Integration and automation of a micro-tissue and microsphere based tissue engineering system and its application in cartilage regeneration and cancer models

Naveen Vijayan Mekhileri

A thesis submitted for the degree of Doctor of Philosophy

University of Otago, Christchurch, New Zealand

December 2016

Abstract

Bottom-up biofabrication approaches for fabricating engineered tissue constructs are emerging strategies in tissue engineering. Few technologies have been developed that are capable of assembling tissue units into 3D Plotted scaffolds. We developed an integrated and automated 3D Bioassembly system for bioassembling engineered tissue constructs. The developed automated bioassembly system consisted of a (i) singularisation module and (ii) an injection module integrated into a commercial 3D bioprinter. The fluidic-based singularisation module delivered single Ø1 mm sized tissue unit at a time to the injection module and the injection module together with the 3D positioning system of the 3D bioprinter delivered the tissue unit into a predefined pore in the 3D Plotted scaffold. The developed automated bioassembly system was capable of either fabricating a construct via a two-step top-down bioassembly approach (fabricating a complete scaffold and insertion of tissue units) or a multistep bottom-up bioassembly approach (alternative layer-by-layer scaffold fabrication and tissue unit co-assembly). The automated bioassembly system was validated for application in cartilage and tumour engineering using tissue units (microspheres and micro-tissues). For cartilage engineering, Ø1 mm sized cartilage micro-tissues were fabricated utilising a previously demonstrated high-throughput 96-well plate format and Ø1 mm sized chondrocytes or chondroprogenitor cells-laden GelMA (gelatin-methacryloyl)-HepMA (methacrylated heparin) (9.5%-0.5%) hydrogel microspheres were fabricated utilising an adopted microfluidic system. For tumour engineering, a co-culture of cancer cells with fibroblasts using a liquid overlay technique was required to fabricate compact spherical Ø1 mm micro-tissues that could be handled by the automated bioassembly system and cancer cell-laden 10% GelMA hydrogel microspheres were fabricated utilising the adopted microfluidic system. Reliable handling of the tissue units was demonstrated by the automated bioassembly system. Bottom-up bioassembly of tissue units into 3D Plotted PEGT/PBT polymer scaffolds was demonstrated with the automated bioassembly system. No difference in viability was observed between the constructs assembled manually and with the automated bioassembly system. The flexibility of the automated tissue bioassembly system was shown by assembling constructs with coloured microspheres (denoting microspheres of different types) in various desired arrangements. The automated bioassembly of an anatomically shaped

construct was also demonstrated. Neocartilage formation was observed in the chondrocyte-laden individual microspheres and assembled constructs when cultured *in vitro* for 35 days. Neocartilage formation was also visualised in the assembled graduated constructs fabricated with human articular chondrocytes (HAC) and mesenchymal stromal cells (MSC). In the *in vitro* micro-tissue tumour model, individual micro-tissues had higher chemoresistance compared to cells in 2D and the co-culture assembled construct had higher chemoresistance compared to individual co-culture micro-tissues. Similarly, in the *in vitro* microsphere tumour model, the assembled constructs were the most chemoresistant followed by individual microspheres and the cell in 2D had the lowest chemoresistance. The novel and flexible automated bioassembly technology that we have developed provides a pathway for fabricating a larger number of anatomically shaped clinically relevant constructs with precise control of the spatial position of the tissues units for application in cartilage engineering and for fabricating *in vitro* cancer models for application for drug discovery and high-throughput screening.

Acknowledgements

I would like to thank my Mother and Father, for the endless support and encouragement and to whom I feel forever obliged for everything they have ever done for me. My lovely brother and cousins – Sharath, Roshni and Suraj.

Thank you to my supervisor, Tim Woodfield for his guidance, and encouragement. I would also like to thank my co-supervisors Khoon Lim for his suggestions, advice, and coffee walks and Kenny Chitcholtan for his advice and scientific input. I would like to thank Julian Murphy and Elisabeth Phillips for their suggestions. Bett Gedye for being super-efficient with the purchase orders.

The CReATErs and the ex-CReATErs for their help and support. Summer students Ben Jar and Jeremy Nicholls. Gabriella Brown for the loony fun times. Isha Mutreja for all the help, support and good times. Jonathon Parrish for the rendered images. All the other people from the MCRG, LCRP, GSFL and the Free radical research group.

I would like to acknowledge funding support from the Royal Society of New Zealand Rutherford Discovery Fellowship, AO Foundation, and the University of Otago PhD scholarship.

I would like to thank my friends at home who I have been awful at keeping in touch with. Roshan Cariappa for being my partner in crime. Nishita D'Souza, for always taking the time to remember me! My friends in Christchurch Noel Guilfoyle, Eva Starostka, Antonio Morote, Maud Martinage, and Lydia Harris who I have a lifetime of stories to share and talk about. Abishek Muralidhar, Stefanie Sperling and Malte Duchow for the little adventures. Lastly, thanks to everyone who helped me in making this thesis a reality.

List of Publications

Journal Publications

The novel work from this thesis has contributed to the manuscripts currently being prepared or is in the process of being submitted to a journal for publication and are listed below.

1. **Mekhileri, N.V.,** K.S. Lim, I. Mutreja, B.S. Schon, G.J. Hooper, and T.B.F. Woodfield, *Integrated system for automated 3D Bioassembly of micro-tissues for biofabrication of hybrid tissue engineered constructs.* Biofabrication. (in submission).

2. **Mekhileri, N.V.,** I. Mutreja, K.S. Lim, G.J. Hooper, and T.B.F. Woodfield, *Automated 3D Bioassembly of micro-tissues for biofabrication of an in vitro 3D cancer model and its evaluation compared to existing 2D and 3D drug screening models*. (in preparation).

3. **Mekhileri, N.V.,** I. Mutreja, K.S. Lim, G.J. Hooper, and T.B.F. Woodfield, *Fabrication and evaluation of physiologically relevant in vitro 3D cancer models using automated 3D Bioassembly of cell-laden microspheres.* (in preparation).

The following journal article has been published from work performed during the course of the PhD thesis but the work has not contributed to the thesis itself.

1. Lim K.S., B.S. Schon, **N.V. Mekhileri,** G.C.J. Brown, C.M. Chia, S. Prabakar, G.J. Hooper, and T.B.F. Woodfield, *New Visible-Light Photoinitiating System for Improved Print Fidelity in Gelatin-Based Bioinks.* ACS Biomaterials Science & Engineering, 2016. **2**(10), 1752-1762

Conference Proceedings

1. **Mekhileri, N.V.,** B.S. Schon, K.S. Lim, I. Mutreja, G.J. Hooper, and T.B.F. Woodfield, *Bioassembly of complex multicellular tissues: an automated 3D microtissue assembly system for tissue-engineering and high throughput screening*. Stem Cell and Regenerative Medicine Symposium. Queenstown Research Week Conference. 2016. Nelson, New Zealand. Poster.

2. Lim K.S., B.S. Schon, **N.V. Mekhileri,** G.J. Hooper, and T.B.F. Woodfield, *3D Bioprinting of Gelatin Constructs with Enhanced Shape Fidelity and Cell Viability via*

Visible Light Photo-Polymerisation. International Conference on Biofabrication. 2016. Wake-Forest, USA. Oral.

3. Lim K.S., G.C.J. Brown, **N.V. Mekhileri,** B.S. Schon, G.J. Hooper, and T.B.F. Woodfield, *The Effect of Oxygen Inhibition in Biofabrication of Photocrosslinked Hydrogels. Proceedings Tissue Engineering and Regenerative Medicine*. International Conference on Biofabrication. 2015. Boston USA. TISSUE ENGINEERING PART A; 21: S32-S32.

4. **Mekhileri, N.V.,** B.S. Schon, K.S. Lim, G.J. Hooper, and T.B.F. Woodfield, *Biofabrication of tissue engineered cartilage constructs via an automated 3D micro-tissue assembly system*. International Conference on Biofabrication. 2015. Utrecht, Netherlands. Oral.

5. Lim K.S., G.C.J. Brown, **N.V. Mekhileri,** B.S. Schon, S. Prabakar, G.J. Hooper, and T.B.F. Woodfield, *Finding the balance between oxygen inhibition and cell viability in biofabrication of photopolymerised hydrogels*. International Conference on Biofabrication. 2015. Utrecht, Netherlands. Oral.

6. **Mekhileri, N.V.,** T.B.F. Woodfield, B.S. Schon, and G.J. Hooper, *A Biofabrication System for 3D Assembly of Micro-tissues for Cartilage Regeneration.* 21st Annual Conference of the Australian and New Zealand Orthopaedic Research Society. 2015. Auckland, New Zealand. Oral.

7. **Mekhileri, N.V.,** T.B.F. Woodfield, M. Lang, B.S. Schon, and G.J. Hooper, *Integrated System for Automated 3D Assembly of Micro-tissues for Cartilage Regeneration.* 24th Annual Conference of the Australasian Society for Biomaterials and Tissue Engineering. 2015. Sydney, Australia. Oral.

8. **Mekhileri, N.V.,** T.B.F. Woodfield, V. Nock, and G.J. Hooper, *An integrated system for automated 3D Assembly of micro-tissues for cartilage regeneration*. MacDiarmid Institute: Theme 4 meeting. 2014. Auckland, New Zealand. Oral.

9. Jar, B., **N. V. Mekhileri,** M. Lang, G.J. Hooper, and T.B.F. Woodfield, *Automated 3D Assembly of micro-tissues for cartilage regeneration*. MedTec in Christchurch. 2014. Christchurch, New Zealand. Poster. *Won the best poster award.*

10. **Mekhileri, N.V.,** M. Lang, G.J. Hooper, and T.B.F. Woodfield, *Integrated system for automated 3D Assembly of micro-tissues for cartilage regeneration*. Otago Health Sciences Research forum. 2014. Dunedin, New Zealand. Poster.

11. **Mekhileri, N.V.,** M. Lang, G.J. Hooper, and T.B.F. Woodfield, *Automated 3D Assembly of micro-tissues for cartilage regeneration*. Recycled poster Expo (Health Research Society of Canterbury). 2014. Christchurch, New Zealand. Poster. *Won the best poster award.*

Table of contents

List of Figures

List of Tables

Chapter 1 Introduction

1.1 Introduction

From time immemorial, humankind has been on a quest to cure the ailments that plague both the body and mind. From the first description of skin grafting in 300 BC to the development of the first tissue-engineered skin constructs in the early 1980s, progress in medical research has come a long way [1, 2]. There is a desperate need for transplantable tissues and organs and millions of people could benefit from laboratory-grown autologous tissues or organs that are ready to be transplanted. The ability to create artificial tissues would also be highly beneficial for the progress of medical research and discovery.

Tissue engineering is a very self-explanatory term where the fundamental intention is to engineer tissues to restore, maintain, or enhance tissue function [3]. Unlike other solutions such as drug based therapies, tissue engineering hopes to provide a permanent solution to organ and tissue failure [4]. However, there are a lot of technical challenges and barriers associated with manufacturing an artificial tissue [4]. Apart from the raw materials required to manufacture the laboratory-grown off-the-shelf tissue such as cells, growth factors and biodegradable 3D scaffold, there is a need for state-of-art technologies to manufacturing the tissue [3-6].

Although there exist various bioassembly and biofabrication techniques to fabricate a tissue construct, as far as we are aware of, there exists no technological platform that can assemble tissue subunits together into a 3D plotted scaffold with the intention of creating a larger organised tissue construct. In this thesis, the primary objective was to develop and validate a bioassembly technology, with special emphasis on cartilage tissue engineering and on 3D cancer models for drug discovery and high-throughput screening.

1.2 Thesis objectives and chapter outline

The focus of this thesis was to develop a novel automated bioassembly system capable of fabricating tissue constructs. The overall objectives of the thesis were to:

I. Design, develop and validate an automated tissue bioassembly system.
II. Validate the system for application in cartilage tissue engineering.
III. Validate the system for fabricating a proof-of-concept 3D cancer model and to characterise the model.

The general outline of the chapters in the thesis is as described below.

The literature regarding fabrication approaches in tissue engineering, cartilage engineering, cancer models and the need for an automated 3D Bioassembly system was reviewed in Chapter 2. The specific aims of this thesis are described at the end of Chapter 2.

Chapter 3 focuses essentially on the development of the integrated and automated 3D Bioassembly system. The aim of this chapter was to describe in detail the design and development of the prototype automated bioassembly system. A complete description of the architecture of the mechanical and electronic systems was explained here.

Chapter 4 reports the validation of the developed integrated automated bioassembly system for application in cartilage tissue engineering with micro-tissues (i.e. spherical aggregates consisting of only cells). The aim of this chapter was to demonstrate and validate the automated bioassembly of cartilage micro-tissues without adversely affecting the living micro-tissues.

Chapter 5 presents the work on bioassembly of microspheres fabricated utilising a micro-fluidic system for application in cartilage tissue engineering. The aim of this chapter was to fabricate cell-laden hydrogel microspheres (i.e. spherical hydrogel bead with encapsulated cells) for application in cartilage engineering, validation of the microspheres with the bioassembly system, demonstrate the flexibility of the bioassembly system and demonstrate cartilage tissue formation in the bioassembled microspheres.

Chapter 6 presents the work on biofabrication of a proof-of-concept *in vitro* 3D cancer model with micro-tissues. The aim of this chapter was to develop, validate and characterise a micro-tissue based *in vitro* 3D cancer model that can be assembled with the bioassembly system.

Chapter 7 reports the work on biofabrication of a proof-of-concept *in vitro* 3D cancer model with microspheres. The aim of this chapter was to develop, validate and characterise a cancer cell-laden microsphere based *in vitro* 3D cancer model that can be assembled with the bioassembly system.

Finally, Chapter 8 presents the conclusions drawn from the thesis and makes recommendations for future work

Chapters 4 and 5 primarily focus on cartilage engineering and Chapters 6 and 7 focus on *in vitro* cancer models. Chapters 4 and 6 are based on micro-tissues (spherical aggregates consisting of only cells, see note below) as the modular tissue unit for bioassembly, whereas Chapters 5 and 7 are based on cell-laden hydrogel microspheres (spherical hydrogel bead with encapsulated cells) as the modular tissue unit for bioassembly.

Please note: aggregates of tumour cells, which is usually referred to as tumour spheroids in the literature has been referred to as micro-tissues in this thesis to keep it consistent with the nomenclature used for chondrocyte micro-tissues and to prevent confusion.

1.3 References

1. Berthiaume F, Maguire TJ, Yarmush ML. Tissue engineering and regenerative medicine: history, progress, and challenges. Annual review of chemical and biomolecular engineering. 2011;2:403-430.
2. O'Connor N, Mulliken J, Banks-Schlegel S, Kehinde O, Green H. Grafting of burns with cultured epithelium prepared from autologous epidermal cells. The Lancet. 1981;317(8211):75-78.
3. Langer R, Vacanti J. Tissue engineering. Science. 1993;260(5110):920-926.
4. Griffith LG, Naughton G. Tissue engineering-current challenges and expanding opportunities. Science. 2002;295(5557):1009-1014.
5. Woodfield TB, Malda J, de Wijn J, Peters F, Riesle J, van Blitterswijk CA. Design of porous scaffolds for cartilage tissue engineering using a three-dimensional fiber-deposition technique. Biomaterials. 2004;25(18):4149-61.
6. Malda J, Visser J, Melchels FP, Jüngst T, Hennink WE, Dhert WJ, Groll J, Hutmacher DW. 25th anniversary article: engineering hydrogels for biofabrication. Advanced Materials. 2013;25(36):5011-5028.

Chapter 2 Literature review

2.1 Introduction

The progress of modern medicine has been highly intertwined with science and technology and the advancement in medical research has led to the extraordinary capacity of being able to engineer artificial tissues in the laboratory. The primary goal of engineering a tissue is to provide a permanent solution to tissue and organ failure [1, 2]. However, the application of engineered tissues is not only being confined to restoring, maintaining, or enhancing tissue functions but is being investigated for application in other avenues such as 3D *in vitro* tissue models for studying disease or high-throughput drug screening e.g. cancer research [1, 2]. Engineering an artificial tissue is a highly complex process and not only requires the raw materials such as cells, growth factors and biodegradable 3D scaffold but also requires cutting-edge technologies to biomanufacture the synthetic tissue [1-4]. Presently a spectrum of futuristic technologies exist to manufacture an artificial tissue, but to our knowledge, we are not aware of a technological platform that can assemble tissue subunits together into a 3D plotted scaffold with the intention of creating a larger engineered tissue. In this thesis, the primary objective was to develop and validate a bioassembly technology platform, with special emphasis on application in cartilage tissue engineering for joint resurfacing and in tumour engineering for drug discovery.

2.2 Tissue engineering and regenerative medicine

Tissue engineering is a relatively young field in health science that aims at the repair and restoration of damaged or degenerated tissue and organs [4, 5]. It is a complex and multidisciplinary area that applies the principle of engineering, physical sciences and medicine to create *ex vivo* tissues and organs substitutes functionally analogous to natural tissue [1]. The typical tissue engineering paradigm involves in isolating the required cells or the substitute cell type with the possible *in vitro* expansion of the cells, seeding the cells with growth factors within a biodegradable 3D scaffold or into a tissue inducing substrate *in vitro*, and then

implanting the artificially engineered construct into the target site [1, 3, 4]. See Figure 2-1 for various tissue engineering strategies for organ development.

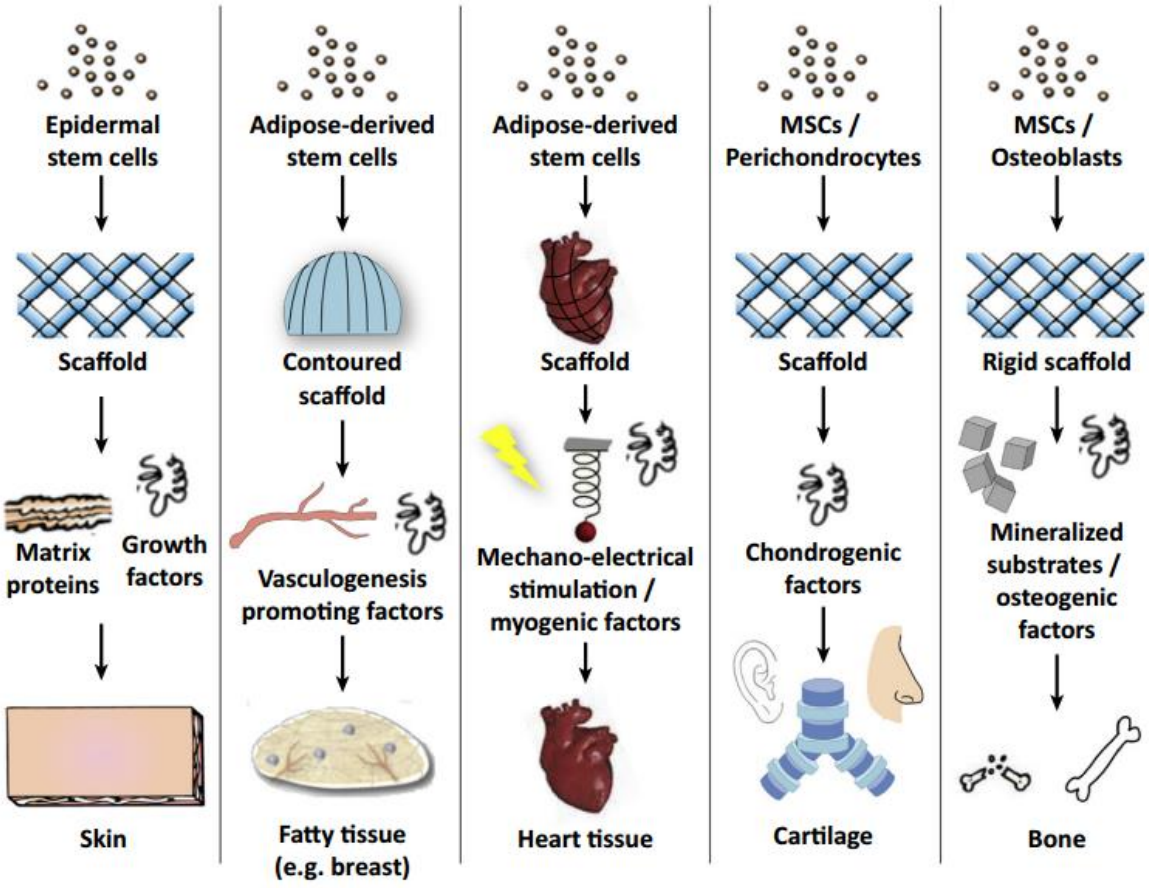

Figure 2-1. Tissue engineering strategies for organ development. Reproduced from Gholipourmalekabadi *et al.* [6].

Regenerative medicine, on the other hand, aims at the repair and restoration of damaged or degenerated tissues and organs by regenerating the part *in vivo* or *ex vivo*. This might require a combination of cells, natural or artificial scaffolding, growth factors, gene manipulation [7-9]. Although the terms "tissue engineering" and "regenerative medicine" have often been used interchangeably and are related with similar objectives, regenerative medicine is oriented more toward the cellular aspect of tissue replacement and tissue engineering is more focused on the engineering and manufacturing aspects of tissue replacement [10]. Tissue engineering can be considered as a partial subset of regenerative medicine [7]. To sum up, the primary aim of both tissue engineering and regenerative medicine is to restore the function of a pathological or damaged tissue or organ [1].

2.3 Cartilage engineering

2.3.1 Structure and function of articular cartilage

Articular cartilage is a load-bearing viscoelastic tissue at the ends of a bone that provides a smooth, low friction and lubricated surface for movement [11]. It is an avascular, aneural and alymphatic tissue consisting of chondrocytes and extracellular matrix (ECM) [11]. The extracellular matrix is synthesised, maintained, and secreted by the chondrocytes and consists of water, dissolved salts, collagen, hyaluronan and proteoglycan, and in lesser quantities non-collagenous proteins and glycoproteins [12, 13]. Collagen is the most abundant structural and load-bearing macromolecule in the extracellular matrix and collagen II is the most abundant type of collagen fibrils. Other types of collagen such as collagen type V, VI, IX, X, XI, XII and XIV are found in lower quantities [13, 14]. Proteoglycans are the second most abundant structural and load-bearing macromolecule in the extracellular matrix after collagen. Articular cartilage is composed of a variety of proteoglycans such as aggrecan, decorin, biglycan, and fibromodulin, and aggrecan is the most abundant proteoglycan by weight [13, 15]. The proteoglycan aggregates are entrapped in the fibrils formed by collagen interaction [14]. This composition of articular cartilage with negatively charged proteoglycans aids retention of water in the extracellular matrix and gives cartilage its mechanical properties [12, 13]. The hydrophilic nature of the proteoglycans aids retention of water and creates a swelling pressure which is balanced by the tensile strength of the collagen matrix at equilibrium. During compression, the interstitial fluid pressure in the cartilage opposes the compressive load and dampens the mechanical impulse [16]. On removal of the compressive load, the interstitial fluid is absorbed back into the cartilage and the cartilage reverts to its original structure. This circulation pattern between the synovial fluid and the tissue is essential for waste and nutrient exchange [17].

Cartilage has a highly organised structure and can histologically be divided into 4 different zones - the superficial zone, the middle zone, the deep zone, and the calcified zone [18]. See Figure 2-2 for an illustration of articular cartilage. The superficial zone makes up the articulating surface and protects the deep layers from shear stress [18]. Unlike the other layers, the superficial layer consists of chondrocytes that have a more elongated and fibroblast-like morphology [13, 18].

This layer consists of a relatively higher quantity of collagen type I and lesser proteoglycan. The collagen fibres of this layer are packed tightly and are aligned parallel to the surface, thereby resisting the tensile forces generated by friction between joints [19]. The middle zone is in between the deep and superficial zone. In this layer, the chondrocytes are more spread out with a lower population density and have a more rounded morphology compared to ones in the superficial layer. The collagen fibres of this layer are arranged obliquely. The deep zone consists of collagen fibres that are parallel to the articular surface. The chondrocytes are arranged in a column fashion. This layer provides the highest resistance to a compressive load. The calcified cartilage is distinguished from the deep zone by a tide mark. The calcified cartilage aids in securing the cartilage to the bone [13].

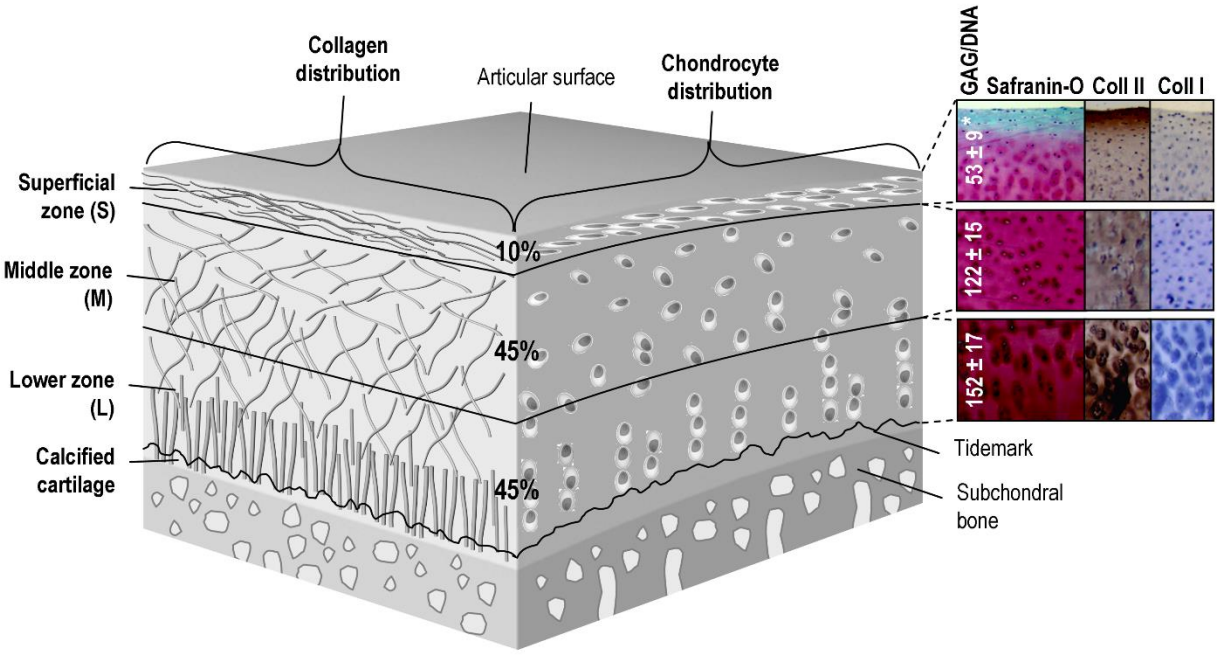

Figure 2-2. Illustration of articular cartilage showing the distribution and orientation of collagen fibres (left) and chondrocytes (right) within the superficial, middle and deep zone. The GAG/DNA content, safranin O staining for GAG, immunohistochemistry for collagen type II and type I for bovine articular cartilage is shown in the box on the right. Reproduced from Woodfield *et al.* [20].

2.3.2 Damage and repair strategies

Due to the avascular nature and low chondrocyte density, cartilage has a limited capacity for repair. Injury to articular cartilage can cause morbidity in young and old patients [13, 14]. Damage to articular cartilage can either be superficial

(Figure 2-3 a) which is a partial thickness defect or can extend till the subchondral plate which is an osteochondral or full-thickness defect (Figure 2-3 b and Figure 2-4) [14]. Superficial defects fail to heal spontaneously and osteochondral defects elicit tissue repair response which produces a mechanically inferior fibrocartilage instead of hyaline cartilage tissue which leads to the accelerated deterioration of the joint [21].

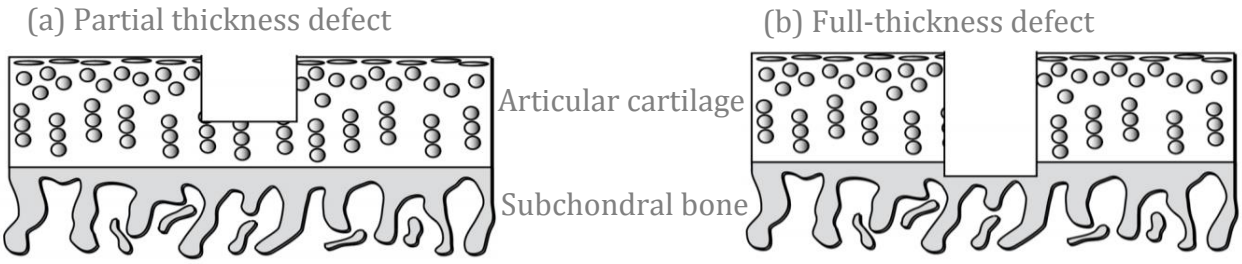

Figure 2-3. Illustration of (a) a superficial partial thickness defect and (b) a full-thickness defect that extends into the subchondral bone in articular cartilage. Reproduced from Redman *et al.* [21].

Figure 2-4. Arthroscopic image of a 20 x 30 mm full-thickness cartilage defect to the medial femoral condyle. Reproduced from Kuroda *et al.* [22].

Many repair strategies have been developed in an attempt to treat articular cartilage defects with the end goal of being able to reduce the patient's symptoms and restore the function of the joint [14]. Studies have suggested that arthroscopic repair procedures such debridement (removal of damaged or calcified tissue) and lavage (irrigation of the joint) do not induce cartilage repair and the results are comparable to placebo [21, 23]. With the microfracture technique (debridement of

damaged tissue down to the subchondral bone), the clinical long-term outcome has been reported to be varied due to the variable nature of the fibrous repair tissue [21, 24]. Clinical results have shown that osteotomy which is the realignment of the articulating surface deteriorates with time, causing recurrent pain and progressive osteoarthritis [25, 26]. With soft tissue grafts where perichondrial/periosteal grafts are placed in the defect, studies have shown better outcomes in young patients and poorer outcomes in older patients [27, 28]. Osteochondral transplantation (Figure 2-5) or mosaicplasty, on the other hand, showed donor site morbidity and the resulting cartilage was more fibrous [29, 30].

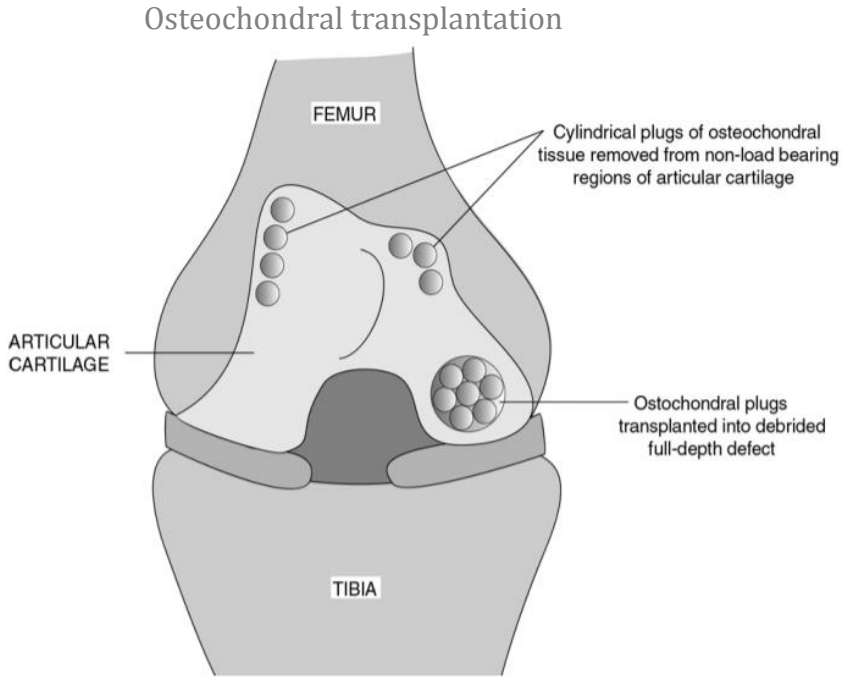

Figure 2-5. Illustration of osteochondral transplantation. Reproduced from Redman *et al.* [21].

Total/partial arthroplasty is the resurfacing of the articulating surface with metal and plastic components and is one of the most common procedures. However the drawback is the requirement of extensive surgery and as it functionally lasts only for about 10-15 years it is limited to older patients [31, 32]. Autologous chondrocyte implantation (ACI), which is a cell-based therapy has shown better outcome compared to other surgical outcomes. The ACI process (Figure 2-6) involves harvesting a healthy biopsy from a non-load bearing region, extracting chondrocytes from the biopsy, expanding the chondrocytes, and injecting the cultured autologous

chondrocytes under a periosteal flap [33]. Considerable cost of the procedure, highly invasive nature of the surgery, donor site morbidity, long rehabilitation time, and limited success in patellar defects are the disadvantages associated with ACI [21]. The matrix-assisted chondrocyte implantation (MACI) is a similar technique to ACI, where cells are immobilised within a collagen-based matrix and the matrix is then implanted into the defect. The use of periosteal flap as in ACI is omitted. However, a two-year study showed no advantage of MACI over ACI [34, 35].

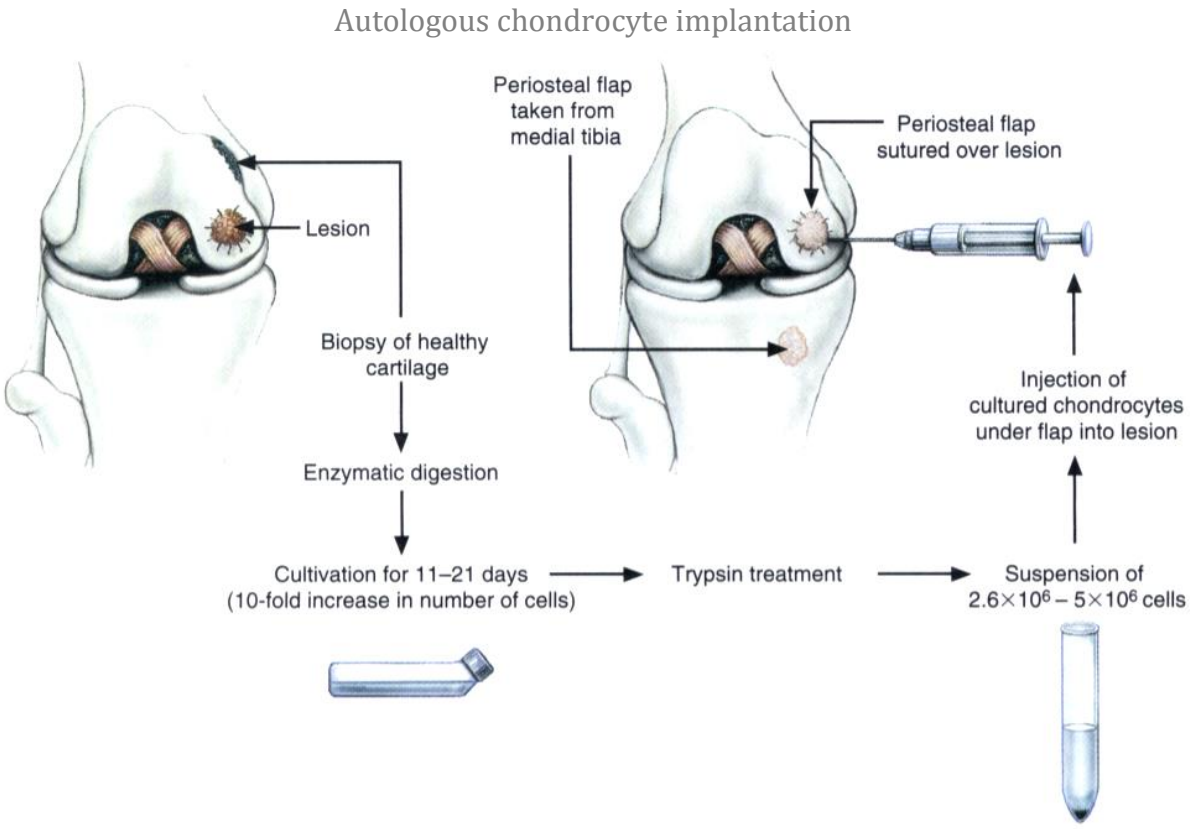

Figure 2-6. Illustration of the autologous chondrocyte implantation (ACI). Reproduced from Brittberg *et al*. [36].

Although some of the above-described procedures are effective in providing symptomatic relief and improved joint function in certain circumstances, there is a need for a strategy with good long-term outcomes. A strategy that can cater to a range of population and lifestyles and tissue engineering and regenerative medicine is one of the areas being looked into.

2.3.3 Tissue engineering and regenerative approaches in cartilage engineering

Cartilage engineering aims at fabricating replacement scaffolds or constructs that have a similar structure, composition and mechanical properties to the native tissue to restore the function of a joint [37]. Although current tissue engineering and regenerative medicine strategies such as ACI and MACI have shown better outcomes compared to other surgical repair strategies, the implanted tissues lack the mechanical properties and organisation of native cartilage and other approaches are being looked into [33-35, 37].

Typically, tissue engineering strategies for cartilage repair adopt either a scaffold only or a scaffold with cell strategy. In repair strategies utilising only scaffolds by themselves, the scaffold material and geometry is designed so that the host progenitor cells would infiltrate into the absorbable scaffold placed in the defect and induce neocartilage formation [38]. For the scaffold with cell strategy, the tissue engineering paradigm for engineering a cartilage involves culturing chondrocytes or chondroprogenitor cells along with chondrogenesis inducing growth factors within a biodegradable 3D scaffold *in vitro* and then implanting the engineered construct into the target site *in vivo* [3]. The fabricated scaffolds for cartilage engineering can either be a single-phase scaffold – which is a scaffold containing a single or several materials but is uniform through or a biphasic or multiphasic scaffold – which is a scaffold where two different materials are used, one for the cartilage phase and the other for the subchondral bone or bone phase [39].

During the expansion of chondrocytes on a 2D surface, chondrocytes undergo dedifferentiation, change from a rounded to fibroblastic morphology, and the ratio of collagen type II to I production decreases [40]. The *in vitro* culture of chondrocytes in a 3D environment guides chondrocytes to redifferentiate, have a more rounded morphology, and produce cartilage extracellular matrix such as collagen type II, GAG and aggrecan [41]. There are two main strategies by which we cultured chondrocytes or chondroprogenitor cells in a 3D environment in this thesis – a micro-mass or pellet culture to fabricate micro-tissues, and the encapsulation of cells in a hydrogel [42]. In a micro-mass or pellet culture, the condensed cellular environment typical during the developmental stages of cartilage growth is

replicated, and this induces the production of hyaline-like neocartilage [42]. In a cell encapsulated hydrogel, the hydrogel provides a hydrated environment, aids the cells in maintaining a rounded morphology, imitates the features of native cartilage and can promote or direct a chondrogenic phenotype [43, 44].

2.3.4 Challenges in cartilage engineering

Presently significant research is ongoing in the area of cartilage repair and there exist numerous challenges in engineering a cartilage. This includes the source of cells, quality of ECM production in the engineered construct, optimal scaffold design, fabricating constructs with similar mechanical properties to native cartilage, recapturing the native microarchitecture, and the automated biofabrication of large complex and constructs [39, 45].

One of the biggest challenges in cartilage engineering is obtaining the required number of cells to fabricate cartilage constructs of clinically relevant size. As the number of chondrocytes that can be isolated from a biopsy is limited, obtaining a large number of cells would require cell expansion. Chondrocytes have a limited proliferative potential and when autologous cells are cultured in 2D, they dedifferentiate and lose their chondrogenic phenotype [40]. Chondrocytes isolated from articular cartilage is the most commonly used cell source in cartilage engineering. Apart articular cartilage, chondrocytes can be isolated from the nasal septum [46]. The use of nasal chondrocytes can be advantageous as nasal septum biopsies can be isolated more easily than articular cartilage biopsies. Nasal chondrocytes have been shown to have a faster proliferation rate and increased chondrogenic capacity compared to articular chondrocytes, and the quality of engineered cartilage from nasal chondrocytes does not seem to depend on the age of the donor, contrary to articular chondrocytes [46-49]. Mesenchymal stromal cells (MSCs) can also be a considered as an alternative source for cartilage engineering as they can be easily isolated, expanded and differentiated into chondrocytes [50]. However, MSCs derived from bone-marrow have a disadvantage in that they have a tendency to undergo hypertrophy and calcification [51].

Designing an optimum scaffold is a challenge for cartilage engineering. The substrate used for the fabricating the 3D cartilage construct could affect the quality

of the tissue in many ways [52]. The scaffold should have a controllable degradation rate, promote cell viability, differentiation and ECM production, should integrate with the surrounding native *in vivo* cartilage, and provide the required mechanical properties for the construct [45]. A wide range of materials have been investigated for scaffold material, including alginate [53], agarose [54], collagen [55], fibrin [56], poly(ethylene glycol) (PEG) [57], poly(ethylene oxide) (PEO)[58] and poly(vinyl alcohol) (PVA) [59] and poly-lactic-glycolic acid (PLGA) [60].

One of the emerging strategies in cartilage engineering is to assemble cartilage micro-tissues into a 3D plotted scaffold (described later). Utilising micro-mass or pellet culture, hyaline-like neocartilage micro-tissues can be fabricated [42]. However, manually assembling a construct of a clinically relevant size (i.e. Ø25 x 2.4 mm) would be extremely tedious in a clinical environment [42, 61, 62]. Moreover, there is a need to be able to fabricate anatomical constructs of complex architecture. The ability to assemble constructs with complex architecture would mean that the fabrication of an osteochondral construct with the zonal arrangement of native articular cartilage, and constructs with a gradient of cell types, bioactive molecules, mechanical properties, hydrogel types or varying cell densities, could potentially be possible [44, 61, 63-67].

2.4 Tumour engineering

2.4.1 Cancer and cancer microenvironment

With 14.1 million new cases in 2012 and with the number of new cases per annum expected to reach over 20 million as early as 2025, cancer is a major cause of morbidity and mortality thereby making research in cancer highly critical [68, 69]. Cancers are generally classified based on the normal cells that they originate from [70]. The commonly diagnosed cancers in 2012 were lung, colorectal and stomach [68, 69]. The most common cause of cancer mortality in 2012 were lung, liver and stomach cancers [69]. Cancer is a group of diseases that can affect any part of the body and the hallmark of cancer is the abnormal growth of cells, loss of architecture and function [69, 71]. The development of cancer has been attributed to the progressive accumulation of genomic changes which lead to the loss of tumour suppression function in the cells [72]. These genomic changes can be caused by

physical (i.e. ultraviolet light), chemical (i.e. asbestos, tobacco or arsenic) or biological (i.e. certain viruses, bacteria or parasites) carcinogens [69]. A high body mass index, a diet with a low fruit and vegetable content, lack of physical activity, tobacco use and alcohol use are behavioural and dietary risks that can increase the incidence of cancer [69]. Approximately 80% of all human cancer cells are carcinomas (originate from epithelial cells) [70]. The other 20% include sarcomas (originate from mesenchymal cells), leukaemias (arise from hematopoietic), and lymphomas (originate from the lymphoid) [70].

Tumours *in vivo* are heterogeneous and comprise a complex microenvironment (see Figure 2-7) [73]. In general, tumours primarily consist of tumour cells and the supporting connective tissue (stroma) [70]. The cell types in a tumour are heterotypic and include cancer stem cells (CSC) [74], primary stem cells, fibroblasts [75, 76], cancer-associated fibroblasts (CAFs) [75, 77, 78], endothelial cells [79] and immune cells [76, 80]. Fibroblasts play an important role in cytokine secretion, the deposition of ECM, tumour capsule formation, in the proliferation and metastasis of cancers, and are associated with cancer in all stages of progression [75, 81-83]. Fibroblasts that are activated and are associated with malignant tumours are called cancer-associated fibroblasts and are known to enhance cancer progression [75, 77, 78]. The growth of tumours beyond 1 - 2 mm require vascularisation [70]. Tumours *in vivo* have deficient or abnormal vascularisation and this can cause a gradient in gases, pH, growth factors, nutrients, and drug [84, 85]. The reduction of oxygen in a growing tumour causes the upregulation of hypoxia-inducible factor (HIF1α) and this promotes transcription of angiogenic factors, including vascular endothelial growth factor (VEGF) [86]. The upregulation of VEGF causes the migration of endothelial cells which form new blood vessels that aid in the transportation of nutrients and oxygen that helps in the proliferation of cancer cells [86]. The presence of immune cells in the tumour also aids neovascularisation by synthesising pro-angiogenesis factors at specific locations [86, 87]. The association of cancer cells and immune cells has been known for a long time [80]. As immune cells produce cytokines, chemokines, pro-angiogenic mediators, metalloproteinases, reactive oxygen species, histamine and other bioactive molecules, the immune cells that infiltrate the tumour play a crucial role in the inhibition and progression of cancer cells [80]. Immune cells inhibit tumour cells by antitumour cytotoxic T-cell

activity and cytokine-mediated lysis of tumour cells [80]. Immune cells promote tumour growth via regulatory T cells that suppress antitumour T-cell response and by the increase in chronic inflammation in the tumour microenvironment caused by the humoral immune responses [80].

Genetic heterogeneities in cancer cells and variation in physical properties (i.e. presence of physical borders) in a tumour microenvironment can result in the formation of a range of biological and phenotypical zones within the tumour [73, 88, 89]. As mentioned earlier, deficient or abnormal vascularisation in tumours can cause a gradient in gases, pH, growth factors, nutrients and drugs, which cause the cells to adopt different metabolic strategies resulting in the formation of biological and phenotypical zones [84, 85]. Likewise, due to extensive ECM deposition, physical borders such as fibrotic areas and tumour capsules are formed in most benign solid tumours dividing the tumour into different zones [73]. These undisrupted physical borders can also inhibit tumour invasiveness and can act as a barrier for anticancer drugs [73, 90, 91].

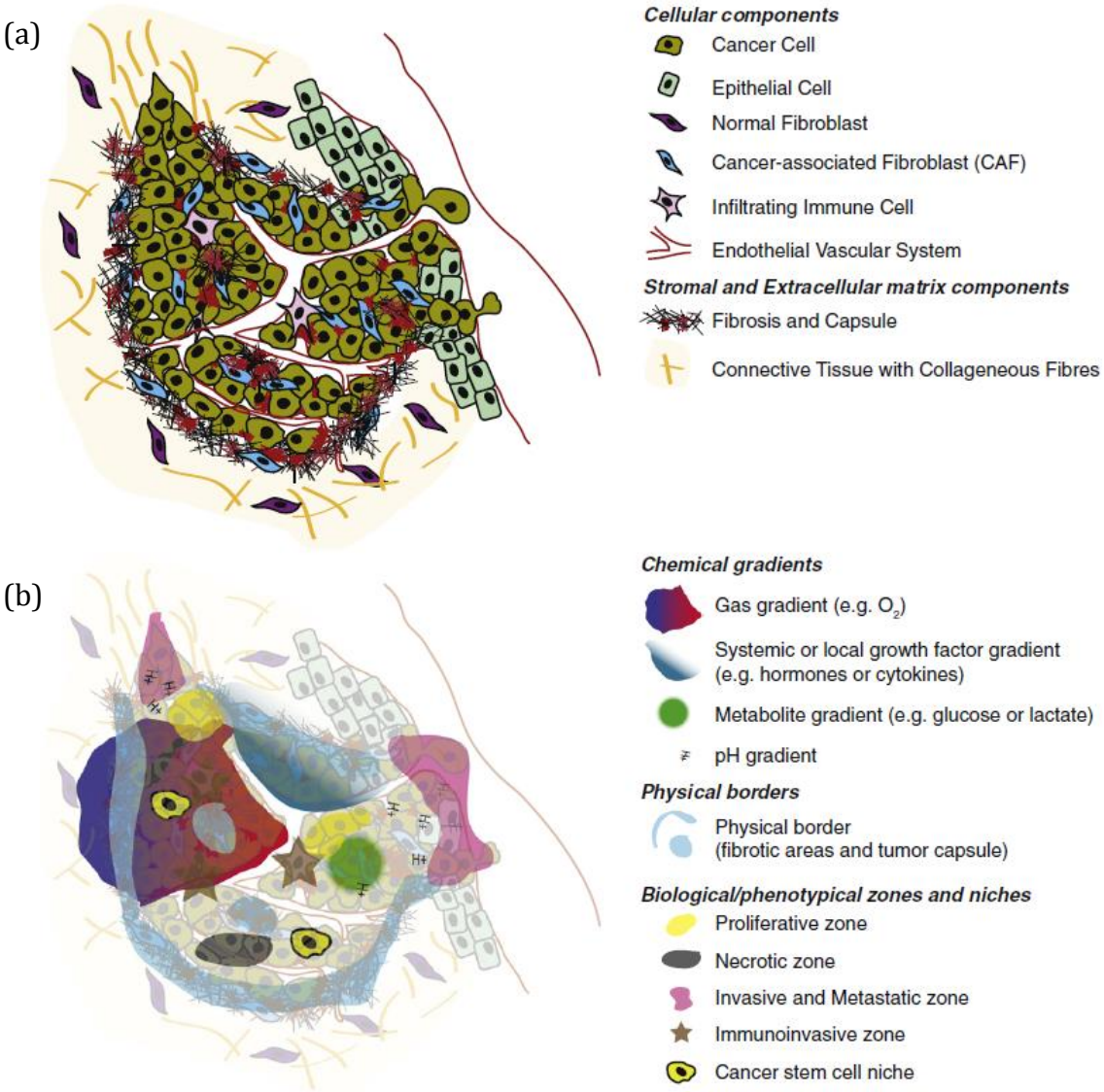

Figure 2-7. Illustration of tumour microenvironment showing (a) the cellular components together with the stromal and extracellular components, and (b) the chemical gradients, physical borders and the biological/phenotypical zones and niches. Reproduced from Thoma *et al*. [73].

2.4.2 Cancer drug development

Treatments for cancer can include a combination of surgery, radiotherapy or chemotherapy [69]. There is a need for better treatment strategies including new anticancer drugs [92]. The use of chemotherapy began at the start of the 20th century and has become standard clinical practice [93]. Clinically used drugs fail either because they do not work or because they are not safe and there is a search for safer and more effective drugs [94]. Drug discovery aims at the development of anticancer drugs that have an improved efficacy and higher selectivity between normal and

cancer cells [95]. The main steps involved in drug discovery are: (i) identification and validation of a target – a target could include proteins, genes or RNA and the structure on which the candidate drug would act on, (ii) hit identification – a hit is identified as a compound which shows the desired activity, hit-to-lead phase – to refine each hit series to try to produce more potent and selective compounds, and (iii) lead optimisation phase – where the properties favourable in the lead compounds are maintained and deficiencies in the lead compound are addressed [94].

The cost of developing a new drug has been estimated to be about US $ 2.6 billion out of which US $ 1.4 billion is spent on research [96]. As the cost of drug development increases drastically during animal testing, it is essential to identify poor cancer drug candidates earlier rather than later [97]. A potential drug that presently enters Phase I trials has a probability of only 8% to be approved for clinical treatment [98]. Clinical trials of cancer drugs have been associated with being highly risky and cancer models have an increasingly important role to play before clinical trials on humans are carried out [99-102]. Tumour models, apart from being an invaluable tool in the development and screening of chemotherapeutic agents, would also aid translational research in cancer [103].

Presently, high-throughput screening (HTS) is the most widely applicable technology delivering chemistry entry points for drug discovery programmes [102]. HTS is a process of rapidly testing a large number of chemical compounds against a target to deliver accurate data based on which a decision is made to identify a hit and lead [94, 104]. HTS is an integral part of pharmaceutical research and is currently the most widely applicable technology delivering chemistry entry points for drug discovery [102]. Commonly used anticancer drugs were discovered by random HTS of synthetic and natural compounds [95]. It is imperative that the models used in HTS are capable of predicting the right candidate drugs so that high fall-out rates in the later stages of drug discovery can be reduced. Quite often the development of drugs has been dependent on high-throughput screening in 2D monolayer system for identifying a potential lead compound, because of the deficit in better 3D models [105, 106]. However, 2D monolayer based HTS has a limited

potential for predicting the *in vivo* efficacy of anticancer drugs as 2D models do not recapitulate the native *in vivo* environment [97].

2.4.3 Tumour models

The two tumour model tools that scientists have long depended on to conduct cancer research have been animal models and two-dimensional (2D) monolayer culture systems. The regulatory and legal requirements and strong clinical tradition have made animal models the gold standard in cancer research [97, 107]. However, animal models tend to be expensive, need ethical approval, are complex and contain many multivariable uncontrollable factors like the presence of the host immune response, differences in liver toxicity, differences in telomerase regulation, contain non-human host cells, differences in hemodynamics, and production of endogenous growth factors [103, 107-109]. Even if a new drug has been tested in an animal model there is no assurance that it would be safe in humans.

On the other hand, the simplicity and convenience of traditional 2D monolayer culture systems have made them a favourable *in vitro* model for cancer research [110]. Native tissues are 3D structures, and it is well recognised that 3D models mimic real tissue better than 2D models [110-112]. The behaviour of cells in a 2D monolayer is unlike the behaviour in a 3D *in vivo* environment, where the cells are in an organised 3D structure surrounded by matrix and other cells. Cells cultured as a monolayer lose the tissue-specific architecture, metabolic gradient, cellular differentiation, cell cycle control, mechanical and biochemical cues, three-dimensional cell–cell and cell–matrix interactions [112, 113]. When the cells are cultured in 3D these physiological interactions are more likely to be re-established [112]. The gene expression of cells cultured in 3D is also known to be different from that of cells cultured in 2D [112]. Most importantly, 2D monolayer cultures are less resistant to anticancer drugs compared to their 3D counterparts, resulting in a lower predictive power of the 2D monolayer model to the drug [114, 115]. It has been reported that over 85% of cancer research groups still routinely use 2D culture systems such as tissue-culture plates, Petri dishes or coverslips and the research outcomes might not be significant in an *in vivo* scenario [116]. Figure 2-8 shows microscope images of cells in 2D and a micro-tissue (3D multicellular spheroid).

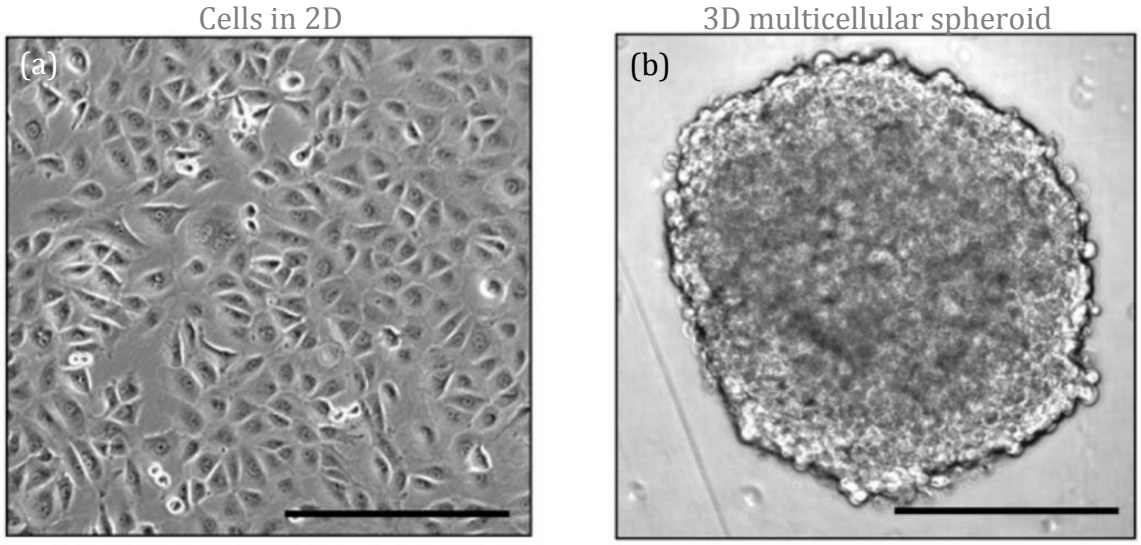

Figure 2-8. Microscope images of human mesotheliomoa cell line (NCI-H226) (a) cells in 2D and (b) 3D multicellular spheroid (micro-tissue). *Scale bar = 400 μm*. Reproduced from Kim *et al.* [117].

Currently, the two major trending and favoured *in vitro* 3D cancer platforms can be broadly divided to include gel systems which involves in embedding cells in gels made of reconstituted basement membrane protein (Matrigel or reconstituted type I collagen) [118, 119] and the use of multicellular spheroids (micro-tissues) (see Figure 2-9) [97, 116].

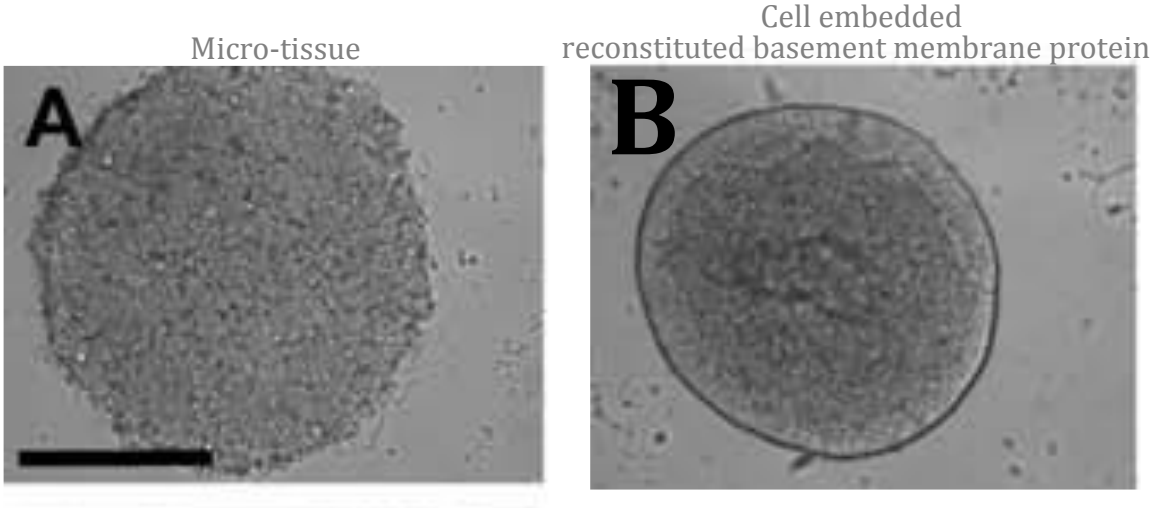

Figure 2-9. Microscope images of renal cancer cell line (HEK 293) (A) micro-tissue (3D multicellular spheroid) and (B) cells embedded reconstituted basement membrane protein. *Scale bar = 500 μm.* Reproduced from Ivascu *et al*. [120].

Micro-tissues are aggregates of cells that can be formed from a broad range of cell types and are the most widely used human tumour model [106]. The size of a micro-tissue varies from 20 μm to 1 mm depending on the cell type, fabricating technique and growth condition [106]. The use of micro-tissues for investigating the action of radiotherapy and chemotherapy drugs has been used since the 1970s [111]. Micro-tissues have been utilised for a wide range of applications including drug screening, research in drug transport and binding, cancer research, tissue morphogenesis, differentiation, tissue engineering, regenerative medicine and stem cell research [121-126].

Hydrogels aid the 3D support of cells *in vitro*, help to recreate the *in vivo* physical and structural environment and can be of natural or synthetic material [110]. Cell-laden hydrogels are advantageous in that 3D models can be fabricated from cell types that do not form micro-tissues [120, 127-129]. Moreover, as micro-tissues only recapitulate certain aspects of the *in vivo* microenvironment alternative hydrogel based substrates are being utilised [106]. The hydrogel themselves can transduce ECM signalling to the cells, but the ECM component can be variable and undefined [106, 110]. The other benefits of hydrogels are that cells can remodel certain hydrogels, cells can be aligned by applying strain to the hydrogel, and the contractions caused by the cells can increase the matrix density [86]. Factors such as the type and composition of the hydrogel and mechanical stiffness are known to affect the cell response [130-133]. Hydrogels can be made from alginate [53], agarose [54], collagen [55], poly(ethylene glycol) (PEG) [57], or poly(vinyl alcohol) (PVA) [59]. Hydrogels are appealing as they can provide a hydrated tissue-like environment and are structurally similar to the native extracellular matrix of many tissues [134, 135]. Other types of hydrogel include basement membrane hydrogels such as Matrigel, Cultrex, or EHS matrix [119].

2.4.4 Challenges in tumour engineering

The idea of engineering tumours for drug discovery and cancer research has gained considerable momentum. Tumour engineering has been defined previously by Ghajar and Bissell *et al.* as "*the construction of complex culture models that recapitulate aspects of the in vivo tumour microenvironment to study the dynamics of tumour development, progression and therapy on multiple scales"* [71]. Many tissue

engineering and regenerative medicine platforms and strategies developed can be easily translated for application in tumour engineering and overlapping challenges exist. The challenges include optimal scaffold design, recapturing the native microarchitecture, and the automated biofabrication of large and complex constructs [86].

Native tumours *in vivo* are complex tissues and consist of different cell types which include cancer stem cells [74], primary stem cells, fibroblasts [75, 76], endothelial [79] and immune cells [76, 80]. The importance of the interactions between cancer cells and non-malignant cells in supporting tumour growth, invasion and metastasis are well known [76]. The presence of non-malignant cells in the *in vitro* model can alter the drug response of the tumour model [76, 136]. Co-culture models would be more representative of models *in vivo* [76]. In tumour biology, most work is done culturing just the tumour cells and the co-culture of more than 3 cell types are rarely reported in the literature [76, 137]. Thus, there is a need for cancer models composed of heterotypic cell types.

Apart from the presence of non-malignant cells, the matrix properties can also affect the behaviour of the cells. The stiffness of the matrix can affect growth rate, viability, resistance to apoptosis, the state of differentiation, motility, alignment and protein expression of the cells [138, 139]. The cell response to a specific hydrogel is known to be cell dependent [140]. The response of the cell is also known to depend on the type of matrix [141, 142]. Therefore, it is essential to choose the right matrix properties to fabricate the desired 3D models.

Tumours *in vivo* are large and have a complex architecture with the average size ranging from 2 to 5 cm in stage II breast cancer [143] to 4.6 to 11.8 cm in ovarian cancer depending on the stage [144]. Cancer micro-tissues are comparatively smaller and the arrangement of cells and the tissue architecture in the gel system and the micro-tissue are less complex than actual tumours that are found *in vivo* [145, 146]. Thus there is a requirement for the ability to fabricate large tumour models of complex architecture comparable to tumours *in vivo* that can be adapted for application in a high-throughput system. The ability to fabricate a cancer construct with an automated system would mean that constructs with a gradient of

cell types, bioactive molecules, mechanical properties, different hydrogel types can potentially be fabricated in a high-throughput fashion [66, 76, 147].

2.5 Tissue engineering fabrication strategies

Tissue engineering fabrication strategies can be divided into top-down and bottom-up strategies.

2.5.1.1 Top-Down tissue engineering fabrication strategy

The top-down approach is a more traditional tissue engineering approach in which cells are seeded into a scaffold and stimulated with bioactive molecules with the intention that they would produce the desired extracellular matrices (Figure 2-10) [148]. Sculpting a statue from stone could be thought of a top-down approach of creating an object. The overall design is created first and then the finer details are added further along. The problem with this approach is the difficulty and challenges in recreating the microstructural features of tissues [148].

2.5.1.2 Bottom-up tissue engineering fabrication strategy or modular tissue assembly

In the bottom-up tissue engineering strategy or modular tissue assembly, smaller nanoscale or microscale functional tissue subunits or modules are assembled to create a macroscale construct with specific microstructural features (Figure 2-10) [148-150]. Using off the shelf parts to assemble a computer can be thought of as an analogy for the bottom-up approach. These modules could potentially be designed to be of different types and could be precisely assembled either by self or direct assembly to create a construct [149, 151]. The challenge with the bottom-up tissue engineering approach is to assemble modules of specific microstructure into a macroscale construct [148]. There is a strong biological basis for using a modular assembly based approach for creating a tissue as many native tissues are often composed of small repeating units that are assembled over several scales, from the molecular level to cell and tissue level [148, 152]. Modular assembly is explained in more detail later in bioassembly.

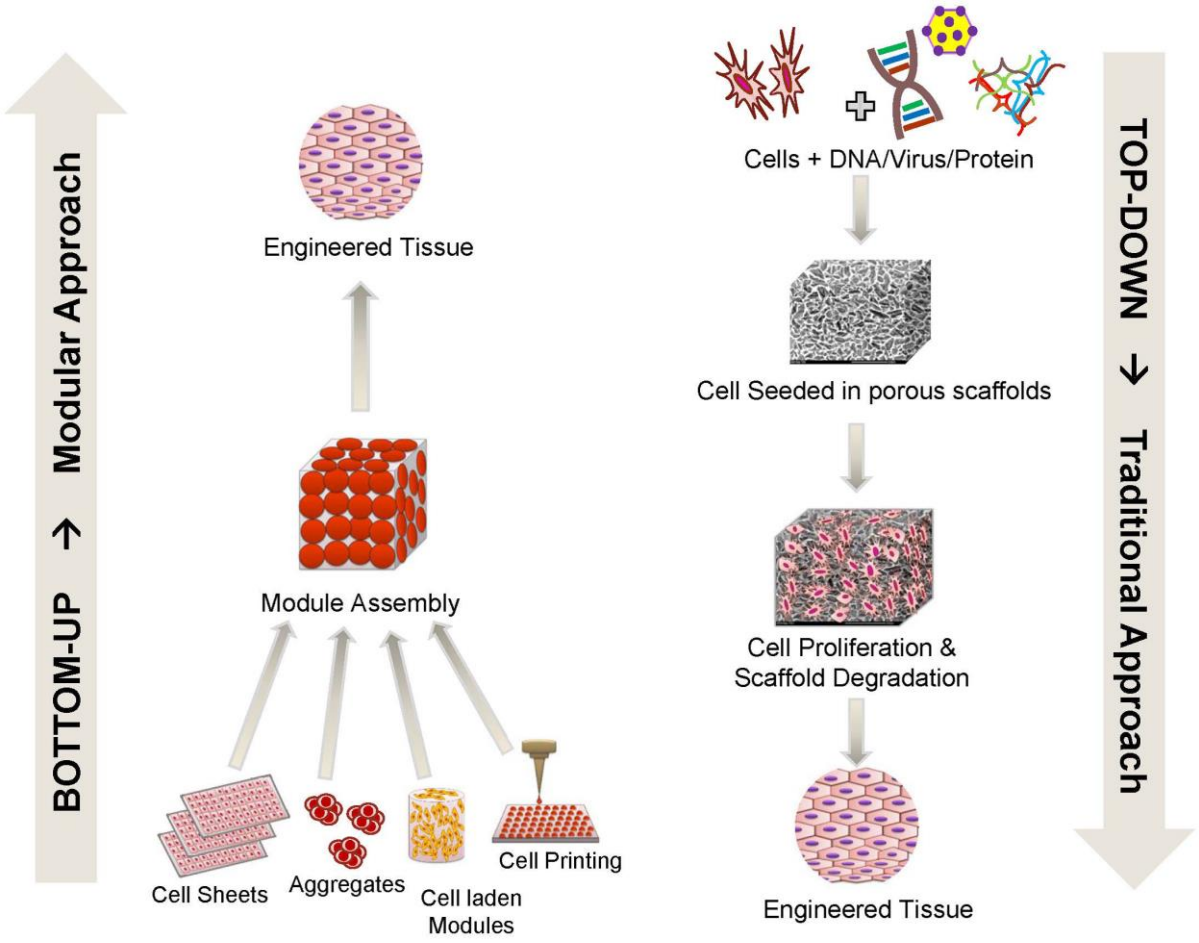

Figure 2-10. A Schematic outline of bottom-up or modular assembly based tissue engineering approaches and top-down or traditional tissue engineering approaches. Reproduced from Tiruvannamalai-Annamalai *et al.* [153].

2.5.2 Biofabrication

Biofabrication is a special branch of tissue engineering and is a technological platform [4]. It is a broad field that describes fabricating materials by living organisms, and with regards to tissue engineering, the most obvious application would be the bioengineering and manufacturing of human tissues and organs for implantation [154, 155]. It is a complex and multidisciplinary field requiring extensive knowledge and skills in cell biology and anatomy, mechanical engineering and material science [154].

The elementary units used are living cells, cell aggregates, tissues, decellularized organ, extracellular matrices, biological molecules, and engineered

biomaterials and the manufactured products are functional living tissue constructs [154, 155]. It essentially involves the use of computer-aided 3D manufacturing strategies such as 3D printing or additive manufacturing for assembling living and non-living material with the desired architecture [4, 155]. This makes it essential to have sophisticated hardware and software. The development of biofabrication technologies would assist the development of organ assembly lines, thereby aiding a smoother commercialisation process. Apart from tissue engineering and regenerative medicine, biofabrication can be potentially applied to a range of cell and tissue-based applications including drug discovery, *in vitro* models of human development and human diseases, and biochips and biosensors [154]. Typical biofabrication approaches for biofabricating bioinks or hydrogels (Figure 2-11) include (a) laser-induced forward transfer, (b) inkjet printing and (c) robotic dispensing and these are described below [4].

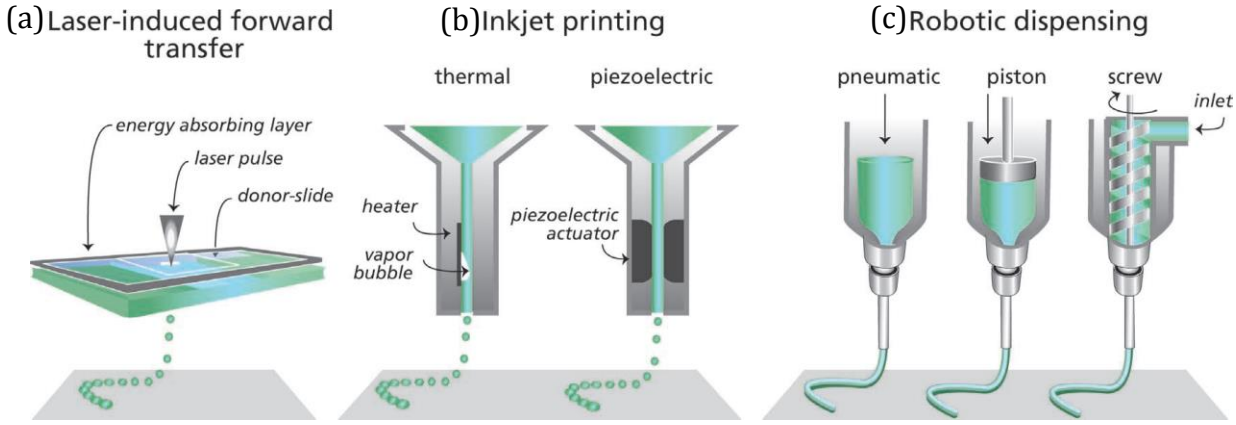

Figure 2-11. Illustration of the three most common biofabrication approaches: (a) laser-induced forward transfer, (b) inkjet printing and (c) robotic dispensing. Reproduced from Malda *et al.* [4].

Laser-induced (Figure 2-11 a) forward transfer bioprinting is a high-resolution nozzle free approach capable of printing with single-cell resolution with bioinks of a wide range of viscosities [4, 156]. Laser-induced forward transfer printers typically consist of a pulsed laser beam, a focusing system, a 'ribbon' which is typically a donor slide covered with an energy absorbing layer and a layer of biological material (i.e. cell suspension) to be printed, and a target substrate [157]. The printing process involves focusing the laser light onto the ribbon and the cell containing material that interacts with the laser is guided and propelled forward onto the target substrate [157, 158]. Although laser-induced forward transfer has a

high printing resolution, preparation of the ribbon is time-consuming, contamination of metallic residues in the printed construct from the energy absorbing layer might occur, and the high-resolution printing requires rapid gelation kinetics to achieve high shape fidelity, which results in a relatively low overall flow rate [4, 157].

Inkjet printing (Figure 2-11 b) involves the precise dispensing of controlled volumes of bioink onto a predefined position on the substrate through a small orifice [4, 157]. Commonly used inkjet printers for cells are either thermal or piezo-electric based [4, 159, 160]. In thermal printing, a small volume of bioink is vaporized by a micro-heater and this creates a pulse that expels the bioink from the print head [4, 159]. The generated heat is detrimental to the cells as transient pores in the cell membrane are formed [4, 159]. In the piezo-electric based approach, the piezo-electric actuator applies a mechanical force to the fluid in the nozzle and this forces the bioink through the nozzle [4, 160]. Limitations in inject printing include an upper viscosity limit of 0.1 Pa s^{-1} that can be used for the bioink [161] and the need for using bioinks with low cell concentrations (<5 × 10^6 cells/ml) to avoid cell clogging [162]. Moreover, the building up of a 3D construct would be challenging as during the printing process the low viscosity inject droplets would spread upon impact on the surface [4].

Robotic dispensing (Figure 2-11 c) is the most commonly employed biofabrication technology [157]. With robotic dispensing anatomical structures can be fabricated [163]. Robotic dispensing consists of a temperature controlled dispensing system, a 3D positioning system and a build platform [157]. In robotic dispensing, high viscosity bioinks are dispensed from a syringe either by pneumatic extrusion, by piston-driven extrusion or screw-driven extrusion onto a build platform [4]. Piston-driven extrusion or screw-driven extrusion gives better control of the bioink extruded compared to the simpler pneumatic extrusion [157]. Materials that possess shear thinning properties and can be either thermally or photo crosslinked are quite often chosen for biofabrication applications [4, 157, 163]. Robotic dispensing is a promising biofabrication technological platform as it allows the fabrication of constructs of clinically relevant size in a realistic timeframe [4].

The above-described methods have been employed for biofabricating bioinks or hydrogels. Where bioink are defined as cytocompatible hydrogel precursor formulations that allow the 3D printing or plotting of living cells [164, 165]. Bioinks can include cell-laden hydrogels, decellularized ECM-based solutions and cell suspensions [164]. To fabricate thermoplastic scaffolds, however, 3D plotting and Fused deposition modelling (FDM) are commonly employed [166].

3D plotting is an additive manufacturing technology and is a versatile method for fabricating porous scaffolds with control of the interconnecting structures for tissue engineering applications [166]. 3D plotting is similar to robotic dispensing. 3D plotting systems consist of a temperature controlled dispensing system, a 3D positioning system, and a build platform [157, 166]. The material is extruded by the dispensing system and deposited via a layer-by-layer process to fabricate a 3D structure. Fused deposition modelling (FDM) is also an additive manufacturing technology similar to 3D plotting except that the material is fed in the form of a filament [167]. The filament is heated to a semi-molten form and is extruded to create a structure utilising the layer-by-layer approach [167]. Rapid prototyping techniques such as 3D plotting and fused deposition modelling (FDM) can overcome limitations of conventional scaffold fabrication techniques such as solvent casting and particulate leaching, gas foaming, fibre meshes and fibre bonding, phase separation, melt moulding, emulsion freeze drying, solution casting and freeze-drying which are incapable of precisely controlling pore size, pore geometry, pore interconnectivity, spatial distribution of pores, and construction of internal channels within the scaffold [167].

3D plotting is a highly flexible platform and complex hybrid scaffolds can be fabricated together with hydrogel bioinks and thermoplastic polymers [168]. Hydrogels can provide a hydrated tissue-like environment that is structurally similar to the native extracellular matrix. However, hydrogels have a limited mechanical strength and need to be reinforced for load-bearing applications [169]. Thermoplastic polymers can reinforce the hydrogel with mechanical strength thereby overcoming the limitation to fabricate constructs with complex shape and size [170]. Kang *et al.* [170] developed an integrated tissue-organ printer (ITOP)

system (Figure 2-12) capable of fabricating 3D hybrid constructs with cell-laden hydrogels and biodegradable thermoplastic polymer (poly(ε-caprolactone) (PCL)) [170]. The ITOP system consisted of a 3D positioning system (3-axis stage controller), multiple cartridges for dispensing different materials (PCL, 2 types of cell-laden hydrogel and sacrificial material), and a temperature and humidity controlled closed chamber [170]. Data from medical imaging (CT or MRI) was used to generate the 3D CAD/CAM model from which a text-based motion control program was generated to control 3D positioning system and other 3D plotting parameters of the system [170]. With the ITOP system the fabrication of mandible and calvarial bone, cartilage and skeletal muscle of clinically relevant size with different types of patterning was demonstrated [170]. Various biofabrication approaches for fabricating hybrid constructs have been reported in the literature and some of these have been listed in Table 2-1.

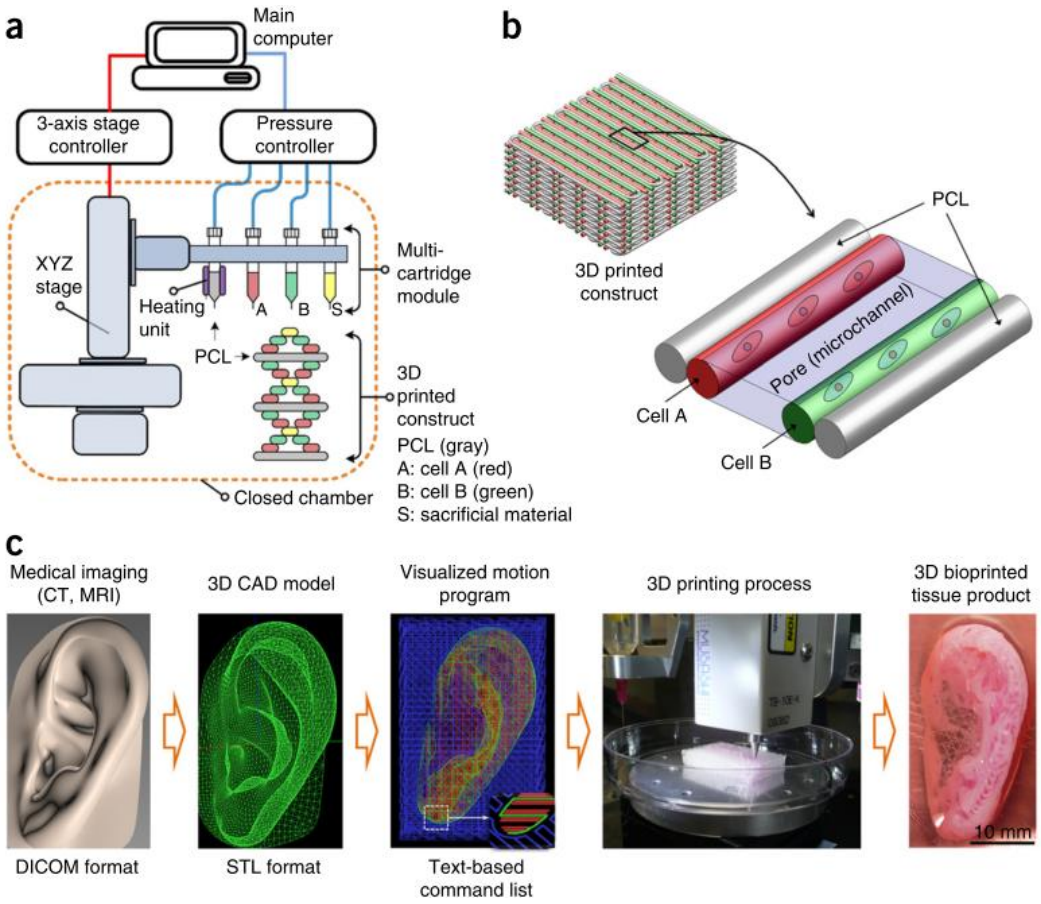

Figure 2-12. Illustration of the (a) integrated tissue-organ printer (ITOP) system, (b) the architecture of the 3D plotted construct, and (c) the CAD/CAM process for automated fabrication of anatomically shaped tissues or organs. The ITOP system consists of a 3D positioning system (3-axis stage controller), multiple cartridges for dispensing different materials, and a temperature-humidity controlled closed chamber. Reproduced from Kang *et al.* [170].

Table 2-1. Various biofabrication approaches for fabricating hybrid constructs and their potential application.

Technique	Material	Cell line	Application	Comments	Author
3D plotting - ITOP system	Thermoplastic polymer – PCL Hydrogel – mixture of gelatin, fibrinogen and glycerol Sacrificial hydrogel - Pluronic F-127	3T3 hAFSC RPAC C2C12	Musculoskeletal engineering (bone, cartilage and skeletal muscle)	The ITOP system was used to fabricate constructs with cell-laden hydrogels and PCL. Microchannels were incorporated into the construct to facilitate diffusion of nutrients to printed cells. See Figure 2-12.	Kang *et al.* [170]
3D plotting – ITOP system	Thermoplastic polymer – blend of PCL and PLCL Hydrogel - fibrin, gelatin and hyaluronic acid	UC SMC	Urethral reconstruction	Tubular scaffold was fabricated with the thermoplastic polymer and UC-laden hydrogel and SMC-laden hydrogel was delivered into the inner and outer layer of the scaffold respectively to fabricate a urethra construct.	Zhang *et al.* [171]
3D plotting	Thermoplastic polymer - PCL Hydrogel - Alginate	C20A4	Broad range including musculoskeletal engineering	3D plotting of alternate layers of PCL and cell-laden alginate. The alginate was cross-linked with calcium chloride solution.	Schuurman *et al.* [168]
Hybrid inkjet printing and electrospinning	Thermoplastic polymer – PCL and Pluronic F-127 Hydrogel – mixture of fibrin and collagen	RPAC	Cartilage engineering	Electrospinning of PCL fibres was alternated with inkjet printing of rabbit primary auricular chondrocyte-laden fibrin-collagen hydrogel.	Xu *et al.* [172]
3D plotting	Thermoplastic polymer – mixture of pHMGC and PCL and mixture of methacrylated pHMGC and PCL Hydrogel – GelMA	PHC	Cartilage engineering	A blend of thermoplastic polymers were 3D plotted and was infused with cell-laden GelMA solution and photopolymerised.	Boere *et al.* [169]

Technique	Material	Cell line	Application	Comments	Author
3D plotting - CMEP system	Thermoplastic polymer - PCL Hydrogel - alginate	L-929	Muscle and nerve repair	A construct was fabricated by melt extruding cell-laden alginate/PCL co-axial fibres using the CMEP system	Cornock *et al.* [173]
3D plotting	Thermoplastic polymer – PCL, PLA and PLGA Hydrogel - alginate	3T3	Tissue engineering	PLA or PLGA was layers were 3D plotted and alternately cell-laden alginate was deposited in the space. PCL was 3D plotted to act as a thermal protective layer for the cell-laden alginate from the PLA or PGLA being 3D plotted. The fabricated construct was immersed in calcium chloride solution to crosslink the alginate.	Kim *et al.* [174]

Abbreviations: C20A4 - Human Chondrocyte Cell Line, 3T3 - mouse embryonic fibroblasts, hAFSC - human amniotic fluid-derived stem cells, RPAC - rabbit primary auricular chondrocytes, C2C12 - mouse myoblasts, PHC - primary human chondrocytes, L-929 - mouse fibroblast cell line, ITOP - integrated tissue-organ printer, pHMGC - poly(hydroxymethylglycolide-co-e-caprolactone), GelMA - gelatin methacrylamide, CMEP - coaxial melt extrusion printing, PLGA - poly (lacticco-glycolic acid), PLA - polylactic acid, UC - urothelial cells, SMC - Smooth muscle cells, PLCL - Poly(lactide-co-caprolactone).

With respect to biofabrication strategies in tissue engineering and regenerative medicine, biofabrication can be thought to consist of two main complementary strategies:

1. Bioprinting - where the minimum fabrication level is molecular [155]. It has been defined by Guillemot *et al.* [155] as *"the use of computer-aided transfer processes for patterning and assembling living and non-living materials with a prescribed 2D or 3D organization in order to produce bioengineered structures serving in regenerative medicine, pharmacokinetic and basic cell biology studies".*

2. Bioassembly - where the minimum fabrication level is with cell containing units [155]. It has been defined by Groll *et al.* [155] as *"the fabrication of hierarchical constructs with a prescribed 2D or 3D organization through automated assembly of pre-formed cell-containing fabrication units generated via cell-driven self-organization or through preparation of hybrid cell-material building blocks, typically by applying enabling technologies, including microfabricated moulds or microfluidics"*.

2.5.2.1 Bioprinting

Bioprinting is one of the major subdivisions of biofabrication. When the minimum level of fabrication is at the molecular level, it can be classified under bioprinting [155, 175]. In the macro scale, the motive of bioprinting is to create anatomically similar structures [175]. Bioprinting is a 3D printing technique used for the fabrication of 3D structures. A layer-by-layer approach is used deposit biomaterials, biomolecules and living cells onto a substrate with precise spatial control to create a predefined architecture [157, 175]. The ITOP system (Figure 2-12) previously described is an example of bioprinting.

2.5.2.2 Bioassembly

Bioassembly is the other major subdivision of biofabrication. When the minimum level of fabrication consists of prefabricated cell containing building blocks that are large enough to be handled by an automated system, it can be classified as bioassembly [155]. Bioassembly is a bottom-up modular approach in which a 3D functional tissue or organ is manufactured using a layer-by-layer process with cell containing units as the building block [176]. Figure 2-13 shows the

approach for bioassembling tissue units to fabricate a tubular construct either in air or in a hydrogel (biopaper) using a bioprinting technology. Figure 2-14 illustrates the concept for bioassembly based organ printing.

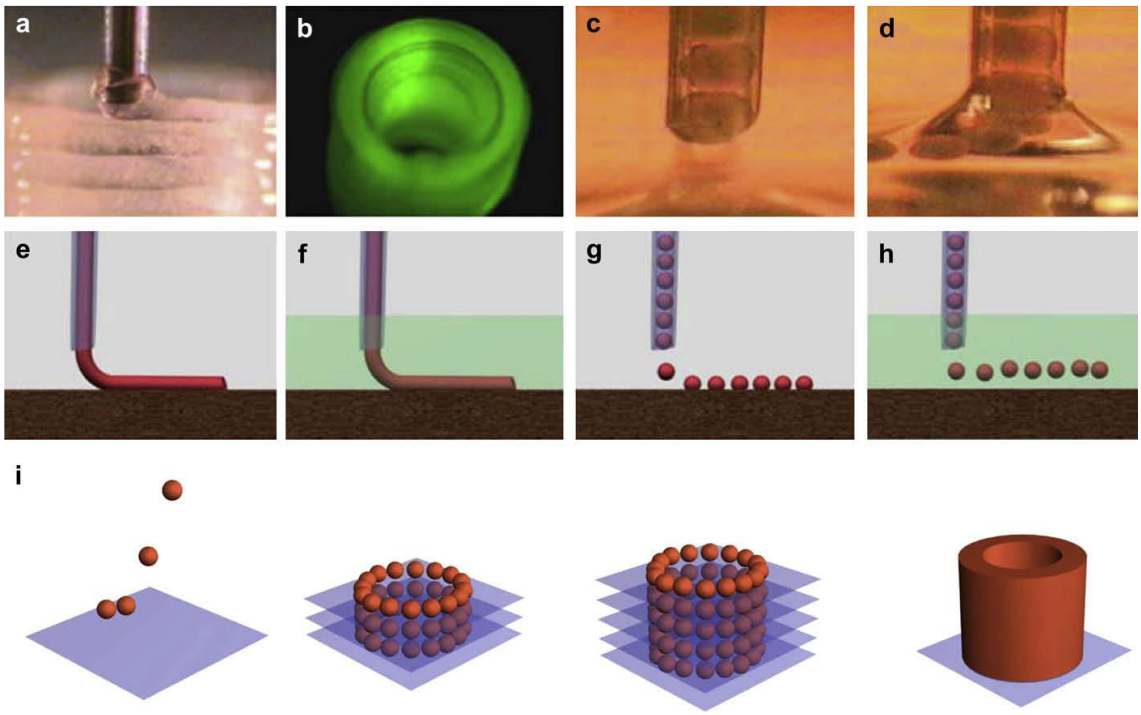

Figure 2-13. Bioprinting technology for bioassembling constructs. Illustration of (a) general view of the bioprinter, (b) bioprinter nozzle, (c) before the tissue unit dispensing process, (d) the tissue unit dispensing process, (e) continuous dispensing in air (f), continuous dispensing in a biopaper, (g) single tissue unit dispensing in air (h) single tissue unit dispensing in a biopaper, and (i) the approach for sequential layer-by-layer bioassembly of a tubular construct. Reproduced from Mironov *et al.* [176].

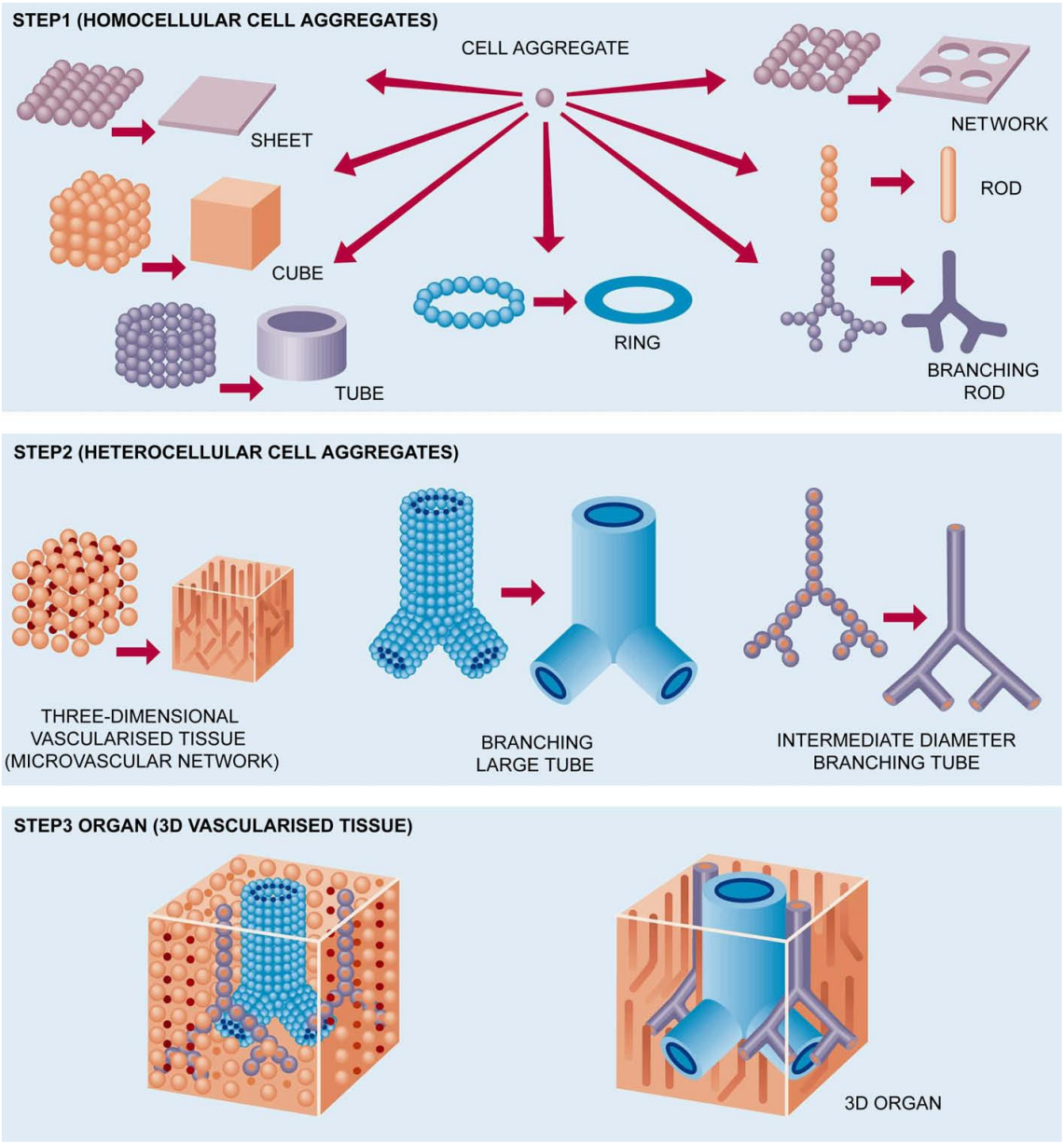

Figure 2-14. Illustration showing the concept of bioassembly based organ printing or robotic additive biomanufacturing. Reproduced from Mironov *et al.* [176].

Numerous bioassembly approaches have been reported in the literature to fabricate higher order assembled constructs using tissue subunits and some of these have been listed in Table 2-2. These approaches have been demonstrated for an extensive range of applications including tumour models [177], vascular engineering [178, 179], cardiac tissue engineering [180, 181], bone tissue engineering [182], trachea tissue engineering [183], dermal tissue engineering [184], liver tissue engineering [185] and cartilage engineering [186].

A spectrum of tissue module types can be fabricated for tissue assembly and this includes cells sheets [180, 187], micro-tissues or cellular aggregates [42, 178, 179, 185, 188], cell-laden microgels [151, 189], microspheres [190] or tissue-rings [183]. The techniques for assembling the modules into a scaffold includes placing micro-tissues in a mold and allowing for tissue fusion [188], stacking of cell sheets [180], random packing of microgels [191], utilising hydrophobic effect for assembling microgels [151], physical manipulation of individual cell-laden microgels [192] assembling micro-tissues into a 3D plotted scaffold [42], vacuum moulding [184, 193], stacking rings on a tube [183]. In this thesis, the two types of fabricated subunits or modules utilised were:

1. Spheroids or micro-tissues

   These consist of an aggregation of cells that can be formed by a broad range of methods including hanging drop technique [194], liquid overlay technique [195], spinner flask [196], pellet culture [42], micromoulding [197] and NASA rotary system [198]. In this thesis, to form chondrocyte micro-tissues, we utilised a high-throughput 96-well plate centrifugation approach and for cancer micro-tissues, we utilised the liquid overlay technique.

2. Cell-laden hydrogel microspheres

   These consist of cells embedded in a hydrogel and can be formed with a wide range of techniques including emulsification [199], photolithography [200], solvent evaporation [201], jetcutting [202], jet breakup [203], and electrostatic droplet generation [204], microfluidic synthesis [190], and micromoulding [189]. In this thesis, a microfluidic system was adapted to generate both chondrocyte or mesenchymal stromal cell encapsulated microspheres and cancer cell encapsulated microspheres.

Our approach toward modular tissue assembly involved assembling the tissue modules or subunits into a 3D plotted scaffold.

Table 2-2. Various bioassembly approaches and their potential application.

Module or subunits	Technique to fabricate module	Material	Cell type	Application	Comments	Author
Micro-tissues	Hanging drop culture	-	HAF HUVEC	Vascular tissue engineering	Micro-tissues were fabricated utilising hanging drop culture. Micro-tissues were assembled using a micro-tissue assembly device.	Kelm *et al.* [178]
Micro-tissues	Hanging drop culture	-	HMF PAC HAC HUVEC C2C12	Vascular tissue engineering	Micro-tissues were fabricated utilising hanging drop culture. The micro-tissues were assembled in a ring-shaped mould.	Kelm *et al.* [179]
Micro-tissues	Micromoulds	-	NHF H35	Investigation of tissue fusion and cell sorting	Micro-tissues were fabricated utilising micromoulds. Larger structures were assembled by resuspending micro-tissues into a second micromould.	Rago *et al.* [205]
Coated spheroids	Microwell device	Collagen	Primary rat hepatocytes HUVEC	Demonstrated perfusion through a construct	Hepatocyte spheroids were fabricated utilising microwells, were collagen-coated and covered with HUVEC. A larger structure was formed by trapping the spheroids in a polyester mesh filter in a culture chamber.	Inamori *et al.* [206]
Aggregates	Microwell arrays	PLLA	Primary rat hepatocytes HUVEC	Liver tissue engineering	Aggregates were fabricated in microwell arrays. The endothelialized aggregates were assembled by packing them in a perfusion bioreactor.	Pang *et al.* [185]

Module or subunits	Technique to fabricate module	Material	Cell type	Application	Comments	Author
Micropellets	Microwell platform	-	hMSC	Biphasic construct - cartilage engineering	Micropellets were fabricated in a microwell platform. The micropellets were cultured separately in chondrogenic medium or osteogenic medium depending on the direction of differentiation required. The micropellets were assembled on separate days on a PDMS mould to form biphasic construct.	Babur *et al.* [186]
Cartilaginous rings	Aggregation in agarose moulds	Gelatin	hMSC	Trachea tissue engineering	Self-assembled cartilaginous rings using annular agarose wells/moulds. The construct was assembled by stacking the rings on silicone tubes.	Dikina *et al.* [183]
Microbeads	Modified double emulsion technique	Gelatin	HDF	Dermis equivalent tissue	Microbeads were fabricated using an emulsion technique and cells were seed into them. The construct was assembled vacuum moulding.	Imparato *et al.* [184]
Microbeads	Water-in-oil emulsion procedure	Collagen Chitosan	Fibroblasts	Multiphase tissue constructs	Microbeads were fabricated using water-in-oil emulsion technique. A multiphase construct was assembled using centrifugation process or vacuum moulding.	Caldwell *et al*. [193]
CultiSpher S Microcarriers	Microcarriers	Gelatin	hAMSC	Bone tissue engineering	Off-the-shelf gelatin microcarriers were seeded with cells. Modules were placed in a cylindrical perfusion culture chamber and assembled through the pulsatile flow of medium.	Chen *et al.* [182]
Gel	Soft-lithographic moulding of gels	Collagen	3T3 HepG2	Tumour model	Gel modules fabricated on patterned hydrophilic PDMS membrane. Gel modules assembled in a microchannel.	Bruzewicz *et al.* [177]
Gel modules	Casting	Collagen Matrigel	CM-rich cell mixture	Cardiac tissue engineering	Cell-laden gel modules were cast. Modules were placed on a nylon mesh to form an assembled single sheet.	Leung and Sefton [181]

Module or subunits	Technique to fabricate module	Material	Cell type	Application	Comments	Author
Gel rods	Casting and cutting	Collagen	HepG2 HUVEC	Demonstrated vascularisation in a construct	Fabricated by gel rods by slicing tubing containing cell-laden collagen. Modules were randomly assembled in a larger tube and media was perfused.	McGuigan and Sefton [191]
Microgels	Photolithography	Methacrylated gelatin Hydroxyapatite	HUVEC MG63	Bone tissue engineering	Osteon-like concentric double ring modules were fabricated with containing HUVECs in the middle and osteoblast-like cells on the outside. The modules were assembled in a hollow tube.	Zuo *et al.* [207]
Microgels	Photolithography	PEG	3T3	Tissue engineering	Fabrication of cell-laden microgels using photolithography. Assembling the microgels by utilizing hydrophobic effect.	Du *et al.* [151]
Microgels	Micromoulding	PEG Hyaluronic acid	3T3 Murine embryonic stem cells	Tissue engineering	Fabrication of cell-laden microgels *via* micromoulding. Microgels were physically arranged in a pattern to assemble a construct.	Yeh *et al.* [189]
Cell-sheet	Temperature-responsive cell culture surfaces	-	Neonatal rat cardiomyocytes	Cardiac tissue engineering	Temperature-responsive detachment of confluent cell sheets. Cell sheets were assembled by stacking the sheets on top of each other.	Shumizu *et al.* [180]
Hydrogel sphere	Dispensing nozzle	Alginate	CPC	Cartilage engineering	Cell-laden alginate scaffold was 3D plotted with a co-axial nozzle and the cell-laden alginate sphere was deposited with a dispensing nozzle into the scaffold.	Ozbolat *et al.* [208]

Abbreviations: PDMS – Polydimethylsiloxane, PLLA - poly-L-lactic acid and PEG - poly(ethylene glycol). Cell types: HepG2 - human liver hepatocellular carcinoma, 3T3 - mouse embryonic fibroblasts, hMSC - human mesenchymal stromal cells, HDF - human dermal fibroblasts, HUVEC - human umbilical vein endothelial cell, HAF - human artery-derived fibroblasts, CM-rich cell mixture - primary neonatal rat

cardiomyocytes and fibroblasts, hAMSC - human amniotic mesenchymal stem cells, NHF - normal neonatal foreskins human fibroblasts, H35 - rat hepatoma cells, ASM - human airway smooth muscle, HMF - human myofibroblasts, PAC - pig articular chondrocytes, HAC - human articular chondrocytes and C2C12 - mouse myoblasts, MG63 - osteoblast-like cells, CPC - Cartilage progenitor cells. Table adapted from Schon *et al*. [209].

2.6 Thesis Aims:

Presently, biofabrication techniques to fabricate large constructs that mimic the microarchitecture in native tissue are limited. The ability to fabricate large complex constructs with an automated bioassembly system would be highly beneficial for advancement in tissue engineering. As seen from Table 2-2, there exists no automated technology that enables the assembly of tissue units (i.e. micro-tissues or microspheres) into a 3D plotted scaffold. We aimed at developing an automated bioassembly system that can assemble tissue units into a 3D plotted thermoplastic scaffold for application in two areas – cartilage engineering and tumour engineering. For cartilage engineering, the engineered cartilage construct can potentially aid joint resurfacing of damaged and degenerated joints. In tumour engineering, the developed cancer construct can potentially be employed for the high-throughput screening of anticancer drugs. The following aims form the basis for the body of work presented in this thesis.

Aim 1: The design and development of a prototype integrated system for automated 3D Bioassembly of tissue units for biofabrication of tissue engineered constructs (Chapter 3).

Aim 2: Validation and characterization of an integrated system for automated 3D Bioassembly of micro-tissues for biofabrication of tissue engineered cartilage constructs (Chapter 4).

Aim 3: Validation of an integrated system for automated 3D Bioassembly of cell-laden microspheres for biofabrication of tissue engineered cartilage constructs, including proof-of-concept and chondrogenic characterisation of the assembled construct (Chapter 5).

Aim 4: Validation of an integrated system for high-throughput fabrication and automated 3D Bioassembly of micro-tissues for biofabrication of an *in vitro* cancer model, including proof-of-concept characterisation of the assembled

tumour construct compared to existing 2D and 3D *in vitro* models (Chapter 6).

Aim 5: Validation of an integrated system for automated 3D Bioassembly of cell-laden microspheres for biofabrication of an *in vitro* cancer model, including proof-of-concept characterisation of the assembled tumour construct compared to existing 2D and 3D *in vitro* models (Chapter 7).

2.7 References

1. Langer R, Vacanti J. Tissue engineering. Science. 1993;260(5110):920-926.
2. Griffith LG, Naughton G. Tissue engineering-current challenges and expanding opportunities. Science. 2002;295(5557):1009-1014.
3. Woodfield TB, Malda J, de Wijn J, Peters F, Riesle J, van Blitterswijk CA. Design of porous scaffolds for cartilage tissue engineering using a three-dimensional fiber-deposition technique. Biomaterials. 2004;25(18):4149-61.
4. Malda J, Visser J, Melchels FP, Jüngst T, Hennink WE, Dhert WJ, Groll J, Hutmacher DW. 25th anniversary article: engineering hydrogels for biofabrication. Advanced Materials. 2013;25(36):5011-5028.
5. Patra S, Young V. A Review of 3D printing techniques and the future in biofabrication of bioprinted tissue. Cell Biochemistry and Biophysics. 2016:1-6.
6. Gholipourmalekabadi M, Zhao S, Harrison BS, Mozafari M, Seifalian AM. Oxygen-generating biomaterials: a new, viable paradigm for tissue engineering? Trends in Biotechnology. 2016;34(12):1010-1021.
7. Katari R, Peloso A, Orlando G. Tissue engineering and regenerative medicine: semantic considerations for an evolving paradigm. Frontiers in Bioengineering and Biotechnology. 2015;2:57.
8. Orlando G, Wood KJ, Stratta RJ, Yoo JJ, Atala A, Soker S. Regenerative medicine and organ transplantation: past, present, and future. Transplantation. 2011;91(12):1310-1317.
9. Health UDo, Services H. 2020: A new vision—a future for regenerative medicine. Washington DC, USA. 2005.
10. Salgado AJ, Oliveira JM, Martins A, Teixeira FG, Silva NA, Neves NM, Sousa N, Reis RL. Tissue engineering and regenerative medicine: past, present, and future. International Review of Neurobiology. 2013;108:1-33.
11. Athanasiou KA, Shah AR, Hernandez RJ, LeBaron RG. Basic science of articular cartilage repair. Clinics in Sports Medicine. 2001;20(2):223-247.
12. Buckwalter J, Mankin H. Articular cartilage: tissue design and chondrocyte-matrix interactions. Instructional Course Lectures. 1997;47:477-486.
13. Fox AJS, Bedi A, Rodeo SA. The basic science of articular cartilage: structure, composition, and function. Sports Health: A Multidisciplinary Approach. 2009;1(6):461-468.
14. Lewis PB, McCarty III LP, Kang RW, Cole BJ. Basic science and treatment options for articular cartilage injuries. Journal of Orthopaedic & Sports Physical Therapy. 2006;36(10):717-727.
15. Kiani C, Liwen C, Wu YJ, Albert JY, Burton BY. Structure and function of aggrecan. Cell Research. 2002;12(1):19-32.
16. Mow VC, Holmes MH, Lai WM. Fluid transport and mechanical properties of articular cartilage: a review. Journal of Biomechanics. 1984;17(5):377-394.
17. Armstrong C, Lai W, Mow V. An analysis of the unconfined compression of articular cartilage. Journal of Biomechanical Engineering. 1984;106(2):165-173.
18. Pearle AD, Warren RF, Rodeo SA. Basic science of articular cartilage and osteoarthritis. Clinics in Sports Medicine. 2005;24(1):1-12.
19. Wong M, Wuethrich P, Eggli P, Hunziker E. Zone-specific cell biosynthetic activity in mature bovine articular cartilage: A new method using confocal

microscopic stereology and quantitative autoradiography. Journal of Orthopaedic Research. 1996;14(3):424-432.
20. Woodfield T, Blitterswijk CV, Wijn JD, Sims T, Hollander A, Riesle J. Polymer scaffolds fabricated with pore-size gradients as a model for studying the zonal organization within tissue-engineered cartilage constructs. Tissue Engineering. 2005;11(9-10):1297-1311.
21. Redman S, Oldfield S, Archer C. Current strategies for articular cartilage repair. European Cells & Materials. 2005;9(23-32):23-32.
22. Kuroda R, Ishida K, Matsumoto T, Akisue T, Fujioka H, Mizuno K, Ohgushi H, Wakitani S, Kurosaka M. Treatment of a full-thickness articular cartilage defect in the femoral condyle of an athlete with autologous bone-marrow stromal cells. Osteoarthritis and Cartilage. 2007;15(2):226-231.
23. Moseley J, O'Malley K, Petersen N, Menke T, Brody B, Kuykendall D, Hollingsworth J, Ashton C, Wray N. Arthroscopic lavage or debridement did not reduce pain more than placebo did in patients with osteoarthritis. The Journal of Bone and Joint Surgery - American Volume. 2003;85(2):387-387.
24. Sledge SL. Microfracture techniques in the treatment of osteochondral injuries. Clinics in Sports Medicine. 2001;20(2):365-378.
25. Buckwalter J, Mankin H. Articular cartilage repair and transplantation. Arthritis & Rheumatism. 1998;41(8):1331-1342.
26. Weisl H. Intertrochanteric osteotomy for osteoarthritis. A long-term follow-up. Bone & Joint Journal. 1980;62(1):37-42.
27. Alfredson H, Lorentzon R. Superior results with continuous passive motion compared to active motion after periosteal transplantation A retrospective study of human patella cartilage defect treatment. Knee Surgery, Sports Traumatology, Arthroscopy. 1999;7(4):232-238.
28. Seradge H, Kutz J, Kleinert H, Lister G, Wolff T, Atasoy E. Perichondrial resurfacing arthroplasty in the hand. The Journal of Hand Surgery. 1984;9(6):880-886.
29. Ahmad CS, Guiney WB, Drinkwater CJ. Evaluation of donor site intrinsic healing response in autologous osteochondral grafting of the knee. Arthroscopy: The Journal of Arthroscopic & Related Surgery. 2002;18(1):95-98.
30. LaPrade RF, Botker JC. Donor-site morbidity after osteochondral autograft transfer procedures. Arthroscopy: The Journal of Arthroscopic & Related Surgery. 2004;20(7):e69-e73.
31. Zhan C, Kaczmarek R, Loyo-Berrios N, Sangl J, Bright RA. Incidence and short-term outcomes of primary and revision hip replacement in the United States. The Journal of Bone and Joint Surgery - American Volume. 2007;89(3):526-533.
32. Carr AJ, Robertsson O, Graves S, Price AJ, Arden NK, Judge A, Beard DJ. Knee replacement. The Lancet. 2012;379(9823):1331-1340.
33. Brittberg M. Autologous chondrocyte transplantation. Clinical Orthopaedics and Related Research. 1999;367:S147-S155.
34. Bachmann G, Basad E, Lommel D, Steinmeyer J. [MRI in the follow-up of matrix-supported autologous chondrocyte transplantation (MACI) and microfracture]. Der Radiologe. 2004;44(8):773-782.
35. Bartlett W, Skinner J, Gooding C, Carrington R, Flanagan A, Briggs T, Bentley G. Autologous chondrocyte implantation versus matrix-induced autologous chondrocyte implantation for osteochondral defects of the knee. Bone & Joint Journal. 2005;87(5):640-645.

36. Brittberg M, Lindahl A, Nilsson A, Ohlsson C, Isaksson O, Peterson L. Treatment of deep cartilage defects in the knee with autologous chondrocyte transplantation. The New England Journal of Medicine. 1994;331(14):889-895.
37. Kock L, van Donkelaar CC, Ito K. Tissue engineering of functional articular cartilage: the current status. Cell and Tissue Research. 2012;347(3):613-627.
38. Siclari A, Mascaro G, Gentili C, Cancedda R, Boux E. A cell-free scaffold-based cartilage repair provides improved function hyaline-like repair at one year. Clinical Orthopaedics and Related Research. 2012;470(3):910-919.
39. Nukavarapu SP, Dorcemus DL. Osteochondral tissue engineering: current strategies and challenges. Biotechnology Advances. 2013;31(5):706-721.
40. Darling EM, Athanasiou KA. Rapid phenotypic changes in passaged articular chondrocyte subpopulations. Journal of Orthopaedic Research. 2005;23(2):425-432.
41. Bernstein P, Dong M, Corbeil D, Gelinsky M, Günther KP, Fickert S. Pellet culture elicits superior chondrogenic redifferentiation than alginate-based systems. Biotechnology Progress. 2009;25(4):1146-1152.
42. Schon BS, Schrobback K, van der Ven M, Stroebel S, Hooper GJ, Woodfield TB. Validation of a high-throughput microtissue fabrication process for 3D assembly of tissue engineered cartilage constructs. Cell and Tissue Research. 2012.
43. Mauck R, Yuan X, Tuan R. Chondrogenic differentiation and functional maturation of bovine mesenchymal stem cells in long-term agarose culture. Osteoarthritis and cartilage. 2006;14(2):179-189.
44. Klein TJ, Rizzi SC, Reichert JC, Georgi N, Malda J, Schuurman W, Crawford RW, Hutmacher DW. Strategies for zonal cartilage repair using hydrogels. Macromolecular Bioscience. 2009;9(11):1049-1058.
45. Chung C, Burdick JA. Engineering cartilage tissue. Advanced Drug Delivery Reviews. 2008;60(2):243-262.
46. Kafienah We, Jakob M, Démarteau O, Frazer A, Barker MD, Martin I, Hollander AP. Three-dimensional tissue engineering of hyaline cartilage: comparison of adult nasal and articular chondrocytes. Tissue Engineering. 2002;8(5):817-826.
47. Rotter N, Bonassar LJ, Tobias G, Lebl M, Roy AK, Vacanti CA. Age dependence of biochemical and biomechanical properties of tissue-engineered human septal cartilage. Biomaterials. 2002;23(15):3087-3094.
48. Barbero A, Grogan S, Schäfer D, Heberer M, Mainil-Varlet P, Martin I. Age related changes in human articular chondrocyte yield, proliferation and post-expansion chondrogenic capacity. Osteoarthritis and Cartilage. 2004;12(6):476-484.
49. Siegel NS, Gliklich RE, Taghizadeh F, Chang Y. Outcomes of septoplasty. Otolaryngology–Head and Neck Surgery. 2000;122(2):228-232.
50. Tuan RS. Stemming cartilage degeneration: adult mesenchymal stem cells as a cell source for articular cartilage tissue engineering. Arthritis & Rheumatism. 2006;54(10):3075-3078.
51. Mueller MB, Tuan RS. Functional characterization of hypertrophy in chondrogenesis of human mesenchymal stem cells. Arthritis & Rheumatism. 2008;58(5):1377-1388.
52. Pelttari K, Wixmerten A, Martin I. Do we really need cartilage tissue engineering. Swiss Medical Weekly. 2009;139(41-42):602-609.

53. Guo J, Jourdian GW, Maccallum DK. Culture and growth characteristics of chondrocytes encapsulated in alginate beads. Connective Tissue Research. 1989;19(2-4):277-297.
54. Benya PD, Shaffer JD. Dedifferentiated chondrocytes reexpress the differentiated collagen phenotype when cultured in agarose gels. Cell. 1982;30(1):215-224.
55. Wakitani S, Goto T, Pineda SJ, Young RG, Mansour JM, Caplan AI, Goldberg VM. Mesenchymal cell-based repair of large, full-thickness defects of articular cartilage. The Journal of Bone and Joint Surgery - American Volume. 1994;76(4):579-592.
56. Silverman RP, Passaretti D, Huang W, Randolph MA, Yaremchuk MJ. Injectable tissue-engineered cartilage using a fibrin glue polymer. Plastic and Reconstructive Surgery. 1999;103(7):1809-1818.
57. Kim T-K, Sharma B, Williams C, Ruffner M, Malik A, McFarland E, Elisseeff JH. Experimental model for cartilage tissue engineering to regenerate the zonal organization of articular cartilage. Osteoarthritis and Cartilage. 2003;11(9):653-664.
58. Elisseeff J, McIntosh W, Fu K, Blunk T, Langer R. Controlled-release of IGF-I and TGF-β1 in a photopolymerizing hydrogel for cartilage tissue engineering. Journal of Orthopaedic Research. 2001;19(6):1098-1104.
59. Spiller KL, Liu Y, Holloway JL, Maher SA, Cao Y, Liu W, Zhou G, Lowman AM. A novel method for the direct fabrication of growth factor-loaded microspheres within porous nondegradable hydrogels: controlled release for cartilage tissue engineering. Journal of Controlled Release. 2012;157(1):39-45.
60. Uematsu K, Hattori K, Ishimoto Y, Yamauchi J, Habata T, Takakura Y, Ohgushi H, Fukuchi T, Sato M. Cartilage regeneration using mesenchymal stem cells and a three-dimensional poly-lactic-glycolic acid (PLGA) scaffold. Biomaterials. 2005;26(20):4273-4279.
61. Hunziker E, Quinn T, Häuselmann H-J. Quantitative structural organization of normal adult human articular cartilage. Osteoarthritis and Cartilage. 2002;10(7):564-572.
62. Woodfield T, Bezemer J, Pieper J, Van Blitterswijk C, Riesle J. Scaffolds for tissue engineering of cartilage. Critical Reviews™ in Eukaryotic Gene Expression. 2002;12(3).
63. Klein T, Schumacher B, Schmidt T, Li K, Voegtline M, Masuda K, Thonar E-M, Sah R. Tissue engineering of stratified articular cartilage from chondrocyte subpopulations. Osteoarthritis and Cartilage. 2003;11(8):595-602.
64. Sharma B, Williams CG, Kim TK, Sun D, Malik A, Khan M, Leong K, Elisseeff JH. Designing zonal organization into tissue-engineered cartilage. Tissue Engineering. 2007;13(2):405-414.
65. Bian L, Zhai DY, Mauck RL, Burdick JA. Coculture of human mesenchymal stem cells and articular chondrocytes reduces hypertrophy and enhances functional properties of engineered cartilage. Tissue Engineering Part A. 2011;17(7-8):1137-45.
66. Ng KW, Wang CCB, Mauck RL, Kelly TAN, Chahine NO, Costa KD, Ateshian GA, Hung CT. A layered agarose approach to fabricate depth-dependent inhomogeneity in chondrocyte-seeded constructs. Journal of Orthopaedic Research. 2005;23(1):134-141.

67. Tuli R, Nandi S, Li W-J, Tuli S, Huang X, Manner PA, Laquerriere P, Nöth U, Hall DJ, Tuan RS. Human mesenchymal progenitor cell-based tissue engineering of a single-unit osteochondral construct. Tissue Engineering. 2004;10(7-8):1169-1179.
68. Ferlay J, Soerjomataram I, Dikshit R, Eser S, Mathers C, Rebelo M, Parkin DM, Forman D, Bray F. Cancer incidence and mortality worldwide: sources, methods and major patterns in GLOBOCAN 2012. International Journal of Cancer. 2015;136(5):E359-E386.
69. Organization WH. Cancer fact sheet N 297. . Retrieved;2014.
70. Dvorak HF, Nagy JA, Feng D, Dvorak AM. Tumor architecture and targeted delivery. Radioimmunotherapy of cancer. New York: Marcel Dekker. 2000:107-35.
71. Ghajar CM, Bissell MJ. Tumor engineering: the other face of tissue engineering. Tissue Engineering Part A. 2010;16(7):2153-2156.
72. Forment JV, Kaidi A, Jackson SP. Chromothripsis and cancer: causes and consequences of chromosome shattering. Nature Reviews Cancer. 2012;12(10):663-670.
73. Thoma CR, Zimmermann M, Agarkova I, Kelm JM, Krek W. 3D cell culture systems modeling tumor growth determinants in cancer target discovery. Advanced Drug Delivery Reviews. 2014;69:29-41.
74. Ebben JD, Treisman DM, Zorniak M, Kutty RG, Clark PA, Kuo JS. The cancer stem cell paradigm: a new understanding of tumor development and treatment. Expert Opinion on Therapeutic Targets. 2010;14(6):621-632.
75. Kalluri R, Zeisberg M. Fibroblasts in cancer. Nature Reviews Cancer. 2006;6(5):392-401.
76. Unger C, Kramer N, Walzl A, Scherzer M, Hengstschläger M, Dolznig H. Modeling human carcinomas: physiologically relevant 3D models to improve anti-cancer drug development. Advanced Drug Delivery Reviews. 2014;79:50-67.
77. Olumi AF, Grossfeld GD, Hayward SW, Carroll PR, Tlsty TD, Cunha GR. Carcinoma-associated fibroblasts direct tumor progression of initiated human prostatic epithelium. Cancer Research. 1999;59(19):5002-5011.
78. Zhang Y, Tang H, Cai J, Zhang T, Guo J, Feng D, Wang Z. Ovarian cancer-associated fibroblasts contribute to epithelial ovarian carcinoma metastasis by promoting angiogenesis, lymphangiogenesis and tumor cell invasion. Cancer Letters. 2011;303(1):47-55.
79. Carmeliet P, Jain RK. Angiogenesis in cancer and other diseases. Nature. 2000;407(6801):249-257.
80. De Visser KE, Eichten A, Coussens LM. Paradoxical roles of the immune system during cancer development. Nature reviews cancer. 2006;6(1):24-37.
81. Mueller MM, Fusenig NE. Friends or foes—bipolar effects of the tumour stroma in cancer. Nature Reviews Cancer. 2004;4(11):839-849.
82. Webb K, Li W, Hitchcock RW, Smeal RM, Gray SD, Tresco PA. Comparison of human fibroblast ECM-related gene expression on elastic three-dimensional substrates relative to two-dimensional films of the same material. Biomaterials. 2003;24(25):4681-4690.
83. Bridle KR, Crawford DH, Powell LW, Ramm GA. Role of myofibroblasts in tumour encapsulation of hepatocellular carcinoma in haemochromatosis. Liver. 2001;21(2):96-104.

84. Brown JM, Giaccia AJ. The unique physiology of solid tumors: opportunities (and problems) for cancer therapy. Cancer Research. 1998;58(7):1408-1416.
85. Bergers G, Benjamin LE. Tumorigenesis and the angiogenic switch. Nature Reviews Cancer. 2003;3(6):401-410.
86. Nyga A, Cheema U, Loizidou M. 3D tumour models: novel in vitro approaches to cancer studies. Journal of Cell Communication and Signaling. 2011;5(3):239-248.
87. Pollard JW. Tumour-educated macrophages promote tumour progression and metastasis. Nature Reviews Cancer. 2004;4(1):71-78.
88. Polyak K, Haviv I, Campbell IG. Co-evolution of tumor cells and their microenvironment. Trends in Genetics. 2009;25(1):30-38.
89. Albini A, Sporn MB. The tumour microenvironment as a target for chemoprevention. Nature Reviews Cancer. 2007;7(2):139-147.
90. Heinemann V, Reni M, Ychou M, Richel D, Macarulla T, Ducreux M. Tumour–stroma interactions in pancreatic ductal adenocarcinoma: rationale and current evidence for new therapeutic strategies. Cancer Treatment Reviews. 2014;40(1):118-128.
91. Jiang B, Mason J, Jewett A, Liu M, Chen W, Qian J, Ding Y, Ding S, Ni M, Zhang X. Tumor-infiltrating immune cells: triggers for tumor capsule disruption and tumor progression. International Journal of Medical Sciences. 2013;10(5):475-497.
92. Siegel R, DeSantis C, Virgo K, Stein K, Mariotto A, Smith T, Cooper D, Gansler T, Lerro C, Fedewa S. Cancer treatment and survivorship statistics, 2012. CA: A Cancer Journal for Clinicians. 2012;62(4):220-241.
93. DeVita VT, Chu E. A history of cancer chemotherapy. Cancer Research. 2008;68(21):8643-8653.
94. Hughes J, Rees S, Kalindjian S, Philpott K. Principles of early drug discovery. British Journal of Pharmacology. 2011;162(6):1239-1249.
95. Balis FM. Evolution of anticancer drug discovery and the role of cell-based screening. Journal of the National Cancer Institute. 2002;94(2):78-79.
96. Avorn J. The $2.6 billion pill—methodologic and policy considerations. New England Journal of Medicine. 2015;372(20):1877-1879.
97. Kunz-Schughart LA, Freyer JP, Hofstaedter F, Ebner R. The use of 3-D cultures for high-throughput screening: the multicellular spheroid model. Journal of Biomolecular Screening. 2004;9(4):273-285.
98. Food, Administration D. Innovation or stagnation: challenge and opportunity on the critical path to new medical products. Food and Drug Administration, Critical Path Report. 2004.
99. Chabner BA, Roberts TG. Chemotherapy and the war on cancer. Nature Reviews Cancer. 2005;5(1):65-72.
100. Solomon SD, McMurray JJ, Pfeffer MA, Wittes J, Fowler R, Finn P, Anderson WF, Zauber A, Hawk E, Bertagnolli M. Cardiovascular risk associated with celecoxib in a clinical trial for colorectal adenoma prevention. New England Journal of Medicine. 2005;352(11):1071-1080.
101. Griffith LG, Swartz MA. Capturing complex 3D tissue physiology in vitro. Nature Reviews Molecular Cell Biology. 2006;7(3):211-224.
102. Bleicher KH, Böhm H-J, Müller K, Alanine AI. Hit and lead generation: beyond high-throughput screening. Nature Reviews Drug discovery. 2003;2(5):369-378.

103. Kim JB, Stein R, O'Hare MJ. Three-dimensional *in vitro* tissue culture models of breast cancer- a review. Breast Cancer Research and Treatment. 2004;85(3):281-91.
104. Liu B, Li S, Hu J. Technological advances in high-throughput screening. American Journal of Pharmacogenomics. 2004;4(4):263-276.
105. Bissell MJ, Hines WC. Why don't we get more cancer? A proposed role of the microenvironment in restraining cancer progression. Nature medicine. 2011;17(3):320-329.
106. Burdett E, Kasper FK, Mikos AG, Ludwig JA. Engineering tumors: a tissue engineering perspective in cancer biology. Tissue Engineering Part B: Reviews. 2010;16(3):351-359.
107. Yamada KM, Cukierman E. Modeling tissue morphogenesis and cancer in 3D. Cell. 2007;130(4):601-610.
108. Rangarajan A, Hong SJ, Gifford A, Weinberg RA. Species-and cell type-specific requirements for cellular transformation. Cancer Cell. 2004;6(2):171-183.
109. Sivaraman A, Leach J, Townsend S, Iida T, Hogan B, Stolz DB, Fry R, Samson L, Tannenbaum S, Griffith L. A microscale in vitro physiological model of the liver: predictive screens for drug metabolism and enzyme induction. Current Drug Metabolism. 2005;6(6):569-591.
110. Kim JB. Three-dimensional tissue culture models in cancer biology. in Seminars in Cancer Biology. 2005. Elsevier.
111. Petersen OW, Rønnov-Jessen L, Howlett AR, Bissell MJ. Interaction with basement membrane serves to rapidly distinguish growth and differentiation pattern of normal and malignant human breast epithelial cells. Proceedings of the National Academy of Sciences. 1992;89(19):9064-9068.
112. Pampaloni F, Reynaud EG, Stelzer EH. The third dimension bridges the gap between cell culture and live tissue. Nature Reviews Molecular Cell Biology. 2007;8(10):839-845.
113. Kimlin LC, Casagrande G, Virador VM. In vitro three-dimensional (3D) models in cancer research: An update. Molecular Carcinogenesis. 2013;52(3):167-182.
114. Kobayashi H, Man S, Graham CH, Kapitain SJ, Teicher BA, Kerbel RS. Acquired multicellular-mediated resistance to alkylating agents in cancer. Proceedings of the National Academy of Sciences. 1993;90(8):3294-3298.
115. Ohmori T, Yang J-L, Price JO, Arteaga CL. Blockade of tumor cell transforming growth factor-βs enhances cell cycle progression and sensitizes human breast carcinoma cells to cytotoxic chemotherapy. Experimental Cell Research. 1998;245(2):350-359.
116. Hutmacher DW, Horch RE, Loessner D, Rizzi S, Sieh S, Reichert JC, Clements JA, Beier JP, Arkudas A, Bleiziffer O. Translating tissue engineering technology platforms into cancer research. Journal of Cellular and Molecular Medicine. 2009;13(8a):1417-1427.
117. Kim H, Phung Y, Ho M. Changes in global gene expression associated with 3D structure of tumors: an ex vivo matrix-free mesothelioma spheroid model. PLOS ONE. 2012;7(6):e39556.
118. Nelson CM, Inman JL, Bissell MJ. Three-dimensional lithographically defined organotypic tissue arrays for quantitative analysis of morphogenesis and neoplastic progression. Nature Protocols. 2008;3(4):674-678.
119. Kleinman HK, Martin GR. Matrigel: basement membrane matrix with biological activity. in Seminars in Cancer Biology. 2005. Elsevier.

120. Ivascu A, Kubbies M. Rapid generation of single-tumor spheroids for high-throughput cell function and toxicity analysis. Journal of biomolecular screening. 2006;11(8):922-932.
121. Bates RC, Edwards NS, Yates JD. Spheroids and cell survival. Critical Reviews in Oncology/Hematology. 2000;36(2):61-74.
122. Kale S, Biermann S, Edwards C, Tarnowski C, Morris M, Long MW. Three-dimensional cellular development is essential for *ex vivo* formation of human bone. Nature Biotechnology. 2000;18(9):954-958.
123. Desoize B. Contribution of three-dimensional culture to cancer research. Critical Reviews in Oncology/Hematology. 2000;36(2):59-60.
124. Jakab K, Neagu A, Mironov V, Markwald RR, Forgacs G. Engineering biological structures of prescribed shape using self-assembling multicellular systems. Proceedings of the National Academy of Sciences of the United States of America. 2004;101(9):2864-2869.
125. Lin R-Z, Chou L-F, Chien C-CM, Chang H-Y. Dynamic analysis of hepatoma spheroid formation: roles of E-cadherin and β1-integrin. Cell and Tissue Research. 2006;324(3):411-422.
126. Friedrich J, Seidel C, Ebner R, Kunz-Schughart LA. Spheroid-based drug screen: considerations and practical approach. Nature Protocols. 2009;4(3):309-324.
127. Ivascu A, Kubbies M. Diversity of cell-mediated adhesions in breast cancer spheroids. International Journal of Oncology. 2007;31(6):1403-1414.
128. Kunz-Schughart LA, Heyder P, Schroeder J, Knuechel R. A heterologous 3-D coculture model of breast tumor cells and fibroblasts to study tumor-associated fibroblast differentiation. Experimental Cell Research. 2001;266(1):74-86.
129. Carlsson J, Nilsson K, Westermark B, Ponten J, Sundstrom C, Larsson E, Bergh J, Pahlman S, Busch C, Collins VP. Formation and growth of multicellular spheroids of human origin. International Journal of Cancer. 1983;31(5):523-33.
130. Stoker A, Streuli C, Martins-Green M, Bissell M. Designer microenvironments for the analysis of cell and tissue function. Current Opinion in Cell Biology. 1990;2(5):864-874.
131. Jones JL, Critchley D, Walker RA. Alteration of stromal protein and integrin expression in breast—a marker of premalignant change? The Journal of Pathology. 1992;167(4):399-406.
132. Howlett AR, Bailey N, Damsky C, Petersen OW, Bissell MJ. Cellular growth and survival are mediated by beta-1 integrins in normal human breast epithelium but not in breast carcinoma. Journal of Cell Science. 1995;108(5):1945-1957.
133. Liang Y, Jeong J, DeVolder RJ, Cha C, Wang F, Tong YW, Kong H. A cell-instructive hydrogel to regulate malignancy of 3D tumor spheroids with matrix rigidity. Biomaterials. 2011;32(35):9308-9315.
134. Nafea EH, Poole-Warren LA, Martens PJ. Structural and permeability characterization of biosynthetic PVA hydrogels designed for cell-based therapy. Journal of Biomaterials Science, Polymer Edition. 2014;25(16):1771-1790.
135. Nicodemus GD, Bryant SJ. Cell encapsulation in biodegradable hydrogels for tissue engineering applications. Tissue Engineering Part B: Reviews. 2008;14(2):149-165.
136. Tiago M, de Oliveira EM, Brohem CA, Pennacchi PC, Paes RD, Haga RB, Campa A, de Moraes Barros SB, Smalley KS, Maria-Engler SS. Fibroblasts protect melanoma cells from the cytotoxic effects of doxorubicin. Tissue engineering Part A. 2014;20(17-18):2412-2421.

137. Smalley KS, Lioni M, Herlyn M. Life ins't flat: Taking cancer biology to the next dimension. In Vitro Cellular & Developmental Biology-Animal. 2006;42(8-9):242-247.
138. Bischofs IB, Schwarz US. Cell organization in soft media due to active mechanosensing. Proceedings of the National Academy of Sciences. 2003;100(16):9274-9279.
139. McDaniel DP, Shaw GA, Elliott JT, Bhadriraju K, Meuse C, Chung K-H, Plant AL. The stiffness of collagen fibrils influences vascular smooth muscle cell phenotype. Biophysical Journal. 2007;92(5):1759-1769.
140. Weigelt B, Ghajar CM, Bissell MJ. The need for complex 3D culture models to unravel novel pathways and identify accurate biomarkers in breast cancer. Advanced Drug Delivery Reviews. 2014;69:42-51.
141. Montanez E, Casaroli-Marano RP, Vilaro S, Pagan R. Comparative study of tube assembly in three-dimensional collagen matrix and on Matrigel coats. Angiogenesis. 2002;5(3):167-172.
142. Grefte S, Vullinghs S, Kuijpers-Jagtman A, Torensma R, Von den Hoff J. Matrigel, but not collagen I, maintains the differentiation capacity of muscle derived cells *in vitro.* Biomedical Materials. 2012;7(5):055004.
143. Rosen PP, Saigo PE, Braun DW, Weathers E, Fracchia AA, Kinne DW. Axillary micro-and macrometastases in breast cancer: prognostic significance of tumor size. Annals of Surgery. 1981;194(5):585.
144. Horvath LE, Werner T, Boucher K, Jones K. The relationship between tumor size and stage in early versus advanced ovarian cancer. Medical Hypotheses. 2013;80(5):684-687.
145. Ivascu A, Kubbies M. Rapid generation of single-tumor spheroids for high-throughput cell function and toxicity analysis. J Biomol Screen. 2006;11(8):922-32.
146. Friedrich J, Seidel C, Ebner R, Kunz-Schughart LA. Spheroid-based drug screen: considerations and practical approach. Nat Protoc. 2009;4(3):309-24.
147. Lynch TJ, Bell DW, Sordella R, Gurubhagavatula S, Okimoto RA, Brannigan BW, Harris PL, Haserlat SM, Supko JG, Haluska FG. Activating mutations in the epidermal growth factor receptor underlying responsiveness of non–small-cell lung cancer to gefitinib. New England Journal of Medicine. 2004;350(21):2129-2139.
148. Nichol JW, Khademhosseini A. Modular tissue engineering: engineering biological tissues from the bottom up. Soft Matter. 2009;5(7):1312-1319.
149. Elbert DL. Bottom-up tissue engineering. Current Opinion in Biotechnology. 2011;22(5):674-680.
150. Khademhosseini A, Langer R. Microengineered hydrogels for tissue engineering. Biomaterials. 2007;28(34):5087-5092.
151. Du Y, Lo E, Ali S, Khademhosseini A. Directed assembly of cell-laden microgels for fabrication of 3D tissue constructs. Proceedings of the National Academy of Sciences. 2008;105(28):9522-9527.
152. Rivron NC, Rouwkema J, Truckenmüller R, Karperien M, De Boer J, Van Blitterswijk CA. Tissue assembly and organization: developmental mechanisms in microfabricated tissues. Biomaterials. 2009;30(28):4851-4858.
153. Tiruvannamalai-Annamalai R, Armant DR, Matthew HW. A glycosaminoglycan based, modular tissue scaffold system for rapid assembly of perfusable, high cell density, engineered tissues. PLOS ONE. 2014;9(1):e84287.

154. Mironov V, Trusk T, Kasyanov V, Little S, Swaja R, Markwald R. Biofabrication: a 21st century manufacturing paradigm. Biofabrication. 2009;1(2):022001.
155. Groll J, Boland T, Blunk T, Burdick JA, Cho D-W, Dalton PD, Derby B, Forgacs G, Li Q, Mironov VA. Biofabrication: reappraising the definition of an evolving field. Biofabrication. 2016;8(1):013001.
156. Nahmias Y, Schwartz RE, Verfaillie CM, Odde DJ. Laser-guided direct writing for three-dimensional tissue engineering. Biotechnology and Bioengineering. 2005;92(2):129-136.
157. Murphy SV, Atala A. 3D bioprinting of tissues and organs. Nature biotechnology. 2014;32(8):773-785.
158. Odde DJ, Renn MJ. Laser-guided direct writing of living cells. Biotechnology and Bioengineering. 2000;67(3):312-318.
159. Cui X, Dean D, Ruggeri ZM, Boland T. Cell damage evaluation of thermal inkjet printed chinese hamster ovary cells. Biotechnology and bioengineering. 2010;106(6):963-969.
160. Derby B. Bioprinting: inkjet printing proteins and hybrid cell-containing materials and structures. Journal of Materials Chemistry. 2008;18(47):5717-5721.
161. Calvert P. Inkjet printing for materials and devices. Chemistry of Materials. 2001;13(10):3299-3305.
162. Xu T, Jin J, Gregory C, Hickman JJ, Boland T. Inkjet printing of viable mammalian cells. Biomaterials. 2005;26(1):93-99.
163. Lim KS, Schon BS, Mekhileri NV, Brown GC, Chia CM, Prabakar S, Hooper GJ, Woodfield TB. New visible-light photoinitiating system for improved print fidelity in gelatin-based bioinks. ACS Biomaterials Science & Engineering. 2016;2(10):1752-1762.
164. Ji S, Guvendiren M. Recent advances in bioink design for 3D bioprinting of tissues and organs. Frontiers in Bioengineering and Biotechnology. 2017;5.
165. Hölzl K, Lin S, Tytgat L, Van Vlierberghe S, Gu L, Ovsianikov A. Bioink properties before, during and after 3D bioprinting. Biofabrication. 2016;8(3):032002.
166. Park SA, Lee SH, Kim WD. Fabrication of porous polycaprolactone/hydroxyapatite (PCL/HA) blend scaffolds using a 3D plotting system for bone tissue engineering. Bioprocess and Biosystems Engineering. 2011;34(4):505-513.
167. Peltola SM, Melchels FP, Grijpma DW, Kellomäki M. A review of rapid prototyping techniques for tissue engineering purposes. Annals of Medicine. 2008;40(4):268-280.
168. Schuurman W, Khristov V, Pot M, Van Weeren P, Dhert W, Malda J. Bioprinting of hybrid tissue constructs with tailorable mechanical properties. Biofabrication. 2011;3(2):021001.
169. Boere KW, Visser J, Seyednejad H, Rahimian S, Gawlitta D, Van Steenbergen MJ, Dhert WJ, Hennink WE, Vermonden T, Malda J. Covalent attachment of a three-dimensionally printed thermoplast to a gelatin hydrogel for mechanically enhanced cartilage constructs. Acta Biomaterialia. 2014;10(6):2602-2611.
170. Kang H-W, Lee SJ, Ko IK, Kengla C, Yoo JJ, Atala A. A 3D bioprinting system to produce human-scale tissue constructs with structural integrity. Nature Biotechnology. 2016;34(3):312-319.
171. Zhang K, Fu Q, Yoo J, Chen X, Chandra P, Mo X, Song L, Atala A, Zhao W. 3D bioprinting of urethra with PCL/PLCL blend and dual autologous cells in fibrin

hydrogel: an in vitro evaluation of biomimetic mechanical property and cell growth environment. Acta Biomaterialia. 2016.
172. Xu T, Binder KW, Albanna MZ, Dice D, Zhao W, Yoo JJ, Atala A. Hybrid printing of mechanically and biologically improved constructs for cartilage tissue engineering applications. Biofabrication. 2012;5(1):015001.
173. Cornock R, Beirne S, Thompson B, Wallace G. Coaxial additive manufacture of biomaterial composite scaffolds for tissue engineering. Biofabrication. 2014;6(2):025002.
174. Kim BS, Jang J, Chae S, Gao G, Kong J-S, Ahn M, Cho D-W. Three-dimensional bioprinting of cell-laden constructs with polycaprolactone protective layers for using various thermoplastic polymers. Biofabrication. 2016;8(3):035013.
175. Mironov V, Reis N, Derby B. Review: bioprinting: a beginning. Tissue Engineering. 2006;12(4):631-634.
176. Mironov V, Visconti RP, Kasyanov V, Forgacs G, Drake CJ, Markwald RR. Organ printing: Tissue spheroids as building blocks. Biomaterials. 2009;30(12):2164-2174.
177. Bruzewicz DA, McGuigan AP, Whitesides GM. Fabrication of a modular tissue construct in a microfluidic chip. Lab on a Chip. 2008;8(5):663-671.
178. Kelm JM, Lorber V, Snedeker JG, Schmidt D, Broggini-Tenzer A, Weisstanner M, Odermatt B, Mol A, Zünd G, Hoerstrup SP. A novel concept for scaffold-free vessel tissue engineering: self-assembly of microtissue building blocks. Journal of Biotechnology. 2010;148(1):46-55.
179. Kelm JM, Djonov V, Ittner LM, Fluri D, Born W, Hoerstrup SP, Fussenegger M. Design of custom-shaped vascularized tissues using microtissue spheroids as minimal building units. Tissue Engineering. 2006;12(8):2151-2160.
180. Shimizu T, Sekine H, Isoi Y, Yamato M, Kikuchi A, Okano T. Long-term survival and growth of pulsatile myocardial tissue grafts engineered by the layering of cardiomyocyte sheets. Tissue Engineering. 2006;12(3):499-507.
181. Leung BM, Sefton MV. A modular approach to cardiac tissue engineering. Tissue Engineering Part A. 2010;16(10):3207-3218.
182. Chen M, Wang X, Ye Z, Zhang Y, Zhou Y, Tan W-S. A modular approach to the engineering of a centimeter-sized bone tissue construct with human amniotic mesenchymal stem cells-laden microcarriers. Biomaterials. 2011;32(30):7532-7542.
183. Dikina AD, Strobel HA, Lai BP, Rolle MW, Alsberg E. Engineered cartilaginous tubes for tracheal tissue replacement via self-assembly and fusion of human mesenchymal stem cell constructs. Biomaterials. 2015;52:452-462.
184. Imparato G, Urciuolo F, Casale C, Netti PA. The role of microscaffold properties in controlling the collagen assembly in 3D dermis equivalent using modular tissue engineering. Biomaterials. 2013;34(32):7851-7861.
185. Pang Y, Montagne K, Shinohara M, Komori K, Sakai Y. Liver tissue engineering based on aggregate assembly: efficient formation of endothelialized rat hepatocyte aggregates and their immobilization with biodegradable fibresThis work was presented at the International Conference on Biofabrication (Toyama, Japan, 6–8 October 2011). Biofabrication. 2012;4(4):045004.
186. Babur BK, Futrega K, Lott WB, Klein TJ, Cooper-White J, Doran MR. High-throughput bone and cartilage micropellet manufacture, followed by assembly of micropellets into biphasic osteochondral tissue. Cell and Tissue Research. 2015;361(3):755-768.

187. Hannachi IE, Yamato M, Okano T. Cell sheet technology and cell patterning for biofabrication. Biofabrication. 2009;1(2):022002.
188. Kelm JM, Djonov V, Ittner LM, Fluri D, Born W, Hoerstrup SP, Fussenegger M. Design of custom-shaped vascularized tissues using microtissue spheroids as minimal building units. Tissue Engineering. 2006;12(8):2151-60.
189. Yeh J, Ling Y, Karp JM, Gantz J, Chandawarkar A, Eng G, Blumling J, 3rd, Langer R, Khademhosseini A. Micromolding of shape-controlled, harvestable cell-laden hydrogels. Biomaterials. 2006;27(31):5391-8.
190. Young C, Rozario K, Serra C, Poole-Warren L, Martens P. Poly (vinyl alcohol)-heparin biosynthetic microspheres produced by microfluidics and ultraviolet photopolymerisation. Biomicrofluidics. 2013;7(4):044109.
191. McGuigan AP, Sefton MV. Vascularized organoid engineered by modular assembly enables blood perfusion. Proceedings of the National Academy of Sciences. 2006;103(31):11461-11466.
192. Yeh J, Ling Y, Karp JM, Gantz J, Chandawarkar A, Eng G, Blumling Iii J, Langer R, Khademhosseini A. Micromolding of shape-controlled, harvestable cell-laden hydrogels. Biomaterials. 2006;27(31):5391-5398.
193. Caldwell DJ, Rao RR, Stegemann JP. Assembly of discrete collagen–chitosan microenvironments into multiphase tissue constructs. Advanced Healthcare Materials. 2013;2(5):673-677.
194. Tung YC, Hsiao AY, Allen SG, Torisawa YS, Ho M, Takayama S. High-throughput 3D spheroid culture and drug testing using a 384 hanging drop array. Analyst. 2011;136(3):473-8.
195. Carlsson J, Yuhas J. Liquid-overlay culture of cellular spheroids. in Spheroids in Cancer Research: Springer; 1984. p. 1-23.
196. Yuhas JM, Li AP, Martinez AO, Ladman AJ. A simplified method for production and growth of multicellular tumor spheroids. Cancer Research. 1977;37(10):3639-3643.
197. Fukuda J, Khademhosseini A, Yeo Y, Yang X, Yeh J, Eng G, Blumling J, Wang C-F, Kohane DS, Langer R. Micromolding of photocrosslinkable chitosan hydrogel for spheroid microarray and co-cultures. Biomaterials. 2006;27(30):5259-5267.
198. Ingram M, Techy G, Saroufeem R, Yazan O, Narayan K, Goodwin T, Spaulding G. Three-dimensional growth patterns of various human tumor cell lines in simulated microgravity of a NASA bioreactor. In Vitro Cellular & Developmental Biology-Animal. 1997;33(6):459-466.
199. Young CJ, Poole-Warren LA, Martens PJ. Combining submerged electrospray and UV photopolymerization for production of synthetic hydrogel microspheres for cell encapsulation. Biotechnology and Bioengineering. 2012;109(6):1561-1570.
200. Hahn MS, Miller JS, West JL. Three-dimensional biochemical and biomechanical patterning of hydrogels for guiding cell behavior. Advanced Materials. 2006;18(20):2679-2684.
201. Cohen S, Yoshioka T, Lucarelli M, Hwang LH, Langer R. Controlled delivery systems for proteins based on poly (lactic/glycolic acid) microspheres. Pharmaceutical Research. 1991;8(6):713-720.
202. Prüße U, Dalluhn J, Breford J, Vorlop KD. Production of spherical beads by JetCutting. Chemical Engineering & Technology. 2000;23(12):1105-1110.
203. Brandenberger HR, Widmer F. Immobilization of highly concentrated cell suspensions using the laminar jet breakup technique. Biotechnology Progress. 1999;15(3):366-372.

204. Bugarski B, Li Q, Goosen MF, Poncelet D, Neufeld RJ, Vunjak G. Electrostatic droplet generation: mechanism of polymer droplet formation. AIChE Journal. 1994;40(6):1026-1031.
205. Rago AP, Dean DM, Morgan JR. Controlling cell position in complex heterotypic 3D microtissues by tissue fusion. Biotechnology and Bioengineering. 2009;102(4):1231-41.
206. Inamori M, Mizumoto H, Kajiwara T. Investigation of medium perfusion through scaffold-free tissue constructs using endothelial cell-covered spheroids in vitro. Biochemical Engineering Journal. 2010;50(3):116-121.
207. Zuo Y, Liu X, Wei D, Sun J, Xiao W, Zhao H, Guo L, Wei Q, Fan H, Zhang X. Photo-cross-linkable methacrylated gelatin and hydroxyapatite hybrid hydrogel for modularly engineering biomimetic osteon. ACS Applied Materials & Interfaces. 2015;7(19):10386-10394.
208. Ozbolat IT, Chen H, Yu Y. Development of 'Multi-arm Bioprinter'for hybrid biofabrication of tissue engineering constructs. Robotics and Computer-Integrated Manufacturing. 2014;30(3):295-304.
209. Schon B, Hooper G, Woodfield T. Modular tissue assembly strategies for biofabrication of engineered cartilage. Annals of Biomedical Engineering. 2016:1-15.

Chapter 3 Development of an integrated system for automated 3D Bioassembly

3.1 Abstract

Presently there exist few technologies that can precisely assemble spherical tissue units (TU, micro-tissues or hydrogel microspheres) into a 3D plotted scaffold. We developed a novel automated and integrated 3D Bioassembly system capable of assembling tissue units into a 3D plotted scaffold. The developed automated bioassembly system consisted primarily of a singularisation module and an injection module. The singularisation module was designed to deliver one tissue unit at a time to the injection module. The injection module was designed to insert the tissue units into the pores of the 3D plotted scaffold with the aid of a 3D positioning system. The mechanical and electronic systems required for the functioning of the fluidics-based automated bioassembly system were designed and manufactured and a prototype of the bioassembly system was successfully constructed and integrated with a commercial Bioscaffolder. The developed prototype would allow us to validate the potential of an automated bioassembly system for application in cartilage engineering and tumour engineering.

3.2 Introduction

Many international tissue engineering centres focus primarily on the biology of tissue culture rather than process engineering and product realization, and this has led to tissue engineering currently being in an inconvenient position to transit from a development-stage industry to a full-fledged one [1]. Automated robotic approaches have been important in the successful development of new commercially profitable automobile and microelectronic industries and would also be highly beneficial to the regenerative medicine and tissue engineering industry [2]. Presently, the development and investigation of tissue engineered constructs are in its early stages. The development of bioassembly technologies would not only benefit current research but would help in laying out the manufacturing process for tissue engineered products. It would also be quite advantageous to address

manufacturing processes way earlier than during the commercialisation phase as a tissue engineered product created via a new manufacturing process might require regulatory reapproval [1]. Likewise, platform technologies developed for tissue engineering can be translated for application in tumour engineering as similar challenges exist [3]. The utilisation of an automated bioassembly system would reduce production variations due to the elimination of human error, would be cheaper and cost-effective as a result of less human involvement, would be easier for large-scale production of complex designs and would provide the necessary level of flexibility for patient-specific, customized organ biofabrication [2, 4]. For the bioassembly technology to become a reality, the design and implementation of an automated system would be the first step, after which the advantages of the developed biofabrication strategy over existing strategies would have to be demonstrated.

A detailed literature search revealed that automated bioassembly technology is still in its infancy, so similar technology that can be translated or adapted for applications in bioassembly was looked into. This included separation and delivery. Much of the developed technology related to the separation of bioparticles was targeted more at single cells separation rather than larger bioparticles. Nomura *at al.* demonstrated a fully automated on-chip imaging flow cytometry system using a micro-fluidic based non-destructive cell-sorting system [5]. Grover *et al.* showed single-cell sorting based on optical trapping and manipulation [6]. Huang *et al.* demonstrated a biochip that can catch, separate and transport bioparticles using dielectrophoretic forces created by non-uniform electric fields [7]. Freyer *et al.* took this one step further and modified a fluorescence-activated cell sorting (FACS) instrument to demonstrate the sorting of multicellular spheroids into uniformly-sized populations with diameters in the range of 50-100 μm [8].

Though there has been not much literature relating to the technology for the separation or singularisation of particles, there has been development relating to the automated production of micro-tissues. The automated production of a variety of micro-tissues for efficacy testing in a standard 96-well format was shown by Drewitz *et al.* [9]. Rezende *et al.* presented data showing that the scalable robotic biofabrication of tissue spheroids is technologically feasible [10]. Tung *et al.* used

liquid handling robots to culture spheroid utilising the traditionally tedious hanging drop technique [11].

Tanol *et al.* and Ozbolat *et al.* developed the two closest technologies that employed spheroids in bioprinting. Tanol *et al.* developed a 3D printing technology to deposit microdroplets of alginate solution on calcium-containing substrates in a layer-by-layer fashion to prepare ring-shaped 3D hydrogel moulds [12]. Ozbolat *et al.* developed a system where a cell-laden alginate scaffold was 3D plotted with a co-axial nozzle and cell-laden alginate spheres that formed at the tip of the dispensing nozzle were deposited within the scaffold [13]. Currently, to our knowledge, there exists no technique or system that can handle macro-sized particles or spherical tissue units (TU, micro-tissues or microspheres) for applications in bioassembly or bioprinting.

To fill in this gap that exists presently in the area of bioassembly, we looked into developing a prototype of an automated tissue assembly system, which is the specific aim of this chapter. Presently, 3D Bioprinters or Bioscaffolders have already the capability to 3D plot biodegradable scaffolds, and essentially to complete the system, all that was needed was a device that can insert tissue units into the pores of the 3D plotted scaffold.

It was crucial and imperative that the designed system included the following aspects: (i) it should be able to insert a spherical tissue unit into the desired pore of the 3D plotted scaffold, (ii) the mechanical stress on the tissue unit while the system is handling it should be as low as possible to avoid destructive effects on the cells in the tissue units, (iii) the tissue units should always be hydrated to prevent drying of the cells which would otherwise have an adverse effects on the cells, (iv) the system should be able to handle slight variations in tissue unit diameter and (v) the system should be capable integration with the Bioscaffolder, and (vi) the system should be capable of handling tissue units with a range of stiffnesses and densities.

Previously Lang *et al.* investigated a mechanical-based and a fluidics-based tissue handling system [14-16]. However, the mechanical based tissue handling system was shown to damage the tested alginate beads [14, 15]. Therefore, a

comparatively gentle fluidics-based system that handles tissue units by varying the hydrodynamic forces was thought would make a more fitting design for an automated bioassembly system [15]. Moreover, the fluid in the fluid system would be able to keep the tissue units in a hydrated environment. The design of an automated bioassembly system involved the development of a system consisting of: (i) a singularisation module that can take up a large number of engineered spherical tissue units and then deliver a tissue unit individually at a time to the injection module, and (ii) an injection module which can seed the tissue unit into a predetermined pore within the 3D plotted scaffold with the aid of a 3D positioning system.

The development of this system was made with the intention that it would be able to handle various types of spheroid-based tissue units primarily for application in cartilage engineering and tumour engineering. With regards to cartilage engineering, the tissue units would include micro-tissues formed with chondrocytes or chondroprogenitor cells or hydrogel microspheres encapsulated with chondrocytes or chondroprogenitor cells for fabricating an assembled living construct suitable for clinical implantation. In tumour engineering, the tissue units would include micro-tissues formed from cancer cells or hydrogel microspheres encapsulated with cancer cells for fabricating a cancer construct which could be utilised for application in translational research in cancer and/or for high-throughput screening (HTS) of drugs.

The specific objective of this chapter was the design and development of a prototype automated 3D bioassembly technology capable of biofabricating tissue engineered constructs. This involved (i) the design and fabrication of the mechanical and electrical components of the fluidics-based automated bioassembly system, (ii) programming of the control module, (iii) assembly and construction of the components of the automated bioassembly system together, and (iv) the calibration of the prototype automated 3D bioassembly technology.

3.3 Methods

The automated bioassembly system consisted mainly of a singularisation module (delivers one tissue unit at a time) and an injection module (delivers the

singularised tissue unit into a predetermined pore within the 3D plotted scaffold) which was assembled to create the tissue unit injection head. The primary mechanical components (the singularisation chamber, pressure tanks and the injection system), the control system components (hardware and software), the tissue unit sensor, the Bioscaffolder-singularisation device communication and the assembly of the tissue unit injection head are described here in the methods section. Work performed previously by Lang *et al.* [14-16] on the automated bioassembly system included: (i) the design and fabrication of the mechanical components of the fluidics-based singularisation system and injection system and (ii) the validation of the singularisation and injection process. Existing components from the previous work which included (i) the singularisation chamber and (ii) the primary components of the injection system were reused here. The remaining components of the prototype were newly fabricated.

3.3.1 Singularisation chamber

The singularisation chamber was where the singularisation process (i.e. the process whereby one tissue unit is released at a time from a collection of tissue units) took place through the manipulation of the hydrodynamic forces within the chamber. The singularisation chamber was fabricated from a polycarbonate block using conventional machining techniques. See Appendix 3.A for mechanical design. Polycarbonate was selected, as the material allows the economical fabrication of the singularisation chamber utilising conventional machining techniques. Moreover, polycarbonate has a higher resistance to ethanol (for sterilisation of the system) compared to materials such as Poly(methyl methacrylate)(PMMA). The work on the singularisation device was based on previous work conducted by Lang *et al.* [14-16]. The block consists of three small vertical ports and a horizontal main chamber (see Figure 3-1). The horizontal main chamber was sized to a diameter of 1.3 mm so that it accommodated tissue units with a diameter of approximately 1 mm. The vertical channels were designed to be 0.7 mm in diameter so that the tissue units did not enter the port but the port was big enough to hold the tissue units in position. The vertical pressure ports – flush port 1, flush port 2 and capture port were fluidically connected to electronically regulated pressure tanks. The fluidic pressure in the vertical pressure ports was controlled by switching ON/OFF the five fluid isolation micro solenoid valves (ASCO Numatics, USA) - hopper valve (H), flush valve 1 (F1),

flush valve 2 (F2), capture port pressure valve (CP) and capture port vacuum valve (CV) (see Figure 3-1). The relative position of the flush port 1 and the capture port was such that when a tissue unit was captured at the capture port, the occurrence of dead volume between the two ports where another tissue unit could potentially be trapped in between the space was minimised. A pinch valve (Sirai, Italy) located downstream from the singularisation chamber not only aided in the control of the hydrodynamic forces but also acted as a gate that allowed the singularised tissue unit to pass through to the injection system. The piping and instrumentation diagram of the singularisation device is shown in Figure 3-2. For a more detailed diagram see Appendix 3.B.

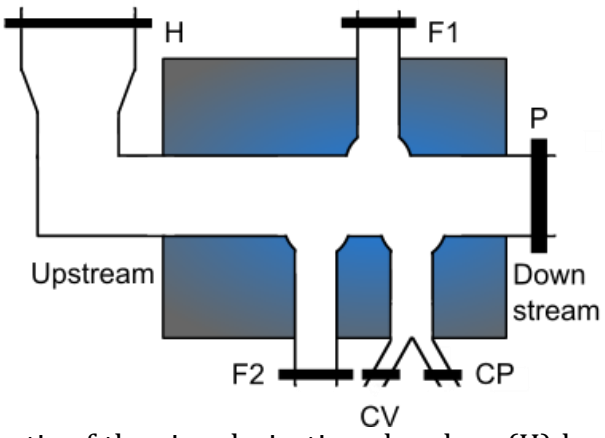

Figure 3-1. Schematic of the singularisation chamber. (H) hopper valve, (F1) flush valve 1, (F2) flush valve 2, (P) pinch valve, (CP) capture port pressure valve and (CV) capture port vacuum valve.

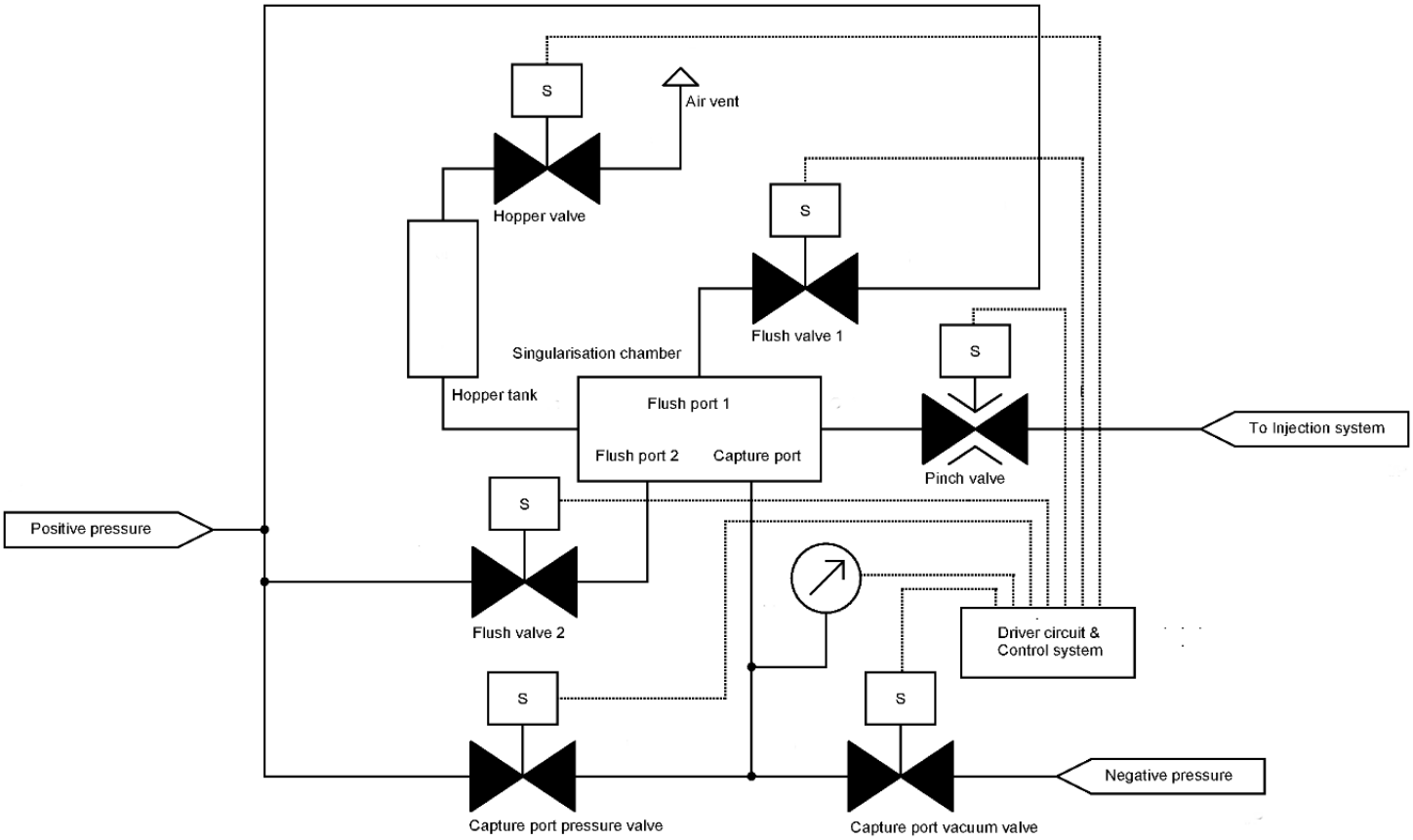

Figure 3-2. Piping and instrumentation diagram showing the layout of the singularisation chamber.

The tubing was coupled to the horizontal main chamber of the singularisation chamber using a flangeless ferrules system (VICI Jour, Canada). The flangeless ferrules system was utilised to ensure a relatively seamless constant inner diameter connection, and to accurately position the tubing. Stainless steel connectors were utilised to connect the tubing to the vertical ports of the singularisation chamber and to the fluidic valves. White nylon luer lock or barb connectors (Nordson medicals, USA) were used for the remaining connections. The fluidic connections were made utilising 1.6 x 3.2 mm flexible Tygon tubing (Saint-Gobain, USA). For the pinch valve section that ran downstream from the exit of the singularisation device to the injection device traversing the pinch valve, 1.6 x 3.2 mm flexible Tygon tubing (Cole-Parmer, USA) compatible with the pinch valve was used. For the fluidic connections to the inlet and outlet of the positive pressure tank and the inlet of the negative pressure tank, polyurethane tubing (Festo, Germany) sized 6 x 8 mm tubing was used. The polyurethane tubing was connected using push-in connectors (Festo, Germany).

3.3.2 Pressure tanks

The manipulation of the tissue unit was performed by varying the hydrodynamic forces within the singularisation chamber. The hydrodynamic forces were varied by switching ON/OFF valves supplying pressurised fluid from the pressure tanks to the singularisation chamber. To supply fluid of different pressures to the singularisation chamber, two electronically regulated pressure tanks were designed - a positive pressure tank and a negative pressure tank. The positive and negative pressure tanks were positive and negative relative to atmospheric pressure. The piping and instrumentation diagram is shown in Figure 3-3. For the positive pressure tank, compressed air line of set pressure (7 bars) was connected to the inlet of the tank. The pressure sensor measures the pressure in the tank and proportional valves (Clippard, USA) which act as release valves were opened as needed by the control system to regulate the pressure in the tank and to obtain the desired set pressure. For the negative pressure tank, a vacuum ejector converts the compressed air line into vacuum. The proportional valves were fed by the output of the vacuum ejector, and the valve was proportionally opened by the control system to maintain the desired vacuum in the tank. The system was controlled by a LabVIEW PID algorithm virtual instrument.

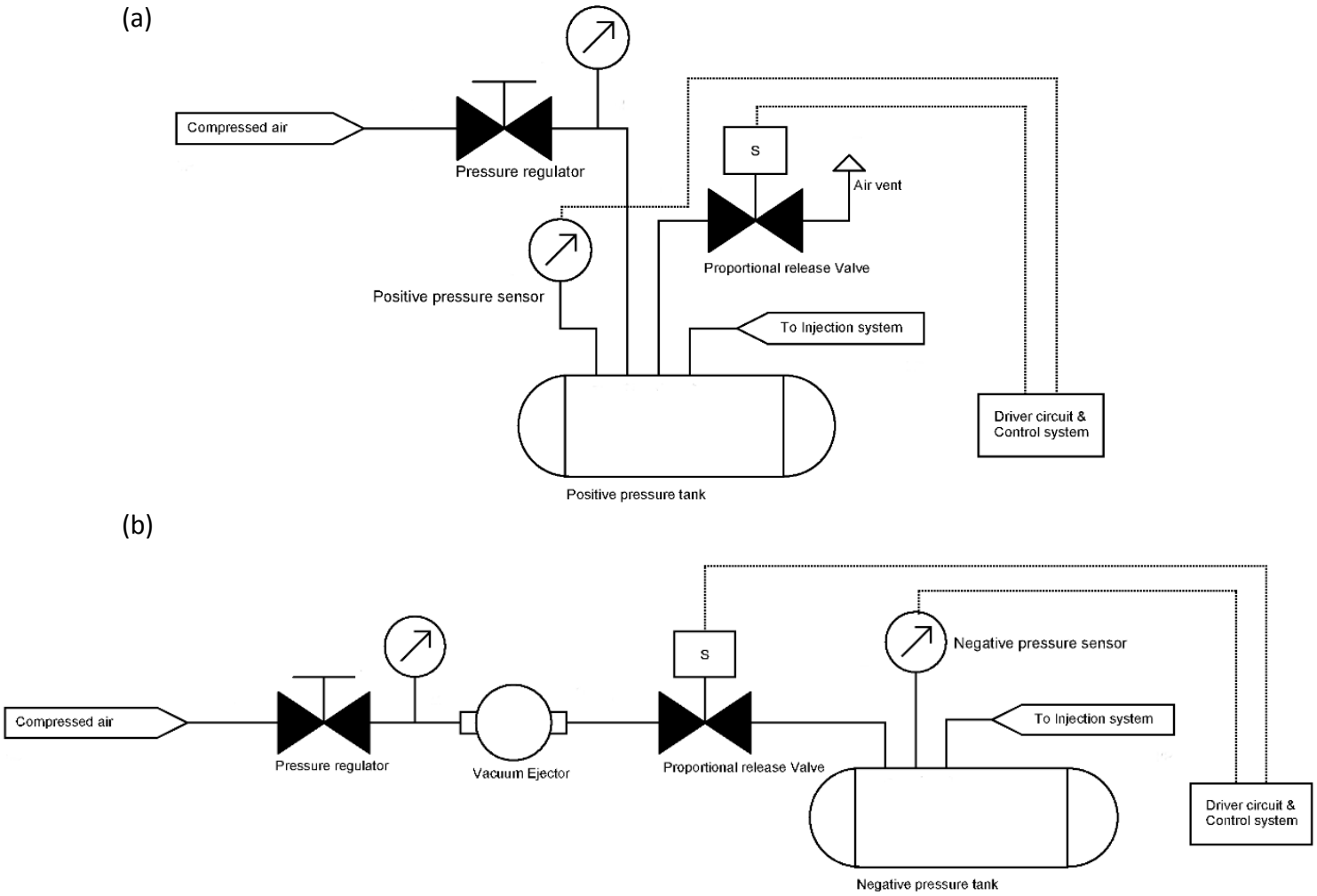

Figure 3-3. Piping and instrumentation diagram showing the layout of the (a) positive and (b) negative pressure tanks.

3.3.3 Injection system

The injection system was designed to insert tissue units into the pores of a 3D plotted scaffold with the aid of a 3D positioning system. The injection system consisted primarily of a nozzle and an expanding rod. The expanding rod was mechanically attached to a solenoid controlled by the singularisation and injection system control module. The downward movement of the expanding rod was designed to aid the movement of the tissue unit and to help in press fitting the tissue unit into the pore of the 3D plotted scaffold. The expanding rod also helps to maintain a smooth profile for the nozzle so that the nozzle does not damage the scaffold fibres during the injection process and also the expanding rod protects the nozzle during the placement of the nozzle on the 3D plotted scaffold fibre. The nozzle was designed to have an inner diameter of 1.06 mm so that it could accommodate

tissue units with a diameter of 1 mm. The remaining components that made up the injection system were for the support of the functional components. For the primary components of the injection system and assembly refer Appendix 3.A. The components of the injection system were machined using either 316 Stainless steel or 7075 Aluminium.

3.3.4 Hardware development of the control module

The core of the control module consisted of the National Instruments myRIO-1900 which is a portable reconfigurable I/O (RIO) device that can be graphically programmed. As the output lines of myRIO had a low output voltage and amperage, driver circuits were essential to power the solenoids in the system. The driver circuits were designed keeping in mind the operating voltage and amperage of the various components and were electrically isolated if required. Power MOSFET (International Rectifier) based driver circuits were wired to run the fixed input voltage injection solenoid and fluid isolation micro solenoid valves. High-Voltage, High-Current Operational Amplifier (Texas Instruments, USA) based driver circuits were rigged to power the variable input voltage proportional valves. The signals from the singularisation chamber and tank pressure sensors (Freescale Semiconductor, USA) were amplified using instrument amplifiers (Texas Instruments, USA) and inputted to the myRIO. A potentiometer was used to set the gain of the instrument amplifier for the singularisation chamber pressure sensor so that the gain could be adjusted if required. The photomicrosensor (Omron, Japan) to detect singularised tissue units was biased and the output signal was inputted to the myRIO. Two one-way communication signal lines, a myRIO to Bioscaffolder line and a Bioscaffolder to myRIO line linked the Bioscaffolder with the myRIO. The communication signal lines were optically isolated and keeping in consideration the different operating voltages (Bioscaffolder – 24 V and myRIO – 5/3.3 V). The hardware circuitries were all fabricated on stripboards. Refer Appendix 3.C for all circuit diagrams and connections. After the hardware was set up, we proceeded to program the system.

3.3.5 Software development of the control module

The myRIO was programmed using LabVIEW. Standard LabVIEW programs or subroutines called virtual instruments were used to program/rig up the virtual

control circuit. The front panel of LabVIEW program consisted of controls (input) and indicators (output) defined by the programmer and was controlled and viewed by the user via a personal computer (PC). Whereas the back panel of LabVIEW program contained the graphical source code.

The LabVIEW virtual instrument that controlled the automated system was programmed so that it consisted of independent sections that ran in parallel to ensure smooth running and to eliminate any cross-talk. The independent sections consisted of the virtual circuits for the control systems for the positive and negative tank, control of the fluid isolation valves and the injection solenoids, the photosensor detector and tissue unit counter, and other processes that would aid in the initialisation and efficient working of the system. The circuit was rigged so that default operating values were hardwired through the back panel and relevant operating values could be modified if required by the user through the front panel while the program is running.

For the pressure tank control system, the PID virtual instrument in LabVIEW which is basically a PID algorithm was utilised as a PI controller to control the system. The process variable for the controller was the amplified pressure sensor voltage and the output of the controller was sent to the driver circuit to control the proportional release valves.

The functions of the various controls and indicators in the front panel of the program are explained in detail in the results section.

3.3.6 Tuning of the PI controllers for the pressure tanks

The PID controller virtual instrument in LabVIEW served as the PI controller for the pressure tanks. The PI controller for each pressure tank was manually tuned. First, the proportional gain (K_p) and integral gain (K_i) was set to 0. Then the K_p was increased until the response to a disturbance was a steady oscillation. The value of K_p was set to half this value. The K_i was then increased to correct any offset in sufficient time. After this, the response of the controller was tested by checking the response to a disturbance or change in set-point with the updated gains and the

values were refined so that the control system worked with the response that we desired.

3.3.7 Tissue unit sensor

The output tubing of the singularisation device carrying the tissue unit to the injection system was made to transverse through a transmissive photomicrosensor. The photomicrosensor (Omron, Japan) circuit, was designed and biased so that every time a tissue unit passed through the sensor, there was a change in the output voltage. To detect a tissue unit and to differentiate it from the background noise caused by the flow of liquid through the tubing, the output voltage was sampled every 200 ms and a value of 0.6 V was added to the average of the last 10 samples, this value was calculated to be the baseline voltage. Whenever the continuously sampled photosensor voltage increased above this baseline voltage, the system would recognise that a tissue unit had passed through.

3.3.8 Communications

Communication between the Bioscaffolder and the myRIO was to be achieved using two lines - Bioscaffolder ready flag (BRF) and a singularisation device ready flag (SRF). When the Bioscaffolder is in position and ready, the next G-code in the Bioscaffolder would then turn the BRF high and wait, this would indicate to the singularisation device that it should begin the cycle of singularisation and injection. After the singularisation and injection process has been completed, the singularisation device would switch the SRF flag high indicating to the Bioscaffolder that it can proceed to the next line of the G-code. Both flags would turn low after a fixed time. For the detailed schematic of the communication, circuits refer Appendix 3.C. The circuit was designed so that the Bioscaffolder and myRIO were optically isolated to avoid any power surges. Although the communication lines between Bioscaffolder and the myRIO were designed and made ready, they could not be interconnected to each other as the manufacturers of the Bioscaffolder had not yet provided us with the architecture of the input and output interface.

3.3.9 Tissue unit injection head

The low-temperature head of the commercial Bioscaffolder (SYS ENG, Germany) was modified so that the injection system could be mounted on it, after which the singularisation system was rigged onto it. The tissue unit injection head

assembly primarily consisted of the singularisation chamber, the injection assembly and solenoid, the singularisation chamber sensor and circuitry, the fluid isolation and pinch valves, and the photosensor circuit to detect the singularised tissue unit. Detachable electric and fluidic lines linked the pressure tanks and circuits located outside the Bioscaffolder to the tissue unit injection head. The system was calibrated so that the length of the new lines was taken into account.

3.4 Results and Discussion

3.4.1 Overall design

The block diagram overview of the whole bioassembly system is illustrated in Figure 3-4. The bioassembly system can be divided into two sections, the Bioscaffolder – around which the whole system is centred – and the singularisation and injection system. The Bioscaffolder is essentially an additive manufacturing device that can generate a physical 3D structure by a layer-by-layer extrusion process. The Bioscaffolder was controlled by the user using the Bioscaffolder program which runs on a PC. Designed CAD files that describe surface geometry of a 3D object such as an STL file was inputted into the Bioscaffolder program with the desired and/or optimised print parameters. The Bioscaffolder program converts the STL file and print parameters into G code (a numerical control programming language for automated machines). Complete control of the polymer deposition head to print a polymer-based scaffold can be executed using this approach. The tissue unit injection head was also positioned in space by the Bioscaffolder's 3D positioning system. The Bioscaffolder has a tool changing system by which the polymer deposition head or the tissue unit injection head can be loaded onto the Bioscaffolder's 3D positioning system and this was controlled by G codes. The 3D positioning system allows movement in X, Y and Z direction enabling control in the three dimensions with a positional and repositioning accuracy of 0.05 mm. As an algorithm for the G-code generation for the tissue unit injection head has yet to be developed, the G-code to control the tissue unit injection head was written by the user. The primary components of the tissue unit injection head – the singularisation and injection system was controlled by an external control module consisting of a myRIO embedded design device and driver circuits to power the components of the system. The Bioscaffolder and the myRIO were linked with communication lines.

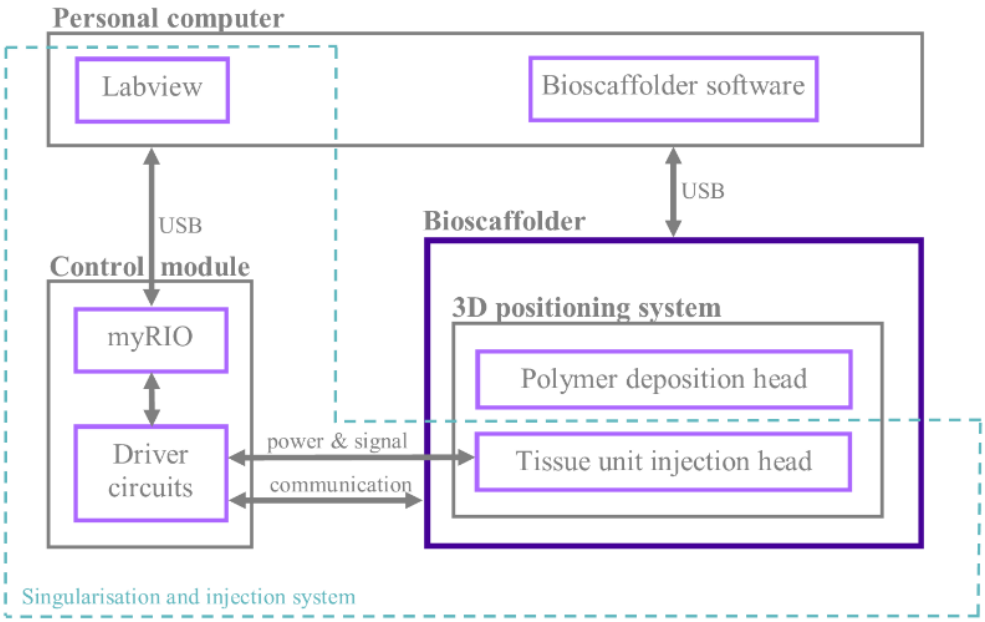

Figure 3-4. The block diagram overview of the whole bioassembly system.

3.4.2 Singularisation chamber

The primary function of the singularisation device was to deliver a single tissue unit at a time to allow complex 3D Bioassembly of tissue units in a layer-by-layer process. The fundamental component of the singularisation system, where the whole singularisation process takes place is the singularisation chamber. The singularisation system was designed to work in a way that it would first try and capture a tissue unit from a train of tissue units that are stored upstream in a tank. Next, the uncaptured tissue units were sent back upstream into the tank and the single captured tissue unit in the singularisation chamber was released downstream.

The singularisation system was successfully assembled. Preliminary tests showed that spherical tissue units could be successfully singularised. The actual working and validation of the singularisation system are described in the next chapter.

3.4.3 Injection System

The main function of the injection system was to reliably deliver with ease a singularised tissue unit within the pore of a 3D plotted scaffold and to ensure that after the tissue unit had been delivered within the pore it remains securely in place.

For the initial design, the injection system was designed so that when the expanding rod and nozzle together was positioned on the scaffold pore, they would first expand and elastically deform the scaffold fibres (Figure 3-5i a and b). After which, when the expanding rod was retracted (Figure 3-5i c), creating an unimpeded path for the delivery of the tissue unit within the scaffold pore (Figure 5i d and e). The idea behind this was that there would be minimal physical stress exerted on the tissue unit decreasing the likelihood of damaging the cells in the tissue unit. This method of injection had a couple of drawbacks. For example, as the nozzle needed extremely thin walls machining the nozzle was challenging, and although the nozzle could be fabricated, it was structurally delicate and needed extreme care while handling it. Given that the tissue unit needed to have a snug fit in the scaffold, the size of tissue unit or the fibre could not be compromised at the cost of a successful injection device. Furthermore, preliminary trials showed that the scaffold fibres had a tendency to be slightly damaged as the thin wall of the nozzle behaved very similar to a drill punch.

To overcome the above issues, the injection method was modified to a more press fit style (Figure 3-5ii). The nozzle would be placed on the topmost fibre that makes the scaffold pore (Figure 3-5ii a-c) by moving the injection head using the 3D positioning system of the Bioscaffolder. Then the singularisation system would singularise a tissue unit and the expanding rod aided with hydrodynamic forces of the liquid flowing through the nozzle would press fit (Figure 3-5ii d-f) the tissue unit within the predetermined pore of the scaffold. This method of inserting the tissue unit was comparable to the process of manually press fitting a tissue unit into the scaffold. The advantage of utilising the press fit method was also that nozzles with thicker walls could be fabricated if required without affecting the performance of the injection system. The actual operation and validation of the injection system is described in the next chapter.

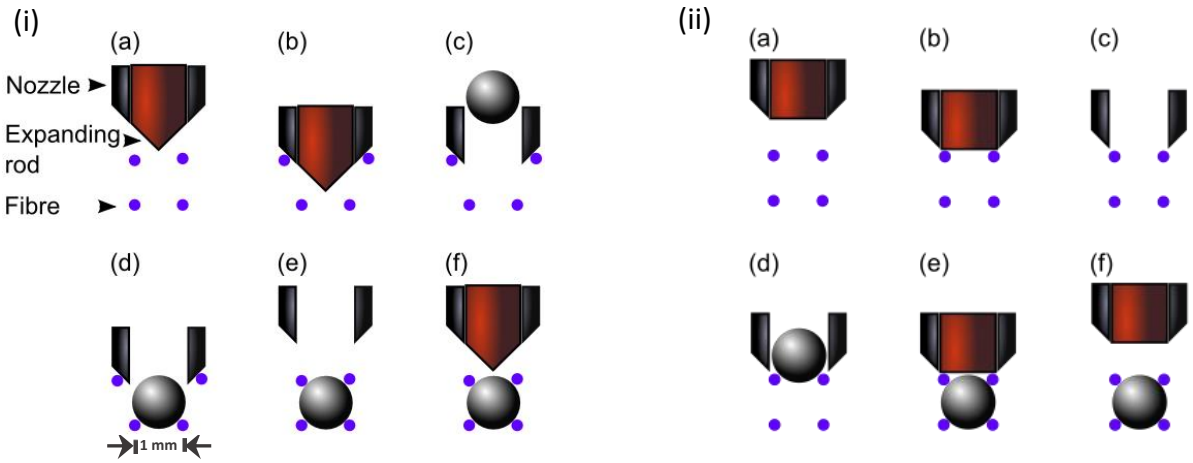

Figure 3-5. The two injection approaches. The (i) elastic deformation based injection concept and (ii) press fit based injection concept

3.4.4 Hardware development of the control module

myRIO was chosen as the core of the control model due to the flexibility in rigging up the hardware, the ease with which it can be graphically programmed and the ability to conveniently modify the timing, control, flow and other required aspects in real-time during the development of the prototype. After the hardware was set up, a simple test to check if the hardware worked as intended was carried out. The driver circuits, when operated by myRIO via LabVIEW, were successful in powering the injection solenoid, the fluid isolation micro solenoid valves and the proportional release valves. LabVIEW via myRIO was able to detect a change in the value of the pressure sensors when a change in pressure at the pressure or vacuum port occurred. The obstruction of the aperture of the photomicrosensor was also detected on LabVIEW via myRIO. The myRIO-Bioscaffolder communication line circuits functioned well, however, the two systems were not linked presently as the hardware blueprint of the various input/output lines of the Bioscaffolder and the corresponding G-codes were not yet available. The whole system was enclosed in a box for protection to make it aesthetically pleasing.

3.4.5 Software development of the control module

The software for myRIO was programmed using LabVIEW - which is a graphical dataflow language. The front panel (Figure 3-6) of the myRIO control

system program that controls the singularisation and injection systems consisted of controls (input) and indicators (output).

The default operating pressure and timing values obtained from preliminary tests were hardwired through the back panel. However, the virtual instrument was programmed such that the hardwired values could be modified by the user if required while the program was still running. This could be done through the front panel by either using the increment/decrement button or entering a desired numerical value in the required data field. The ability to modify the data values was extremely useful while debugging the system or while determining the optimum timing for different types of tissue units.

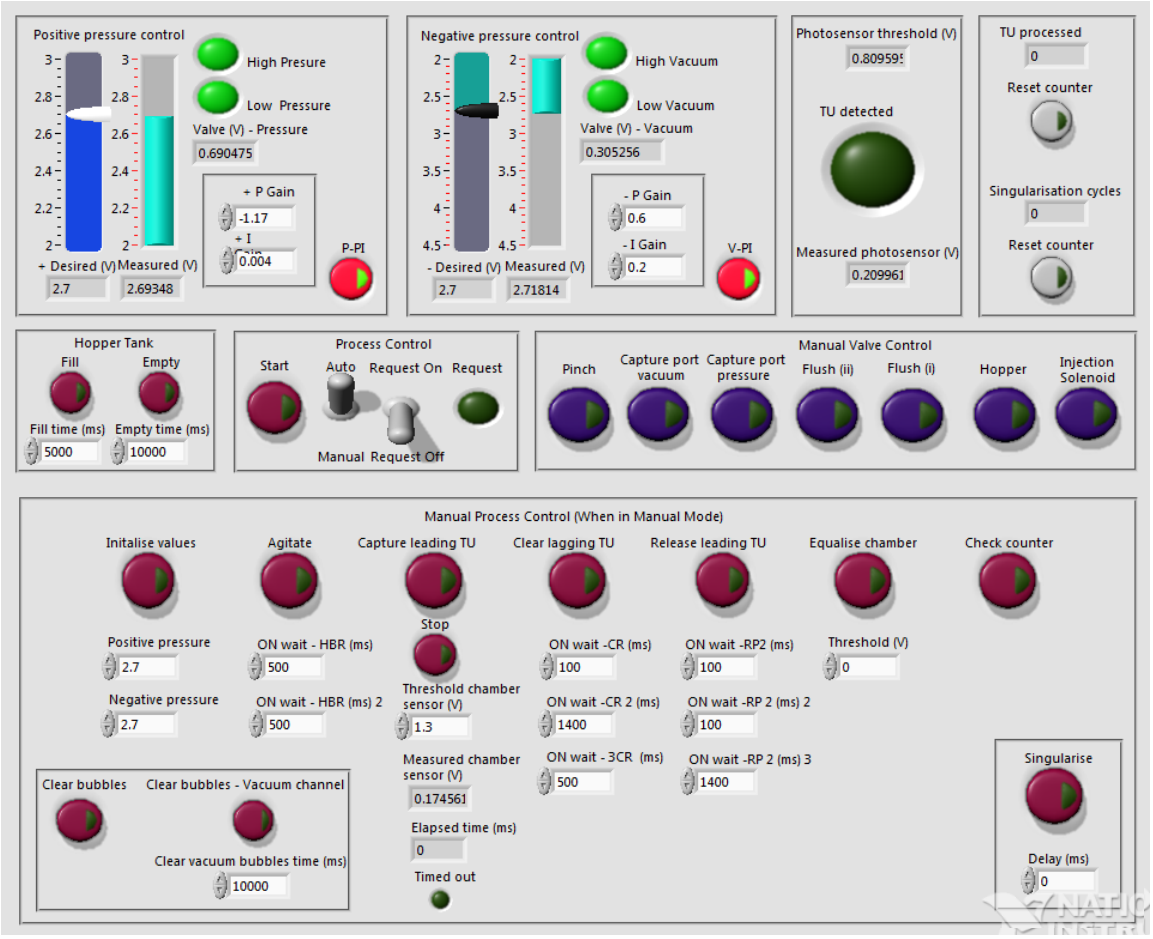

Figure 3-6. Screenshot of the front panel of the myRIO control system that controls the singularisation and injection system.

The functions of all the buttons and indicators in the front panel of the designed program are as described below.

The manual valve controls allow the user to manually control the fluid isolation valves, pinch valve and the injection solenoid.

In the hopper tank section, the fill button increases the fluid level in the hopper tank and the empty button decreases the fluid level in the hopper tank. The fill/empty time could be set so that hopper tank was filled/emptied with a predetermined volume of liquid.

In the process control section, the start button manually starts the singularisation cycle. The auto/man switch could be used to choose either automatic singularisation (normal working) or manuals singularisation. During the singularisation cycle, if the switch was in manual singularisation, the program does not automatically move to the next singularisation step and this was helpful while debugging or optimising the system.

The request ON/OFF switch could be used to choose whether the start of the singularisation cycle was triggered either by the Bioscaffolder via the Bioscaffolder-myRIO communications (BRF line) or manually by the user. When the Bioscaffolder sends a request to myRIO, the request indicator turns ON.

Air bubbles in the singularisation device could inhibit its normal working and could also result in erroneous tissue unit detection by the photomicrosensor. To remove the bubbles, the clear bubbles button switches ON/OFF the valves so that the bubbles in the singularisation device were cleared.

Air bubbles in the line to the negative pressure tank could severely handicap the functioning of the singularisation device and the clear-bubbles – vacuum channel button specifically removes any bubbles in the line to the negative pressure tank.

In the manual process control section, the functions of the buttons are defined so that each button executes each of the steps in the singularisation cycle. The timing for switching ON and OFF the various valves, the pressure of the tanks and the chamber sensor threshold are all wired through the back panel and can be modified

when the program is running through the front panel. In the automatic mode, the buttons are wired so that the 4 primary steps of the singularisation step (Figure 3-7) are executed sequentially.

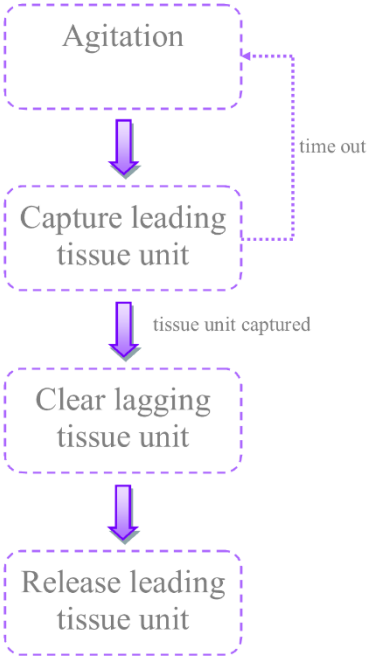

Figure 3-7. Flow diagram of the primary steps in the singularisation cycle.

Agitation – this removes any blockages that might be present in the singularisation chamber and hopper tank, dislodges tissue units stuck to the sides of the hopper tank, and causes the tissue units to float making the singularisation process easier. This step works by sending fluid upstream into the hopper tank through the ports of the singularisation chamber. The agitation was initiated for a set period of time.

Capture leading TU – during this step an attempt was made to try and capture the leading tissue unit at the capture port. This step takes place right after the agitation step so that the tissue units are not very close to each other. An attempt to capture a tissue unit was made by changing the valve sequence so that there was a slight negative pressure at the capture port. If a tissue unit was captured at the captured port, it causes a reduction of pressure at the capture port, which was detected by the singularisation chamber sensor. The singularisation chamber sensor then triggered the clear lagging TU step. If there was a failure to capture a tissue unit at the capture port within the set time, the timeout indicator turns ON

and the agitation step was retriggered. If the capture leading tissue unit and agitation enters an infinite loop, the stop button could be switched ON by the user to break the loop.

Clear lagging TU – by maintaining the negative pressure at the capture port the captured tissue unit is held in place. However by increasing the pressure in flush port 1 and flush port 2. The lagging tissue units behind the captured tissue units are sent back upstream into the hopper tank.

Release leading TU – the injection solenoid was switched OFF causing the spring-loaded expanding rod to retract. This cleared the path for the captured tissue unit to the injection chamber. The capture tissue unit was then released downstream to the injection chamber. It is here that the photomicrosensor detects whether a tissue unit has been singularised or not and if it has, the tissue unit detected indicator turns green and the number of tissue units singularised were updated in the tissue units processed counter.

Apart from the 4 buttons described above that execute the primary singularisation steps, the other buttons aid the various steps. The initialise valve button switches off all valves and sets the desired pressure values in the tank to the desired initial value. The equalise chamber button flushes the singularisation chamber, detects if there is an abnormal pressure reading in the singularisation chamber sensor, initialises valves, checks tissue unit counters and switches ON the injection solenoid thereby lowering the expanding rod. Check counter checks if there is a mismatch between the tallied number of singularisation cycles and tissue unit processed.

In the pressure control sections, the V-PI and P-PI buttons were used to switch ON the pressure tank control system and valves. If the input compressed air or vacuum to the tanks were too high or low for the controller, the high/low pressure/vacuum indicator would turn from green to red. When the indicator turned red, necessary adjustments had to be made by the user to the compressed air regulator to restore the normal functioning of the pressure tanks.

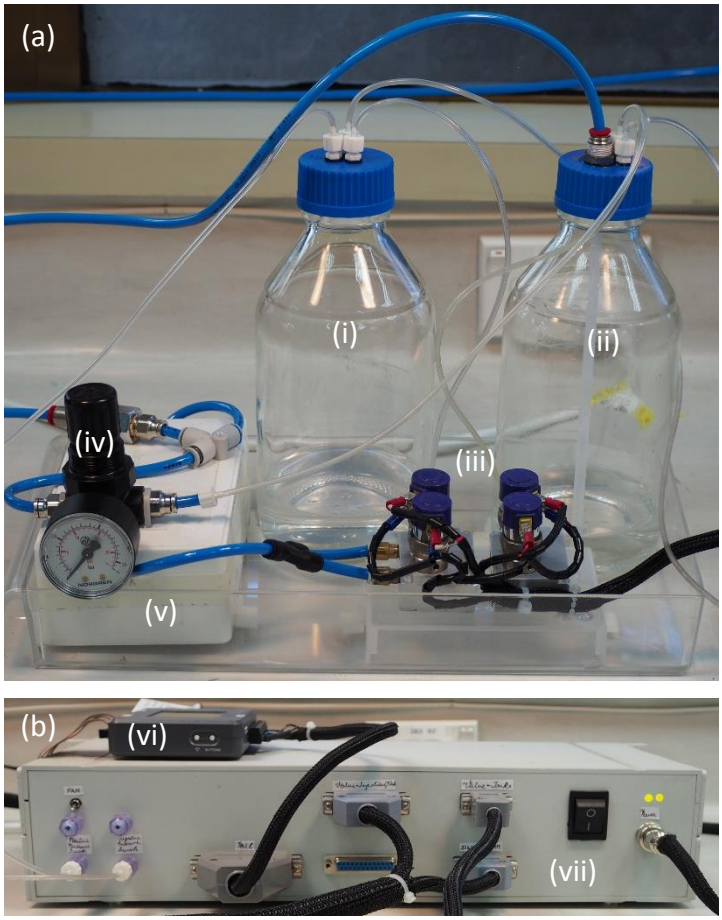

Figure 3-8. Photograph of the (a) positive and negative pressure tank setup and (b) the box containing the control system module showing the (i) negative pressure tank, (ii) positive pressure tank, (iii) proportional release valves, (iv) pressure regulator, (v) enclosure containing the pressure ejector, (vi) myRIO and (vii) enclosure containing driver circuits and sensors.

3.4.6 Tuning of the PI controllers for the pressure tanks:

Manually tuning of the PI controllers for the pressure tanks gave an approximate range of the gains. Fine-tuning the gains around the obtained approximate range by checking the response to a disturbance or change in set-point gave us the most favourable K_p and K_i values for the controllers. The fine-tuned optimal K_p and K_i values were determined to be (i) 1.17 and 0.004 for the positive tank PI controller, and (ii) 0.6 and 0.2 for the negative tank PI controller. As long as the input pressure line to the vacuum ejector was about 7 bars and the input pressure line to the positive pressure tank was about 1.1 bar, the response of the

control system with the above gains was stable during the normal operation of the singularisation device. With the above input pressure and gain vales, the control system was also sufficiently quick enough to respond when the set-point value was changed.

3.4.7 Tissue unit injection head

The singularisation system and injection system was successfully integrated with the low-temperature head of the Bioscaffolder. This included the placement of the singularisation chamber, the injection assembly and solenoid, the singularisation chamber sensor and circuitry, hopper tank, the fluid isolation and pinch valves, and the photosensor. The head was mounted on the tool magazine and preliminary tests showed that the head could be moved in space by the 3D positioning system without any problem or obstacles. The communication lines between the Bioscaffolder and the myRIO could not be connected to each other as the manufacturers of the Bioscaffolder did not provide us with the architecture of the input and output interface of the Bioscaffolder which was required for the integration of the communication lines. To overcome this the Bioscaffolder ready flag (BRF) and a singularisation device ready flag (SRF) were manually switched ON/OFF. However, the communication between the devices should be possible once we have the details of the lines input and output interface. Further testing of the device has been explained in detail in the next chapter. Photograph of the injection head is shown in Figure 3-9.

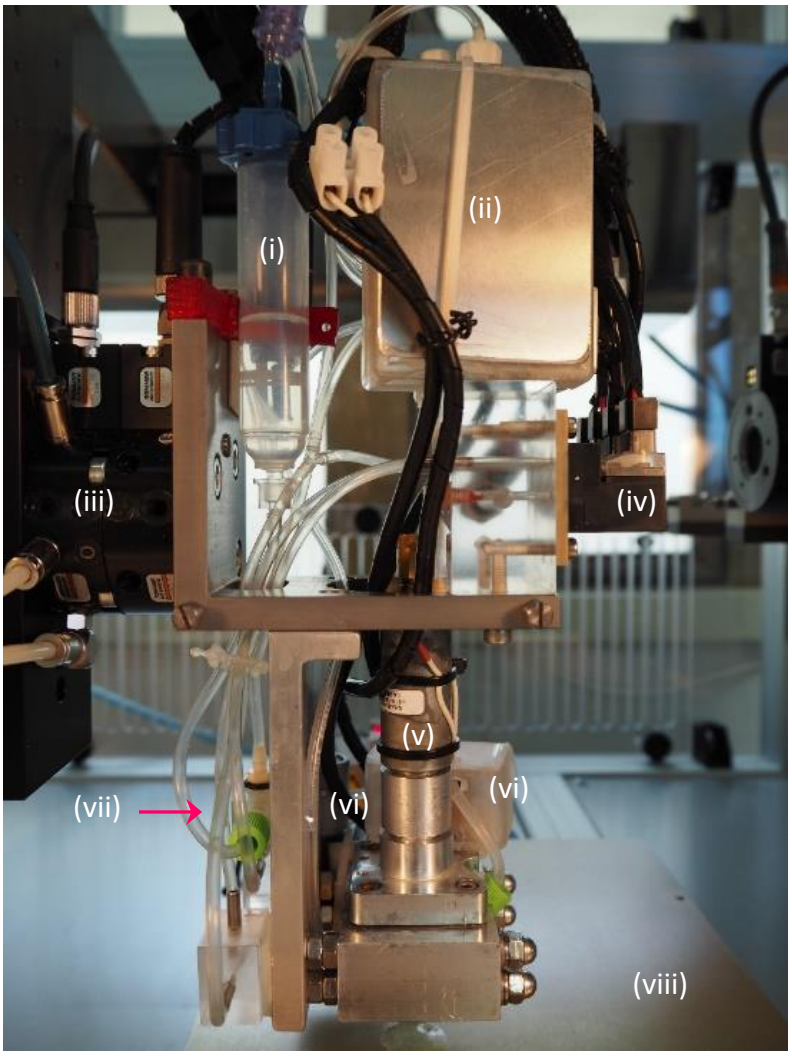

Figure 3-9. Photograph of the injection head with labels showing the position of (i) hopper tank, (ii) singularisation chamber sensor and circuitry, (iii) Bioscaffolder 3D positioning head, (iv) fluid isolation, (v) injection solenoid, (vi) photosensor, (vii) singularisation chamber and (viii) Bioscaffolder base plate.

3.5 Conclusions

We have described an approach undertaken to design and successfully build and construct a prototype, fluid-based automated bioassembly system. This included the complete architecture of the mechanical and electronic systems required for the functioning of the device. The constructed singularisation module had the capability to take up large numbers of engineered tissue units (micro-tissue or microspheres) and then deliver a tissue unit individually at a time to the injection module, which with the aid of the 3D positioning system could deliver a tissue unit

to a predetermined pore within the bioscaffold. The immense flexibility of the constructed prototype allowed for the adjustment and optimisation of the essential soft parameters with ease. The ability to tailor these soft parameters allowed the easy and effective optimisation of the system for handling different types and sizes of tissue units. This prototype allowed us to further validate the capabilities of the automated assembly system for bioassembly applications.

3.6 References

1. Archer R, Williams DJ. Why tissue engineering needs process engineering. Nature Biotechnology. 2005;23(11):1353-1355.
2. Mironov V, Visconti RP, Kasyanov V, Forgacs G, Drake CJ, Markwald RR. Organ printing: Tissue spheroids as building blocks. Biomaterials. 2009;30(12):2164-2174.
3. Hutmacher DW, Horch RE, Loessner D, Rizzi S, Sieh S, Reichert JC, Clements JA, Beier JP, Arkudas A, Bleiziffer O. Translating tissue engineering technology platforms into cancer research. Journal of Cellular and Molecular Medicine. 2009;13(8a):1417-1427.
4. Williams D, Sebastine I. Tissue engineering and regenerative medicine: manufacturing challenges. in IEE Proceedings - Nanobiotechnology. 2005. IET.
5. Yasuda K, Hattori A, Kim H, Terazono H, Hayashi M, Takei H, Kaneko T, Nomura F. Non-destructive on-chip imaging flow cell-sorting system for on-chip cellomics. Microfluidics and Nanofluidics. 2013;14(6):907-931.
6. Grover SC, Skirtach AG, Gauthier RC, Grover CP. Automated single-cell sorting system based on optical trapping. Journal of Biomedical Optics. 2001;6(1):14-22.
7. Huang JT, Wang GC, Tseng KM, Fang SB. A chip for catching, separating, and transporting bio-particles with dielectrophoresis. Journal of Industrial Microbiology & Biotechnology. 2008;35(11):1551-7.
8. Freyer JP, Wilder ME, Jett JH. Viable sorting of intact multicellular spheroids by flow cytometry. Cytometry. 1987;8(4):427-436.
9. Drewitz M, Helbling M, Fried N, Bieri M, Moritz W, Lichtenberg J, Kelm JM. Towards automated production and drug sensitivity testing using scaffold-free spherical tumor microtissues. Biotechnology Journal. 2011;6(12):1488-1496.
10. Rezende R, Pereira F, Kasyanov V, Kemmoku D, Maia I, Da Silva J, Mironov V. Scalable biofabrication of tissue spheroids for organ printing. Procedia CIRP. 2013;5:276-281.
11. Tung YC, Hsiao AY, Allen SG, Torisawa YS, Ho M, Takayama S. High-throughput 3D spheroid culture and drug testing using a 384 hanging drop array. Analyst. 2011;136(3):473-8.
12. Tan Y, Richards DJ, Trusk TC, Visconti RP, Yost MJ, Kindy MS, Drake CJ, Argraves WS, Markwald RR, Mei Y. 3D printing facilitated scaffold-free tissue unit fabrication. Biofabrication. 2014;6(2):024111.
13. Ozbolat IT, Chen H, Yu Y. Development of 'Multi-arm Bioprinter'for hybrid biofabrication of tissue engineering constructs. Robotics and Computer-Integrated Manufacturing. 2014;30(3):295-304.
14. Lang M, Wang W, Chen X, Woodfield T. Integrated system for 3D assembly of bio-scaffolds and cells. in 2010 IEEE International Conference on Automation Science and Engineering. 2010. IEEE.
15. Lang M. Systems for the automated 3D assembly of micro-tissue and bio-printing of tissue engineered constructs. 2012.
16. Lang M, Chen X, Wang W, Woodfield TB. Injection system for cellular assembly of 3D bio-tissue engineered constructs. in 2012 IEEE International Conference on Automation Science and Engineering (CASE). 2012. IEEE.

Chapter 4 Integrated system for automated 3D Bioassembly of micro-tissues for biofabrication of hybrid tissue engineered constructs

The work from this chapter has contributed to the manuscript that is currently in the process of being submitted to the journal Biofabrication.

Mekhileri, N.V., K.S. Lim, I. Mutreja, B.S. Schon, G.J. Hooper, and T.B.F. Woodfield, *Integrated system for automated 3D Bioassembly of micro-tissues for biofabrication of hybrid tissue engineered constructs.* Biofabrication. (in submission).

4.1 Abstract

Bottom-up biofabrication approaches combining micro-tissue fabrication techniques with 3D plotted scaffolds are emerging strategies in tissue engineering. These strategies promote cell-cell/stem cell interactions and cell differentiation capacity. Few technologies have been developed to automate the precise assembly of micro-tissues into 3D plotted scaffolds. We developed a cutting-edge automated 3D Bioassembly system capable of fabricating: (i) simple constructs via a two-step top-down bioassembly strategy and (ii) complex hybrid hierarchical constructs via a multistep bottom-up bioassembly strategy. The prototype automated micro-tissue bioassembly system consisted of a fluidics-based singularisation and injection module incorporated into a commercial 3D bioprinter. The singularisation module delivered individual micro-tissues to an injection module, for insertion into specific locations in a 3D plotted scaffold. Chondrocytes were isolated and Ø1 mm micro-tissues were generated utilising a high-throughput 96-well plate format. Micro-tissues were singularised with an efficiency of 96.0 ± 5.1%. There was no significant difference in size, shape or viability of micro-tissues before and after automated singularisation and injection. A layer-by-layer approach or aforementioned bottom-up bioassembly scheme was employed to fabricate a bilayered construct by alternatively 3D plotting a PEGT/PBT polymer scaffold and inserting pre-differentiated chondrogenic micro-tissues utilising the bioassembly system. No significant difference in viability between the construct assembled utilising the automated bioassembly system and manually assembled construct was observed.

This technology provides an automated and scalable pathway for Bioassembly of both simple and complex 3D, multicellular tissues of clinically relevant size and shape.

4.2 Introduction

Physical impact or degenerative diseases such as osteoarthritis and related disorders can damage articular cartilage causing severe pain, deformity and loss of joint motion [1]. Cartilage, being an avascular tissue structure with constrained oxygen supply has a limited capacity for self-repair [2]. Many repair strategies such as microfracture, mosaicplasty, autologous chondrocyte implantation, and matrix-assisted chondrocyte implantation have been developed in an attempt to treat articular cartilage defects, although short-term clinical results are satisfactory long-term results are typically associated with the formation of fibrocartilage which has inferior mechanical properties compared to native hyaline cartilage [3-5]. This has prompted the search for alternative treatments based on tissue engineering strategies and other approaches to circumvent the limitations of existing therapies [6, 7].

The typical tissue engineering paradigm for cartilage involves growing chondrocytes or chondroprogenitor cells (e.g. mesenchymal stromal cells isolated from bone marrow) in combination with cell phenotype modulating growth factors within a biodegradable 3D scaffold *in vitro* and then implanting the engineered construct into the target site [8]. This approach may offer advantages over existing surgical techniques in that the desired scaffold shape can be tailored to meet the needs of an individual patient while providing the initial mechanical properties, cells and extracellular matrix (ECM) components required to elicit regeneration and repair. Ideally, over time the biodegradable scaffold would be completely replaced by mature ECM deposited by the cells, resulting in a functional cartilage repair [7]. Although significant advances have been made in tissue engineering, major challenges are yet to be conquered before cartilage tissue engineering strategies can be applied in a clinical setting [9].

Chondrocytes, however, need to be guided to prevent dedifferentiation and promote the generation of quality repair tissue *in vitro* or *in vivo* that mimics the

complex cellular and extracellular matrix (ECM) organisation in native hyaline cartilage to allow normal load bearing and long-term function of the joint [10]. Micro-mass or pellet culture of chondrocytes or chondroprogenitor cells are well-established methods for generating small micro-tissues of cartilage tissue, and more recent studies have investigated high-throughput approaches for micro-tissue formation [11, 12]. A previous study by Schon *et al.* [11], demonstrated a high-throughput technique for producing *ex vivo* cartilage-like micro-tissues. In these micro-tissue, the 3D niche promotes a large number of cell–cell interactions [13], thereby replicating the cellular condensation environment typical during developmental stages of cartilage growth, allowing the production of hyaline-like *ex vivo* neocartilage expressing collagen type II and aggrecan [11] typical of mature hyaline cartilage. A large body of work around the high-throughput generation of micro-tissues exists and has been demonstrated with hanging drop technology for cartilage engineering [14], with a 96-well plate format for cartilage engineering [11], to assess chondrogenesis [15, 16] and for the screening of antirheumatic compounds [17], and with a 384-well plates format for high-throughput screening (HTS) of chondrogenesis in mesenchymal stromal cells [18]. Therefore, a significant opportunity exists if high-throughput cultured micro-tissues could be assembled into a scaffold to obtain a functional tissue engineered construct consisting of a large number of pre-differentiated micro-tissues primed for promoting ECM formation.

In tissue engineering and regenerative medicine (TERM), the conventional "top-down" strategies revolve around populating cells in a scaffold [19]. Recreating the microarchitecture of native tissue utilising top-down approaches is however challenging [19]. This drawback can be addressed by undertaking a "bottom-up" strategy where smaller nanoscale or microscale tissue units are assembled to create a larger more complex engineered tissue construct with a more controlled architecture [20]. With regards to bottom-up approach, Livoti and Morgan *et al.* [21, 22] reported on a tissue fusion technique, where a printing approach was used to produce complex shapes that were assembled using micro-tissues as building units on agarose moulds. Jakab *et al.* [23] demonstrated a system for the self-assembly of micro-tissues using a bio-printer with a device that cuts and extrudes cellular slurry into cylindrical aggregates and then delivers it into a printed hydrogel producing a tissue unit. Apart from this, a spectrum of techniques have been demonstrated to

assemble prefabricated tissue modules or units into a higher order tissue structure and this includes stacking of cell sheets [24], random packing of microgels [25], utilizing hydrophobic effect for assembling microgels [26], physical manipulation of individual cell-laden microgels [27] assembling micro-tissues into 3D plotted scaffolds [11], vacuum moulding [28, 29] or stacking rings on a tube [30].

Presently, bottom-up modular fabrication or tissue assembly technologies suffer from the inability to precisely place micro-tissues into a 3D plotted scaffold [31] and the manual assembly of micro-tissue spheroids has currently been limited to small, simple constructs. To our knowledge, there are currently no techniques available for the combination of automated top-down and bottom-up bioassembly approaches for hierarchical biofabrication and direct 3D bioassembly of micro-tissues in complex, anatomically-shaped 3D scaffolds.

The absence of a roadmap for scalable, reproducible, automated, large-scale biofabrication of tissue engineered products with a high level of cell-cell interaction, cellular self-assembly and co-location in combination with structurally reinforcing scaffolds offers opportunities to develop modular bioassembly technologies [32]. The requirements of such a system would include: (i) high degree of automation and scalability, (ii) ability to assemble micro-tissues of different cell types with controlled spatial resolution (e.g. osteochondral biphasic constructs [33]), (iii) ability to fabricate large, complex and high fidelity constructs of clinically relevant size. The system must also be able to promote rapid cell differentiation and ECM formation that mimics the complex 3D architecture of the native tissue as well as reduce overall construct fabrication time.

For the advancement of biofabrication approaches, any 3D bioassembly technology should preferably offer flexibility and be highly capable of fabricating both simple and anatomically complex hybrid tissue constructs. We envisioned that the 3D Bioassembly process should be capable of two specific bioassembly strategies: (i) a simple or top-down bioassembly strategy which is a two-step process involving the fabrication of a 3D plotted scaffold and the assembly of specific tissue units into targeted locations in the fabricated 3D plotted scaffold allowing the fabrication of simple constructs and (ii) hybrid or bottom-up bioassembly strategy

which is a layer-by-layer multistep process involving the alternating 3D plotting of a scaffold layer and co-assembly of specific tissue units into targeted locations in the 3D plotted scaffold layer enabling the fabrication of complex hybrid constructs. Figure 4-1. illustrates the opportunities offered by advanced modular tissue bioassembly for fabricating both simple and hybrid scaffolds for tissue engineering.

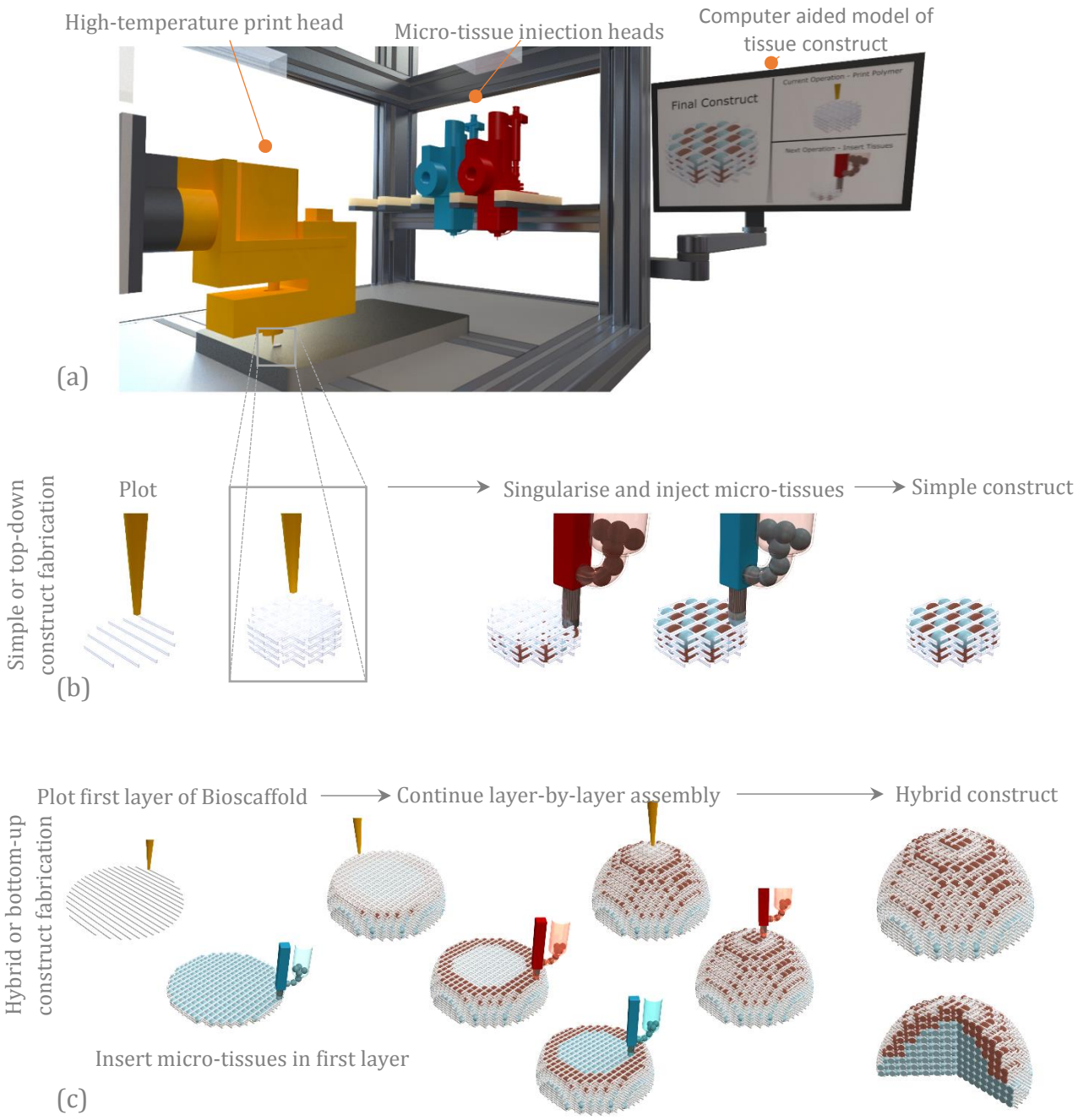

Figure 4-1. Illustration of the envisioned automated 3D Bioassembly process. (a) A three dimensional design is translated from a computer aided model to a plotted construct. (b) Simple or top-down fabrication: two step simple assembly involving 3D plotting a scaffold and subsequent spatial assembly of micro-tissues and (b) hybrid or bottom-up fabrication: multistep layer-by-layer assembly which involves in alternatively 3D plotting a layer and inserting micro-tissues to create a hybrid assembled construct.

The specific aim of this study was therefore to develop an automated biofabrication strategy combining 3D micro-tissue bioassembly and 3D plotting of

thermoplastic polymer scaffolds. This involved the development of a system consisting of (i) a singularisation module that is able to separate large numbers of engineered spheroids or micro-tissues and then deliver them individually to an injection module, and (ii) an injection module which can assemble or seed the micro-tissue at a pre-determined location within a defined scaffold architecture with the aid of a 3D positioning system. The ultimate goal of this technology was the development of an automated biofabrication system capable of assembling living constructs suitable for clinical translation, preliminarily targeting cartilage repair strategies.

4.3 Methods

4.3.1 Scaffold fabrication

Biodegradable poly(ethylene glycol)-terephthalate-poly(butylene terephthalate) block copolymers (Polyactive 300PEGT55PBT45, PolyVation, The Netherlands) with a PEG molecular weight (MW) of 300 g/mol and a PEGT:PBT weight percent (wt%) ratio of 55:45 were used to fabricate scaffolds with a specific pore size and architecture. PEGT/PBT copolymer composition was selected as a model scaffold based on previous studies demonstrating applicability across multiple processing techniques (e.g. melt extrusion), mechanical properties mimicking native tissue, as well as the capacity to modulate cell, adhesion, proliferation, differentiation and extra cellular matrix formation [8, 11, 34-38]. Porous scaffolds (15 × 15 × 3.52 mm), with accurately defined and controlled pore architecture for micro-tissue incorporation, were 3D plotted using a Bioscaffolder system (SYS ENG, Germany). Fibres were oriented in a repeating 0-90°-90°-0° pattern in order to provide porosity in both the x-y and x-z planes for assembly of 1 mm diameter micro-tissues. During the melt dispensing process the following 3D plotting parameters were applied: (i) fibre spacing of 1 mm in both x and y-direction, (ii) fibre height offset of 0.22 mm, (iii) dispense head and plotting temperature of 200° and 5 bar pressure, (iv) dispense head auger speed of 63 RPM and (v) 25 gauge dispense head nozzle moving at an x-y traverse speed of 500 mm/min.

4.3.2 Scaffold characterisation

3D plotted scaffold architectures designed for Bioassembly were gold sputter-coated (Emitech K957X), after which scanning electron microscopy (SEM) images

were taken using a Jeol 7000F FE-SEM with secondary electron detection used at an acceleration voltage of 15 kV. The interconnecting pore size of the 3D plotted scaffolds in the x-y plane and z plane and the fibre diameter was measured from calibrated SEM images. Rendered images illustrating the bioassembly scaffold design, interconnecting pore size and fibre diameter measurements are shown in Figure 4-2.

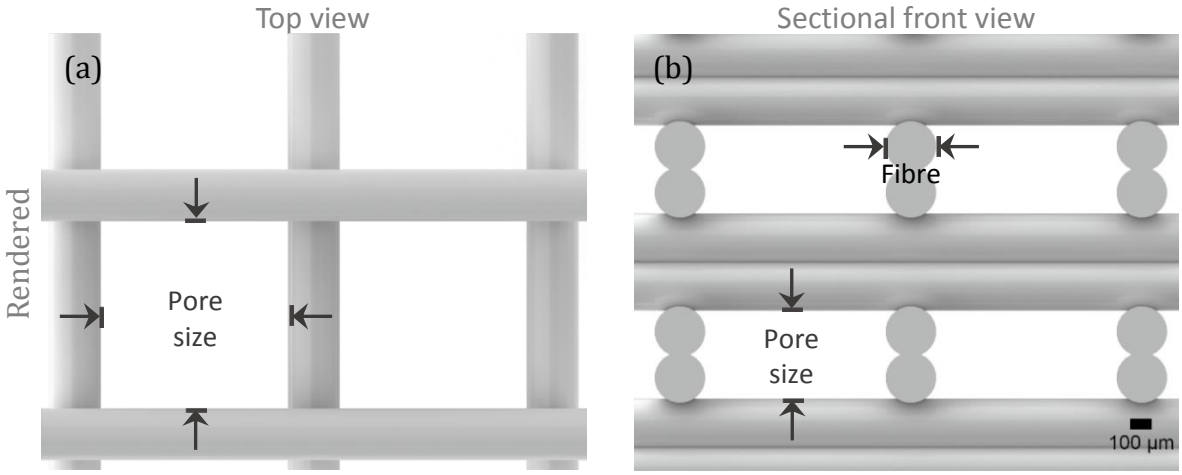

Figure 4-2. Rendered images of the top view and sectional front view of the 3D plotted scaffold. *Scale bar = 100 µm for all images.*

The volume percentage porosity (*Vol% porosity*$_{scaffold}$) of the 3D plotted scaffold was determined by mass-volume method using Equation 4-1 as described previously [8]. The length ($l_{scaffold}$), breath ($b_{scaffold}$), height ($h_{scaffold}$) and the mass ($m_{scaffold}$) of the 3D plotted scaffold was measured.

$$Vol\%\ porosity_{scaffold} = 1 - \frac{m_{\text{scaffold}}}{m_{\text{solid material}}}\ x\ 100 \qquad \textbf{4-1}$$

Where $m_{solid\ material}$ was determined using equation 4-2 and 4-3 and the density of Polyactive 300PEGT55PBT45 ($\rho_{solid\ material}$ = 1.25 g/cm^3) was based on the value previously reported and the theoretical value of porosity was also determined as described earlier [8].

$$m_{\text{solid material}} = V_{\text{scaffold}} \times \rho_{\text{ solid material}} \qquad \textbf{4-2}$$

$$V_{\text{scaffold}} = l_{\text{ scaffold}} \times b_{\text{ scaffold}} \times h_{\text{ scaffold}} \qquad \textbf{4-3}$$

The unconfined dynamic stiffness (compressive modulus) of the 3D plotted scaffolds was measured using an MTS Criterion® 42 mechanical test machine incorporating a 500N load cell. 3D plotted scaffolds with a dimension of 5 × 5 × 1.8 mm were tested at room temperature under dry conditions. A preload of 0.1 N was applied to ensure that the machine crosshead was in contact with the sample. The dynamic stiffness was determined by applying a uniaxial unconfined cyclic compression between 1% and 5% strain (liner region of the stress-strain curve) at a frequency of 1 Hz. During cyclic compression, the equilibrium peak force was reached after approximately 70 cycles out of a total of 100 compression cycles. The dynamic stiffness was calculated by taking the average modulus for the last 10 cycles.

4.3.3 Cartilage excision and cell isolation

Human chondrocytes were isolated, expanded and formed into micro-tissues as described previously [11]. Briefly, nasal or articular cartilage biopsies were obtained following ethics approval from consenting patients undergoing septoplasty surgery or cruciate ligament reconstruction respectively (*n=2*; 18, 25 years of age). The cartilage was diced into 1 mm cubes and digested overnight in basic chondrocyte media containing DMEM (high glucose, GlutaMAX Supplement, pyruvate; GIBCO, USA) with 10% fetal bovine serum (FBS; GIBCO, New Zealand), 0.1 mM non-essential amino acids (NEAA; GIBCO, USA), 10 mM HEPES (GIBCO, Taiwan), 0.2 mM L-ascorbic acid-2-phosphate (Sigma-Aldrich, USA), 0.4 mM L-proline (Sigma-Aldrich, USA), 100 units/mL penicillin (GIBCO, USA) and 100 µg/mL streptomycin (GIBCO, USA) containing 0.15% (w/v) collagenase type II (Worthington, USA). The suspension was then filtered through a 100 µm cell strainer (BD Biosciences, USA) and centrifuged at 700 g for 4 minutes.

4.3.4 Cell expansion

Freshly isolated human articular chondrocytes (HACs) or human nasal chondrocytes (HNCs) were seeded at a density of 3,000 cells/cm^2 in tissue culture flasks (BD Biosciences, USA) in basic chondrocyte media. Cells were expanded at 37°C in a humidified 5% CO_2/95% air incubator and media changed twice a week. After approximately 7 days, subconfluent passage one (P_1) cells were washed with

phosphate-buffered saline (PBS; GIBCO, USA), detached using 0.25% trypsin/EDTA (Gibco, Canada), counted by trypan blue exclusion in a haemocytometer and plated in a tissue culture flask at 3,000 cells/cm^2. Passage 2 (P_2) cells were harvested similarly and utilised to form micro-tissues.

4.3.5 High-throughput micro-tissue fabrication

Micro-tissues each consisting of 0.25 x 10^6 chondrocytes were formed in a high-throughput manner [11] and cultured in serum-free basic chondrocyte media supplemented with 1 % ITS+ (1 mg/ml insulin from bovine pancreas, 0.55 mg/ml human transferrin, 0.5 µg/ml sodium selenite, 50 mg/ml bovine serum albumin and 470 µg/ml linoleic acid; Sigma), 0.1 x 10^{-6} M dexamethasone (Sigma, USA), 1.25 mg/ml bovine serum albumin (GIBCO, New Zealand) and 10 ng/ml recombinant human transforming growth factor-β1 (TGF-β1; R&D systems, USA). Cell suspensions consisting of 0.25 x 10^6 chondrocytes in 290 µL media was pipetted into each well of a polypropylene 96-well V-bottom plate (Raylab, New Zealand), and centrifuged (Eppendorf 5810) at 200 g for 4 minutes and placed in an incubator at 37°C, 5% CO_2. The following day, the newly formed micro-tissue was gently detached from the bottom of the V-plate by pipetting. During the micro-tissue culture period, the media was changed 3 times per week and samples harvested at day 7.

4.3.6 Design of the Singularisation system

The singularisation device is a subsystem of the integrated tissue assembly device that takes the pooled micro-tissues from the high-throughput fabrication process in a reservoir hopper and then delivers a single micro-tissue at a time when required. The singularisation system consisted of a fluidic block fabricated with polycarbonate. The fluidic block was designed so that the hydrodynamic forces in the block could be varied sequentially using hydraulic valves and a pinch valve to manipulate and trap the micro-tissues and to achieve singularisation.

The block consisted of three small vertical pressure ports and a horizontal main chamber. The arrangement of chambers is illustrated in Figure 4-3. The vertical pressure ports – flush port 1, flush port 2 and capture port were connected to pressurised reservoirs, with the fluidic pressure in the ports controlled by the four

fluidic valves - hopper valve (H), flush valve 1 (F1), flush valve 2 (F2), capture port pressure valve (CP) and capture port vacuum valve (CV).

In this study, the main fluidic chamber was designed with an internal diameter of 1.3 mm to accommodate micro-tissues (or any other spherical aggregate or bioassembly tissue unit) with a diameter of 1 mm [11] for initial proof of concept, and also prevented horizontal stacking of the micro-tissues. The pressure ports were designed with a reduced diameter of 0.7 mm, in order to restrict micro-tissue entry into the ports and to either capture or trap them in position. The distance between the pressure ports on the main chamber was designed to be minimal to reduce the presence of a dead volume where micro-tissues may become trapped. A pressure sensor at the capture port measured the pressure as a feedback-loop to identify successful micro-tissue capture or if blockages were present. Furthermore, a photomicrosensor downstream of the singularisation system was used to provide feedback if successful singularisation (i.e. the delivery of a single micro-tissue to the injection system) had occurred or not.

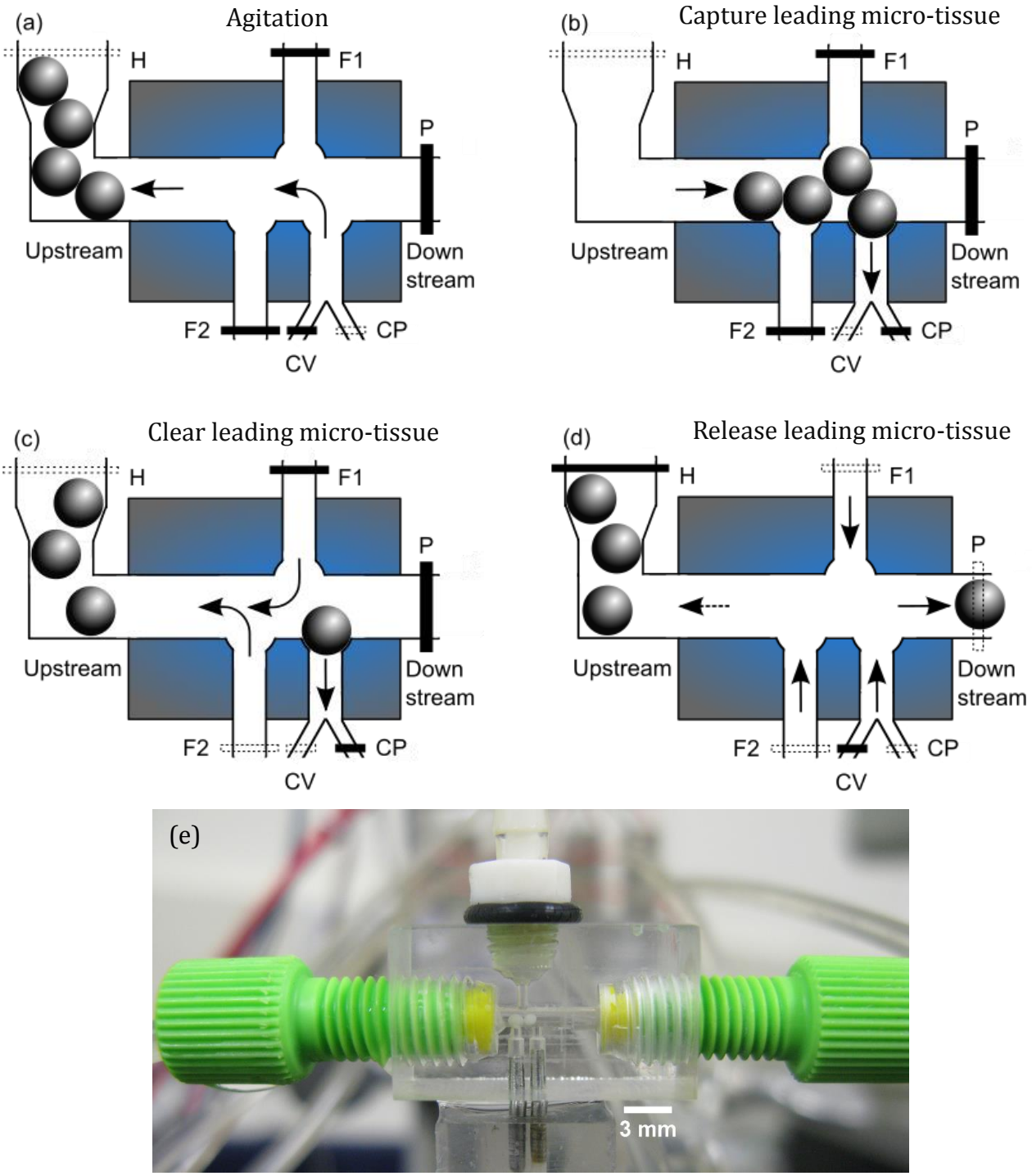

Figure 4-3. The singularisation concept. (a) agitation in the chamber to clear any blocks that might be present, (b) the capture port capturing the leading micro-tissue (c) flush back of the lagging micro-tissues and (d) the release and exit of the leading micro-tissue. The arrows show the direction of fluid and the dotted arrow indicates the direction of pressure. (H) hopper valve, (F1) flush valve 1, (F2) flush valve 2, (P) pinch valve, (CP) capture port pressure valve and (CV) capture port vacuum valve. Dotted boxes indicate that the valve is open and the solid boxes indicate that the valve is closed. (e) a photograph of the singularisation chamber, with the leading micro-tissue captured and the lagging micro-tissues trailing behind.

A summary of the singularisation process is illustrated Figure 4-3, and can primarily be broken down into 4 main steps - agitation, capture of leading micro-tissue, clearing of micro-tissue and release of leading micro-tissue. Micro-tissues entered the horizontal main chamber from the hopper reservoir (micro-tissue were transferred into the hopper tank manually by the user utilising a Pasteur pipette) which had a pneumatic hopper valve (H) to let air in the tank. Expulsion of micro-tissues from the singularisation device was controlled by a pinch valve (P). Pneumatic valves and pressure sensors were used to regulate the pressurised reservoirs containing media. Control software (LabVIEW, National Instruments, USA) and user interface was designed which took inputs from pressure sensors, the control system processes and feedback, user inputs as well as also sequentially controlling the valves and their timings. Preliminary tests using formalin fixed micro-tissues were used to determine the optimal valve timing and pressure settings for optimisation of the singularisation system.

4.3.7 Design of the Injection system

For the integrated tissue assembly device, a delivery subsystem was also required to automate the delivery of micro-tissues via two specific top-down and bottom-up fabrication strategies: (i) bioassembly of micro-tissues at target locations within a prefabricated scaffold with defined pore spacing (i.e. top-down), or (ii) bioassembly of micro-tissues at a target location via alternating layer-by-layer scaffold fabrication and assembly approach (i.e. bottom-up). To achieve this, an injection system was designed to successfully achieve both of these flexible bioassembly strategies and to minimise damage to the micro-tissues during the assembly process.

Figure 4-4 describes the steps involved in the injection concept in detail and also demonstrates the process for successful injection of Ø1 mm micro-tissues into a pore of a 3D plotted scaffold. Briefly, the assembly process begins with accurate positioning of the injection nozzle over the centre of the scaffold pore using the Bioscaffolder tool path calculated via the programming code (g-code) used to fabricate the scaffold. A solenoid operated expanding rod located within the core of the injection nozzle was then retracted to make way for the micro-tissue. The movement of the micro-tissue through the injection system was fluidically

controlled again by triggering the appropriate valves with specific control over valve timing via LabVIEW software interface (see Figure 4-7). Along with fluid flow of, the downward movement of the expanding rod (Figure 4-4 e) aided the delivery of the micro-tissue into the pore spacing. Apart from aiding the press-fit delivery of the micro-tissue into the pore, the expanding rod further helped to maintain a smooth profile for the nozzle so that the nozzle did not damage the scaffold fibres during the injection process and also protected the delicate nozzle during the placement of the nozzle on the scaffold fibre.

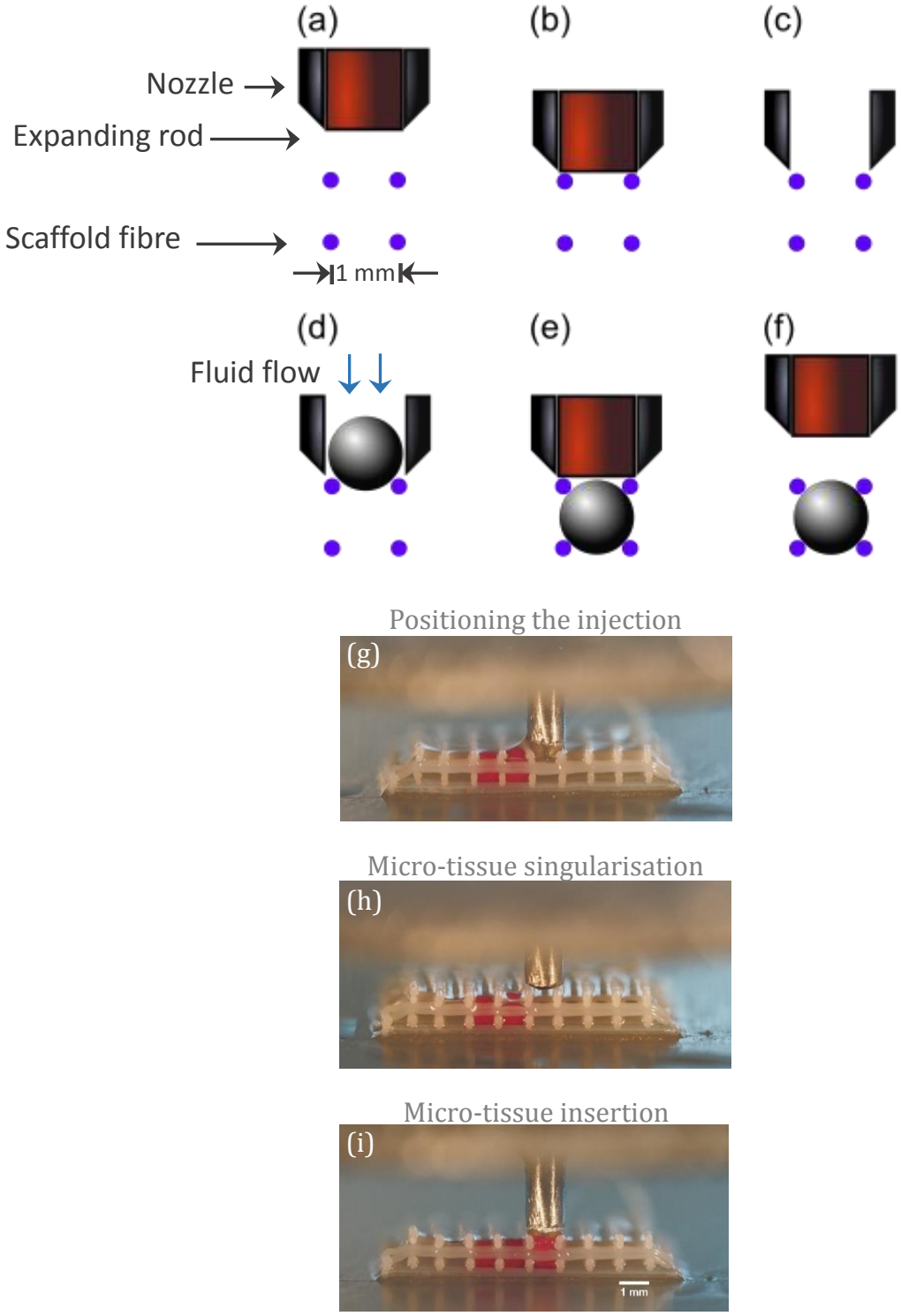

Figure 4-4. The Injection concept. (a) The injection system is positioned above the scaffold pore spacing where the micro-tissue is to be delivered, (b) it is then vertically lowered so that the expanding rod and nozzle sit on top of the upper fibres, (c) the expanding rod is retracted enabling (d) the delivery of the micro-tissue to the pore, (e) the expanding rod is lowered and pushes the micro-tissue in place if necessary and (f) the injection system is raised about the scaffold and is ready for the next insertion. The injection process. (a) Positioning the injection head, (b) micro-tissue singularisation and rod retraction and (c) micro-tissue insertion. *Scale bar = 1 mm for images g to i.*

4.3.8 The integrated tissue assembly system

The integrated platform for the fabrication of 3D plotted scaffolds and automated assembly of micro-tissues consisted of the 3D Bioscaffolder and LabVIEW controlled singularisation and injection device. The 3D Bioscaffolder allowed scaffolds to be plotted via fibre deposition (Figure 4-5 a) and also served as a 3D positioning system for the micro-tissue injection head (Figure 4-5 b). The desired head could be mounted on the printer head with the use of a tool changer interface. The transport of single micro-tissues from the singularisation system to the injection system under fluid flow was achieved through a coupling tube.

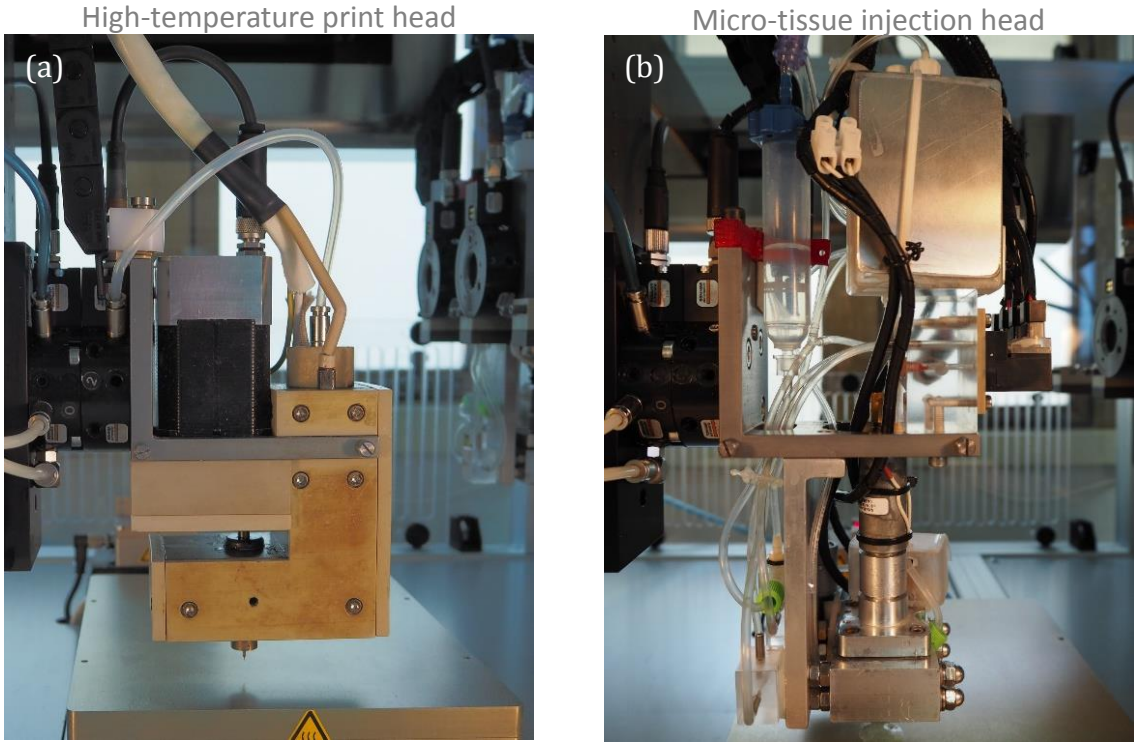

Figure 4-5. Illustration of (a) the high-temperature plotting head and the micro-tissue injection head. Each head could be alternated or activated through the use of the tool changer mounting.

For construct biofabrication, a scaffold layer (0º-90º-90º-0º fibre orientation with desired fibre spacing) was 3D plotted with the high-temperature thermoplastic polymer print head, after which a micro-tissue was singularised and precisely assembled into the desired location within the scaffold via the injection system. The multistep process was repeated to create a bioassembled hybrid construct.

4.3.9 Micro-tissue shape characterization before and after singularisation

Micro-tissue (*n=9*) dimensions were analysed both before and after undergoing the singularisation process. Samples were fixed overnight with 4% neutral buffered formalin and imaged using a bright-field microscope. The major and minor diameters were measured using the image measurement function in the Micrometrics SE Premium 4 software. Following imaging and measurement, micro-tissues were put through the singularisation device and then imaged and measured again as above, for comparison.

4.3.10 Reliability and efficiency of the singularisation device

Preliminary tests with the singularisation device demonstrated that micro-tissues with a major diameter less than 0.82 ± 0.06 mm (*n=3*) became lodged into the pressure ports (diameter of 0.7 mm) of the fluidic chamber. The smaller micro-tissues would be sucked into the negative pressure tank through the capture port, by increasing the pressure in the negative pressure tank. Whereas micro-tissues that had a major diameter greater than 1.26 ± 0.02 mm (*n=3*) did not enter the fluidic chamber (diameter of 1.3 mm). The larger micro-tissue were purged back into the hopper tank and would have to be manually removed by the user utilising a Pasteur pipette. The singularisation device could handle micro-tissues with a major diameter in between this range. To determine the optimal size range for reliable and efficient operation of the device and determine the efficiency of the singularisation device at the upper or lower limits of the micro-tissue diameter, the fabricated micro-tissues were fixed and sorted into two size ranges - group A and group B (see Table 4-1).

Table 4-1. Average major and minor diameter of micro-tissues.

	Average diameter	
	Major	Minor
Group A	1.14 ± 0.12 mm	1.03 ± 0.18 mm
Group B	0.95 ± 0.07 mm	0.84 ± 0.06 mm

[a] Group A (*n*=6 microspheres)
[b] Group B (*n*=9 microspheres)

Micro-tissues belonging to group A was then singularised in sets of 6 and repeated 17 times whereas micro-tissues belonging to group B were singularised in

sets of 9 and repeated 12 times, with percentage success rate for singularisation recorded. The total number of successful singularisation cycles was used to determine the overall efficiency of the singularisation system (Equation 4-4). The number of successful detection of singularisation cycles was used to determine photomicrosensor detection efficiency (Equation 4-5).

$$efficiency\ of\ singularisation = \frac{successful\ micro\text{-}tissue\ singularisation}{total\ attempted\ number\ of\ micro\text{-}tissue\ singularisation} \quad \textbf{4-4}$$

$$photomicrosensor\ detection\ efficiency = \frac{number\ of\ successful\ detection\ of\ singularisation\ cycles}{total\ \ number\ of\ singularisation\ cycles} \quad \textbf{4-5}$$

Micro-tissues that were that were too small to be handled by the singularisation device (i.e. micro-tissues smaller than the diameter of the capture port (0.7 mm) would be), would pass through the capture port and end up in the negative pressure tank.

4.3.11 Viability of the micro-tissue

In order to determine if any of the automated fluidic-based steps for singularisation, transport and injection influenced cell viability, micro-tissues were divided into 4 groups, a control group (i.e. not put through the device), a singularised group (i.e. put through the singularisation device only), an injected group (i.e. put through the injection device only) and a singularised and injected group (i.e. put through both the singularisation and injection devices). The viability of the micro-tissues was determined using the live/dead assay and the trypan blue exclusion assay.

For the live/dead assay, samples were incubated at 37°C in 0.5 ml of Dulbecco's phosphate-buffered saline (DPBS; Invitrogen, USA) with 1 µM Calcein AM (Molecular Probes, USA) for 15 minutes, then 1.5 µM Propidium Iodide (Molecular Probes, USA) was added and incubated for 10 further minutes. Samples were then washed twice with DPBS and a z-stack of the sample was imaged using a Zeiss Axioimager Z1 microscope (FITC and Texas Red filter-set).

For the trypan blue exclusion assay, micro-tissue samples were digested overnight with 0.15% (w/v) collagenase type II (Worthington, USA) in basic chondrocyte media as described previously [11]. The cells were then diluted in an equal amount of 0.04% trypan blue (GIBCO, USA) and the viability of the cells was quantified by imaging and counting of stained cells using a Zeiss Axioimager Z1 microscope.

4.3.12 Automated micro-tissue bioassembly

To validate the process for automated bioassembly of a 3D construct, a bilayered scaffold was designed and 3D plotted to incorporate 16 micro-tissues in each layer adopting a layer-by-layer scaffold fabrication and micro-tissue bioassembly (bottom-up) approach. For the first layer of the construct, 8 fibre layers were plotted and subsequently, 16 viable HAC micro-tissues were singularised and inserted using the automated assembly system. This process was similarly repeated for the second layer.

During the micro-tissue insertion process, the fluid flowing naturally through the nozzle was sufficient to keep the micro-tissues in the construct hydrated and the surface tension ensured that the fluid remained around the construct. For the 3D plotting of the subsequent layer of the scaffold, the fluid level around the construct was manually adjusted with a pipette so that the fluid level remained below the topmost scaffold fibre so that the micro-tissues were still hydrated and also allowed the adhesion of the fibre being 3D plotted onto the construct. Although we have presently controlled the fluid level manually, developing a fluid control system along with a chamber in which the media level can be controlled and the construct fabrication takes place would not be challenging.

4.3.13 Efficiency of micro-tissue insertion

A bilayered scaffold ($n=6$) was printed with 4 micro-tissues in each layer using the layer-by-layer approach described earlier. The efficiency of micro-tissue insertion into the scaffold was determined by the ratio of successful micro-tissues inserted into the target scaffold pore to the total attempted number of micro-tissues inserted with the automated system (Equation 4-6).

$$efficiency\ of\ micro\text{-}tissue\ insertion = \frac{successful\ micro\text{-}tissue\ insertion}{total\ attempted\ number\ of\ micro\text{-}tissue\ insertion} \quad \textbf{4-6}$$

4.3.14 Determination of viability of assembled construct

The layer-by-layer approach based bilayered scaffold (*n=3*) with 4 viable micro-tissues per layer was assembled using the automated system. Furthermore, a manually assembled scaffold (*n=3*) was prepared as a control to compare against bioassembled constructs with the automated system. In the latter case, the scaffold was 3D plotted and micro-tissues were inserted manually by hand into pre-fabricated scaffold pores using a pipette fitted with a 1 mL pipette tip.

Live/dead assay was performed on manual and automated assembled constructs as described for micro-tissues above. To quantify metabolic activity of bioassembled constructs, the AlamarBlue® assay was performed. AlamarBlue® (Invitrogen, USA) was added to the serum-free basic chondrocyte media so that the final concentration was 10% (v/v) and the samples were incubated at 37°C for 3.5 hours. The reduction in AlamarBlue® reagent was calculated colorimetrically using the equations provided by the manufacturer after measuring the absorbance at 570 nm, using 600 nm as a reference wavelength (Fluostar Galaxy BMG Labtechnology, Germany).

4.3.15 Statistical analysis

Data was presented graphically as mean ± standard deviation. Data were analysed using GraphPad Prism v.6.0. Statistical analysis was performed using 1-way ANOVA or paired t-test, with $p<0.05$ set as criterion for statistical significance.

4.4 Results

4.4.1 Scaffold characterisation

The SEM images (Figure 4-6) of the 3D plotted scaffold showed regular interconnecting pores in the in the x-y plane and z plane for the specific scaffold architecture and 3D plotting parameters adopted.

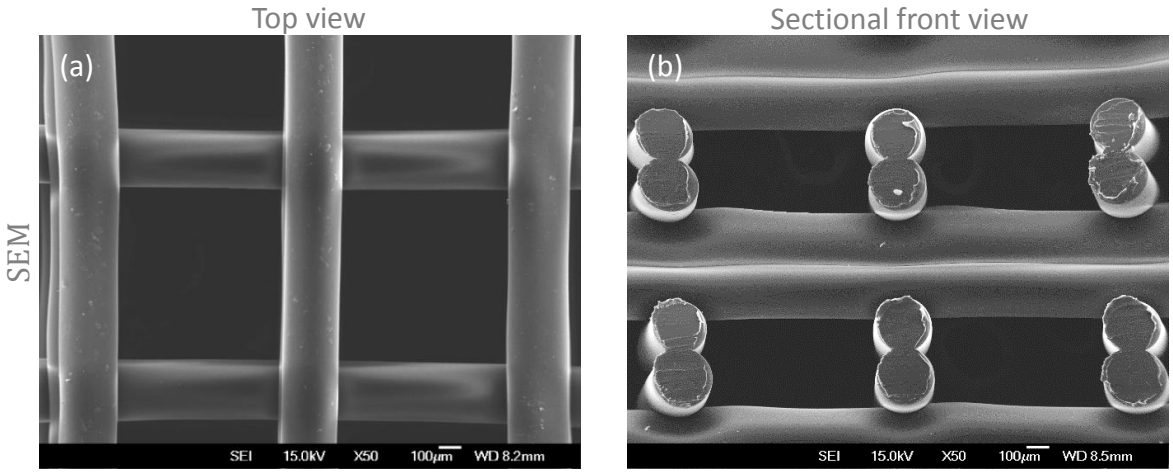

Figure 4-6. Scanning electron microscopy (SEM) images (x50) of the top view and sectional front view of the 3D plotted scaffold.

The theoretical and measured values of interconnecting pore size in the x-y plane and z-plane, the volume percent (*Vol% porosity*$_{scaffold}$) porosity and the fibre diameter for the 3D plotted scaffold are indicated in Table 4-2. The theoretical values for interconnecting pore size, *Vol% porosity*$_{scaffold}$ and fibre diameter were comparable with the measured values, where the average interconnecting pore size in the x-y plane was specifically designed at approximately 780 μm to allow a slight press-fit of the Ø1 mm micro-tissues. It was essential that the interconnecting pore size and *Vol% porosity*$_{scaffold}$ were accurately designed and fabricated so that the micro-tissues could reliably be inserted into the pore by the automated bioassembly system, while at the same timing ensuring they remain in place and not dislodged after insertion.

Table 4-2. Characterization of 3D plotted scaffold.

	Interconnecting pore size		*Vol% porosity*$_{scaffold}$	Fibre diameter (μm)
	x-y plane (μm)	z plane (μm)		
Theoretical	780	440	84.17	220
Measured	767.02 ± 16.54	427.25 ± 9.78	78.17 ± 2.26	218.50 ± 7.94

[a] (n=4)

The mechanical properties of the 3D plotted scaffold can be influenced by the architecture of the scaffold [8, 39]. For the particular architecture used in this study

where the fibres were 3D plotted in a 0-90°-90°-0° pattern, the unconfined dynamic stiffness of the empty scaffold was determined to be 6.91 ± 0.62 MPa at 1 Hz. For articular cartilage, 1 Hz is in the range of physiological frequency representative of light to moderate activity [40]. In comparison, the dynamic stiffness of bovine cartilage under cyclic compression at 1 Hz has been reported to be approximately 9.6 MPa [39], whereas for bovine carpometacarpal cartilage a dynamic stiffness of 7.0 MPa at 1 Hz of cyclic compression has been reported [41]. The dynamic stiffness for human articular femoral cartilage at 1 Hz has been reported to be 4.5 MPa [42]. Therefore our data suggest that the dynamic stiffness of the scaffold design adopted for bioassembly in this study are similar to that of articular cartilage.

4.4.2 Timing of the singularisation system

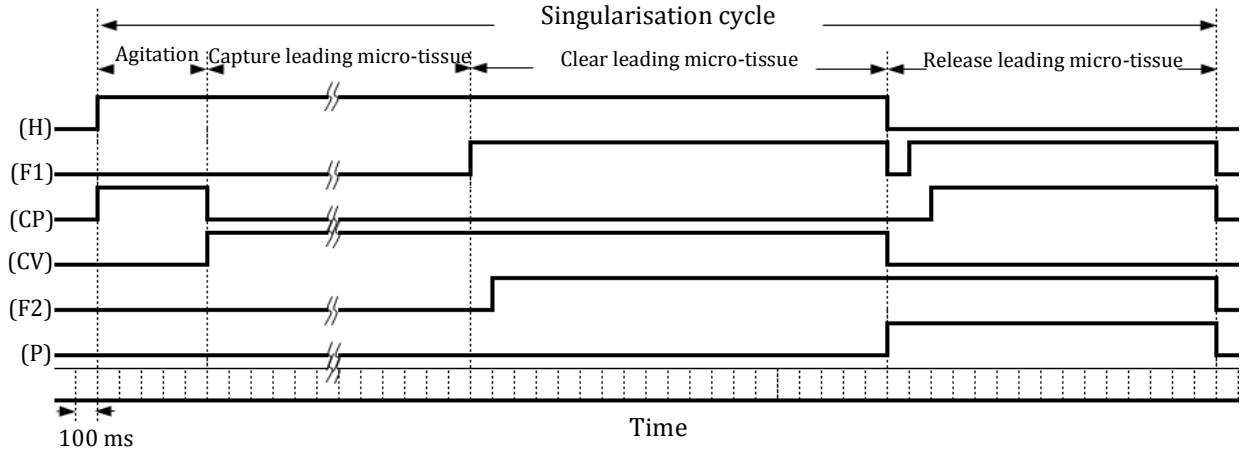

Figure 4-7. Timing diagram of the valve sequence for a single cycle of singularisation. For valve positions see (H) hopper valve, (F1) flush valve 1, (CP) capture port pressure valve(CV), capture port vacuum valve, (F2) flush valve 2 and (P) pinch valve.

Initially, a prototype singularisation and injection system were designed and fabricated. After which, we examined and determined the most optimal valve and fluid flow timing sequences for the system to allow successful automated assembly. Figure 4-7 shows the timing diagram of the valve sequence for a single singularisation cycle. This particular valve sequence timing was specific for a 10 cm long fluidic tube connecting the singularisation chamber and the hopper tank, a positive pressure of 105.7 kPa in the positive pressure tank, a negative pressure of 93.5 kPa in the negative pressure tank. A feedback control system that assumed whenever the pressure at the capture port had decreased to a value less than 96.5

kPa, a micro-tissue had been captured at the port, signalling to the control system to change the valve sequence from capturing the leading micro-tissue to clearing lagging micro-tissues. Varying any of the above parameters would require a recalibration of the valve timing sequence. This sequence formed the initial framework for the operation of the device.

4.4.3 Size comparison before and after singularisation

To understand and scrutinize any physical deformation and mechanical impact on micro-tissues after being passed through the singularisation system, micro-tissues were imaged and measured before and after singularisation. The average percentage change in the major and minor diameter of micro-tissues (*n=9*) measured before and after singularisation is listed in Table 4-3. The values demonstrated that there was no significant change in micro-tissue size and shape (*p>0.05*) as a result of being handled by the device.

Table 4-3. Average diameter of the micro-tissues before and after singularisation and percentage change in diameter after singularisation in paired samples.

	Average diameter		Percentage change in diameter after singularisation[a]
	Before singularisation	After singularisation	
Major diameter	1.04 ± 0.16 mm	1.03 ± 0.16 mm	2.2 ± 2.8%
Minor diameter	0.99 ± 0.17 mm	0.98 ± 0.15 mm	2.7 ± 3.4%

[a] In paired samples.
[b] *Statistical analysis: paired t-test*

4.4.4 Reliability and efficiency of the singularisation device

The reliability of the singularisation device was quantified by determining the successful singularisation of micro-tissues expressed in terms of efficiency. As demonstrated in Table 4-4, the singularisation efficiency for micro-tissues of larger sizes (group A) was 97.0 ± 6.6%, whereas it was 86.0 ± 13.8% for the smaller micro-tissue group (group B). This result indicates that micro-tissues with a diameter closer to the upper limit of the device have better singularisation efficiency as long as they are not large enough to obstruct and cause a blockage in the singularisation chamber. Successful operation of the tissue bioassembly system, therefore, depends on the ability to fabricate tightly controlled regular-sized spherical micro-tissues

and our group has previously described a high-throughput approach demonstrating this [11].

Table 4-4. Efficiency of singularisation.

	Average diameter		Singularisation efficiency
	Major	Minor	
Group A	1.14 ± 0.12 mm	1.03 ± 0.18 mm	97.0 ± 6.6%
Group B	0.95 ± 0.07 mm	0.84 ± 0.06 mm	86.0 ± 13.8%

[a] (n=100) number of singularisation.

During the experiment, the situations which resulted in singularisation failures included: (i) capture of 2 micro-tissue at a time, (ii) failure to trigger the capture pressure sensor even when a micro-tissue had been captured, (iii) accidental release of micro-tissue upstream rather than downstream, (iv) blocking of pressure ports by the micro-tissues, and (v) accidental dislodging of the captured micro-tissue. Nevertheless, the determined efficiency of approximately 97% for the targeted (group A) micro-tissues was deemed be acceptable for its application in tissue assembly. The singularisation failures that occurred were not critical and did not cause the failure of the device nor the inability to completely assemble all available micro-tissues. For example, in the event of a failure, the singularisation cycle could be repeated if the device had failed to release a micro-tissue, or in the case of a blockage, the device could be purged with fluid so as to dislodge the blocked micro-tissue and clear the bioassembly system after which normal operation was resumed. In the case of these failures, however, the overall bioassembly time for the entire construct would increase slightly.

The photomicrosensor detection efficiency or the reliability of the photomicrosensor to detect a successfully singularised micro-tissue was based on the number of successfully detected singularised micro-tissues and this was determined to be 96.0 ± 5.2%.

4.4.5 Viability of micro-tissues

Significant attention was invested in designing the bioassembly system to ensure that the environment within the device was favourable for cell survival and

that, size or shape of the micro-tissues was not adversely affected. For that reason, a fully fluidic approach was adopted for singularisation and delivery of the micro-tissues. To ascertain that the cells in the micro-tissues were not negatively affected during their passage through the device, a live/dead assay was carried out to inspect cell viability on the surface of micro-tissues. In addition, a trypan blue exclusion assay was performed to quantify cell viability throughout the entire micro-tissue.

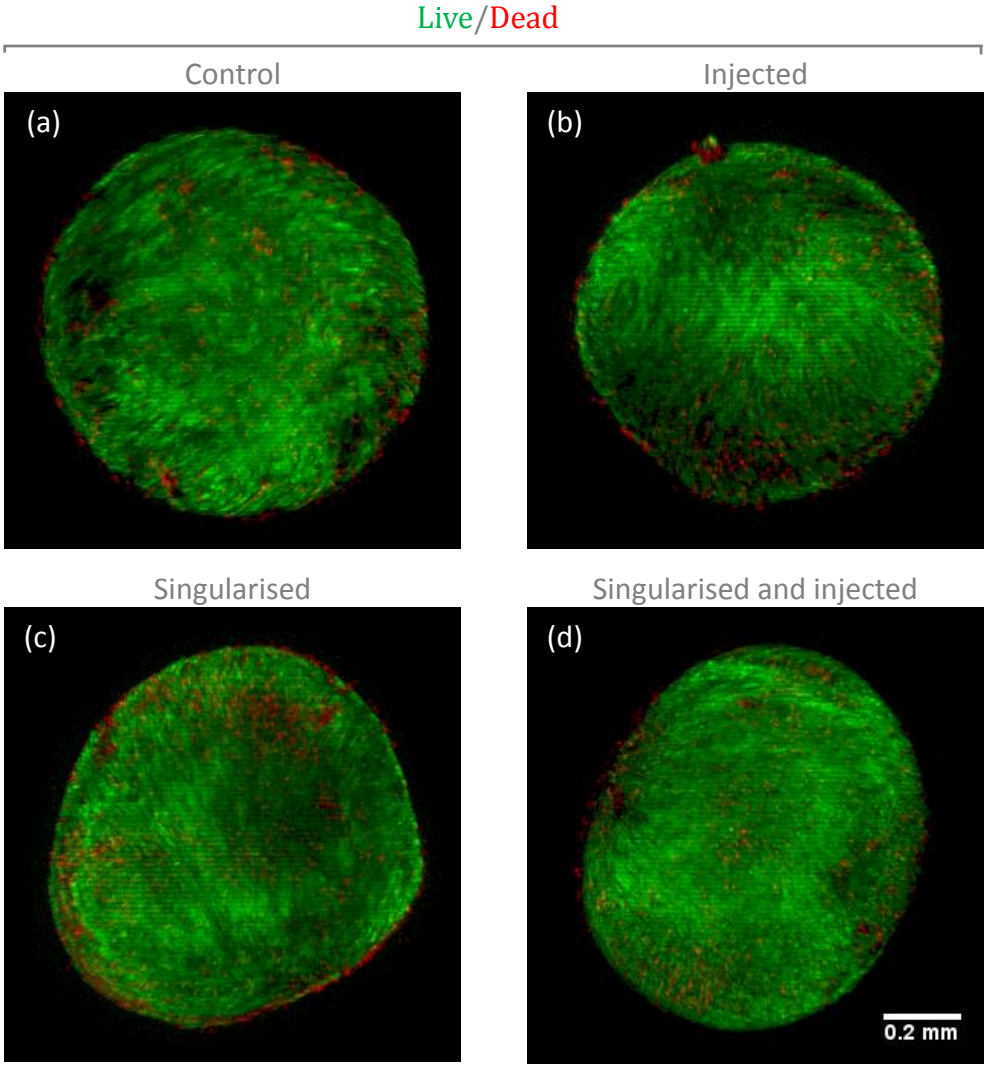

Figure 4-8. Fluorescence microscopy images of (a) control (b) singularised (c) injected and (d) singularised and injected micro-tissues stained with Calcein AM (live cells, green) and Propidium Iodide (dead cells, red) on day 0. *Scale bar = 0.2 mm for all images.*

Fluorescence microscopy images (Figure 4-8) obtained from the live/dead assay of the micro-tissues indicated that the cells at the surface of micro-tissues that were most prone to mechanical or physical deformation were predominantly viable and unaffected by the singularisation and injection process. This was further

validated by trypan blue exclusion assay (Figure 4-9) indicating no significant difference (p>0.05) in percentage of viable cells between the control (80.45 ± 4.77%; non-singularised/non-injected micro-tissue) and either singularised (83.45 ± 3.43%) or injected (78.38 ± 2.37%) or both singularised and injected (83.55 ± 5.53%) micro-tissues. This data suggests that the automated bioassembly system presented in this study does not appear to impart adverse effects on micro-tissues.

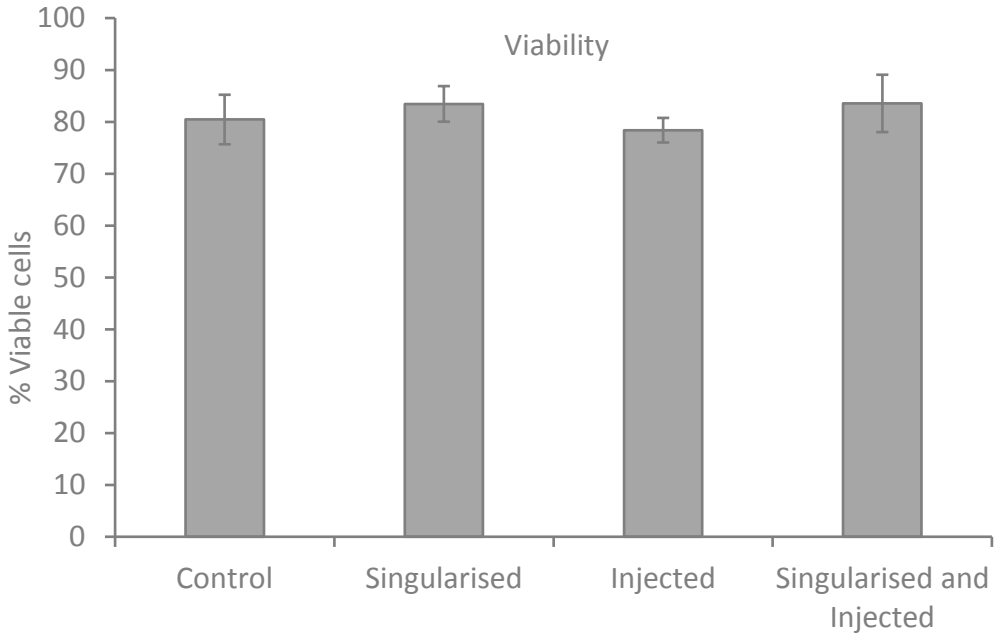

Figure 4-9. Percentage of viable cells determined using the Trypan blue exclusion assay for control, singulation, injected, and injected and singulated micro-tissues on day 0. The data is presented as mean ± SD (*n=4*). *No significant difference (p>0.05). Statistical analysis: 1-way ANOVA.*

4.4.6 Automated tissue assembly

The ability of the automated tissue bioassembly system to assemble a hybrid construct was demonstrated following the validation of the individual bioassembly device components. A scaffold consisting of 1 mm fibre spacing was 3D plotted with the high-temperature plotting head (see Figure 4-5 a) as described above, and fixed HAC micro-tissues stained with Safranin O were inserted into the pores using the micro-tissue injection head (Figure 4-5 b). The steps involved in the layer-by-layer 3D plotting and micro-tissue assembly of a bilayered construct with the aid of the automated bioassembly system as shown in Figure 4-10.

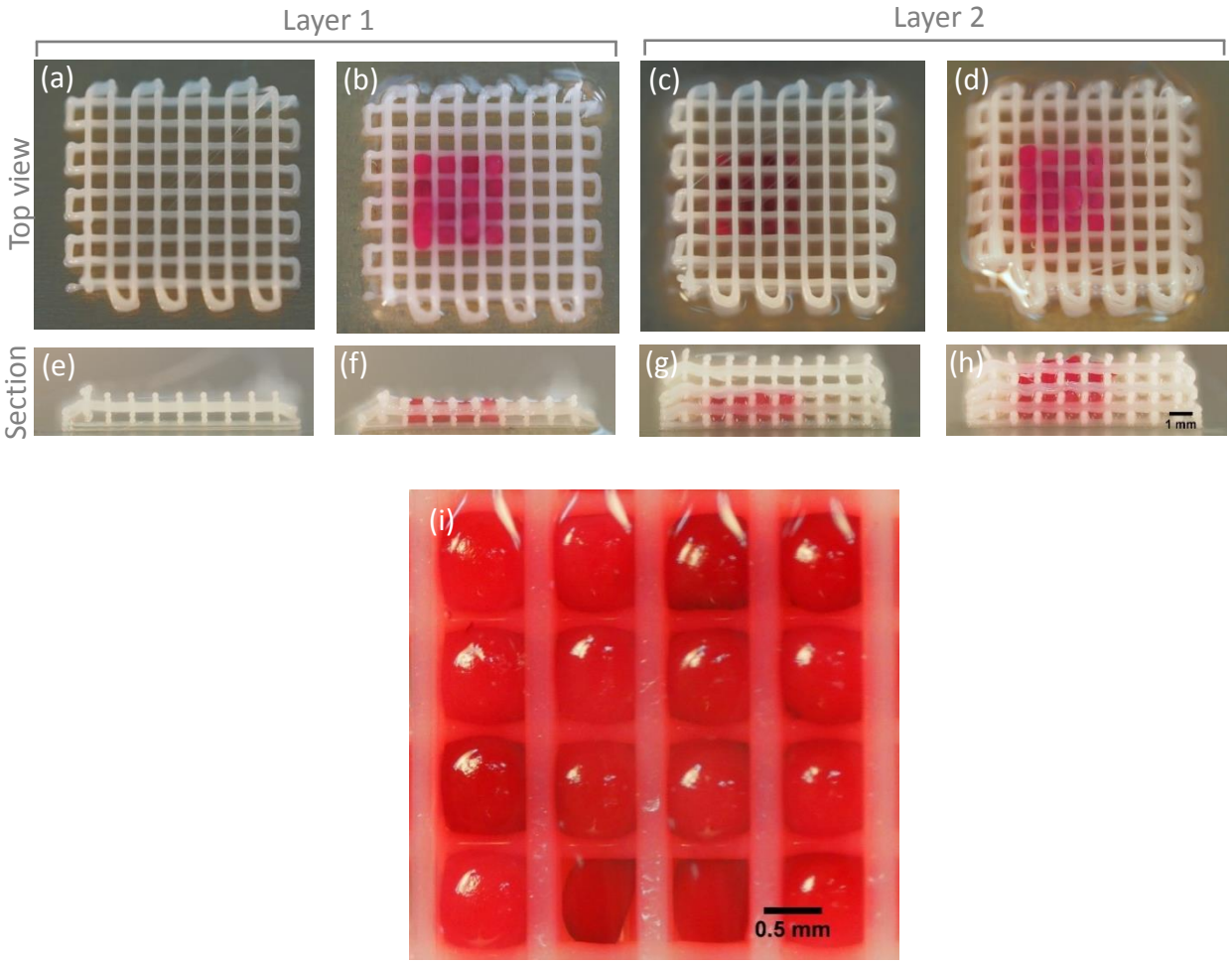

Figure 4-10. (a-h, *Scale bar = 1 mm*) Top view and sectional front view photographs of the steps involved in the layer-by-layer plotting and assembly of a bioassembled construct consisting of high-throughout fabricated HAC micro-tissues with the aid of the automated system. The construct contains 32 micro-tissues, arranged in 2 layers with 16 micro-tissues in each layer. (i) higher magnification image of the assembled construct. The micro-tissues were stained with Safranin O.

4.4.7 Efficiency of micro-tissue insertion

The efficiency of successful micro-tissue insertion into the scaffold was determined to be 79.2 ± 18.8%. Although there were micro-tissues that failed to be inserted into the scaffold, the scaffold was visually inspected by the user for errors at the end of assembling every layer and the micro-tissue insertion process was repeated for pores not containing a micro-tissue, thereby allowing the complete scaffold bioassembly as designed.

4.4.8 Viability of bioassembled constructs

After demonstrating that our fully fluidic approach did not damage the micro-tissues, we had to ascertain that the micro-tissues were not affected by the

automated system inserting the micro-tissues within the designated pores of the plotted scaffold. The dispensing temperature in the high-temperature print head was approximately 200°, although the extruded material rapidly solidifies and cools to ambient temperature. Therefore, during the layer-by-layer plotting process, we had to ensure that the molten polymer being plotted on the previous layer of assembled micro-tissues did not affect cell viability.

The visual inspection of the live/dead fluorescence microscopy images of the manually assembled construct (i.e. micro-tissues were press-fit by hand into a 3D plotted scaffold) and the construct assembled using the bioassembly system showed no obvious differences (Figure 4-11). Furthermore, this observation was validated from the AlamarBlue® assay (Figure 4-12), which demonstrated no significant difference (p>0.05) in the percentage of AlamarBlue® reduced between the manually assembled construct (62.31 ± 4.12%) and construct assembled with the automated bioassembly system (58.40 ± 6.93%).

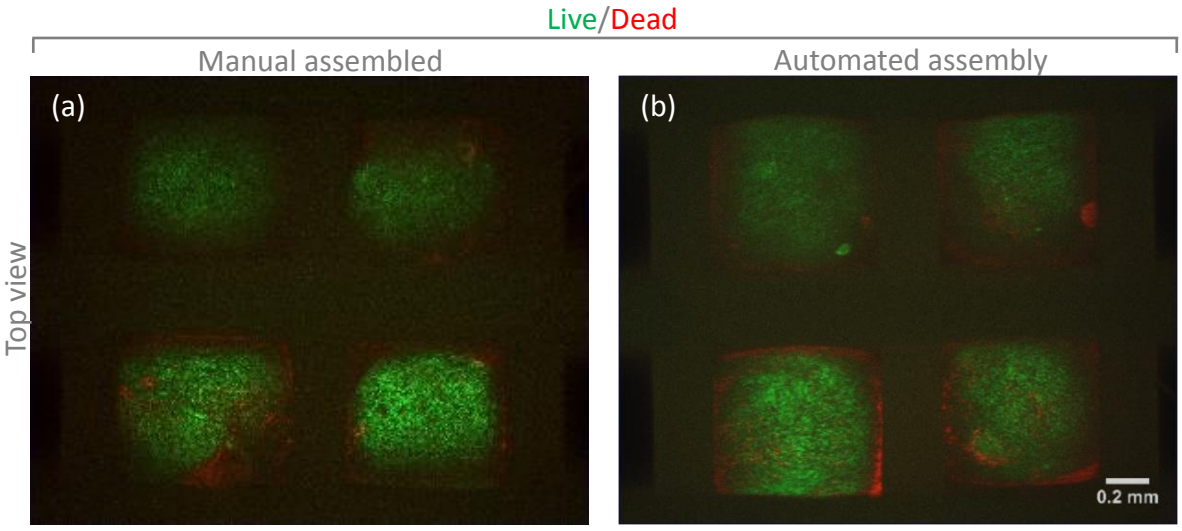

Figure 4-11. Fluorescence microscopy images of (a) manually assembled construct and a (b) construct assembled using the bioassembly system stained with Calcein AM (live cells, green) and Propidium Iodide (dead cells, red) on day 0. *Scale bar = 0.2 mm for all images.*

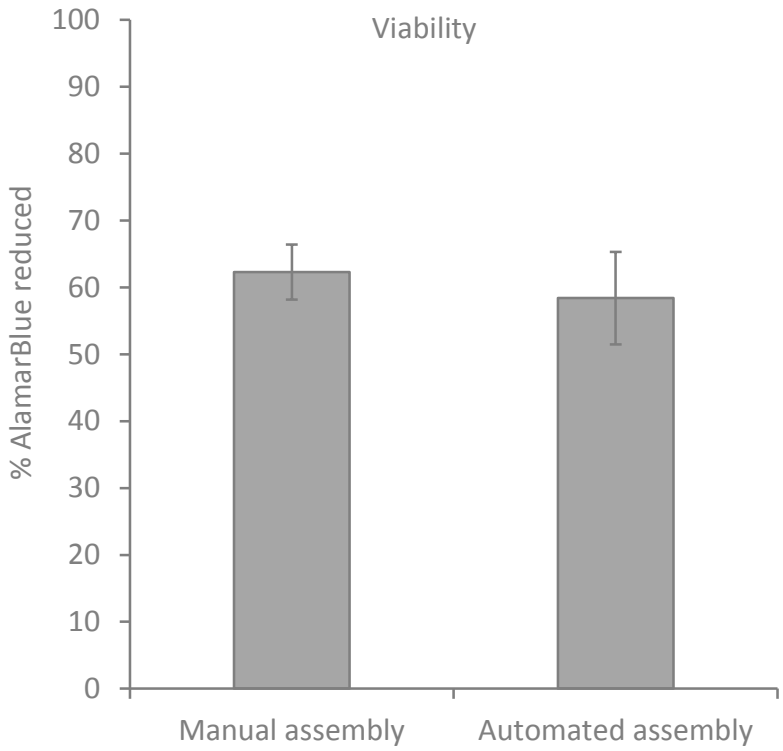

Figure 4-12. Percentage of AlamarBlue® reduced to determine the viability of the manually assembled construct and the construct assembled using the automated system on day 0. The data is presented as mean ± SD (*n=3*). *No significant difference (p>0.05). Statistical analysis: 1-way ANOVA.*

4.5 Discussion

Typically, traditional tissue engineering strategies employ a "top-down" biofabrication approach, where cells are seeded into a pre-fabricated biomaterial scaffold to create an engineered tissue. However, "top-down" approaches with their inability to precisely control the spatial distribution of the cells and support material have difficulty recreating the intricate microstructural features of tissues [19]. On the other hand, "bottom-up" biofabrication approaches or modular tissue engineering focus on fabricating engineered tissue by the self-assembly or directed-assembly of a tissue from smaller components or modules with specific micro-architectural features [20, 43]. Furthermore, as many tissues are comprised of repeating functional units there is a strong biological basis for using bottom-up approaches [19] to biofabricate complex hierarchical and functional engineered tissue constructs.

Modular tissue engineering aims to create biomimetic structures by designing modular tissues that can be used as building blocks to create larger tissues [19]. These modules can be created via a number of approaches, such as self-assembled aggregation [44], micro-fabrication of cell-laden hydrogels [45], creation of cell sheets [46], direct printing of cells [47] or via high-throughput pellet or micro-mass culture techniques [11] as described herein.

The absence of an automated system that assembles micro-tissue "modules" into a bioscaffold to produce an assembled tissue and also the increasing focus on tissues engineered cartilage repair makes it essential and highly relevant to have an automated assembly system. By successfully testing and establishing a reliable and efficient blueprint for such a scheme, we have overcome a barrier to building large and complex high quality living constructs of clinically relevant sizes, with precision, in large numbers, and with a reduced construction time.

Having an automated system means that tissues based on mathematical models or anatomical models generated through non-invasive imaging techniques such as computed tomography (CT) or magnetic resonance imaging (MRI) can easily be translated into a computer-aided design and computer aided manufacturing (CAD/CAM) file and inputted into a bio-plotter [48]. The application of computer-aided technologies has led to the development of a new emerging field of computer-aided tissue engineering (CATE) [49]. We believe that we have paved a path that employs computer-aided technology to create scaffolds with a wide array of properties and geometries, and the system described in this article can be thought of as a submodule of a computer-controlled tooling process for assembling tissue via computer-aided design models.

The described fluidic based system offer advantages over other methods such as laser-based writing or jetting techniques where the cells experience an extreme kinematic profile during the cell transfer process [50-52]. Cell-based constructs fabricated using cell direct writing techniques also have a downfall in that they lack an initial support structure and the maturation of the bioactive tissue must be rapid so as to have the necessary structural support [51]. From our studies, the absence of any detrimental effect on the viability and shape of the micro-tissue after being put

through and assembled using our system reflects the gentle nature of the designed fluidic system. This gentle nature and the reduced human involvement which eliminates human error would encourage end-users to employ the system for their application.

Although the described system works efficiently with micro-tissue sizes that are within the designed size range, the system has an innate shortcoming in that micro-tissues above or below the designed size range cannot be efficiently handled. By suitably modifying the size of the singularisation chamber and the injection nozzle and expanding rod, the tissue assembly system can be adopted for micro-tissues of other desired sizes. Alternately, micro-tissue size can be optimised and adjusted to fit the device using strategies such as adjusting seeding densities during micro-tissue formation.

With the use of parallel singularisation devices rigged up to an injection device, this system can potentially be used to assemble micro-tissues of different cell types in a specific order. The use of the technology in this fashion would have important implications in co-culture systems where two or more cell types are brought together in the same culture environment either to enhance tissue formation of a specific lineage and/or to form a multicellular tissue or organ replacement [33]. In cartilage engineering, this can be applied to chondrocytes and synovial fibroblasts [33], chondrocytes and osteoblasts [33], primary and passaged chondrocytes [53], and mesenchymal stromal cells (MSC) and chondrocyte [54, 55] co-cultures.

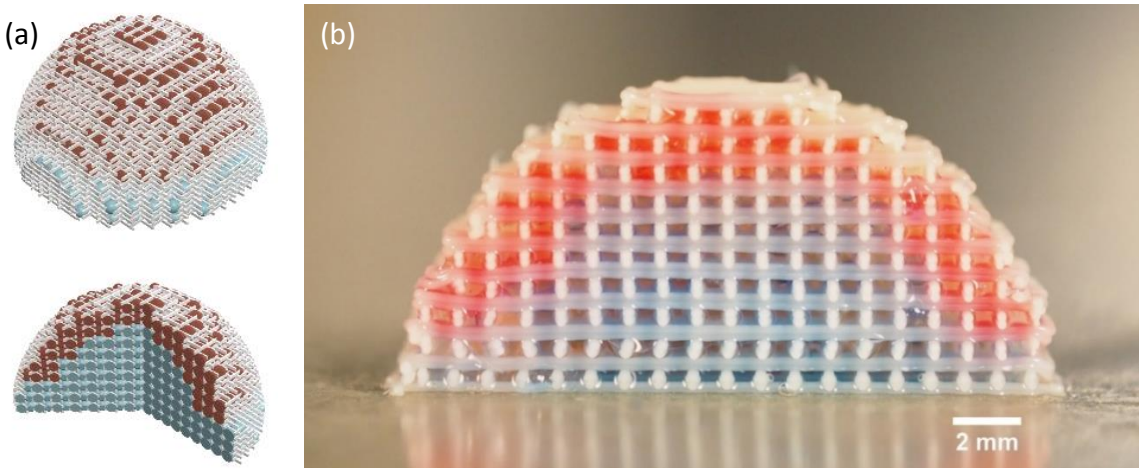

Figure 4-13. (a) Illustration of an assembled hemisphere. (b) a hemisphere assembled with coloured beads employing the automated tissue bioassembly system. This demonstrates possibility of bioassembling a biphasic osteochondral anatomically shaped construct.

The automated bioassembly could be used to assemble a top-down based simple construct where a complete scaffold is prefabricated using 3D plotting, and micro-tissues are assembled into the scaffold or a more complex bottom-up or hybrid approach involving layer-by-layer fabrication where the scaffold is 3D plotted and micro-tissues are co-assembled alternatively to generate complex hierarchical constructs. The impact of this would be the ability to create anatomically shaped complex hybrid constructs (Figure 4-13).

The bioassembly system can also be applied for micro-tissue based applications in other areas. Assembled cancer tissues might play a valuable role in translational research in cancer by potentially recreating the natural physical and structural environment of living tissues, and the use of a tissue assembly system is a natural choice [56]. However, cancer spheroids tend to have a large variation in aggregation pattern between different cell types and this would potentially require modification of the system to accommodate the assembly of certain types cancer spheroids [57].

High-throughput screening (HTS) is another area where the system could be used to handle micro-tissues. In HTS, the use of micro-tissues as a 3D cell culture

system is a better reflection of the *in vivo* behaviour of most cell types rather than monolayer or suspension cultures [58]. HTS in drug testing is frequently carried out on small spheroids of up to 200 μm, which is thought to be sufficient to reflect the 3D cell-cell and cell-matrix interactions [59, 60].

To allow the efficient handling of the smaller sized micro-tissues in HTS, the developed tissue assembly system would have to be a modified for this application. However, with miniaturisation of the system, laminar flow, surface tension, diffusion and fluidic resistance begin to dominate the system [61] and the handling of micro-tissues of very small sizes would require a miniaturized microfluidics-based system to handle the micro-tissues efficiently, making necessary further research on the design and development of a miniaturised system.

4.6 Conclusions

We have described here a novel integrated system applied to the automated 3D bio-assembly of micro-tissues in 3D plotted scaffolds. The singularisation system can effectively deliver a single micro-tissue to the injection system which with the aid of the 3D positioning system can deliver the micro-tissue to any desired point in the bioscaffold. Our results indicate that the system is efficient and that the micro-tissues are unaffected by being handled through the singularisation and injection systems. No difference in viability was observed in a construct assembly manually and with the automated bioassembly system. With the automated bioassembly system, simple constructs could be either fabricated via a top-down approach involving 3D plotting of a complete scaffold and injection of micro-tissues or a flexible bottom-up approach combining layer-by-layer scaffold fabrication and micro-tissues co-assembly to generate complex hierarchical constructs. This technology paves the way to use an automated system to produce complex assembled tissues of clinically relevant sizes.

4.7 References

1. Buckwalter JA, Lane NE. Athletics and osteoarthritis. The American Journal of Sports Medicine. 1997;25(6):873-881.
2. Hunziker EB. Articular cartilage repair: basic science and clinical progress. A review of the current status and prospects. Osteoarthritis and Cartilage. 2002;10(6):432-463.
3. Brittberg M. Autologous chondrocyte transplantation. Clinical Orthopaedics and Related Research. 1999;367:S147-S155.
4. Lewis PB, McCarty III LP, Kang RW, Cole BJ. Basic science and treatment options for articular cartilage injuries. Journal of Orthopaedic & Sports Physical Therapy. 2006;36(10):717-727.
5. Hangody L, Füles P. Autologous osteochondral mosaicplasty for the treatment of full-thickness defects of weight-bearing joints. The Journal of Bone and Joint Surgery - American Volume. 2003;85(suppl 2):25-32.
6. Lalan S, Pomerantseva I, Vacanti JP. Tissue engineering and its potential impact on surgery. The World Journal of Surgery. 2001;25(11):1458-66.
7. Ikada Y. Challenges in tissue engineering. Journal of The Royal Society Interface. 2006;3(10):589-601.
8. Woodfield TB, Malda J, de Wijn J, Peters F, Riesle J, van Blitterswijk CA. Design of porous scaffolds for cartilage tissue engineering using a three-dimensional fiber-deposition technique. Biomaterials. 2004;25(18):4149-61.
9. Keeney M, Lai JH, Yang F. Recent progress in cartilage tissue engineering. Current Opinion in Biotechnology. 2011;22(5):734-740.
10. Schulze-Tanzil G, de Souza P, Villegas Castrejon H, John T, Merker HJ, Scheid A, Shakibaei M. Redifferentiation of dedifferentiated human chondrocytes in high-density cultures. Cell and Tissue Research. 2002;308(3):371-9.
11. Schon BS, Schrobback K, van der Ven M, Stroebel S, Hooper GJ, Woodfield TB. Validation of a high-throughput microtissue fabrication process for 3D assembly of tissue engineered cartilage constructs. Cell and Tissue Research. 2012.
12. Babur BK, Futrega K, Lott WB, Klein TJ, Cooper-White J, Doran MR. High-throughput bone and cartilage micropellet manufacture, followed by assembly of micropellets into biphasic osteochondral tissue. Cell and Tissue Research. 2015;361(3):755-768.
13. Schrobback K, Klein TJ, Woodfield TB. The importance of connexin hemichannels during chondroprogenitor cell differentiation in hydrogel versus microtissue culture models. Tissue Engineering Part A. 2015;21(11-12):1785-1794.
14. Kelm JM, Djonov V, Ittner LM, Fluri D, Born W, Hoerstrup SP, Fussenegger M. Design of custom-shaped vascularized tissues using microtissue spheroids as minimal building units. Tissue Engineering. 2006;12(8):2151-60.
15. Penick KJ, Solchaga LA, Welter JF. High-throughput aggregate culture system to assess the chondrogenic potential of mesenchymal stem cells. Biotechniques. 2005;39(5):687.
16. Welter JF, Solchaga LA, Penick KJ. Simplification of aggregate culture of human mesenchymal stem cells as a chondrogenic screening assay. Biotechniques. 2007;42(6):732.
17. Ibold Y, Frauenschuh S, Kaps C, Sittinger M, Ringe J, Goetz PM. Development of a high-throughput screening assay based on the 3-dimensional pannus model for rheumatoid arthritis. Journal of biomolecular screening. 2007;12(7):956-965.
18. Huang AH, Motlekar NA, Stein A, Diamond SL, Shore EM, Mauck RL. High-throughput screening for modulators of mesenchymal stem cell chondrogenesis. Annals of Biomedical Engineering. 2008;36(11):1909-1921.
19. Nichol JW, Khademhosseini A. Modular tissue engineering: engineering biological tissues from the bottom up. Soft Matter. 2009;5(7):1312-1319.

20. Elbert DL. Bottom-up tissue engineering. Current Opinion in Biotechnology. 2011;22(5):674-80.
21. Livoti CM, Morgan JR. Self-assembly and tissue fusion of toroid-shaped minimal building units. Tissue Engineering Part A. 2010;16(6):2051-61.
22. Rago AP, Dean DM, Morgan JR. Controlling cell position in complex heterotypic 3D microtissues by tissue fusion. Biotechnology and Bioengineering. 2009;102(4):1231-41.
23. Jakab K, Norotte C, Damon B, Marga F, Neagu A, Besch-Williford CL, Kachurin A, Church KH, Park H, Mironov V, Markwald R, Vunjak-Novakovic G, Forgacs G. Tissue engineering by self-assembly of cells printed into topologically defined structures. Tissue Engineering Part A. 2008;14(3):413-21.
24. Shimizu T, Sekine H, Isoi Y, Yamato M, Kikuchi A, Okano T. Long-term survival and growth of pulsatile myocardial tissue grafts engineered by the layering of cardiomyocyte sheets. Tissue Engineering. 2006;12(3):499-507.
25. McGuigan AP, Sefton MV. Vascularized organoid engineered by modular assembly enables blood perfusion. Proceedings of the National Academy of Sciences. 2006;103(31):11461-11466.
26. Du Y, Lo E, Ali S, Khademhosseini A. Directed assembly of cell-laden microgels for fabrication of 3D tissue constructs. Proceedings of the National Academy of Sciences. 2008;105(28):9522-9527.
27. Yeh J, Ling Y, Karp JM, Gantz J, Chandawarkar A, Eng G, Blumling Iii J, Langer R, Khademhosseini A. Micromolding of shape-controlled, harvestable cell-laden hydrogels. Biomaterials. 2006;27(31):5391-5398.
28. Imparato G, Urciuolo F, Casale C, Netti PA. The role of microscaffold properties in controlling the collagen assembly in 3D dermis equivalent using modular tissue engineering. Biomaterials. 2013;34(32):7851-7861.
29. Caldwell DJ, Rao RR, Stegemann JP. Assembly of discrete collagen–chitosan microenvironments into multiphase tissue constructs. Advanced Healthcare Materials. 2013;2(5):673-677.
30. Dikina AD, Strobel HA, Lai BP, Rolle MW, Alsberg E. Engineered cartilaginous tubes for tracheal tissue replacement via self-assembly and fusion of human mesenchymal stem cell constructs. Biomaterials. 2015;52:452-462.
31. Mironov V, Kasyanov V, Drake C, Markwald RR. Organ printing: promises and challenges. Regenerative Medicine. 2008;3(1):93-103.
32. Mironov V, Visconti RP, Kasyanov V, Forgacs G, Drake CJ, Markwald RR. Organ printing: Tissue spheroids as building blocks. Biomaterials. 2009;30(12):2164-2174.
33. Hendriks J, Riesle J, van Blitterswijk CA. Co-culture in cartilage tissue engineering. J Tissue Eng Regen Med. 2007;1(3):170-8.
34. Woodfield TBF, Guggenheim M, von Rechenberg B, Riesle J, van Blitterswijk CA, Wedler V. Rapid prototyping of anatomically shaped, tissue-engineered implants for restoring congruent articulating surfaces in small joints. Cell Proliferation. 2009;42(4):485-497.
35. Woodfield TB, Miot S, Martin I, van Blitterswijk CA, Riesle J. The regulation of expanded human nasal chondrocyte re-differentiation capacity by substrate composition and gas plasma surface modification. Biomaterials. 2006;27(7):1043-1053.
36. Miot S, Woodfield T, Daniels AU, Suetterlin R, Peterschmitt I, Heberer M, Van Blitterswijk CA, Riesle J, Martin I. Effects of scaffold composition and architecture on human nasal chondrocyte redifferentiation and cartilaginous matrix deposition. Biomaterials. 2005;26(15):2479-2489.
37. Woodfield T, Guggenheim M, Von Rechenberg B, Riesle J, Van Blitterswijk C, Wedler V. Rapid prototyping of anatomically shaped, tissue-engineered implants for restoring congruent articulating surfaces in small joints. Cell Proliferation. 2009;42(4):485-497.

38. Woodfield TB, Moroni L, Malda J. Combinatorial approaches to controlling cell behaviour and tissue formation in 3D via rapid-prototyping and smart scaffold design. Combinatorial Chemistry & High Throughput Screening. 2009;12(6):562-579.
39. Moroni L, De Wijn J, Van Blitterswijk C. 3D fiber-deposited scaffolds for tissue engineering: influence of pores geometry and architecture on dynamic mechanical properties. Biomaterials. 2006;27(7):974-985.
40. Park S, Hung C, Ateshian G. Mechanical response of bovine articular cartilage under dynamic unconfined compression loading at physiological stress levels. Osteoarthritis and cartilage. 2004;12(1):65-73.
41. Mauck R, Wang C-B, Oswald E, Ateshian G, Hung C. The role of cell seeding density and nutrient supply for articular cartilage tissue engineering with deformational loading. Osteoarthritis and Cartilage. 2003;11(12):879-890.
42. Treppo S, Koepp H, Quan EC, Cole AA, Kuettner KE, Grodzinsky AJ. Comparison of biomechanical and biochemical properties of cartilage from human knee and ankle pairs. Journal of Orthopaedic Research. 2000;18(5):739-748.
43. Schon B, Hooper G, Woodfield T. Modular tissue assembly strategies for biofabrication of engineered cartilage. Annals of Biomedical Engineering. 2016:1-15.
44. Dean DM, Napolitano AP, Youssef J, Morgan JR. Rods, tori, and honeycombs: the directed self-assembly of microtissues with prescribed microscale geometries. The FASEB Journal. 2007;21(14):4005-12.
45. Yeh J, Ling Y, Karp JM, Gantz J, Chandawarkar A, Eng G, Blumling J, 3rd, Langer R, Khademhosseini A. Micromolding of shape-controlled, harvestable cell-laden hydrogels. Biomaterials. 2006;27(31):5391-8.
46. L'Heureux N, Paquet S, Labbe R, Germain L, Auger FA. A completely biological tissue-engineered human blood vessel. The FASEB Journal. 1998;12(1):47-56.
47. Mironov V, Boland T, Trusk T, Forgacs G, Markwald RR. Organ printing: computer-aided jet-based 3D tissue engineering. Trends in Biotechnology. 2003;21(4):157-61.
48. Agarwala MK, Jamalabad VR, Langrana NA, Safari A, Whalen PJ, Danforth SC. Structural quality of parts processed by fused deposition. Rapid Prototyping Journal. 1996;2(4):4-19.
49. Sun W, Lal P. Recent development on computer aided tissue engineering - a review. Computer Methods and Programs in Biomedicine. 2002;67(2):85-103.
50. Smausz T, Hopp B, Kecskemeti G, Bor Z. Study on metal microparticle content of the material transferred with absorbing film assisted laser induced forward transfer when using silver absorbing layer. Applied Surface Science. 2006;252(13):4738-4742.
51. Schiele NR, Corr DT, Huang Y, Raof NA, Xie Y, Chrisey DB. Laser-based direct-write techniques for cell printing. Biofabrication. 2010;2(3):032001.
52. Jayasinghe SN. Cell engineering: spearheading the next generation in healthcare. Biomedical Materials. 2008;3(3):034004.
53. Gan L, Kandel RA. *In vitro* cartilage tissue formation by co-culture of primary and passaged chondrocytes. Tissue Engineering. 2007;13(4):831-42.
54. Acharya C, Adesida A, Zajac P, Mumme M, Riesle J, Martin I, Barbero A. Enhanced chondrocyte proliferation and mesenchymal stromal cells chondrogenesis in coculture pellets mediate improved cartilage formation. Journal of Cellular Physiology. 2012;227(1):88-97.
55. Bian L, Zhai DY, Mauck RL, Burdick JA. Coculture of human mesenchymal stem cells and articular chondrocytes reduces hypertrophy and enhances functional properties of engineered cartilage. Tissue Engineering Part A. 2011;17(7-8):1137-45.
56. Kim JB, Stein R, O'Hare MJ. Three-dimensional *in vitro* tissue culture models of breast cancer- a review. Breast Cancer Research and Treatment. 2004;85(3):281-91.
57. Carlsson J, Nilsson K, Westermark B, Ponten J, Sundstrom C, Larsson E, Bergh J, Pahlman S, Busch C, Collins VP. Formation and growth of multicellular spheroids of human origin. International Journal of Cancer. 1983;31(5):523-33.

58. Kunz-Schughart LA, Freyer JP, Hofstaedter F, Ebner R. The use of 3-D cultures for high-throughput screening: the multicellular spheroid model. J Biomol Screen. 2004;9(4):273-85.
59. Ivascu A, Kubbies M. Rapid generation of single-tumor spheroids for high-throughput cell function and toxicity analysis. J Biomol Screen. 2006;11(8):922-32.
60. Friedrich J, Seidel C, Ebner R, Kunz-Schughart LA. Spheroid-based drug screen: considerations and practical approach. Nat Protoc. 2009;4(3):309-24.
61. Beebe DJ, Mensing GA, Walker GM. Physics and applications of microfluidics in biology. Annual Review of Biomedical Engineering. 2002;4:261-86.

Chapter 5 Automated 3D Bioassembly of cell-laden microspheres for biofabricating tissue engineered cartilage constructs

5.1 Abstract

Encapsulating chondrocytes in hydrogels is an emerging tissue engineering strategy. Hydrogels are appealing as they can mimic the hydrated 3D environment in native cartilage. However, controlling the microarchitecture of a hydrogel construct is challenging and one of the strategies to overcome this is to exploit modular assembly based tissue engineering approaches to fabricate complex hybrid constructs. Not many technologies have been developed to automate the precise assembly of hydrogel modules into 3D plotted scaffolds. We fabricated GelMA microspheres and human articular chondrocyte (HAC)-laden 9.5% GelMA-0.5% HepMA hydrogel microspheres of Ø1 mm with a microfluidic device to be used as tissue units. Previously, we had developed a fluidic based 3D tissue bioassembly system that precisely assembles microspheres into 3D plotted scaffolds for fabricating large, complex tissue-engineered constructs. The fabricated microspheres were reliably and efficiently handled by the automated bioassembly system. Different arrangements of the various coloured (representing different microsphere types) microspheres were assembled into 3D plotted scaffolds to demonstrate the flexibility of the automated bioassembly system. Layer-by-layer 3D Bioassembly of 8 HAC-laden microspheres into a 3D plotted PEGT/PBT polymer scaffold with the automated tissue bioassembly system showed no significant difference in viability when compared with manually assembled bilayered constructs. Individual HAC-laden microspheres and assembled constructs were cultured for 5 weeks. Fixed frozen sections were stained for aggrecan and they revealed neocartilage formation. Higher aggrecan was visualized in the assembled construct compared to the individual microspheres. Furthermore, we demonstrated the fabrication of a graduated construct with Qtracker labelled HAC, co-culture (50% HAC and 50% mesenchymal stromal cells (MSC)) and MSC laden microspheres and the immunofluorescence staining for aggrecan revealed cartilage tissue formation.

This technology demonstrates the feasibility of bioassembling large complex constructs with hydrogel microspheres.

5.2 Introduction

The repair of injured or damaged cartilage is, unfortunately, challenging due to its limited ability to heal. It has been acknowledged by the research and medical community that tissue engineering and regenerative medicine (TERM) strategies could possibly be employed for clinical repair or regeneration of cartilage and hopefully be able to overcome the limitations of current repair strategies [1, 2]. The tissue engineering paradigm, the rational for tissue engineering of cartilage and the need for developing an automated system, has been discussed earlier (chapter 4), but an outline with respect to hydrogels is explained here.

Biofabrication of a cartilage construct containing pre-formed high cell density micro-tissues has shown promising outcomes with respect to chondrogenic capacity, extracellular matrix (ECM) formation and tissue fusion during *in vitro* culture [3]. Creating a cartilage construct of clinically relevant size with micro-tissues requires substantial cell expansion thereby making it expensive. Assuming a single 1 mm diameter micro-tissue contains 0.25 million cells, merely fabricating a clinically relevant sized construct of Ø25 mm and 2.4 mm thickness with micro-tissues would require approximately 247 million cells [3-5]. Moreover, chondrocytes have a limited proliferative potential and when autologous cells are cultured in a monolayer, they dedifferentiate and lose their chondrogenic phenotype [6].

An alternative route to fabricating micro-tissues would be to encapsulate chondrocytes or chondroprogenitor cells (mesenchymal stromal cells (MSCs)) within hydrogel microspheres. Hydrogels are appealing as fabricating a tissue construct with a hydrogel requires a lesser number of cells compared to a micro-tissue based construct of the same size [3, 7, 8]. Moreover, hydrogels can promote cell survival and imitate the features of natural cartilage including providing a hydrated 3D environment [9]. A wide range of hydrogel systems such alginate [10], agarose [11], collagen [12], fibrin [13], poly(ethylene glycol) (PEG) [14], poly(ethylene oxide) (PEO)[15] and poly(vinyl alcohol) (PVA) [16] hydrogels have been researched for cartilage engineering. We chose gelatin-methacryloyl (GelMA)

which is a functionalised gelatin that allows for the irreversible covalent crosslinking as it has been shown to support cartilage formation and can be photocrosslinked with visible light making it less detrimental to cells [8, 17, 18]. GelMA is also appealing as it is inexpensive, is water soluble, contain cell binding motifs, can be derived from a wide variety of sources, is biocompatible, can be easily processed and its stiffness can be modulated [19, 20]. Moreover, GelMA based hydrogels can also be functionalised with cartilage specific matrix compounds like hyaluronic acid [8, 21], chondroitin sulphate [21] and can also be incorporated with bioactive molecules like TGF-β1 [15, 22] to promote cartilage formation.

Populating cells in a scaffold is the conventional tissue engineering paradigm for regenerative medicine strategies [23-26]. Hydrogel constructs are typically fabricated via casting approaches in a mould ultimately to be utilised for minimally invasive delivery of reparative cells [26]. A disadvantage of this approach is the limited ability to directly control the exact location or 3D spatial resolution of cells, multiple cell types and/or ECM components [27]. Current biofabrication or 3D Bioprinting strategies offer an alternative solution via top-down dispensing of multiple bioinks to fabricate complex layers of cell-laden hydrogel fibres, with each bioink comprising of multiple cell sources or combinations of ECM components, dispersed around 3D plotted structural thermoplastic biomaterial scaffolds to provide mechanical integrity to the hybrid construct [28, 29]. On the other hand, modular assembly based bottom-up approaches may allow the biofabrication of large constructs of complex geometry with specific cellular arrangement and microarchitectural features [23, 30]. In modular assembly based bottom-up strategies, larger macro-scale tissues are assembled using smaller tissue units [27]. A range of tissue module types can be fabricated for tissue assembly and these include cell sheets [31, 32], micro-tissues (which we have previously utilised for the demonstration of an assembled cartilage construct (Chapter 4)) or cellular aggregates [3, 33-36], cell-laden microgels [37, 38], tissue-rings [39] or cell-laden hydrogel microspheres [40]. A modular hydrogel system would enable the fabrication of large constructs of complex architecture. The approach would enable the assembly of zonal constructs with different zonal subpopulations thereby recreating the zonal arrangement of native articular cartilage [7, 35]. Bioassembly of an osteochondral construct assembled with chondrocytes and osteoprogenitor

cells would be possible [36]. This bioassembly technique could also be used to fabricate constructs with a gradient or different cell types, bioactive molecules, mechanical properties, hydrogel types or varying cell densities [7, 37]. The advantage of the bioassembly technique would be that it would allow the automated and controlled fabrication of functional engineered tissues which mimics the native tissue architecture and mechanical properties.

Substantial work has been performed on the development of biofabrication techniques to control the architecture of an engineered construct. 3D plotting of cell-laden photocurable bioinks for application in cartilage tissue engineering has been demonstrated by Costantini *et al.* and Lim *et al.* [18, 41]. Boere *et al*. engineered a hybrid 3D plotted cartilage constructs with improved mechanical properties by reinforcing the hydrogel with a 3D plotted thermoplastic [42]. Vissers *et al.* demonstrated the fabrication of a composite hydrogel construct mechanically reinforced with thermoplastic using melt electrospinning writing [43]. Specifically, with regards to bioassembly, the utilisation of hydrogel subunits or modules to assemble larger tissue structures have been demonstrated for cardiac tissue engineering [44], bone tissue engineering [45], vascularisation in a construct [46] and for general application in tissue engineering [37, 38]. Ozbolat *et al.* developed a system in which cell-laden alginate scaffold was 3D plotted with a co-axial nozzle and cell-laden alginate spheres that formed at the tip of the dispensing nozzle were deposited into the scaffold [47]. The arrangement of cell-laden microgels in specific configurations using a micromanipulator has also been shown [48]. As far as we know, there exists no fabrication technique or technology where cell-laden hydrogel microspheres can be assembled into a 3D plotted thermoplastic polymer scaffold to create a custom cartilage or musculoskeletal construct of complex architecture.

We have previously developed a prototype automated tissue bioassembly system that can precisely assemble tissue units into a 3D plotted scaffold using a bottom-up approach based on the simultaneous layer-by-layer scaffold and micro-tissue assembly strategy. The developed 3D Bioassembly system was capable of fabricating (i) simple constructs using top-down bioassembly strategy which is a two-step strategy involving the 3D plotting of a scaffold and the assembly of tissue units into the desired location in the scaffold, and (ii) hybrid constructs using a

bottom-up bioassembly strategy which is a multistep strategy involving the alternative 3D plotting and assembly of tissue units into the scaffold to generate the hybrid construct (see Chapter 4). The bioassembly of a hydrogel based construct requires the fabrication of hydrogel microsphere module or units. To fabricate the hydrogel microsphere modules or units, a diverse range of techniques including electrospraying [49], polyelectrolyte complexation [50], solvent evaporation [51], jet cutting [52], jet breakup [53], and electrostatic droplet generation [54] exist. We utilised a simple droplet microfluidic setup coupled with photopolymerisation [55]. This setup was adapted from Serra *et al.* as its ability to produce microspheres within a controlled size range with minimum variation was previously demonstrated [40, 55]. The commonly reported method of photopolymerising GelMA has been combining the photoinitiator, Irgacure 2959 with UV light irradiation [19, 56, 57]. However, UV light has been shown to be detrimental to cell cytocompatibility as it can cause chromosomal and genetic instability [20, 58]. Our group has previously developed a visible light based photopolymerisation system that showed an improved cytocompatibility and viability, which was adapted herein [18].

The specific objective of this study was the development and validation of an automated 3D Bioassembly of cell-laden hydrogel microspheres for biofabricating a tissue engineered cartilage construct. This involved (i) adopting a high-throughput microfluidic system to fabricate Ø1 mm cell-laden hydrogel microspheres that can be handled by the automated bioassembly system, (ii) validating the flexibility of the automated tissue bioassembly system by demonstrating different arrangements of the microspheres in a scaffold, (iii) demonstrating the ability to bioassemble cell-laden hydrogel microspheres and fabricate a complex 3D construct utilising automated tissue bioassembly system without affecting the viability, (iv) assessing tissue formation *in vitro* in HAC-laden GelMA-HepMA hydrogels in individual microspheres and in 3D bioassembled constructs cultured in vitro (v) and demonstrating the fabrication of a complex 3D gradient construct containing HAC, MSC and co-culture GelMA-HepMA microspheres and assessing tissue formation *in vitro*.

5.3 Methods

5.3.1 Chondrocytes and mesenchymal stromal cells (MSCs) isolation

Human articular chondrocytes (HACs) were isolated and expanded using the method described previously by Schon *et al.* [3]. Briefly, articular cartilage biopsies were obtained with ethics approval from consenting patients undergoing cruciate (knee) ligament reconstruction (*n=2*, 18, 25 years of age). The cartilage was diced into cubes sized around 1 mm and digested overnight in basic chondrocyte media containing DMEM (high glucose, GlutaMAX Supplement, pyruvate; GIBCO, USA) with 10% foetal bovine serum (FBS; GIBCO, New Zealand), 0.1 mM non-essential amino acids (NEAA; GIBCO, USA), 10 mM HEPES (GIBCO, Taiwan), 0.2 mM L-ascorbic acid-2-phosphate (Sigma-Aldrich, USA), 0.4 mM L-proline (Sigma-Aldrich, USA), 100 units/mL penicillin (GIBCO, USA) and 100 µg/mL streptomycin (GIBCO, USA) and along with 0.15% (w/v) collagenase type II (Worthington, USA). The suspension was then filtered through a 100 µm pore cell strainer (Corning, USA) and centrifuged at 700 g for 4 minutes.

Human mesenchymal stromal cells (MSCs) were obtained from an iliac crest bone marrow aspirate. The aspirate was obtained from a healthy donor (*n=1*, 33 years of age) undergoing upper limb procedure where an iliac crest bone graft was required. The MSCs were isolated from the bone marrow aspirate by plastic adhesion. The bone marrow aspirates were diluted 1:4 in basic MSC media containing MEM Alpha (GlutaMAX Supplement; GIBCO, USA) with 10% FBS, 100 units/mL penicillin, 100 µg/mL streptomycin, and 1 ng/mL basic Fibroblast growth factor (bFGF; R&D systems, USA) and then plated into a tissue culture flask. The next day, the flasks were washed with PBS to remove any non-adherent cells and fresh basic MSC media was added.

5.3.2 Cell expansion

Freshly isolated HACs were seeded at a density of 3,000 cells/cm^2 in tissue culture flasks (Falcon, USA) in basic chondrocyte media. Cells were expanded at 37°C in a humidified 5% CO_2/95% air incubator and the media was changed twice a week. After approximately 7 days, subconfluent first passage cells (P_1) were washed with phosphate-buffered saline (PBS; GIBCO, USA), detached using 0.25% trypsin/EDTA

(Gibco, Canada), counted by trypan blue exclusion (GIBCO, USA) in a haemocytometer and plated in a tissue culture flask at 3,000 cells/cm^2. The third passage (P_3) cells were harvested similarly, suspended in basic chondrocyte media and made ready to be encapsulated.

The MSCs were seeded at a density of 5,000 cells/cm^2 and expanded similarly to HACs but with basic MSC media.

5.3.3 Cell labelling with Qtracker

Qtracker cell labelling kit (Life technologies, USA) was used to track cells in a co-culture environment. HACs were labelled with Qtracker 655 and MSCs with Qtracker 800. To label the cells with Qtracker, cells were concentrated to 10 x 10^6 cells/ml by centrifugation at 700 g for 5 minutes and resuspended in DMEM. A 10 nM labelling solution was prepared by mixing 1 µL of the Qtracker Component A and 1 µL of the Qtracker Component B in a 1.5 ml microcentrifuge tube and incubated at room temperature for 5 minutes. 0.2 ml of DMEM was added to the mixture and vortexed for 30 seconds. 10^6 cells were added to the labelling mixture and incubated for 60 minutes. The cells were subsequently washed twice with DMEM and re-suspended in basic chondrocyte media for use.

5.3.4 Synthesis of gelatin-methacryloyl (GelMA) and methacrylated heparin (HepMA)

Gelatin (porcine skin, type A, 300g Bloom strength) (Sigma-Aldrich, USA) was dissolved in phosphate-buffered saline (PBS; GIBCO, USA) at a 10 wt% concentration. 0.6 g of methacrylic anhydride (Sigma-Aldrich, USA) per gram of gelatin was added to the gelatin solution, and left to react for 1 h at 50˚C under constant stirring [59], followed by dialysis against deionised water to remove unreacted methacrylic anhydride. The purified GelMA solution was filtered through a 0.2 µm sterile filter (Ahlstrom, Germany), then lyophilised under sterile conditions. The degree of methacryloyl substitution was quantified to be 60% (data not shown) using ^{1}H-proton nuclear magnetic resonance spectroscopy (Bruker Avance 400 MHz).

Methacrylated heparin (HepMA) was synthesized based on methods described by Smeds *et al.* [60]. Heparin sodium salt (porcine intestinal mucosa, grade I-A) (Sigma-Aldrich, USA) was dissolved in PBS at a 1 wt% concentration. Methacrylate anhydride was added 10-fold molar excess over primary amine and hydroxyl groups. The reaction mixture was kept at 4˚C under constant stirring while repeatedly adjusting the pH to 8 for 24 hours. The remaining steps were carried out similar to GelMA.

5.3.5 Micro-fluidic device

Figure 5-1 shows the schematic of the microfluidic system. The system was adapted from the setup described by Serra *et al*. [55]. The micro-fluidic system consisted of fused silica capillary, T-junction and Tygon tubing. The T-junction was fabricated from Perspex using conventional machining techniques. A fused silica capillary (PostNova, Germany) with an ID x OD 530 x 660 μm was inserted into the T-junction along its horizontal axis. The tip of the fused silica capillary was positioned so that it exited from the T-junction at the centre of the outlet Tygon tubing ID x OD 1.6 x 3.2 mm. Two syringe pumps (New Era, USA) were used to deliver the continuous and dispersed phases at a specific flow rate. The dispersed phase was injected via the fused silica capillary while the continuous phase was injected through the horizontal port of the T-junction. Tygon tubing connected the syringes (BD Biosciences, USA) through a gauge-16 needle (BD Biosciences, USA) to the ports of the T-junction. The output port of the microfluidic system was connected to a long coil of transparent Tygon tubing which was positioned under the light source fitted with a collimator to crosslink the formed microspheres under the light. The length of the coil was so that each microsphere was exposed to the light source for 2 minutes. The syringe containing the macromer (the pre-polymerised monomers) and the inlet tubing to the T-junction was wrapped in aluminium foil to prevent crosslinking of the macromer before the microspheres were formed.

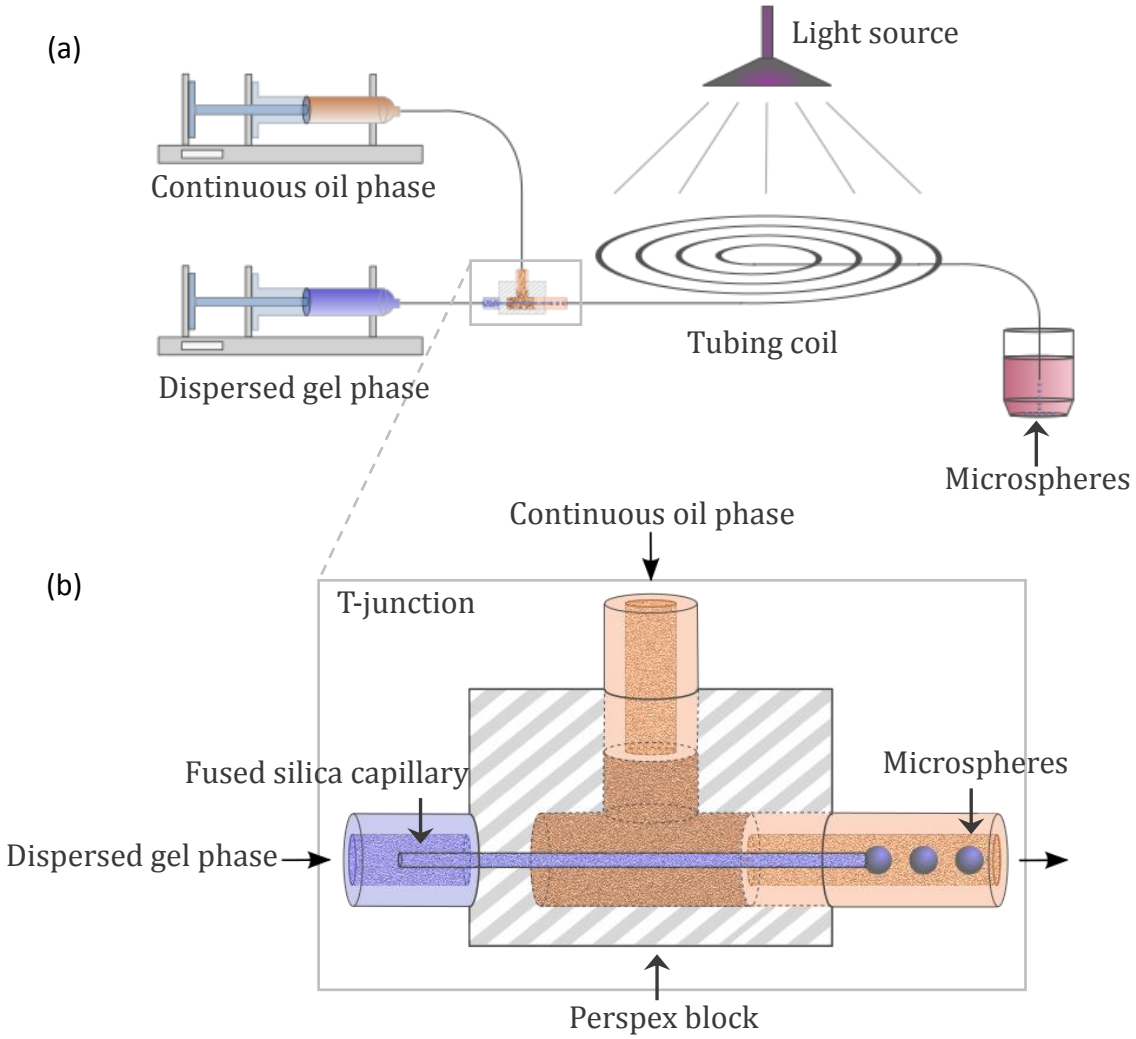

Figure 5-1. (a) Schematic of the arrangement of the microfluidic system to form microspheres and (b) a magnified schematic of the T-junction, adapted from Serra *et al.* [55].

5.3.6 Fabrication of cell-free GelMA hydrogel microspheres

To fabricate the cell-free GelMA hydrogel microspheres, dried sterile GelMA (5 wt% and 10 wt%) was dissolved in PBS at 37˚C and left to cool overnight at room temperature. A visible light system was chosen to crosslink the microspheres as UV light can be detrimental to the cells compared to visible light [18]. Prior to crosslinking, 0.2 mM tris(2,2-bipyridyl)dichlororuthenium(II) hexahydrate (Ru; Sigma-Aldrich, USA) and 2mM sodium persulfate (SPS; Sigma-Aldrich, USA) was added to the GelMA solution and the solution was loaded into the syringe. Food

grade sunflower oil was used as the continuous phase and the GelMA solution containing the photoinitiator made up the dispersed phase. For the continuous oil phase, the flow rate was set to 1 ml/minute and the dispersed gel phase it was set to 40 µl/min to fabricate Ø1 mm microspheres, based on previous work by Young *et al.* [61] The formed microspheres were then irradiated with visible light (OmniCure® S1500, Excelitas Technologies). The light was irradiated through a light filter (Rosco IR/UV filter) where only light of 400 – 450 nm wavelength was allowed to pass through with a final intensity of 100 mW/cm^2. The light intensity and exposure time were selected based on previous work by Lim *et al.* [18]. The formed microspheres were collected in polypropylene (Falcon, USA) centrifuge tubes containing PBS. To separate the oil from the microspheres, the centrifuge tube was centrifuged at 0.1 g for 5 minutes. The oil was then aspirated and the pellet of microspheres in PBS was collected using a Pasteur pipette. The microspheres were then resuspended in fresh PBS and the washing step was repeated.

5.3.7 Cell encapsulation in GelMA-HepMA hydrogel microspheres

The prepared chondrocyte suspension was added to the 9.5% wt GelMA-0.5% wt HepMA macromer solution containing sterile filtered initiators to give a final concentration of 15 x 10^6 HACs/ml. The cell encapsulated microspheres were then fabricated and visible light crosslinked as outlined previously. Each microsphere was transferred to well in a 96-well polystyrene plate (Falcon, USA). 150 µL of serum-free basic chondrocyte media that was supplemented with 1% ITS+1 (1 mg/ml insulin from bovine pancreas, 0.55 mg/ml human transferrin, 0.5 µg/ml sodium selenite, 50 mg/ml bovine serum albumin and 470 µg/ml linoleic acid; Sigma-Aldrich, USA), 0.1 x 10^{-6} M dexamethasone (Sigma-Aldrich, USA), 1.25 mg/ml bovine serum albumin (GIBCO, New Zealand) and 10 ng/ml recombinant human transforming growth factor-β1 (TGF-β1; R&D systems, USA) was then pipetted into the wells and placed in an incubator at 37°C, 5% of CO_2. During the microsphere culture period, the media was changed 2 times per week.

Cell-free 9.5% GelMA-0.5% HepMA and Qtracker labelled HAC, MSC and co-culture (50% HAC and 50% MSC) 9.5% GelMA-0.5% HepMA microspheres were fabricated similarly.

5.3.8 Characterisation of microspheres

The size distribution of the fabricated microspheres was determined by measuring the size of the microspheres for the cell-free 5% and 10% GelMA microspheres and the HAC-laden 9.5% GelMA-0.5% HepMA microspheres. Fabricated microspheres (*n=50*) were stained with Coomassie brilliant blue (Thermo Fisher Scientific, USA) for 15 minutes and were imaged using the Zeiss Axioimager Z1 microscope. The major and minor diameters were measured using the particle analysis function in ImageJ. The average of the major and minor diameter was calculated and normal distribution of the average diameter was plotted. The coefficient of variation was tabulated to gauge the microsphere size distribution.

The DNA content of the HAC-laden 9.5% GelMA-0.5% HepMA microspheres (*n=4*, 8 microspheres/sample) were quantified using a CyQUANT kit (Molecular Probes, USA) on Day 0. The samples were first digested overnight at 56˚C in 500 µL of 1 mg/ml proteinase-K (Sigma-Aldrich, USA) solution. Post proteinase-K digestion, the cells in the sample were lysed and the RNA was degraded by using the provided lysis buffer with RNase A (1.35 KU/ml; Thermo Fisher Scientific, Lithuania) for an hour at room temperature. Samples were pipetted into 96-well white polypropylene plates (Nunc, Denmark) and GR-dye solution was added. The plate was then incubated at room temperature for 60 minutes in the dark and fluorescence was measured (Fluostar Galaxy BMG Labtechnology, Germany). A DNA standard curve was constructed using the λ-DNA provided in the kit and a cell standard curve was constructed using HACs to determine the cell number.

The theoretical value (*theoretical cell number*$_{microsphere}$) of the number of cells encapsulated per microsphere for day 0 was calculated by calculating the volume ($V_{microsphere}$) of the microsphere ($d_{microsphere}$) and then calculating the number of cells in that volume when the concentration of cells in the solution is 15 x 10^6 cells/mL (*cell concentration*). The *theoretical cell number*$_{microsphere}$ was calculated using equation 5-1 and 5-2.

$$V_{microsphere} = \frac{\pi}{6} d^3_{microsphere} \quad \textbf{5-1}$$

$$theoretical\ cell\ number_{microsphere} = V_{microsphere}\ x\ cell\ concentration \quad \textbf{5-2}$$

5.3.9 Reliability and efficiency of the singularisation device with the microspheres

To determine the reliability of the singularisation device with the microspheres, cell-free 5% and 10% GelMA microspheres and HAC-laden 9.5% GelMA-0.5% HepMA microspheres were put through the device. The microspheres were put into the singularisation device in sets of 10 and repeated 10 times, with the success or failure in singularisation being noted. The total number of successful singularisation was used to determine the overall efficiency of the singularisation system (equation 5-3).

$$efficiency\ of\ singularisation = \frac{successful\ micro\text{-}tissue\ singularisation}{total\ attempted\ number\ of\ micro\text{-}tissue\ singularisation} \times 100 \quad \textbf{5-3}$$

5.3.10 Scaffold fabrication

Biodegradable poly(ethylene glycol)-terephthalate-poly(butylene terephthalate) block copolymers (Polyactive 300PEGT55PBT45, PolyVation, The Netherlands) with a PEG molecular weight (MW) of 300 g/mol and a PEGT:PBT weight percent (wt%) ratio of 55:45 were used to fabricate scaffolds with a specific pore size and architecture. PEGT/PBT copolymer composition was selected as a model scaffold based on previous studies demonstrating applicability across multiple processing techniques (e.g. melt extrusion), mechanical properties mimicking native tissue, as well as the capacity to modulate cell, adhesion, proliferation, differentiation and extracellular matrix formation [3, 62-67]. Porous scaffolds (25 × 25 × 2.64 mm), with accurately defined and controlled pore architecture for microsphere incorporation, were 3D plotted using a Bioscaffolder system (SYS ENG, Germany). Fibres were oriented in a repeating 0-90°-90°-0° pattern in order to provide porosity in both the x-y and x-z planes for assembly of 1 mm diameter microspheres. During the melt dispensing process the following 3D plotting parameters were applied: (i) fibre spacing of 1 mm in both x and y-direction, (ii) fibre height offset of 0.22 mm, (iii) print head reservoir containing the polymer heated to a temperature of 200° and pressurised to 5 Bar, (iv) an auger speed of 63

RPM and (v) print head fitted with a 25 gauge nozzle moving with a traverse speed of 500 mm/min.

5.3.11 Automated tissue assembly with microspheres

The automated assembly of a tissue construct with microspheres was demonstrated by 3D plotting a scaffold utilising a high-temperature print head containing Polyactive 300PEGT55PBT45 and then inserting microspheres using the microsphere injection head. To 3D plot the assembled construct a layer-by-layer approach was opted so as to not limit the height of the scaffold that can be constructed using the system. In this scheme, the first layer of the scaffold (8 layers of fibre strands) was 3D plotted (as described earlier) and then 16 (4 x 4 fashion) fixed microspheres were inserted into the pores of the 3D plotted scaffold. The 3D plotting was repeated on top of the first layer to generate the second layer of the scaffold (8 layers of fibre strands) and then 16 more microspheres were inserted into the second layer.

Microspheres of different colours (which represented microspheres of different cell types, hydrogel types or microspheres containing different types of bioactive molecules), were inserted into specific locations in an alternating and concentric pattern in a single-layered scaffold similarly as described above. Microspheres of a particular colour were loaded into the microsphere injection head, the program containing the G code with the specific locations of where the microspheres were to be inserted was executed and the microspheres were inserted within the 3D plotted scaffold. Subsequently, the other coloured microspheres were similarly assembled.

To validate the viability of the assembled constructs, HAC-laden 9.5% GelMA-0.5% HepMA microspheres were assembled. Utilising a layer-by-layer approach as described above, the automated tissue assembly system was used to create a 2 layered construct with 8 microspheres per layer (4 x 4 fashion). For the manually assembled scaffold, the whole scaffold was 3D plotted at once and the microspheres were inserted manually by hand into the pre-plotted scaffolds in a similar format to the ones assembled with the automated system. The constructs assembled with the

automated tissue assembly system and the manually assembled construct were compared with the live/dead assay and AlamarBlue® assay.

For the live/dead assay, the samples were incubated at 37°C in 0.5 ml of PBS with 1 μM Calcein AM (Molecular Probes, USA) for 15 minutes. 1 μM Propidium Iodide (Molecular Probes, USA) was then added and the samples were incubated for 10 more minutes. After this, the samples were washed twice with PBS and a z-stack of the sample was imaged using the Zeiss Axioimager Z1 microscope (FITC and Texas Red filter-set).

For the AlamarBlue® assay, AlamarBlue® (Invitrogen, USA) was added to the media containing FBS so that the final concentration was 10% (v/v) and the samples were incubated at 37°C for 20 hours. The reduction in AlamarBlue® reagent was calculated colorimetrically using the equations provided by the manufacturer after measuring the absorbance at 570 nm, using 600 nm as a reference wavelength (Fluostar Galaxy BMG Labtechnology, Germany).

5.3.12 Efficiency of microsphere insertion

A bilayered scaffold (*n=8* scaffolds, *n=64* microspheres) was assembled with 4 microspheres in each layer using the layer-by-layer approach described earlier. The efficiency of microsphere insertion into the scaffold was determined by the number of successful microsphere insertion into the scaffold pore to the total attempted number of microsphere insertion with the automated system (equation 5-4).

$$efficiency\ of\ microsphere\ insertion = \frac{successful\ microsphere\ insertion}{total\ attempted\ number\ of\ microsphere\ insertion} \times 100 \qquad \textbf{5-4}$$

5.3.13 Glycosaminoglycan (GAG) and DNA quantification

After 1 day of fabricating the HAC-laden 9.5% GelMA-0.5% HepMA microspheres, the microspheres were assembled into a 3D plotted scaffold. The bilayered scaffold contained 8 microspheres in total with 4 microspheres in each layer in a 2 x 2 manner. The HAC-laden individual microspheres and assembled constructs were cultured up to 5 weeks. GAG and DNA were quantified and the

samples were sectioned for histology and immunofluorescence. Live/dead assay was also performed on the samples as described earlier after 1, 14 and 35 days of culture.

The GAG and DNA content for individual HAC-laden 9.5% GelMA-0.5% HepMA microspheres (8 individually cultured microspheres were pooled together to make one sample) and HAC-laden 9.5% GelMA-0.5% HepMA assembled constructs (8 microspheres per sample) were measured as described previously [3, 68] on day 0, 14 and 35. The samples were digested overnight at 56˚C in 500 µL of 1 mg/ml proteinase-K solution to digest the cells, matrix and the hydrogel. The DNA in the samples were quantified as described earlier.

To quantify the total GAG retained in the gel, the digested samples were reacted with dimethyl-methylene blue dye (DMMB; Sigma-Aldrich). The absorbance of the samples was then measured on a plate reader at 520 nm (Fluostar Galaxy BMG Labtechnology). GAG content was calculated from a standard curve constructed using known concentrations of chondroitin sulphate B (Sigma-Aldrich). The normalised GAG was calculated using (equation 5-5).

$$normalised\ GAG = sample\ GAG - sample\ without\ cells\ GAG \quad \textbf{5-5}$$

The GAG and DNA values for the assembled construct on day 0 was considered to be same as the individual microspheres. The normalised GAG, DNA and (normalised GAG)/DNA values were all calculated and plotted per microsphere so that the values of the individual microspheres could be compared with the assembled construct.

5.3.14 Histology and immunofluorescence

The cultured HAC-laden 9.5% GelMA-0.5% HepMA microspheres and HAC-laden 9.5% GelMA-0.5% HepMA assembled constructs were washed in PBS, fixed in 10% neutral buffered formalin for an hour, washed in PBS again and then immersed in OCT (Ted Pella, Inc. USA) overnight at 4˚C. The samples were then embedded in OCT and were cryosectioned (30 µm thick sections).

For safranin O staining, the slides were stained with Gill's haematoxylin (Merck, Germany) and 0.001% (w/v) Fast Green solution (Sigma-Aldrich, USA) for cells and collagens respectively, and with 0.1% (w/v) safranin O (Sigma-Aldrich, USA), for sulphated glycosaminoglycans as described previously [3, 68]. The stained sections were imaged using a Zeiss Axioimager Z1 microscope.

For immunofluorescence, the slides with the sections were rinsed with cold PBS thoroughly and were incubated in 0.1% (w/v) hyaluronidase (Sigma, USA) in PBS for 30 minutes for antigen retrieval. The sections were rinsed with cold PBS and were exposed to 2% (w/v) BSA in PBS at a pH 7.4 for 60 minutes at room temperature. They were then rinsed with cold PBS and incubated with rabbit polyclonal anti-collagen I antibody (1:150 dilution; ab34710, abcam, USA) and mouse monoclonal anti-chicken collagen II antibody (1:150 dilution; II-II6B3; DSHB, USA), and mouse monoclonal anti-human aggrecan (1:200 dilution; 969D4D11, Invitrogen, USA) anti-bodies at 4˚C overnight. The sections were washed in PBS and were incubated with secondary antibodies, goat Alexa Fluor 488 anti-mouse (1:400 dilution; Thermo Fisher Scientific, USA) and goat Alexa Fluor 555 anti-rabbit (1:400 dilution; abcam, USA) at 37˚C for an hour. Following further washing, the sections were counterstained with 4.5μM Hoechst 33342 (Invitrogen, USA) in PBS. Finally, the slides were washed with 0.05% Tween-20 (Sigma-Aldrich, USA) in cold PBS, rinsed in PBS and then coverslipped. The samples were imaged using a Zeiss Axioimager Z1 microscope (DAPI, FITC and Texas Red filter-set).

5.3.15 Graduated construct assembly

After 1 day of forming the Qtracker labelled HAC, MSC and co-culture (50:50 HAC:MSC) 9.5% GelMA-0.5% HepMA microspheres, the microspheres were assembled into a 3D plotted scaffold. The bilayered co-culture graduated assembled construct contained 12 microspheres in each layer in a 4 x 3 manner with 4 microspheres of each cell type. The samples were cultured up to 35 days and the samples were cryosectioned for histology and immunofluorescence as described earlier.

5.3.16 Statistical analysis

Data was presented graphically as mean ± standard deviation. Data were analysed using GraphPad Prism v.6.0. Statistical analysis was performed using 1-way ANOVA or 2-way ANOVA (if required Tukey's multiple comparisons test) or paired t-test, with $p<0.05$ set as a criterion for statistical significance.

5.4 Results

5.4.1 Microsphere fabrication

The reliable and efficient operation of the current automated bioassembly system requires microspheres of Ø1 mm as a model tissue unit of regular size and shape. This subsection describes the setup of the microfluidic system to fabricate Ø1 mm sized microspheres with the desired requirements.

5.4.1.1 Fabrication of GelMA microsphere hydrogels

With the microfluidic system setup, and with the right flowrates for the continuous oil phase and the dispersed hydrogel phase, it was possible to generate GelMA based microspheres. A higher flow rate of the dispersed gel phase resulted in jetting of the dispersed phase. The droplet formation was characterised by the development of a droplet at the tip of the fused silica capillary (Figure 5-2 a), elongation of the neck to which the droplet is attached to the tip of the capillary (Figure 5-2 b) and the detachment of the droplet from the tip of the capillary (Figure 5-2 c). The detached droplet then flows downstream through the coil where they are irradiated with light to be crosslinked and then collected. Cell-free 5% and 10% GelMA microspheres and cell-laden 9.5% GelMA-0.5% HepMA microspheres were fabricated using the system. Figure 5-2 (e and f) shows an image of the cell-free 10% GelMA microspheres and Figure 5-2 g shows an image of HAC-laden 9.5% GelMA-0.5% HepMA microspheres.

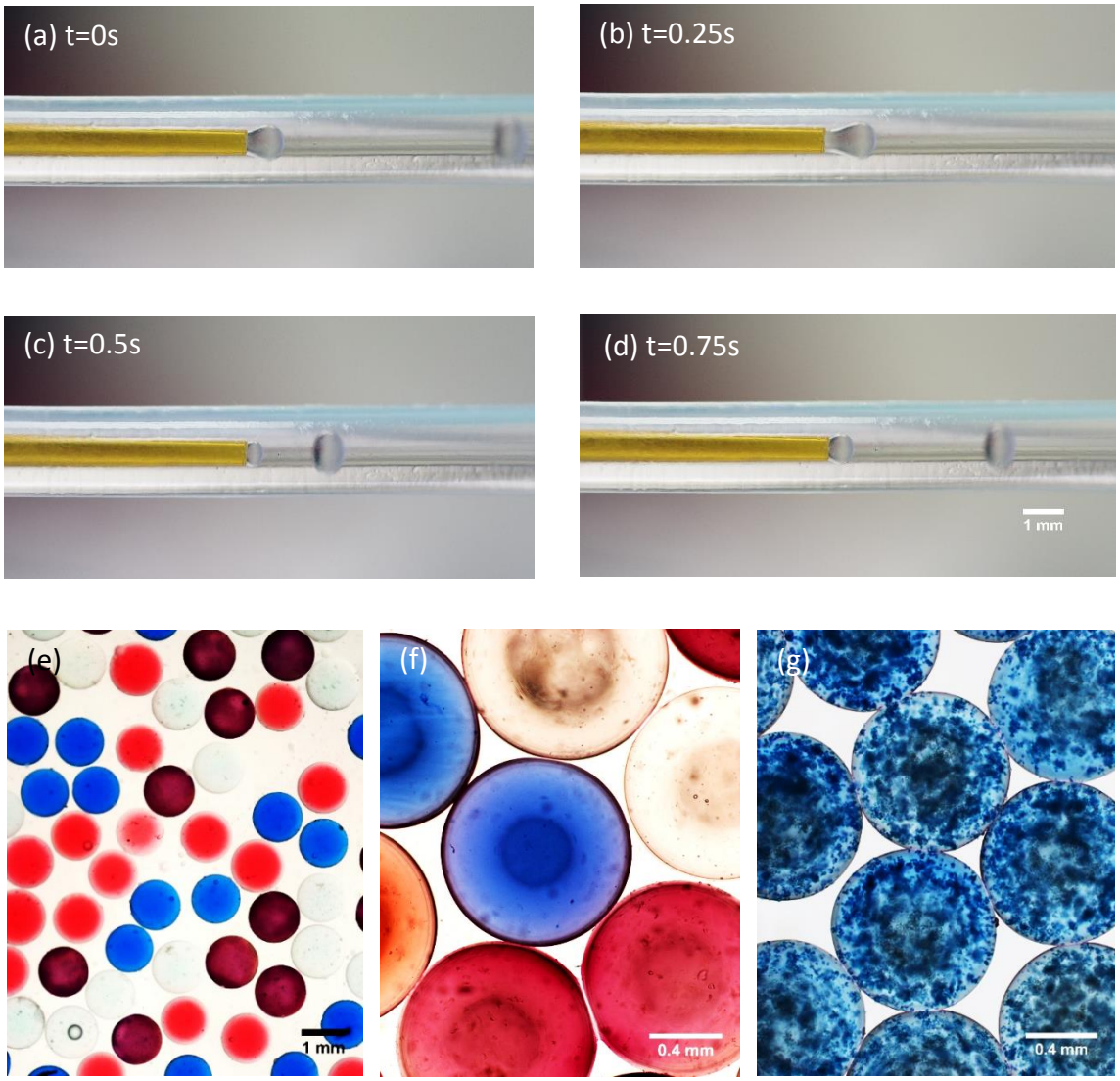

Figure 5-2. Snapshots (a, b, c, and d, *scale bar = 1 mm*) of microsphere generation using sunflower oil which is the continuous oil phase flowing at a flow rate of 1 ml/minute and 10% GelMA which is the dispersed gel phase flowing at flowrate of 40 µl/min. The fused silica capillary (yellow) is upstream and the droplet exits downstream. Brightfield microscope image of (e and f) coloured cell-free 10% GelMA microspheres and (g) HAC-laden 9.5% GelMA-0.5% HepMA microspheres (stained with Coomassie brilliant blue). Microspheres can be seen to have a uniform size and a smooth and regular morphology.

5.4.1.2 Characterisation of microspheres

Cell-free 5% and 10% GelMA hydrogel microspheres and cell-laden 9.5% GelMA-0.5% HepMA microspheres were successfully fabricated with the micro-fluidic system. The size distribution of the microspheres is plotted in Figure 5-3. There was a significant difference ($p<0.05$) in the average diameter (Table 5-1) between all conditions. The cell-free 10% (1.294 ± 0.052 mm) GelMA microspheres

had a larger average diameter than the cell-free 5% (1.193 ± 0.070 mm) microspheres and the HAC-laden 9.5% GelMA-0.5% HepMA microspheres (0.955 ± 0.031 mm) had the smallest average diameter. For a constant flow rate of the dispersed phase and continues phase, the viscosity, surface tension and density of the dispersed phase could affect the size of the microsphere [69, 70]. The different macromer concentrations, the presence of HepMA, and the presence of cells could all contribute to the difference in viscosity, surface tension and density of the dispersed phase thereby affecting the size of the fabricated microspheres. The coefficient of variation (Table 5-1) tells us that the dispersion in microsphere size is quite low. This uniformity of the microsphere was critical and essential for the efficient handling of the microspheres by the automated tissue assembly system.

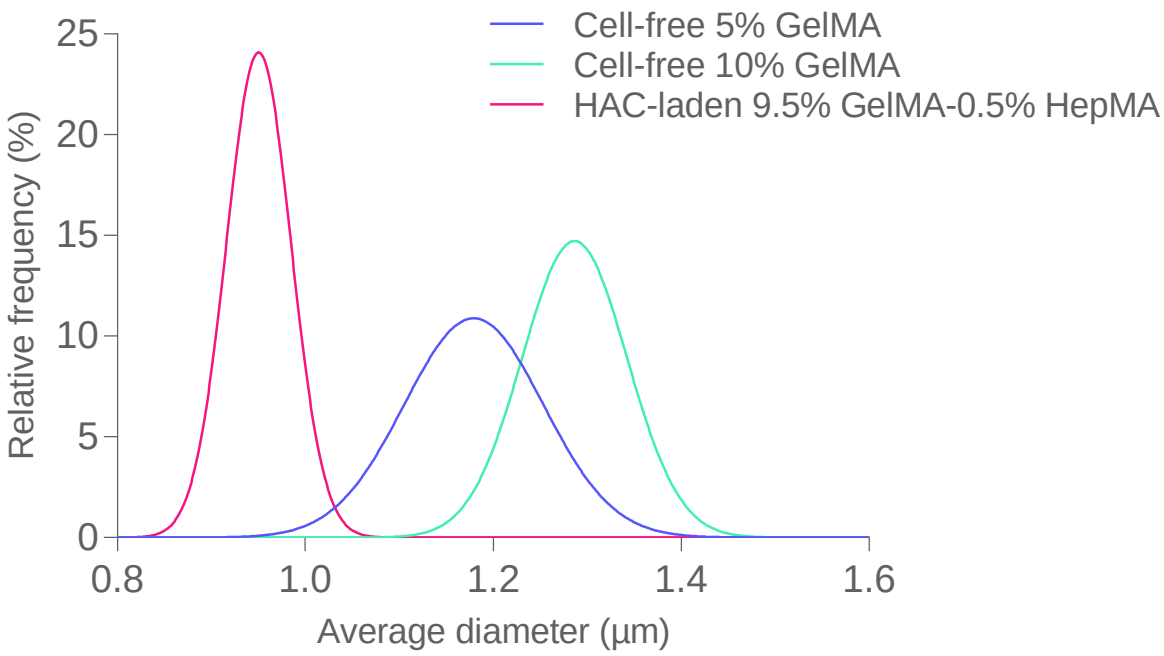

Figure 5-3. Size (average diameter of the microspheres) distribution curves of (a) cell-free 5% GelMA, (b) cell-free 10% GelMA, and (c) HAC-laden 9.5% GelMA-0.5% HepMA microspheres. (*n=50*)

Table 5-1. Average diameter and coefficient of variation for microspheres fabricated with different conditions.

Microsphere type	Cell-free 5% GelMA	Cell-free 10% GelMA		HAC-laden 9.5% GelMA-0.5% HepMA
Average diameter (mm)	1.193 ± 0.070	1.294 ± 0.052		0.955 ± 0. 031
Coefficient of variation	0.058	0.04		0.033

[a] Distribution plotted in Figure 5-3.
[b] n=50
[c] **Significant difference ($p<0.05$) was observed between all conditions. Statistical analysis: 2-way ANOVA.*

After fabricating the HAC-laden 9.5% GelMA-0.5% HepMA microspheres, the number of cells per microsphere (Table 5-2) was determined. The determined value of cells per microsphere was significantly higher (*$p<0.05$*) compared to the expected or theoretical value. The coefficient of variation shows that the variation in the cells per microsphere was low.

Table 5-2. Cells per microsphere after fabrication (day 0).

Cells	HAC-laden 9.5% GelMA-0.5% HepMA	Theoretical
Cells per microsphere	10337 ± 1019	7853.99
Coefficient of variation	0.099	-

[a] n=4
[b] *Significant difference ($p<0.05$) between HAC-laden 9.5% GelMA-0.5% HepMA microsphere and the theoretical value.*
[c] Theoretical value is the calculated number of cells for a microsphere of Ø1 mm formed with macromer containing a cell density of 15 x 10^6 cells/ml.

5.4.2 3D Bioassembly of microspheres

In this subsection, the ability of the automated tissue assembly system to handle the microspheres was investigated. After which, the flexibility of the automated tissue assembly system was demonstrated by assembling microspheres of different colours (the different colours representing microspheres of different cell types, hydrogel types or microspheres containing different types of bioactive molecules) into a construct. Constructs were also assembled with cell-laden hydrogel microspheres to demonstrate that the automated bioassembly system does not affect the viability of the assembled construct.

5.4.2.1 Reliability and efficiency of the singularisation device with the microspheres

The efficiency of singularisation (*n=100*) determined for microspheres is listed in Table 5-3. The HAC-laden 9.5% GelMA-0.5% HepMA microspheres had a significantly higher (*p<0.05*) singularisation efficiency compared to the cell-free 5% GelMA microspheres. However, there was no significant difference (*p>0.05*) in singularisation efficiency between the cell-free 5% and 10% GelMA microspheres or the cell-free 10% GelMA microspheres and the HAC-laden 9.5% GelMA-0.5 HepMA microspheres. The higher efficiency of the HAC-laden 9.5% GelMA-0.5 HepMA microspheres compared to the cell-free 5% GelMA microspheres could possibly be due to two reasons. Firstly, the higher stiffness of the HAC-laden 9.5% GelMA-0.5% HepMA microspheres caused by a higher macromer concentration could have resulted in the better handling of the microspheres by the automated tissue assembly system. Secondly, as the average diameter of HAC-laden 9.5% GelMA-0.5% HepMA microspheres was closer to 1 mm (the diameter for which the automated tissue assembly system was designed for) compared to the cell-free 5% GelMA microspheres, this could also have contributed to the better handling of the microspheres.

Table 5-3. The efficiency of singularisation for microspheres fabricated with different conditions.

Microsphere type	Cell-free 5% GelMA	Cell-free 10% GelMA		HAC-laden 9.5% GelMA-0.5% HepMA
Singularisation efficiency	82 ± 11.35%	89 ± 7.38%		94 ± 9.66%

[a] *n*=100.
[b] *Significant difference (p<0.05) only between 5% cell laden microspheres and HAC-laden 9.5% GelMA-0.5% HepMA microspheres. Statistical analysis: 1-way ANOVA.*

During the experiment, the reasons for singularisation failures were due to, either, the release of 2 microspheres at a time, or due to the microsphere being sucked into the vacuum pressure port. In the event of a singularisation failure, the singularisation cycle could be repeated to release a microsphere. If the microsphere has blocked the ports of the singularisation device, the device can be purged with fluid to dislodge the microsphere after which normal operation of the device can be resumed. The singularisation failures that occurred were not critical and did not

cause the failure of the device. The photomicrosensor that was fitted to detect singularised micro-tissues could not detect the microspheres as they were not opaque to light and did not trigger the photomicrosensor. The successful singularisation was visually inspected by the user.

5.4.2.2 Automated tissue assembly with microspheres

Layer-by-layer assembly (Figure 5-4) of a construct was successfully demonstrated with cell-free 10% GelMA microspheres. The 10% GelMA macromer concentration was chosen based on previous studies on cartilage engineering [71]. 2 layers with 16 (4 x 4 fashion) microspheres per layer was assembled. Microsphere of different colours were inserted into specific location (which includes a checked and concentric pattern) in a single layer scaffold (Figure 5-5) to demonstrate the flexibility of the automated bioassembly system.

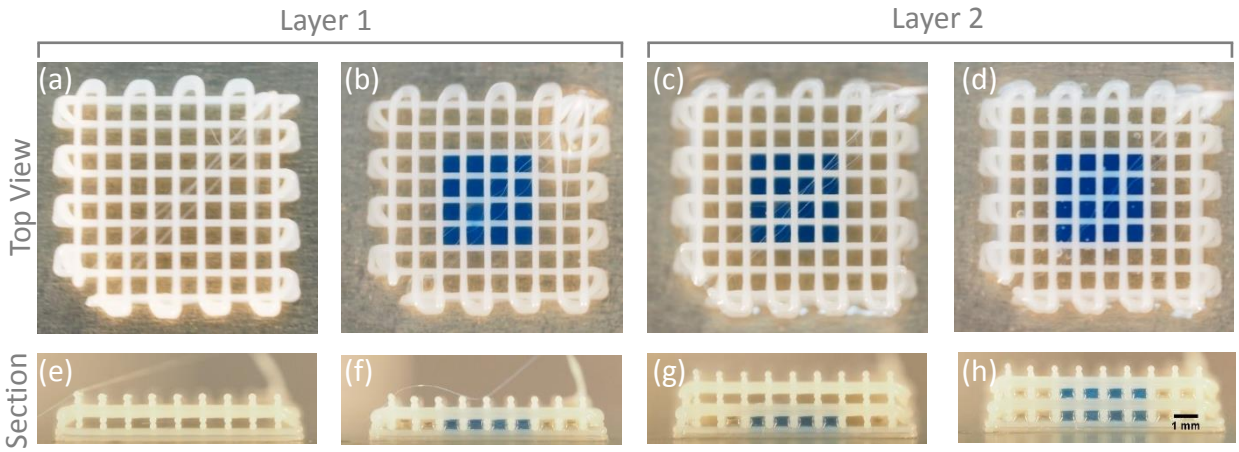

Figure 5-4. Top-view and cross sectional-view photographs of the steps involved in the layer-by-layer printing and assembly of a microsphere assembled construct with the aid of the automated assembly system. Contains 32 microspheres, arranged in 2 layers with 16 microspheres in each layer. *Scale bar = 1 mm for all images.*

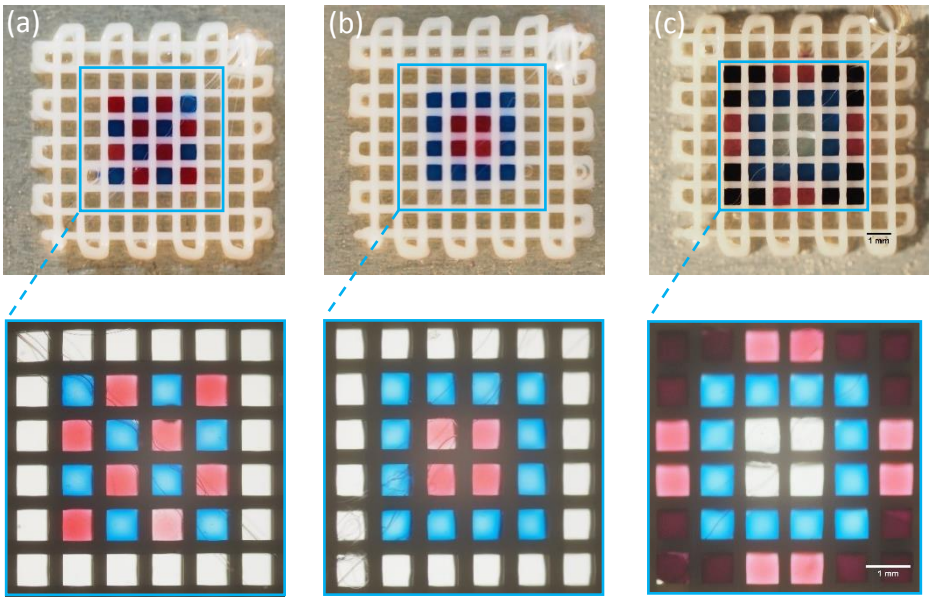

Figure 5-5. Top-view of a microsphere assembled construct with the aid of the automated assembly device to demonstrate the flexibility of the system. Different coloured microspheres were inserted into specific 3D locations, (a-b) contains 16 microspheres arranged in a single layer and (c) contains 36 microspheres arranged in a single layer. *Scale bar = 1 mm for all images.*

5.4.2.3 Efficiency of microsphere insertion

The efficiency of successful microsphere insertion into the scaffold was determined to be 90.6 ± 11.0% (*n=8* scaffolds, *n=64* microspheres) for the cell-free 10% GelMA microspheres. Although there were microspheres that failed being inserted into the scaffold, the scaffold was inspected for the missed microsphere insertions and the microsphere insertion process was repeated for the failed pores and the scaffold was completely filled as planned.

5.4.2.4 Viability of assembled construct

The print head containing the thermoplastic material is heated to approximately 200°C and during the 3D plotting process, the extruded fibre rapidly cools. However, it was essential to ascertain that the extruded molten polymer coming in contact with microspheres during the layer-by-layer assembly process and the handling of the microspheres by the automated bioassembly system did not affect the viability of encapsulated cells. HAC-laden 9.5% GelMA-0.5% HepMA microspheres were assembled manually and using the automated tissue assembly system. The visual inspection of the live/dead fluorescence microscopy images

(Figure 5-6) of the manually assembled scaffold and the construct assembled using the assembly system showed no obvious differences and this was validated with the AlamarBlue® assay (Figure 5-7). There was no significant difference (*p>0.05*) in the percentage of AlamarBlue® reduced by the manually assembled scaffold (55.12 ± 4.51%) and the construct assembled using the automated bioassembly system (52.82 ± 6.89%).

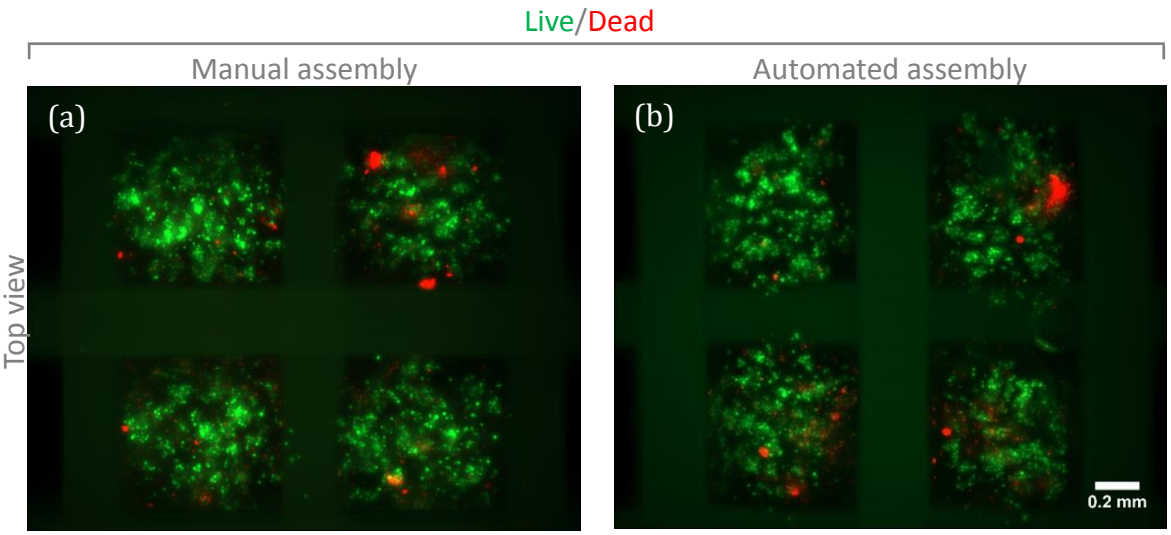

Figure 5-6. Fluorescence microscopy images of (a) manually assembled construct and a (b) construct assembled using the assembly system assembled with HAC-laden 9.5% GelMA-0.5% HepMA microspheres stained with Calcein AM (live cells, green) and Propidium Iodide (dead cells, red) on day 0. *Scale bar = 0.2 mm for all images.*

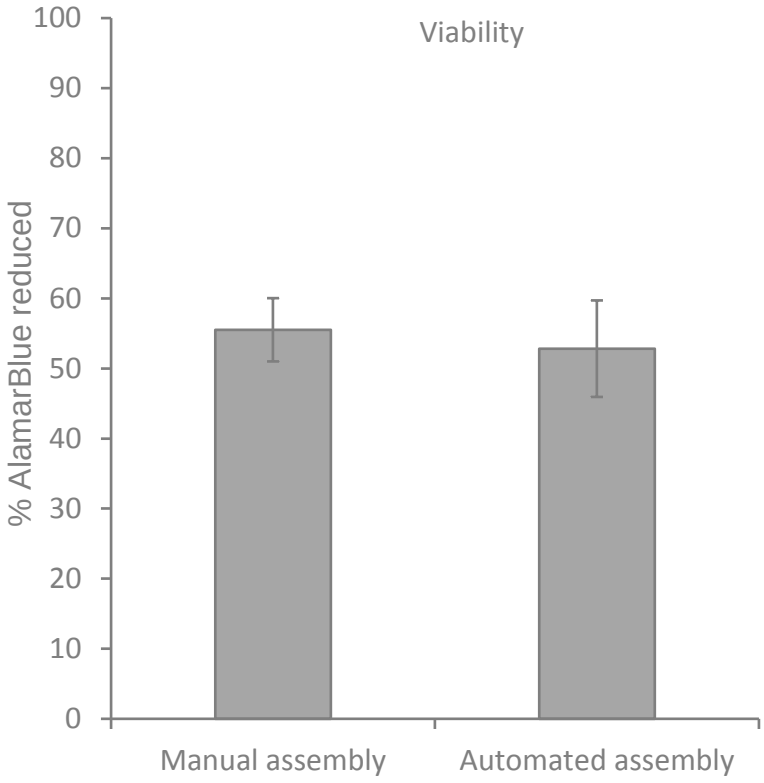

Figure 5-7. Percentage of AlamarBlue® reduced to determine the viability of the manually assembled construct and the construct assembled using the automated system with HAC-laden 9.5% GelMA-0.5% HepMA microspheres on day 0. The data is presented as mean ± SD (*n=4*). *(p>0.05)*.

The live/dead images of HAC-laden 9.5% GelMA-0.5% HepMA microspheres and manually assembled construct cultured over time (day 0, 14 and 35) is shown in Figure 5-8 . Visual inspection did not reveal a significant population of dead cells in any of the samples cultured *in vitro*.

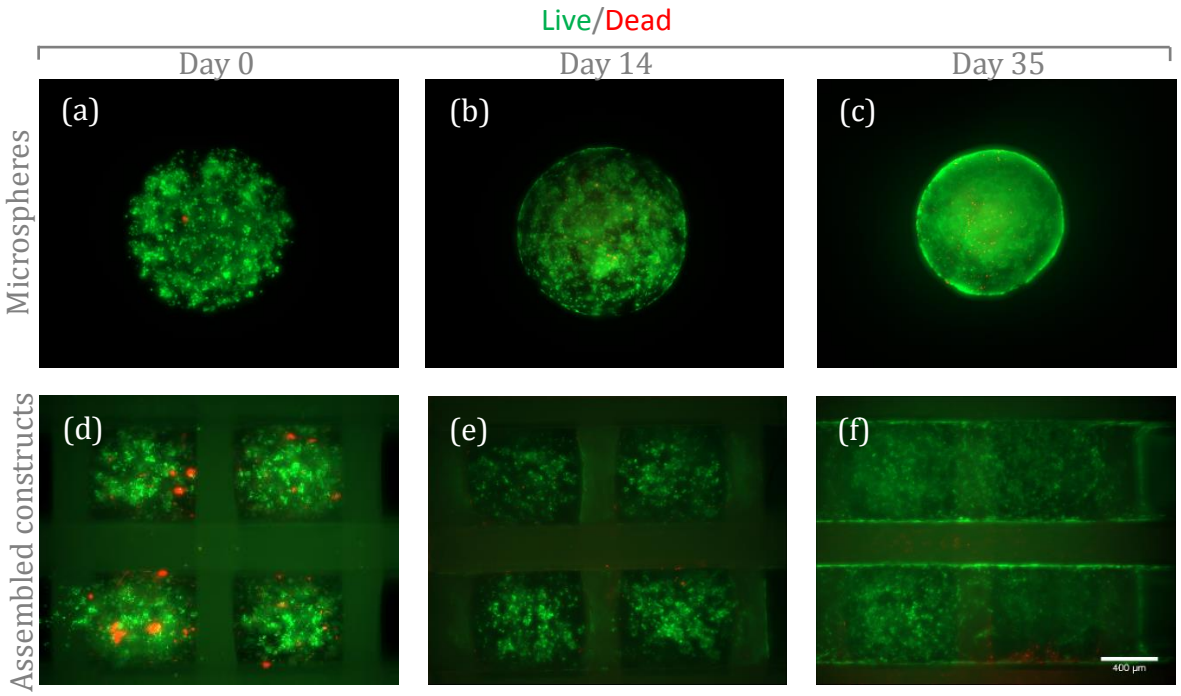

Figure 5-8. Fluorescence microscopy images HAC-laden 9.5% GelMA-0.5% HepMA microspheres and assembled constructs on day 0, 14 and 35 stained with Calcein AM (live cells, green) and Propidium Iodide (dead cells, red). *Scale bar = 400 µm for all images.*

5.4.3 Assessment of cartilage tissue formation

In this subsection, cartilage tissue formation *in vitro* in the HAC-laden 9.5% GelMA-0.5% HepMA hydrogel microspheres and assembled constructs were assessed.

5.4.3.1 GAG and DNA quantification

The DMMB assay was utilised to quantify the glycosaminoglycan (GAG) produced. However, the DMMB assay quantifies not only the GAG produced by the chondrocytes but also the heparin that is present in the HepMA hydrogel that was incorporated during the microsphere fabrication. Therefore, interpreting the data with high basal GAG values caused by the presence of HepMA was challenging [72]. To try and overcome this and to measure the quantity of GAG produced over time by the chondrocytes, the GAG values of the cell-laden 9.5% GelMA-0.5% HepMA samples (individual microspheres and assembled constructs) were normalised by subtracting the GAG values from cell-free 9.5% GelMA-0.5% HepMA hydrogel microspheres. The normalised GAG per microsphere for the individual microspheres and the assembled construct is plotted in Figure 5-9 a. A decrease in normalised GAG

(*p<0.05*) was observed in the individual microspheres between day 0 (0.31 ± 0.05 μg/microsphere) and 14 (0.12 ± 0.07 μg/microsphere). This decrease could be due to the leaching out of the HepMA from the microspheres and the remodelling of the HepMA by the cells [72]. The decrease from day 0 (0.31 ± 0.05 μg/microsphere) to 14 (0.20 ± 0.08 μg/microsphere) was possibly less pronounced in the assembled construct due to higher production of GAG compared to the individual microspheres. In the assembled construct, the normalised GAG increased (*p<0.05*) from day 14 (0.20 ± 0.08 μg/microsphere) to 35 (0.42 ± 0.09 μg/microsphere). Higher normalised GAG (*p<0.05*) was observed in the assembled construct (0.42 ± 0.09 μg/microsphere) compared to the individual microspheres (0.25 ± 0.10 μg/microsphere) after 35 days in culture.

The DNA content per microsphere for the individual microspheres and assembled constructs is plotted in Figure 5-9 b. The DNA content observed in the individual microspheres decreased (*p<0.05*) between day 0 (80.20 ± 8.15 ng/microsphere) and 14 (63.62 ± 5.85 ng/microsphere). In the assembled construct, the DNA content significantly increased (*p<0.05*) from day 14 (67.03 ± 10.97 ng/microsphere) to 35 (98.72 ± 10.27 ng/microsphere). A higher (*p<0.05*) DNA content was observed between the assembled construct (98.72 ± 10.27 ng/microsphere) compared to the individual microspheres (72.91 ± 4.46 ng/microsphere) on day 35. With the normalised GAG per DNA (Figure 5-9 c), a significant change (*p<0.05*) was observed only in the individual microspheres where the normalised GAG per DNA decreased from day 0 (3.88 ± 0.90 g/g) to 14 (1.87 ± 1.04 g/g).

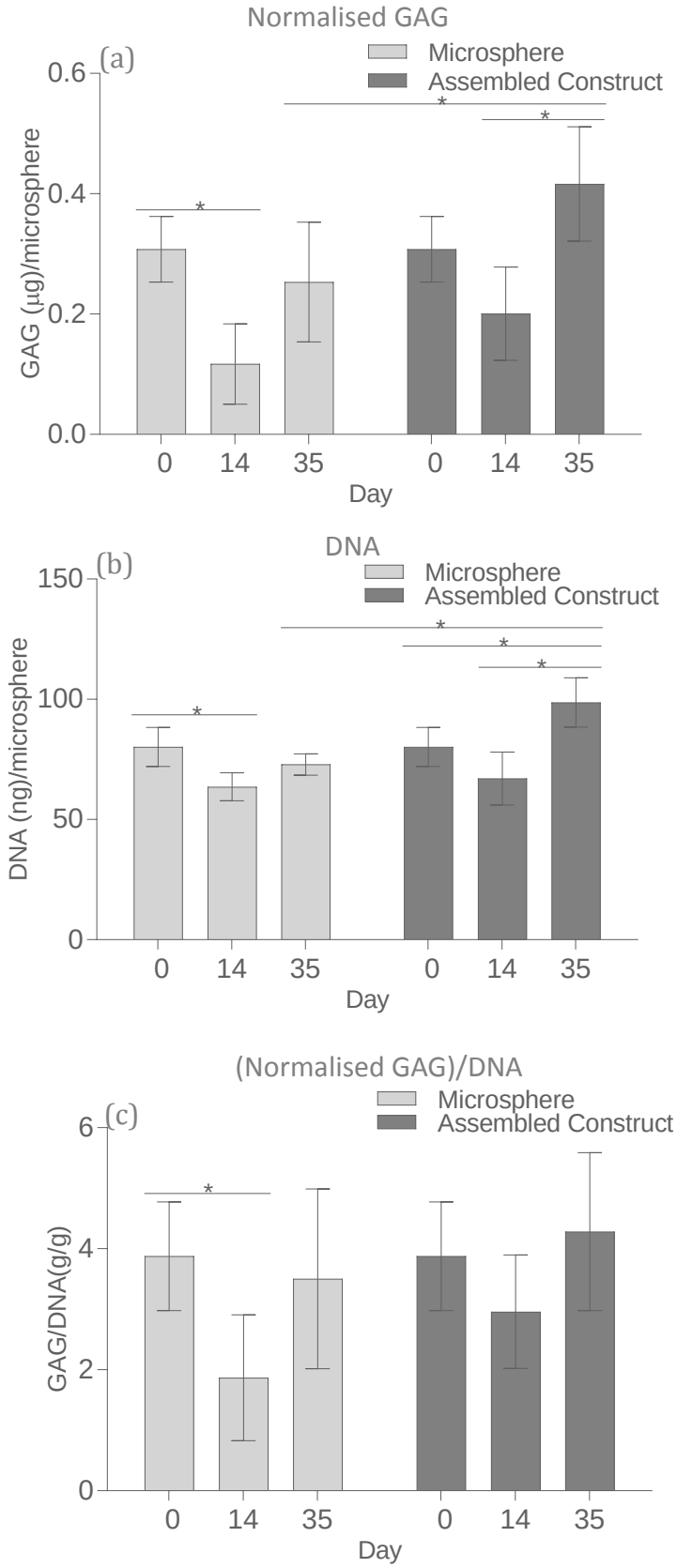

Figure 5-9. (a) normalised GAG per microsphere, (b) DNA per microsphere and (c) (normalised GAG)/DNA for HAC-laden 9.5% GelMA-0.5% HepMA microspheres and assembled construct at day 0, 14 and 35. The data is presented as mean ± SD (*n=4*). **Significant differences between columns below each end of lines (p<0.05). Statistical analysis: 2-way ANOVA. See appendix for total GAG per microsphere*

5.4.3.2 Histology and immunofluorescence

The cryosections were stained with safranin O (Figure 5-10) to visually investigate GAG production in microspheres and assembled constructs. GAG is one of the major components of articular cartilage and is responsible for the elasticity and resilience of cartilage [73]. However, the presence of HepMA incorporated during the microsphere fabrication process caused high background staining for GAG. The background staining can be seen in the control microspheres without cells (Figure 5-10 a and b).

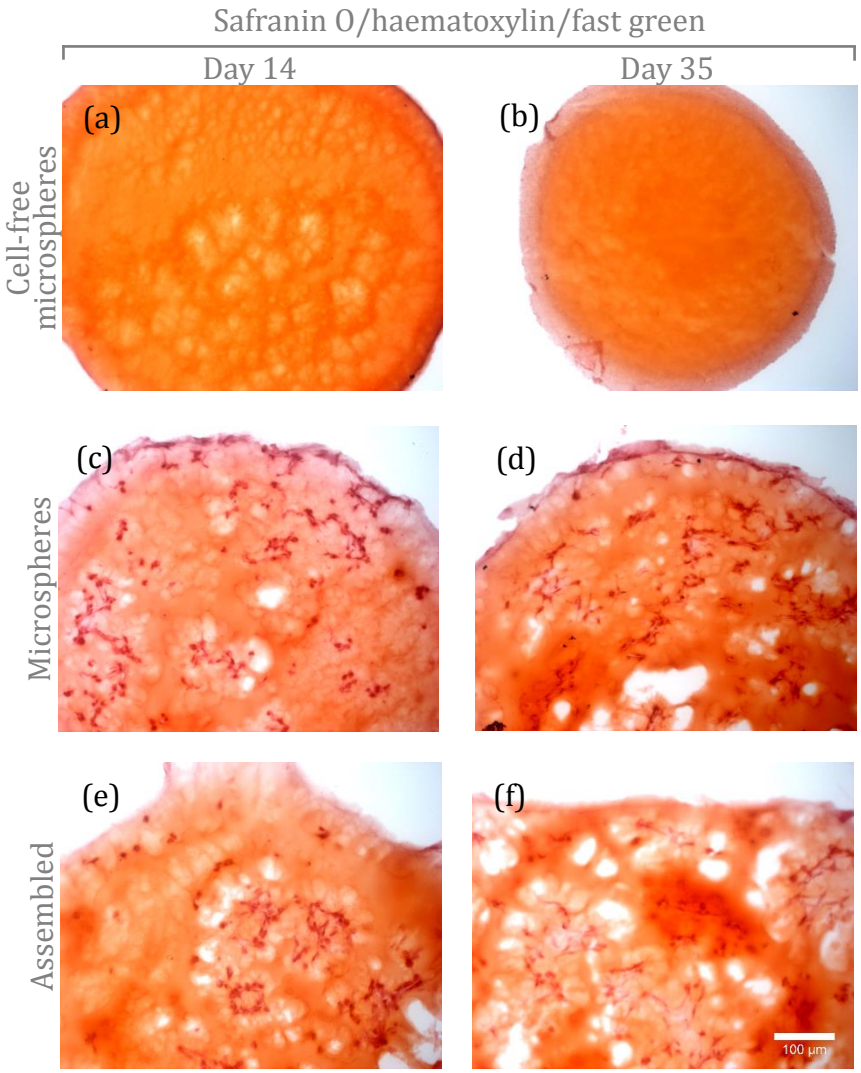

Figure 5-10. Histological staining (safranin O/haematoxylin/fast green) for cell-free 9.5% GelMA-0.5% HepMA individual microspheres, HAC-laden 9.5% GelMA-0.5% HepMA individual microspheres and assembled constructs on day 14 and 35. For lower magnification images see Figure 5.A-v, Appendix 5.A. *Scale bar = 100 µm for all images.*

Immunofluorescence staining on cryosections for aggrecan is shown in Figure 5-11 for HAC-laden 9.5% GelMA-0.5% HepMA individual microspheres and assembled constructs. Aggrecan is a large proteoglycan present in the extracellular matrix and aids cartilage in withstanding compressive loads [74]. Visual inspection for aggrecan suggest that higher aggrecan can be observed on day 35 (Figure 5.A-vi. b and d) compared to day 14 (Figure 5-11 a and c) for both individual microspheres and assembled construct. The assembled construct (Figure 5-11 a and b) was observed to have produced higher aggrecan compared to the individual microspheres (Figure 5-11 c and d) on both day 14 and 35.

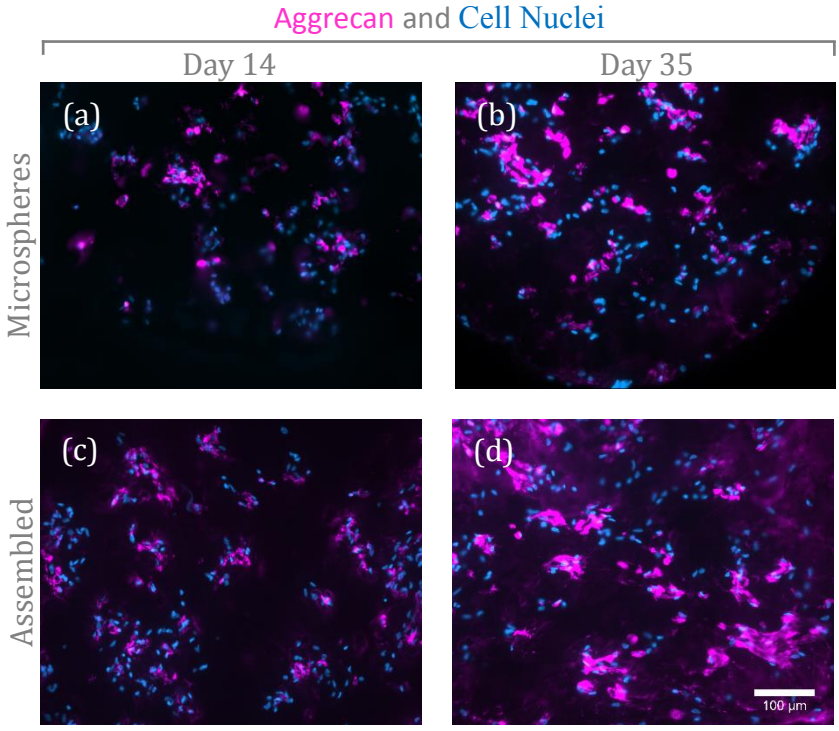

Figure 5-11. Immunofluorescence staining for Aggrecan and Hoechst 33342(Cell Nuclei) imaged using a fluorescence microscopy for HAC-laden 9.5% GelMA-0.5% HepMA individual microspheres and assembled constructs on day 14 and 35. For lower magnification images see Figure 5.A-vi, Appendix 5.A. *Scale bar = 100 µm for all images.*

5.4.4 Graduated construct assembly

As chondrocytes have limited source and *in vitro* proliferative potential, MSCs can potentially serve an alternative cell source for cartilage engineering [6, 75-77]. In this subsection, the fabrication of a graduated construct with HAC, MSC and co-culture microspheres was demonstrated.

The cells in the graduated assembled construct were labelled with Qtracker to track the rearrangement and self-assembly of the cells in the construct. See Figure 5.A-xv, Appendix 5.A for the confocal microscopy images of the cryosectioned graduated assembled construct. The visual inspection revealed that the intensity of the Qtracker was very low to track the rearrangement and self-assembly of the cells and no conclusion could be deduced.

The cryosections of the graduated assembled construct were stained with safranin O (Figure 5-12) to visually investigate GAG production. As seen previously, the incorporation of HepMA during the microsphere fabrication resulted in a high background staining for GAG. The background staining of HepMA made it challenging to investigate GAG production via safranin O staining.

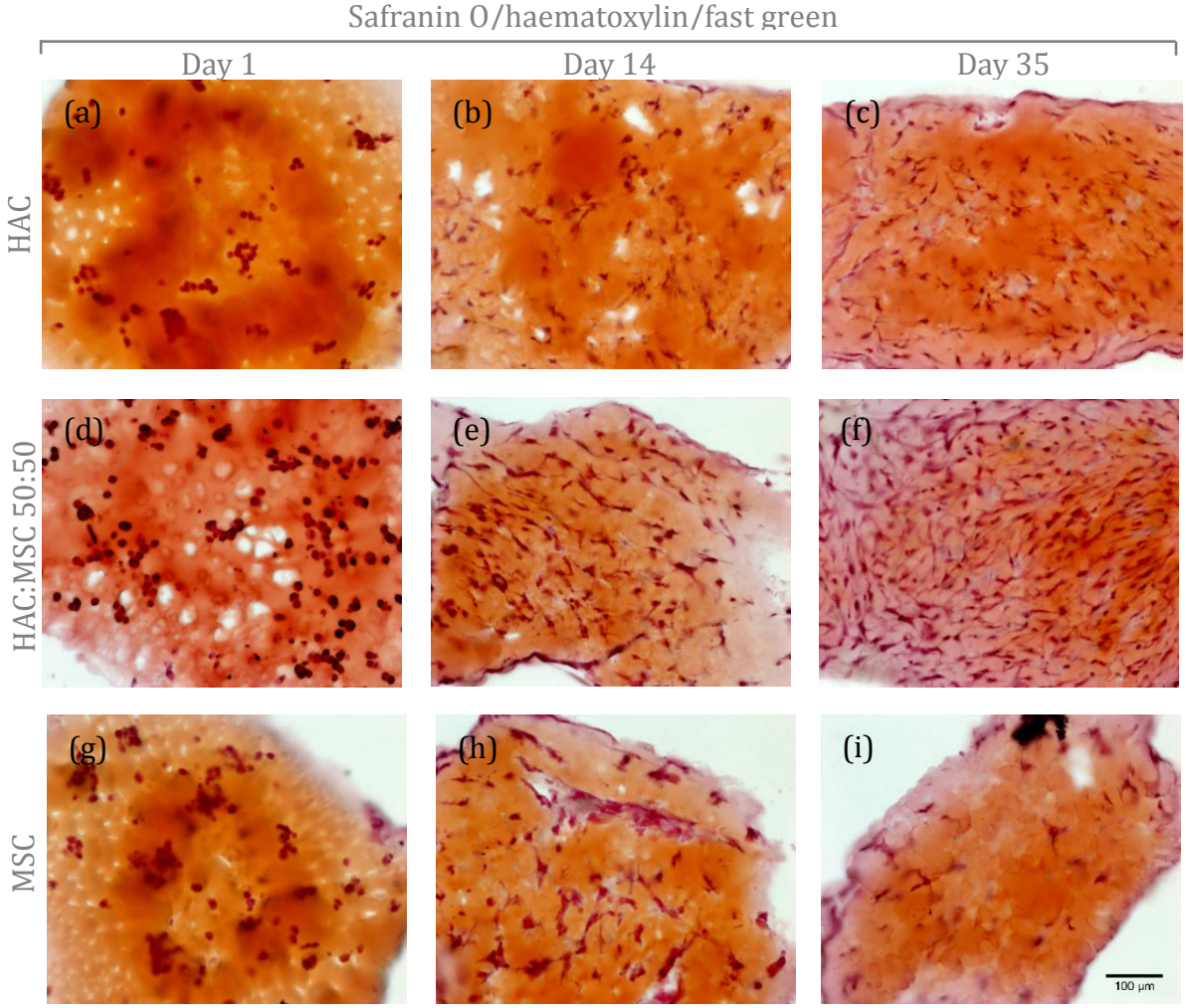

Figure 5-12. Histological staining (safranin O/haematoxylin/fast green) for HAC, co-culture (50% HAC and 50% MSC) and MSC laden 9.5% GelMA-0.5% HepMA microspheres that were assembled as a construct on day 1, 14 and 35. For lower magnification images see Figure 5.A-x, Appendix 5.A. *Scale bar = 100 µm for all images.*

Immunofluorescence staining on cryosections for aggrecan for the whole graduated assembled construct is shown in Figure 5-13 and the higher magnification images are shown in Figure 5-14. On day 1, the observed aggrecan staining appeared to be pericellular and was observed only in the HAC microspheres (Figure 5-14 a) and the co-culture microspheres (Figure 5-14 d). No noticeable pericellular aggrecan staining could be visualised in the MSC microspheres (Figure 5-14 g) on day 1. With the day 14 images (Figure 5-14 b and e), higher aggrecan was observed in the HAC and co-culture microspheres compared to the day 1 images suggesting aggrecan production. The visualisation of aggrecan observed in day 14 MSC microspheres (Figure 5-14 h) was higher than the day 1 MSC microspheres

(Figure 5-14 g) however the expression seemed comparatively lower than in the day 14 HAC (Figure 5-14 b) and co-culture (Figure 5-14 e) microspheres. The aggrecan staining in the day 35 images (Figure 5-14 c and f, and Figure 5-13 b) appeared to be slightly higher compared to the day 14 images (Figure 5-14 b and e, and Figure 5-13 a) in the HAC and co-culture microspheres. Similar to the day 14 data, the aggrecan staining in MSC microspheres at day 35 was visualised to be lower than the HAC and co-culture microspheres (Figure 5-14 I and Figure 5-13 b). The increased aggrecan staining observed by the visual inspection of the graduated assembled construct revealed aggrecan production and therefore neocartilage production over time.

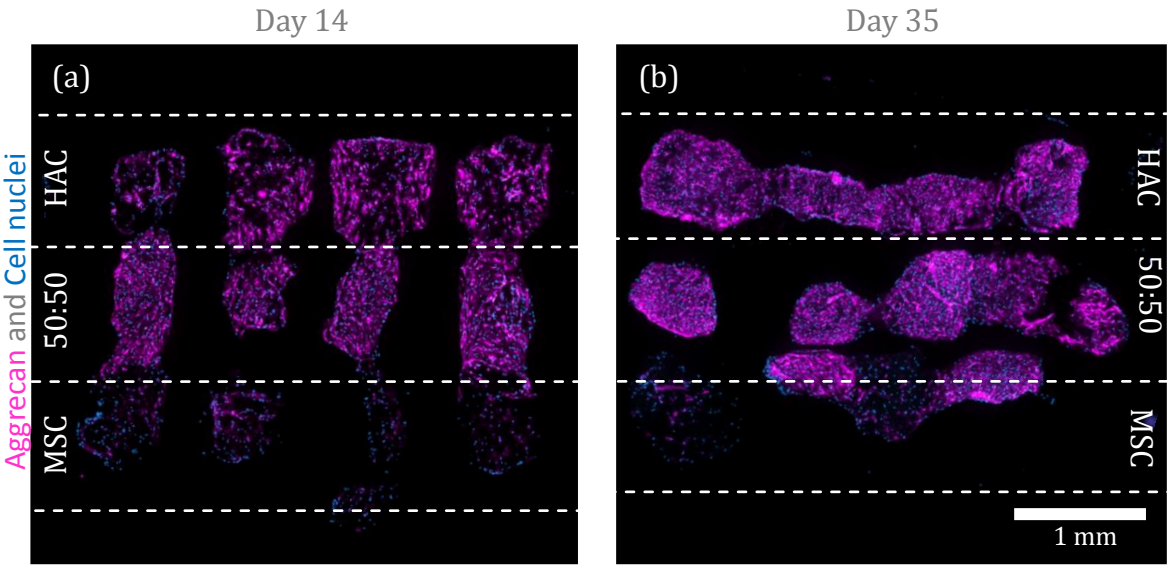

Figure 5-13. Immunofluorescence staining for Aggrecan and Hoechst 33342 (cell nuclei) imaged using a confocal fluorescence microscopy for a graduated assembled construct (HAC, co-culture (50% HAC and 50% MSC) and MSC-laden 9.5% GelMA-0.5% HepMA microspheres) on day 14 and 35. The dotted lines shows the division in the construct with different cell types. *Scale bar = 1 mm for all images.*

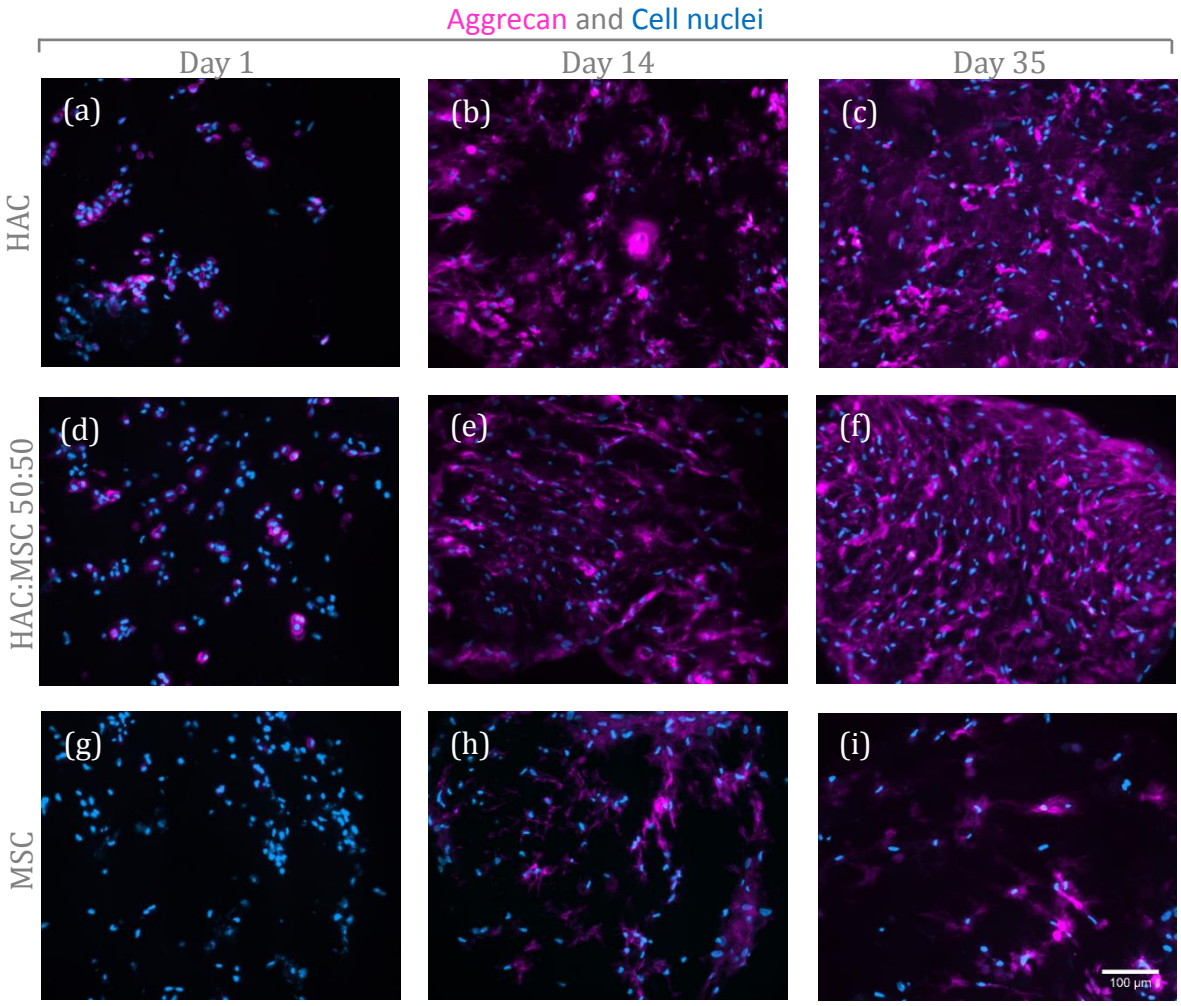

Figure 5-14. Immunofluorescence staining for Aggrecan and Hoechst 33342 (cell nuclei) imaged using a fluorescence microscopy for HAC, co-culture (50% HAC and 50% MSC) and MSC laden 9.5% GelMA-0.5% HepMA microspheres that were assembled as a construct on day 1, 14 and 35. *Scale bar = 100 µm for all images.*

5.5 Discussion

We have demonstrated the automated 3D Bioassembly of cell-laden hydrogel microspheres for biofabricating a tissue engineered cartilage construct via a bottom-up tissue engineering strategy. Bottom-up modular tissue engineering approaches are attractive alternatives given that larger tissue engineered constructs can be biofabricated from smaller tissue modules or subunits with specific micro-architectural features [78, 79]. The advantage of bottom-up strategies over top-down strategies is that the precise control of the spatial distribution of the cells and support material to recreate the microstructural features of tissues is possible [23].

As many native tissues are composed of repeating functional units, there is a strong biological reasoning for employing bottom-up strategies [23]. Utilising the layer-by-layer strategy, we demonstrated the use of a prototype automated biofabrication system to bioassemble cartilage constructs without affecting the viability of the individual tissue subunits. By successfully validating the automated bioassembly system with microspheres, we have opened a pathway to precisely build large and complex constructs of clinically relevant sizes in large numbers with a reduced construction time. Mathematical models or anatomical models generated via imaging techniques such as computed tomography (CT) or magnetic resonance imaging (MRI) can be inputted into a bio-plotter and easily translated to create an assembled construct [80].

Encapsulating cells in hydrogels is an attractive strategy to engineer multiple tissue modules in a short amount of time. In particular, GelMA based hydrogels do not only provide a hydrated 3D environment similar to native cartilage, but also enable the incorporation of bioactive molecules or compounds to further promote cartilage formation. Besides that, by tuning the stiffness of the GelMA hydrogels, encapsulated cells can be forced to maintain a rounded morphology to promote or direct a pro-chondrogenic phenotype [8, 9, 15, 19, 22, 81]. Encapsulating cells would be beneficial in a single surgery strategy, where, following harvesting of the tissue, chondrocytes could be isolated, encapsulated, bioassembled into a scaffold quickly and then the construct could be immediately transplanted into the patient. Moreover, one of the criteria for the cell scaffolds used in tissue engineering is that the scaffold should be completely degraded and replaced over time by the ECM produced by the cells [82]. As GelMA is prone to enzymatic degradation (GelMA contains MMP degradable motifs), the cartilage construct implanted *in situ* over time would eventually be degraded to be completely replaced by neocartilage [83, 84].

The major advantage of utilising cell-laden hydrogel microspheres over micro-tissues is the number of cells required. Fabricating an individual cell-laden Ø1 mm microsphere required approximately 8,000 cells at a concentration of 15 million cells/ml. In comparison, fabricating a Ø1 mm micro-tissue required 250,000 cells which is approximately 31-folds higher [3]. Based on these numbers, fabricating a construct of Ø25 mm and 2.4 mm thickness with microspheres would require only

8 million cells in comparison to fabricating a construct with micro-tissues which would require 247 million cells as mentioned earlier [3, 4]. Moreover, microspheres do not require the rate-limiting step of culturing the cell pellet for 7 days to form the micro-tissues before they can be bioassembled. These advantages with the microsphere based construct would aid in saving time, resources and man-power. With the microfluidic system that we have adopted, a large number of uniformly sized microspheres with a narrow size distribution of about Ø1 mm could be fabricated in a convenient and high-throughput manner. In an emulsion (macromer solution and oil), the surface tension causes the droplets to contract into a sphere to minimise the surface energy and this leads to the formation of microspheres at the edge of the fused capillary in the microfluidic system [40, 85]. The microspheres fabricated in this manner has been previously shown to be smooth and spherical [40].

A difference in average diameter was observed in the microspheres fabricated with different conditions. The average diameter of the cell-free 10% GelMA microspheres (1.294 ± 0.052 mm) was larger than the cell-free 5% GelMA microspheres (1.193 ± 0.070 mm) and the HAC-laden 9.5% GelMA-0.5% HepMA microspheres (0.955 ± 0.031 mm) had the smallest average diameter of all the conditions. The macromer concentrations and the addition of HepMA and cells could all possibly cause a change in viscosity, surface tension or density of the dispersed phase causing the variation in the size of the fabricated microspheres among different conditions [69, 70]. A significantly higher ($p<0.05$) singularisation efficiency was observed in the HAC-laden 9.5% GelMA-0.5% HepMA microspheres (94 ± 9.66%) compared to the cell-free 5% GelMA microspheres (82 ± 11.35%). It is likely that the higher macromer concentration increases the stiffness of the HAC-laden 9.5% GelMA-0.5% HepMA microspheres which improves the singularisation efficiency as microspheres of higher stiffness are trapped more effectively than softer microspheres which tend to get deformed or become lodged in the pressure ports of the singularisation chamber (see Chapter 4). The average diameter of the HAC-laden 9.5% GelMA-0.5% HepMA microspheres was closer to 1 mm (the diameter the tissue assembly system was designed to handle) compared to the cell-free 5% GelMA microspheres which could have also contributed to the higher efficiency.

The incorporation of heparin in a hydrogel scaffold has previously been shown to stimulate the redifferentiation of dedifferentiated chondrocytes [86]. The increase neocartilage synthesis in the presence of HepMA has been observed by our group [87]. Heparin and heparan sulphate is part of the GAG family and HepMA has been shown to exhibit a similar anticoagulant and growth factor signalling properties to heparin [72]. It has been suggested that the role of heparin could be to capture endogenous and exogenous growth factors produced by the cells when added into the media [86, 88]. These growth factors could signal the redifferentiation of the cells back into a more chondrogenic like phenotype [86]. The presence of heparin has also been shown to improve expression of chondrogenic markers [86, 88]. Due to the above potential of heparin for cartilage engineering, HepMA was incorporated into the cell-laden GelMA microspheres.

The individual microspheres and assembled constructs were cultured for 35 days to evaluate neocartilage formation. The presence of HepMA in the microspheres interfered with GAG quantification as the DMMB assay quantifies the heparin present in the HepMA microspheres. Likewise, the visual inspection for the presence of synthesised GAG was challenging with the safranin O stained sections as the presence of HepMA in the microspheres resulted in a high background staining [72]. To overcome this, the total GAG in the samples were normalised by subtracting the GAG values of the cell-free microspheres from the GAG values of the samples to evaluate the GAG production in the microspheres with the assumption that the HepMA content in the cell-free and cell-laden microspheres are similar over time. The decrease in normalised GAG per microsphere from day 0 (0.31 ± 0.05 μg/microsphere) to day 14 (0.12 ± 0.07 μg/microsphere) observed in the individual microspheres could possibly be due to HepMA leaching of the out of the hydrogel and the remodelling of the hydrogel by the chondrocytes [72]. However, the decrease in normalised GAG per microsphere from day 0 (0.31 ± 0.05 μg/microsphere) to 14 (0.20 ± 0.08 μg/microsphere) is less pronounced in assembled constructs and could possibly be due to higher GAG production by the cells in the assembled construct. Likewise, an increase in normalised GAG was seen in the assembled construct from day 14 (0.20 ± 0.08 μg/microsphere) to 35 (0.42 ± 0.09 μg/microsphere) but the increase was not significant in the individual microsphere possibly due to lower GAG

synthesis and retention. It has been previously shown that the GAG incorporated in an assembled micro-tissue construct is higher than that in individual micro-tissues [89]. This difference seen in the study was attributed to the reduced surface area to volume resulting in improved retention of GAG in the assembled construct [89]. It is also known that a hypoxic environment stimulates chondrocyte redifferentiation and extracellular matrix production in vitro and the assembled construct being larger could be more hypoxic compared to the individual microspheres resulting in the higher extracellular matrix production [90, 91]. The staining for aggrecan revealed neocartilage formation [92]. Higher aggrecan staining was visualised in the assembled construct compared the individual microspheres on day 35 and this is in line with the trend observed with the normalised GAG.

Although a higher normalised GAG per microsphere (Figure 5-9 a) was observed in the assembled construct (0.42 ± 0.09 μg/microsphere) compared to the individual microspheres (0.25 ± 0.10 μg/microsphere) on day 35, a higher normalised GAG per DNA was not observed in the assembled construct compared to the individual microspheres. This could be due to the higher DNA content (Figure 5-9 b) in the assembled construct (98.72 ± 10.27 ng/microsphere) compared to the individual microspheres (72.91 ± 4.46 ng/microsphere) due to the proliferation of cells on the fibres of the scaffold. The live/dead images on day 35 confirm the presence of cells on the scaffold fibres (Figure 5-8 f). Significant chondrocyte proliferation on Polyactive 300PEGT55PBT45 has previously been reported [62, 93]. It is known that the production of GAG by chondrocytes is lower in a 2D environment compared to cells in 3D [94]. Therefore, even though there was an increase in cell number on the surface of the scaffold fibres they might not be producing sufficient GAG comparable to the cells encapsulated within the hydrogel. As mentioned earlier, we are also of the opinion that we might be underestimating the production of GAG as the cells might be remodelling the incorporated HepMA and the quantity of HepMA leaching out in the cell-free microspheres might be different from the cell-laden microspheres. As the presence of HepMA incorporated in the hydrogel interfered with quantification and histology of GAG, other approaches to quantify neocartilage tissue formation is required. Further studies investigating the gene expression of collagen type I and II and aggrecan could potentially be more informative [17]. While there was no significant difference observed in normalised

GAG/DNA in the individual microspheres compared to the assembled construct, the normalised GAG per microsphere values and aggrecan staining observed in the assembled construct compared to the individual microspheres are encouraging as it suggests improved production of neocartilage in the assembled construct compared to the individual microspheres.

MSCs are considered as a relevant alternative source to chondrocytes for cartilage engineering as they can be easily isolated, expanded and differentiated into chondrocytes [75]. We have demonstrated the assembly of a graduated cartilage construct with HAC, co-culture and MSC laden 9.5% GelMA-0.5% HepMA microspheres. The cells in the graduated assembled construct were labelled with Qtracker (photostable fluorophores) to investigate any rearrangement and self-assembly of the cells. As Qtracker has previously been shown to not affect the viability of the cells and as it photo-bleaches very little over time, it was employed to track the cells [95, 96]. However, the faint signal of the Qtracker labelled cells (see Figure 5.A-xv, Appendix 5.A) made it challenging to precisely track the cells and the rearrangement and self-assembly of cells in the graduated assembled construct could not be concluded. Future experiments to track the rearrangement and self-assembly of the cells could potentially be carried out by labelling the cells with green fluorescent protein (GFP) and red fluorescent protein (RFP) [95].

With regards to tissue formation, higher aggrecan staining (Figure 5-13 and Figure 5-14) was visualised in the graduated assembled construct over time suggesting neocartilage formation. The production of aggrecan was however not uniform in the graduated assembled construct. The visualisation of aggrecan in the MSC microspheres (Figure 5-14 h and i and Figure 5-13) was comparatively lower to the HAC (Figure 5-14 b and c and Figure 5-13) and co-culture (Figure 5-14 e and f and Figure 5-13) microspheres in the construct on day 14 and 35 suggesting that MSC-laden microspheres had a lower matrix production, and is comparable to previous similar studies. For example, it has been shown that chondrogenesis does occur in MSC-laden agarose hydrogels, however, the quantity of matrix formed was lower than that produced by chondrocytes [81]. Furthermore, studies have shown that the expression of aggrecan and collagen type II is higher in MSC and HAC co-culture hydrogels compared to MSC only laden hydrogels [76]. This study also

suggests that a close proximity is required between MSCs and HACs for the promotion of chondrogenesis in MSCs [76] and can be related to cell-cell signalling via the establishment of gap junctions and also paracrine signalling mechanisms between cells and respective endogenous secretion of growth factors. This could possibly be the reason why the aggrecan staining was higher in the co-culture microspheres compared to the MSC only microspheres (Figure 5-14 and Figure 5-13). It has also been shown that the co-culture of MSCs with HACs reduced hypertrophy in MSCs [76, 77]. Moreover, the inhibition of chondrogenesis in MSCs could be due to the presence of RGD sequences in GelMA. It has been reported that RGD sequences can inhibit chondrogenesis of MSCs within alginate hydrogels and a similar behaviour might be occurring in our microspheres [97, 98].

We have demonstrated the flexibility of the system by assembling microspheres of different colours representing microspheres consisting of either different cell types or hydrogel compositions. Although this was performed with just one singularisation device rigged up to an injection device, potentially, parallel singularisation devices containing different types of microspheres can be rigged to an injection device to assemble microspheres of different cell types in a specific order. In cartilage engineering, assembling microspheres in a particular organisation can be of significant importance. Zonal constructs with different zonal subpopulations of cells could be assembled to recreate the arrangement in native articular cartilage [9, 99, 100]. A biphasic osteochondral construct with chondrocytes and osteoblasts/osteocytes could be assembled, with the potential advantage that an osteochondral construct would allow for fixation of the construct in the bony section of the defect and better integration of the cartilage with the bone [5, 101] compared to a single-phase chondral construct. Assembling vascularised bone modules for the bony region of the construct would allow diffusion of nutrients, gases and waste products and aid in avoiding necrosis in an osteochondral construct [27, 57]. Constructs with a gradient of cell types or different cell types (e.g. chondrocytes, MSCs or osteoblasts) could be fabricated to recapitulate a specific desired tissue structure [9, 76]. Furthermore, hydrogels of different mechanical properties could be assembled to induce chondrocytes to behave like cells from different zones [9, 102]. The cell density varies in different zones of cartilage, with higher cell density in the superficial zone compared to the middle and deep zones

[4]. The variation in cell density could be recapitulated in the assembled construct by assembling microspheres of different cell density [4]. Bioactive molecules such as basic fibroblast growth factor (bFGF) [103], TGF-β1 [15, 22] or insulin-like growth factor I (IGF-I) [15] could be incorporated into a microsphere with different concentrations and a construct with a gradient in bioactive molecules could be fabricated, this would be beneficial in zonal chondrogenesis of MSCs and chondrocytes [9]. Furthermore, even a micro-tissue and microsphere hybrid construct could potentially be assembled. For example, chondrogenic differentiation of MSCs in a micromass culture was demonstrated in the presence of hyaluronic acid microspheres which behaved as a growth factor delivery system delivering bone morphogenetic protein 2 (BMP-2) in a controlled manner and similarly a hybrid construct with micro-tissues and microspheres delivering growth factors could be fabricated [104].

Hydrogels possess limited mechanical strength and for application in cartilage tissue engineering, they need mechanical reinforcement to enhance their load-bearing ability [8, 42, 43]. The reinforcement of the hydrogel with thermoplastics to create a composite construct has previously been demonstrated, but the respective fabrication technique did not allow control over the microarchitecture [42, 43]. In the previous chapter we have shown that the stiffness of the fabricated scaffold is comparable to native cartilage and by assembling cell-laden microspheres into thermoplastic scaffold not only provide mechanical reinforcement for the hydrogels but also allowed spatial control over the construct's microarchitecture [8, 42, 43]. The reinforced hydrogel constructs would allow the implantation of a construct consisting of relatively immature neo-cartilage matrix thereby reducing *in vitro* culture time [5]. Previous studies have suggested that integration of engineered cartilage with host cartilage is improved when a more immature construct is implanted as opposed to a more mature *in vitro* cultured construct [105, 106]. Moreover, a study has also reported a higher chondrogenic expression in mechanically reinforced hydrogels compared to non-reinforced hydrogels when mechanically stimulated [43]. Apart from the mechanical reinforcement of the hydrogel, the pores present in between the microspheres after bioassembly could potentially also allow for easier diffusion of nutrients during early stages of tissue formation compared to a single solid casted hydrogel scaffold [107].

Previous studies have shown that physiological mechanical stimuli which include cyclic dynamic compression, fluid-induced shear, and hydrostatic pressure can positively influence cartilage ECM production [108-110]. Likewise, a low oxygen environment has been demonstrated to stimulate chondrocyte redifferentiation *in vitro* [90]. Further studies on the assembled construct in a hypoxic environment or with mechanical stimuli for optimal neocartilage synthesis would be beneficial in producing cartilage of higher quality [91, 108].

The fabrication of microspheres for a wide range of microsphere sizes (50-3000 μm) has previously been demonstrated [40, 49, 115, 116]. Presently, we have only validated the automated bioassembly system with microspheres of approximately 1 mm diameter and to be able to accommodate and handle microspheres outside this range, the physical components and the soft parameters of the automated tissue assembly system would have to be suitably modified. The miniaturisation of the system could unavoidably cause additional problems due to the nature of physics. Laminar flow, surface tension, diffusion and fluidic resistance start influencing the system as the design of the system approaches the microscale range, requiring further research or redesign of the system [117].

5.6 Conclusions

We demonstrated here the automated 3D Bioassembly of cell-laden hydrogel microspheres into a 3D plotted scaffold for biofabricating a tissue engineered cartilage construct. Microspheres of Ø1 mm that could be reliability handled by the automated bioassembly system were fabricated with a microfluidic system. The bioassembly system could effectively handle the fabricated microspheres and with the aid of the 3D positioning system could deliver the microspheres to any desired point in the 3D plotted scaffold. The flexibility of the automated tissue assembly system was demonstrated by assembling constructs with different arrangements of the various coloured microspheres into a 3D plotted scaffold. The layer-by-layer assembly of a cartilage construct with human articular chondrocyte (HAC)-laden hydrogel microspheres utilising the automated bioassembly system was demonstrated. No significant difference in viability was observed between manually assembled constructs and constructs assembled with the automated bioassembly

system. HAC-laden 9.5% GelMA-0.5% HepMA hydrogel microspheres were assembled and cultured up to 35 days. Immunofluorescence staining for aggrecan revealed cartilage tissue formation with a higher amount of aggrecan visualised in the assembled constructs compared to the individual microspheres. Furthermore, we demonstrated the fabrication of a graduated construct consisting of HAC, co-culture (50% HAC and 50% MSC) and MSC laden microspheres and the immunofluorescence staining for aggrecan revealed cartilage tissue formation over time. With this technology, large complex constructs of clinically relevant sizes can be fabricated.

5.7 References

1. Yang, S., et al., *The design of scaffolds for use in tissue engineering. Part I. Traditional factors.* Tissue engineering, 2001. **7**(6): p. 679-689.
2. Solchaga, L.A., V.M. Goldberg, and A.I. Caplan, *Cartilage regeneration using principles of tissue engineering.* Clinical Orthopaedics and Related Research, 2001. **391**: p. S161-S170.
3. Schon, B.S., et al., *Validation of a high-throughput microtissue fabrication process for 3D assembly of tissue engineered cartilage constructs.* Cell Tissue Res, 2012.
4. Hunziker, E., T. Quinn, and H.-J. Häuselmann, *Quantitative structural organization of normal adult human articular cartilage.* Osteoarthritis and Cartilage, 2002. **10**(7): p. 564-572.
5. Woodfield, T., et al., *Scaffolds for tissue engineering of cartilage.* Critical Reviews™ in Eukaryotic Gene Expression, 2002. **12**(3).
6. Darling, E.M. and K.A. Athanasiou, *Rapid phenotypic changes in passaged articular chondrocyte subpopulations.* Journal of Orthopaedic Research, 2005. **23**(2): p. 425-432.
7. Oliveira, J.T., et al., *Gellan gum injectable hydrogels for cartilage tissue engineering applications: in vitro studies and preliminary in vivo evaluation.* Tissue Engineering Part A, 2009. **16**(1): p. 343-353.
8. Schuurman, W., et al., *Gelatin-Methacrylamide Hydrogels as Potential Biomaterials for Fabrication of Tissue-Engineered Cartilage Constructs.* Macromolecular bioscience, 2013. **13**(5): p. 551-561.
9. Klein, T.J., et al., *Strategies for zonal cartilage repair using hydrogels.* Macromolecular bioscience, 2009. **9**(11): p. 1049-1058.
10. Guo, J., G.W. Jourdian, and D.K. Maccallum, *Culture and growth characteristics of chondrocytes encapsulated in alginate beads.* Connective tissue research, 1989. **19**(2-4): p. 277-297.
11. Benya, P.D. and J.D. Shaffer, *Dedifferentiated chondrocytes reexpress the differentiated collagen phenotype when cultured in agarose gels.* Cell, 1982. **30**(1): p. 215-224.
12. Wakitani, S., et al., *Mesenchymal cell-based repair of large, full-thickness defects of articular cartilage.* J Bone Joint Surg Am, 1994. **76**(4): p. 579-592.
13. Silverman, R.P., et al., *Injectable tissue-engineered cartilage using a fibrin glue polymer.* Plastic and reconstructive surgery, 1999. **103**(7): p. 1809-1818.
14. Kim, T.-K., et al., *Experimental model for cartilage tissue engineering to regenerate the zonal organization of articular cartilage.* Osteoarthritis and cartilage, 2003. **11**(9): p. 653-664.
15. Elisseeff, J., et al., *Controlled-release of IGF-I and TGF-β1 in a photopolymerizing hydrogel for cartilage tissue engineering.* Journal of Orthopaedic Research, 2001. **19**(6): p. 1098-1104.
16. Spiller, K.L., et al., *A novel method for the direct fabrication of growth factor-loaded microspheres within porous nondegradable hydrogels: controlled release for cartilage tissue engineering.* Journal of controlled release, 2012. **157**(1): p. 39-45.

17. Levett, P.A., et al., *A biomimetic extracellular matrix for cartilage tissue engineering centered on photocurable gelatin, hyaluronic acid and chondroitin sulfate.* Acta biomaterialia, 2014. **10**(1): p. 214-223.
18. Lim, K.S., et al., *New Visible-Light Photoinitiating System for Improved Print Fidelity in Gelatin-Based Bioinks.* 2016.
19. Nichol, J.W., et al., *Cell-laden microengineered gelatin methacrylate hydrogels.* Biomaterials, 2010. **31**(21): p. 5536-5544.
20. Bartnikowski, M., et al., *Protective effects of reactive functional groups on chondrocytes in photocrosslinkable hydrogel systems.* Acta biomaterialia, 2015. **27**: p. 66-76.
21. Hwang, N.S., et al., *Response of zonal chondrocytes to extracellular matrix-hydrogels.* FEBS letters, 2007. **581**(22): p. 4172-4178.
22. Mann, B.K., R.H. Schmedlen, and J.L. West, *Tethered-TGF-β increases extracellular matrix production of vascular smooth muscle cells.* Biomaterials, 2001. **22**(5): p. 439-444.
23. Nichol, J.W. and A. Khademhosseini, *Modular Tissue Engineering: Engineering Biological Tissues from the Bottom Up.* Soft Matter, 2009. **5**(7): p. 1312-1319.
24. Annabi, N., et al., *25th anniversary article: rational design and applications of hydrogels in regenerative medicine.* Advanced Materials, 2014. **26**(1): p. 85-124.
25. Annabi, N., et al., *Controlling the porosity and microarchitecture of hydrogels for tissue engineering.* Tissue Engineering Part B: Reviews, 2010. **16**(4): p. 371-383.
26. Miller, J.S., et al., *Rapid casting of patterned vascular networks for perfusable engineered three-dimensional tissues.* Nature materials, 2012. **11**(9): p. 768-774.
27. Khademhosseini, A. and R. Langer, *Microengineered hydrogels for tissue engineering.* Biomaterials, 2007. **28**(34): p. 5087-5092.
28. Kolesky, D.B., et al., *3D bioprinting of vascularized, heterogeneous cell-laden tissue constructs.* Advanced materials, 2014. **26**(19): p. 3124-3130.
29. Kang, H.-W., et al., *A 3D bioprinting system to produce human-scale tissue constructs with structural integrity.* Nature biotechnology, 2016. **34**(3): p. 312-319.
30. Lu, T., Y. Li, and T. Chen, *Techniques for fabrication and construction of three-dimensional scaffolds for tissue engineering.* International journal of nanomedicine, 2013. **8**: p. 337.
31. Hannachi, I.E., M. Yamato, and T. Okano, *Cell sheet technology and cell patterning for biofabrication.* Biofabrication, 2009. **1**(2): p. 022002.
32. Shimizu, T., et al., *Long-term survival and growth of pulsatile myocardial tissue grafts engineered by the layering of cardiomyocyte sheets.* Tissue engineering, 2006. **12**(3): p. 499-507.
33. Kelm, J.M., et al., *Design of custom-shaped vascularized tissues using microtissue spheroids as minimal building units.* Tissue Eng, 2006. **12**(8): p. 2151-60.
34. Pang, Y., et al., *Liver tissue engineering based on aggregate assembly: efficient formation of endothelialized rat hepatocyte aggregates and their immobilization with biodegradable fibresThis work was presented at the International Conference on Biofabrication (Toyama, Japan, 6–8 October 2011).* Biofabrication, 2012. **4**(4): p. 045004.
35. Kelm, J.M., et al., *A novel concept for scaffold-free vessel tissue engineering: self-assembly of microtissue building blocks.* Journal of biotechnology, 2010. **148**(1): p. 46-55.

36. Kelm, J.M., et al., *Design of custom-shaped vascularized tissues using microtissue spheroids as minimal building units.* Tissue engineering, 2006. **12**(8): p. 2151-2160.
37. Du, Y., et al., *Directed assembly of cell-laden microgels for fabrication of 3D tissue constructs.* Proceedings of the National Academy of Sciences, 2008. **105**(28): p. 9522-9527.
38. Yeh, J., et al., *Micromolding of shape-controlled, harvestable cell-laden hydrogels.* Biomaterials, 2006. **27**(31): p. 5391-8.
39. Dikina, A.D., et al., *Engineered cartilaginous tubes for tracheal tissue replacement via self-assembly and fusion of human mesenchymal stem cell constructs.* Biomaterials, 2015. **52**: p. 452-462.
40. Young, C., et al., *Poly (vinyl alcohol)-heparin biosynthetic microspheres produced by microfluidics and ultraviolet photopolymerisation.* Biomicrofluidics, 2013. **7**(4): p. 044109.
41. Costantini, M., et al., *3D bioprinting of BM-MSCs-loaded ECM biomimetic hydrogels for in vitro neocartilage formation.* Biofabrication, 2016. **8**(3): p. 035002.
42. Boere, K.W., et al., *Covalent attachment of a three-dimensionally printed thermoplast to a gelatin hydrogel for mechanically enhanced cartilage constructs.* Acta biomaterialia, 2014. **10**(6): p. 2602-2611.
43. Visser, J., et al., *Reinforcement of hydrogels using three-dimensionally printed microfibres.* Nature communications, 2015. **6**.
44. Leung, B.M. and M.V. Sefton, *A modular approach to cardiac tissue engineering.* Tissue Engineering Part A, 2010. **16**(10): p. 3207-3218.
45. Zuo, Y., et al., *Photo-cross-linkable methacrylated gelatin and hydroxyapatite hybrid hydrogel for modularly engineering biomimetic osteon.* ACS applied materials & interfaces, 2015. **7**(19): p. 10386-10394.
46. McGuigan, A.P. and M.V. Sefton, *Vascularized organoid engineered by modular assembly enables blood perfusion.* Proceedings of the National Academy of Sciences, 2006. **103**(31): p. 11461-11466.
47. Ozbolat, I.T., H. Chen, and Y. Yu, *Development of 'Multi-arm Bioprinter'for hybrid biofabrication of tissue engineering constructs.* Robotics and Computer-Integrated Manufacturing, 2014. **30**(3): p. 295-304.
48. Yeh, J., et al., *Micromolding of shape-controlled, harvestable cell-laden hydrogels.* Biomaterials, 2006. **27**(31): p. 5391-5398.
49. Young, C.J., L.A. Poole-Warren, and P.J. Martens, *Combining submerged electrospray and UV photopolymerization for production of synthetic hydrogel microspheres for cell encapsulation.* Biotechnology and bioengineering, 2012. **109**(6): p. 1561-1570.
50. Lacik, I., et al., *New capsule with tailored properties for the encapsulation of living cells.* Journal of biomedical materials research, 1998. **39**(1): p. 52-60.
51. Cohen, S., et al., *Controlled delivery systems for proteins based on poly (lactic/glycolic acid) microspheres.* Pharmaceutical research, 1991. **8**(6): p. 713-720.
52. Prüße, U., et al., *Production of spherical beads by JetCutting.* Chemical engineering & technology, 2000. **23**(12): p. 1105-1110.
53. Brandenberger, H.R. and F. Widmer, *Immobilization of highly concentrated cell suspensions using the laminar jet breakup technique.* Biotechnology progress, 1999. **15**(3): p. 366-372.

54. Bugarski, B., et al., *Electrostatic droplet generation: mechanism of polymer droplet formation.* AIChE Journal, 1994. **40**(6): p. 1026-1031.
55. Serra, C., et al., *A predictive approach of the influence of the operating parameters on the size of polymer particles synthesized in a simplified microfluidic system.* Langmuir, 2007. **23**(14): p. 7745-7750.
56. Bae, H., et al., *Cell-laden microengineered pullulan methacrylate hydrogels promote cell proliferation and 3D cluster formation.* Soft Matter, 2011. **7**(5): p. 1903-1911.
57. Klotz, B.J., et al., *Gelatin-Methacryloyl Hydrogels: Towards Biofabrication-Based Tissue Repair.* Trends in biotechnology, 2016. **34**(5): p. 394-407.
58. Dahle, J., E. Kvam, and T. Stokke, *Bystander effects in UV-induced genomic instability: antioxidants inhibit delayed mutagenesis induced by ultraviolet A and B radiation.* Journal of carcinogenesis, 2005. **4**(1): p. 11.
59. Van Den Bulcke, A.I., et al., *Structural and Rheological Properties of Methacrylamide Modified Gelatin Hydrogels.* Biomacromolecules, 2000. **1**(1): p. 31-38.
60. Smeds, K.A. and M.W. Grinstaff, *Photocrosslinkable polysaccharides for in situ hydrogel formation.* Journal of biomedical materials research, 2001. **54**(1): p. 115-121.
61. Young, C., *Fabrication and characterisation of poly(vinyl alcohol) and heparin biosynthetic hydrogel microspheres for cell microencapsulation*, in *Graduate School of Biomedical Engineering, Faculty of Engineering* 2012, University of New South Wales.
62. Woodfield, T.B., et al., *Design of porous scaffolds for cartilage tissue engineering using a three-dimensional fiber-deposition technique.* Biomaterials, 2004. **25**(18): p. 4149-61.
63. Woodfield, T.B.F., et al., *Rapid prototyping of anatomically shaped, tissue-engineered implants for restoring congruent articulating surfaces in small joints.* Cell Proliferation, 2009. **42**(4): p. 485-497.
64. Woodfield, T.B., et al., *The regulation of expanded human nasal chondrocyte re-differentiation capacity by substrate composition and gas plasma surface modification.* Biomaterials, 2006. **27**(7): p. 1043-1053.
65. Miot, S., et al., *Effects of scaffold composition and architecture on human nasal chondrocyte redifferentiation and cartilaginous matrix deposition.* Biomaterials, 2005. **26**(15): p. 2479-2489.
66. Woodfield, T., et al., *Rapid prototyping of anatomically shaped, tissue-engineered implants for restoring congruent articulating surfaces in small joints.* Cell proliferation, 2009. **42**(4): p. 485-497.
67. Woodfield, T.B., L. Moroni, and J. Malda, *Combinatorial approaches to controlling cell behaviour and tissue formation in 3D via rapid-prototyping and smart scaffold design.* Combinatorial chemistry & high throughput screening, 2009. **12**(6): p. 562-579.
68. Woodfield, T.B.F., et al., *Polymer scaffolds fabricated with pore-size gradients as a model for studying the zonal organization within tissue-engineered cartilage constructs.* Tissue Engineering, 2005. **11**(9-10): p. 1297-1311.
69. Utada, A.S., et al., *Dripping to jetting transitions in coflowing liquid streams.* Physical review letters, 2007. **99**(9): p. 094502.

70. Nie, Z., et al., *Polymer particles with various shapes and morphologies produced in continuous microfluidic reactors.* Journal of the American chemical society, 2005. **127**(22): p. 8058-8063.
71. Li, X., et al., *3D Culture of Chondrocytes in Gelatin Hydrogels with Different Stiffness.* Polymers, 2016. **8**(8): p. 269.
72. Nilasaroya, A., et al., *Structural and functional characterisation of poly (vinyl alcohol) and heparin hydrogels.* Biomaterials, 2008. **29**(35): p. 4658-4664.
73. Kiviranta, I., et al., *Microspectrophotometric quantitation of glycosaminoglycans in articular cartilage sections stained with Safranin O.* Histochemistry, 1985. **82**(3): p. 249-255.
74. Roughley, P.J. and J.S. Mort, *The role of aggrecan in normal and osteoarthritic cartilage.* Journal of experimental orthopaedics, 2014. **1**(1): p. 1.
75. Tuan, R.S., *Stemming cartilage degeneration: adult mesenchymal stem cells as a cell source for articular cartilage tissue engineering.* Arthritis & Rheumatism, 2006. **54**(10): p. 3075-3078.
76. Bian, L., et al., *Coculture of human mesenchymal stem cells and articular chondrocytes reduces hypertrophy and enhances functional properties of engineered cartilage.* Tissue Eng Part A, 2011. **17**(7-8): p. 1137-45.
77. Giovannini, S., et al., *Micromass co-culture of human articular chondrocytes and human bone marrow mesenchymal stem cells to investigate stable neocartilage tissue formation in vitro.* Eur Cell Mater, 2010. **20**(245): p. 59.
78. Elbert, D.L., *Bottom-up tissue engineering.* Curr Opin Biotechnol, 2011. **22**(5): p. 674-80.
79. Schon, B., G. Hooper, and T. Woodfield, *Modular Tissue Assembly Strategies for Biofabrication of Engineered Cartilage.* Annals of biomedical engineering, 2016: p. 1-15.
80. Agarwala, M.K., et al., *Structural quality of parts processed by fused deposition.* Rapid Prototyping Journal, 1996. **2**(4): p. 4-19.
81. Mauck, R., X. Yuan, and R. Tuan, *Chondrogenic differentiation and functional maturation of bovine mesenchymal stem cells in long-term agarose culture.* Osteoarthritis and cartilage, 2006. **14**(2): p. 179-189.
82. Langer, R., *Biodegradable polymer scaffolds for tissue engineering.* Nat. Biotechnol, 1994.
83. Hutson, C.B., et al., *Synthesis and characterization of tunable poly (ethylene glycol): gelatin methacrylate composite hydrogels.* Tissue Engineering Part A, 2011. **17**(13-14): p. 1713-1723.
84. Yue, K., et al., *Synthesis, properties, and biomedical applications of gelatin methacryloyl (GelMA) hydrogels.* Biomaterials, 2015. **73**: p. 254-271.
85. Okubo, M., et al., *Studies on suspension and emulsion. XLVII. Anomalous composite polymer emulsion particles with voids produced by seeded emulsion polymerization.* Journal of Polymer Science: Polymer Letters Edition, 1981. **19**(3): p. 143-147.
86. Recha-Sancho, L. and C.E. Semino, *Heparin-based self-assembling peptide scaffold reestablish chondrogenic phenotype of expanded de-differentiated human chondrocytes.* Journal of Biomedical Materials Research Part A, 2016. **104**(7): p. 1694-1706.
87. Brown, G.C., et al., *Fabrication of gelatin-heparin hydrogels with enhanced chondrogenic differentiation and tunable degradation.*

88. Kim, M., et al., *Composite system of PLCL scaffold and heparin-based hydrogel for regeneration of partial-thickness cartilage defects.* Biomacromolecules, 2012. **13**(8): p. 2287-2298.
89. Schuurman, W., et al., *Three-dimensional assembly of tissue-engineered cartilage constructs results in cartilaginous tissue formation without retainment of zonal characteristics.* Journal of tissue engineering and regenerative medicine, 2013.
90. Malda, J., et al., *Low oxygen tension stimulates the redifferentiation of dedifferentiated adult human nasal chondrocytes.* Osteoarthritis and cartilage, 2004. **12**(4): p. 306-313.
91. Domm, C., et al., *Redifferentiation of dedifferentiated bovine articular chondrocytes in alginate culture under low oxygen tension.* Osteoarthritis and Cartilage, 2002. **10**(1): p. 13-22.
92. Aigner, J., et al., *Cartilage tissue engineering with novel nonwoven structured biomaterial based on hyaluronic acid benzyl ester.* Journal of biomedical materials research, 1998. **42**(2): p. 172-181.
93. Papadaki, M., et al., *The different behaviors of skeletal muscle cells and chondrocytes on PEGT/PBT block copolymers are related to the surface properties of the substrate.* Journal of biomedical materials research, 2001. **54**(1): p. 47-58.
94. Caron, M., et al., *Redifferentiation of dedifferentiated human articular chondrocytes: comparison of 2D and 3D cultures.* Osteoarthritis and Cartilage, 2012. **20**(10): p. 1170-1178.
95. Fotos, J.S., J.T. Koh, and D.S. Galileo, *Vital labeling, time-lapse microscopy, and quantitative motility analysis of C6 glioma tumor cells.* Cancer Research, 2005. **65**(9 Supplement): p. 1332-1332.
96. Shuman, L., et al., *Use of Qtracker™ 655 to monitor the interaction of metastatic breast cancer cells with osteoblasts in co-culture.* Cancer Research, 2007. **67**(9 Supplement): p. 2805-2805.
97. Connelly, J.T., A.J. García, and M.E. Levenston, *Inhibition of in vitro chondrogenesis in RGD-modified three-dimensional alginate gels.* Biomaterials, 2007. **28**(6): p. 1071-1083.
98. Shirahama, H., et al., *Precise tuning of facile one-pot gelatin methacryloyl (GeLMA) synthesis.* Scientific Reports, 2016. **6**.
99. Klein, T., et al., *Tissue engineering of stratified articular cartilage from chondrocyte subpopulations.* Osteoarthritis and cartilage, 2003. **11**(8): p. 595-602.
100. Sharma, B., et al., *Designing zonal organization into tissue-engineered cartilage.* Tissue engineering, 2007. **13**(2): p. 405-414.
101. Tuli, R., et al., *Human mesenchymal progenitor cell-based tissue engineering of a single-unit osteochondral construct.* Tissue engineering, 2004. **10**(7-8): p. 1169-1179.
102. Ng, K.W., et al., *A layered agarose approach to fabricate depth-dependent inhomogeneity in chondrocyte-seeded constructs.* Journal of Orthopaedic Research, 2005. **23**(1): p. 134-141.
103. DeLong, S.A., J.J. Moon, and J.L. West, *Covalently immobilized gradients of bFGF on hydrogel scaffolds for directed cell migration.* Biomaterials, 2005. **26**(16): p. 3227-3234.

104. Jha, A.K., et al., *Perlecan domain I-conjugated, hyaluronic acid-based hydrogel particles for enhanced chondrogenic differentiation via BMP-2 release.* Biomaterials, 2009. **30**(36): p. 6964-6975.
105. Miot, S., et al., *Influence of in vitro maturation of engineered cartilage on the outcome of osteochondral repair in a goat model.* Eur Cell Mater, 2012. **23**: p. 222-236.
106. Obradovic, B., et al., *Integration of engineered cartilage.* Journal of Orthopaedic Research, 2001. **19**(6): p. 1089-1097.
107. Shipley, R., et al., *Design criteria for a printed tissue engineering construct: a mathematical homogenization approach.* Journal of theoretical biology, 2009. **259**(3): p. 489-502.
108. Vinatier, C., et al., *Cartilage engineering: a crucial combination of cells, biomaterials and biofactors.* Trends in biotechnology, 2009. **27**(5): p. 307-314.
109. Mauck, R.L., et al., *Functional tissue engineering of articular cartilage through dynamic loading of chondrocyte-seeded agarose gels.* Journal of biomechanical engineering, 2000. **122**(3): p. 252-260.
110. Elder, S.H., et al., *Chondrocyte differentiation is modulated by frequency and duration of cyclic compressive loading.* Annals of biomedical engineering, 2001. **29**(6): p. 476-482.
111. Ivascu, A. and M. Kubbies, *Rapid generation of single-tumor spheroids for throughput cell function and toxicity analysis.* Journal of biomolecular screening, 2006. **11**(8): p. 922-932.
112. Ivascu, A. and M. Kubbies, *Diversity of cell-mediated adhesions in breast cancer spheroids.* International journal of oncology, 2007. **31**(6): p. 1403-1414.
113. Kunz-Schughart, L.A., et al., *A heterologous 3-D coculture model of breast tumor cells and fibroblasts to study tumor-associated fibroblast differentiation.* Experimental cell research, 2001. **266**(1): p. 74-86.
114. Carlsson, J., et al., *Formation and growth of multicellular spheroids of human origin.* Int J Cancer, 1983. **31**(5): p. 523-33.
115. Rossow, T., et al., *Controlled synthesis of cell-laden microgels by radical-free gelation in droplet microfluidics.* Journal of the American Chemical Society, 2012. **134**(10): p. 4983-4989.
116. Kim, C., et al., *Generation of core-shell microcapsules with three-dimensional focusing device for efficient formation of cell spheroid.* Lab on a Chip, 2011. **11**(2): p. 246-252.
117. Beebe, D.J., G.A. Mensing, and G.M. Walker, *Physics and applications of microfluidics in biology.* Annu Rev Biomed Eng, 2002. **4**: p. 261-86.

Chapter 6 Automated 3D Bioassembly of micro-tissues for biofabrication of an *in vitro* 3D cancer model and its evaluation compared to existing 2D and 3D drug screening models

6.1 Abstract

3D *in vitro* cancer models have an invaluable role in cancer research and drug discovery. Presently, high-throughput fabrication of complex 3D cancer constructs with the precise arrangement of micro-tissues in 3D plotted scaffolds has been limited. We aimed at the automated 3D Bioassembly of micro-tissues for biofabricating a modular assembly based cancer construct for application as an *in vitro* 3D cancer model. Compact and spherical Ø1 mm cancer micro-tissues that can be handled by the automated bioassembly system were fabricated by co-culturing SKOV3 (human ovarian adenocarcinoma cell-line) with human foreskin fibroblasts (HFF) using liquid overlay technique and were characterised. Qtracker labelled micro-tissues showed that the cells self-segregated to form a fibroblastic core enveloped by SKOV3s. A bilayered cancer construct containing 4 micro-tissues per layer was fabricated via a layer-by-layer approach by alternately 3D plotting a PEGT/PBT polymer scaffold and inserting the cancer micro-tissues using a prototype automated bioassembly system. No significant difference in viability between the construct assembled using the automated system and the manually assembled construct was observed. For the chemosensitivity test, cells cultured in 2D, micro-tissues and assembled cancer constructs were exposed to doxorubicin for 4 days and the metabolic activity was measured using the AlamarBlue® assay. The chemosensitivity test revealed a cell-dependent chemoresistance and higher chemoresistance in 3D models compared to cells in 2D. Fixed frozen sections were stained for Ki67 and γ-H2AX. A cell-dependent Ki67 expression was visualised. Higher γ-H2AX was visualized at higher drug concentrations demonstrating double-stranded DNA breakage caused by the drug. This model and technology opens the path for the automated bioassembly of large modular assembly based cancer constructs with complex 3D architecture.

6.2 Introduction

With cancer becoming a major cause of morbidity and mortality, research in cancer is highly imperative [1]. Understanding cancer progression *in situ* can be very long and impractical. Also, clinical trials of probable anticancer drugs tend to have risks associated with it, are expensive and need ethical approval [2]. Thus there is an indispensable need to develop cancer models that can be employed to provide some very important insights into the process of tumorigenesis, to help in accelerating translational research in cancer and also facilitate the development and screening of novel tumour-specific drugs [2].

Two-dimensional (2D) monolayer culture systems and animal models have long been relied upon by researchers as cancer models to conduct cancer research. 2D culture systems are too simplistic and primitive and do not recapitulate the anatomy or physiology of a tissue [3]. When cells are grown as a monolayer on a plastic or glass substrate, the tissue-specific architecture, metabolic gradient, cellular differentiation, cell cycle control, mechanical cues, biochemical cues, three-dimensional (3D) cell–cell and cell–matrix interactions are lost [4, 5]. Furthermore, cells cultured in 2D have a lower resistance to chemotherapy compared to cells cultured in a 3D environment, resulting in poor negative screening power during drug screening [6].

With regards to animal models, the transplantable tumour model in rodents was developed as early as the start of the 20th century, which allowed for the testing of anticancer drugs [7]. Animal models are currently the gold standard in cancer research and are critical in drug testing. However, they tend to be expensive, require ethical approval, and are complex and containing many multivariable uncontrollable factors, such as, the presence of the host immune response, differences in liver toxicity, differences in telomerase regulation, contain non-human host cells, differences in haemodynamics, and production of endogenous growth factors [2, 8-10].

The high cost of drug research and development means there is a need for selecting the most promising candidates in the earlier stages of screening rather than later [11]. Due to the disadvantages of monolayer culture systems and the cost

and ethical issues associated with animal models, there is a need for *in vitro* 3D models with increased predictive power that can more accurately anticipate the outcome of a candidate drug in tumours *in vivo* before animal testing and clinical trials [4, 12].

Multicellular spheroids (micro-tissues) [13, 14] along with gel systems which allow cell encapsulation in 3D hydrogels [15, 16] make up the two major frequently used *in vitro* 3D cancer platforms. Micro-tissues are an aggregation of cells used in a wide range of research fields including drug screening, research in drug transport and binding, cancer research, tissue morphogenesis, differentiation, tissue engineering, regenerative medicine and stem cell research [17-22]. Although the drug response of tumours *in vivo* is more similar to micro-tissues in comparison to cells in 2D, micro-tissues are comparatively smaller and the drug response is altered compared to larger tumour tissues [23, 24]. In general, cancer micro-tissues of approximately Ø70 μm up to Ø1 mm have been fabricated, where the micro-tissue size is dependent on the cell type, seeding density and culture time [22, 25, 26]. However, these sizes are not necessarily clinically relevant as most tumours *in vivo* are much larger in size [27]. For example for stage 2 breast cancer, the tumour size varies from 2 to 5 cm [28]. Similarly, with regards to ovarian cancer, the average cancer tumour size varies from 4.6 to 11.8 cm depending on the stage [29]. Moreover, the tissue architecture in micro-tissues is less complex than actual tumours that are found *in vivo* [22, 30, 31]. Therefore, there is a need for an improved fabrication approach that can tailor make large 3D cancer models to recreate tumour niches of complex architecture and is also adaptable with high-throughput analysis systems.

Research in tissue engineering and regenerative medicine (TERM) has led to advances in biofabrication enabling the control of macro and microscale structure and architecture of an engineered construct. These TERM concepts can potentially be translated for application in cancer research. Advances in biofabrication relating to the bioassembly of micro-tissues for application in tissue engineering such as vascular tissue engineering [32] and cartilage engineering [33, 34] have been reported. Nevertheless, little focus has been given to bioassembly of micro-tissues for tumour engineering. With regards to tumour cells, Rago *et al.* demonstrated the

fabrication of co-culture micro-tissues with rat hepatoma cells and human fibroblasts and assembled the micro-tissues into a larger complex structure by seeding the micro-tissues into micromoulds [35]. However, this model was used to demonstrate tissue fusion and cell sorting and not for application as a tumour model.

To our knowledge, there exists no system - either manual or automated, to tailor make a well-defined and reproducible complex tumour model based on modular assembly. By applying the principles of bioassembly, a target oncological model could be stripped down to its basic elements and different types of prefabricated modules or subunits can be potentially assembled into one complex biologically relevant assembled cancer construct via a modular assembly based bottom-up approach. As many tissues are composed of repeating functional units, there is a biological basis for using the modular assembly approach [36]. The fabrication of such cancer models may allow higher spatial control of the arrangement of cells/prefabricated modules to be possible. The developed model and complementary automated bioassembly system would be highly beneficial for fabricating large-scale cancer constructs in a high-throughput fashion for cancer research and drug discovery.

The specific aims of this study were to validate the process for automated 3D bioassembly of micro-tissues for biofabrication of an *in vitro* 3D cancer construct and to evaluate the performance of this 3D tumour model compared to existing 2D and 3D drug screening models. This study involved: (i) the fabrication of compact and spherical Ø1 mm cancer micro-tissues that could be handled by the automated bioassembly system, (ii) demonstrating the fabrication of cancer constructs with micro-tissues using the automated tissue bioassembly system without affecting cell viability, (iii) and the investigation and characterization of the response of the engineered cancer construct to an anticancer drug – doxorubicin, compared to commonly adopted 2D and 3D drug screening models.

6.3 Methods

6.3.1 Cell expansion

Experiments were carried out with human breast adenocarcinoma cell lines MCF-7 and MDA-MB-231, human ovarian adenocarcinoma cell-line SKOV3 and normal human foreskin fibroblasts (HFF). SKOV3 and HFF were cultured in media containing DMEM (high glucose, GlutaMAX Supplement, pyruvate) (GIBCO, USA) with 5% foetal bovine serum (FBS; GIBCO, New Zealand), 100 units/mL penicillin (GIBCO, USA) and 100 µg/mL streptomycin (GIBCO, USA). MCF-7 and MDA-MB-231 cells lines were cultured with the above media composition but with 10% foetal bovine serum. The cells were seeded at a density of 3,000 cells/cm^2 in tissue culture flasks (BD Biosciences). Cells were expanded at 37°C in a humidified 5% CO_2/95% air incubator and media changed twice a week.

After approximately 7 days, subconfluent passage cells were washed with phosphate-buffered saline (PBS; GIBCO, USA), detached using 0.25% trypsin/EDTA (Gibco, Canada), counted by trypan blue exclusion in a haemocytometer and plated in a tissue culture flask at 3,000 cells/cm^2. The cells were passaged until there were a sufficient number of cells, after which the cells harvested to form micro-tissues.

6.3.2 Preliminary experiment – high-throughput micro-tissue fabrication

Preliminary experiments to form spherical micro-tissues were conducted. Micro-tissues were cultured using a liquid-overlay technique [37]. SKOV3, MDA-MB-231 and MCF-7 cells lines were seeded at 80,000 cells/well in a 2% agarose (Invitrogen, USA) coated 48-well plate and placed in an incubator at 37°C, 5% of CO_2. During the micro-tissue culture period, the media was changed twice a week and culture until day 7.

None of the different cells types formed satisfactory spherical micro-tissues. Further preliminary experiments were performed with SKOV3s as it formed the most regular compact circular flat spheroid (discoid). SKOV3s were seeded at 80,000 cells/well in a 2% agarose coated 48-well plate with DMEM, 10 ng/ml EGF, 10 ng/ml bFGF, 5 µg/ml Insulin and 0.4% BSA and DMEM and 5% FBS and placed in an incubator at 37°C, 5% of CO_2. The media was similarly changed twice a week and

cultured until day 7. The addition of supplement did not result in satisfactory spherical micro-tissues either.

Finally SKOV3s and HFFs at different percentage co-culture ratios of 100:0, 99:1, 95:5, 90:10, 75:25, 50:50, 25:75 and 0:100 were suspended at 80,000 cells in 500 µL of DMEM with 5% FBS and were pipetted into a 2% agarose coated 48-well plate and placed in an incubator at 37°C, 5% of CO_2. This gave us successful results in forming compact non-discoid spherical micro-tissues.

6.3.3 Cell labelling with fluorescent nanoparticle

A Qtracker cell labelling kit (Life technologies, USA) was used to track cells in a co-culture environment. HFFs were labelled with Qtracker 655 and the SKOV3s with Qtracker 800. To label the cells with Qtracker, cells were concentrated to 10^7 cells/ml by centrifugation at 700g for 5 minutes and resuspended in DMEM. A 10 nM labelling solution was prepared by mixing 1 µL of the Qtracker Component A and 1 µL of the Qtracker Component B in a 1.5 ml microcentrifuge tube and incubated at room temperature for 5 minutes. 0.2 ml of DMEM was added to the mixture and vortexed for 30 seconds. 10^6 cells at a concentration of 10 x 10^6 cells/ml were added to the labelling mixture and incubated for 60 minutes. The cells were subsequently washed twice with media and resuspended in media for use.

6.3.4 Percent co-culture ratio versus sphericity

To determine how spherical micro-tissues of different co-culture ratios of SKOV3 to HFF were, the sphericity of the micro-tissues was determined. The sphericity is a measure of how spherical an object is [38]. Labelled SKOV3 and HFF at different percentage ratio of 100:0, 99:1, 95:5, 90:10, 75:25, 50:50, 25:75 and 0:100 were cultured as described earlier at a seeding density of 80,000 cells/well for 7 days. The micro-tissues were fixed overnight in 10% neutral buffered formalin and imaged using the Zeiss Axioimager Z1 microscope. The major and minor diameters were measured using the image measurement function in ImageJ. The axial measurement function in the microscope was used to measure the height between the centre to the periphery. The micro-tissue was then flipped and the height between the centre to the periphery was measured again. The sum of these

two measured heights was taken to be the diameter of the micro-tissue in the z-axis. Using the approximated equation for sphericity as given by Krumbein [39], the sphericity of the micro-tissues was calculated using Equation 6-1.

$$sphericity = \left(\frac{bc}{a^2}\right)^{\frac{1}{3}} \quad \textbf{6-1}$$

In the equation $a>b>c$, where a was assigned to the major diameter of the micro-tissue, b was the minor diameter and c was the diameter of the micro-tissue in the z-axis. A sphericity value of 1 indicated that theoretically the micro-tissue was a perfect sphere and a value of 0 indicated that the micro-tissue was least spherical.

The Qtracker labelled whole micro-tissues and cryosections were imaged using a Leica TCS SP5 confocal microscope to investigate the distribution of different cell types in the micro-tissues.

6.3.5 Seeding density per well versus micro-tissue size

To determine the relationship between the cell seeding density per well versus the size of the micro-tissue 60,000, 80,000, 100,000, 120,000, 140,000 and 160,000 cells in the chosen percent ratio of 75% SKOV3 and 25% HFF were seeded in a 2% agarose coated 48-well plate. They were cultured for 7 days and the micro-tissues were fixed overnight in 10% neutral buffered formalin and imaged using the Zeiss Axioimager Z1 microscope. The average diameter of each micro-tissue was obtained by taking the average of the measured major and minor diameter using the image measurement function in ImageJ.

6.3.6 Scaffold fabrication

Biodegradable poly(ethylene glycol)-terephthalate-poly(butylene terephthalate) block copolymers (Polyactive 300PEGT55PBT45, PolyVation, The Netherlands) with a PEG molecular weight (MW) of 300 g/mol and a PEGT:PBT weight percent (wt%) ratio of 55:45 were used to fabricate scaffolds with a specific pore size and architecture. The material and composition were selected based on previous studies demonstrating its applicability for 3D plotting and biofabrication techniques [40, 41].

Porous scaffolds (15 × 15 × 1.8 mm), with accurately defined and controlled pore architecture for micro-tissue incorporation, were 3D plotted using a Bioscaffolder system (SYS ENG, Germany). Fibres were oriented in a repeating 0-90°-90°-0° pattern in order to provide porosity in both the x-y and x-z planes for assembly of 1 mm diameter micro-tissues. During the melt dispensing process the following 3D plotting parameters were applied: (i) fibre spacing of 0.7, 0.8 and 0.9 mm in both x and y-direction, (ii) fibre height offset of 0.22 mm, (iii) dispense head and plotting temperature of 200° and 5 bar pressure, (iv) dispense head auger speed of 63 RPM and (v) 25 gauge dispense head nozzle moving at an x-y traverse speed of 500 mm/min.

6.3.7 Assembled cancer construct – fibre spacing

Co-culture micro-tissues seeded at a density of 120,000 cells per well with a percent ratio of 75:25 of SKOV3s and HFFs were cultured for 7 days and then inserted into the pores of a sterile 3D plotted scaffold. 8 micro-tissues were assembled into the scaffold with 4 micro-tissues in each layer of the bilayered scaffold. Constructs with fibre spacing of 0.7, 0.8 and 0.9 mm were assembled. The cancer constructs were cultured for 5 days after assembly. The samples were imaged using the Zeiss Axioimager Z1 microscope and the DNA content was quantified using a CyQUANT kit (Molecular Probes, USA). For the CyQUANT assay, the samples were first digested overnight at 56 ˚C in 500 µL of 1 mg/ml proteinase-K (Sigma-Aldrich, USA) solution. Post proteinase-K digestion, the cells in the sample were lysed and the RNA was degraded by using the provided lysis buffer with RNase A (1.35 KU/ml; Thermofisher, Lithuania) added for an hour at room temperature. Samples were pipetted into 96-well white polypropylene plates (Nunc, Denmark) and GR-dye solution was added. The plate was then incubated at room temperature for 60 minutes and fluorescence was measured (Fluostar Galaxy BMG Labtechnology, Germany). A standard curve was constructed using the λ-DNA provided in the kit.

6.3.8 Reliability of the singularisation device with cancer micro-tissues

To determine the reliability of the singularisation device (see Chapter 4, Figure 4-3) with cancer micro-tissues, cancer micro-tissues formed with a co-culture of 75% SKOV3 and 25% HFF at a seeding density of 80,000 and 120,000 cells per well were put through the device. Preliminary tests showed that micro-tissues formed

with a seeding density of 80,000 could not be handled by the device. So only micro-tissues formed at a seeding density of 120,000 cells per well was selected. The micro-tissues were put into the singularisation device in sets of 10 and repeated 10 times, with the success or failure in singularisation being noted. The total number of successful singularisation cycles was used to determine the overall efficiency of the singularisation system using Equation 6-2.

$$efficiency\ of\ singularisation = \frac{successful\ micro\text{-}tissue\ singularisation}{total\ attempted\ number\ of\ micro\text{-}tissue\ singularisation} \quad \textbf{6-2}$$

6.3.9 Automated bioassembly with cancer micro-tissues

The automated assembly of a construct with cancer micro-tissues was demonstrated by printing a scaffold using the high-temperature print head containing Polyactive 300PEGT55PBT45 and then inserting the co-culture micro-tissues (75% SKOV3s and 25% HFFs) using the micro-tissue injection head. To fabricate our assembled construct a layer-by-layer approach was opted so as to not limit the height of the scaffold that can be constructed using the system. In this scheme, the first layer of the scaffold (6 layers of fibre strands) was 3D plotted (as described earlier) and then 4 micro-tissues were inserted into the pores of the 3D plotted scaffold. The 3D plotting was repeated on top of the first layer to generate the second layer of the scaffold (2 layers of fibre strands) and then 4 more micro-tissues were inserted into the second layer.

The layer-by-layer approach based bilayered scaffold (*n=3*) with 4 live micro-tissues per layer was assembled using our automated tissue assembly system. For the manually assembled scaffold (*n=3*), the whole scaffold was 3D plotted at once and the micro-tissues were inserted manually by hand into pre-plotted scaffolds. The manually assembled constructs were assembled in a similar format to the constructs assembled with the automated system. The manual insertion of the micro-tissues into the pore involved in placing the micro-tissues on top of the scaffold pore with a Pasteur pipette and press-fitting the micro-tissues into the scaffold pore with a spatula. There is a possibility that the shear force experienced during the manual press-fitting process could damage the micro-tissues, however, the modular assembly strategy that we have employed makes this unavoidable.

For the live/dead assay, the samples were incubated at 37°C in 0.5 ml of PBS with 1 µM Calcein AM (Molecular Probes, USA) for 15 minutes, then 1 µM Propidium Iodide (Molecular Probes, USA) was added and incubated for 10 more minutes. After this, the samples were washed twice with PBS and a z-stack of the sample was imaged using the Zeiss Axioimager Z1 microscope (FITC and Texas Red filter-set).

For the AlamarBlue® assay, AlamarBlue® (Invitrogen, USA) was added to the media containing FBS so that the final concentration was 10% (v/v) and the samples were incubated at 37°C for 24 hours. The reduction in AlamarBlue® reagent was calculated colourimetrically using the equations provided by the manufacturer after measuring the absorbance at 570 nm, using 600 nm as a reference wavelength (Fluostar Galaxy BMG Labtechnology, Germany).

6.3.10 Efficiency of cancer micro-tissue insertion

A bilayered scaffold (*n=6*) was 3D plotted with 4 micro-tissues in each layer using the layer-by-layer approach described earlier. The efficiency of micro-tissue insertion (see Chapter 4, Figure 4-4) into the scaffold was determined (Equation 6-3) by the number of successful micro-tissue insertion into the scaffold pore to the total attempted number of micro-tissue insertion with the automated system.

$$efficiency\ of\ micro\text{-}tissue\ insertion = \frac{successful\ micro\text{-}tissue\ insertion}{total\ attempted\ number\ of\ micro\text{-}tissue\ insertion} \quad \textbf{6-3}$$

6.3.11 Chemosensitivity test

To evaluate the tumour models, cells in 2D, micro-tissues and assembled tumour constructs were exposed to varying concentrations of doxorubicin (see Figure 6-1). Doxorubicin was dissolved in DMSO so that the maximum final concentration of DMSO in the media did not exceed 0.5% v/v of DMSO. On day 7 of forming the micro-tissues, cancer constructs were manually assembled and transferred to a 2% agarose coated 24-well plate with 1.2 ml of media per well. SKOV3, HFF and co-culture micro-tissues were transferred to a 2% agarose coated 96-well plate and 150 µl of media per well was added. For the chemosensitivity test

in the 2D model, SKOV3s, HFFs and co-culture (SKOV3:HFF 75:25) cells were seeded onto a 48-well plate at 30,000 cells and 200 µl of media per well. The next day, the samples were treated with different concentrations of doxorubicin – no drug control, 0.001 µM, 0.01 µM, 0.1 µM, 1 µM, 10 µM. Media with 5% FBS containing the specific concentration of drug was changed every 2 days. After 4 days of exposure to the drug, AlamarBlue® assay was conducted to measure metabolic activity of the samples. For the AlamarBlue® assay, AlamarBlue® (Invitrogen, USA) was added to the media containing FBS so that the final concentration was 10% (v/v). After which the micro-tissues and assembled constructs was incubated for 20 hours and the cells in 2D were incubated for 3.5 hours at 37°C. Fluorometric measurements were made at an excitation wavelength of 545 nm and an emission wavelength of 590 nm and these values were curve fitted to estimate the half maximal inhibitory concentration (IC_{50}) using GraphPad Prism v.6.0. The samples from the chemosensitivity test were also quantified for DNA content. The DNA was purified by ethanol precipitation as described earlier [42] for the assembled constructs but not for the micro-tissues. The purification was performed as the AlamarBlue® used to measure the metabolic activity stained the scaffold fibres, leached out during the DNA isolation process and interfered with the CYQUANT assay.

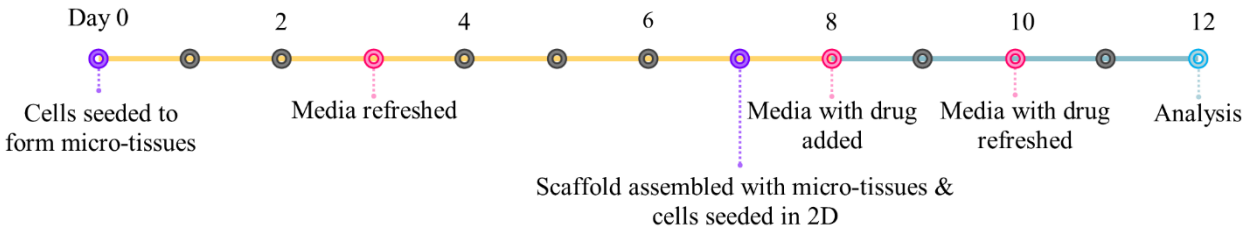

Figure 6-1. Timeline of chemosensitivity test.

6.3.12 Histology and immunofluorescence

After the AlamarBlue® assay, the micro-tissues and cancer constructs from the chemosensitivity tests were fixed in 10% neutral buffered formalin for an hour, washed in PBS, immersed for an hour in 15% (w/v) sucrose in PBS and then immersed overnight in 30% (w/v) sucrose in PBS at 4˚C. The samples were then embedded in OCT and were cryo-sectioned (15 µm thick sections). The slides with the sections were rinsed in cold PBS thoroughly and were permeabilized with 0.25% (v/v) Triton X-100 in PBS for 30 minutes. The sections were rinsed in cold PBS and were exposed to 5% (w/v) BSA in PBS at pH 7.4 for 60 minutes at room temperature.

They were then rinsed with cold PBS and incubated with monoclonal anti-Ki67 (1:100 dilution: abcam, USA) and polyclonal anti-gamma H2AX (1:5,000 dilution: abcam, USA) anti-bodies at 4˚C overnight. The sections were washed in PBS and were incubated with secondary antibodies, goat Alexa Fluor 488 anti-mouse (1:500 dilution: Thermofisher, USA) and goat Alexa Fluor 555 anti-rabbit (1:500 dilution: abcam, USA) at 37˚C for an hour. Following further washing, the sections were counterstained with 4.5 μM Hoechst 33342 in PBS. Finally, the slides were washed with 0.05% (v/v) Tween-20 in cold PBS, rinsed in PBS and then coverslipped. The samples were imaged using a Leica TCS SP5 confocal microscope.

6.3.13 Statistical analysis

Data was presented graphically as mean ± standard deviation. Data were analysed using GraphPad Prism v.6.0. Statistical analysis was performed using 1-way ANOVA or 2-way ANOVA (if required Tukey's multiple comparisons test) or paired t-test, with $p<0.05$ set as a criterion for statistical significance.

6.4 Results

6.4.1 High-throughput fabrication of compact micro-tissues of regular spherical size and shape

The efficient and reliable working of the automated bioassembly system as discussed and shown in Chapter 4 requires compact spherical micro-tissues with a diameter of 1 mm. This subsection describes the results to fabricate cancer micro-tissues with the desired requirements.

6.4.1.1 Preliminary experiment – effect of single cell source on micro-tissue spheroid fabrication

MCF-7, MDA-MB-231 and SKOV3 cell-lines were cultured for 7 days in our attempt to form compact spherical micro-tissues. These cell-lines were selected based on the prior experience we have of working with them, their availability in our laboratory and our intention of engineering a tumour construct. MCF-7 formed a delicate loose aggregate (Figure 6-2 a), MDA-MB-231 formed a slightly denser irregular micro-tissue of no particular shape (Figure 6-2 b) and SKOV3 formed a compact discoid shaped micro-tissue (Figure 6-2 c).

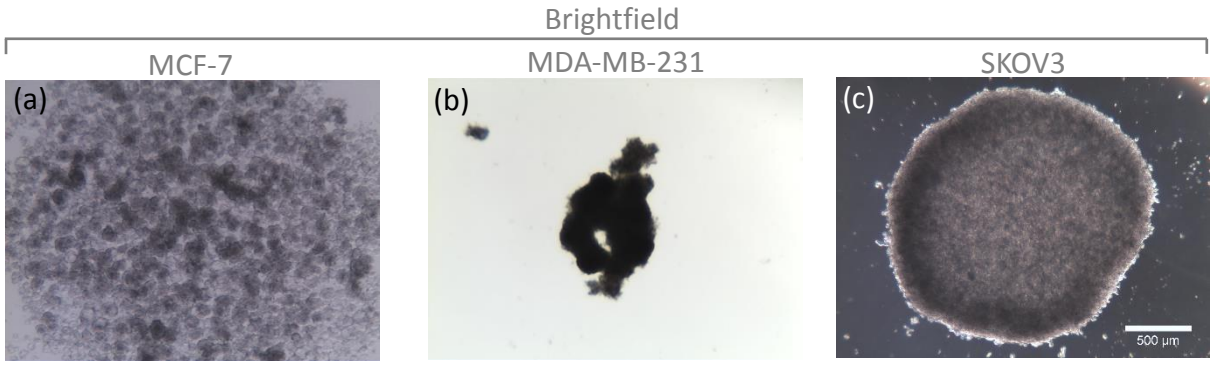

Figure 6-2. Brightfield images of (a) MDA-MB-231, (b) MCF-7 and (c) SKOV3 micro-tissues on day 7 at 80,000 cells/well. *Scale bar = 500 µm for all images.*

As the discoid shaped SKOV3 spheroids were not spherical and compact, it would not be able to be handled by the automated tissue assembly system. So further attempts were made to form spherical micro-tissues by culturing SKOV3s in media supplemented with EGF, bFGF, Insulin and BSA for 7 days (Figure 6-3 b) which still resulted in a discoid shaped micro-tissue.

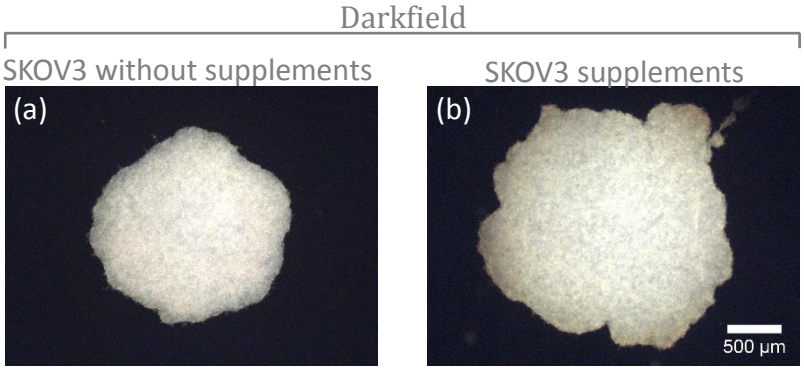

Figure 6-3. Darkfield images of (d) SKOV3 without supplements (e) SKOV3 supplemented with EGF, bFGF, Insulin and BSA on day 7 at 80,000 cells/well. *Scale bar = 500 µm for all images.*

Cadherins play an important role in micro-tissues formation and fibroblasts are known to express multiple types of cadherin [21, 43]. Moreover, fibroblasts are known to produce and maintain extracellular matrix (ECM) by which they are interconnected [44]. Therefore, we investigated the co-culture of SKOV3s with human foreskin fibroblasts (HFFs) and this led to the successful formation of a more spherical shaped compact micro-tissue (Figure 6-4 c) compared to a discoid shaped micro-tissues formed from the SKOV3 monoculture. Apart from aiding the formation of compact spherical micro-tissues, the addition of fibroblasts to the 3D model is

valuable. Fibroblasts are one of the cellular components that make up tumours. They are known to have an important role in the progression, growth and spread of cancers and are associated with cancer cells in all stages of progression [45, 46]. The co-culture micro-tissue was investigated further for application with the automated tissue assembly system.

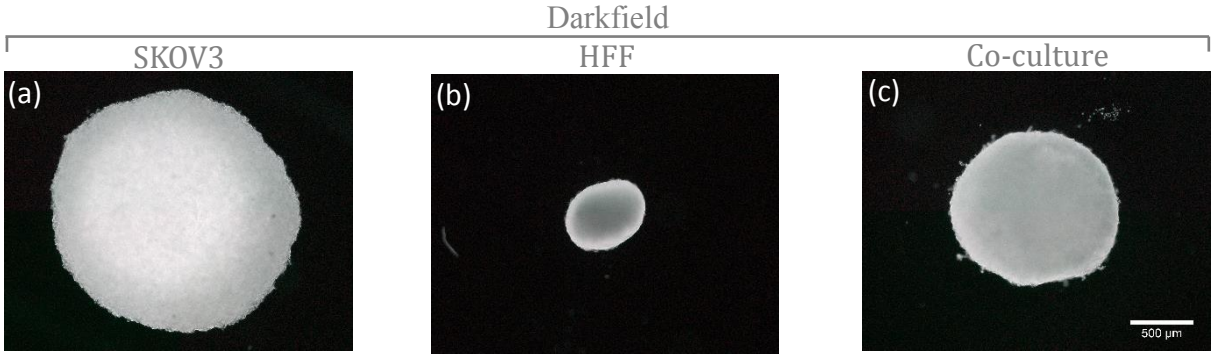

Figure 6-4. Darkfield images of (a) SKOV3 (b) HFF and (c) co-culture (SKOV3:HFF 75:25) micro-tissues on day 7 at 80,000 cells/well. *Scale bar = 500 µm for all images.*

6.4.1.2 Effect of cell co-culture ratio on micro-tissue sphericity

The sphericity of the micro-tissue is important for the reliable functioning of the automated tissue bioassembly system. A spherical-shaped micro-tissue can easily move and be fluidically manipulated through the cylindrically shaped ports and tubes of the automated bioassembly system compared to a non-spherical shaped micro-tissue. Moreover, it was essential that the micro-tissues are compact so that they can withstand the fluidic forces while being handed by the fluidic tissue bioassembly system and that the micro-tissues do not end up falling apart or being dispersed. For the sphericity, a value closer to 1 indicates that theoretically, the micro-tissue is more spherical. Micro-tissues formed with percentage ratios of 100:0 (0.47 ± 0.01), 99:1 (0.49 ± 0.02), 95:5 (0.49 ± 0.02), 90:10 (0.55 ± 0.08) of SKOV3 to HFF were more disc-shaped and there was no significant difference ($p>0.05$) (Figure 6-5) in sphericity between them. However, with the percentage of HFF equal to 25% or more, the micro-tissues were more spherical in shape. The sphericity was significantly different ($p<0.05$) between micro-tissue ratios of 90:10 (0.55 ± 0.08) and 75:25 (0.71 ± 0.02), and 75:25 (0.71 ± 0.02) and 50:50 (0.82 ± 0.05). There was no significant difference ($p>0.05$) in sphericity between micro-tissues with a percentage ratios of 50:50 (0.82 ± 0.05), 25:75 (0.78± 0.01) and 100:0 (0.80 ± 0.06) of SKOV3 to HFFs. A ratio of 75:25 of SKOV3 to HFF was selected for the remaining experiments as it was the ratio that contained the lowest proportion of HFFs that

resulted in micro-tissues spherical enough to be handled by the automated tissue bioassembly system.

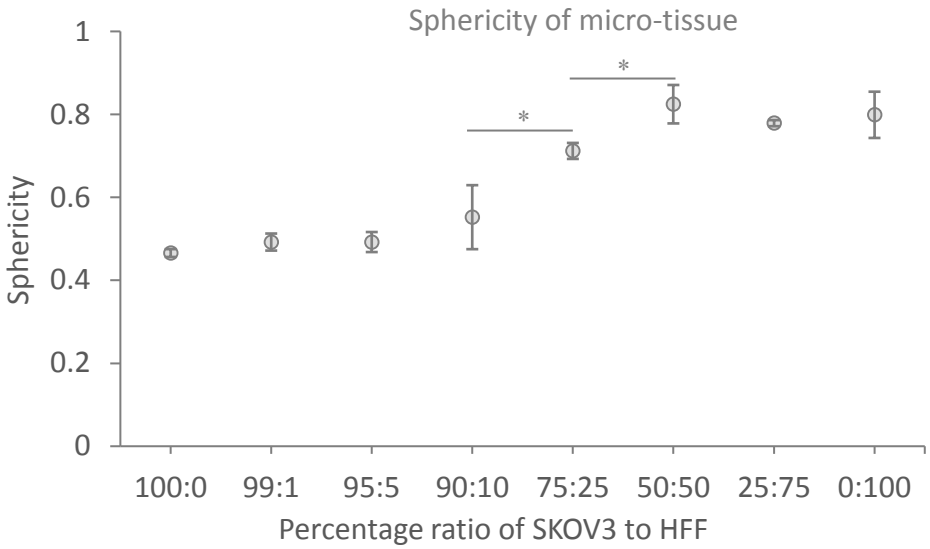

Figure 6-5. Sphericity of micro-tissues for different percentage ratios of SKOV3 to HFF (*n=4*). **Significant difference (p<0.05) between neighbouring values. Statistical analysis: 1-way ANOVA.*

6.4.1.3 Effect of cell seeding density on micro-tissue spheroid size

The automated bioassembly system was designed for the reliable handling of micro-tissues with a diameter of 1 mm (deviation from the designed size could cause blockage or improper functioning of the system). Therefore, it was necessary that the fabricated micro-tissues have a diameter around 1 mm. Increasing the cell seeding density increased the average diameter of the co-culture micro-tissues. There was no significant difference (*p>0.05*) (Figure 6-6) in average diameter for micro-tissues formed with a seeding density of 100,000 (0.97 ± 0.03 mm) and 120,000 (0.99 ± 0.02 mm), 120,000 and 140,000 (1.04 ± 0.02 mm), and 140,000 and 160,000 (1.06 ± 0.04 mm) cells per well. All other conditions were significantly different (*p<0.05*). A cell seeding density of 120,000 (0.99 ± 0.02 mm) cells per well was chosen for the remaining experiments as it produced micro-tissues with an average diameter closest to 1 mm and could be handled by the automated tissue bioassembly system.

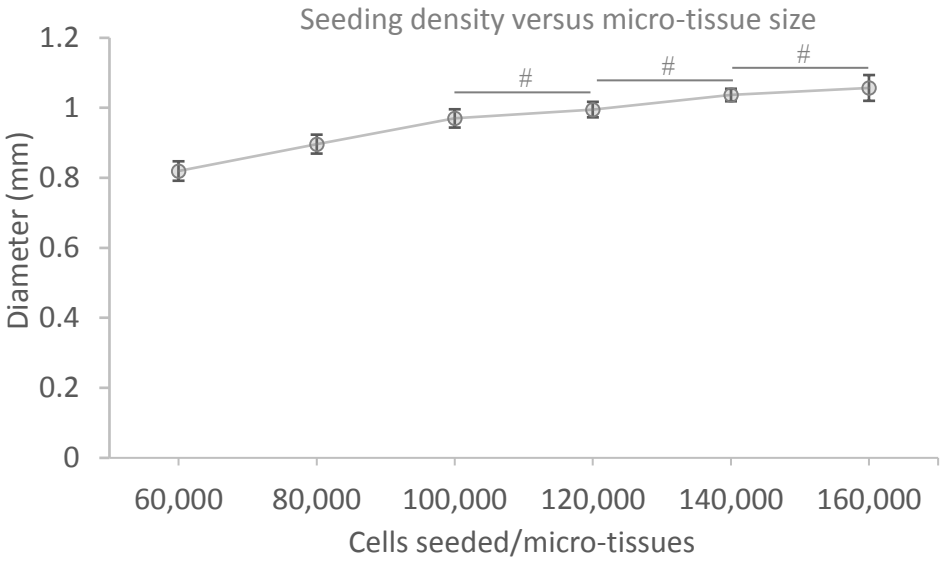

Figure 6-6. Cell seeding density versus micro-tissues size on Day 7 for co-culture micro-tissues (SKOV3:HFF 75:25). *# No significant difference (p>0.05) between neighbouring values. Statistical analysis: 1-way ANOVA.*

6.4.1.4 Cell distribution in co-cultured micro-tissues

The SKOV3 and HFF cells were labelled with Qtracker 800 and 655 respectively and micro-tissue were fabricated with the labelled cells. Figure 6-7 displays the whole and sectioned fluorescence microscope images of the monoculture and co-culture (SKOV3:HFF 75:25) micro-tissues cultured for 7 days. The distribution of the two cell types in the co-culture micro-tissues are not homogenous and there is a clear rearrangement of cells that can be visualized (Figure 6-7 g). The micro-tissue contains a core predominantly containing HFFs and a periphery predominately with SKOV3s. Although the cell seeding density in all the micro-tissues were the same, the monoculture SKOV3 micro-tissue (Figure 6-7 a, b, c and d) formed a discoid with a larger diameter, the monoculture HFF micro-tissue (Figure 6-7 i, j, k and l) was compact and spherical with a smaller diameter and the co-culture micro-tissue was in between the two (Figure 6-7 e, f, g and h).

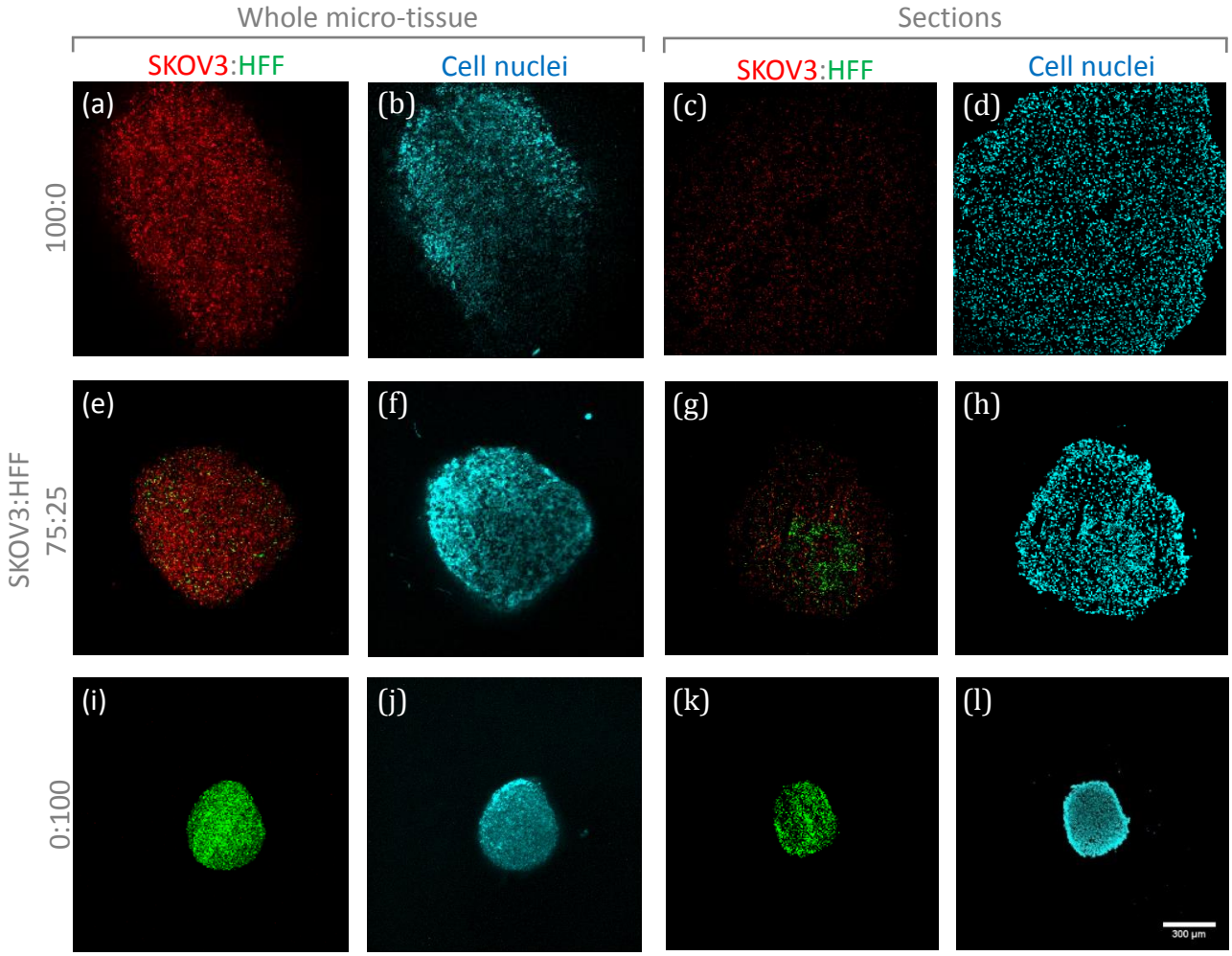

Figure 6-7. Fluorescence microscope images of whole micro-tissues and micro-tissue sections with SKOV3 (Qtracker 800, red) and HFF (Qtracker 655, green), and Hoechst 33342 (cell, nuclei blue). The ratio of SKOV3 to HFF are in rows. See Figure 6.A-i, Appendix 6.A for other co-culture ratios. *Scale bar = 300 µm for all images.*

6.4.2 Cancer construct bioassembly

After successful fabrication of the desired compact spherical micro-tissue of 1 mm diameter, we scrutinized the ability of the prototype automated bioassembly system to handle the cancer micro-tissues and validated the bioassembly of a cancer construct with the automated tissue bioassembly system.

6.4.2.1 Assembled cancer construct – effect of fibre spacing

A perfect fit of the micro-tissue within the scaffold pore was required so that the micro-tissues were not displaced out of the scaffold or that there were no gaps in the assembled construct when cultured over time. Therefore, the optimal fibre spacing for the 3D plotted scaffold for a Ø1 mm cancer micro-tissue was determined. After 5 days of culture of the assembled cancer construct, the darkfield images (Figure 6-8) showed that the assembled construct with a fibre spacing of 0.7 mm

(Figure 6-8 a) was substantially full and intact but the 0.8 (Figure 6-8 b) and 0.9 mm (Figure 6-8 c) constructs had pockets of space. The quantified DNA (Figure 6-9) did not show any significant difference (*p>0.05*) between constructs of different fibre spacing (0.7 mm - 12.27 ± 0.48 µg, 0.8 mm - 13.82 ± 2.41 µg, 0.9 mm - 13.16 ± 0.51 µg). This suggests that the proliferation and attrition rate was constant across all fibre spacing. Based on these observations, scaffolds with a fibre spacing of 0.7 mm was selected for all further experiments.

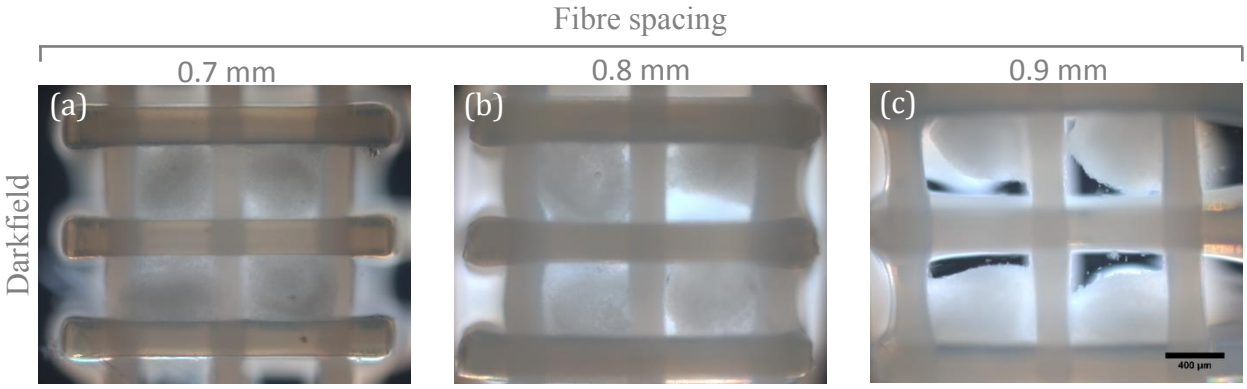

Figure 6-8. Darkfield images imaged after 5 days of culture of assembled cancer constructs with fibre spacing of (a) 0.7, (b) 0.8 and (c) 0.9 mm. *Scale bar = 400 µm for all images.*

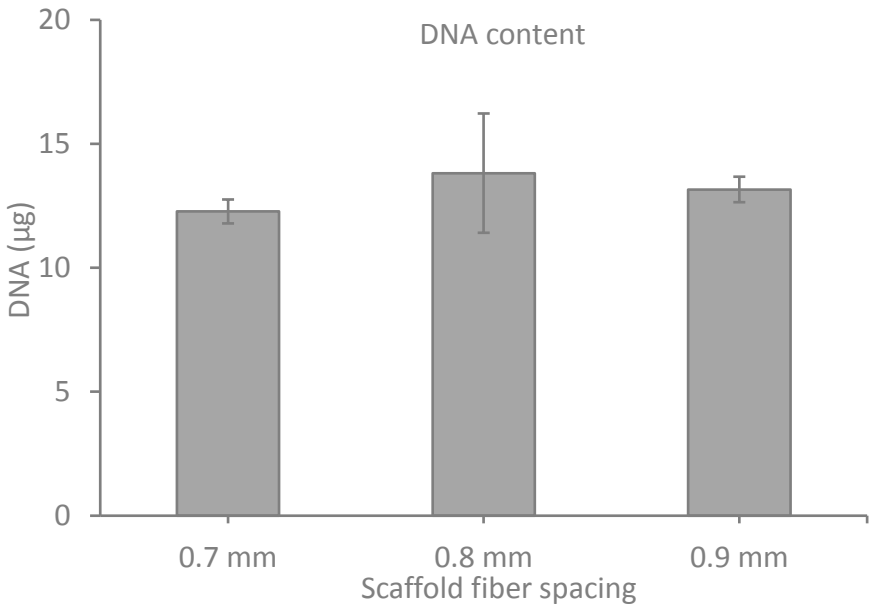

Figure 6-9. DNA content (each scaffold containing 8 micro-tissues) after 5 days of culture for assembled cancer constructs with fibre spacing of (a) 0.7, (b) 0.8 and (c) 0.9 mm. *No significant difference (p>0.05). Statistical analysis: 1-way ANOVA.*

6.4.2.2 Reliability and efficiency of the singularisation device with cancer micro-tissues

The efficiency of singularisation for the co-culture cancer micro-tissues was determined to be 97 ± 4.83%. During the experiment, the reasons for singularisation failures included either the release of 2 micro-tissues at a time or due to the micro-tissues being sucked into the vacuum pressure port. The singularisation failures that occurred were not critical and did not cause the failure of the device. In the event of a failure, either the singularisation cycle can be repeated if the device has failed to release a micro-tissue or in the case of a blockage the device can be purged with fluid so as to dislodge the blocking micro-tissue and clear the bioassembly system after which normal working can be resumed.

6.4.2.3 Efficiency of cancer micro-tissue insertion

The efficiency of successful micro-tissue insertion into the scaffold for the first layer (bottom) was 87.5 ± 13.69% and for the second layer (top) was 33.33 ± 25.81%. The total efficiency was found to be 60.42 ± 12.29% (*n=6* scaffolds, 8 micro-tissues per scaffold). The smaller fibre spacing (0.7 mm) together with fewer fibre layers could have made it harder for the automated system to insert the second layer of cancer micro-tissues into the scaffold. Nevertheless, the scaffolds were visually examined by the user for missed micro-tissues insertions at the end of the assembly process for each layer, and the micro-tissue insertion process was repeated for pores without micro-tissues and the scaffold was completely assembled as intended.

6.4.2.4 Cell viability of bioassembled cancer constructs

During the 3D plotting process, the temperature in the high-temperature print head was approximately 200°C. Although the extruded material cools down rapidly during the layer-by-layer plotting, we had to ascertain that the molten polymer being plotted on the micro-tissues did not affect the viability of the micro-tissues and also that the handling of the micro-tissues by the automated bioassembly system did not affect the viability of the micro-tissues.

To ascertain that the micro-tissues were not affected by the automated bioassembly process, cancer constructs were assembled automatically using the assembly system and compared with manually assembled constructs (the micro-

tissues were press-fitted by hand into a 3D plotted scaffold). The visual inspection of the live/dead fluorescence microscopy images (Figure 6-10) of the manually assembled scaffold and the construct assembled using the assembly system showed no obvious differences. This result was further validated with the AlamarBlue® assay (Figure 6-11). There was no significant difference ($p>0.05$) in the percentage of AlamarBlue® reduced by the manually assembled construct (92.75 ± 6.89%) and the construct assembled using the automated assembly system (82.08 ± 3.78%).

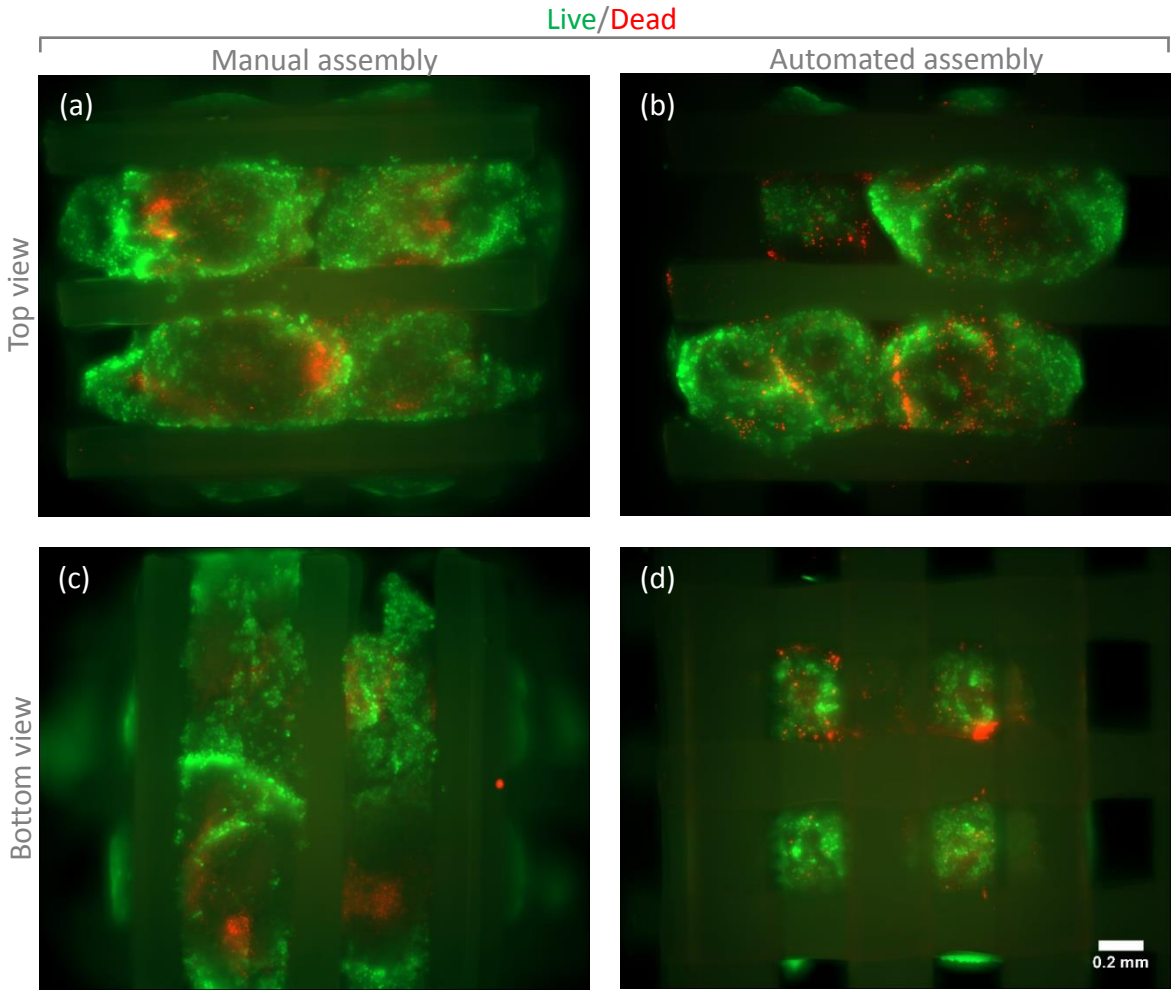

Figure 6-10. Fluorescence microscopy images of a manually assembled construct (a) top view and (b) bottom view and (c) top view and (d) bottom view of a construct assembled using the automated assembly system assembled with cancer micro-tissues stained with Calcein AM (live cells, green) and Propidium Iodide (dead cells, red). *Scale bar = 0.2 mm for all images.*

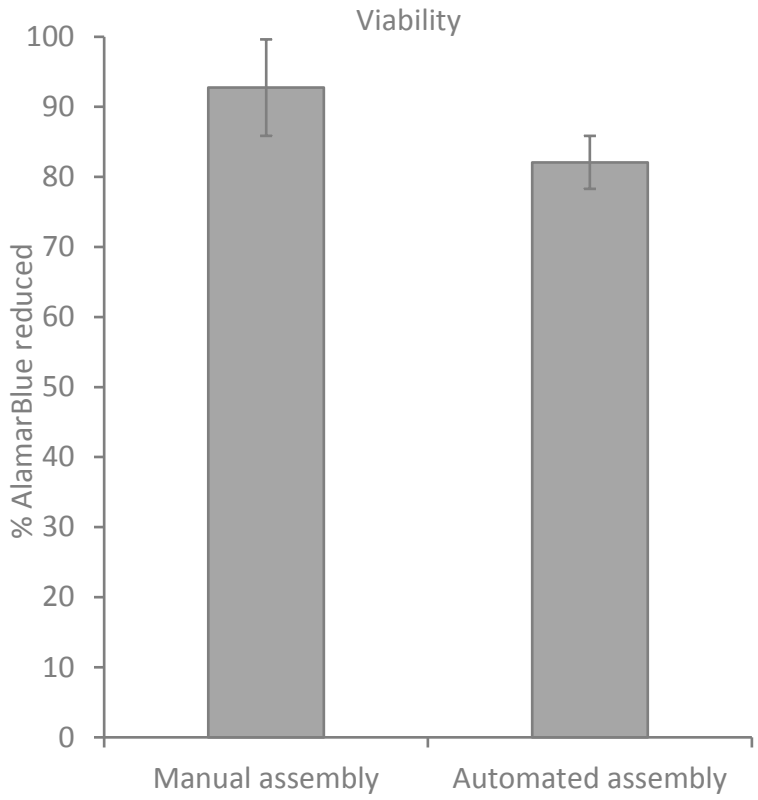

Figure 6-11. Percentage of AlamarBlue® reduced to determine the viability of the manually assembled construct and the construct assembled using the automated system with cancer micro-tissues. The data is presented as mean ± SD (*n=3*). *No significant difference (p>0.05). Statistical analysis: 1-way ANOVA.*

6.4.3 Drug response

After successful fabrication of the desired micro-tissue and bioassembly of the tumour construct, the response of the engineered cancer constructs was further assessed with a chemotherapeutic drug - doxorubicin. Doxorubicin is a clinically relevant anticancer drug often used in combination chemotherapy to treat a range of tumours including ovarian cancer [47-49]. Therefore, doxorubicin was adopted as a model anticancer drug for evaluating the chemosensitivity in the 2D and 3D cancer models. Doxorubicin works by preferentially killing dividing or cycling cells [50]. The drug response was evaluated only for the co-culture assembled constructs as (described earlier) it was not possible to form compact and spherical SKOV3 micro-tissues for assembly into a construct.

6.4.3.1 Chemosensitivity test

Chemosensitivity to doxorubicin was determined *in vitro* for cells in 2D, individual 3D micro-tissues and assembled 3D cancer construct following a 4-day

exposure, and their dose-response curves were plotted in Figure 6-12. The accurate IC_{50} estimation requires a sufficient number of values in the upper and lower plateau regions of the dose-response curves [51]. A maximum drug concentration value of 10 μM was selected for the experiment based on the previously reported value of 3.75 μM for the peak concentration of free doxorubicin available to act on the cells in clinical chemotherapy [52]. However, the dose-response curves (Figure 6-12 b) of the micro-tissues (especially the HFF micro-tissues) and assembled constructs did not achieve a lower plateau region unlike the cells in 2D (Figure 6-12 a) making the IC_{50} estimates less accurate. Nevertheless, the IC_{50} estimates based on the available dose-response curves were used to evaluate the models. A significant increase ($p<0.05$) in the percentage of cell viability was observed in the HFF micro-tissues with increasing drug concentration from 0.1 μM (106.04 ± 14.82%) to 1 μM (126.30 ± 12.90%). It has been previously shown that the treatment of fibroblasts with doxorubicin can cause a decrease in the production of procollagen which is a precursor of the extracellular matrix protein collagen [53]. The decreased production of procollagen with increasing drug concentration could potentially result in better diffusion of nutrients, drug, and also AlamarBlue® which was used to measure the metabolic activity. This increased diffusion could have resulted in the observed higher percentage of growth control from 0.1 to 1 μM concentration of drug seen in the HFF micro-tissues [54, 55].

The estimated IC_{50} values were higher for the individual 3D micro-tissue (SKOV3 - 0.17 μM, HFF - 7.05 μM, co-culture - 0.33 μM) and assembled 3D tumour construct (co-culture - 1.19 μM) respectively compared to cells in 2D (SKOV3 - 0.05 μM, HFF - 0.05 μM, co-culture - 0.08 μM) (Figure 6-12 and Table 6-1). The differences in the IC_{50} values observed in cells in 2D versus 3D micro-tissues depended on the cell type. For the SKOV3s and the co-culture there was a 3-4 fold increase, but for the HFFs there was a 45 fold increase in IC_{50} values between cells in 2D and 3D micro-tissues. The higher drug resistance of the individual 3D micro-tissue models compared to the cells in 2D shows the need for testing candidate drugs on 3D models which are more analogous to tissues *in vivo*. Moreover, the cell-dependent response emphasizes the importance of complex co-culture 3D models. A 15 fold increase between cells in 2D and the assembled construct and a 4 fold increase in IC_{50} value between individual co-cultured micro-tissue and the assembled construct was also

observed. This higher drug resistance of the assembled constructs compared to co-culture micro-tissues highlights the significance of a larger more complex assembled construct model compared to a smaller micro-tissue model. It also suggests that the assembled construct model could potentially be a more efficient and reliable drug screening model.

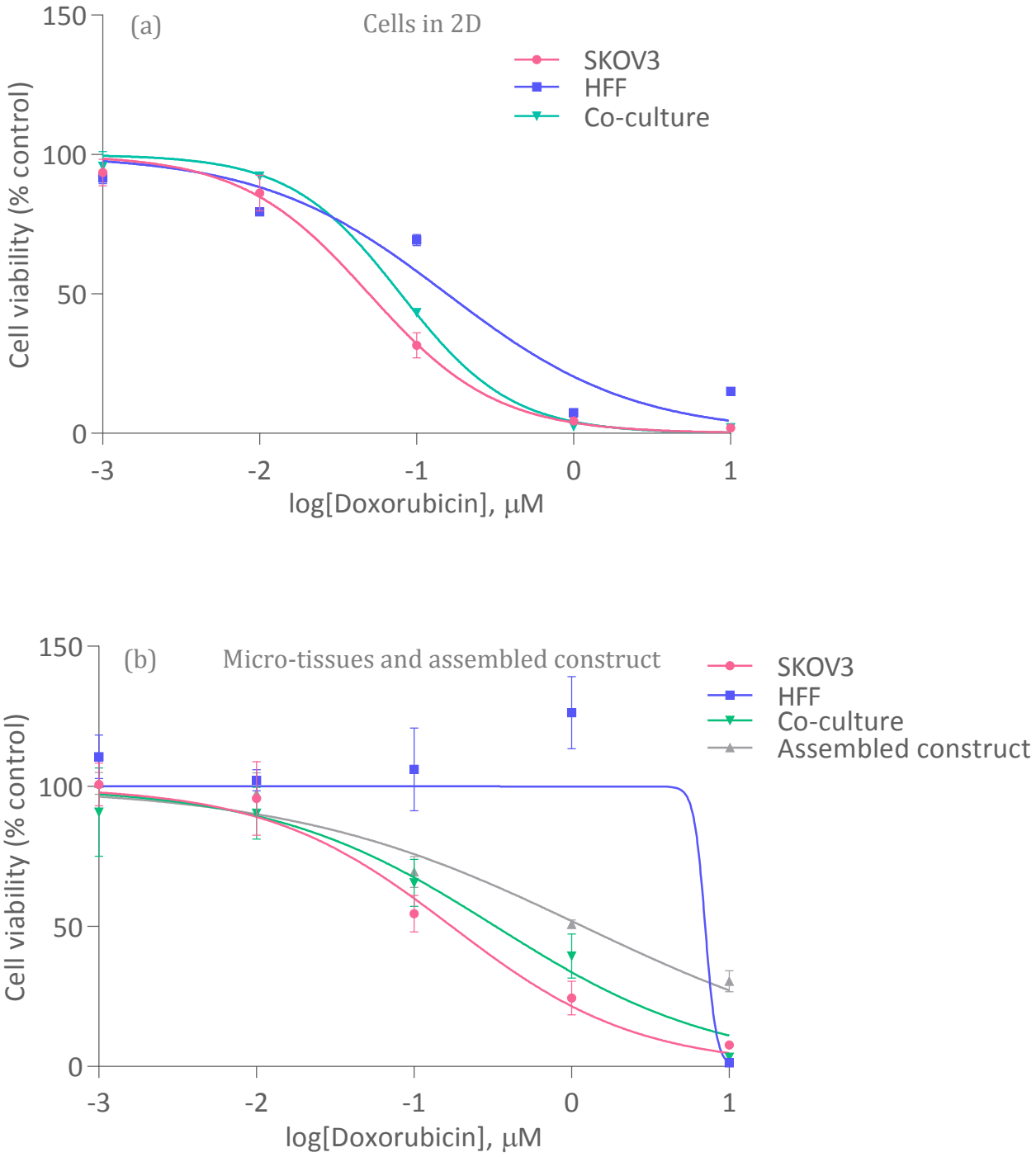

Figure 6-12. Dose-response curves for doxorubicin for (a) cells in a 2D (b) micro-tissues and assembled construct. The response of SKOV3s, HFF, and co-culture cells were measured after 4 days of exposure to the drug. (*n=4*)

Table 6-1. Chemosensitivity of doxorubicin.

Cells	IC_{50} (μM)			Fold change in IC_{50}		
	2D	Micro-tissue	Assembled construct	Micro-tissue/ 2D	Assembled construct/ micro-tissue	Assembled construct/ 2D
SKOV3	0.05	0.17		3.48		
HFF	0.16	7.05		45.05		
Co-culture	0.08	0.33	1.19	4.17	3.59	14.97

[a] Data obtained from Figure 6-12.

The DNA content expressed in percentage of control against drug concentration for the micro-tissues and assembled construct is shown in Figure 6-13. The DNA content of SKOV3 and co-culture micro-tissues reflected their dose-response curve (Figure 6-12 b) and showed a similar trend of decrease in DNA content with increasing concentration of the drug. The normalised DNA content in the SKOV3 micro-tissues decreased significantly ($p<0.05$) from 0.01 (107.89 ± 0.57%) to 0.1 μM (74.84 ± 0.57%) and from 0.1 (74.84 ± 0.57%) to 1 μM (19.88 ± 23.74%). In the co-culture micro-tissues, a significant decrease ($p<0.05$) in normalised DNA content was observed from 0.1 (81.77 ± 1.92%) to 1 (43.24 ± 1.15%) μM and from 1 (43.24 ± 1.15%) to 10 μM (0.00 ± 0.45%). In the HFF micro-tissues the significant decrease ($p<0.05$) in normalised DNA content was only observed from 1 (83.81 ± 4.94%) to 10 μM (0.00 ± 2.19%) of drug concentration. Whereas the dose-response (Figure 6-12 b) of HFF micro-tissues increased with increasing drug concentration, peaked at 1 μM of drug and steeply fell at 10 μM. The significant decrease in normalised DNA content was observed at lower drug concentrations in the SKOV3 micro-tissues (0.01 – 0.1 μM) compared to the co-culture micro-tissues (0.1 - 1 μM) and at a higher drug concentration in the HFF micro-tissues (1 μM). The normalised DNA content for the assembled construct decreased from 0.01 (118.31 ± 9.35%) to 0.1 μM (77.59 ± 26.48%) and from 1 (55.08 ± 9.93%) to 10 μM (0.00 ± 2.22%). This decrease in normalised DNA content is consistent with the darkfield microscopy images (Figure 6-14) of the assembled construct which revealed that at higher concentration of drug there was an atrophy of the tissue present in the construct. The tissue atrophy was especially noticeable at 1 μM concentration (Figure 6-14 e) of the drug and at 10 μM (Figure 6-14 f) there was almost no tissue present within the construct. The larger error bars observed in

the assembled construct could be due to the ethanol precipitation method used to purify DNA in which the yield of purified DNA can vary resulting variability in among the samples. At 1 µM of drug concentration, there was a significant difference (*p<0.05*) in normalised DNA content between all the 3D models apart from the difference between the 3D assembled constructs and co-culture 3D microspheres (SKOV3 – 19.88 ± 23.74%, HFF – 83.81 ± 4.94%, co-culture – 43.24 ± 1.15%, and assembled construct – 55.08 ± 9.93%).

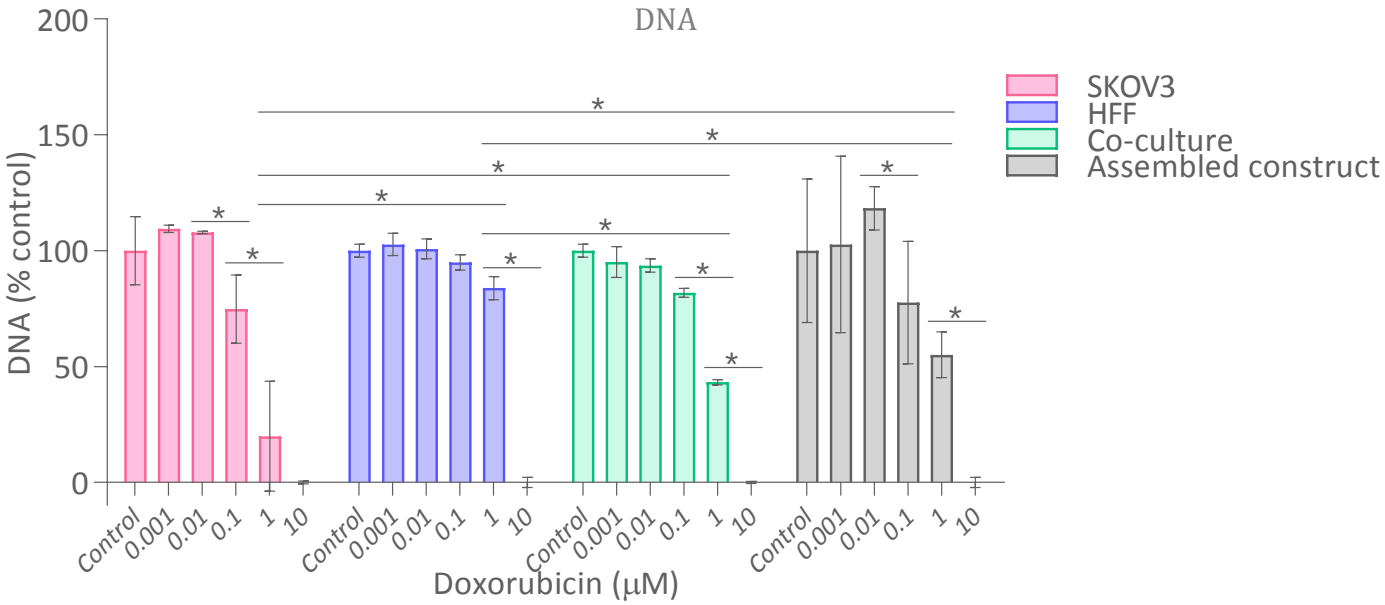

Figure 6-13. Doxorubicin dose dependent DNA content normalised to control and expressed in percentage of control for SKOV3, HFF and co-culture micro-tissues and assembled construct with co-culture micro-tissues measured after 4 days of exposure to the drug. The data is presented as mean ± SD (*n=4*). **Significant differences between columns are below the ends of each line (p<0.05). Statistical analysis: 2-way ANOVA.*

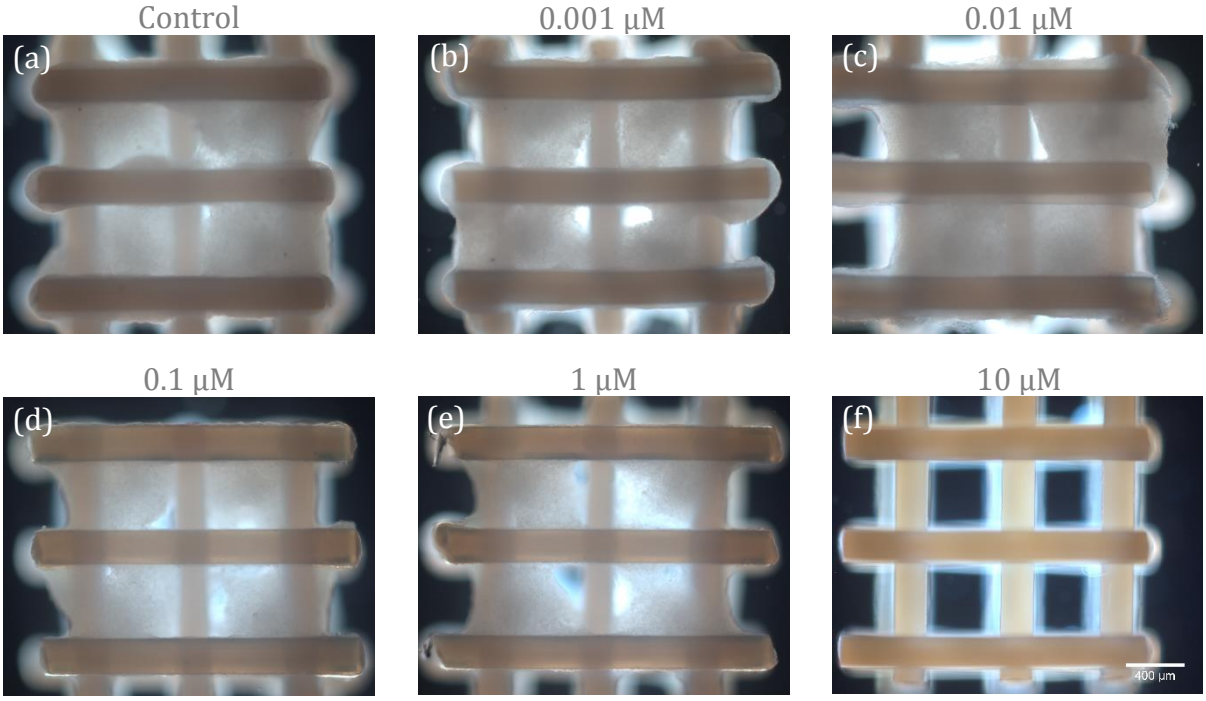

Figure 6-14. Darkfield images of the assembled cancer construct imaged after 4 days of exposure to anticancer drug. (a) control, (b) 0.001, (c) 0.01, (d) 0.1, (e) 1 and (f) 10 µM of doxorubicin. *Scale bar = 400 µm for all images.*

6.4.3.2 Histology and immunofluorescence

Immunofluorescence staining for Ki67, γ-H2AX and Hoechst 33342 on cryosections of SKOV3, HFF, co-culture micro-tissues is shown in Figure 6-15 and for assembled cancer constructs in Figure 6-17 respectively. Ki67 protein is a proliferation nuclear marker that is required for maintaining cell proliferation and is present in all active phases of the cell cycle apart from G_0 phase or the quiescent state [56, 57]. In SKOV3 micro-tissues, the expression of Ki67 was observed mostly at the periphery of the micro-tissues (Figure 6-15 f-j). In the co-cultured micro-tissues (Figure 6-15 aj-an), Ki67 expression was also observed mostly at the periphery. The fluorescence staining observed in the core (Figure 6-15 aj-an and Figure 6-17 c and d) was due to autofluorescence of the HFF core and disappears at a higher magnification (see Figure 6-16 f and h). However, limited Ki67 expression was observed in HFFs (Figure 6-15 u-y). The cells in the cancer constructs (Figure 6-17 c and d) expressed Ki67 suggesting the presence of proliferating cells and – as in the case of the co-culture micro-tissues – the fluorescence staining observed in the core of the assembled construct was due to autofluorescence of the HFF core.

Doxorubicin causes double-strand breaks in DNA which correlates with the cytotoxicity of the drug [58]. Double-strand breaks in DNA can be visualised by the formation of γ-H2AX which is a precise and a highly amplified response [59, 60]. In SKOV3 micro-tissues, the expression of γ-H2AX observed in control (Figure 6-15 k) and 0.001 μM (Figure 6-15 l) concentration of the doxorubicin was very low but present. At 0.01 μM (Figure 6-15 m) concentration of the drug, the expression of γ-H2AX observed was high and towards the periphery of the micro-tissue. At 0.1 (Figure 6-15 n) and 1 μM (Figure 6-15 o) concentration of the drug, lower expression of γ-H2AX compared to 0.01 μM (Figure 6-15 m) was observed. This reduction in γ-H2AX visualisation at 0.1 and 1 μM compared to 0.01 μM drug concentration in the SKOV3 micro-tissues could be due to the lower cell number and density as seen from the Hoechst staining (Figure 6-15 c, d and e). The higher expression of DNA damage marker that we observed in the SKOV3 micro-tissues correlated with the higher proportion of proliferating cells, earlier significant decrease (at 0.01 μM) in normalised DNA content and lowest IC_{50} value (0.17 μM) among the 3D models. In HFF micro-tissues, expression of γ-H2AX was only observed at 1 μM (Figure 6-15 ad) concentration of the drug and the expression of γ-H2AX observed was very low. The lower DNA damage observed in the HFF micro-tissues correlated with a lower proportion of proliferating cells, a later significant decrease (at 1 μM) in normalized DNA content and the highest IC_{50} value (7.05 μM) among the 3D models. In the co-culture micro-tissues, expression of γ-H2AX was low in the control (Figure 6-15 ao), 0.001 (Figure 6-15 ap) and 0.01 μM (Figure 6-15 aq) concentration of doxorubicin. The expression of γ-H2AX observed (Figure 6-15 ao-as) was more toward the periphery of the micro-tissue where the distribution of SKOV3 cells are higher (from the Qtracker labelling of the cells – Figure 6-15 at-ax). At 0.1 μM (Figure 6-15 ar) concentration of the drug, the expression of γ-H2AX observed was higher, and the expression of γ-H2AX was highest at 1 μM (Figure 6-15 as). Even at 1 μM of doxorubicin, the expression of γ-H2AX observed was more toward the periphery of the micro-tissue (Figure 6-16 k) whereas in the SKOV3 (Figure 6-16 o) micro-tissue it was distributed throughout. In the assembled cancer construct, the γ-H2AX expression observed at 1 μM (Figure 6-17 f) concentration of drug was higher than the control (Figure 6-17 e) and the expression was higher at the periphery of the assembled construct itself. The co-culture micro-tissues and assembled constructs displayed a DNA damage response in between the SKOV3 and HFF micro-tissues and

this correlated with the median level in the proportion of proliferating cells and IC_{50} values (co-culture micro-tissues - 0.33 μM and assembled construct - 1.19 μM). The increased drug resistance of the assembled construct compared to the co-culture micro-tissues could be due to the larger size of the construct resulting in the reduced drug, oxygen and nutrient concentration [23, 61].

It has been suggested that the uptake of doxorubicin is significantly reduced in larger micro-tissues [23]. The decreased penetration of the drug along with the higher nutrient constraint and lower proliferation would have a protective effect on the cancer construct from the drug. This situation is comparable to an *in vivo* environment where due to deficient or abnormal vascularisation in a tumour, there is a concentration gradient of oxygen, nutrients and drug [61].

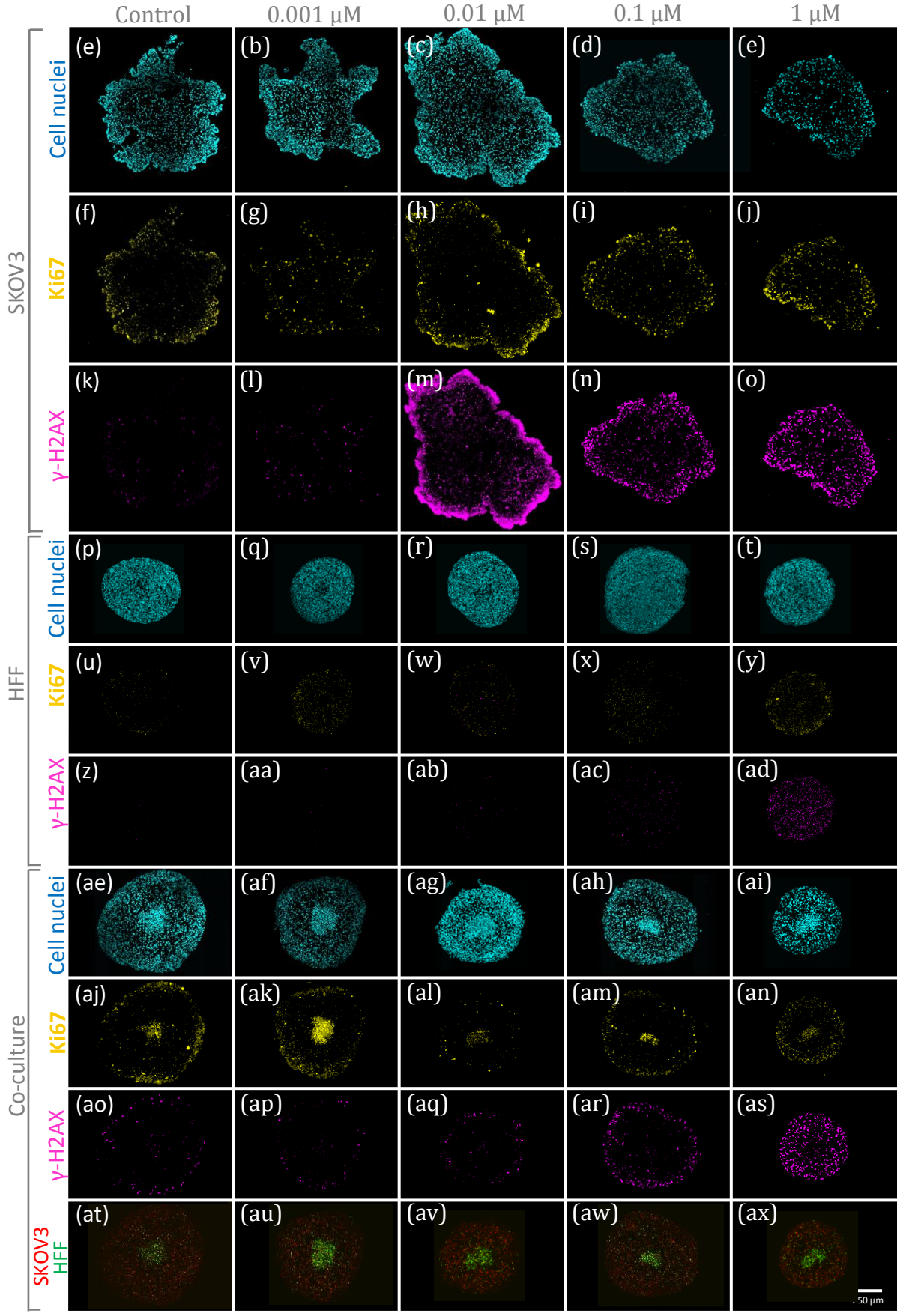

Figure 6-15. Immunofluorescence staining for Ki67 (yellow), γ-H2AX (magenta), Hoechst 33342 (cell nuclei, blue), and SKOV3 (Qtracker 800, red) and HFF (Qtracker 655, green) imaged using a confocal microscope for SKOV3, HFF and co-culture micro-tissues for no drug control, 0.001 µM, 0.01 µM, 0.1 µM and 1 µM concentration of doxorubicin. *Scale bar = 50 µm for all images.*

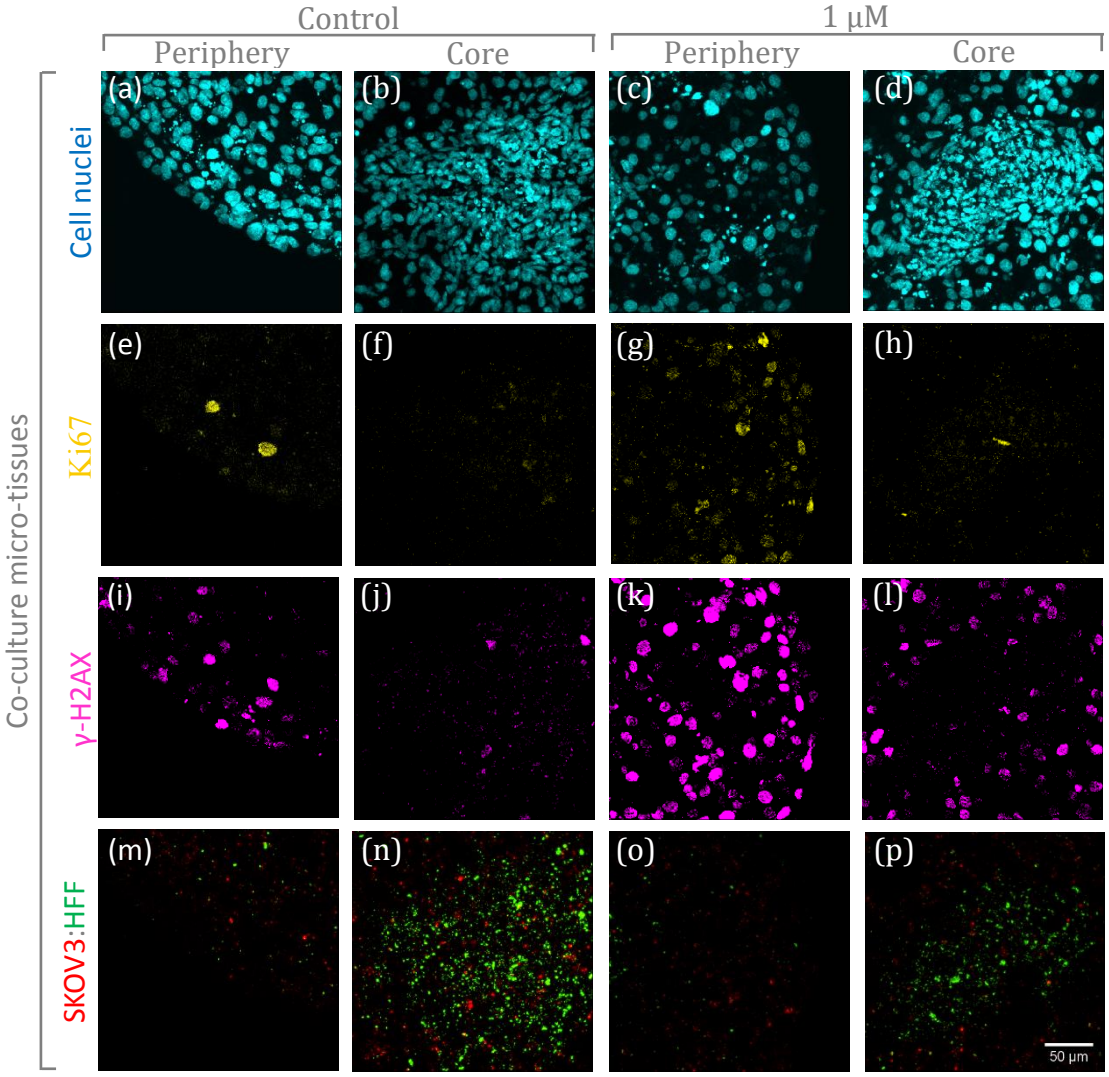

Figure 6-16. Immunofluorescence staining for Ki67 (yellow), γ-H2AX (magenta), Hoechst 33342 (cell nuclei, blue), and SKOV3 (Qtracker 800, red) and HFF (Qtracker 655, green) imaged using a confocal microscope for co-culture micro-tissues at the periphery and core for no drug control and 1 μM concentration of doxorubicin. *Scale bar = 50 μm for all images.*

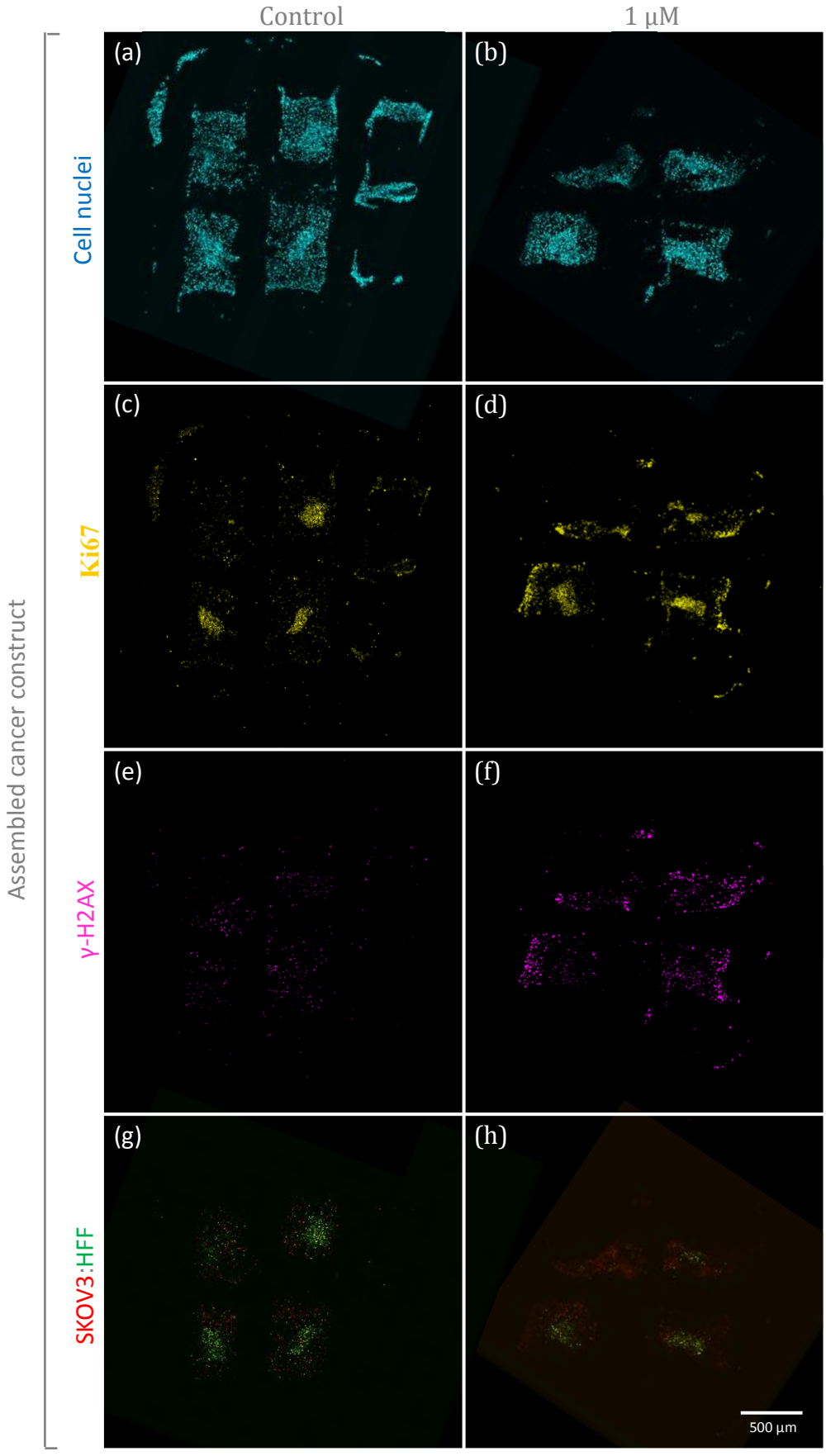

Figure 6-17. Immunofluorescence staining for Ki67 (yellow), γ-H2AX (magenta), Hoechst 33342 (blue), and SKOV3 (Qtracker 800, red) and HFF (Qtracker 655, green) imaged using a confocal microscope for assembled cancer constructs for control and 1 µm concentration of doxorubicin. *Scale bar = 500 µm for all images.*

6.5 Discussion

In this study, a modular bioassembly based approach was employed for biofabrication of an *in vitro* 3D cancer model. The cancer model was developed by adopting a "bottom-up" or modular assembly strategy currently being developed for tissue engineering applications [36, 62]. Modular tissue engineering aims at the development of complex, multi-cellular tissue constructs with hierarchical cell organization, through the use of smaller self-assembled or direct-assembled tissue modules or building blocks [62]. Modular tissue engineering approaches offer potential in recreating the intricate microstructural features of native tissues [36]. As many tissues are composed of repeating functional units, there exists a rational for using modular tissue engineering approaches to fabricate larger tissues from smaller tissue units [36].

We have developed a prototype automated bioassembly system that can assemble smaller tissue units (i.e. micro-tissues) into a 3D plotted scaffold. Our data demonstrated the reliable and efficient handling of cancer micro-tissues by the automated bioassembly system. The prototype fluidic-based automated bioassembly system was developed to provide a flow path and micro-tissue handling solution that did not damage the micro-tissues and no significant effect on cell viability were observed in constructs assembled with the automated bioassembly system (Figure 6-10 and Figure 6-11). This platform thereby provided a pathway for investigating automated modular assembly of 3D cancer micro-tissues for *in vitro* drug screening. With the automated bioassembly system, mathematical models or anatomical models can be easily translated into a computer aided manufacturing (CAD/CAM) file and inputted into a bio-plotter [63]. This, along with the layer-by-layer strategy, would enable the fabrication of complex constructs, or constructs with an array of desired combinations of micro-tissues assembled with the required geometry in precision and in large numbers.

For the purpose of initial validation, the automated tissue assembly system was designed for optimal handling of spherical Ø1 mm sized tissue units, therefore, it was essential that the fabricated micro-tissues were compact, spherical and of Ø1 mm in size. Many cancer cell lines form only loose aggregates or association of cells when cultured in 3D and formation of compact micro-tissues is limited to a few cell

lines [31]. Previous studies have reported scales such as a "compactness index" to quantify compactness of micro-tissues [21, 64]. Unfortunately, much of the compactness of micro-tissues reported in the literature for a particular cell-line type tend to be descriptive and not quantitative, making it challenging to select a compact micro-tissue forming cell-line. MCF-7 (a non-invasive cell-line [65]) has been reported to form compact micro-tissues, SKOV3 (invasive cell-line [66]) an aggregate and MDA-MB-231 (invasive cell-line [65]) a loose aggregate after 24 hours of culture on poly-HEMA coated plates [31, 67, 68]. On the contrary, it has also been suggested that the ability to form compact spheroids in cancer cell-lines is associated with an invasive phenotype [67, 69]. However, from our preliminary experiments, we were only able to form discoid (flat and circular) SKOV3 micro-tissues after 7 days of culture using a liquid overlay technique. The discrepancy in the ability to form compact micro-tissues across different studies reported and our experiment could be due to the cells, culture techniques or even the targeted micro-tissue size. The formation of micro-tissues has been associated with the expression of integrins and cadherins [21]. The major adhesion molecule that maintains tight cell-cell interaction has reported to be E-cadherin and has been correlated to the formation of compact micro-tissues [67]. The reduction or the loss of expression of adhesion molecules can alter the ability of the cells to aggregate into a compact micro-tissue [67]. The loss of E-cadherin expression in MDA-MB-231 could be the possible reason that they do not form compact micro-tissues [67]. With MCF-7s, they have been reported to express E-cadherin and form compact micro-tissues, but their inability to form compact micro-tissues in this study was unexpected [31, 67]. One possible explanation could be the difference in the technique used for the micro-tissue fabrication which caused an altered E-cadherin expression. In studies reported by Ivascu *et al*. micro-tissues were fabricated by seeding 5000 cells per well in a poly-HEMA coated 96-well plate with centrifugation after seeding the cells which resulted in compact micro-tissues after culture for 24 hours [31, 67]. However, we seeded 80,000 cells per well in an agarose coated 48-well plate without centrifugation which did not result in the formation of compact micro-tissues after 7 days of culture. Genotypic and phenotypic drifts can occur in cell lines and biological differences have been observed in MCF-7s obtained from different laboratories and this could also possibly contribute to the difference in the ability to form compact micro-tissues [70, 71]. Nevertheless, a co-culture of human foreskin fibroblasts

(HFFs) with SKOV3 yielded a compact spherical micro-tissue of 1 mm diameter that could successfully be handled by the tissue assembly system for assembling cancer constructs.

With respect to the self-assembly and arrangement of co-cultured HFFs and SKOV3s in micro-tissues, Qtracker labelling (Figure 6-7) revealed an inhomogeneous cell distribution, with the cells self-segregating to form a predominantly HFF core surrounded by SKOV3s in the periphery. When the micro-tissues were assembled in a scaffold, the cells did not rearrange again and maintained their original arrangement they had as an individual micro-tissue. A similar rearrangement of cells has been reported by Rago *et al.* with normal human fibroblasts and rat hepatoma cells [35]. The self-segregation of cells in a micro-tissue can be explained based on the differential adhesion hypothesis (DAH). According to the DAH, cellular aggregates form a spherical structure to maximize intercellular adhesion and to minimize free energy, and cells in the micro-tissue self-segregate due to differences in cell-cell adhesion or apparent surface tension [72]. Cells with a higher cohesion are located on the inside and cells with a lower cohesion are located on the outside [72]. It has been reported that in a co-culture system, cells that produced similar levels of N-cadherin did not segregate, but when the levels were moderately different they segregated with the cells with a higher N-cadherin expression on the inside and the cells with a lower N-cadherin expression on the outside [73]. Cancer cells with a more fibroblastic phenotype and reduced E-cadherin expression have been suggested to be more invasive [74]. SKOV3 is an invasive cancer cell-line in which the E-cadherin DNA is highly methylated and also it has been reported that hypoxia reduces E-cadherin expression in SKOV3 cells [75, 76]. The reduced cadherin expression in SKOV3 cell-line could explain the formation of a less compact discoid in SKOV3 only micro-tissues and the formation of a more compact spherical micro-tissue that self-segregate when SKOV3 is co-cultured with fibroblasts which express multiple types of cadherin [43]. Fibroblasts and myofibroblasts represent the majority of the cells in a tumour stroma, and tumour stroma plays an important role in the support and progression of epithelial cancer cells [77, 78]. The observed rearrangement of fibroblasts and SKOV3s could potentially partly simulate the tumour cell-stroma interactions in tumours *in vivo,* where the tumour stroma supports the tumour cells. This observed arrangement

could potentially be investigated for chemotherapy targeting tumour-associated stroma [78].

Fibroblasts are known to play an important role in the progression, growth and spread of cancers and are associated with cancer cells at all stages of progression [45, 46]. Activated fibroblasts associated with malignant tumours – called cancer-associated fibroblasts (CAFs) – are known to enhance tumour progression [45, 79, 80]. Co-culture cancer models with normal (non-cancer-associated) fibroblasts are thought to envisage early stages of tumour development and dissemination compared to co-culture with cancer-associated fibroblasts which reflect later stages [68]. This could mean that our model could potentially be made to resemble an early or late stage tumour based on whether the model is composed of normal or cancer-associated fibroblast.

The efficacy of the drug on cells in 2D, individual micro-tissues and assembled constructs were evaluated by exposing the models to varying concentrations of doxorubicin. An enhanced chemoresistance indicated by the higher IC_{50} values (Table 6-1) was observed in the 3D models compared to cells in 2D, which is in agreement with other studies [5, 81-84]. There are many possible reasons for the higher chemoresistance of doxorubicin in 3D models compared to the cells in 2D. Micro-tissues have a larger number of non-proliferating cells especially in the core compared to cells in 2D where most cells are proliferating. The toxicity of doxorubicin is dependent on the proliferating rate of cells and a lower proliferation rate in 3D models results in a lower number of doxorubicin induced DNA strand breaks [84]. This is in agreement with our Ki67 (marker for proliferation) and γ-H2AX (marker for double-strand breaks in DNA) immunofluorescence staining (Figure 6-15 and Figure 6-16) which were expressed at a greater intensity at the periphery of the micro-tissue than in the core. Other possible reasons for the higher chemoresistance in 3D models could be attributed due to the reduced drug penetration, hypoxia, cell-cell interaction, gene and protein expression, and increased extracellular matrix components [24, 85-88]. The proliferating cells at the periphery of the micro-tissues observed predominantly in the SKOV3 micro-tissues and to a certain extent in the co-culture micro-tissues has been reported previously,

and has been attributed to the inefficient mass transport towards the core of the micro-tissue [84, 89].

From the dose-response curves (Figure 6-12) and IC_{50} values (Table 6-1), a cell type-dependent response to the drug was observed. Co-cultured micro-tissues (0.33 μM) containing SKOV3 and HFF had a higher IC_{50} value compared to SKOV3 only monoculture micro-tissues (0.17 μM). HFF micro-tissues (7.05 μM) were the most chemoresistant and had the highest IC_{50} value. The higher chemoresistance of fibroblasts to tumour cells and increased chemoresistance of tumour cells in the presence of fibroblasts has been previously been reported [90, 91]. The higher resistance of fibroblasts and co-culture micro-tissues could be caused by a physiological resistance due to the extracellular matrix secreted resulting in the reduced penetration of anticancer drug [45, 92]. Moreover, in the HFF micro-tissues, low Ki67 expression (Figure 6-15 u-y) was observed suggesting a low proliferation rate resulting in a low number of doxorubicin-induced DNA strand breaks observed by the low γ-H2AX expression (Figure 6-15 z-ad). This observation is consistent with the high IC_{50} value (7.05 μM) as well as the observed significant decrease in normalised DNA content (1 - 10 μM) at a higher drug concentration (Figure 6-13). The lower γ-H2AX expression in the HFF micro-tissues could also be attributed to the ability of non-proliferating cells to repair damaged DNA caused by the drug [93]. With the SKOV3 micro-tissues, the higher proliferation rate as seen from the Ki67 expression (Figure 6-15 f-j) leaves the SKOV3 micro-tissues at a higher susceptibility to the number of doxorubicin-induced DNA strand breaks. This observation is in line with the lower IC_{50} value (0.17 μM), the higher levels of γ-H2AX visualised for a particular concentration of drug compared to the co-culture and HFF micro-tissues and also the observed significant decrease in normalised DNA content (0.01 – 0.1 μM) at a lower drug concentration (Figure 6-13). With the co-culture micro-tissues (Figure 6-15 aj-an), the fraction of proliferating cells was observed to be lower compared to the SKOV3 micro-tissues but higher compared to the HFF micro-tissues and can be confirmed by the Ki67 staining (Figure 6-15). This Ki67 expression correlated with the median level in the expression of γ-H2AX estimated IC_{50} values (0.33 μM) and also the observed significant decrease in normalised DNA content (0.1 - 1 μM) all of which was in-between the response for the SKOV3 and HFF micro-tissues. In the co-culture micro-tissues, expression of γ-H2AX (Figure 6-15 ao-as and

Figure 6-16) observed with increasing drug concentration was more toward the periphery of the micro-tissue where the distribution of SKOV3 is higher and a higher proportion of proliferating cells are located. Micro-tissues that are more compact have also been correlated to have a higher drug resistance and the difference we observed in the chemoresistance could be due to the difference in the micro-tissue compaction between micro-tissues of different cell types [94]. The increased micro-tissue compaction is associated with increased intercellular adhesion which causes a lower fraction of proliferating cells thereby possibly resulting in higher chemoresistance [94].

A higher background levels of γ-H2AX was visualised in the control SKOV3 micro-tissue (Figure 6-15 k). Similarly in the control co-culture micro-tissues, a higher background level of γ-H2AX expression (Figure 6-15 ao) was visualised in the periphery of the micro-tissues where the SKOV3s are located (Figure 6-15 at) compared to the HFF core where no noticeable expression of γ-H2AX was observed. However, in the control HFF micro-tissues, no noticeable expression of γ-H2AX (Figure 6-15 z) was observed. The higher background levels of γ-H2AX visualised in the SKOV3 micro-tissues and in the SKOV3s in the co-culture micro-tissues (inferred from the Qtracker labelling and γ-H2AX expression) without drug treatment, could be due to the presence of double-stranded breaks caused by the higher rate of mutations in genes involved in DNA repair and unregulated cell cycle checkpoints in cancer cells as reported previously [59, 95-97].

The 3D assembled co-culture construct had a higher chemoresistance compared to individual 3D co-culture micro-tissue. A 4-fold increase in IC_{50} values between co-culture micro-tissues (0.33 μM) and the co-culture assembled constructs (1.19 μM) was observed. As in the case of ECM in tumours *in vivo* the ECM in the 3D models can slow down the diffusion of nutrients, drugs and oxygen resulting in a concentration gradient of these molecules and these gradients could be greater in the larger assembled construct compared to the smaller micro-tissues [23, 24, 85]. The lower diffusion of nutrients and oxygen in the larger assembled construct compared to the micro-tissues would result in the lower proliferation rate in the assembled construct and lower efficacy of the drug as doxorubicin preferentially targets cycling cells [24, 85]. It has been previously suggested that the

uptake of doxorubicin is significantly reduced in larger micro-tissues [23]. The reduced diffusion and increased concentration gradient of doxorubicin towards the core in the larger assembled construct compared to the smaller micro-tissues would result in the drug being less effective on the cells distal to the periphery of the assembled construct, consequently causing an increased chemoresistance of the assembled construct compared to the micro-tissues [24, 85]. As the treatment of tumours becomes more challenging with increasing tumour size, the size-dependent response highly is relevant for the treatment of tumours *in vivo* (as mentioned earlier, the average ovarian cancer tumour size can range from 4.6 to 11.8 cm) [27, 29]. Despite the fact that small (<200 μm) micro-tissues are commonly used in high-throughput screening models to reproduce cell-cell and cell-matrix interactions, the observed size depended on the response of the 3D models to the drug also need to be factored in during the screening of candidate anticancer drugs. Therefore, larger (>1.6 mm which is the size we used in the study here) assembled constructs as an *in vitro* 3D model would be more relevant compared to 2D models or individual micro-tissues for predicting promising drug candidates for larger *in situ* tumours.

The 3D models investigated in this study consisted only of ovarian cancer cells and fibroblasts, however, native *in vivo* tumour tissues are composed of heterotypic cell types which includes cancer stem cells [98], primary stem cells, fibroblasts [45], endothelial [99] and immune cells [100], where modelling a more clinically relevant *in vivo* like a tumour would require the incorporation of these cells into the model [101]. Even though there exists abundant literature on the co-culture of 2 different cell types, little research has focused on the development of *in vitro* models with 3 or more cell types [101, 102]. Further development of the 3D bioassembly model to incorporate other cell types found in tumours would be the next step. For example, the stroma consists of connective tissues, blood vessels, and inflammatory cells and plays an essential role in the progress or inhibition of cancer [46, 103]. To potentially recapitulate the tumour-stroma interaction *in vivo*, a biphasic construct with a phase containing tumour micro-tissues and the other containing micro-tissues fabricated with elements of the stroma could be assembled to fabricate a 3D model. The drug and toxin metabolism *in vivo* by the liver could be simulated by assembling a tumour construct with tumour micro-tissues along with hepatocyte micro-tissues [104, 105]. Similarly, tumour micro-tissues could be

assembled with bone micro-tissues to simulate a metastatic model to investigate bone invasion and osteolysis [106]. The automated tissue assembly system could be used to assemble mono-culture or co-culture micro-tissue modules of healthy or tumour origin cells into a 3D plotted scaffold in a predetermined desired arrangement. The construct can be assembled in a high-throughput format and interaction between different types of micro-tissues and the cells targeted by the drug can be investigated and analysed [101]. An alternative approach to investigating complex tumours would be a modular assembly based deconstruction-reconstruction approach. Here, complex tumours are deconstructed to its individual basic cell type after which the deconstructed component is added to the model to vary the complexity of the cancer model. This would enable understanding both the individual components and collective components of the tumour as a whole [101].

The application of Biofabrication and 3D plotted models for drug development has grown rapidly from an abstract concept and has received considerable recent attention from researchers and commercial entities alike. Organovo, an early-stage medical laboratory and research company has even begun offering services to evaluate drug exposure on a bioprinted human liver model [107]. Developing a new drug by the pharmaceutical industry is a billion dollar process of which a major portion is spent on research [108]. Screening new drugs with 3D tissue culture models have an increasingly important role to play before clinical trials on humans [109, 110]. For a model to be efficient and effectively suited for preclinical testing especially in an industrial environment it is essential to be able to scale it for medium or high-throughput screening (HTS) [4]. The prototype, fluidic based automated assembly system developed in this study could serve as a template for developing an industry standard system that can be integrated with commercial liquid handling systems currently being used. The potential to transform the prototype technology into an industrial system would make the technology attractive to pharmaceutical researchers and companies which in turn would attract investment. Given our oncological model can be fabricated in a high-throughput fashion, a large number of complex tumour constructs can be potentially fabricated to be implanted into an animal model for *in vivo* studies.

In the near future, we could see our organotypic *in vitro* 3D cancer model adapted to generate a personalised patient-specific model for screening cancer drugs from a repertoire and select a patient-specific drug [98]. The model could contain cells of both normal and tumour phenotype and the impact of different anticancer drugs could be examined to predict and foresee the benefits of treatment and the impact on quality of life of the patient.

The primary drawback of the micro-tissue based system is that only cells that can form or induce the formation of compact spheroids can currently be used with our automated tissue assembly system. One alternative approach would be to forcefully encapsulate the cells in a 3D matrix - an approach to be described and tackled in the next chapter [31, 111]. Encapsulation of cells would also cut short the rate-limiting step of the long culture time required before a robust compact micro-tissue can be formed.

Currently, the tissue assembly system has an innate shortcoming in that micro-tissues need to be of a fairly uniform size and micro-tissues above or below the designed size range of 1 mm diameter cannot be efficiently handled. Though spheroids can be formed over a wide range of sizes, quite often micro-tissues of up to 200 μm in diameter are used for high-throughput screening, which is thought to be sufficient to reflect the 3D cell-cell and cell-matrix interactions [22, 31]. For the automated bioassembly system to be capable of handling micro-tissues smaller or larger than the designed range, the physical components (i.e. tubing singularisation chamber and injection nozzle, see chapter 3 and 4) and the soft parameters (i.e. valve timing, fluid pressure) of the automated bioassembly system would have to be modified to accommodate the new desired size. Therefore, as we approach smaller sizes the system might become strongly influenced by laminar flow, surface tension, diffusion and fluidic resistance making the development of a new system inevitable [112].

We forecast that our developed model and tissue assembly system can cater to a range of applications in translational cancer research and drug testing.

6.6 Conclusions

We have reported the 3D Bioassembly of micro-tissues for biofabricating cancer constructs for application as an *in vitro* 3D cancer model. The co-culture of ovarian cancer cells with fibroblasts was necessary to form compact and spherical Ø1 mm cancer micro-tissues that can be handled by the automated bioassembly system. The cells in the micro-tissue self-segregated to form a predominantly fibroblast core surrounded by SKOV3 in the periphery and this arrangement was maintained when the micro-tissues were assembled into a scaffold. Using our prototype automated tissue bioassembly system, we successfully demonstrated the fabrication of a cancer construct. Our results indicate that the bioassembly system efficiently handles the cancer micro-tissues and that the cancer micro-tissues are unaffected by being handled by the automated tissue bioassembly system. We then characterised and studied the response of the micro-tissues and the cancer construct to an anticancer drug - doxorubicin. The results show an obvious difference between the response of the cells in the 2D model and the 3D model, and micro-tissues of different cell types and the co-culture assembled construct. With its flexibility, the technology and the cancer model would have a broad utility and could be used for a wide range of applications including as 3D model for investigation cancer and for anticancer drug testing in a high-throughput format.

6.7 References

1. Ferlay J, Soerjomataram I, Dikshit R, Eser S, Mathers C, Rebelo M, Parkin DM, Forman D, Bray F. Cancer incidence and mortality worldwide: sources, methods and major patterns in GLOBOCAN 2012. International Journal of Cancer. 2015;136(5):E359-E386.
2. Kim JB, Stein R, O'Hare MJ. Three-dimensional *in vitro* tissue culture models of breast cancer- a review. Breast Cancer Research and Treatment. 2004;85(3):281-91.
3. Haycock JW. 3D cell culture: a review of current approaches and techniques. 3D Cell Culture: Methods and Protocols. 2011:1-15.
4. Pampaloni F, Reynaud EG, Stelzer EH. The third dimension bridges the gap between cell culture and live tissue. Nature Reviews Molecular Cell Biology. 2007;8(10):839-845.
5. Kimlin LC, Casagrande G, Virador VM. In vitro three-dimensional (3D) models in cancer research: An update. Molecular Carcinogenesis. 2013;52(3):167-182.
6. Loessner D, Stok KS, Lutolf MP, Hutmacher DW, Clements JA, Rizzi SC. Bioengineered 3D platform to explore cell–ECM interactions and drug resistance of epithelial ovarian cancer cells. Biomaterials. 2010;31(32):8494-8506.
7. DeVita VT, Chu E. A history of cancer chemotherapy. Cancer Research. 2008;68(21):8643-8653.
8. Rangarajan A, Hong SJ, Gifford A, Weinberg RA. Species-and cell type-specific requirements for cellular transformation. Cancer Cell. 2004;6(2):171-183.
9. Sivaraman A, Leach J, Townsend S, Iida T, Hogan B, Stolz DB, Fry R, Samson L, Tannenbaum S, Griffith L. A microscale in vitro physiological model of the liver: predictive screens for drug metabolism and enzyme induction. Current Drug Metabolism. 2005;6(6):569-591.
10. Yamada KM, Cukierman E. Modeling tissue morphogenesis and cancer in 3D. Cell. 2007;130(4):601-610.
11. Hirschhaeuser F, Menne H, Dittfeld C, West J, Mueller-Klieser W, Kunz-Schughart LA. Multicellular tumor spheroids: an underestimated tool is catching up again. Journal of Biotechnology. 2010;148(1):3-15.
12. Pang Y, Montagne K, Shinohara M, Komori K, Sakai Y. Liver tissue engineering based on aggregate assembly: efficient formation of endothelialized rat hepatocyte aggregates and their immobilization with biodegradable fibresThis work was presented at the International Conference on Biofabrication (Toyama, Japan, 6–8 October 2011). Biofabrication. 2012;4(4):045004.
13. Hutmacher DW, Horch RE, Loessner D, Rizzi S, Sieh S, Reichert JC, Clements JA, Beier JP, Arkudas A, Bleiziffer O. Translating tissue engineering technology platforms into cancer research. Journal of Cellular and Molecular Medicine. 2009;13(8a):1417-1427.
14. Kunz-Schughart LA, Freyer JP, Hofstaedter F, Ebner R. The use of 3-D cultures for high-throughput screening: the multicellular spheroid model. Journal of Biomolecular Screening. 2004;9(4):273-285.
15. Nelson CM, Inman JL, Bissell MJ. Three-dimensional lithographically defined organotypic tissue arrays for quantitative analysis of morphogenesis and neoplastic progression. Nature Protocols. 2008;3(4):674-678.

16. Kleinman HK, Martin GR. Matrigel: basement membrane matrix with biological activity. in Seminars in Cancer Biology. 2005. Elsevier.
17. Bates RC, Edwards NS, Yates JD. Spheroids and cell survival. Critical Reviews in Oncology/Hematology. 2000;36(2):61-74.
18. Kale S, Biermann S, Edwards C, Tarnowski C, Morris M, Long MW. Three-dimensional cellular development is essential for *ex vivo* formation of human bone. Nature Biotechnology. 2000;18(9):954-958.
19. Desoize B. Contribution of three-dimensional culture to cancer research. Critical Reviews in Oncology/Hematology. 2000;36(2):59-60.
20. Jakab K, Neagu A, Mironov V, Markwald RR, Forgacs G. Engineering biological structures of prescribed shape using self-assembling multicellular systems. Proceedings of the National Academy of Sciences of the United States of America. 2004;101(9):2864-2869.
21. Lin R-Z, Chou L-F, Chien C-CM, Chang H-Y. Dynamic analysis of hepatoma spheroid formation: roles of E-cadherin and β1-integrin. Cell and Tissue Research. 2006;324(3):411-422.
22. Friedrich J, Seidel C, Ebner R, Kunz-Schughart LA. Spheroid-based drug screen: considerations and practical approach. Nature Protocols. 2009;4(3):309-324.
23. Wartenberg M, Frey C, Diedershagen H, Ritgen J, Hescheler J, Sauer H. Development of an intrinsic P-glycoprotein-mediated doxorubicin resistance in quiescent cell layers of large, multicellular prostate tumor spheroids. International Journal of Cancer. 1998;75(6):855-863.
24. Minchinton AI, Tannock IF. Drug penetration in solid tumours. Nature Reviews Cancer. 2006;6(8):583-592.
25. Vantangoli MM, Madnick SJ, Huse SM, Weston P, Boekelheide K. MCF-7 human breast cancer cells Form differentiated microtissues in scaffold-free hydrogels. PLOS ONE. 2015;10(8):e0135426.
26. Markovitz-Bishitz Y, Tauber Y, Afrimzon E, Zurgil N, Sobolev M, Shafran Y, Deutsch A, Howitz S, Deutsch M. A polymer microstructure array for the formation, culturing, and high throughput drug screening of breast cancer spheroids. Biomaterials. 2010;31(32):8436-8444.
27. Grimer RJ. Size matters for sarcomas! The Annals of The Royal College of Surgeons of England. 2006;88(6):519-524.
28. Rosen PP, Saigo PE, Braun DW, Weathers E, Fracchia AA, Kinne DW. Axillary micro-and macrometastases in breast cancer: prognostic significance of tumor size. Annals of Surgery. 1981;194(5):585.
29. Horvath LE, Werner T, Boucher K, Jones K. The relationship between tumor size and stage in early versus advanced ovarian cancer. Medical Hypotheses. 2013;80(5):684-687.
30. Breslin S, O'Driscoll L. Three-dimensional cell culture: the missing link in drug discovery. Drug Discovery Today. 2013;18(5):240-249.
31. Ivascu A, Kubbies M. Rapid generation of single-tumor spheroids for high-throughput cell function and toxicity analysis. Journal of biomolecular screening. 2006;11(8):922-932.
32. Kelm JM, Djonov V, Ittner LM, Fluri D, Born W, Hoerstrup SP, Fussenegger M. Design of custom-shaped vascularized tissues using microtissue spheroids as minimal building units. Tissue Engineering. 2006;12(8):2151-2160.

33. Schon BS, Schrobback K, van der Ven M, Stroebel S, Hooper GJ, Woodfield TB. Validation of a high-throughput microtissue fabrication process for 3D assembly of tissue engineered cartilage constructs. Cell and Tissue Research. 2012.
34. Babur BK, Futrega K, Lott WB, Klein TJ, Cooper-White J, Doran MR. High-throughput bone and cartilage micropellet manufacture, followed by assembly of micropellets into biphasic osteochondral tissue. Cell and Tissue Research. 2015;361(3):755-768.
35. Rago AP, Dean DM, Morgan JR. Controlling cell position in complex heterotypic 3D microtissues by tissue fusion. Biotechnology and Bioengineering. 2009;102(4):1231-41.
36. Nichol JW, Khademhosseini A. Modular tissue engineering: engineering biological tissues from the bottom up. Soft Matter. 2009;5(7):1312-1319.
37. Carlsson J, Yuhas J. Liquid-overlay culture of cellular spheroids. in Spheroids in Cancer Research: Springer; 1984. p. 1-23.
38. Wadell H. Volume, shape, and roundness of rock particles. The Journal of Geology. 1932:443-451.
39. Krumbein WC. Measurement and geological significance of shape and roundness of sedimentary particles. Journal of Sedimentary Research. 1941;11(2).
40. Woodfield TB, Malda J, de Wijn J, Peters F, Riesle J, van Blitterswijk CA. Design of porous scaffolds for cartilage tissue engineering using a three-dimensional fiber-deposition technique. Biomaterials. 2004;25(18):4149-61.
41. Woodfield TBF, Guggenheim M, von Rechenberg B, Riesle J, van Blitterswijk CA, Wedler V. Rapid prototyping of anatomically shaped, tissue-engineered implants for restoring congruent articulating surfaces in small joints. Cell Proliferation. 2009;42(4):485-497.
42. Struhl K. Synthesizing proteins *in vitro* by transcription and translation of cloned genes. Wiley Online Library; 1998.
43. Matsuyoshi N, Imamura S. Multiple cadherins are expressed in human fibroblasts. Biochemical and Biophysical Research Communications. 1997;235(2):355-358.
44. Webb K, Li W, Hitchcock RW, Smeal RM, Gray SD, Tresco PA. Comparison of human fibroblast ECM-related gene expression on elastic three-dimensional substrates relative to two-dimensional films of the same material. Biomaterials. 2003;24(25):4681-4690.
45. Kalluri R, Zeisberg M. Fibroblasts in cancer. Nature Reviews Cancer. 2006;6(5):392-401.
46. Mueller MM, Fusenig NE. Friends or foes—bipolar effects of the tumour stroma in cancer. Nature Reviews Cancer. 2004;4(11):839-849.
47. Tacar O, Sriamornsak P, Dass CR. Doxorubicin: an update on anticancer molecular action, toxicity and novel drug delivery systems. Journal of Pharmacy and Pharmacology. 2013;65(2):157-170.
48. A'hern R, Gore M. Impact of doxorubicin on survival in advanced ovarian cancer. Journal of Clinical Oncology. 1995;13(3):726-732.
49. Aletti GD, Gallenberg MM, Cliby WA, Jatoi A, Hartmann LC. Current management strategies for ovarian cancer. in Mayo Clinic Proceedings. 2007. Elsevier.
50. Kim SH, Kim J. Lethal effect of adriamycin on the division cycle of HeLa cells. Cancer Research. 1972;32(2):323-325.

51. Sebaugh J. Guidelines for accurate EC50/IC50 estimation. Pharmaceutical Statistics. 2011;10(2):128-134.
52. Liu J, Zheng H, Tang M, Ryu Y-C, Wang X. A therapeutic dose of doxorubicin activates ubiquitin-proteasome system-mediated proteolysis by acting on both the ubiquitination apparatus and proteasome. American Journal of Physiology-Heart and Circulatory Physiology. 2008;295(6):H2541-H2550.
53. Arif I, Hooper C, Greco F, Williams A, Boateng S. Increasing doxorubicin activity against breast cancer cells using PPARγ-ligands and by exploiting circadian rhythms. British Journal of Pharmacology. 2013;169(5):1178-1188.
54. Dittmer J, Leyh B. The impact of tumor stroma on drug response in breast cancer. in Seminars in Cancer Biology. 2015. Elsevier.
55. Loeffler M, Krüger JA, Niethammer AG, Reisfeld RA. Targeting tumor-associated fibroblasts improves cancer chemotherapy by increasing intratumoral drug uptake. The Journal of Clinical Investigation. 2006;116(7):1955-1962.
56. Scholzen T, Gerdes J. The Ki-67 protein: from the known and the unknown. Journal of Cellular Physiology. 2000;182(3):311-322.
57. Schlüter C, Duchrow M, Wohlenberg C, Becker M, Key G, Flad H-D, Gerdes J. The cell proliferation-associated antigen of antibody Ki-67: a very large, ubiquitous nuclear protein with numerous repeated elements, representing a new kind of cell cycle-maintaining proteins. The Journal of Cell Biology. 1993;123(3):513-522.
58. Banáth JP, Olive PL. Expression of phosphorylated histone H2AX as a surrogate of cell killing by drugs that create DNA double-strand breaks. Cancer Research. 2003;63(15):4347-4350.
59. Kuo LJ, Yang L-X. γ-H2AX-a novel biomarker for DNA double-strand breaks. In Vivo. 2008;22(3):305-309.
60. Pilch DR, Sedelnikova OA, Redon C, Celeste A, Nussenzweig A, Bonner WM. Characteristics of γ-H2AX foci at DNA double-strand breaks sites. Biochemistry and Cell Biology. 2003;81(3):123-129.
61. Brown JM, Giaccia AJ. The unique physiology of solid tumors: opportunities (and problems) for cancer therapy. Cancer Research. 1998;58(7):1408-1416.
62. Elbert DL. Bottom-up tissue engineering. Current Opinion in Biotechnology. 2011;22(5):674-80.
63. Agarwala MK, Jamalabad VR, Langrana NA, Safari A, Whalen PJ, Danforth SC. Structural quality of parts processed by fused deposition. Rapid Prototyping Journal. 1996;2(4):4-19.
64. Lin R-Z, Chu W-C, Chiang C-C, Lai C-H, Chang H-Y. Magnetic reconstruction of three-dimensional tissues from multicellular spheroids. Tissue Engineering Part C: Methods. 2008;14(3):197-205.
65. Lacroix M, Leclercq G. Relevance of breast cancer cell lines as models for breast tumours: an update. Breast Cancer Research and Treatment. 2004;83(3):249-289.
66. Kobayashi M, Salomon C, Tapia J, Illanes SE, Mitchell MD, Rice GE. Ovarian cancer cell invasiveness is associated with discordant exosomal sequestration of Let-7 miRNA and miR-200. Journal of Translational Medicine. 2014;12(1):1.
67. Ivascu A, Kubbies M. Diversity of cell-mediated adhesions in breast cancer spheroids. International Journal of Oncology. 2007;31(6):1403-1414.

68. Kunz-Schughart LA, Heyder P, Schroeder J, Knuechel R. A heterologous 3-D coculture model of breast tumor cells and fibroblasts to study tumor-associated fibroblast differentiation. Experimental Cell Research. 2001;266(1):74-86.
69. Sodek KL, Ringuette MJ, Brown TJ. Compact spheroid formation by ovarian cancer cells is associated with contractile behavior and an invasive phenotype. International journal of cancer. 2009;124(9):2060-2070.
70. Osborne CK, Hobbs K, Trent JM. Biological differences among MCF-7 human breast cancer cell lines from different laboratories. Breast Cancer Research and Treatment. 1987;9(2):111-121.
71. Burdall SE, Hanby AM, Lansdown MR, Speirs V. Breast cancer cell lines: friend or foe? Breast Cancer Research. 2003;5(2):1.
72. Napolitano AP, Chai P, Dean DM, Morgan JR. Dynamics of the self-assembly of complex cellular aggregates on micromolded nonadhesive hydrogels. Tissue Engineering. 2007;13(8):2087-2094.
73. Foty RA, Steinberg MS. Cadherin-mediated cell-cell adhesion and tissue segregation in relation to malignancy. International Journal of Developmental Biology. 2004;48(5-6):397-409.
74. Frixen UH, Behrens J, Sachs M, Eberle G, Voss B, Warda A, Löchner D, Birchmeier W. E-cadherin-mediated cell-cell adhesion prevents invasiveness of human carcinoma cells. The Journal of Cell Biology. 1991;113(1):173-185.
75. Imai T, Horiuchi A, Wang C, Oka K, Ohira S, Nikaido T, Konishi I. Hypoxia attenuates the expression of E-cadherin via up-regulation of SNAIL in ovarian carcinoma cells. The American Journal of Pathology. 2003;163(4):1437-1447.
76. Yuecheng Y, Hongmei L, Xiaoyan X. Clinical evaluation of E-cadherin expression and its regulation mechanism in epithelial ovarian cancer. Clinical & Experimental Metastasis. 2006;23(1):65-74.
77. Bremnes RM, Dønnem T, Al-Saad S, Al-Shibli K, Andersen S, Sirera R, Camps C, Marinez I, Busund L-T. The role of tumor stroma in cancer progression and prognosis: emphasis on carcinoma-associated fibroblasts and non-small cell lung cancer. Journal of Thoracic Oncology. 2011;6(1):209-217.
78. Orimo A, Weinberg RA. Stromal fibroblasts in cancer: a novel tumor-promoting cell type. Cell Cycle. 2006;5(15):1597-1601.
79. Olumi AF, Grossfeld GD, Hayward SW, Carroll PR, Tlsty TD, Cunha GR. Carcinoma-associated fibroblasts direct tumor progression of initiated human prostatic epithelium. Cancer Research. 1999;59(19):5002-5011.
80. Zhang Y, Tang H, Cai J, Zhang T, Guo J, Feng D, Wang Z. Ovarian cancer-associated fibroblasts contribute to epithelial ovarian carcinoma metastasis by promoting angiogenesis, lymphangiogenesis and tumor cell invasion. Cancer Letters. 2011;303(1):47-55.
81. Dhiman HK, Ray AR, Panda AK. Three-dimensional chitosan scaffold-based MCF-7 cell culture for the determination of the cytotoxicity of tamoxifen. Biomaterials. 2005;26(9):979-986.
82. Padrón JM, Peters GJ. Cytotoxicity of sphingoid marine compound analogs in mono-and multilayered solid tumor cell cultures. Investigational New Drugs. 2006;24(3):195-202.
83. Fischbach C, Chen R, Matsumoto T, Schmelzle T, Brugge JS, Polverini PJ, Mooney DJ. Engineering tumors with 3D scaffolds. Nature methods. 2007;4(10):855-860.

84. Chitcholtan K, Sykes PH, Evans JJ. The resistance of intracellular mediators to doxorubicin and cisplatin are distinct in 3D and 2D endometrial cancer. Journal of Translational Medicine. 2012;10(1):1.
85. Sutherland RM, Eddy HA, Bareham B, Reich K, Vanantwerp D. Resistance to adriamycin in multicellular spheroids. International Journal of Radiation Oncology* Biology* Physics. 1979;5(8):1225-1230.
86. Hamilton G. Multicellular spheroids as an in vitro tumor model. Cancer Letters. 1998;131(1):29-34.
87. Miller BE, Miller FR, Heppner GH. Factors affecting growth and drug sensitivity of mouse mammary tumor lines in collagen gel cultures. Cancer Research. 1985;45(9):4200-4205.
88. Edmondson R, Broglie JJ, Adcock AF, Yang L. Three-dimensional cell culture systems and their applications in drug discovery and cell-based biosensors. Assay and Drug Development Technologies. 2014;12(4):207-218.
89. Alvarez-Pérez J, Ballesteros P, Cerdán S. Microscopic images of intraspheroidal pH by 1H magnetic resonance chemical shift imaging of pH sensitive indicators. Magnetic Resonance Materials in Physics, Biology and Medicine. 2005;18(6):293-301.
90. Tiago M, de Oliveira EM, Brohem CA, Pennacchi PC, Paes RD, Haga RB, Campa A, de Moraes Barros SB, Smalley KS, Maria-Engler SS. Fibroblasts protect melanoma cells from the cytotoxic effects of doxorubicin. Tissue engineering Part A. 2014;20(17-18):2412-2421.
91. andYi Lu LL. Optimizing a 3D culture system to study the interaction between epithelial breast cancer and its surrounding fibroblasts. Journal of Cancer. 2011;2:458-466.
92. Netti PA, Berk DA, Swartz MA, Grodzinsky AJ, Jain RK. Role of extracellular matrix assembly in interstitial transport in solid tumors. Cancer Research. 2000;60(9):2497-2503.
93. Barcellos-Hoff M, Marton L, Deen DF. Differential drug sensitivity conferred by growth status detected in a mixed population of cycling and noncycling cells. Cancer Research. 1990;50(12):3551-3555.
94. Croix BS, Rak JW, Kapitain S, Sheehan C, Graham CH, Kerbel RS. Reversal by hyaluronidase of adhesion-dependent multicellular drug resistance in mammary carcinoma cells. Journal of the National Cancer Institute. 1996;88(18):1285-1296.
95. Hinchcliffe EH, Day CA, Karanjeet KB, Fadness S, Langfald A, Vaughan KT, Dong Z. Chromosome missegregation during anaphase triggers p53 cell cycle arrest through histone H3. 3 Ser31 phosphorylation. Nature cell biology. 2016.
96. Kastan MB, Bartek J. Cell-cycle checkpoints and cancer. Nature. 2004;432(7015):316-323.
97. Banáth JP, MacPhail SH, Olive PL. Radiation sensitivity, H2AX phosphorylation, and kinetics of repair of DNA strand breaks in irradiated cervical cancer cell lines. Cancer Research. 2004;64(19):7144-7149.
98. Ebben JD, Treisman DM, Zorniak M, Kutty RG, Clark PA, Kuo JS. The cancer stem cell paradigm: a new understanding of tumor development and treatment. Expert Opinion on Therapeutic Targets. 2010;14(6):621-632.
99. Carmeliet P, Jain RK. Angiogenesis in cancer and other diseases. Nature. 2000;407(6801):249-257.

100. De Visser KE, Eichten A, Coussens LM. Paradoxical roles of the immune system during cancer development. Nature reviews cancer. 2006;6(1):24-37.
101. Unger C, Kramer N, Walzl A, Scherzer M, Hengstschläger M, Dolznig H. Modeling human carcinomas: physiologically relevant 3D models to improve anti-cancer drug development. Advanced Drug Delivery Reviews. 2014;79:50-67.
102. Linde N, Gutschalk CM, Hoffmann C, Yilmaz D, Mueller MM. Integrating macrophages into organotypic co-cultures: a 3D in vitro model to study tumor-associated macrophages. PLOS ONE. 2012;7(7):e40058.
103. Connolly JL, Schnitt SJ, Wang HH, Longtine JA, Dvorak A, Dvorak HF. Tumor structure and tumor stroma generation. 2003.
104. Peshwa MV, Wu FJ, Follstad BD, Cerra FB, Hu WS. Kinetics of hepatocyte spheroid formation. Biotechnology Progress. 1994;10(5):460-466.
105. Nyberg SL, Shatford RA, Peshwa MV, White JG, Cerra FB, Hu WS. Evaluation of a hepatocyte-entrapment hollow fiber bioreactor: A potential bioartificial liver. Biotechnology and Bioengineering. 1993;41(2):194-203.
106. Wacnik PW, Eikmeier LJ, Ruggles TR, Ramnaraine ML, Walcheck BK, Beitz AJ, Wilcox GL. Functional interactions between tumor and peripheral nerve: morphology, algogen identification, and behavioral characterization of a new murine model of cancer pain. The Journal of Neuroscience. 2001;21(23):9355-9366.
107. Vaidya M. Startups tout commercially 3D-printed tissue for drug screening. Nature medicine. 2015;21(1):2-2.
108. Avorn J. The $2.6 billion pill—methodologic and policy considerations. New England Journal of Medicine. 2015;372(20):1877-1879.
109. Griffith LG, Swartz MA. Capturing complex 3D tissue physiology in vitro. Nature Reviews Molecular Cell Biology. 2006;7(3):211-224.
110. Bleicher KH, Böhm H-J, Müller K, Alanine AI. Hit and lead generation: beyond high-throughput screening. Nature Reviews Drug discovery. 2003;2(5):369-378.
111. Carlsson J, Nilsson K, Westermark B, Ponten J, Sundstrom C, Larsson E, Bergh J, Pahlman S, Busch C, Collins VP. Formation and growth of multicellular spheroids of human origin. International Journal of Cancer. 1983;31(5):523-33.
112. Beebe DJ, Mensing GA, Walker GM. Physics and applications of microfluidics in biology. Annual Review of Biomedical Engineering. 2002;4:261-86.

Chapter 7 Automated 3D Bioassembly of cell-laden microspheres for biofabrication of an *in vitro* 3D cancer model and its evaluation compared to existing 2D and 3D drug screening models

7.1 Abstract

Oncological models are imperative for investigating cancer and for the development of therapeutics. 2D cultures are primitive and animal models are expensive, complex and need ethical approval. 3D models provide a more attractive intermediate solution. However, methods describing the high-throughput fabrication of large 3D cancer constructs with complex architecture have been limited. We aimed at the automated 3D Bioassembly of cell-laden microspheres for biofabricating modular assembly based cancer constructs for application as *in vitro* 3D cancer models. SKOV3, human foreskin fibroblast (HFF) and co-culture cell-laden GelMA microspheres of Ø1 mm were fabricated with a microfluidic device and characterised. The microspheres were reliably and efficiently handled by the automated bioassembly system. Layer-by-layer assembly of 8 microspheres into a 3D plotted PEGT/PBT polymer scaffold utilising the automated tissue bioassembly system showed no significant difference in viability when compared with manually assembled bilayered constructs. For evaluating the chemosensitivity, cells in 2D, microspheres and assembled cancer constructs were exposed to doxorubicin for 4 days and the metabolic activity was measured using AlamarBlue® assay. Fixed frozen sections were stained for Ki67 and γ-H2AX. Chemosensitivity testing demonstrated that the 3D assembled constructs had the highest chemoresistance, the cells in 2D were the most vulnerable to the drug, whereas 3D microspheres showed an intermediate chemoresistance. The chemoresistance to the drug was also cell dependent. This model and technology demonstrated the feasibility of bioassembling large multicellular models of complex 3D architecture for high-throughput screening.

7.2 Introduction

It is generally recognised that 3D *in vitro* models are able to more accurately mimic tissues *in vivo* than 2D models as they are a more physiologically relevant model system [1, 2]. 2D culture systems differ considerably in the proliferation, apoptosis, differentiation, and gene expression and do not recapitulate the 3D anatomy or physiology of native tissue [3, 4]. Furthermore, cells cultured in 2D have an altered drug response and sensitivity compared to cells in a 3D environment, resulting in the poor negative screening of candidate antitumour drugs [5]. Animal models, on the other hand, are complex, expensive and require ethical approval [4]. With the drawbacks of 2D monolayer systems and animal models, there is a need for 3D models that can bridge the gap between 2D drug screening models and animal models, to improve the reliability of current drug screening protocols before implementation in clinical trials [1, 6].

In the previous chapters, we described the development of an automated 3D tissue bioassembly system and forged an *in vitro* 3D cancer model that was populated with micro-tissues. Unfortunately, the formation of compact micro-tissues is only limited to a small subset of cancer cells and is highly dependent on the cell phenotype [7-10]. For example, we showed that breast cancer cell lines such as MCF-7 and MDA-MB-231 could not be fabricated into compact spherical micro-tissues, whereas the ovarian cancer cell line (SKOV3) required to be co-cultured with fibroblasts to form compact spherical micro-tissues that could be handled and assembled by the automated bioassembly system. This drawback of not being able to form compact spherical micro-tissues would seriously hinder the application of the developed model for a wider range of cell types. The alternative path to conquer this issue would be to encapsulate the cells in a 3D hydrated polymeric network, i.e. hydrogel microspheres that can be handled by the automated bioassembly system.

Encapsulating cells in a hydrogel is appealing as it provides a hydrated tissue-like environment which is structurally similar to the native extracellular matrix (ECM) of many tissues [11, 12]. A wide range of 3D hydrogel-based matrices for cancer models have been described, such as reconstituted basement membrane protein (Matrigel) [13], fibrin [14], type I collagen [12], polyethylene glycol (PEG)

[5] and silk fibroin [15]. However, gelatine-methacryloyl (GelMA) hydrogels are an appealing alternative given that it is inexpensive, water soluble, can be derived from a wide variety of natural sources, biocompatible, and can be photocrosslinked with tailorable physicomechanical properties [16, 17]. In the literature, various techniques have been employed to fabricate hydrogel microspheres, such as electrospraying [18], polyelectrolyte complexation [19], solvent evaporation [20], jet cutting [21], jet breakup [22], and electrostatic droplet generation [23]. In this chapter, we adapted a simple droplet microfluidic setup coupled with photopolymerisation from Serra *et al*. [24] to produce microspheres of a uniform size range [25]. The setup was presented earlier (Chapter 5, Figure 5-1) to form GelMA microspheres encapsulated with chondrocytes. We adopted the technique to fabricate cancer cell encapsulated GelMA microspheres as described herein.

By employing bottom-up tissue engineering strategies, smaller subunits or building blocks such as microspheres can be assembled to generate large constructs of complex and precise architecture [26]. Clinically relevant tumours *in vivo* are often quite large. Rosen *et al*. reported that tumour sizes in stage II breast cancer varied from 2.1 to 5 cm and Horvath *et al.* reported that average ovarian cancer tumours range from 4.6 to 11.8 cm respectively [27-29]. The ability to generate larger cancer constructs that mimic *in vivo* tumours would be advantageous for high-throughput drug screening given that larger 3D models potentially provide a more realistic drug response compared to a smaller 3D model [30, 31]. Essentially, there exists a need for a state-of-the-art fabrication technique that can custom-make cancer models to recreate tumour niches of complex architecture and is also adaptable with commonly adopted high-throughput approaches.

Biofabrication techniques have been developed for tissue engineering and regenerative medicine (TERM) to allow the control of macro and micro scale structure, as well as the architecture of an engineered construct. These techniques can be potentially adapted for application in cancer research. Recent progress in hydrogel-based fabrication of 3D cancer models includes a temperature controlled cell printing system to print hepatocellular carcinoma and epithelial cell-laden Matrigel for application as a disease model [32]. 3D *in vitro* cervical [33] and liver [34] tumour models have been created by plotting hydrogels containing a mixture

of cells, gelatin, alginate and fibrinogen. Specifically, advances in biofabrication involving the bioassembly of hydrogel subunits have been demonstrated for cardiac tissue engineering [35], vascularisation [36] and for general applications in tissue engineering [37, 38]. With tumour cells, Bruzewicz *et al.* assembled liver hepatocellular carcinoma and fibroblast cell-laden collagen gel modules in a micro-channel to demonstrate the ability to assemble constructs of multiple cell types with spatial organisation [39]. Apart from these few studies, little progress has been made in the bioassembly of hydrogel subunits or modules for tumour engineering.

To our knowledge, there are no studies which have described a system where prefabricated cell encapsulated microspheres can be precisely inserted into a 3D plotted scaffold in a layer-by-layer approach to custom-make large well-defined and reproducible complex-tumour models (see Chapter 4, Figure 4-1). Fundamentally to fabricate the model, we have employed a modular assembly based bottom-up strategy. Here, a hydrogel is used to encapsulate cells to form modular cell-laden hydrogel microspheres which would make up prefabricated subunits or building blocks. These prefabricated subunits can be potentially assembled into a 3D plotted scaffold to create a more complex biologically relevant tumour construct. By using this biofabrication approach, tumour models with a higher control of the spatial position of prefabricated modules would be possible. The biological rationale for adopting a modular assembly strategy to construct tissues of higher order is related to the ability to mimic the *in vivo* tissue structure using repeating functional units [40]. Furthermore, the technique would allow the fabrication of larger and more clinically relevant models in an automated and repeatable manner. The novel model would be a relevant research tool in cancer biology for translational research and drug discovery [4].

Therefore, the specific aim of this study was to develop an automated process for 3D Bioassembly of cell-laden hydrogel (GelMA) microspheres and biofabrication of complex cancer constructs for application as an *in vitro* 3D cancer model. This study involved (i) the fabrication of Ø1 mm cell-laden GelMA microspheres using a simple microfluidic setup that can be integrated with the automated bioassembly system, (ii) demonstrating the fabrication of a cancer construct via automated

microsphere bioassembly without affecting cell viability, (iii) and to investigate and characterise the response of the engineered cancer construct to a clinically relevant anticancer drug – doxorubicin compared to existing 2D and 3D drug screening models.

7.3 Methods

7.3.1 Cell expansion

Experiments were carried out with human ovarian adenocarcinoma cell line (SKOV3) and normal human foreskin fibroblasts (HFF). SKOV3 and HFF were cultured in media containing DMEM (high glucose, GlutaMAX Supplement, pyruvate) (GIBCO, USA) with 5% foetal bovine serum (FBS; GIBCO, New Zealand), 100 units/mL penicillin (GIBCO, USA) and 100 µg/mL streptomycin (GIBCO, USA). The cells were seeded at a density of 3,000 cells/cm^2 in tissue culture flasks (Corning, USA). Cells were expanded at 37°C in a humidified 5% CO_2/95% air incubator and media was changed twice a week. After approximately 4-7 days, subconfluent passage cells were washed with phosphate-buffered saline (PBS; GIBCO, USA), detached using 0.25% trypsin/EDTA (Gibco, Canada), counted by trypan blue exclusion in a haemocytometer and plated in a tissue culture flask at 3,000 cells/cm^2. The cells were passaged until there was a sufficient number of cells, after which the cells were harvested to form cell encapsulated microspheres. All HFFs used for this study were between passages 24 and 28 and SKOV3 were between passage 44 and 48.

7.3.2 Cell labelling with fluorescent nanoparticle

A Qtracker cell labelling kit (Life technologies, USA) was used to track cells in a co-culture environment. HFFs were labelled with Qtracker 655 and the SKOV3s with Qtracker 800. To label the cells with Qtracker, cells were concentrated to 10 x 10^6 cells/ml by centrifugation at 700 g for 5 minutes and resuspended in media. A 10 nM labelling solution was prepared by mixing 1 µL of the Qtracker Component A and 1 µL of the Qtracker Component B in a 1.5 ml microcentrifuge tube and incubated at room temperature for 5 minutes. 0.2 ml of DMEM was added to the mixture and vortexed for 30 seconds. 10^6 cells were added to the labelling mixture

and incubated for 60 minutes. The cells were subsequently washed twice with media and resuspended in media for use.

7.3.3 Synthesis of gelatine-methacryloyl (GelMA)

Gelatine (porcine skin, type A, 300g Bloom strength) (Sigma-Aldrich, USA) was dissolved in phosphate-buffered saline (PBS; GIBCO, USA) at a 10 wt% concentration. 0.6 g of methacrylic anhydride (Sigma-Aldrich, USA) per gram of gelatine was added to the gelatine solution and left to react for 1 hour at 50˚C under constant stirring [41], followed by dialysis against deionised water to remove unreacted methacrylic anhydride. The purified GelMA solution was filtered through a 0.22 µm sterile filter, then lyophilised under sterile conditions. The degree of methacryloyl substitution was quantified to be 60% (data not shown) using ^{1}H-proton nuclear magnetic resonance spectroscopy (Bruker Avance 400 MHz).

7.3.4 Cancer cell encapsulation in GelMA hydrogel microspheres

Non-labelled cells were used to form SKOV3 microspheres and HFF microspheres. Labelled SKOV3 and HFF were mixed so that the ratio of SKOV3 to HFF in the mixture was 75:25 and was used to form the co-culture microspheres. The microspheres were formed as outlined previously in Chapter 5, Briefly, dried sterile 10% (w/v) GelMA was dissolved in PBS at 37˚C and left to cool overnight at room temperature. A cell pellet was formed by centrifuging the cells at 700 g and the supernatant was discarded. The cell pellet was then resuspended in 10% wt GelMA (preliminary experiments showed that SKOV3 degraded the 5% (w/v) GelMA when culture for 7 days) macromer solution containing sterile filtered initiators (0.2 mM tris(2,2-bipyridyl)dichlororuthenium(II) hexahydrate (Ru; Sigma-Aldrich, USA) and 2 mM sodium persulfate (SPS; Sigma-Aldrich, USA)) to give a final concentration of 10 x 10^{6} cells/ml. The solution containing the cells was loaded into a syringe. Food grade sunflower oil was used as the continuous phase and the GelMA solution containing the photoinitiator and cells made up the dispersed phase. For the continuous oil phase the flow rate was set to 1 ml/minute and the dispersed gel phase it was set to 40 µl/min, this was based on studies by Young *et al.* [42]. The formed microspheres were then irradiated with visible light (OmniCure® S1500, Excelitas Technologies). The light was irradiated through a light filter (Rosco IR/UV filter) where only light between the wavelength 400 – 450 nm was allowed to pass

through and had a final intensity of 100 mW/cm^2. The light intensity and exposure time were selected based on previous work by Lim *et al.* [43]. The formed microspheres were collected in polypropylene (Falcon, USA) centrifuge tubes containing PBS. To separate the oil from the microspheres, the centrifuge tube was centrifuged at 0.1 g for 5 minutes. The oil was then aspirated and the pellet of microspheres in PBS was collected using a Pasteur pipette. The microspheres were then suspended in fresh PBS and the washing step was repeated. Each cell encapsulated microspheres was then transferred into a well in a 96-well polystyrene plate (Falcon, USA). 150 µL of cell culture media was then pipetted into the wells and placed in the incubator. The media was changed twice a week.

7.3.5 Size distribution of cell encapsulated microspheres

The size distribution of the fabricated microspheres was determined by measuring the size of the SKOV3, HFF and co-culture encapsulated microspheres. Fabricated microspheres (*n=50*) were stained with Coomassie brilliant blue (Thermo Fisher Scientific, USA) for 15 minutes and were imaged using the Zeiss Axioimager Z1 microscope. The major and minor diameters were measured using the particle analysis function in ImageJ. The average of the major and minor diameter was calculated and normal distribution of the average was plotted. The coefficient of variation was tabulated to gauge the microsphere size distribution.

7.3.6 DNA content – microspheres

The DNA content of the fabricated cell-laden microspheres was measured to quantify if a consistent number of cells were encapsulated in the microspheres as well as to investigate cell proliferation during culture. The DNA content of the microspheres (*n=3*, 4 microspheres/sample) was quantified using a CyQUANT kit (Molecular Probes, USA) on Day 0, 7 and 12. The samples were first digested overnight at 56 ˚C in 400 µL of 1 mg/ml proteinase-K (Sigma-Aldrich, USA) solution. Post proteinase-K digestion, the cells in the sample were lysed and the RNA was degraded by adding the provided lysis buffer with RNase A (1.35 KU/ml; Thermofisher, Lithuania) and incubating for an hour at room temperature. Samples were pipetted into 96-well white polypropylene plates (Nunc, Denmark) and GR-dye solution was added. The plate was then incubated at room temperature for 60 minutes in the dark and fluorescence was measured (Fluostar Galaxy BMG

Labtechnology, Germany). A DNA standard curve was constructed using the λ-DNA provided in the kit to determine the DNA quantity and a cell standard curve was constructed using SKOV3, HFF, and 75% SKOV3 and 25% HFF to determine the cell number.

7.3.7 Reliability and efficiency of microsphere singularisation

To determine the reliability of the singularisation device (see Chapter 4, Figure 4-3) to successfully assemble individual cancer microspheres, (SKOV3, HFF and co-culture) cell encapsulated microspheres were put through the device. The microspheres were put into the singularisation device in sets of 10 and repeated 10 times, with the success or failure in singularisation being noted. The total number of successful singularisation events was used to determine the overall efficiency of the singularisation system (Equation 7-1).

$$efficiency\ of\ singularisation = \frac{successful\ micro\text{-}tissue\ singularisation}{total\ attempted\ number\ of\ micro\text{-}tissue\ singularisation} \quad \textbf{7-1}$$

7.3.8 Scaffold fabrication

Biodegradable poly(ethylene glycol)-terephthalate-poly(butylene terephthalate) block copolymers (Polyactive 300PEGT55PBT45, PolyVation, The Netherlands) with a PEG molecular weight (MW) of 300 g/mol and a PEGT:PBT weight percent (wt%) ratio of 55:45 were used to fabricate scaffolds with a specific pore size and architecture. The material and composition were selected based on previous studies demonstrating its applicability for 3D plotting of extruded fibre scaffolds with controlled properties and stability both *in vitro* and *in vivo* [44, 45].

Porous scaffolds (25×25×2.64 mm), with accurately defined and controlled pore architecture for microsphere incorporation, were 3D plotted using a Bioscaffolder system (SYS ENG, Germany). Fibres were oriented in a repeating 0-90°-90°-0° pattern in order to provide porosity in both the x-y and x-z planes for assembly of 1 mm diameter microspheres. During the melt dispensing process the following 3D plotting parameters were applied: (i) fibre spacing of 1 mm in both x and y-direction, (ii) fibre height offset of 0.22 mm, (iii) print head reservoir

containing the polymer heated to a temperature of 200° and pressurised to 5 Bar, (iv) an auger speed of 63 RPM and (v) print head fitted with a 25 gauge nozzle moving with a traverse speed of 500 mm/min.

7.3.9 Automated bioassembly with cancer microspheres

The automated assembly of a construct with cancer microspheres was demonstrated by 3D plotting a scaffold using the high-temperature print head containing Polyactive 300PEGT55PBT45 and then inserting the cell (75% SKOV3 and 25% HFF) encapsulated microspheres using the microsphere injection head. To plot our assembled construct (*n=3*) a layer-by-layer scaffold fabrication and microsphere bioassembly (bottom-up) approach were adopted. In this scheme, the first layer of the scaffold (8 layers of fibre strands) was 3D plotted (as described earlier) and then 4 (2 x 2 fashion) live microspheres were inserted into the pores of the 3D plotted scaffold. The 3D plotting was repeated on top of the first layer to generate the second layer of the scaffold (4 layers of fibre strands) and then 4 more microspheres were inserted into the second layer. For the manually assembled construct, the whole scaffold was 3D plotted at once and the microspheres were inserted manually by hand into the pre-plotted scaffolds in a similar format to the ones assembled with the automated system. The manual insertion of the microsphere into the pore involved manually placing the microsphere on top of the scaffold pore with a pipette and press-fitting the microsphere into the scaffold pore with a spatula.

For the live/dead assay, the samples were incubated at 37°C in 0.5 ml of PBS with 1 µM Calcein AM (Molecular Probes, USA) for 15 minutes, then 1 µM Propidium Iodide (Molecular Probes, USA) was added and incubated for 10 more minutes. After this, the samples were washed twice with PBS and a z-stack of the sample was imaged using the Zeiss Axioimager Z1 microscope (FITC and Texas Red filter-set).

For the AlamarBlue® assay, AlamarBlue® (Invitrogen, USA) was added to the media containing FBS so that the final concentration was 10% (v/v) and the samples were incubated at 37°C for 20 hours. The reduction in AlamarBlue® reagent was calculated colourimetrically using the equations provided by the manufacturer after

measuring the absorbance at 570 nm, using 600 nm as a reference wavelength (Fluostar Galaxy BMG Labtechnology, Germany).

7.3.10 Efficiency of microsphere insertion

A bilayered scaffold (n=8) was 3D plotted with 4 microspheres in each layer using the layer-by-layer approach described earlier. The efficiency of microsphere insertion (see Chapter 4, Figure 4-4) within the scaffold pore was determined by the number of successful microsphere insertion within the scaffold pore to the total attempted number of microsphere insertion with the automated system (Equation 7-2).

$$efficiency\ of\ microsphere\ insertion = \frac{successful\ microsphere\ insertion}{total\ attempted\ number\ of\ microsphere\ insertion} \quad \textbf{7-2}$$

7.3.11 Construct assembly

After 1 day of fabricating the microspheres, 4 microspheres per layer (2 x 2 manner) were assembled into a 3D plotted bilayered scaffold. SKOV3 constructs, HFF constructs and co-culture constructs were assembled. Each assembled construct was transferred to a well in a 24-well polystyrene plate (Corning, USA). 1200 µL of cell culture media was then pipetted into the wells and the plate was placed in the incubator. The media was changed twice a week.

7.3.12 Viability of microspheres and assembled constructs over time

Live/dead assay was performed as described earlier on SKOV3, HFF and co-culture encapsulated microspheres and assembled constructs on day 1, 7 and 12 of the chemosensitivity timeline (see Figure 7-1).

7.3.13 Chemosensitivity test

The chemosensitivity test was used to evaluate *in vitro* antitumor activity of doxorubicin on cells in 2D, microspheres and assembled cancer constructs (see Figure 7-1 for a timeline of the chemosensitivity test). Doxorubicin was dissolved in DMSO so that the maximum final concentration of DMSO in media did not exceed 0.5% (v/v) of DMSO. On Day 0, the fabricated SKOV3, HFF and co-culture

microspheres were transferred to a 96-well plate and 150 µl of media with 5% FBS per well was added. On day 1 of forming the microspheres, SKOV3, HFF and co-culture cancer constructs were manually assembled (as described earlier) and transferred 24-well plate with 1.2 ml of media per well. On day 7, for the chemosensitivity test on 2D model, SKOV3, HFF and co-culture (75% SKOV3 and 25% HFF) cells were seeded onto a 48-well plate at 30,000 cells and 200 µl of media with 5% FBS per well. The next day (day 8), all samples were treated with different concentrations of doxorubicin – no drug control, 0.001 µM, 0.01 µM, 0.1 µM, 1 µM, 10 µM. Media with 5% FBS containing the specific concentration of drug was changed every 2 days. After 4 days of exposure to the drug, AlamarBlue® assay was conducted to measure metabolic activity of the samples. For the AlamarBlue® assay, all samples were transferred to a fresh well plate, AlamarBlue® was added to the media containing FBS so that the final concentration was 10% (v/v) and the and the microspheres and assembled construct were incubated for 20 hours and the cells in 2D were incubated for 3.5 hours at 37°C. Fluorometric measurements were made at an excitation wavelength of 545 nm and an emission wavelength of 590 nm and these values were curve fitted to estimate the half maximal inhibitory concentration (IC_{50}) using GraphPad Prism v.6.0. The microspheres from the chemosensitivity test were also quantified for DNA content as described earlier.

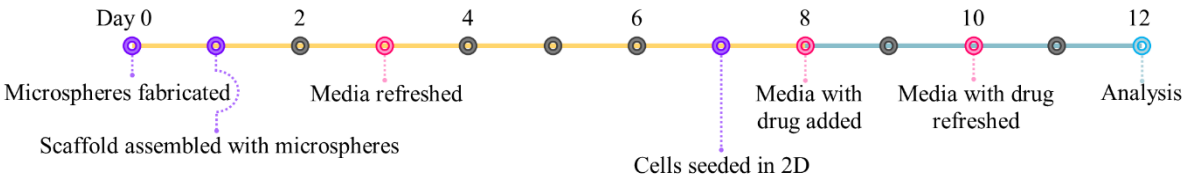

Figure 7-1. Timeline of the chemosensitivity test.

7.3.14 Histology and immunofluorescence

Following the AlamarBlue® assay, cell-laden microspheres and cancer constructs from the chemosensitivity test were washed in PBS, fixed in 10% neutral buffered formalin for an hour, washed in PBS again, immersed for an hour in 15% (w/v) sucrose in PBS and then immersed overnight in 30% (w/v) sucrose in PBS at 4°C. The samples were then embedded in OCT (Ted Pella, Inc. USA) and were cryosectioned (15 µm thick sections). The slides with the sections were rinsed in cold PBS thoroughly and were permeabilized with 0.25% (v/v) Triton X-100 (Sigma, USA) in PBS for 30 minutes. The sections were rinsed in cold PBS and were exposed

to 5% (w/v) BSA in PBS at a pH 7.4 for 60 minutes at room temperature. They were then rinsed in cold PBS and incubated with monoclonal anti-Ki67 (1:100 dilution; abcam, USA) and polyclonal anti-gamma H2AX (1:5,000 dilution; abcam, USA) antibodies at 4˚C overnight. The sections were washed in PBS and were incubated with secondary antibodies, goat Alexa Fluor 488 anti-mouse (1:500 dilution; Thermofisher, USA) and goat Alexa Fluor 555 anti-rabbit (1:500 dilution; abcam, USA) at 37˚C for an hour. Following further washing, the sections were counterstained with 4.5 μM Hoechst 33342 (Invitrogen, USA) in PBS. Finally, the slides were washed with 0.05% Tween-20 (Sigma, USA) in cold PBS, rinsed in PBS and then coverslipped. The samples were imaged using a Leica TCS SP5 confocal microscope. The rendered images of the microspheres and assembled construct (Figure 7-2) shows the plane at which the cryosections were performed and the approximate region imaged for immunofluorescence staining. A pixel count of γ-H2AX expression and Hoechst 33342 staining was performed on the images utilising the colour pixel counter plugin in ImageJ. The pixel count of γ-H2AX expression was expressed as a percentage of the pixel count of Hoechst 33342 staining.

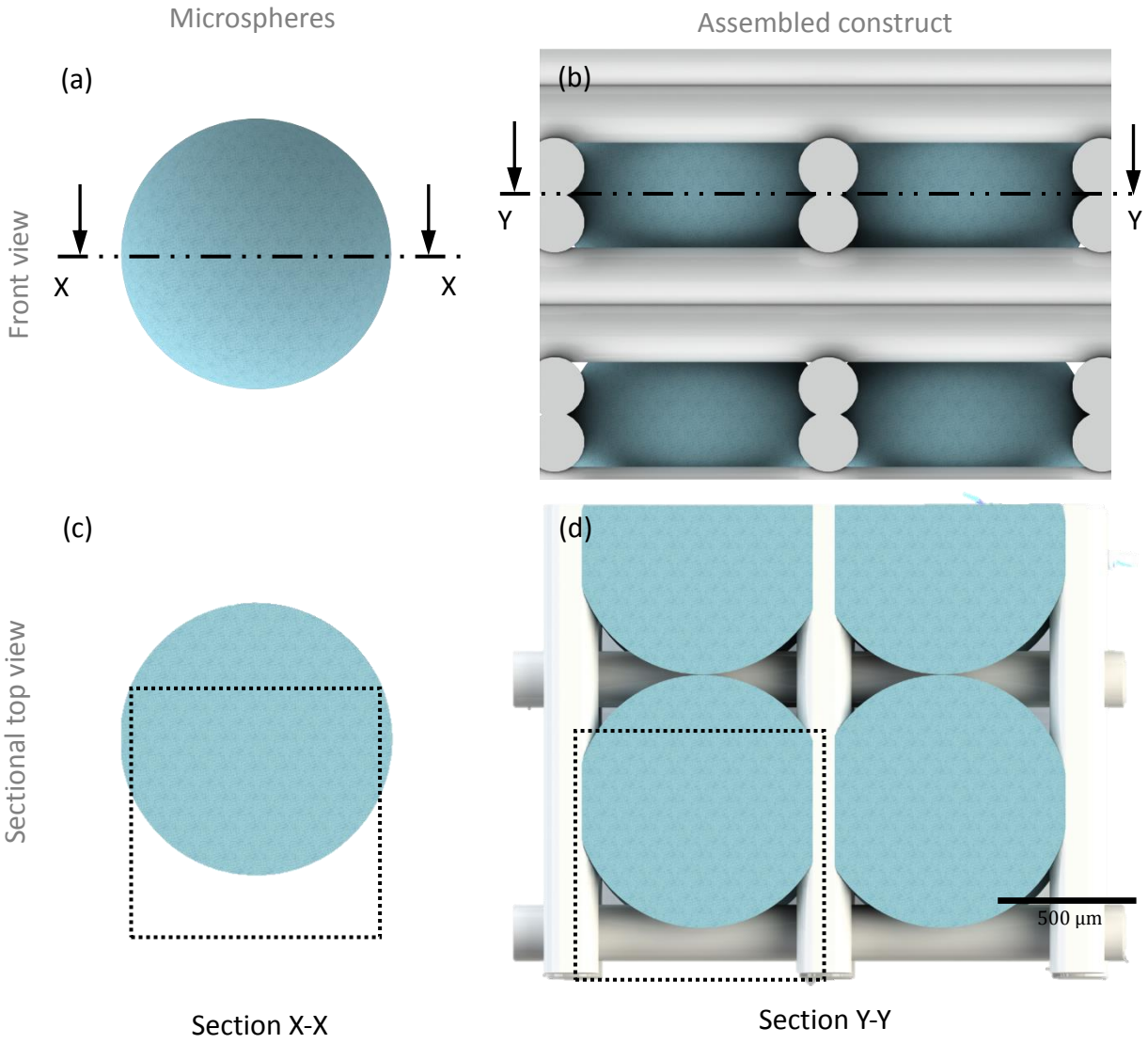

Figure 7-2. Rendered images of front view of the (a) microspheres and (b) assembled construct showing the plane at which the cryosection was performed (X-X in the microsphere and Y-Y in the assembled construct) and the sectional top view of the (c) microsphere and (d) assembled construct. The dotted rectangle shows the approximate region imaged for the immunofluorescence staining.

7.3.15 Statistical analysis

Data was presented graphically as mean ± standard deviation. Data were analysed using GraphPad Prism v.6.0. Statistical analysis was performed using 1-way ANOVA or 2-way ANOVA (if required Tukey's multiple comparisons test) or paired t-test, with $p<0.05$ set as a criterion for statistical significance.

7.4 Results

7.4.1 Microsphere fabrication

For validation of the automated tissue bioassembly system, Ø1 mm microspheres of regular size and shape were required. The requirement for Ø1 mm tissue units has been discussed and shown in Chapter 4. This subsection describes the fabrication of cancer cell-laden GelMA microspheres to meet these desired requirements along with a consistent number of encapsulated cells in the microspheres. The viability and proliferation of the cells in the microspheres was also investigated.

7.4.1.1 Size distribution of fabricated cell-laden microspheres

SKOV3, HFF and co-culture microspheres were successfully fabricated with the microfluidic device. For the purpose of initial validation, the automated tissue assembly system was designed for optimal handling of Ø1 mm sized tissue units. Therefore, microspheres with a uniform size distribution of Ø1 mm was essential for the efficient handling of the microspheres by the automated tissue assembly system. The size distribution of the microspheres is plotted in Figure 7-3.

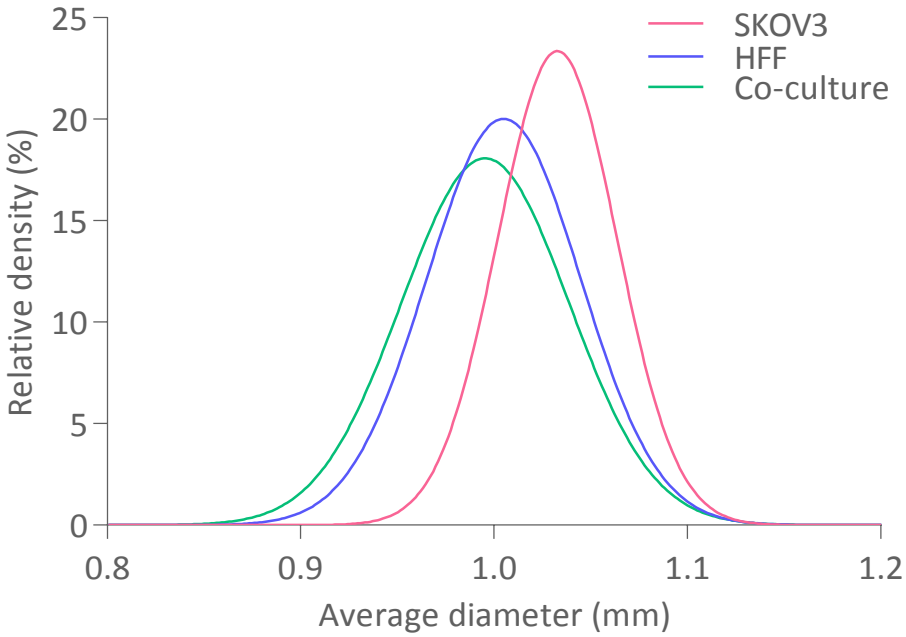

Figure 7-3. Size (average diameter of the microspheres) distribution curves of (a) SKOV3 (b) HFF and (c) co-culture encapsulated microspheres in 10% GelMA visible light crosslinked microspheres.

The average diameter (Table 7-1) of the microspheres encapsulated with different cell types varied from 0.995 mm to 1.015 mm. There was also no significant difference (p>0.05) between the average diameter (Table 7-1) of the SKOV3, HFF or co-culture encapsulated microspheres. The coefficient of variation reveals that the dispersion in microsphere size is low and that the microfluidics process adopted is able to fabricate microspheres in large quantity and with a very accurate and uniform size distribution.

Table 7-1. Average diameter (mm) and coefficient of variation for different types of cells encapsulated in microspheres.

Cells	SKOV3	HFF	Co-culture
Average diameter (mm)	1.015 ± 0.054	0.996 ± 0.042	0.995 ± 0.045
Coefficient of variation	0.054	0.043	0.0455

[a] Distribution plotted in Figure 7-3.
[b] n=50
[c] *No significant difference (p>0.05) between microspheres of different cell types*.
[d] *Statistical analysis: 1-way ANOVA.*

7.4.1.2 DNA content – microspheres

After fabricating the microspheres, the number of cells per microsphere (Table 7-2) was determined for day 0 to confirm that the variation in the cells per microspheres was low. The determined average cell number for the specific cell types varied from 5610 to 6168 cells per microsphere and there was no significant difference (p>0.05) in the cells per microsphere for SKOV3, HFF or co-culture microspheres. The coefficient of variation affirms that the variation in the cells per microsphere between the samples was low. This shows that with the micro-fluidic system, it is possible to fabricate microspheres in a high-throughput fashion with consistent cell number per microspheres irrespective of cell type.

Table 7-2. Cells per microsphere after fabrication (day 0).

Cells	SKOV3	HFF	Co-culture
Cells per microsphere	5828.63 ± 263.31	6168.01 ± 158.77	5609.71 ± 540.06
Coefficient of variation	0.045	0.025	0.096

[a] n=3
[b] *No significant difference (p>0.05) between microspheres of different cell types*.
[d] *Statistical analysis: 1-way ANOVA.*

7.4.1.3 Cell viability and proliferation of microspheres over time

The DNA content was quantified and live/dead assay was performed on the microspheres to assess if the cells were affected during the microsphere fabrication process and also to assess if the cells proliferated and remained viable over time in *in vitro* culture. The viability of the SKOV3, HFF, and co-culture encapsulated microspheres (Figure 7-4) on day 1, 7 and 12 was visualised from the live/dead fluorescence microscopy images. The day 1 images of the microspheres (Figure 7-4 a, b and c) do not indicate a noticeable number of dead cells suggesting that the viability of the cells were not affected during the microsphere fabrication process. In the SKOV3 and co-culture microspheres, a greater number of dead cells were visualised on day 7 and 12. However, in the HFF microspheres, fewer dead cells were observed. A thick cell monolayer formed around the co-culture microspheres on day 7 and 12 (Figure 7-4f and I). The monolayer had a tendency to easily separate from the day 12 microsphere sample during the washing step of the live/dead staining, hence the more non-uniform cell monolayer (i.e. monolayer still present only on certain parts of the microsphere after staining) around the microsphere (Figure 7-4 f).

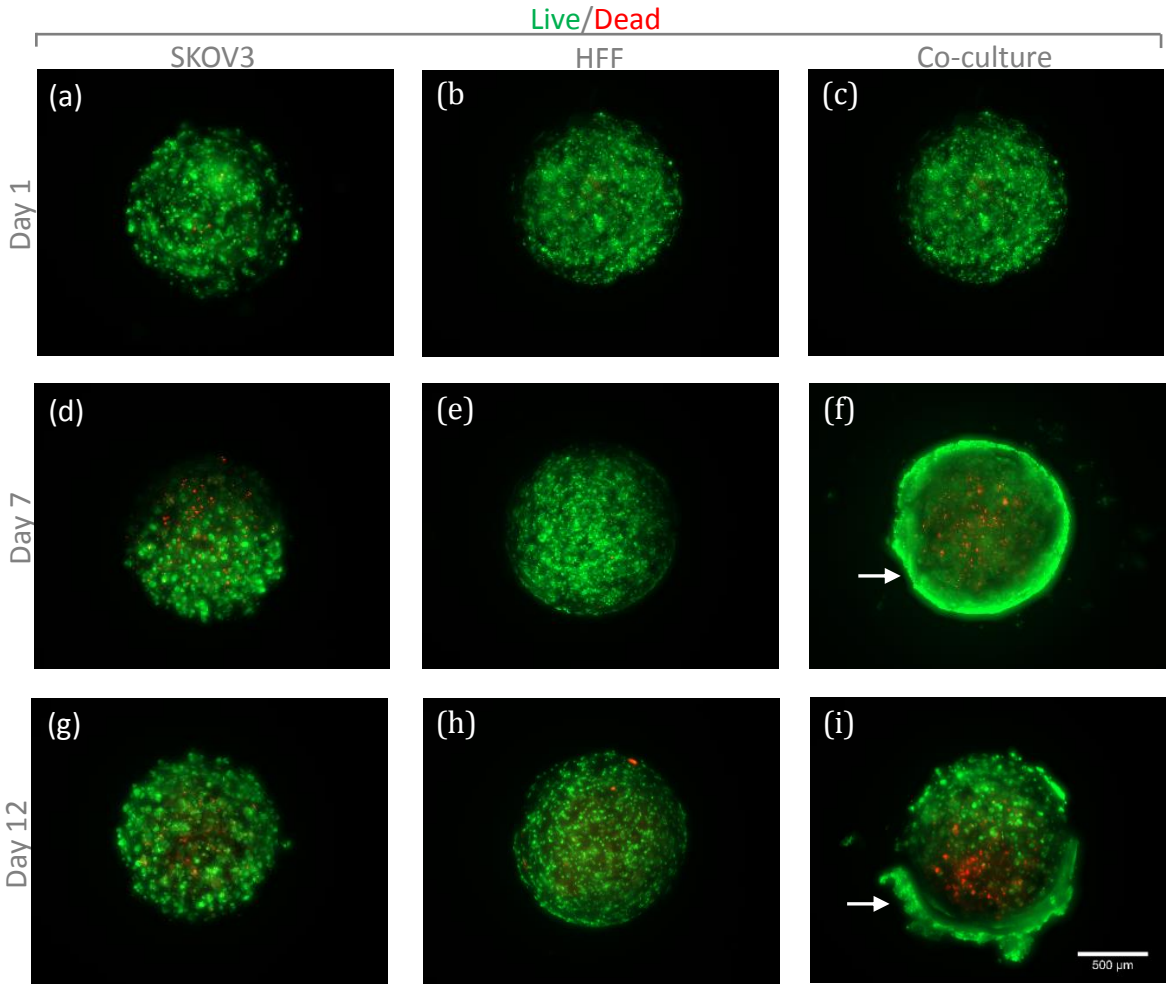

Figure 7-4. Fluorescence microscopy images of SKOV3, co-culture and HFF encapsulated microspheres on day 1, 7 and 12 stained with Calcein AM (live cells, green) and Propidium Iodide (dead cells, red). Arrows point to the monolayer. *Scale bar = 500 µm for all images.* For higher magnification image see Appendix 7.A.

The n-fold change in DNA content for SKOV3, HFF and co-culture microspheres cultured up to day 12 is shown in Figure 7-5. There was a significant difference (p<0.05) between the n-fold change in DNA content from day 0 to 12 in all the samples (SKOV3 - 1.75 ± 0.34, HFF - 1.02 ± 0.07, co-culture - 4.53 ± 0.73 fold increase). There were no significant changes (p>0.05) in DNA content of HFF microspheres over time (constant across time), indicating no proliferation. However, there was a significant increase (p<0.05) in DNA between day 0 and 12 (1.75 ± 0.34 fold increase) for the SKOV3 microspheres suggesting that the cells proliferated. Similarly with the co-culture microspheres, a significant increase in DNA content

(p<0.05) was observed from day 0 to day 12 (4.53 ± 0.73 fold increase), which was at a much higher level compared to the SKOV3 microspheres suggesting a higher proliferation rate. This observation suggested that there might be a paracrine signalling effect between both HFF and SKOV3 when co-cultured to promote cell proliferation.

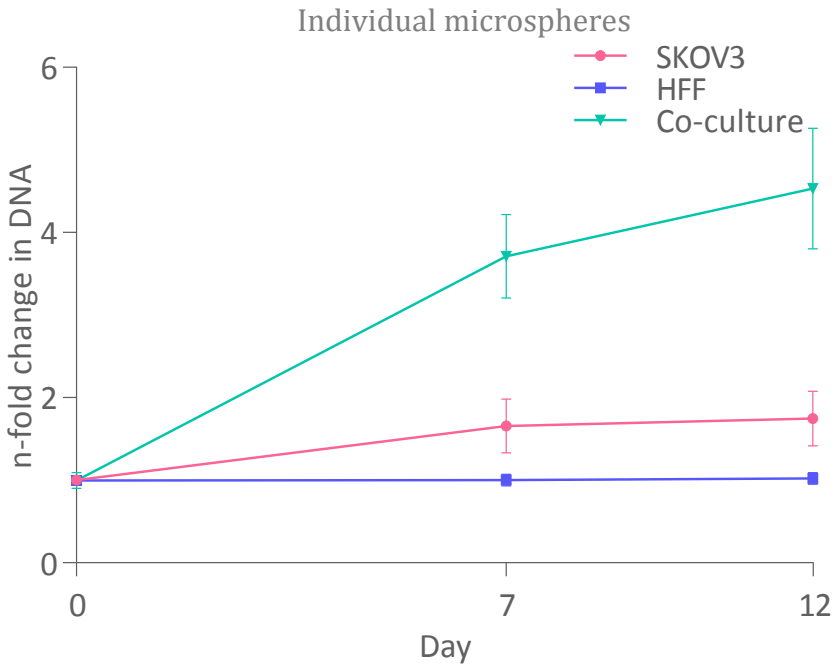

Figure 7-5. n-fold change in DNA content (n=3) for SKOV3, HFF and co-culture individually cultured microspheres measured on Day 0, 7 and 12.

7.4.2 Cancer construct bioassembly

In this subsection, we report the capacity of the prototype automated bioassembly system to viably handle and assemble the fabricated cancer cell-laden hydrogel microspheres into a construct.

7.4.2.1 Reliability and efficiency of microsphere singularisation

The efficiency of singularisation ($n=100$) (see Chapter 4, Figure 4-3) was determined for the SKOV3, HFF and co-culture microspheres and is listed in Table 7-3. The efficiency of singularisation for the microspheres varied from 93% to 97% depending on the specific cell type. The main causes of singularisation failure included the release of 2 microspheres at a time or a microsphere being sucked into the vacuum pressure port. If a singularisation failure has occurred and the device has failed to release a microsphere, the singularisation cycle can be repeated. If a

blockage has occurred, the device can be purged with fluid to dislodge the blocking microsphere and clear the bioassembly system after which normal operation of the device can be continued. None of the singularisation failures were critical to prevent further operation of the device.

Table 7-3. The efficiency of singularisation for microspheres encapsulated with cells.

Cells	SKOV3	HFF	Co-culture
Singularisation efficiency	97 ± 4.83%	95 ± 5.27%	93 ± 6.75%

[a] n=100.

7.4.2.2 Efficiency of microsphere insertion

The efficiency of successful microsphere insertion into the scaffold was ascertained to be 92.19 ± 9.3% (n=8 scaffolds, 64 microspheres). After the insertion process for a layer, the scaffold was visually scrutinized by the user for pores without microspheres after the microsphere insertion process for each layer. Next, the microsphere insertion process was repeated for the pores without microspheres and the scaffold was completely filled as designed.

7.4.2.3 Viability of assembled construct

During the 3D plotting process, the temperature in the thermoplastic print head was approximately 200°C. Even though the extruded fibre cools down quickly, we had to ascertain whether the molten polymer being plotted on the first layer of assembled construct during the layer-by-layer plotting did not affect the viability of the microspheres. Likewise, we had to determine that the handling of the microspheres by the automated bioassembly system did not affect the viability of the microspheres.

Cancer constructs were assembled using the automated tissue bioassembly system with co-culture microspheres via the layer-by-layer approach and were compared for viability with the manually assembled construct. Visual inspection of the live/dead fluorescence microscopy images (Figure 7-6) of the manually assembled construct and the construct assembled using the assembly system showed no obvious differences. The results from the AlamarBlue® assay (Figure 7-7)

supported this observation as there was no significant difference (*p>0.05*) in the percentage of AlamarBlue® reduced between the manually assembled construct (60.93 ± 1.62%) and the construct assembled using the automated tissue assembly system (58.59 ± 2.10%).

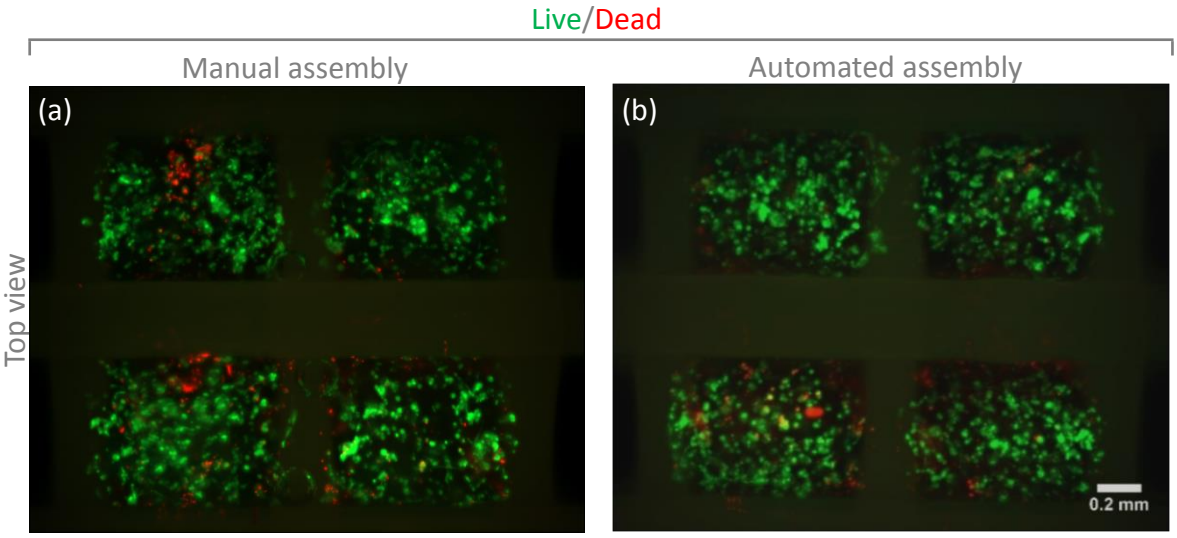

Figure 7-6. Fluorescence microscopy images of (a) manually assembled construct and a (b) construct assembled using the automated tissue assembly system inserted with microspheres encapsulated with (SKOV3:HFF 75:25) stained with Calcein AM (live cells, green) and Propidium Iodide (dead cells, red). *Scale bar = 0.2 mm for all images.*

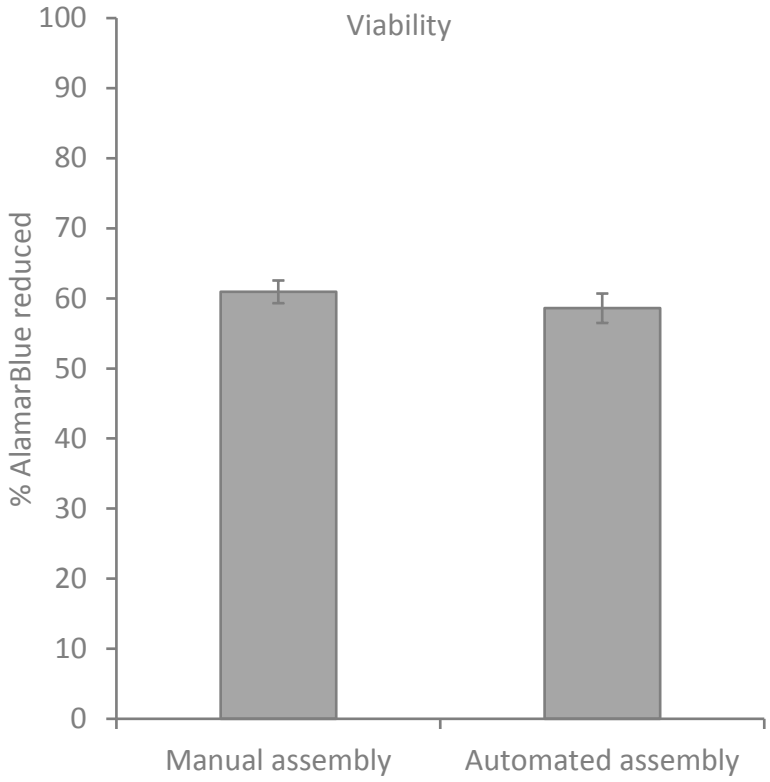

Figure 7-7**.** Percentage of AlamarBlue reduced to determine the viability of the manually assembled construct and the construct assembled using the automated system with cancer cell (SKOV3:HFF 75:25) encapsulated microspheres. The data is presented as mean ± SD (*n=4*). *No significant difference (p>0.05). Statistical analysis: 1-way ANOVA.*

7.4.2.4 Viability of assembled constructs over time

Live/dead assay was performed to assess the viability of the assembled construct cultured *in vitro*. The viability of the constructs assembled with SKOV3, HFF and co-culture microspheres (Figure 7-8) was visualised from the live/dead fluorescence microscopy images on day 1, 7 and 12. There were very few dead cells observed in the SKOV3 and co-culture assembled constructs on day 1 (Figure 7-8 a and c), however on day 7 (Figure 7-8 d and f) and 12 (Figure 7-8 g and i), a considerably greater number of dead cells was visualised. In the HFF assembled constructs (Figure 7-8 b, e and h), a fewer number of dead cells was observed over time. Similar to the co-culture microspheres (Figure 7-4 f and I), an uneven cell monolayer was observed on the SKOV3 and co-culture assembled constructs on day

7 (Figure 7-8 d and f) and 12 (Figure 7-8 g and i), and in addition, the cells appeared to proliferate on the scaffold fibres. As in the case of the microspheres, the monolayer in the assembled construct had a tendency to separate from the construct during the washing step of the live/dead staining.

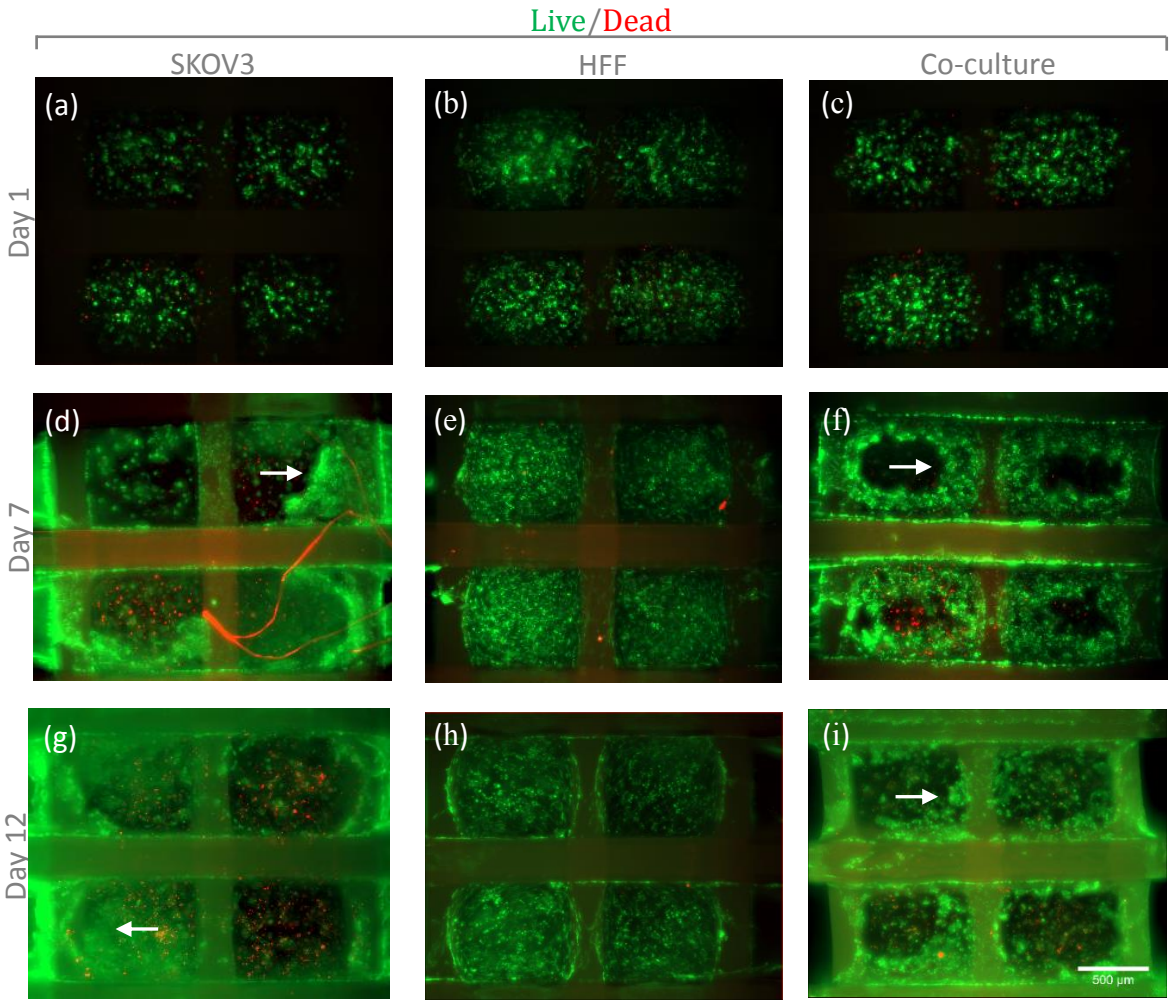

Figure 7-8. Fluorescence microscopy images of SKOV3, assembled constructs and HFF on day 1, 7 and 12 stained with Calcein AM (live cells, green) and Propidium Iodide (dead cells, red). Arrows point to the monolayer. *Scale bar = 500 µm for all images.*

7.4.2.5 Cell distribution in co-culture microspheres and assembled construct

The SKOV3 and HFF cells were labelled with Qtracker 800 and 655 respectively and the co-culture (SKOV3:HFF 75:25) microspheres and assembled constructs were fabricated and cultured. See Appendix 7.A for sectioned fluorescence microscope images of the microspheres and assembled construct on day 1 and 12 of culture. The visual inspection revealed that the intensity of the samples was less

intense on day 12 compared to day 1. The reduction of the Qtracker signal from day 1 to 12 could possibly be due to the proliferation of cells which led to a lower number of fluorophores per cell resulting in a fainter fluorescence signal. The low intensity made the tracking of the labelled cells challenging. However, close examination of the day 12 images suggested no particular redistribution of the two cells types either in the microspheres or in the assembled construct.

7.4.3 Drug response

In this subsection, the response of cells in 2D, individual microspheres and engineered cancer constructs were assessed with varying concentrations of doxorubicin. Doxorubicin is a clinically relevant anticancer drug used to treat a range of tumours including ovarian cancer and is often used in combination chemotherapy [46-48]. Dividing or cycling cells are preferentially targeted by doxorubicin [49].

7.4.3.1 Chemosensitivity test

Cells in 2D, microspheres and the assembled constructs were exposed to doxorubicin for 4 days to evaluate the anticancer activity of the drug *in vitro* and their dose-response curves are plotted in Figure 7-9. The accurate IC_{50} estimation requires a sufficient number of values in the upper and lower plateau region of the dose-response curves [50]. A maximum drug concentration of 10 μM for the experiment was selected based on the value of 3.75 μM reported for the peak concentration of free doxorubicin available to act on the cells in clinical chemotherapy [51]. However, the dose-response curves of the assembled constructs (Figure 7-9 c) did not achieve a lower plateau region. Moreover, the lowest value of the percentage growth control values were just slightly below 50% of growth control (SKOV3 – 37.38 ± 1.96% (at 10 μM), HFF – 37.98 ± 4.90% (at 1 μM), and co-culture – 41.36 ± 2.65% (at 10 μM)), unlike the cells in 2D (Figure 7-9 a) and microspheres (Figure 7-9 b), making the IC_{50} estimation for the assembled constructs less accurate. Nevertheless, the estimated IC_{50} values based on the available dose-response curves were used for comparative purposes among the different models.

It was observed that for cells cultured in 2D, HFF had the highest IC_{50} value (0.16 μM) compared to SKOV3s (0.05 μM) or co-culture (0.08 μM) samples (Table 7-4). However, when the cells are encapsulated in microspheres, the co-culture

microspheres had the highest IC_{50} value (0.29 µM), followed by HFF (0.18 µM) and SKOV3 (0.15 µM) microspheres. A similar trend was observed in the assembled constructs, where the co-culture samples had a much higher IC_{50} value (5.56 µM), compared to HFF (3.81 µM) and SKOV3 (2.41 µM). Comparison between all the different models (2D, microspheres, assembled constructs) revealed a general trend where the IC_{50} values (Table 7-4) were the lowest for cells in 2D, slightly higher for the microspheres (1-4 fold increase compared to cells in 2D) and highest for the assembled constructs (48-70 fold increase compared to cells in 2D, 16-21 fold increase compared to microspheres). The higher drug resistance of the assembled constructs compared to microspheres highlights the significance of a larger more complex assembled 3D construct model compared to a smaller microsphere model or 2D model and could potentially be more efficient and reliable drug screening model. Likewise, the cell-dependent response of the 3D models accentuates the need for complex co-culture 3D models.

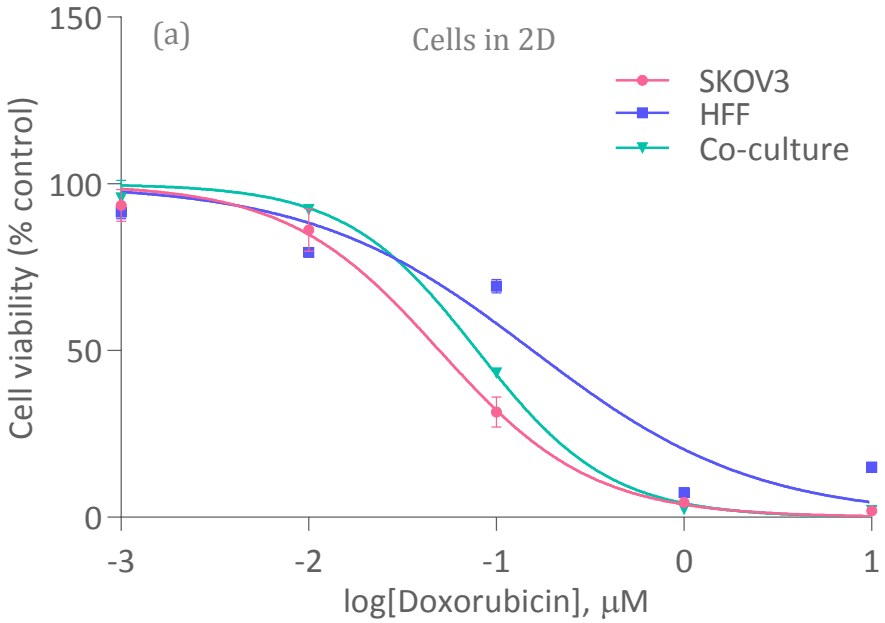

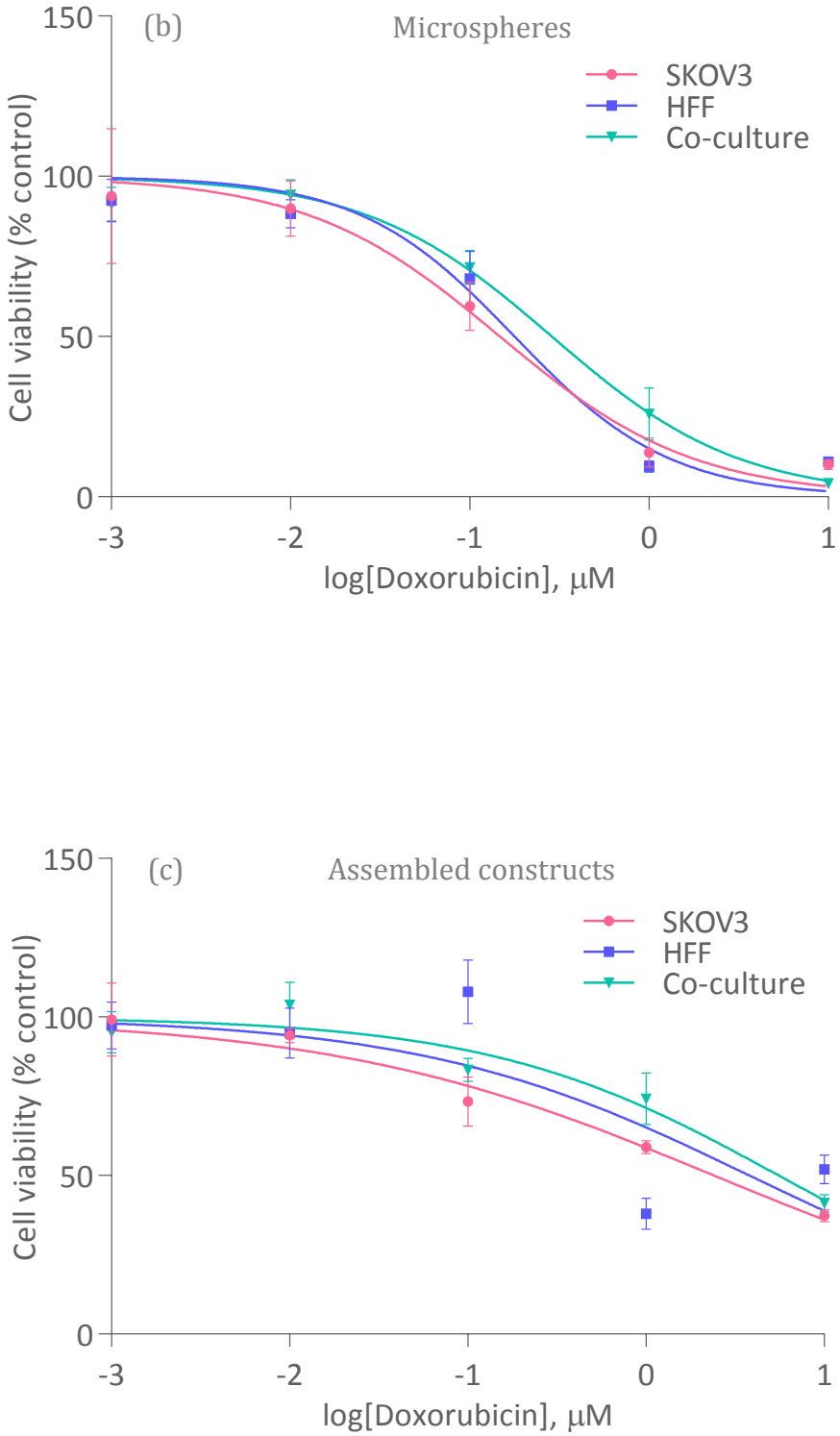

Figure 7-9. Dose-response curves for doxorubicin for (a) cells in a 2D (b) microspheres (c) assembled constructs. The response was for SKOV3, HFF, and co-culture cells measured after 4 days of exposure to the drug. *(n=4)*

Table 7-4. Chemosensitivity of doxorubicin.

Cells	IC50 (μM)			Fold change in IC50		
	2D	Microsphere	Assembled construct	Microsphere/ 2D	Assembled construct/ microsphere	Assembled construct/ 2D
SKOV3	0.05	0.15	2.41	2.96	16.33	48.32
HFF	0.16	0.18	3.81	1.14	21.41	24.32
Co-culture	0.08	0.29	5.56	3.63	19.34	70.14

[a] Data obtained from Figure 7-9.

The DNA content expressed in percentage of control against drug concentration for the microspheres is shown in Figure 7-10. The trend of decreasing DNA content normalised to control with increasing drug concentration is similar to the dose-response curve (Figure 7-9 b). In the SKOV3 and co-culture microspheres, there was significant decrease ($p<0.05$) in normalised DNA content from 0.01 (SKOV3 - 77.48 ± 25.28%, co-culture - 72.40 ± 26.52%) to 0.1 μM (SKOV3 - 36.20 ± 4.09%, co-culture - 33.99 ± 2.22%) concentration of drug. With the HFF microspheres, there was a lag in the reduction of normalised DNA content with increasing drug concentration compared to SKOV3 and co-culture microspheres and the significant decrease ($p<0.05$) in DNA content was seen from 0.1 (85.01 ± 11.19%) to 1 μM (11.03 ± 1.78%) of concentration of drug. There was also a significant difference in normalised DNA content at 0.001 μM between the HFF (96.40 ± 13.16%) and co-culture (69.76 ± 12.10%) microspheres.

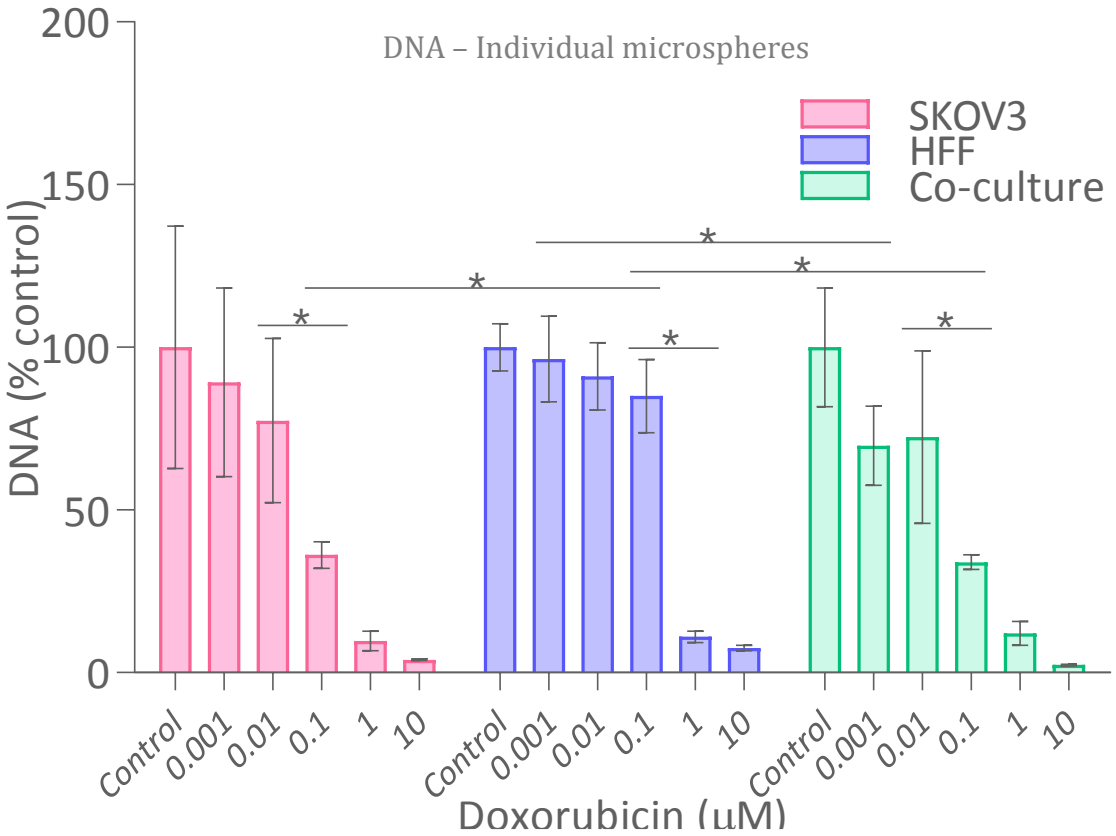

Figure 7-10. Doxorubicin dose dependent DNA content normalised to no drug control for SKOV3, HFF and co-culture individual microspheres measured after 4 days of exposure to the drug. The data is presented as mean ± SD (*n=6*). **Significant differences between columns are below the ends of each line (p<0.05). Statistical analysis: 2-way ANOVA.*

7.4.3.2 Histology and immunofluorescence

Immunofluorescence staining for Ki67, γ-H2AX and Hoechst 33342 were performed on cryosections of SKOV3, HFF, co-culture microspheres and assembled cancer constructs after the chemosensitivity test.

From the Hoechst 33342 staining, a cell monolayer can be observed around the periphery of the SKOV3 (Figure 7-11 a) and co-culture (Figure 7-11 i) microspheres and SKOV3 (Figure 7-11 c) and co-culture (Figure 7-11 k) assembled construct as indicated by the arrow in the images, but not in the HFF microspheres (Figure 7-11 e) or HFF assembled constructs (Figure 7-11 g). The non-uniform monolayer seen in the samples with the monolayer (especially the control co-culture assembled construct (Figure 7-11 k)) was due to the tendency of the monolayer around the samples to easily separate and move. Although the monolayer was visible in the

live/dead staining of the co-culture microsphere (Figure 7-4 i), the monolayer on the SKOV3 microsphere (Figure 7-4 a) was not obvious and observable from the day 12 live/dead staining compared to the sectioned Hoechst 33342 staining of the SKOV3 microsphere (Figure 7-11 a).

Interestingly a higher Ki67 expression was not specifically observed in the monolayer on the surface of the SKOV3 (Figure 7-11 a and b), co-culture (Figure 7-11 i and j) microspheres, and SKOV3 (Figure 7-11 c and d) and co-culture (Figure 7-11 k and l) assembled construct, but proportionally a higher number of cells expressing Ki67 was observed in cells within the microspheres and assembled constructs. Ki67 protein is a nuclear marker that is strictly associated with cell proliferation and is present in all active phases of the cell cycle and exclusively not present in the G_0 phase or the quiescent state [52, 53].

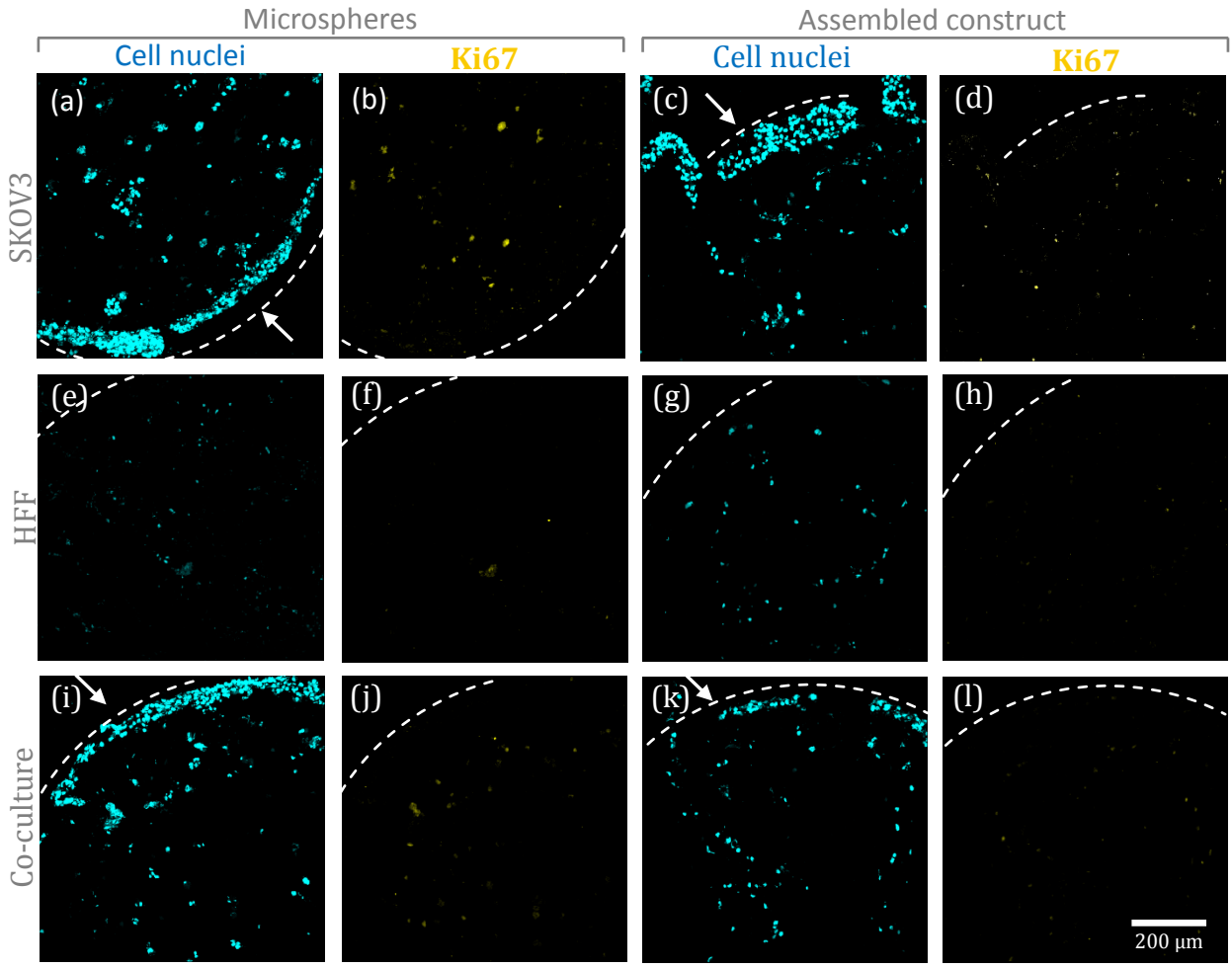

Figure 7-11. Immunofluorescence staining for Ki67 (yellow) and Hoechst 33342 (cell nuclei, blue) imaged using a confocal microscope for SKOV3, HFF co-culture microspheres and assembled construct for no drug control. Arrows point to the monolayer and the dotted lines represent the outer edge of the sample. *Scale bar = 200 µm for all images.* See Appendix 7.A for higher magnification images and other concentrations of drug.

Doxorubicin causes double-strand breaks in DNA which correlates with the drug cytotoxicity [54]. These double-stranded breaks in DNA causes the phosphorylation of H2AX which is a highly amplified response [55, 56]. The pixel count of γ-H2AX expressed in percentage of Hoechst 33342 for SKOV3, HFF and co-culture microspheres and assembled construct exposed to different concentrations of the drug are shown in Figure 7-12. The pixel count of γ-H2AX expressed in percentage of Hoechst 33342 (see Figure 7-12) confirmed a significantly higher ($p<0.05$) expression of γ-H2AX in all 3D models at 0.1 µM (SKOV3 microspheres - 35.52 ± 9.98%, HFF microspheres - 32.75 ± 2.87%, co-culture microspheres - 46.31

± 4.92%, SKOV3 assembled construct - 42.91 ± 3.02%, HFF assembled construct - 35.85 ± 3.50%, co-culture assembled construct - 35.03 ± 5.86%) compared to no drug control and lower concentrations of drug (at 0.01 μM; SKOV3 microspheres - 2.14 ± 0.74%, HFF microspheres - 11.97 ± 3.50%, co-culture microspheres - 10.46 ± 3.20%, SKOV3 assembled construct - 6.43 ± 0.55%, HFF assembled construct - 12.37 ± 3.90%, co-culture assembled construct - 22.72 ± 5.76%). The immunofluorescence staining for γ-H2AX and Hoechst 33342 staining for selected concentration of drugs (for drug control, 0.1 μM and 1 μM) for microspheres and assembled construct is shown in Figure 7-13 and Figure 7-14 respectively. From the visualisation of the immunofluorescence staining for γ-H2AX and Hoechst 33342 staining it can be observed that the proportion of cells expressing γ-H2AX is higher at 0.1 μM concentration of drug for all 3D models.

At 1 μM of doxorubicin, the Hoechst 33342 staining and also γ-H2AX expression was observed only in the SKOV3 (Figure 7-14 c and f) and co-culture (Figure 7-14 o and s) assembled constructs and the staining was negligible in the SKOV3 (Figure 7-13 c and f) and co-culture (Figure 7-13 o and s) microspheres and in the HFF microsphere (Figure 7-13 i and l) and assembled construct (Figure 7-14 i and l). The pixel count of γ-H2AX expressed in percentage of Hoechst 33342 (Figure 7-12) was therefore only plotted for the SKOV3 and co-culture assembled constructs at a drug concentration of 1 μM, as the very low value of pixel count might lead to erroneous values. The proportion of cells that expressed γ-H2AX in the SKOV3 (Figure 7-14 c and f) and co-culture (Figure 7-14 o and s) assembled constructs at 1 μM of the drug was visualised to be high. The pixel count of γ-H2AX expressed in percentage of Hoechst 33342 (Figure 7-12) suggested a significantly higher ($p<0.05$) expression of γ-H2AX in the SKOV3 and co-culture assembled constructs at 1 μM (SKOV3 assembled construct – 56.72 ± 5.32%, co-culture assembled construct - 65.22 ± 5.40%) compared to 0.1 μM (SKOV3 assembled construct - 42.91 ± 3.02%, co-culture assembled construct - 35.03 ± 5.86%). With an increasing drug concentration, the monolayer around the SKOV3 and co-culture 3D models reduced (see Figure 7-13 a, b, c, m, n and o, Figure 7-14 a, b, c, m, n and o, and Appendix 7.A) demonstrating the chemotherapeutic effect of the drug on monolayer.

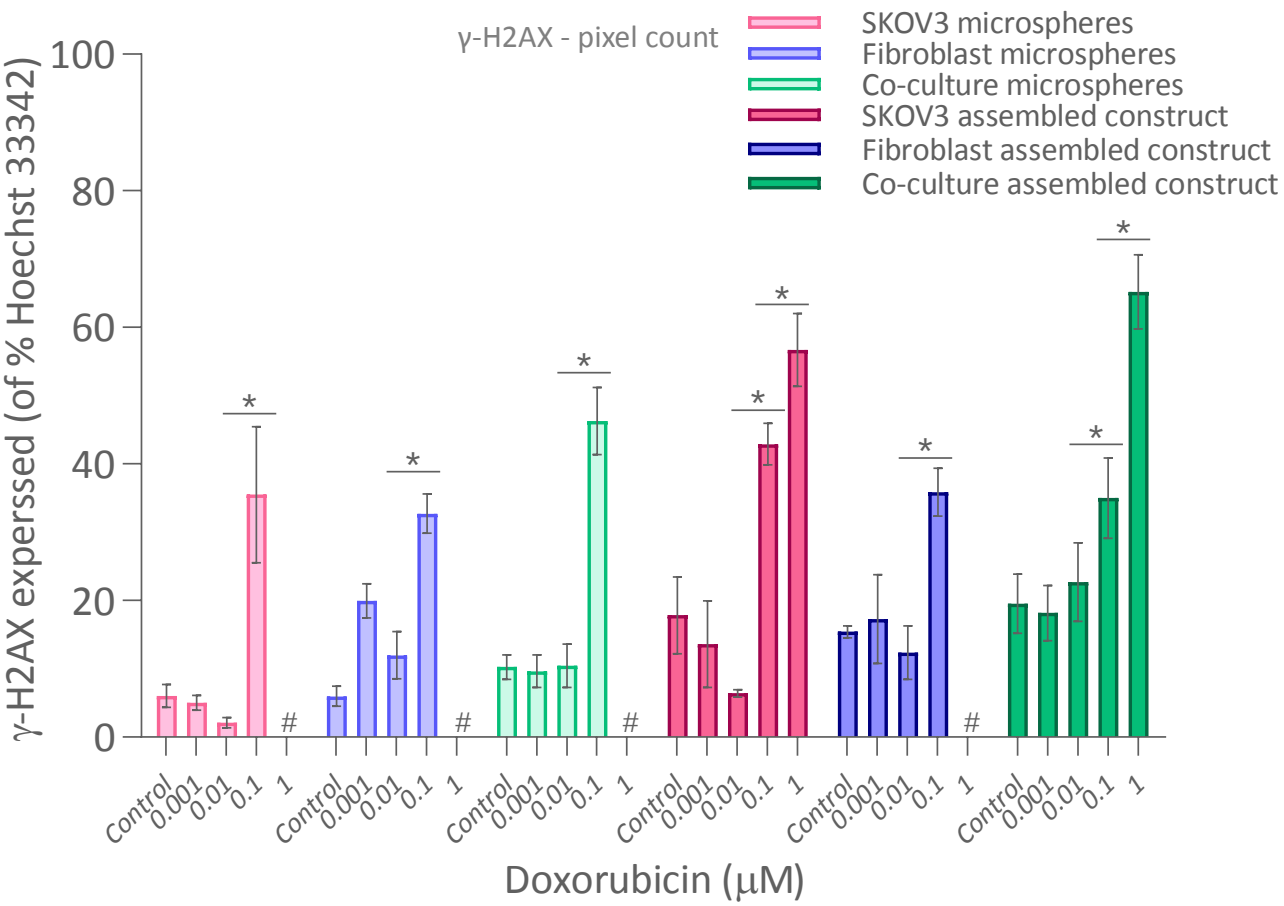

Figure 7-12. Pixel count of γ-H2AX expressed in percentage of Hoechst 33342 for SKOV3, HFF and co-culture (SKOV3:HFF 75:25) microspheres and assembled construct for no drug control, 0.001 μM, 0.01 μM, 0.1 μM and 1 μM concentration of doxorubicin. Data obtained from Figures 7.A-vi to 7.A-xi, Appendix 7.A. The data is presented as mean ± SD (*n=4*). **Significant differences between columns are below the ends of each line (p<0.05). #the values were not determined at 1 μM for these samples as the Hoechst 33342 staining was negligible. (n=3)*

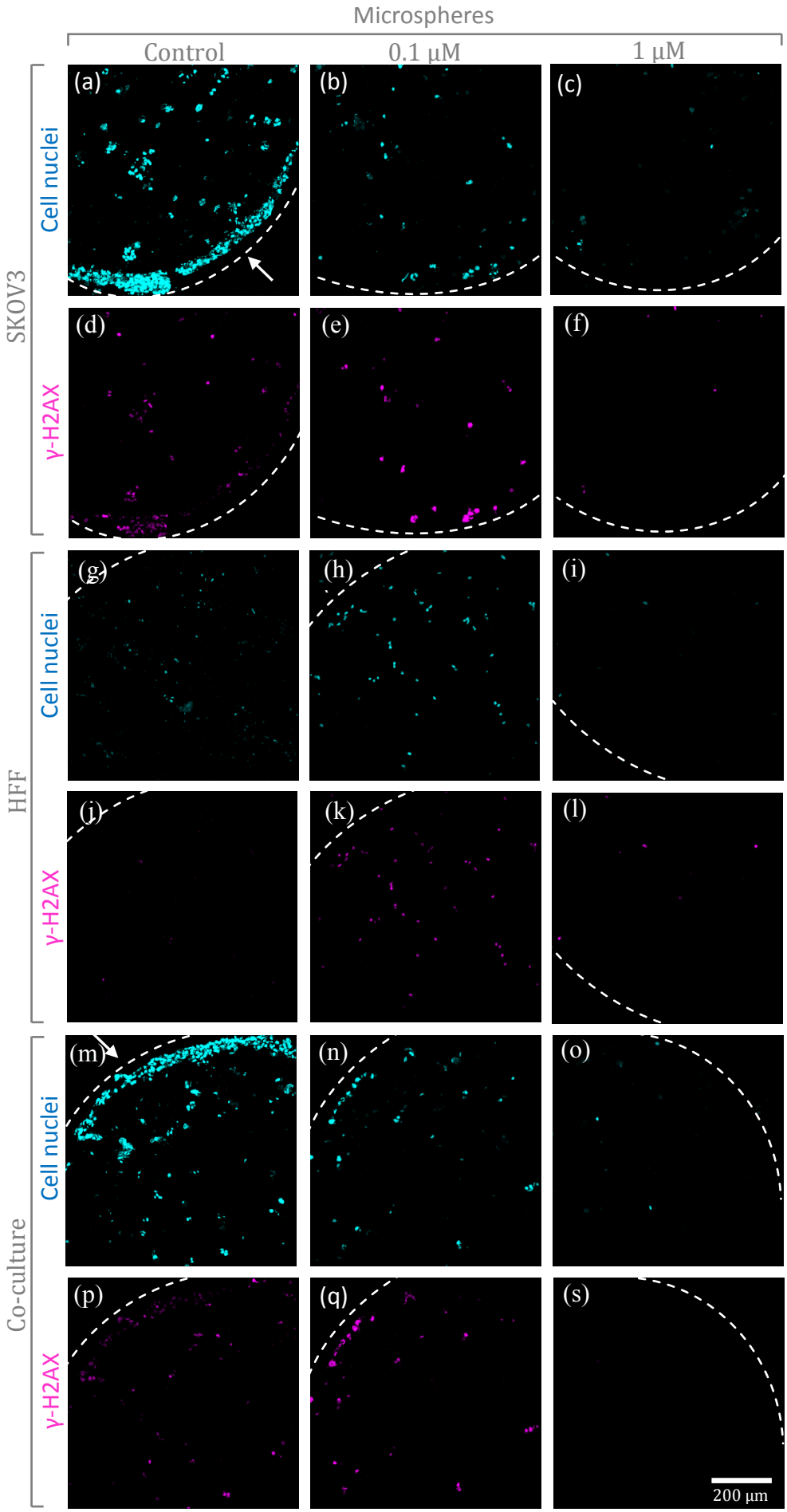

Figure 7-13. Immunofluorescence staining for γ-H2AX (magenta) and Hoechst 33342 (cell nuclei, blue) imaged using a confocal microscope for SKOV3, HFF and co-culture (SKOV3:HFF 75:25) microspheres for no drug control, 0.1 µM and 1 µM concentration of doxorubicin. The dotted line represent the outer edge of the sample. *Scale bar = 200 µm for all images.* See Appendix 7.A for higher magnification images other concentrations of drug.

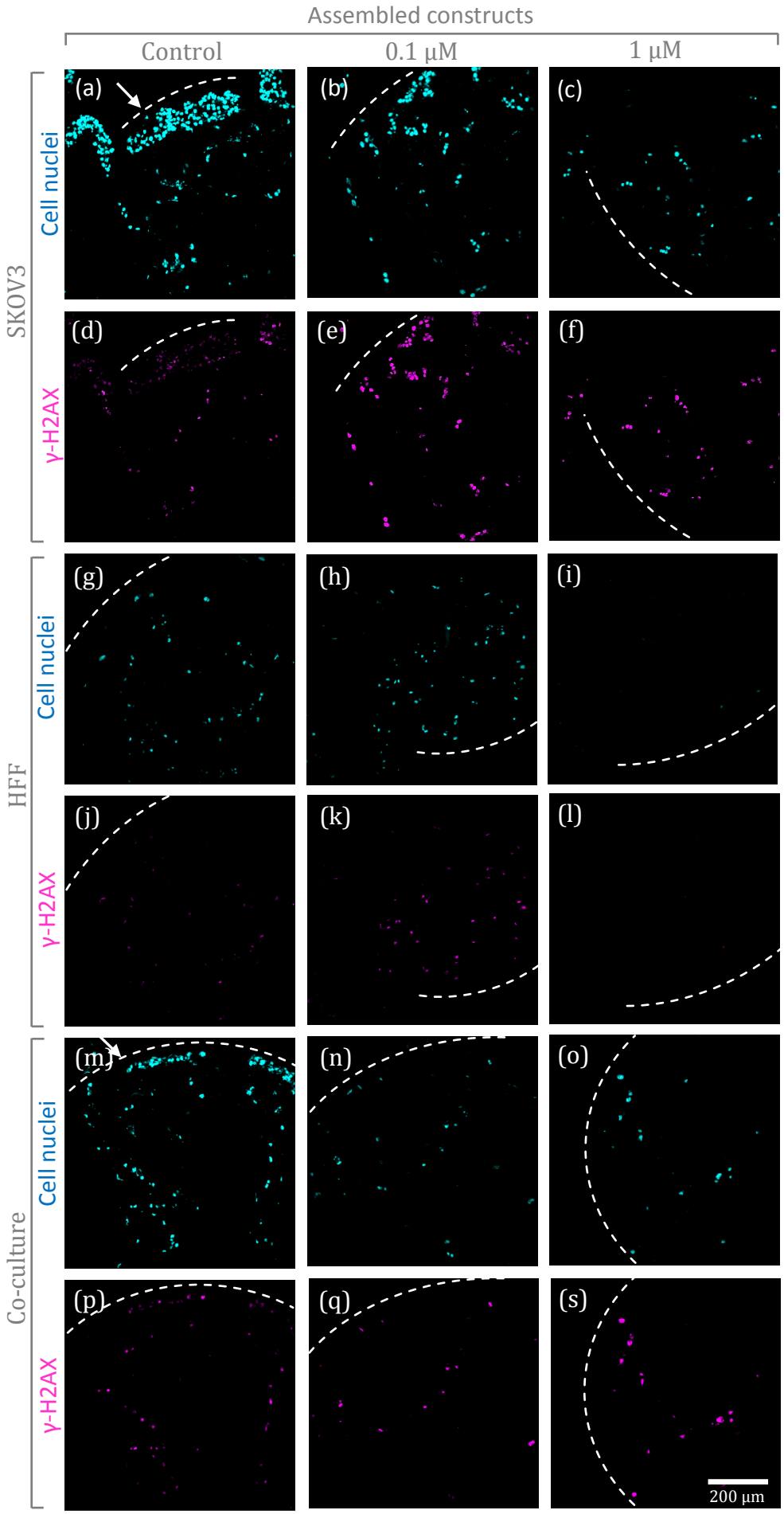

Figure 7-14. Immunofluorescence staining for γ-H2AX (magenta) and Hoechst 33342 (cell, nuclei, blue) imaged using a confocal microscope for SKOV3, HFF and co-culture (SKOV3:HFF 75:25) assembled constructs for no drug control, 0.1 μM and 1 μM concentration of doxorubicin. The dotted line represent the outer edge of the sample. *Scale bar = 200 μm for all images.* See Appendix 7.A for higher magnification images other concentrations of drug.

7.5 Discussion

We biofabricated an *in vitro* 3D cancer model assembled with cell-laden hydrogel microspheres. The cancer construct was manufactured using a bottom-up or modular assembly based tissue engineering strategy which focuses on the assembly of cancer cell-laden micro-scale tissue units or modules (i.e. microspheres) into a larger macro-scale object (i.e. cancer construct) [57, 58]. Bottom-up approaches offer potential advantage in recreating the micro-architectural features of native tissues [40]. As many native tissues consist of repeating functional units, it is logical to go down the path of assembling smaller tissue modules to fabricate a larger tissue [40]. Utilising the prototype automated bioassembly system that we built, cancer constructs were successfully assembled without affecting the viability of the individual subunits. The developed flexible prototype automated bioassembly system was proven to reliably and efficiently handle the microspheres by tweaking the system's soft parameters and did not inflict any adverse effects by handling the microspheres or assembling the construct. Large constructs of complex architecture based on mathematical models or anatomical models can be fabricated using the layer-by-layer strategy that we have employed.

Previously, we created an *in vitro* 3D cancer model assembled with cell-only micro-tissues using a modular assembly based approach (see Chapter 6). The innate problem with the micro-tissue based model was that the manual or automated tissue bioassembly is possible with only compact micro-tissues and not all cell types form compact micro-tissues thereby limiting its application to a narrow range of cells types [7-10]. To overcome this, we alternatively encapsulated the cells in a GelMA hydrogel microsphere and assembled the microspheres to fabricate an *in vitro* 3D cancer model.

Apart from enabling us to fabricate microspheres with cells that tend not to form compact micro-tissues, encapsulating cells in a hydrogel eliminates a rate limiting step by reducing the time required for the formation of a robust compact micro-tissues. Depending on the method and cell type used, the formation of a micro-tissue can range from 24 hours to several days [59]. Micro-tissues had to be cultured for up to 7 days to obtain the relevant compactness to be compatible with

the automated bioassembly system (see chapter 6). On the other hand, fabricating the microspheres (approximately 500 microspheres) when the microfluidic system has already been setup takes less than an hour. Moreover, about 6,000 cells per microsphere is required at a concentration of 10 million cells/ml, whereas the fabrication of Ø1 mm micro-tissues required 120,000 cells. Therefore, the number of cells required to fabricate each modular subunit for the microsphere model was reduced by approximately 20 fold compared to the micro-tissue model. The above-stated advantages would also allow shorter experimental timelines and a reduction in man-power and resources, adding to the cost and complexity of the screening process.

In resorting to a microfluidic system to fabricate the microspheres, a large number of uniform microspheres can be quickly and conveniently fabricated. Studies by Young *et al.* demonstrated that the microspheres exhibit a smooth, spherical morphology, and was due to the fact that in an emulsion the surface tension causes the droplets to contract into a sphere to minimise the surface energy [25, 60].

By using GelMA, the mechanical properties, pore size, degradation rates, and swelling ratio can be tuned by varying either the polymer or photo-initiator concentrations, the degree of functionalization or the light exposure time to suit a desired cell type or application [61, 62]. Previous studies in the literature have utilised a UV light photopolymerisation system, however, we adopted a visible light photopolymerisation system in this study which has been shown to result in significantly greater cell viability compared to UV polymerisation [43]. One drawback of using GelMA, however, is that the gel needs to be optimised (i.e. stiffness) for different cell types and applications and there could be batch-to-batch variations in GelMA making it impractical to correlate work from different lab groups [61, 63].

Fibroblasts are known to have a well-recognised role in cancer development and progression, making their presence critical in a cancer model [64]. Our data suggest that the co-culture of SKOV3 and fibroblasts (HFFs) has a synergistic proliferation effect on each other, where the observed significant increase in DNA content over time of the co-culture microspheres was greater than the SKOV3 only

microspheres, or the HFF only microspheres (Figure 7-5). This is in line with most *in vitro* co-culture studies that have shown that the presence of fibroblasts can promote proliferation of tumour cells [65-68]. However, there is some controversy in the literature and the inhibition of tumour cells by fibroblasts has also been reported [69, 70]. Early stages of tumour development and dissemination are thought to be represented by cancer models co-cultured with normal (non-cancer-associated) fibroblasts rather than the co-culturing cancer cells with cancer-associated fibroblasts (CAF), which tend to reflect later stages of tumour development [9]. Cancer-associated fibroblasts are activated fibroblasts associated with malignant tumours and are known to enhance tumour progression [71-73]. Our model could be made to signify early or late-stage cancer model depending on whether the model is co-cultured with normal or cancer-associated fibroblast.

To track the distribution of the SKOV3 and HFF cells and to investigate any self-assembly or arrangement of cells in the co-culture microspheres and assembled construct, the cells were labelled with Qtracker (photostable fluorophores). Qtracker has previously been shown to not affect cell viability and photo-bleaches very little over time [74, 75]. However, the loss of the cell labelling Qtracker nanoparticles over the culture time made it challenging to precisely track the position of fibroblasts and SKOV3 cells in the co-culture microspheres and assembled constructs. Nevertheless, the faint signal from the confocal images did not suggest any specific arrangement (see Appendix 7.A). We could also not conclude if the predominantly proliferating cells in the co-culture microspheres and assembled construct were SKOV3s or HFFs. However, live/dead images of the co-culture microspheres and assembled constructs resembled the SKOV3 microspheres and assembled constructs rather than the HFF microspheres or assembled constructs, potentially suggesting that the prominently proliferating cells on the surface of the microspheres and assembled construct could be SKOV3s. The loss in the Qtracker signal could possibly be due to the proliferation of cells which resulted in a reduction in the number of fluorophores per cell and therefore a fainter fluorescence signal. Alternatively, in future experiments, the cells could potentially be labelled with green fluorescent protein (GFP) and red fluorescent protein (RFP) to track the cells [74].

During our preliminary experiments, the 5% wt GelMA SKOV3 and co-culture microspheres that were fabricated and cultured *in vitro* degraded over time (data not presented). It is well known that matrix metalloproteinases (MMPs) play an important role in ECM remodelling, tumour invasion and proliferation and GelMA contains MMP degradable motifs [62, 76]. The secretion of MMPs by SKOV3s in the SKOV3 and co-culture microspheres could have resulted in the degradation of the 5% wt GelMA microspheres [77]. However with the stiffer 10% wt GelMA hydrogel microspheres and assembled constructs which we utilised for this experiment, the MMPs produced during the culture time was probably not sufficient to completely degrade the hydrogels.

The proliferation of cells in the hydrogel is known to be affected by the hydrogel type, stiffness and cell type [5, 78, 79]. An increase in DNA content (Figure 7-5) was observed over time (day 0 to 12) in the SKOV3 and co-culture microspheres but not in the HFF microspheres. As GelMA contains MMP degradable motifs and SKOV3s produces MMPs, the MMPs produced by the SKOV3s could be aiding the remodelling of the hydrogel and aiding cell proliferation [62, 76, 77]. It has been previously shown that with cell spheroids in a hydrogel, their proliferation in a MMP-sensitive hydrogel was enhanced compared to a MMP-insensitive hydrogel suggesting the importance of the role of MMPs and hydrogel type in cell proliferation [5]. The proliferation rate of cells in a hydrogels is also dependent on the stiffness of the hydrogels. With SKOV3s, the proliferation rate has been reported to be higher in less stiff hydrogels and contrastingly with fibroblasts, it has been reported to be higher in more stiff hydrogels [5, 79]. The observed increase in DNA content (Figure 7-5) over time (day 0 to 12) in the SKOV3 (Figure 7-11 a) and co-culture (Figure 7-11 i) microspheres also correlates in part with the formation of a monolayer around the microspheres which was not seen in the HFF microspheres (Figure 7-11 e). Interestingly, a higher Ki67 (marker for proliferation) expression was not specifically observed in the monolayer on the surface of the microspheres (Figure 7-11 b and j), but proportionally a higher number of cells expressing Ki67 was observed in cells within the microsphere. It has been shown that the fraction of cycling cells in a confluent monolayer culture is lesser than a subconfluent monolayer and this could be why a reduced Ki67 expression was observed in the confluent like monolayer around the microspheres [80].

In this study, the efficacy of cancer drug on cells in 2D, microspheres and assembled constructs was evaluated by exposing the models to varying concentrations of doxorubicin. The observed higher chemoresistance seen in 3D models as opposed to the 2D model (1-4 fold increase in chemoresistance for microspheres and 48-70 fold increase in chemoresistance for assembled constructs compared to cells in 2D, Table 7-4) is in agreement with other studies and could be possibly attributed to many reasons [81-84]. The proportion of proliferating cancer cells in 2D is higher than that in 3D hydrogels [85]. As doxorubicin preferentially targets proliferating cells, the lower proportion of proliferating cells in the 3D hydrogel would lead to a lower proportion of doxorubicin-induced double-stranded breaks in the DNA resulting in a higher chemoresistance [86]. The hydrogel itself can act as an extracellular matrix diffusion barrier to the drug and decrease the penetration of the drug which would result in an increased chemoresistance of the cells in the 3D hydrogel [87]. As the ECM in tumours *in vivo* can be mimicked by the hydrogel and proliferation rate in tumours *in vivo* is comparable to the 3D models than cells in 2D, *in vitro* 3D models offer greater potential for recapitulating the *in vivo* tumour environment [85, 88]. The increased chemoresistance in 3D models compared to the cells in 2D monolayer could also be due to hypoxia, the difference in gene and protein expression, cell-cell interaction, and increased extracellular matrix components [31, 89-92].

The response of the cells to the drug was noted to be dependent on the cell type. In the 2D model, HFFs (IC_{50} - 0.16 μM) was the most drug-resistant, followed by the co-culture (IC_{50} - 0.08 μM) and SKOV3 (IC_{50} - 0.05 μM) the least (Table 7-4). Fibroblasts are known to be less responsive to doxorubicin compared to cancer cells and an increased chemoresistance of cancer cells when co-cultured with fibroblasts via the secretion of growth factors, cytokines, and MMP has previously been reported [93]. However, with the microspheres and assembled constructs, co-culture microspheres (IC_{50} - 0.29 μM) and assembled constructs (IC_{50} - 5.56 μM) were the most resistant, followed by the HFF microspheres (IC_{50} - 0.18 μM) and assembled constructs (IC_{50} - 5.56 μM) and the SKOV3 microspheres (IC_{50} - 0.15 μM) and assembled constructs (IC_{50} - 2.41 μM) the least. Along with being aided by the protective nature of fibroblasts in the co-culture microspheres and assembled

constructs, the higher chemoresistance of the co-culture models could also be due to the presence of the confluent like monolayer of cells around the hydrogel with a low fraction of cycling cells (Figure 7-11 i, j, k and l) making the models less effective against the anticancer drug [93-95]. Also, the high density of the monolayer could cause a decreased penetration of the drug thereby assisting in the higher chemoresistance [96]. The monolayer observed in the periphery of the microspheres and assembled constructs could potentially reflect the vascularized regions of tumours *in vivo* where there is better delivery of oxygen, nutrients and drug to the tumour cells [31]. The monolayer could also represent the superficially invasive nature of ovarian cancer cells that disseminate in within the peritoneal cavity [97]. The observed significant decrease ($p<0.05$) in normalised DNA content (Figure 7-10) was from 0.01 to 0.1 μM concentration of drug in the SKOV3 and co-culture microspheres, but in the HFF microspheres it was at a higher drug concentration which was from 0.1 to 1 μM. Although the observed trend where a decrease in normalised DNA content correlated with the trend for the IC_{50} values for the HFF (0.18 μM) and SKOV3 (0.15 μM) microspheres, the trend was not in line with the IC_{50} values for co-culture (0.29 μM) and HFF (0.18 μM) microspheres. The SKOV3 (Figure 7-13 a, b and c) and co-culture (Figure 7-13 m, n and o) microspheres have a monolayer which reduced with increasing drug concentration resulting in a greater decrease of DNA content in the samples treated with the drug compared to the control. However, in the HFF microspheres (Figure 7-13), as the monolayer is not present, the decrease in DNA content was less pronounced in the samples treated with the drug compared to the control. This, along with the cell-dependent response of the cells to the drug, could possibly be why the observed significant decrease in DNA content was at a higher drug concentration in the HFF microspheres compared to the co-culture or SKOV3 microspheres.

The assembled constructs were less vulnerable (16-21 fold increase in IC_{50} values compared to the microspheres, Table 7-4) to the anticancer drug compared to the individual microspheres and this could be attributed to many reasons. Likewise, at 1 μM concentration of the drug, in the SKOV3 and co-culture microspheres, negligible Hoechst 33342 staining could be observed, however in the SKOV3 and co-culture assembled constructs the Hoechst 33342 staining and also γ-H2AX expression could be visualised potentially suggesting the higher

chemoresistance of the microspheres compared the assembled construct. The hydrogel matrix as in the case of the ECM in tumours *in vivo* can slow down the movement of nutrients, drugs and oxygen resulting in a concentration gradient of these molecules [31, 87, 89, 91]. The reduced diffusion and increased concentration gradient of the anticancer drug towards the core in the larger assembled construct compared to the microspheres would mean that the effectiveness of the drug on the cells distal to the periphery to the construct would be compromised, resulting in the increased chemoresistance of the assembled construct compared to the microspheres [31, 89]. The size-dependent response is relevant to tumours *in vivo* (average ovarian cancer tumour size can range from 4.6 to 11.8 cm) as the treatment of tumours becomes more challenging with increasing tumour size [27, 29]. The higher chemoresistance of the larger assembled construct compared to the smaller microspheres accentuates the need for larger 3D models for the reliable screening of candidate anticancer drugs.

Native *in vivo* tumour tissues are composed of heterotypic cell types which include cancer stem cells [98], primary stem cells, fibroblasts [71], endothelial [99] and immune cells [100]. However, one drawback of the oncological model that we have fabricated is that it consisted of only ovarian cancer cells and fibroblasts, and creating a model analogous to an *in vivo* tumour would make the incorporation of other tumour cells types into the model necessary [101]. For example, the tumour models could also include a combination of microspheres fabricated from different types of cells which could also be either healthy or tumour origin cells to investigate and analyse the effect on targeted and non-targeted cells by the drug [101]. Likewise metastatic models can be fabricated, for example, microspheres encapsulated with tumour cells could potentially be assembled into a construct with microspheres encapsulated with bone cells to simulate osteolysis and bone invasion or with nerve cells to simulate tumour invasion of nerves [102, 103]. The liver plays an important role in drug metabolism, and models including hepatocyte encapsulated microspheres could be included to simulate drug and toxin metabolism [104, 105]. Furthermore, by utilising the deconstruction-reconstruction approach, complex tumours could be deconstructed to its individual basic cell type and a cancer model of varying complexity could be shaped. This would be beneficial in understanding both the individual components and collective components of a tumour as a whole

[101]. It is well known that the stroma plays an important role in the progress or inhibition of cancer [106]. The stroma consists of connective tissues, blood vessels, and inflammatory cells [107]. A biphasic construct with one phase containing the tumor cells and the other containing elements of the stroma could be potentially fabricated a 3D model that recapitulates the tumour-stroma interaction *in vivo*. The above described schemes for a 3D plotted tumour model could be easily fabricated in a desired predetermined arrangement using the automated tissue assembly system described herein.

Drug discovery is a costly process with a low success rate [108]. Presently, cost of developing a new drug is about US $ 2.6 billion and the probability that a candidate drug that enters Phase I trial would reach the market is just 8% [109, 110]. The monetary and ethical implications of a failed candidate drug is higher when they are narrowed down for animal testing and clinical trials on humans [111, 112]. It is crucial to accurately screen candidate drugs earlier during the drug discovery process to predict whether they would potentially fail or not in the later stages [111, 112]. Therefore, *in vitro* 3D oncological models that can reliably predict the outcomes of the candidate drugs have an increasingly significant part to play in drug screening [111, 112]. High-throughput screening (HTS) has been vital in biology and drug discovery and to be able to rapidly screen a large number of drugs in an industrial environment it is essential to be able to adapt the model for medium or high-throughput screening [1, 113]. To handle a large number of compounds being tested, laboratories employ robots and liquid handling devices to execute the high-throughput screening of candidate drugs in standard well-plate formats [114]. Our fluidic-based prototype automated tissue assembly system could serve as a blue print for developing a state-of-art industrial standard tissue handling system that can be integrated with liquid handling systems presently being used. Furthermore, the tumour model that we have developed could then be adopted to easily fabricate and produce large and complex custom tumour constructs in a high-throughput fashion using the automated assembly system for both *in vitro* and *in vivo* applications.

Frequently, high-throughput screening is carried out in cell spheroids of up to 200 μm in diameter, which is thought to be sufficient to simulate the 3D cell-cell and

cell-matrix interactions and approximate and 3D cancer environment [115-117]. However, micro-tissues greater than 500 μm in diameter have a pH, nutrient and waste removal gradient, become compact and compartmentalized and tend to show a more similar characteristics to *in vivo* solid tumours [118]. For this reason it is essential to be able to cater to a wide range of microsphere sizes and microspheres from 50-3000 μm have been previously fabricated [18, 25, 119, 120]. However, the automated tissue assembly system that we have developed can only efficiently handle microspheres of around 1 mm diameter. Consequently, to handle microsphere outside this range, the physical components (i.e. tubing singularisation chamber and injection nozzle, see chapter 3 and 4) and the soft parameters (i.e. valve timing, fluid pressure) of the automated tissue assembly system would have to be modified. Moreover, with the maturation of the system, laminar flow, surface tension, diffusion and fluidic resistance start influencing the system and the research and development of an alternative tissue assembly system that takes these factors into consideration becomes unavoidable [121].

An artificial tissue-specific environment that simulates the physiological environment *in vivo* can potentially be created in a bioreactor [122]. The development of a 96-format bioreactor is under progress in our lab and we intend to culture the developed tumour model in the bioreactor. An *in vitro* metastasis model could be designed and constructed by fabricating constructs of different tissue types and culturing them in interconnected wells through which media flows and the migration of cancer cells could be studied [3].

We envisage in the foreseeable future that the cancer model that we have developed could be tailored to create a personalised patient specific model to assess and screen potential drugs for treatment [98]. The response of different anticancer drugs to normal and tumour cells of the patient could be used to predict the treatment efficacy and the impact on the quality of life of the patient.

The possibility of specifically arranging cell-laden microspheres or self-assembled micro-tissues of different types of cells in a scaffold to potentially recreate the complex organisation and architecture of native tissues and organs in a medium or high-throughput fashion is appealing. We predict that our modular

assembly based cancer model and tissue assembly system can cater to spectrum of applications especially in translational research in cancer and drug discovery.

7.6 Conclusions

We have described an innovative method for 3D Bioassembly of cell-laden microspheres for biofabricating cancer constructs for application as an *in vitro* 3D cancer model. This model can be used to assemble 3D constructs with cells types that do not form compact micro-tissues. We fabricated uniform cell-laden GelMA SKOV3, fibroblast and co-culture microspheres using the microfluidic system. The fabricated microspheres were Ø1mm and spherical so that they can be handled by the automated bioassembly system. With our prototype automated tissue assembly system, we successfully demonstrated the efficient and reliable handling of the co-culture microspheres and the layer-by-layer assembly of a construct without significantly affecting the viability of the cells. The response of the cells in 2D, individual microsphere and the assembled construct to an anticancer drug - doxorubicin was quantified. 3D Bioassembled constructs showed the highest chemoresistance, whereas cells in 2D showed lowest resistance and the microsphere showed an intermediate resistance. A cell-dependent response was also observed. A broad range of high-throughput format based application in cancer biology research and in drug screening can be catered to by employing the malleable technology and flexible cancer model that we have developed.

7.7 References

1. Pampaloni F, Reynaud EG, Stelzer EH. The third dimension bridges the gap between cell culture and live tissue. Nature Reviews Molecular Cell Biology. 2007;8(10):839-845.
2. Kim JB. Three-dimensional tissue culture models in cancer biology. in Seminars in Cancer Biology. 2005. Elsevier.
3. Haycock JW. 3D cell culture: a review of current approaches and techniques. 3D Cell Culture: Methods and Protocols. 2011:1-15.
4. Kim JB, Stein R, O'Hare MJ. Three-dimensional *in vitro* tissue culture models of breast cancer- a review. Breast Cancer Research and Treatment. 2004;85(3):281-91.
5. Loessner D, Stok KS, Lutolf MP, Hutmacher DW, Clements JA, Rizzi SC. Bioengineered 3D platform to explore cell–ECM interactions and drug resistance of epithelial ovarian cancer cells. Biomaterials. 2010;31(32):8494-8506.
6. Pang Y, Montagne K, Shinohara M, Komori K, Sakai Y. Liver tissue engineering based on aggregate assembly: efficient formation of endothelialized rat hepatocyte aggregates and their immobilization with biodegradable fibresThis work was presented at the International Conference on Biofabrication (Toyama, Japan, 6–8 October 2011). Biofabrication. 2012;4(4):045004.
7. Ivascu A, Kubbies M. Rapid generation of single-tumor spheroids for high-throughput cell function and toxicity analysis. Journal of biomolecular screening. 2006;11(8):922-932.
8. Ivascu A, Kubbies M. Diversity of cell-mediated adhesions in breast cancer spheroids. International Journal of Oncology. 2007;31(6):1403-1414.
9. Kunz-Schughart LA, Heyder P, Schroeder J, Knuechel R. A heterologous 3-D coculture model of breast tumor cells and fibroblasts to study tumor-associated fibroblast differentiation. Experimental Cell Research. 2001;266(1):74-86.
10. Carlsson J, Nilsson K, Westermark B, Ponten J, Sundstrom C, Larsson E, Bergh J, Pahlman S, Busch C, Collins VP. Formation and growth of multicellular spheroids of human origin. International Journal of Cancer. 1983;31(5):523-33.
11. Nafea EH, Poole-Warren LA, Martens PJ. Structural and permeability characterization of biosynthetic PVA hydrogels designed for cell-based therapy. Journal of Biomaterials Science, Polymer Edition. 2014;25(16):1771-1790.
12. Nicodemus GD, Bryant SJ. Cell encapsulation in biodegradable hydrogels for tissue engineering applications. Tissue Engineering Part B: Reviews. 2008;14(2):149-165.
13. Kleinman HK, Martin GR. Matrigel: basement membrane matrix with biological activity. in Seminars in Cancer Biology. 2005. Elsevier.
14. Liu J, Tan Y, Zhang H, Zhang Y, Xu P, Chen J, Poh Y-C, Tang K, Wang N, Huang B. Soft fibrin gels promote selection and growth of tumorigenic cells. Nature materials. 2012;11(8):734-741.
15. Talukdar S, Kundu SC. Engineered 3D silk-based metastasis models: interactions between human breast adenocarcinoma, mesenchymal stem cells and osteoblast-like Cells. Advanced Functional Materials. 2013;23(42):5249-5260.
16. Nichol JW, Koshy ST, Bae H, Hwang CM, Yamanlar S, Khademhosseini A. Cell-laden microengineered gelatin methacrylate hydrogels. Biomaterials. 2010;31(21):5536-5544.

17. Schuurman W, Levett PA, Pot MW, van Weeren PR, Dhert WJ, Hutmacher DW, Melchels FP, Klein TJ, Malda J. Gelatin-Methacrylamide Hydrogels as Potential Biomaterials for Fabrication of Tissue-Engineered Cartilage Constructs. Macromolecular Bioscience. 2013;13(5):551-561.
18. Young CJ, Poole-Warren LA, Martens PJ. Combining submerged electrospray and UV photopolymerization for production of synthetic hydrogel microspheres for cell encapsulation. Biotechnology and Bioengineering. 2012;109(6):1561-1570.
19. Lacik I, Briššová M, Anilkumar A, Powers A, Wang T. New capsule with tailored properties for the encapsulation of living cells. Journal of Biomedical Materials Research. 1998;39(1):52-60.
20. Cohen S, Yoshioka T, Lucarelli M, Hwang LH, Langer R. Controlled delivery systems for proteins based on poly (lactic/glycolic acid) microspheres. Pharmaceutical Research. 1991;8(6):713-720.
21. Prüße U, Dalluhn J, Breford J, Vorlop KD. Production of spherical beads by JetCutting. Chemical Engineering & Technology. 2000;23(12):1105-1110.
22. Brandenberger HR, Widmer F. Immobilization of highly concentrated cell suspensions using the laminar jet breakup technique. Biotechnology Progress. 1999;15(3):366-372.
23. Bugarski B, Li Q, Goosen MF, Poncelet D, Neufeld RJ, Vunjak G. Electrostatic droplet generation: mechanism of polymer droplet formation. AIChE Journal. 1994;40(6):1026-1031.
24. Serra C, Berton N, Bouquey M, Prat L, Hadziioannou G. A predictive approach of the influence of the operating parameters on the size of polymer particles synthesized in a simplified microfluidic system. Langmuir. 2007;23(14):7745-7750.
25. Young C, Rozario K, Serra C, Poole-Warren L, Martens P. Poly (vinyl alcohol)-heparin biosynthetic microspheres produced by microfluidics and ultraviolet photopolymerisation. Biomicrofluidics. 2013;7(4):044109.
26. Khademhosseini A, Langer R. Microengineered hydrogels for tissue engineering. Biomaterials. 2007;28(34):5087-5092.
27. Grimer RJ. Size matters for sarcomas! The Annals of The Royal College of Surgeons of England. 2006;88(6):519-524.
28. Rosen PP, Saigo PE, Braun DW, Weathers E, Fracchia AA, Kinne DW. Axillary micro-and macrometastases in breast cancer: prognostic significance of tumor size. Annals of Surgery. 1981;194(5):585.
29. Horvath LE, Werner T, Boucher K, Jones K. The relationship between tumor size and stage in early versus advanced ovarian cancer. Medical Hypotheses. 2013;80(5):684-687.
30. Wartenberg M, Frey C, Diedershagen H, Ritgen J, Hescheler J, Sauer H. Development of an intrinsic P-glycoprotein-mediated doxorubicin resistance in quiescent cell layers of large, multicellular prostate tumor spheroids. International Journal of Cancer. 1998;75(6):855-863.
31. Minchinton AI, Tannock IF. Drug penetration in solid tumours. Nature Reviews Cancer. 2006;6(8):583-592.
32. Snyder J, Hamid Q, Wang C, Chang R, Emami K, Wu H, Sun W. Bioprinting cell-laden matrigel for radioprotection study of liver by pro-drug conversion in a dual-tissue microfluidic chip. Biofabrication. 2011;3(3):034112.

33. Zhao Y, Yao R, Ouyang L, Ding H, Zhang T, Zhang K, Cheng S, Sun W. Three-dimensional printing of Hela cells for cervical tumor model in vitro. Biofabrication. 2014;6(3):035001.
34. Zhou X, Zhou X, Liu C, Wang X. A 3D bioprinting liver tumor model for drug screening. World Journal of Pharmaceutical Sciences. 2016.
35. Leung BM, Sefton MV. A modular approach to cardiac tissue engineering. Tissue Engineering Part A. 2010;16(10):3207-3218.
36. McGuigan AP, Sefton MV. Vascularized organoid engineered by modular assembly enables blood perfusion. Proceedings of the National Academy of Sciences. 2006;103(31):11461-11466.
37. Du Y, Lo E, Ali S, Khademhosseini A. Directed assembly of cell-laden microgels for fabrication of 3D tissue constructs. Proceedings of the National Academy of Sciences. 2008;105(28):9522-9527.
38. Yeh J, Ling Y, Karp JM, Gantz J, Chandawarkar A, Eng G, Blumling J, 3rd, Langer R, Khademhosseini A. Micromolding of shape-controlled, harvestable cell-laden hydrogels. Biomaterials. 2006;27(31):5391-8.
39. Bruzewicz DA, McGuigan AP, Whitesides GM. Fabrication of a modular tissue construct in a microfluidic chip. Lab on a Chip. 2008;8(5):663-671.
40. Nichol JW, Khademhosseini A. Modular tissue engineering: engineering biological tissues from the bottom up. Soft Matter. 2009;5(7):1312-1319.
41. Van Den Bulcke AI, Bogdanov B, De Rooze N, Schacht EH, Cornelissen M, Berghmans H. Structural and Rheological Properties of Methacrylamide Modified Gelatin Hydrogels. Biomacromolecules. 2000;1(1):31-38.
42. Young C. Fabrication and characterisation of poly(vinyl alcohol) and heparin biosynthetic hydrogel microspheres for cell microencapsulation. in Graduate School of Biomedical Engineering, Faculty of Engineering University of New South Wales;2012.
43. Lim KS, Schon BS, Mekhileri NV, Brown GC, Chia CM, Prabakar S, Hooper GJ, Woodfield TB. New visible-light photoinitiating system for improved print fidelity in gelatin-based bioinks. ACS Biomaterials Science & Engineering. 2016;2(10):1752-1762.
44. Woodfield TB, Malda J, de Wijn J, Peters F, Riesle J, van Blitterswijk CA. Design of porous scaffolds for cartilage tissue engineering using a three-dimensional fiber-deposition technique. Biomaterials. 2004;25(18):4149-61.
45. Woodfield TBF, Guggenheim M, von Rechenberg B, Riesle J, van Blitterswijk CA, Wedler V. Rapid prototyping of anatomically shaped, tissue-engineered implants for restoring congruent articulating surfaces in small joints. Cell Proliferation. 2009;42(4):485-497.
46. Tacar O, Sriamornsak P, Dass CR. Doxorubicin: an update on anticancer molecular action, toxicity and novel drug delivery systems. Journal of Pharmacy and Pharmacology. 2013;65(2):157-170.
47. A'hern R, Gore M. Impact of doxorubicin on survival in advanced ovarian cancer. Journal of Clinical Oncology. 1995;13(3):726-732.
48. Aletti GD, Gallenberg MM, Cliby WA, Jatoi A, Hartmann LC. Current management strategies for ovarian cancer. in Mayo Clinic Proceedings. 2007. Elsevier.
49. Kim SH, Kim J. Lethal effect of adriamycin on the division cycle of HeLa cells. Cancer Research. 1972;32(2):323-325.

50. Sebaugh J. Guidelines for accurate EC50/IC50 estimation. Pharmaceutical Statistics. 2011;10(2):128-134.
51. Liu J, Zheng H, Tang M, Ryu Y-C, Wang X. A therapeutic dose of doxorubicin activates ubiquitin-proteasome system-mediated proteolysis by acting on both the ubiquitination apparatus and proteasome. American Journal of Physiology-Heart and Circulatory Physiology. 2008;295(6):H2541-H2550.
52. Scholzen T, Gerdes J. The Ki-67 protein: from the known and the unknown. Journal of Cellular Physiology. 2000;182(3):311-322.
53. Schlüter C, Duchrow M, Wohlenberg C, Becker M, Key G, Flad H-D, Gerdes J. The cell proliferation-associated antigen of antibody Ki-67: a very large, ubiquitous nuclear protein with numerous repeated elements, representing a new kind of cell cycle-maintaining proteins. The Journal of Cell Biology. 1993;123(3):513-522.
54. Banáth JP, Olive PL. Expression of phosphorylated histone H2AX as a surrogate of cell killing by drugs that create DNA double-strand breaks. Cancer Research. 2003;63(15):4347-4350.
55. Kuo LJ, Yang L-X. γ-H2AX-a novel biomarker for DNA double-strand breaks. In Vivo. 2008;22(3):305-309.
56. Pilch DR, Sedelnikova OA, Redon C, Celeste A, Nussenzweig A, Bonner WM. Characteristics of γ-H2AX foci at DNA double-strand breaks sites. Biochemistry and Cell Biology. 2003;81(3):123-129.
57. Elbert DL. Bottom-up tissue engineering. Current Opinion in Biotechnology. 2011;22(5):674-80.
58. Schon B, Hooper G, Woodfield T. Modular tissue assembly strategies for biofabrication of engineered cartilage. Annals of Biomedical Engineering. 2016:1-15.
59. Lin RZ, Chang HY. Recent advances in three-dimensional multicellular spheroid culture for biomedical research. Biotechnology Journal. 2008;3(9-10):1172-1184.
60. Okubo M, Ando M, Yamada A, Katsuta Y, Matsumoto T. Studies on suspension and emulsion. XLVII. Anomalous composite polymer emulsion particles with voids produced by seeded emulsion polymerization. Journal of Polymer Science: Polymer Letters Edition. 1981;19(3):143-147.
61. Loessner D, Meinert C, Kaemmerer E, Martine LC, Yue K, Levett PA, Klein TJ, Melchels FP, Khademhosseini A, Hutmacher DW. Functionalization, preparation and use of cell-laden gelatin methacryloyl-based hydrogels as modular tissue culture platforms. Nature protocols. 2016;11(4):727-746.
62. Yue K, Trujillo-de Santiago G, Alvarez MM, Tamayol A, Annabi N, Khademhosseini A. Synthesis, properties, and biomedical applications of gelatin methacryloyl (GelMA) hydrogels. Biomaterials. 2015;73:254-271.
63. Hutmacher DW. Biomaterials offer cancer research the third dimension. Nature materials. 2010;9(2):90-93.
64. Bhowmick NA, Neilson EG, Moses HL. Stromal fibroblasts in cancer initiation and progression. Nature. 2004;432(7015):332-337.
65. Gache C, Berthois Y, Cvitkovic E, Martin PM, Saez S. Differential regulation of normal and tumoral breast epithelial cell growth by fibroblasts and 1, 25-dihydroxyvitamin D3. Breast Cancer Research and Treatment. 1999;55(1):29-39.

66. Ryan M, Orr D, Horgan K. Fibroblast stimulation of breast cancer cell growth in a serum-free system. British Journal of Cancer. 1993;67(6):1268.
67. Van Roozendaal C, Van Ooijen B, Klijn J, Claassen C, Eggermont A, Henzen-Logmans S, Foekens J. Stromal influences on breast cancer cell growth. British Journal of Cancer. 1992;65(1):77.
68. Brouty-Boyé D, Mainguené C, Magnien V, Israel L, Beaupain R. Fibroblast-mediated differentiation in human breast carcinoma cells (MCF-7) grown as nodules *in vitro.* International Journal of Cancer. 1994;56(5):731-735.
69. Sadlonova A, Novak Z, Johnson MR, Bowe DB, Gault SR, Page GP, Thottassery JV, Welch DR, Frost AR. Breast fibroblasts modulate epithelial cell proliferation in three-dimensional *in vitro* co-culture. Breast Cancer Research. 2004;7(1):1.
70. Dong-Le Bourhis X, Berthois Y, Millot G, Degeorges A, Sylvi M, Martin P-M, Calvo F. Effect of stromal and epithelial cells derived from normal and tumorous breast tissue on the proliferation of human breast cancer cell lines in co-culture. International Journal of Cancer. 1997;71(1):42-48.
71. Kalluri R, Zeisberg M. Fibroblasts in cancer. Nature Reviews Cancer. 2006;6(5):392-401.
72. Olumi AF, Grossfeld GD, Hayward SW, Carroll PR, Tlsty TD, Cunha GR. Carcinoma-associated fibroblasts direct tumor progression of initiated human prostatic epithelium. Cancer Research. 1999;59(19):5002-5011.
73. Zhang Y, Tang H, Cai J, Zhang T, Guo J, Feng D, Wang Z. Ovarian cancer-associated fibroblasts contribute to epithelial ovarian carcinoma metastasis by promoting angiogenesis, lymphangiogenesis and tumor cell invasion. Cancer Letters. 2011;303(1):47-55.
74. Fotos JS, Koh JT, Galileo DS. Vital labeling, time-lapse microscopy, and quantitative motility analysis of C6 glioma tumor cells. Cancer Research. 2005;65(9 Supplement):1332-1332.
75. Shuman L, Dhurjati R, Krishnan V, Ning G, Vogler E, Mastro A. Use of Qtracker™ 655 to monitor the interaction of metastatic breast cancer cells with osteoblasts in co-culture. Cancer Research. 2007;67(9 Supplement):2805-2805.
76. Vu TH, Werb Z. Matrix metalloproteinases: effectors of development and normal physiology. Genes & Development. 2000;14(17):2123-2133.
77. Rabinovich A, Medina L, Piura B, Segal S, Huleihel M. Regulation of ovarian carcinoma SKOV-3 cell proliferation and secretion of MMPs by autocrine IL-6. Anticancer Research. 2007;27(1A):267-272.
78. Kaemmerer E, Melchels FP, Holzapfel BM, Meckel T, Hutmacher DW, Loessner D. Gelatine methacrylamide-based hydrogels: an alternative three-dimensional cancer cell culture system. Acta Biomaterialia. 2014;10(6):2551-2562.
79. Pandit V, Zuidema JM, Venuto KN, Macione J, Dai G, Gilbert RJ, Kotha SP. Evaluation of multifunctional polysaccharide hydrogels with varying stiffness for bone tissue engineering. Tissue Engineering Part A. 2013;19(21-22):2452-2463.
80. Endl E, Steinbach P, Knüchel R, Hofstädter F. Analysis of cell cycle-related Ki-67 and p120 expression by flow cytometric BrdUrd-Hoechst/7AAD and immunolabeling technique. Cytometry. 1997;29(3):233-241.
81. Dhiman HK, Ray AR, Panda AK. Three-dimensional chitosan scaffold-based MCF-7 cell culture for the determination of the cytotoxicity of tamoxifen. Biomaterials. 2005;26(9):979-986.

82. Kimlin LC, Casagrande G, Virador VM. In vitro three-dimensional (3D) models in cancer research: An update. Molecular Carcinogenesis. 2013;52(3):167-182.
83. Padrón JM, Peters GJ. Cytotoxicity of sphingoid marine compound analogs in mono-and multilayered solid tumor cell cultures. Investigational New Drugs. 2006;24(3):195-202.
84. Fischbach C, Chen R, Matsumoto T, Schmelzle T, Brugge JS, Polverini PJ, Mooney DJ. Engineering tumors with 3D scaffolds. Nature methods. 2007;4(10):855-860.
85. Chitcholtan K, Asselin E, Parent S, Sykes PH, Evans JJ. Differences in growth properties of endometrial cancer in three dimensional (3D) culture and 2D cell monolayer. Experimental Cell Research. 2013;319(1):75-87.
86. Chitcholtan K, Sykes PH, Evans JJ. The resistance of intracellular mediators to doxorubicin and cisplatin are distinct in 3D and 2D endometrial cancer. Journal of Translational Medicine. 2012;10(1):1.
87. Yip D, Cho CH. A multicellular 3D heterospheroid model of liver tumor and stromal cells in collagen gel for anti-cancer drug testing. Biochemical and biophysical research communications. 2013;433(3):327-332.
88. Tibbitt MW, Anseth KS. Hydrogels as extracellular matrix mimics for 3D cell culture. Biotechnology and Bioengineering. 2009;103(4):655-663.
89. Sutherland RM, Eddy HA, Bareham B, Reich K, Vanantwerp D. Resistance to adriamycin in multicellular spheroids. International Journal of Radiation Oncology* Biology* Physics. 1979;5(8):1225-1230.
90. Hamilton G. Multicellular spheroids as an in vitro tumor model. Cancer Letters. 1998;131(1):29-34.
91. Miller BE, Miller FR, Heppner GH. Factors affecting growth and drug sensitivity of mouse mammary tumor lines in collagen gel cultures. Cancer Research. 1985;45(9):4200-4205.
92. Edmondson R, Broglie JJ, Adcock AF, Yang L. Three-dimensional cell culture systems and their applications in drug discovery and cell-based biosensors. Assay and Drug Development Technologies. 2014;12(4):207-218.
93. Tiago M, de Oliveira EM, Brohem CA, Pennacchi PC, Paes RD, Haga RB, Campa A, de Moraes Barros SB, Smalley KS, Maria-Engler SS. Fibroblasts protect melanoma cells from the cytotoxic effects of doxorubicin. Tissue engineering Part A. 2014;20(17-18):2412-2421.
94. Fang Y, Sullivan R, Graham CH. Confluence-dependent resistance to doxorubicin in human MDA-MB-231 breast carcinoma cells requires hypoxia-inducible factor-1 activity. Experimental Cell Research. 2007;313(5):867-877.
95. Gomez-Roman N, Sahasrabudhe NM, McGregor F, Chalmers AJ, Cassidy J, Plumb J. Hypoxia-inducible factor 1 alpha is required for the tumourigenic and aggressive phenotype associated with Rab25 expression in ovarian cancer. Oncotarget. 2016;7(16):22650-22664.
96. Netti PA, Berk DA, Swartz MA, Grodzinsky AJ, Jain RK. Role of extracellular matrix assembly in interstitial transport in solid tumors. Cancer Research. 2000;60(9):2497-2503.
97. Lengyel E. Ovarian cancer development and metastasis. The American Journal of Pathology. 2010;177(3):1053-1064.

98. Ebben JD, Treisman DM, Zorniak M, Kutty RG, Clark PA, Kuo JS. The cancer stem cell paradigm: a new understanding of tumor development and treatment. Expert Opinion on Therapeutic Targets. 2010;14(6):621-632.
99. Carmeliet P, Jain RK. Angiogenesis in cancer and other diseases. Nature. 2000;407(6801):249-257.
100. De Visser KE, Eichten A, Coussens LM. Paradoxical roles of the immune system during cancer development. Nature reviews cancer. 2006;6(1):24-37.
101. Unger C, Kramer N, Walzl A, Scherzer M, Hengstschläger M, Dolznig H. Modeling human carcinomas: physiologically relevant 3D models to improve anti-cancer drug development. Advanced Drug Delivery Reviews. 2014;79:50-67.
102. Wacnik PW, Eikmeier LJ, Ruggles TR, Ramnaraine ML, Walcheck BK, Beitz AJ, Wilcox GL. Functional interactions between tumor and peripheral nerve: morphology, algogen identification, and behavioral characterization of a new murine model of cancer pain. The Journal of Neuroscience. 2001;21(23):9355-9366.
103. Shields CL, Shields JA, Baez K, Cater JR, de Potter P. Optic nerve invasion of retinoblastoma. Metastatic potential and clinical risk factors. Cancer. 1994;73(3):692-698.
104. Peshwa MV, Wu FJ, Follstad BD, Cerra FB, Hu WS. Kinetics of hepatocyte spheroid formation. Biotechnology Progress. 1994;10(5):460-466.
105. Nyberg SL, Shatford RA, Peshwa MV, White JG, Cerra FB, Hu WS. Evaluation of a hepatocyte-entrapment hollow fiber bioreactor: A potential bioartificial liver. Biotechnology and Bioengineering. 1993;41(2):194-203.
106. Mueller MM, Fusenig NE. Friends or foes—bipolar effects of the tumour stroma in cancer. Nature Reviews Cancer. 2004;4(11):839-849.
107. Connolly JL, Schnitt SJ, Wang HH, Longtine JA, Dvorak A, Dvorak HF. Tumor structure and tumor stroma generation. 2003.
108. Kola I, Landis J. Can the pharmaceutical industry reduce attrition rates? Nature reviews Drug discovery. 2004;3(8):711-716.
109. Food, Administration D. Innovation or stagnation: challenge and opportunity on the critical path to new medical products. Food and Drug Administration, Critical Path Report. 2004.
110. Avorn J. The $2.6 billion pill—methodologic and policy considerations. New England Journal of Medicine. 2015;372(20):1877-1879.
111. Griffith LG, Swartz MA. Capturing complex 3D tissue physiology in vitro. Nature Reviews Molecular Cell Biology. 2006;7(3):211-224.
112. Bleicher KH, Böhm H-J, Müller K, Alanine AI. Hit and lead generation: beyond high-throughput screening. Nature Reviews Drug discovery. 2003;2(5):369-378.
113. Hubbell JA. Biomaterials science and high-throughput screening. Nature Biotechnology. 2004;22(7):828-829.
114. Hertzberg RP, Pope AJ. High-throughput screening: new technology for the 21st century. Current Opinion in Chemical Biology. 2000;4(4):445-451.
115. Ivascu A, Kubbies M. Rapid generation of single-tumor spheroids for high-throughput cell function and toxicity analysis. J Biomol Screen. 2006;11(8):922-32.
116. Friedrich J, Seidel C, Ebner R, Kunz-Schughart LA. Spheroid-based drug screen: considerations and practical approach. Nat Protoc. 2009;4(3):309-24.

117. Friedrich J, Seidel C, Ebner R, Kunz-Schughart LA. Spheroid-based drug screen: considerations and practical approach. Nature Protocols. 2009;4(3):309-324.
118. LaBarbera DV, Reid BG, Yoo BH. The multicellular tumor spheroid model for high-throughput cancer drug discovery. Expert Opinion on Drug Discovery. 2012;7(9):819-830.
119. Rossow T, Heyman JA, Ehrlicher AJ, Langhoff A, Weitz DA, Haag R, Seiffert S. Controlled synthesis of cell-laden microgels by radical-free gelation in droplet microfluidics. Journal of the American Chemical Society. 2012;134(10):4983-4989.
120. Kim C, Chung S, Kim YE, Lee KS, Lee SH, Oh KW, Kang JY. Generation of core-shell microcapsules with three-dimensional focusing device for efficient formation of cell spheroid. Lab on a Chip. 2011;11(2):246-252.
121. Beebe DJ, Mensing GA, Walker GM. Physics and applications of microfluidics in biology. Annual Review of Biomedical Engineering. 2002;4:261-86.
122. Hansmann J, Groeber F, Kahlig A, Kleinhans C, Walles H. Bioreactors in tissue engineering—principles, applications and commercial constraints. Biotechnology Journal. 2013;8(3):298-307.

Chapter 8 Conclusions and future work

8.1 Introduction

The *in vitro* fabrication of artificial living tissues is a complex process with a magnitude of scientific challenges. Engineering tissues not only requires components such as cells, growth factors and biodegradable 3D scaffolds but also the technologies to manufacture the tissue [1-4]. Presently, we are unaware of any existing technologies in the area of biofabrication or bioassembly that can assemble tissue subunits together into a 3D plotted scaffold to create a larger engineered tissue with a specific architecture. Therefore, in this thesis, we aimed at developing an automated bioassembly system that can assemble tissue units into a 3D plotted thermoplastic scaffold for application in two areas – cartilage engineering and tumour engineering.

8.2 Thesis conclusions

8.2.1 The design and development of a prototype integrated system for automated 3D Bioassembly of tissue units for biofabrication of tissue engineered constructs.

We developed a novel and flexible 3D Bioassembly platform capable of automated bioassembly of tissue units into a 3D plotted scaffold. The developed system essentially consisted of two parts (i) a singularisation module and (ii) an injection module. The singularisation module was designed to separate a large number of Ø1 mm sized tissue units and deliver an individual tissue unit to the injection module. The injection module with the aid of the 3D positioning system could insert the tissue unit into a target location within a 3D plotted thermoplastic polymer scaffold. The developed singularisation and injection module were incorporated into a commercial 3D bioprinter and this made up the automated bioassembly system. The flexibility of the constructed prototype tissue assembly system permitted the simple adjustment of the various soft parameters (i.e. valve

timings, pressure), thereby allowing the optimization of the device to handle different types of tissue units for the desired modular tissue assembly approach. The prototype device developed allowed us to validate the automated bioassembly system for cartilage and tumour engineering applications. Furthermore, mathematical models or anatomical models generated through imaging techniques (i.e. computed tomography (CT) or magnetic resonance imaging (MRI)) could also potentially be translated to a computer aided manufacturing (CAD/CAM) file. These CAD/CAM flies can then be converted to G-code to fabricate constructs of a desired shape, size, geometry and arrangement of tissue units [5, 6].

8.2.2 Validation and characterisation of an integrated system for automated 3D Bioassembly of micro-tissues for biofabrication of tissue engineered cartilage constructs

The developed integrated automated 3D Bioassembly system was validated for using cartilage engineering as a model application for biofabricating a micro-tissue based tissue engineered construct. We demonstrated that the developed device could efficiently (singularisation efficiency of 97.0 ± 6.6%) and reliably handle cartilage micro-tissues and could also insert the micro-tissues into the 3D plotted scaffold with an efficiency of 79.2 ± 18.8%. The viability of micro-tissues was not affected by being handled by the fluidic approach for micro-tissue capture, singularisation and bioassembly. The automated bioassembly system was designed so constructs could be bioassembled via both top-down and bottom-up bioassembly approaches to maximize the flexibility of the biofabrication process. The top-down bioassembly approach involved 3D plotting of a complete scaffold and injection of specific tissue units into the scaffold to fabricate a simple construct. The bottom-up approach involved a layer-by-layer strategy that combined 3D plotting of a scaffold layer and co-assembly of specific tissue units into the scaffold to allow fabrication of complex hybrid constructs. The layer-by-layer or bottom-up bioassembly of a cartilage construct was demonstrated and there was no difference in viability observed between the construct assembled manually and with the automated bioassembly system. The absence of any noticeable detrimental effect on the viability and shape of the micro-tissue after being handled by the automated tissue assemble system suggests the gentle nature of the designed fluidic-based system. A hemisphere construct (chapter 4, Figure 4-13) was also assembled with the

automated tissue bioassembly system demonstrating the possibility of bioassembling biphasic osteochondral anatomically shaped constructs.

Presently, as many cartilage repair strategies have a poor long-term outcome due to fibrocartilage formation other repair strategies which include tissue engineering and regenerative medicine are being investigated [7-9]. High-throughput fabrication techniques have been previously been demonstrated for generating *ex vivo* cartilage-like micro-tissues [10, 11]. The ability to assemble large numbers of the cartilage micro-tissues into a scaffold would be highly beneficial in fabricating tissue engineered constructs that can be employed as an alternative cartilage repair strategy. The approach would provide the cells and ECM components for simulating cartilage repair and regeneration and would also provide the required initial mechanical properties. The fabricated cartilage construct would then be completely be replaced by mature ECM over time leading to the formation of a functional cartilage [12]. However, one of the challenges with the envisaged cartilage repair strategy was the lack of an automated bioassembly system capable of fabricating the tissue engineered construct. We have established an automated tissue assembly technology that would facilitate the fabrication of complex anatomically-shaped 3D constructs of clinically relevant sizes that can be fabricated with the desired geometry and controlled spatial position of the micro-tissues, with precision, in large numbers, and with reduced construction time. The constructs could be tailor-made to suit the needs of an individual patient. Moreover, the employment of an automated system to fabricate a tissue construct would reduce human involvement and would also reduce human error in the tissue fabrication process.

8.2.3 Validation an integrated system for automated 3D Bioassembly of cell-laden microspheres for biofabrication of tissue engineered cartilage constructs including proof-of-concept and chondrogenic characterisation of the assembled construct

The developed integrated automated 3D Bioassembly system was validated for application in cartilage engineering for biofabricating a cell-laden hydrogel microsphere based cartilage construct. Visible light photopolymerised cell-free 5% and 10% GelMA microspheres and human articular chondrocyte (HAC)-laden 9.5%

GelMA-0.5% HepMA microspheres were fabricated utilising the microfluidic system. The generated microspheres showed a condition dependent average diameter close to Ø1 mm size with a narrow size distribution. We demonstrated that the automated bioassembly system can efficiently and reliably handle and deliver microspheres into a 3D plotted scaffold. The flexibility of the automated tissue bioassembly system was shown by assembling constructs with coloured microspheres which represented microspheres of either different cell types, hydrogel types or microspheres containing different bioactive molecules in various desired arrangements. The layer-by-layer or bottom-up bioassembly of a cartilage construct with HAC-laden 9.5% GelMA-0.5% HepMA hydrogel microspheres was demonstrated and there was no difference in viability observed between the construct assembled manually and with the automated bioassembly system. Individual HAC-laden 9.5% GelMA-0.5% HepMA hydrogel microspheres and assembled constructs (8 microspheres arranged in a 2 x 2 x 2 fashion) were cultured *in vitro* over time. The immunofluorescence staining for aggrecan showed neocartilage formation. Higher aggrecan expression was visualised in the assembled constructs compared to individual microspheres. A graduated assembled construct (arranged in a 4 x 3 x 2 fashion) with HAC, co-culture (50% HAC and 50% MSC) and MSC laden HAC-laden 9.5% GelMA-0.5% HepMA microspheres was cultured *in vitro* over time and staining for aggrecan showed neocartilage formation. The aggrecan visualised in the MSC only microspheres was lower than the HAC or co-culture microspheres. We further established the potential of the automated tissue assembly system to fabricate complex constructs with microspheres and demonstrated neocartilage formation for application in cartilage engineering.

Encapsulating cells in a hydrogel provides a hydrated 3D native tissue-like environment to the cells and a pro-chondrogenic phenotype can be promoted or directed by forcing the cells to maintain a rounded morphology [13-18]. Encapsulating chondrocytes or chondroprogenitor cells in hydrogels can overcome some of the drawbacks of employing a micro-tissue based strategy (chapter 5). Fabricating a Ø1 mm micro-tissue (250,000 cells) requires 31-fold higher number of cells in comparison to fabricating a Ø1 mm hydrogel microspheres (at a concentration of 15 million cells/ml). As chondrocytes have a limited proliferative potential when expanded by culturing in 2D, it is highly favourable to utilise a

strategy that requires lesser cells. The rate-limiting step of culturing the cell pellet (7 days) to form the micro-tissues before they can be assembled into a construct can be eliminated with the hydrogel microspheres. A hydrogel microsphere based system would also be highly beneficial in a single surgery strategy where the tissue is harvested, chondrocytes or chondroprogenitor cells are isolated from the tissue and encapsulated, the cartilage construct is fabricated with the cell encapsulated hydrogel microspheres and transplanted into the patient straight away. Although we have utilised GelMA, other hydrogels that have been researched for cartilage engineering such as alginate [19], agarose [20], collagen [21], fibrin [22], poly(ethylene glycol) (PEG) [23], poly(ethylene oxide) (PEO)[16] and poly(vinyl alcohol) (PVA) [24] could also potentially be adapted to similarly fabricate a cartilage construct.

8.2.4 Validation of an integrated system for high-throughput fabrication and automated 3D Bioassembly of micro-tissues for biofabrication of an *in vitro* cancer model, including proof-of-concept characterisation of the assembled tumour construct compared to existing 2D and 3D *in vitro* models

The developed integrated automated 3D Bioassembly system was validated for application in tumour engineering by biofabricating a cancer micro-tissue based *in vitro* 3D cancer model. Fabrication of compact and spherical Ø1 mm cancer micro-tissues that could be handled by the automated bioassembly system required the co-culture of SKOV3s with human foreskin fibroblasts (HFFs). The cells in the co-culture micro-tissues self-segregated to form a predominantly fibroblast core enveloped by ovarian cancer cells in the periphery. When the micro-tissues were assembled into a scaffold, the cells in the assembled construct maintained their micro-tissue arrangement. Fibroblasts are an integral part of tumours and they are known to play a significant role in the progress, growth and spread of cancers and are associated with cancer cells at all stages of progression [25, 26]. Tumour stroma supports the tumour cells *in vivo* and the rearrangement of SKOV3s and HFFs could potentially mimic the *in vivo* tumour cell-stroma interactions [27]. We demonstrated the reliable and efficient handling of the cancer co-culture (75% SKOV3 and 25% HFF) micro-tissues by the automated bioassembly system. The layer-by-layer or bottom-

up bioassembly of a cancer construct was demonstrated and there was no difference in viability observed between the construct assembled manually and with the automated bioassembly system. The response of cells in 2D monolayer, 3D micro-tissues and the co-culture 3D assembled cancer construct was evaluated with doxorubicin. An increased chemoresistance was observed in the 3D micro-tissues compared to cells in 2D and this enhanced chemoresistance observed in 3D models is in line with other studies [28-32]. A cell-dependent response was observed between SKOV3, HFF and co-culture individual micro-tissues and cells in 2D. A higher chemoresistance was observed in the co-culture assembled construct compared to the co-culture micro-tissues. The observed higher chemoresistance of the assembled construct compared to the individual micro-tissues could possibly be due to the larger gradients in nutrients, drugs and oxygen in the larger assembled construct compared to the smaller individual micro-tissues which resulted in lower drug efficacy [33-35]. Form the immunohistochemistry, the expression of Ki67 was observed to be cell dependent. The expression of γ-H2AX was visualized to be higher at higher drug concentrations demonstrating DNA double-stranded breaks caused by the drug. The developed model and bioassembly technology together open the platform for the fabricating modular assembly based tailor-made cancer constructs with controlled spatial position of micro-tissues that could potentially be applied in cancer research and high-throughput screening of anticancer drugs. Moreover, the average ovarian cancer tumour size *in vivo* can range from 4.6 to 11.8 cm and a larger assembled construct tumour model would be more relevant for anticancer drug testing compared to a smaller micro-tissue model [36, 37]. However, the developed cancer micro-tissue *in vitro* model can only be fabricated with cell types that form compact spherical micro-tissues.

8.2.5 Validation of an integrated system for automated 3D Bioassembly of cell-laden microspheres for biofabrication of an *in vitro* cancer model, including proof-of-concept characterisation of the assembled tumour construct compared to existing 2D and 3D *in vitro* models

The developed integrated automated 3D Bioassembly system was validated for application in tumour engineering by biofabricating a cell-laden hydrogel microsphere based *in vitro* 3D cancer model. Cell-laden 10% GelMA SKOV3, HFF and co-culture (75% SKOV3 and 25% HFF) microspheres were fabricated with the

microfluidic system. The generated microspheres had an average diameter close to 1 mm size with a narrow size distribution. We demonstrated that the automated bioassembly system can efficiently and reliably handle the microspheres. The layer-by-layer or bottom-up bioassembly of a cancer construct was demonstrated and there was no difference in viability observed between the construct assembled manually and with the automated bioassembly system. The response of SKOV3, fibroblast and co-cultures in 2D monolayer, individual microspheres and assembled constructs was evaluated with doxorubicin. The 3D assembled constructs were more chemoresistant than the individual microspheres and the cells in 2D had the lowest chemoresistance. A cell-dependent drug response was also observed. The expression of γ-H2AX was visualized to be higher at higher drug concentrations in all 3D models demonstrating DNA double-stranded breaks caused by the drug. By encapsulating cells in hydrogel microspheres, 3D cancer constructs could be fabricated with cell types that do not form compact micro-tissues. This enables the fabrication of modular assembly based cancer constructs with controllable spatial position of microspheres with cells types that do not form compact spherical micro-tissues. A hydrogel based model is also advantageous in that lower number of cells are required and the rate limiting step (24 hours to several days) of fabricating a micro-tissue can be eliminated compared to fabricating a micro-tissue based model [38]. Moreover, encapsulating cells in a hydrogel is attractive as it provides a hydrated tissue-like environment similar to the native extracellular matrix (ECM) of many tissues. The developed tailorable *in vitro* 3D cancer model could potentially be employed in cancer research and high-throughput screening of anticancer drugs.

The downside of employing GelMA to encapsulate the cells is that there could be batch-to-batch variations in manufactured GelMA making it impracticable to correlate work form different laboratories and also the properties of the hydrogel would have to be optimised (i.e. stiffness) depending on the cell type and application [39, 40]. The fabrication of microspheres with hydrogel-based matrices such as reconstituted basement membrane protein (Matrigel) [41] and type I collagen [42] which are commonly used to fabricate cancer models could potentially be possible with few modifications of the micro-fluidic system (i.e. temperature controlled environment for the temperature sensitive Matrigel) and the automated

bioassembly system. The fabricated microspheres could then be assembled to create Matrigel or type I collagen-based cancer constructs.

In both the micro-tissue and hydrogel microspheres models, a higher chemoresistance was seen in the individual microspheres or micro-tissues compared to cells in 2D and a higher chemoresistance was observed in the assembled constructs compared to the individual microspheres or micro-tissues. The observed trend of higher chemoresistance in 3D models compared to cells in 2D is comparable to other studies reported in the literature [28-32]. The trend also highlights the need for conducting drug testing in 3D models and more importantly with larger 3D models as their response would be more comparable to tumours *in situ*. Although we have fabricated cancer constructs with only fibroblasts and SKOV3, tumour models of different cell types (including a combination of healthy and tumour cells) could potentially be assembled into a construct with complex architecture. The assembled tumour models could also potentially be fabricated to simulate and investigate other aspects in drug testing and cancer research such as drug and toxin metabolism, tumour-stroma interaction, osteolysis, tumour invasion of bone or tumour invasion of nerves [43-46].

8.3 Future work

8.3.1 Hypoxic culture of cell-laden individual hydrogel microspheres and assembled constructs for cartilage engineering

The oxygen concentration in a healthy articular cartilage is low - typically around 1% and oxygen apart from being an essential nutrient is known to direct and influence cartilage formation [47, 48]. The significance of a hypoxic environment for chondrocyte differentiation have been reported inconsistently [47]. However, numerous studies have shown that a hypoxic environment simulates chondrogenic differentiation *in vitro* [49-51]. Moreover, we have shown that the expression of aggrecan to be higher in an assembled construct compared to an individual microsphere. This difference in the aggrecan expression could possibly be due to an oxygen gradient and a more hypoxic environment in the assembled constructs compared to the individual microspheres. We cultured the microspheres and assembled constructs in a normoxic condition. Further studies to investigate the

effect of a hypoxic environment by carrying out the experiment in a hypoxic chamber at different oxygen tensions on both individual microspheres and assembled constructs would be beneficial in revealing the optimum oxygen tension for promoting chondrogenic differentiation and neocartilage formation. Moreover, the microsphere model could be compared with the micro-tissue based model to assess cartilage formation. As the HepMA incorporated into the hydrogel interferes with the GAG quantification and safranin-O staining for GAG, methods that do not cause interference by the incorporation of HepMA such as immunofluorescence staining and gene expression of collagen type I and II and aggrecan would give us a clearer insight into neocartilage formation [52]. The developed cartilage construct could also be potentially implanted *in vivo* in an animal (i.e. sheep, goat or rabbit) to investigate the effect of a low oxygen environment and the outcome it has on tissue formation and integration of the transplanted construct with the surrounding tissue.

8.3.2 Fabrication of an osteochondral construct

An osteochondral construct could cater to a full thickness lesion of articular cartilage and it would also allow for improved fixation of the construct with the bony section of the defect and the integration of the construct with the surrounding cartilage [53, 54]. Ideally, an osteochondral construct would have a similar distribution and organization of cells and ECM components to native articular cartilage [54]. We demonstrated the fabrication of an anatomically shaped construct (chapter 4, Figure 4-11), a chondral construct (chapter 5, Figure 5-11), and a graduated chondral construct with MSCs and HACs (chapter 5, Figure 5-13) [55]. Based on similar principles, the developed automated bioassembly system could potentially be utilised to fabricate a biphasic osteochondral construct with pre-differentiated micro-tissues or microspheres or both. The fabricated microspheres and micro-tissues could be produced from either a combination of chondrocytes/MSCs or osteoblasts/osteocytes/MSCs. The automated aspect of the bioassembly system would aid the large-scale fabrication of the complex biphasic osteochondral constructs. The constructs could be cultured in media formulated to maintain both chondrogenesis and osteogenesis. Chondrogenesis associated genes such as collagen type II and aggrecan and osteogenesis-associated genes such as alkaline phosphatase, bone sialoprotein and osteocalcin could be investigated to assess neotissue formation [52, 54]. Likewise, histological examination with alizarin

red for bone and alcian blue or immunofluorescence staining for aggrecan and collagen type II for cartilage could be visually examined for neotissue formation in the chondral layer, transition zone and the osseous layer [52, 54]. *In vivo* animal studies could also be undertaken to investigate the tissue formation and integration of the transplanted construct with the surrounding tissue with the developed cartilage construct.

8.3.3 Vascularisation of the *in vitro* cancer model

Tumours *in vivo* have abnormal vascularisation and angiogenesis is required for tumour growth, invasion, progression, and metastasis [29, 56]. Vascularisation of a cancer constructs would not only mimic and recapitulate the *in vivo* tumour environment but would be also essential for the long-term survival of cells in larger constructs [29, 57]. Improved vascularisation in a tumour would lead to the better drug and oxygen infiltration to the cells in a tumour and could have an impact on the outcome of chemotherapy [58]. Patients with intermediately vascularised tumours have been shown to respond better to chemotherapy than patients with low or high vascularisation [58]. A vascularised model could have a higher capacity to anticipate the outcome of a candidate drug during drug screening. Co-culture cancer (SKOV3s and fibroblasts) micro-tissues or cancer cell-laden microspheres could be coated with endothelial cells and cultured so that they form a confluent layer on the surface after which they could be assembled as desired into a cancer construct and be fabricated in large numbers with the developed automated bioassembly system [59]. The interstitial spaces between the assembled microspheres or micro-tissues would potentially form the interconnected vascular structure [59]. Alternatively, endothelial cells could be co-cultured with cancer cells and fibroblasts to fabricate cancer micro-tissues or endothelial and cancer cells together could be used to fabricate cell-laden hydrogel microspheres and the micro-tissues or microspheres could be assembled into a construct with the intention that the structure would vascularise over time [57]. The constructs would have to be cultured in a media formulation containing exogenous growth factors for vascularisation [57]. IC_{50} values could be determined to gauge the model and immunofluorescence staining for CD31 which is expressed by endothelial cells [60] Ki67 which is a marker for proliferation [61, 62], and γ-H2AX which is a marker for double-stranded breaks in

DNA [63, 64] could be performed no the samples to investigate the distribution of cells, cell proliferation and the effect of the drug on the vascularised constructs.

8.3.4 Validating the *in vitro* cancer model with different cancer cell types

The ability to fabricate *in vitro* cancer models from a range of different cell lines is highly significant as this would allow the specific screening of anticancer drugs which are tumour specific or receptor-specific [65]. We have already demonstrated the fabrication of an ovarian cancer *in vitro* tumour model based on cancer micro-tissues and cancer cell-laden microspheres with SKOV3s with the automated tissue assembly system. Further studies could be aimed at validating the plausibility of fabricating cancer constructs from cancer cell lines originating from different tissues types including breast, prostate, bone, lung, colon or liver or with receptor positive or negative cell lines such as estrogen receptor-positive MCF-7 and estrogen receptor-negative MDA-MB-231 [65]. The validation would demonstrate the ability to fabricate *in vitro* cancer models from a range of cancer cell types with the automated tissue assembly system for application in high-throughput screening of anticancer drugs. We had previously shown that we were not able to fabricate compact spherical micro-tissues with MDA-MB-231s and MCF-7s and we could investigate co-culturing these cell lines with fibroblasts to try and fabricate compact spherical micro-tissues. Likewise, the MDA-MB-231s and MCF-7s could also be encapsulated into the hydrogel microspheres to fabricate a microsphere based construct. As we have previously executed, IC_{50} values could be determined to gauge the model and immunofluorescence staining for Ki67 [61, 62] and γ-H2AX [63, 64] could be performed on the samples to investigate cell proliferation and the effect of the drug on the constructs.

8.4 References

1. Woodfield, T.B., et al., *Design of porous scaffolds for cartilage tissue engineering using a three-dimensional fiber-deposition technique.* Biomaterials, 2004. **25**(18): p. 4149-61.
2. Malda, J., et al., *25th anniversary article: engineering hydrogels for biofabrication.* Advanced materials, 2013. **25**(36): p. 5011-5028.
3. Langer, R. and J. Vacanti, *Tissue engineering.* Science, 1993. **260**(5110): p. 920-926.
4. Griffith, L.G. and G. Naughton, *Tissue engineering--current challenges and expanding opportunities.* Science, 2002. **295**(5557): p. 1009-1014.
5. Agarwala, M.K., et al., *Structural quality of parts processed by fused deposition.* Rapid Prototyping Journal, 1996. **2**(4): p. 4-19.
6. Sun, W. and P. Lal, *Recent development on computer aided tissue engineering - a review.* Computer Methods and Programs in Biomedicine, 2002. **67**(2): p. 85-103.
7. Brittberg, M., *Autologous chondrocyte transplantation.* Clinical orthopaedics and related research, 1999. **367**: p. S147-S155.
8. Lewis, P.B., et al., *Basic science and treatment options for articular cartilage injuries.* Journal of Orthopaedic & Sports Physical Therapy, 2006. **36**(10): p. 717-727.
9. Hangody, L. and P. Füles, *Autologous osteochondral mosaicplasty for the treatment of full-thickness defects of weight-bearing joints.* J Bone Joint Surg Am, 2003. **85**(suppl 2): p. 25-32.
10. Schon, B.S., et al., *Validation of a high-throughput microtissue fabrication process for 3D assembly of tissue engineered cartilage constructs.* Cell Tissue Res, 2012.
11. Babur, B.K., et al., *High-throughput bone and cartilage micropellet manufacture, followed by assembly of micropellets into biphasic osteochondral tissue.* Cell and tissue research, 2015. **361**(3): p. 755-768.
12. Ikada, Y., *Challenges in tissue engineering.* J R Soc Interface, 2006. **3**(10): p. 589-601.
13. Nichol, J.W., et al., *Cell-laden microengineered gelatin methacrylate hydrogels.* Biomaterials, 2010. **31**(21): p. 5536-5544.
14. Schuurman, W., et al., *Gelatin-Methacrylamide Hydrogels as Potential Biomaterials for Fabrication of Tissue-Engineered Cartilage Constructs.* Macromolecular bioscience, 2013. **13**(5): p. 551-561.
15. Mann, B.K., R.H. Schmedlen, and J.L. West, *Tethered-TGF-β increases extracellular matrix production of vascular smooth muscle cells.* Biomaterials, 2001. **22**(5): p. 439-444.
16. Elisseeff, J., et al., *Controlled-release of IGF-I and TGF-β1 in a photopolymerizing hydrogel for cartilage tissue engineering.* Journal of Orthopaedic Research, 2001. **19**(6): p. 1098-1104.
17. Mauck, R., X. Yuan, and R. Tuan, *Chondrogenic differentiation and functional maturation of bovine mesenchymal stem cells in long-term agarose culture.* Osteoarthritis and cartilage, 2006. **14**(2): p. 179-189.
18. Klein, T.J., et al., *Strategies for zonal cartilage repair using hydrogels.* Macromolecular bioscience, 2009. **9**(11): p. 1049-1058.

19. Guo, J., G.W. Jourdian, and D.K. Maccallum, *Culture and growth characteristics of chondrocytes encapsulated in alginate beads.* Connective tissue research, 1989. **19**(2-4): p. 277-297.
20. Benya, P.D. and J.D. Shaffer, *Dedifferentiated chondrocytes reexpress the differentiated collagen phenotype when cultured in agarose gels.* Cell, 1982. **30**(1): p. 215-224.
21. Wakitani, S., et al., *Mesenchymal cell-based repair of large, full-thickness defects of articular cartilage.* J Bone Joint Surg Am, 1994. **76**(4): p. 579-592.
22. Silverman, R.P., et al., *Injectable tissue-engineered cartilage using a fibrin glue polymer.* Plastic and reconstructive surgery, 1999. **103**(7): p. 1809-1818.
23. Kim, T.-K., et al., *Experimental model for cartilage tissue engineering to regenerate the zonal organization of articular cartilage.* Osteoarthritis and cartilage, 2003. **11**(9): p. 653-664.
24. Spiller, K.L., et al., *A novel method for the direct fabrication of growth factor-loaded microspheres within porous nondegradable hydrogels: controlled release for cartilage tissue engineering.* Journal of controlled release, 2012. **157**(1): p. 39-45.
25. Kalluri, R. and M. Zeisberg, *Fibroblasts in cancer.* Nature Reviews Cancer, 2006. **6**(5): p. 392-401.
26. Mueller, M.M. and N.E. Fusenig, *Friends or foes—bipolar effects of the tumour stroma in cancer.* Nature Reviews Cancer, 2004. **4**(11): p. 839-849.
27. Orimo, A. and R.A. Weinberg, *Stromal fibroblasts in cancer: a novel tumor-promoting cell type.* Cell cycle, 2006. **5**(15): p. 1597-1601.
28. Dhiman, H.K., A.R. Ray, and A.K. Panda, *Three-dimensional chitosan scaffold-based MCF-7 cell culture for the determination of the cytotoxicity of tamoxifen.* Biomaterials, 2005. **26**(9): p. 979-986.
29. Kimlin, L.C., G. Casagrande, and V.M. Virador, *In vitro three-dimensional (3D) models in cancer research: An update.* Molecular carcinogenesis, 2013. **52**(3): p. 167-182.
30. Padrón, J.M. and G.J. Peters, *Cytotoxicity of sphingoid marine compound analogs in mono-and multilayered solid tumor cell cultures.* Investigational new drugs, 2006. **24**(3): p. 195-202.
31. Fischbach, C., et al., *Engineering tumors with 3D scaffolds.* Nature methods, 2007. **4**(10): p. 855-860.
32. Chitcholtan, K., P.H. Sykes, and J.J. Evans, *The resistance of intracellular mediators to doxorubicin and cisplatin are distinct in 3D and 2D endometrial cancer.* Journal of translational medicine, 2012. **10**(1): p. 1.
33. Minchinton, A.I. and I.F. Tannock, *Drug penetration in solid tumours.* Nature Reviews Cancer, 2006. **6**(8): p. 583-592.
34. Sutherland, R.M., et al., *Resistance to adriamycin in multicellular spheroids.* International Journal of Radiation Oncology* Biology* Physics, 1979. **5**(8): p. 1225-1230.
35. Wartenberg, M., et al., *Development of an intrinsic P-glycoprotein-mediated doxorubicin resistance in quiescent cell layers of large, multicellular prostate tumor spheroids.* International journal of cancer, 1998. **75**(6): p. 855-863.
36. Horvath, L.E., et al., *The relationship between tumor size and stage in early versus advanced ovarian cancer.* Medical hypotheses, 2013. **80**(5): p. 684-687.
37. Grimer, R.J., *Size matters for sarcomas!* The Annals of The Royal College of Surgeons of England, 2006. **88**(6): p. 519-524.

38. Lin, R.Z. and H.Y. Chang, *Recent advances in three-dimensional multicellular spheroid culture for biomedical research.* Biotechnology journal, 2008. **3**(9-10): p. 1172-1184.
39. Loessner, D., et al., *Functionalization, preparation and use of cell-laden gelatin methacryloyl-based hydrogels as modular tissue culture platforms.* Nature protocols, 2016. **11**(4): p. 727-746.
40. Hutmacher, D.W., *Biomaterials offer cancer research the third dimension.* Nature materials, 2010. **9**(2): p. 90-93.
41. Kleinman, H.K. and G.R. Martin. *Matrigel: basement membrane matrix with biological activity*. in *Seminars in cancer biology*. 2005. Elsevier.
42. Nicodemus, G.D. and S.J. Bryant, *Cell encapsulation in biodegradable hydrogels for tissue engineering applications.* Tissue Engineering Part B: Reviews, 2008. **14**(2): p. 149-165.
43. Wacnik, P.W., et al., *Functional interactions between tumor and peripheral nerve: morphology, algogen identification, and behavioral characterization of a new murine model of cancer pain.* The Journal of Neuroscience, 2001. **21**(23): p. 9355-9366.
44. Shields, C.L., et al., *Optic nerve invasion of retinoblastoma. Metastatic potential and clinical risk factors.* Cancer, 1994. **73**(3): p. 692-698.
45. Peshwa, M.V., et al., *Kinetics of hepatocyte spheroid formation.* Biotechnology progress, 1994. **10**(5): p. 460-466.
46. Nyberg, S.L., et al., *Evaluation of a hepatocyte-entrapment hollow fiber bioreactor: A potential bioartificial liver.* Biotechnology and bioengineering, 1993. **41**(2): p. 194-203.
47. Malda, J., et al., *Cartilage tissue engineering: controversy in the effect of oxygen.* Critical reviews in biotechnology, 2003. **23**(3): p. 175-194.
48. BRIGHTON, C.T. and R.B. HEPPENSTALL, *Oxygen tension in zones of the epiphyseal plate, the metaphysis and diaphysis.* J Bone Joint Surg Am, 1971. **53**(4): p. 719-728.
49. Malda, J., et al., *Low oxygen tension stimulates the redifferentiation of dedifferentiated adult human nasal chondrocytes.* Osteoarthritis and cartilage, 2004. **12**(4): p. 306-313.
50. Pawelek, J.M., *Effects of thyroxine and low oxygen tension on chondrogenic expression in cell culture.* Developmental biology, 1969. **19**(1): p. 52-72.
51. Domm, C., et al., *Redifferentiation of dedifferentiated bovine articular chondrocytes in alginate culture under low oxygen tension.* Osteoarthritis and Cartilage, 2002. **10**(1): p. 13-22.
52. Levett, P.A., et al., *A biomimetic extracellular matrix for cartilage tissue engineering centered on photocurable gelatin, hyaluronic acid and chondroitin sulfate.* Acta biomaterialia, 2014. **10**(1): p. 214-223.
53. Woodfield, T., et al., *Scaffolds for tissue engineering of cartilage.* Critical Reviews™ in Eukaryotic Gene Expression, 2002. **12**(3).
54. Tuli, R., et al., *Human mesenchymal progenitor cell-based tissue engineering of a single-unit osteochondral construct.* Tissue engineering, 2004. **10**(7-8): p. 1169-1179.
55. Schon, B., et al., *Validation of a high-throughput microtissue fabrication process for 3D assembly of tissue engineered cartilage constructs.* Cell and tissue research, 2012. **347**(3): p. 629-642.

56. Brown, J.M. and A.J. Giaccia, *The unique physiology of solid tumors: opportunities (and problems) for cancer therapy.* Cancer research, 1998. **58**(7): p. 1408-1416.
57. Eckermann, C.W., et al., *Characterization and modulation of fibroblast/endothelial cell co-cultures for the in vitro preformation of three-dimensional tubular networks.* Cell biology international, 2011. **35**(11): p. 1097-1110.
58. Koukourakis, M.I., et al., *Cancer vascularization: implications in radiotherapy?* International Journal of Radiation Oncology* Biology* Physics, 2000. **48**(2): p. 545-553.
59. McGuigan, A.P. and M.V. Sefton, *Vascularized organoid engineered by modular assembly enables blood perfusion.* Proceedings of the National Academy of Sciences, 2006. **103**(31): p. 11461-11466.
60. Treutiger, C.J., et al., *PECAM-1/CD31, an endothelial receptor for binding Plasmodium falciparum-infected erythrocytes.* Nature medicine, 1997. **3**(12): p. 1405-1408.
61. Scholzen, T. and J. Gerdes, *The Ki-67 protein: from the known and the unknown.* Journal of cellular physiology, 2000. **182**(3): p. 311-322.
62. Schlüter, C., et al., *The cell proliferation-associated antigen of antibody Ki-67: a very large, ubiquitous nuclear protein with numerous repeated elements, representing a new kind of cell cycle-maintaining proteins.* The Journal of cell biology, 1993. **123**(3): p. 513-522.
63. Kuo, L.J. and L.-X. Yang, *γ-H2AX-a novel biomarker for DNA double-strand breaks.* In vivo, 2008. **22**(3): p. 305-309.
64. Pilch, D.R., et al., *Characteristics of γ-H2AX foci at DNA double-strand breaks sites.* Biochemistry and cell biology, 2003. **81**(3): p. 123-129.
65. Engel, L.W. and N.A. Young, *Human breast carcinoma cells in continuous culture: a review.* Cancer research, 1978. **38**(11 Part 2): p. 4327-4339.

Appendices

Appendix 3.A

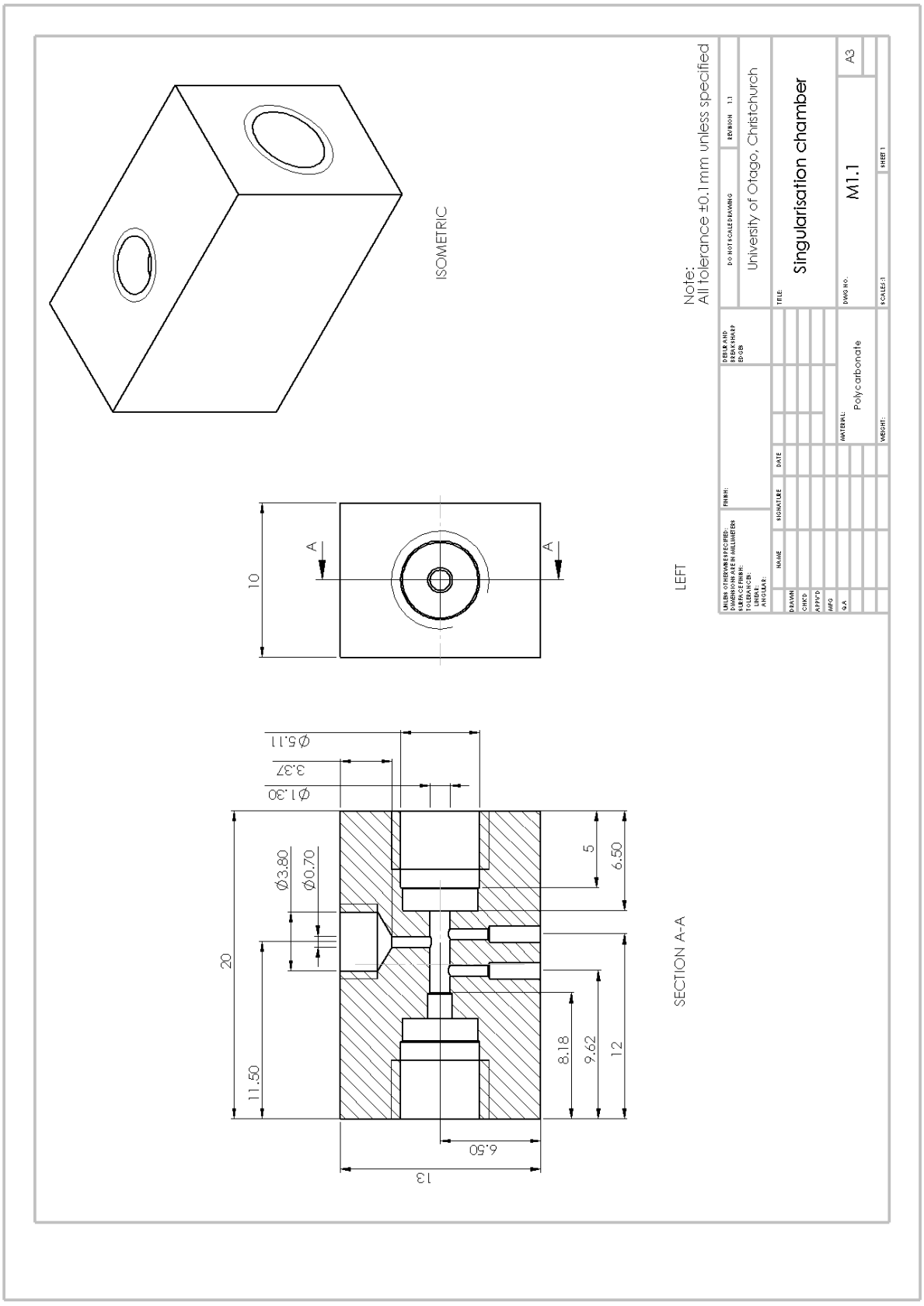

Figure 3.A-i. Mechanical diagram of the singularisation chamber.

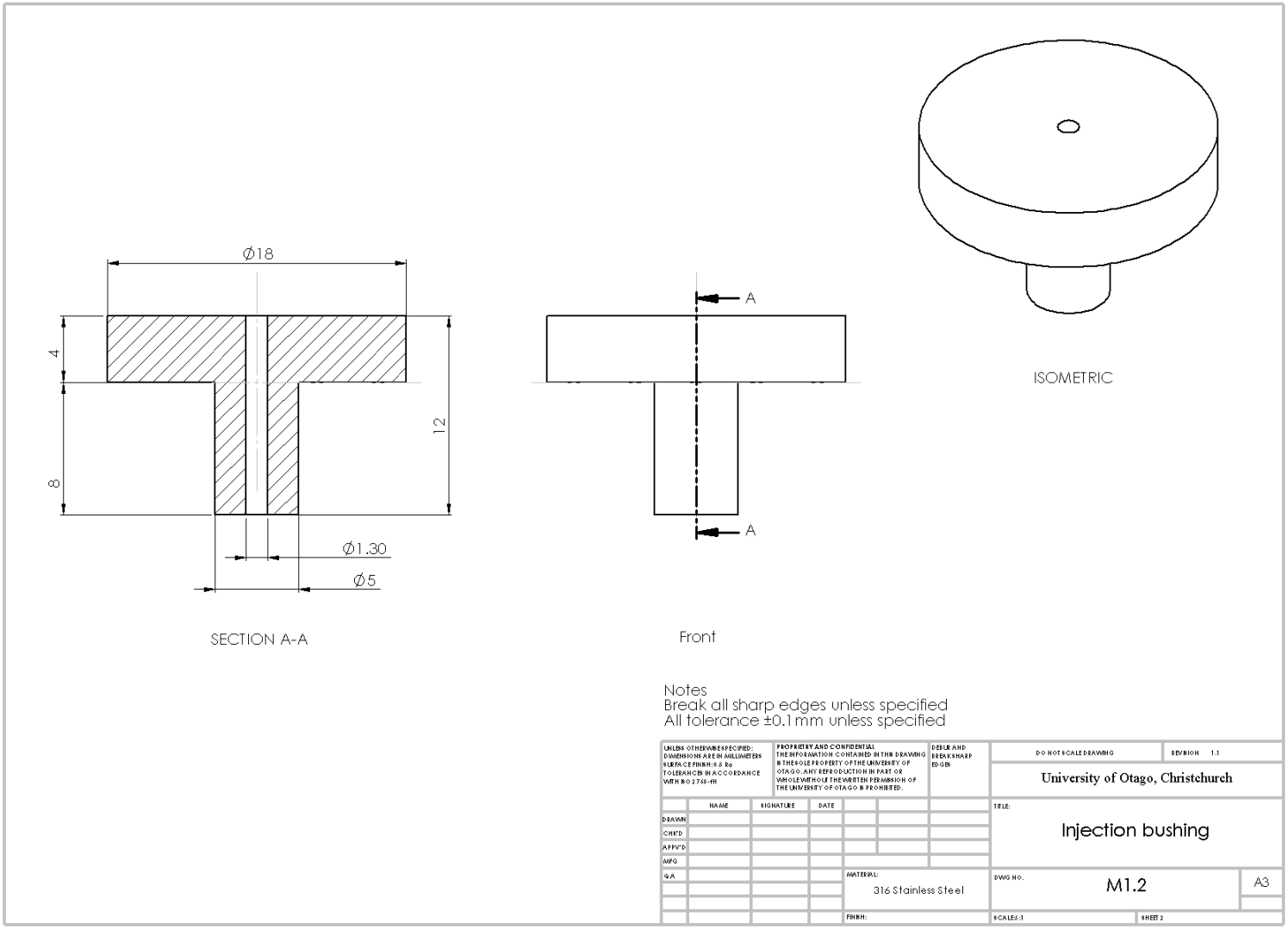

Figure 3.A-ii. Mechanical diagram of the Injection bushing.

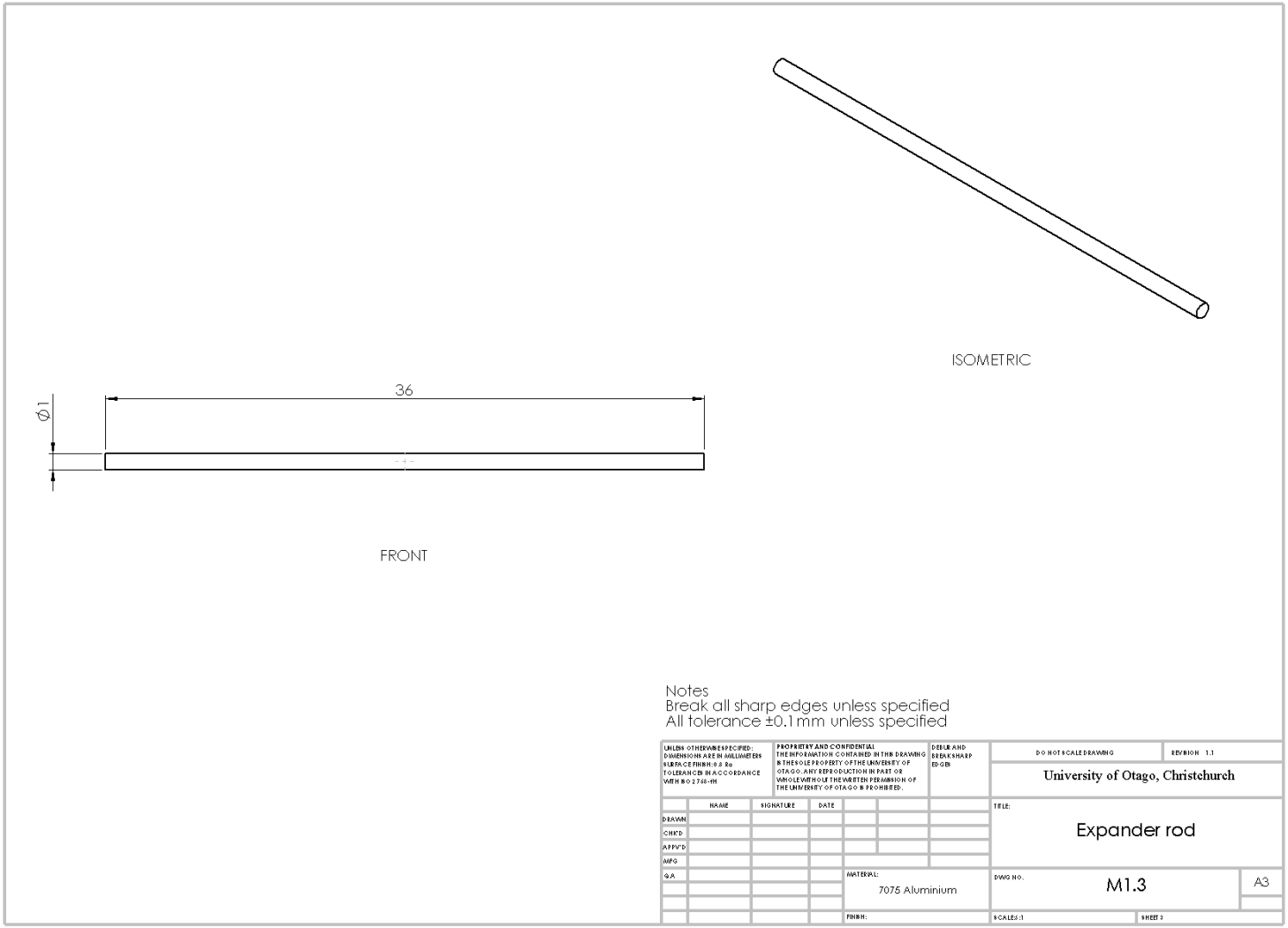

Figure 3.A-iii. Mechanical diagram of the expander rod.

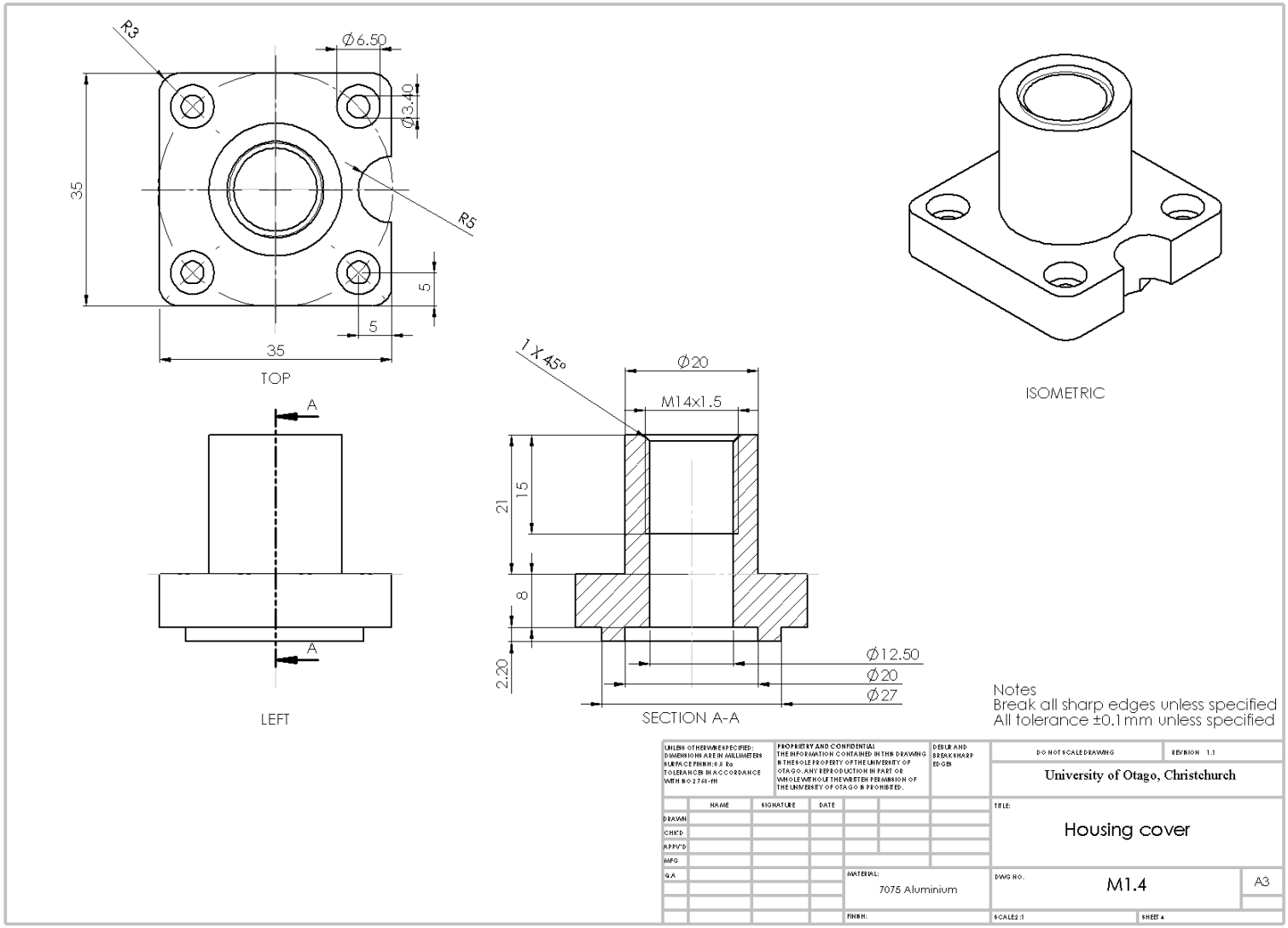

Figure 3.A-iv. Mechanical diagram of the Housing cover.

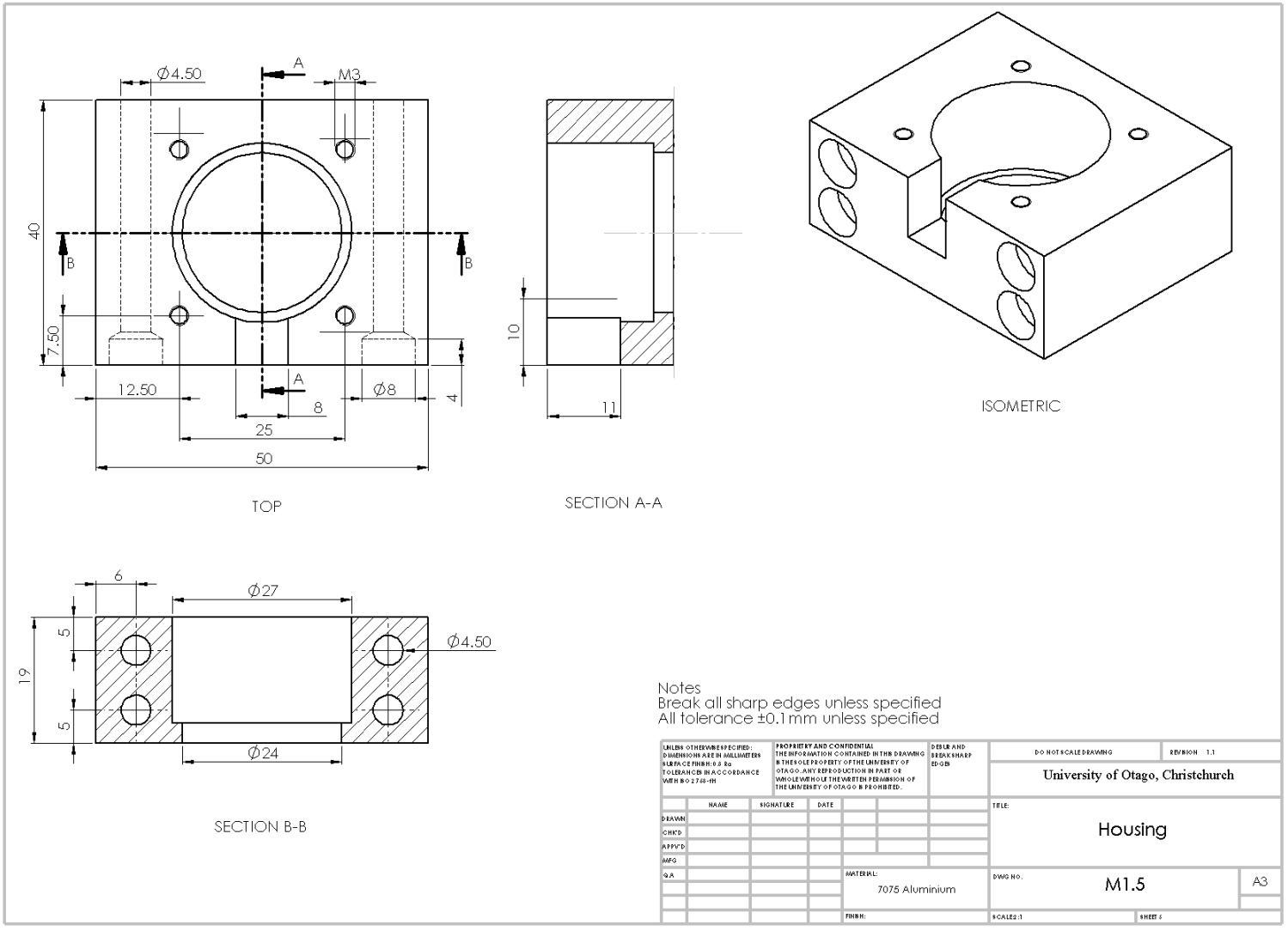

Figure 3.A-v. Mechanical diagram of the Housing.

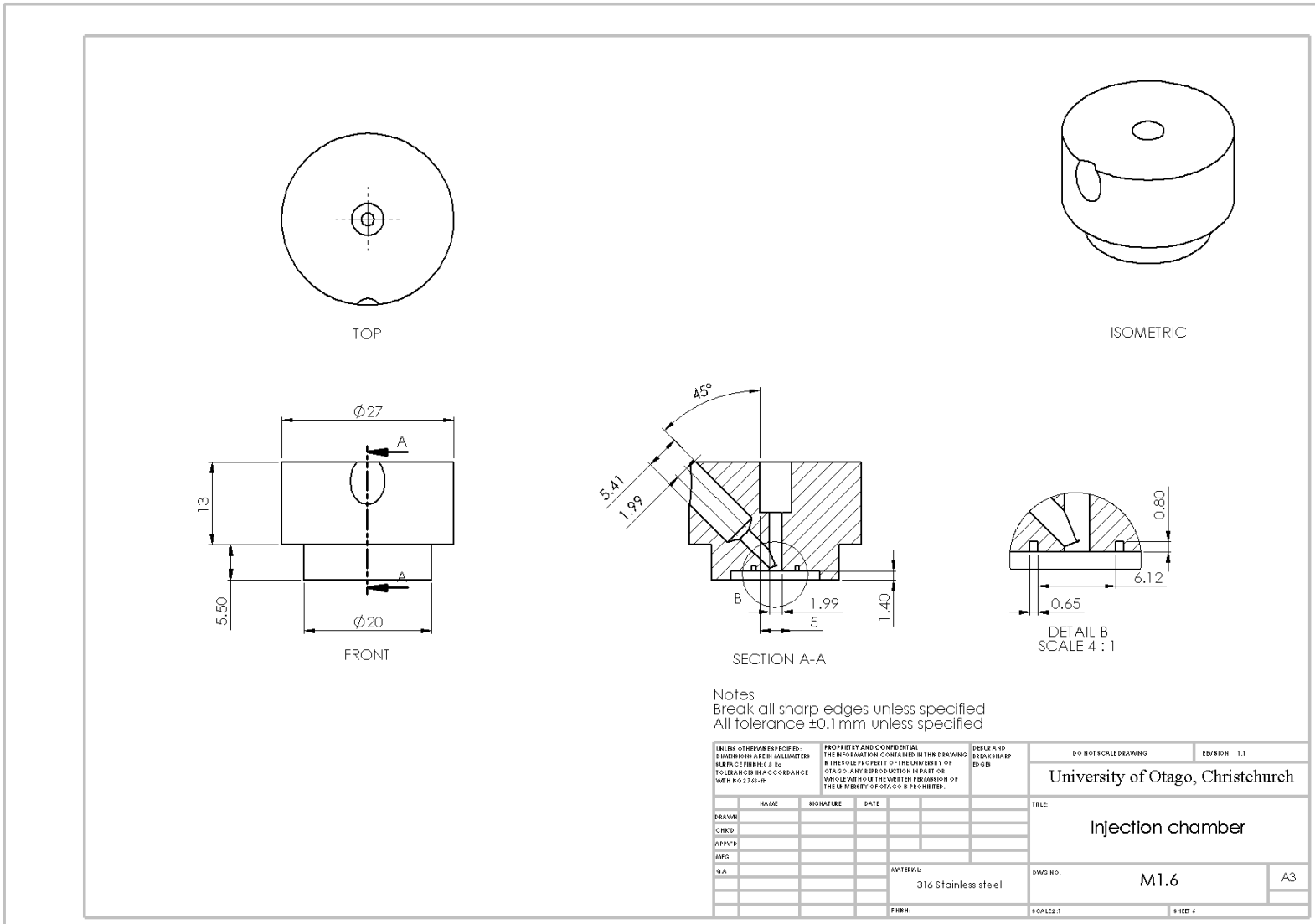

Figure 3.A-vi. Mechanical diagram of the Injection chamber.

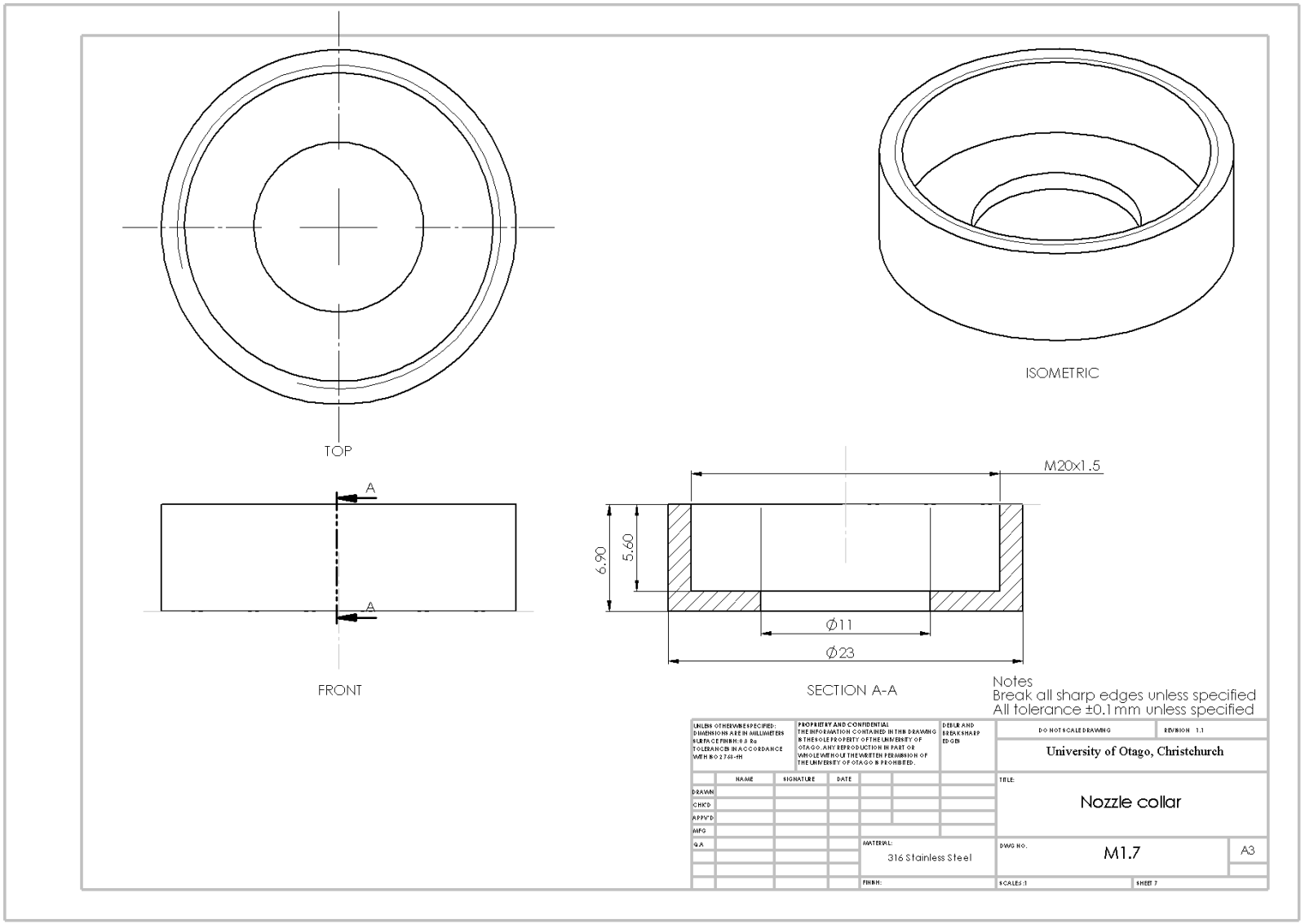

Figure 3.A-vii. Mechanical diagram of the Nozzle collar.

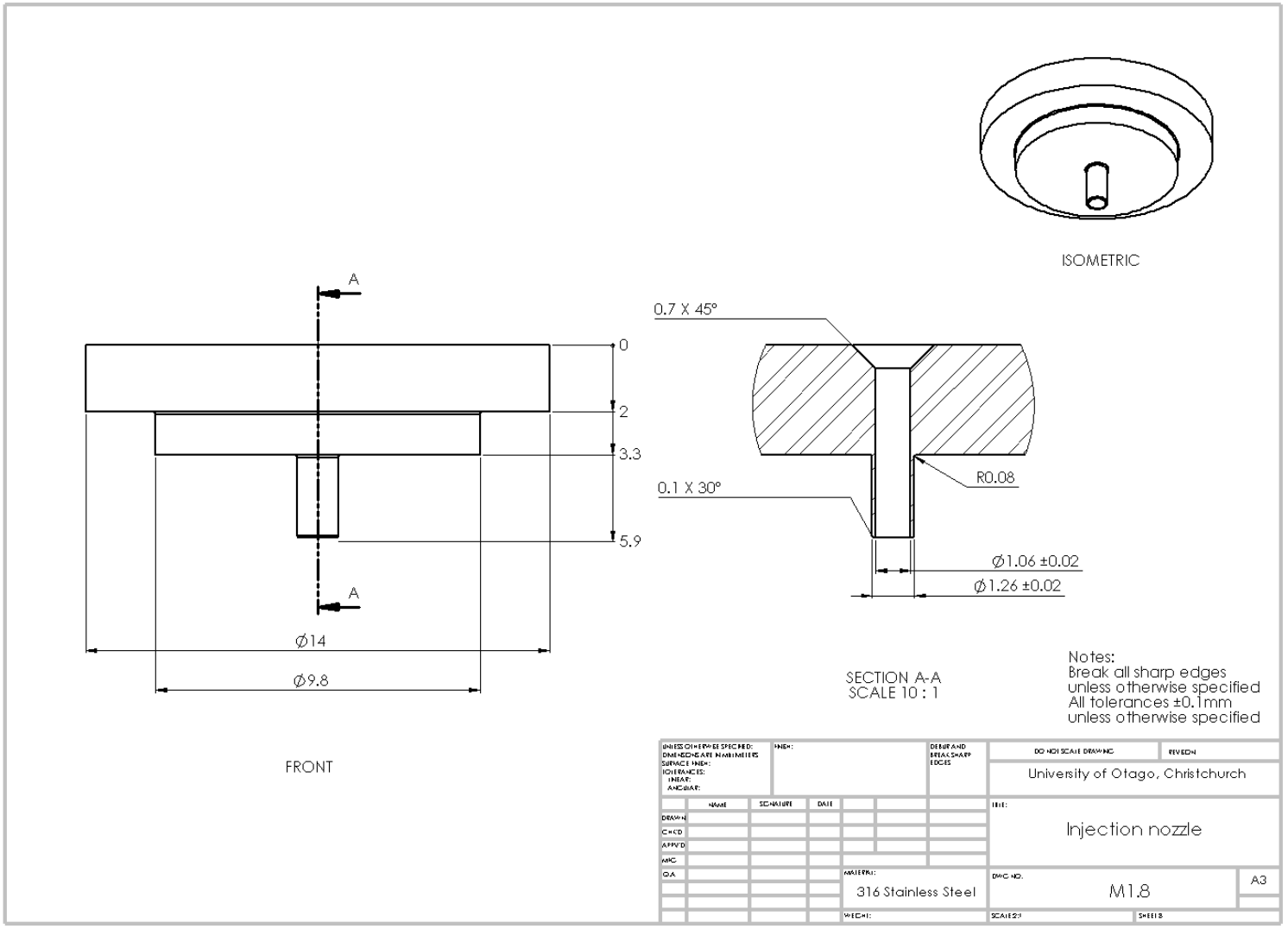

Figure 3.A-viii. Mechanical diagram of the Injection nozzle.

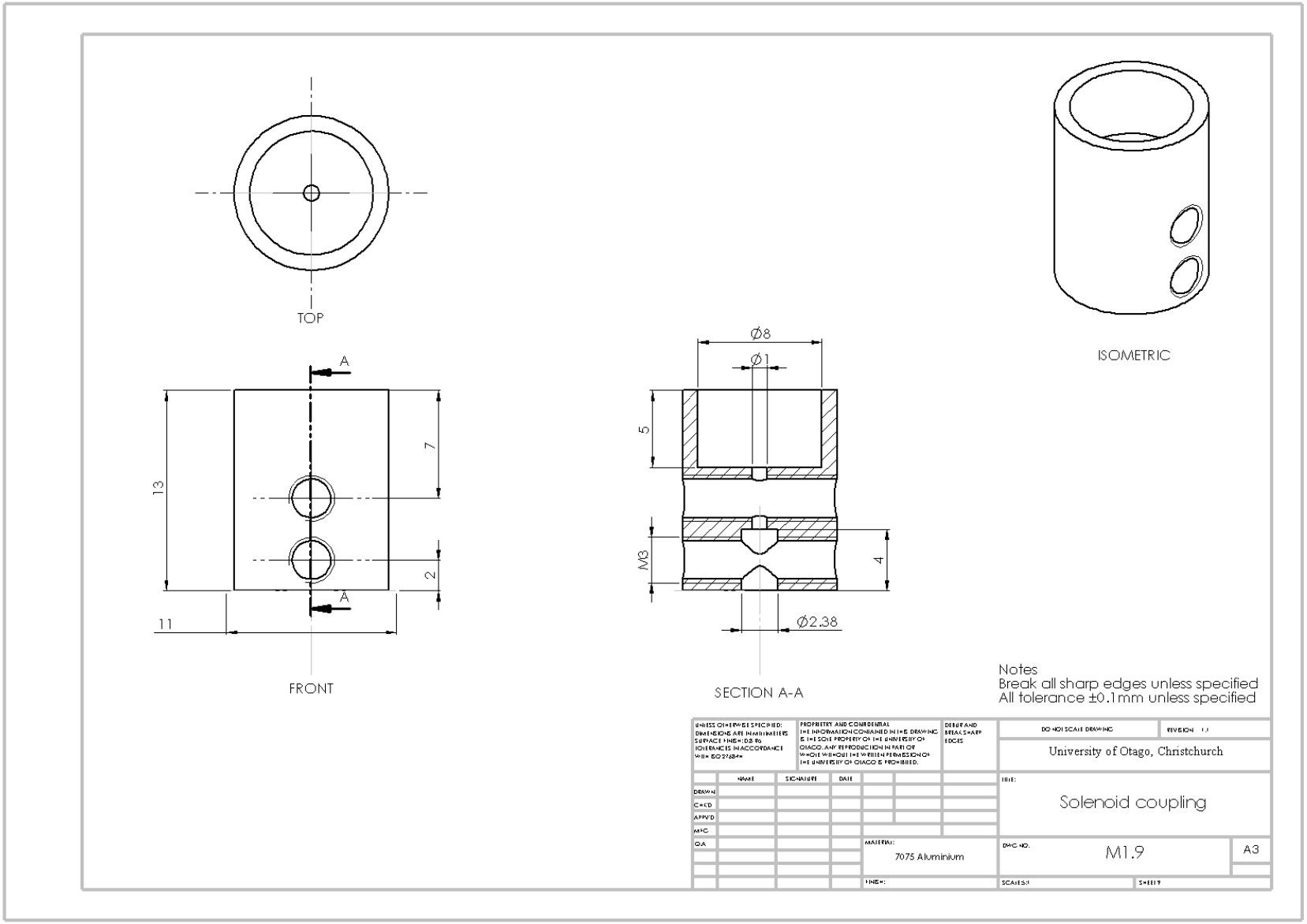

Figure 3.A-ix. Mechanical diagram of the Solenoid coupling.

Appendix 3.B

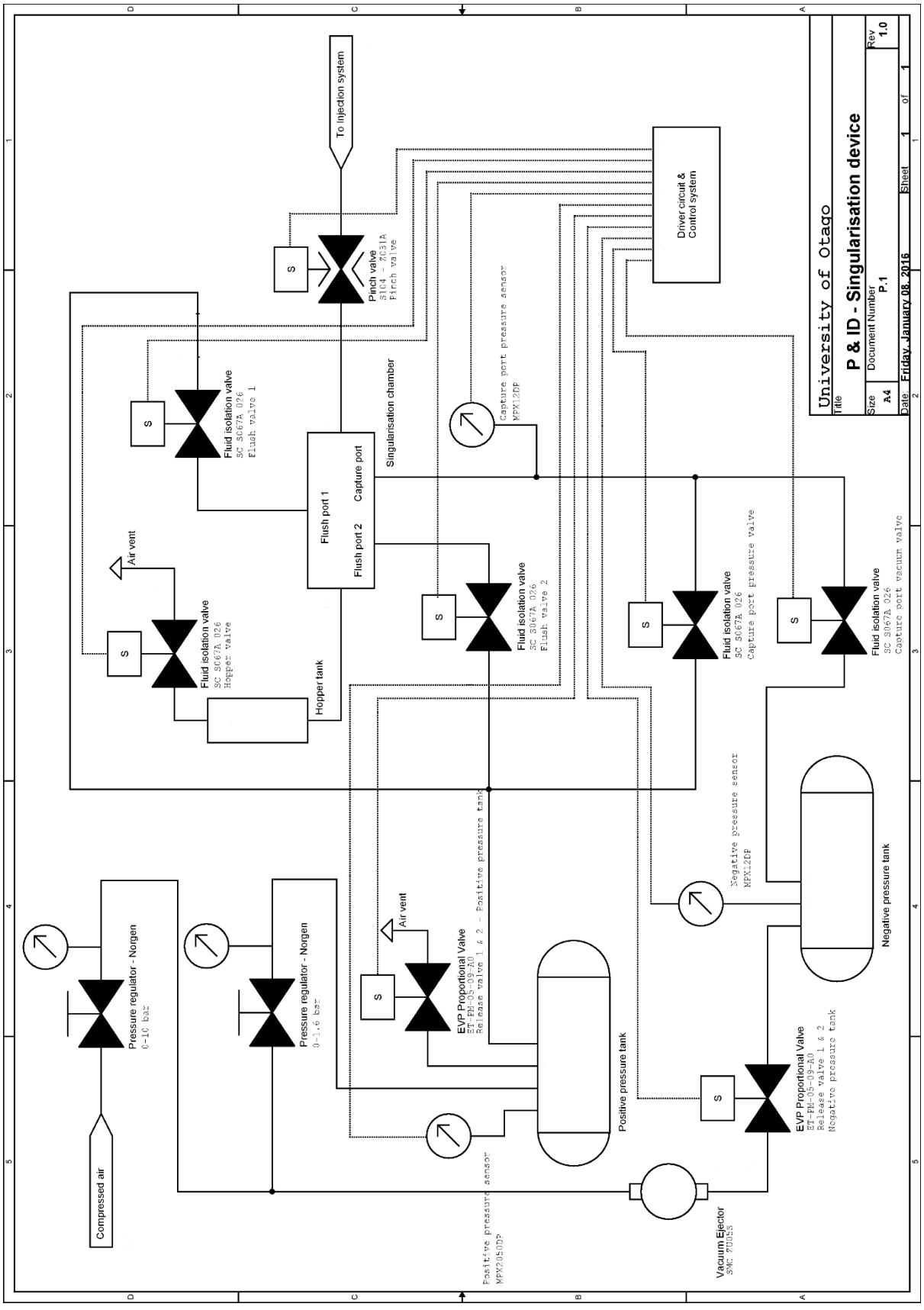

Figure 3.B-i. Piping and instrumentation diagram of the singularisation device.

Appendix 3.C

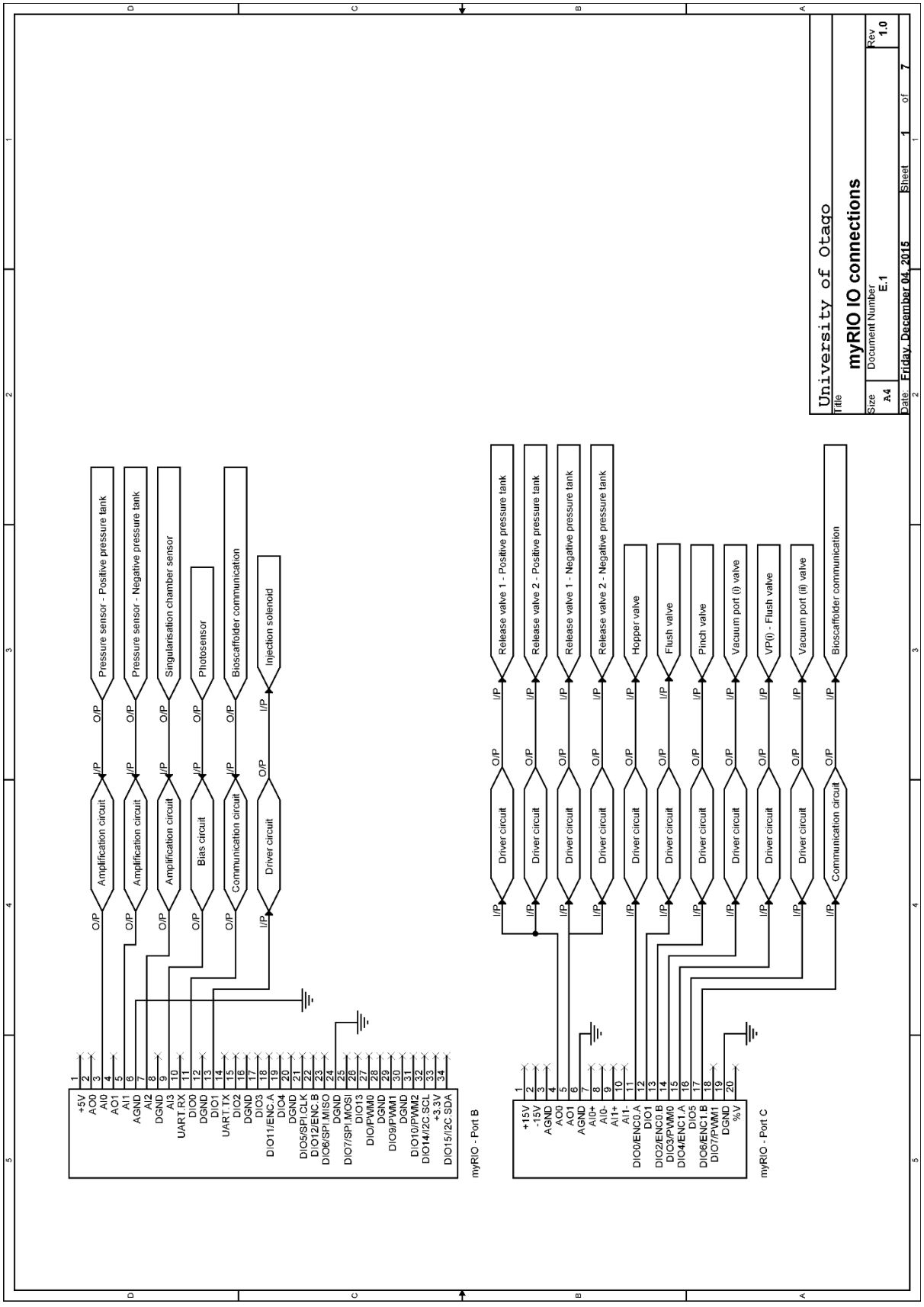

Figure 3.C-i. Schematic of the myRIO IO connections.

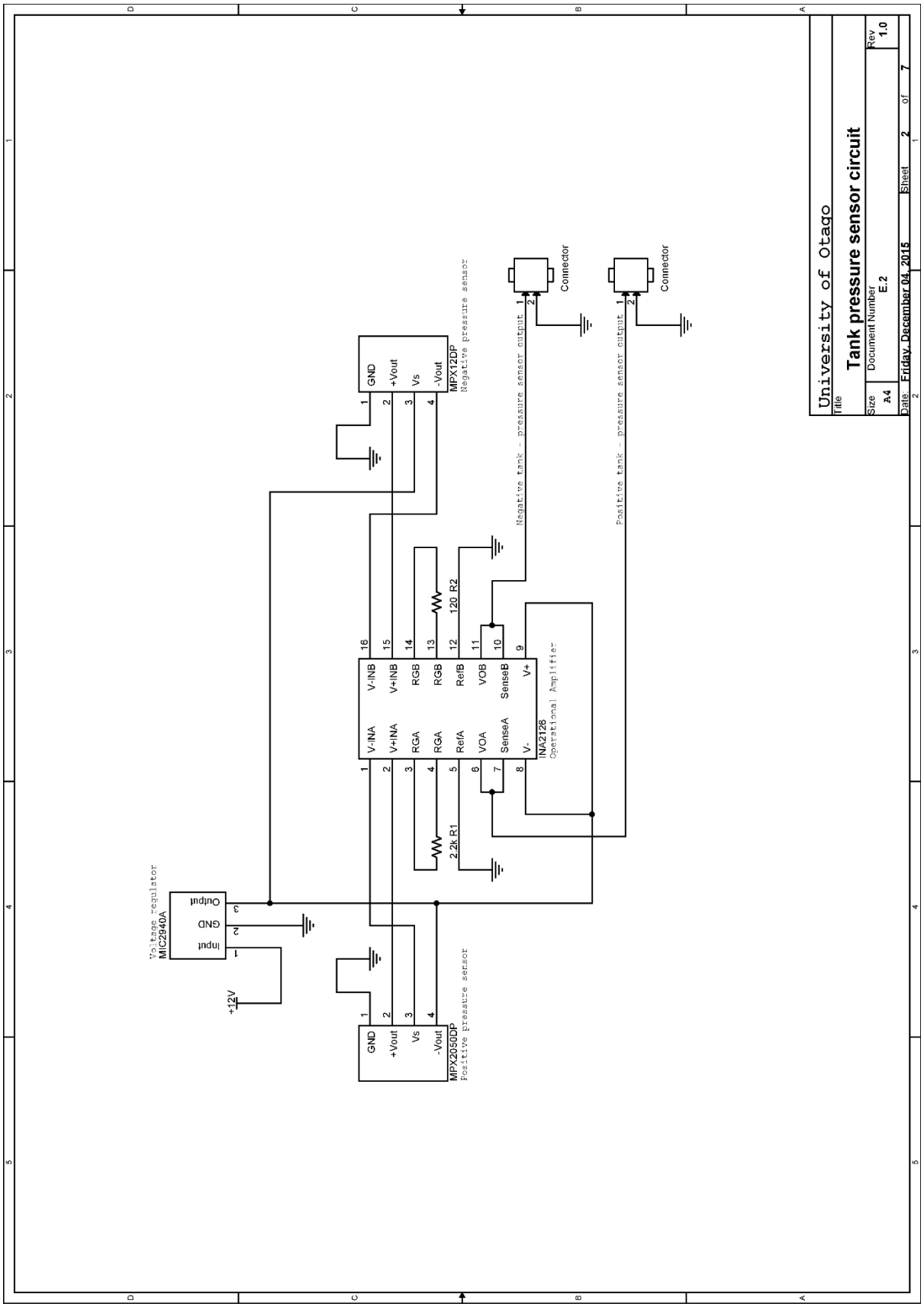

Figure 3.C-ii. Schematic tank pressure sensor circuit.

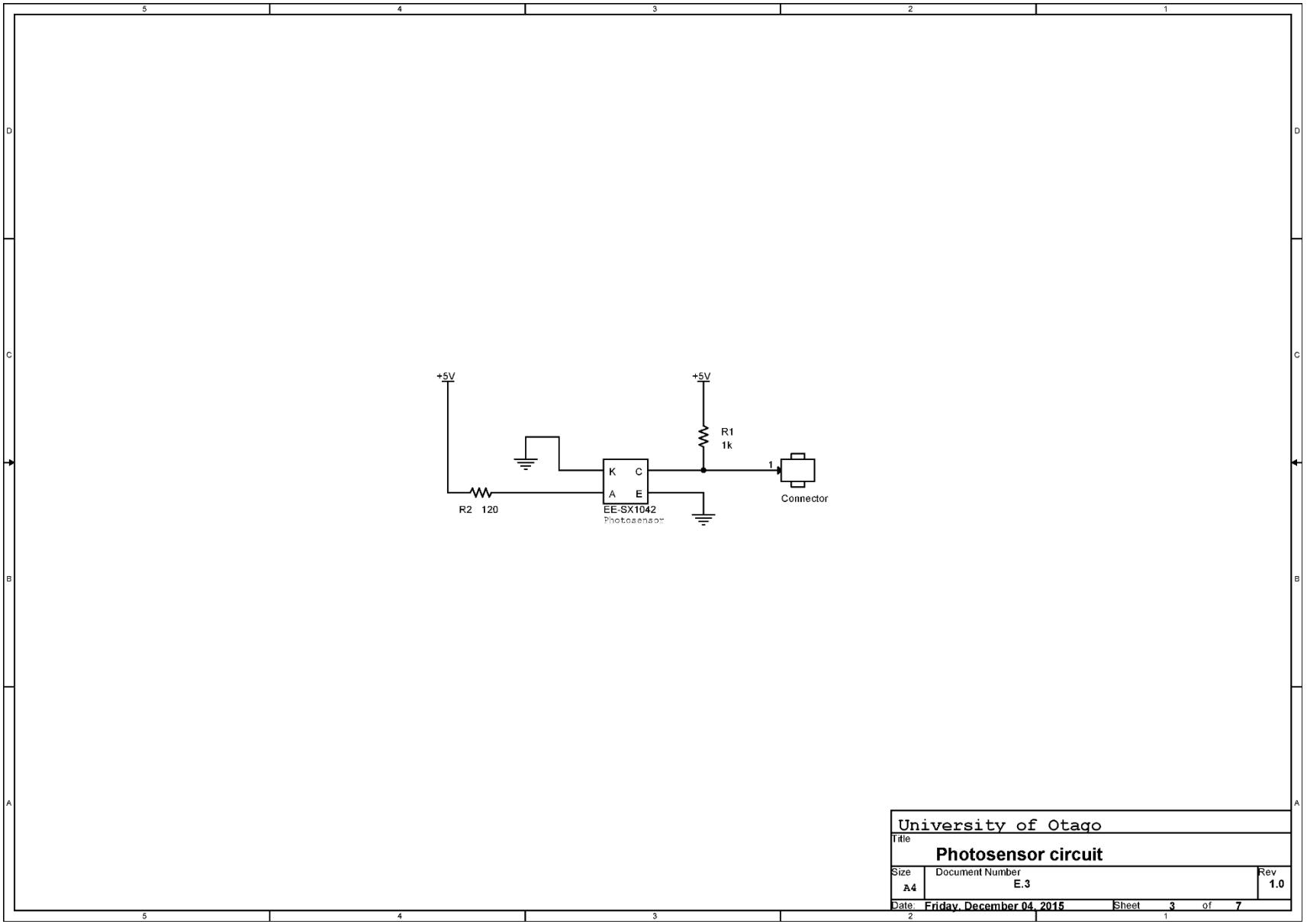

Figure 3.C-iii. Schematic of the photosensor circuit.

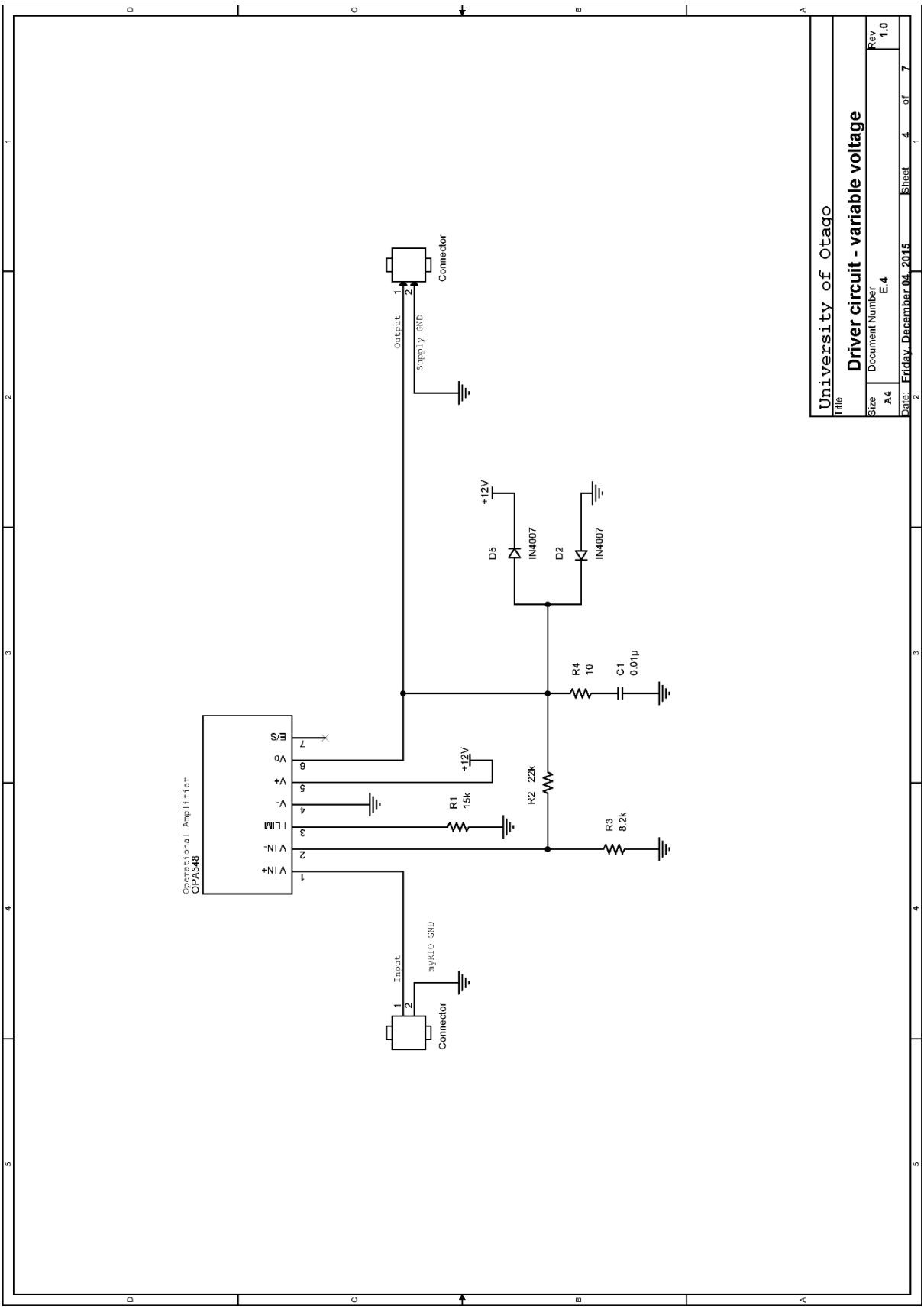

Figure 3.C-iv. Schematic of valve variable voltage driver circuit.

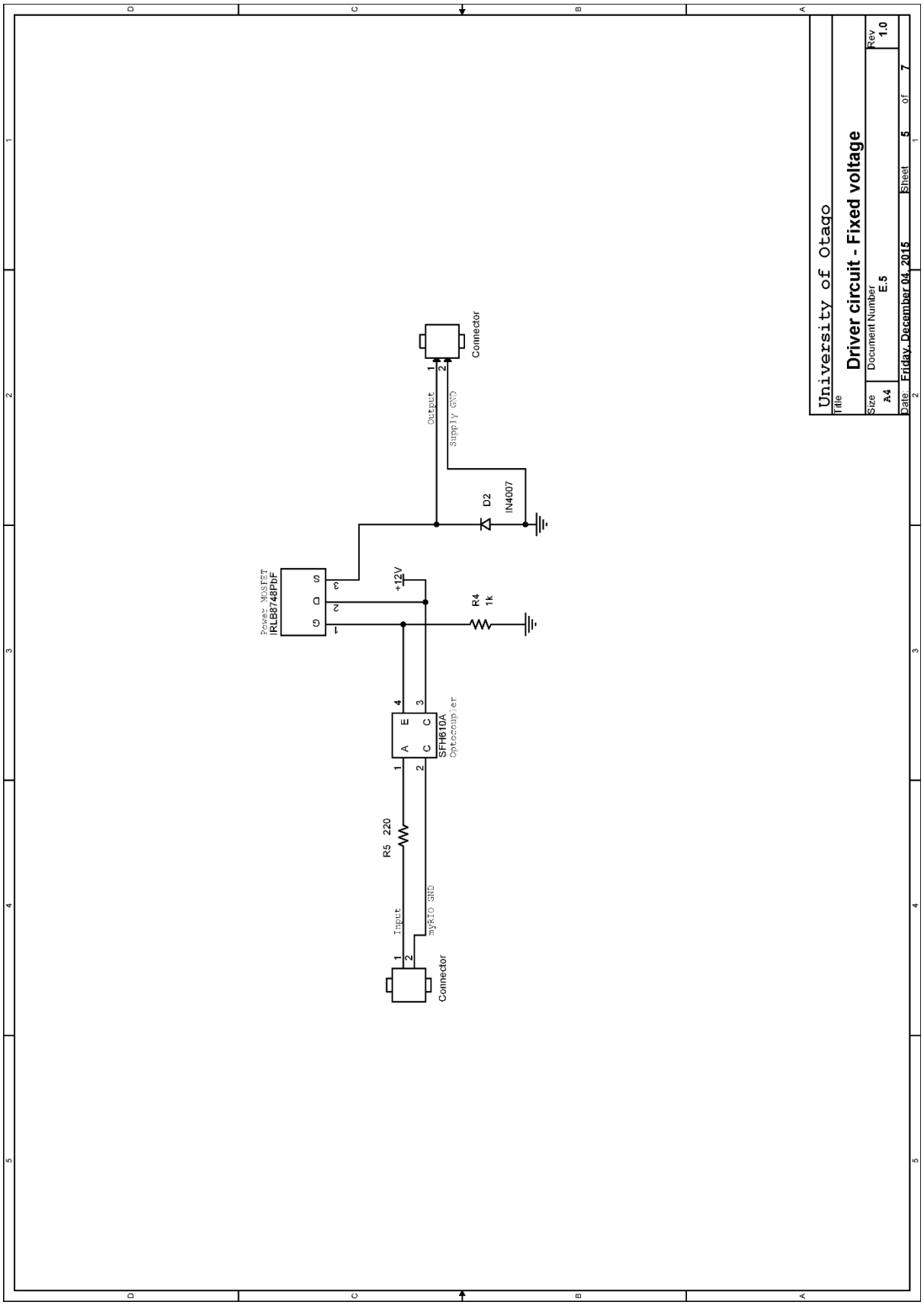

Figure 3.C-v. Schematic of the valve driver circuit.

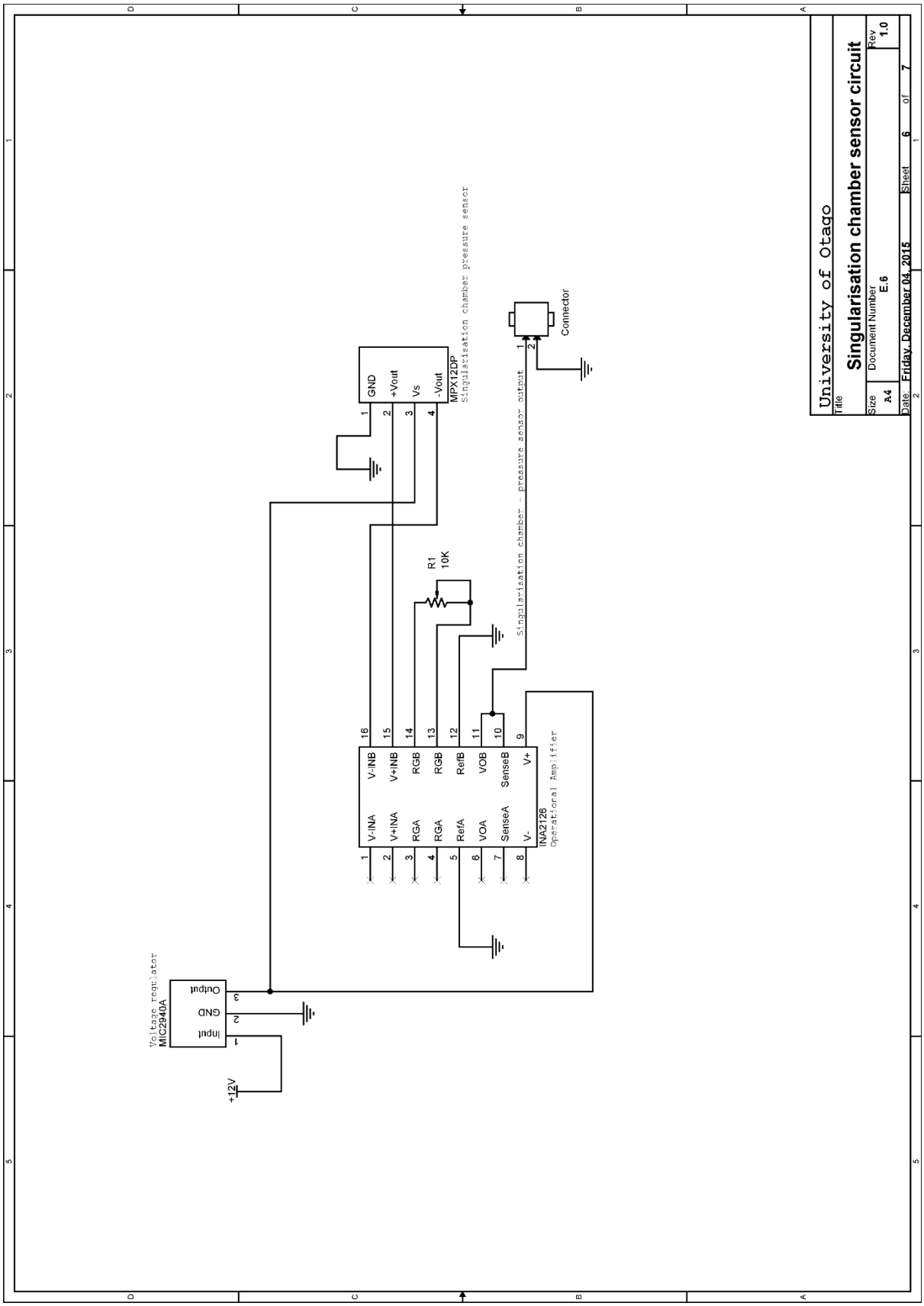

Figure 3.C-vi. Schematic of the singularisation chamber (capture port) sensor circuit.

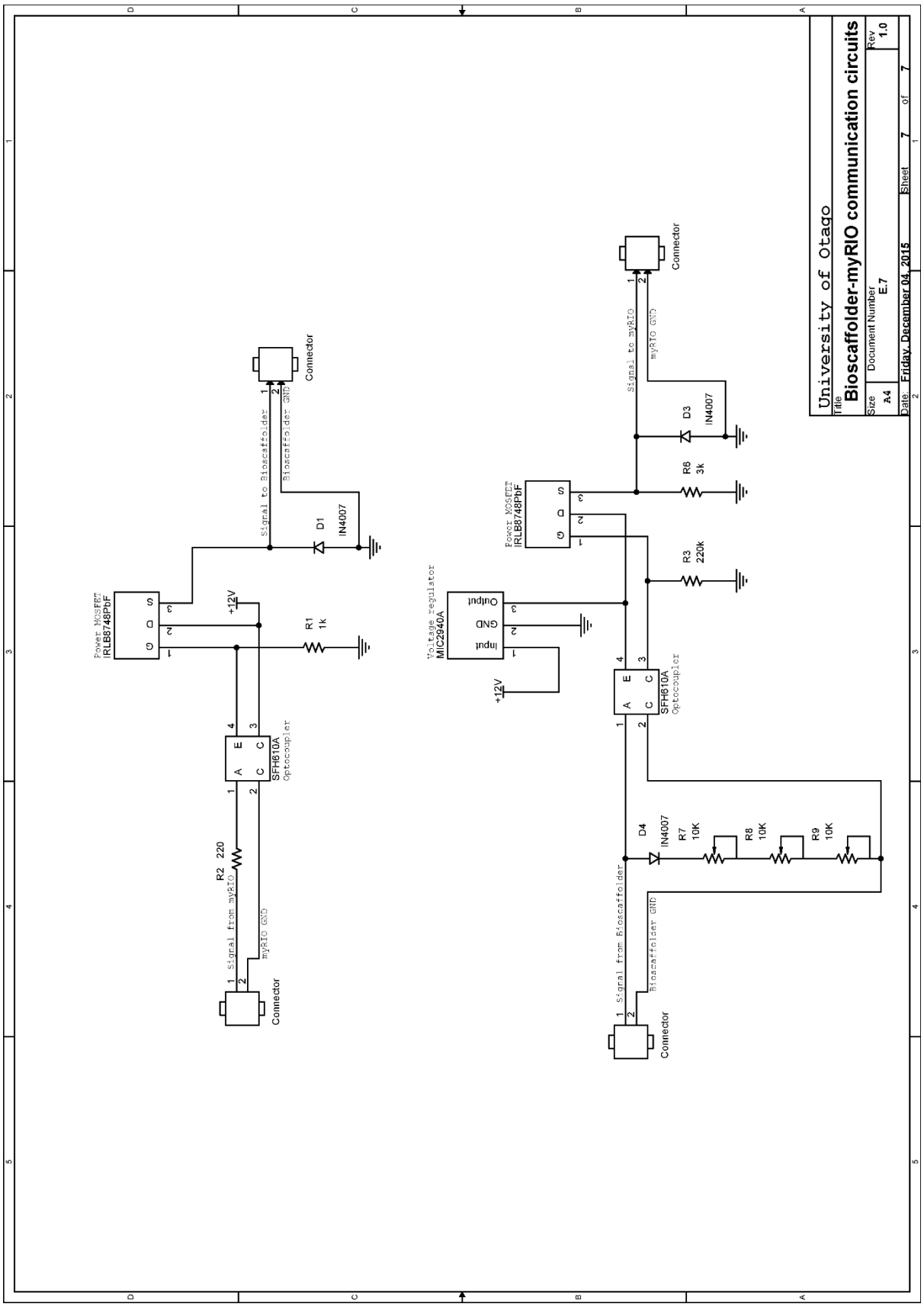

Figure 3.C-vii. Schematic of the Bioscaffolder-myRIO communication circuit.

Appendix 5.A

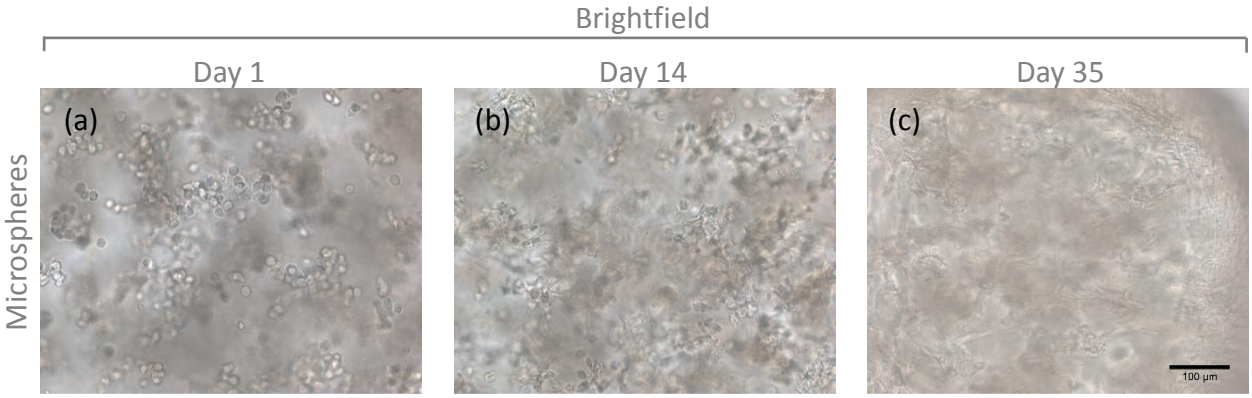

Figure 5.A-i. Brightfield microscopy images of HAC-laden 9.5% GelMA-0.5% HepMA microspheres on day 1, 14 and 35. *Scale bar = 100 µm for all images.*

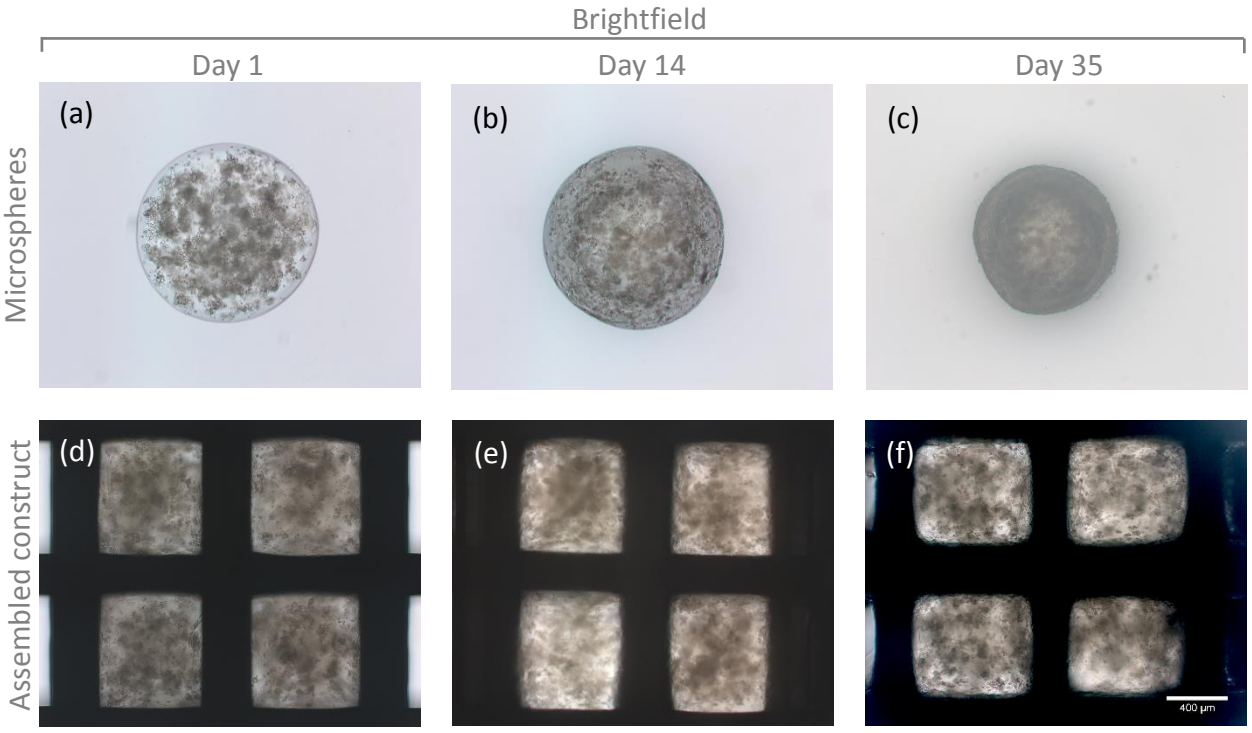

Figure 5.A-ii. Brightfield microscopy images of HAC-laden 9.5% GelMA-0.5% HepMA microspheres on day 1, 14 and 35. *Scale bar = 400 µm for all images.*

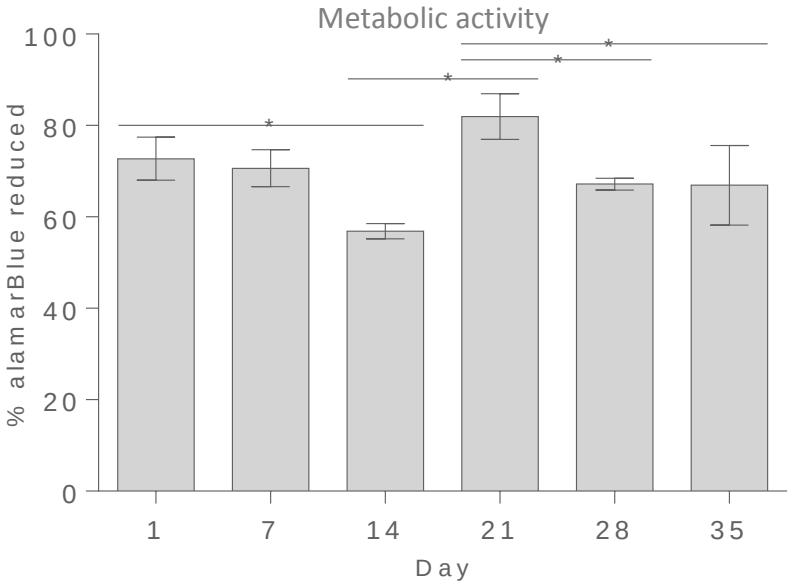

Figure 5.A-iii. Metabolic activity expressed in terms of percentage of AlamarBlue® reduced at day 1, 7, 14, 21, 28 and 35 of the graduated assembled construct with HAC, co-culture (50% HAC and 50% MSC) and MSC encapsulated 9.5% GelMA-0.5% HepMA microspheres assembled in a 4 x 3 x 2 fashion. The data is presented as mean ± SD (*n=3*). **Significant differences between columns below each end of lines (p<0.05).*

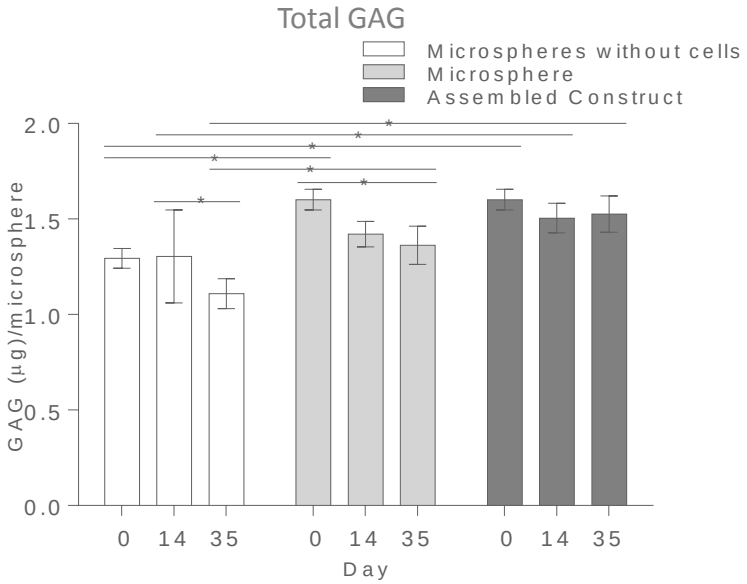

Figure 5.A-iv. Total GAG per microsphere for light crosslinked individual 9.5% GelMA-0.5% HepMA microspheres without cells, HAC-laden individual microspheres and assembled constructs on day 0, 14 and 35. The data is presented as mean ± SD (*n=4*). **Significant differences between columns below each end of lines (p<0.05).*

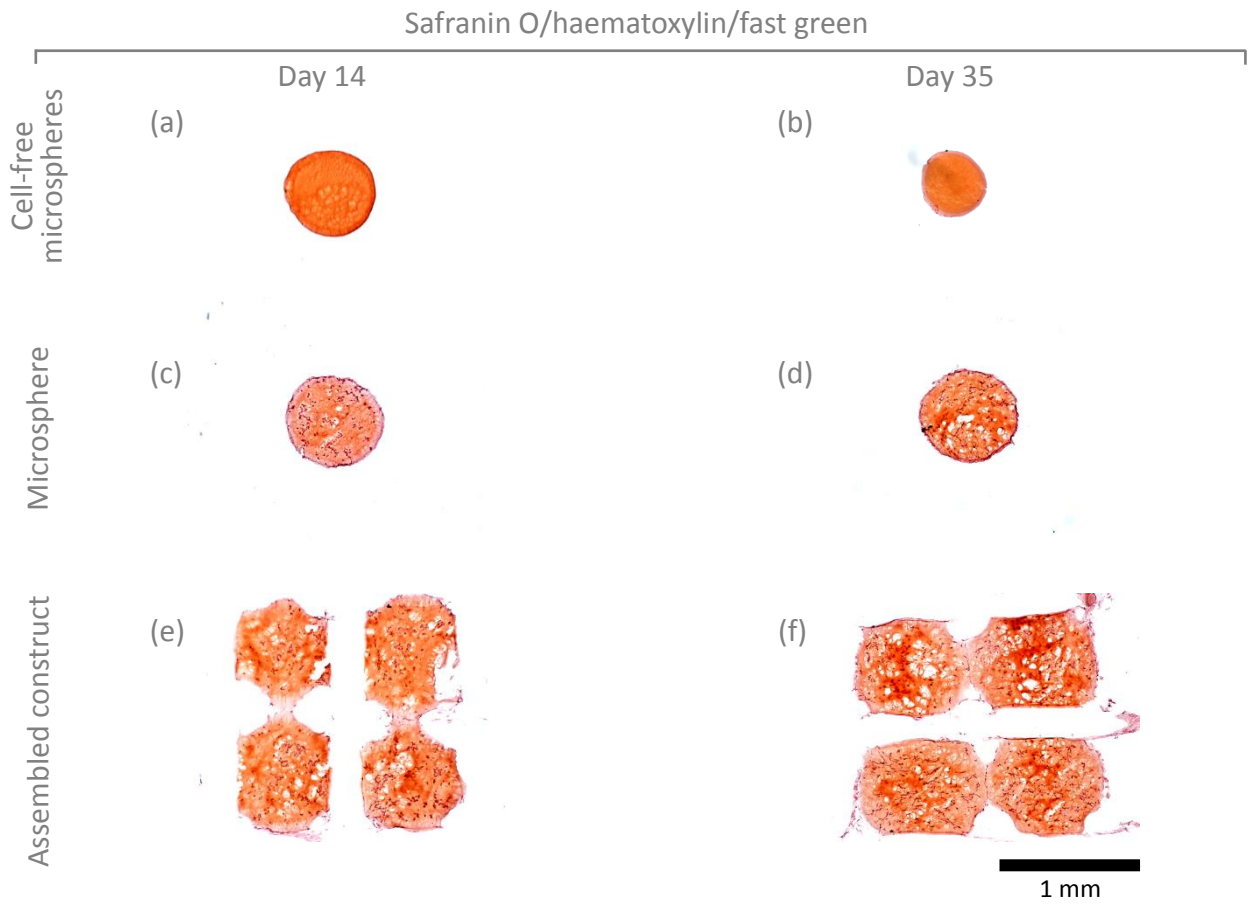

Figure 5.A-v. Histological staining (safranin O/haematoxylin/fast green) for cell-free 9.5% GelMA-0.5% HepMA microspheres, HAC-laden 9.5% GelMA-0.5 HepMA microspheres, HAC-laden 9.5% GelMA-0.5% HepMA assembled constructs on day 14 and 35. *Scale bar = 1 mm for all images.*

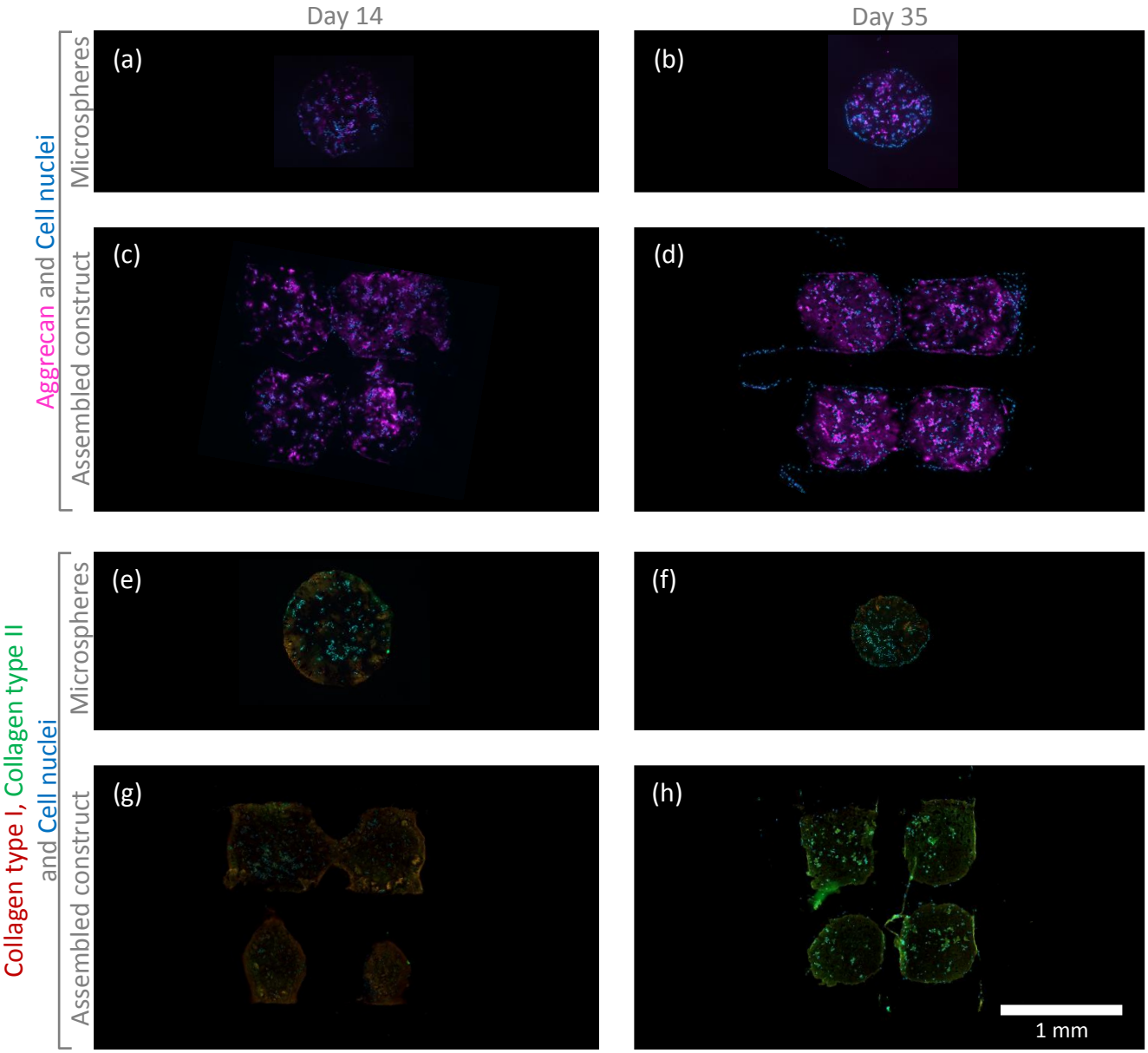

Figure 5.A-vi. Immunofluorescence staining for Aggrecan and Hoechst 33342 (cell nuclei) and Collagen type I, Collagen type II and Hoechst 33342 (overlaid) imaged using a fluorescence microscopy for HAC-laden 9.5% GelMA-0.5% HepMA microspheres and assembled constructs on day 14 and 35. *Scale bar = 1 mm for all images.*

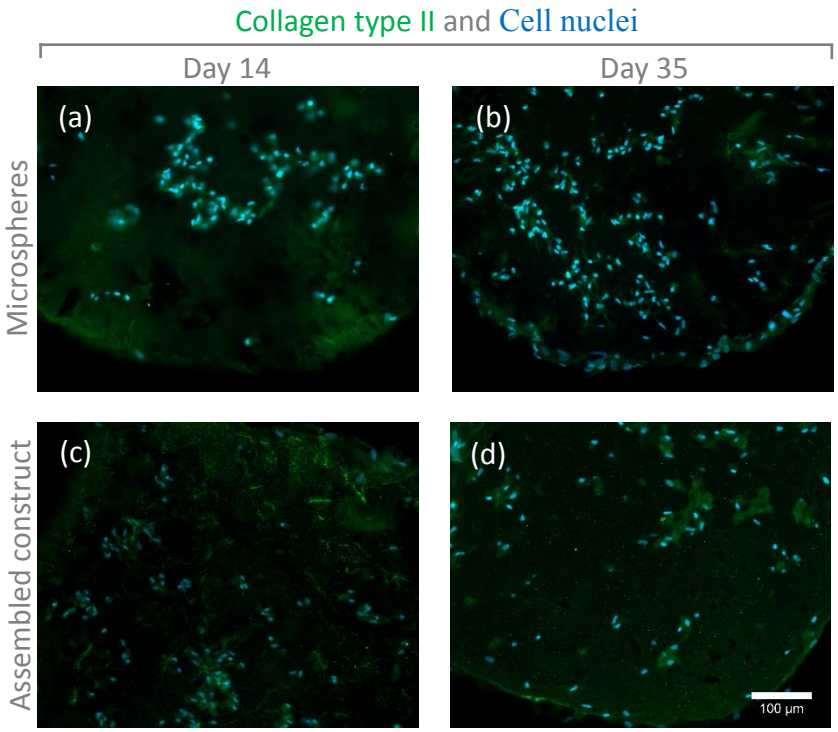

Figure 5.A-vii. Immunofluorescence staining for Collagen type II and Hoechst 33342 (cell nuclei) imaged using a fluorescence microscopy for HAC-laden 9.5% GelMA-0.5% HepMA individual microspheres and assembled constructs on day 14 and 35. *Scale bar = 100 µm for all images.*

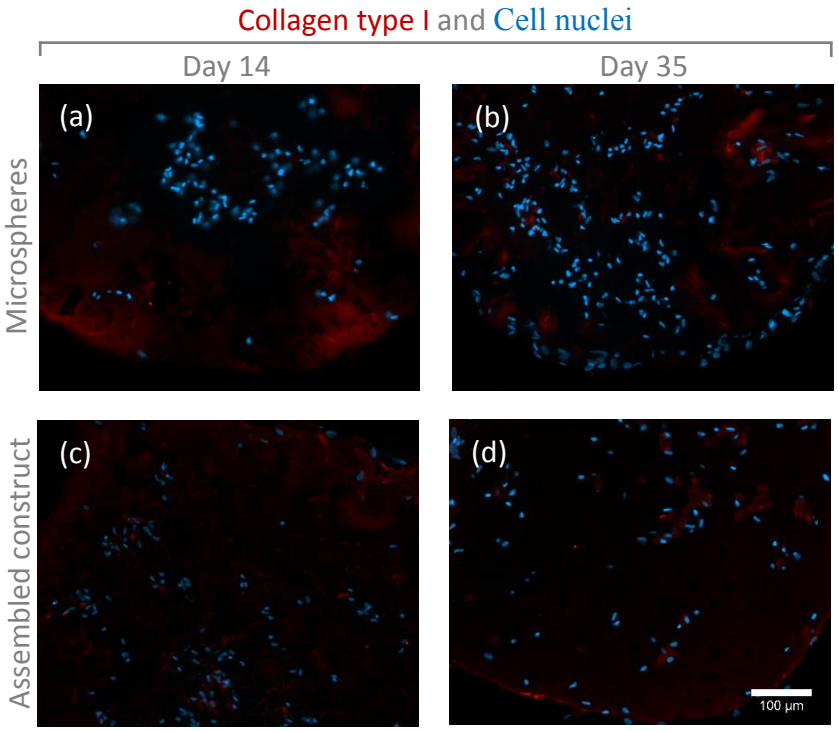

Figure 5.A-viii. Immunofluorescence staining for Collagen type I and Hoechst 33342 (cell nuclei) imaged using a fluorescence microscopy for HAC-laden 9.5% GelMA-0.5% HepMA individual microspheres and assembled constructs on day 14 and 35. *Scale bar = 100 µm for all images.*

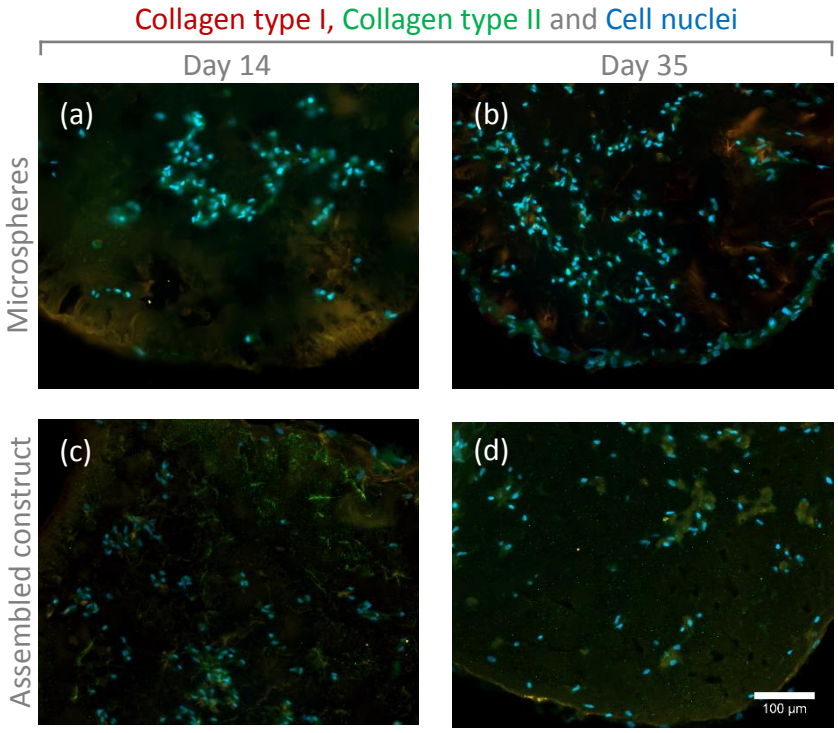

Figure 5.A-ix. Immunofluorescence staining for (overlaid) Collagen type I, Collagen type II and Hoechst 33342 imaged using a fluorescence microscopy for HAC-laden 9.5% GelMA-0.5% HepMA individual microspheres and assembled constructs on day 14 and 35. *Scale bar = 100 µm for all images.*

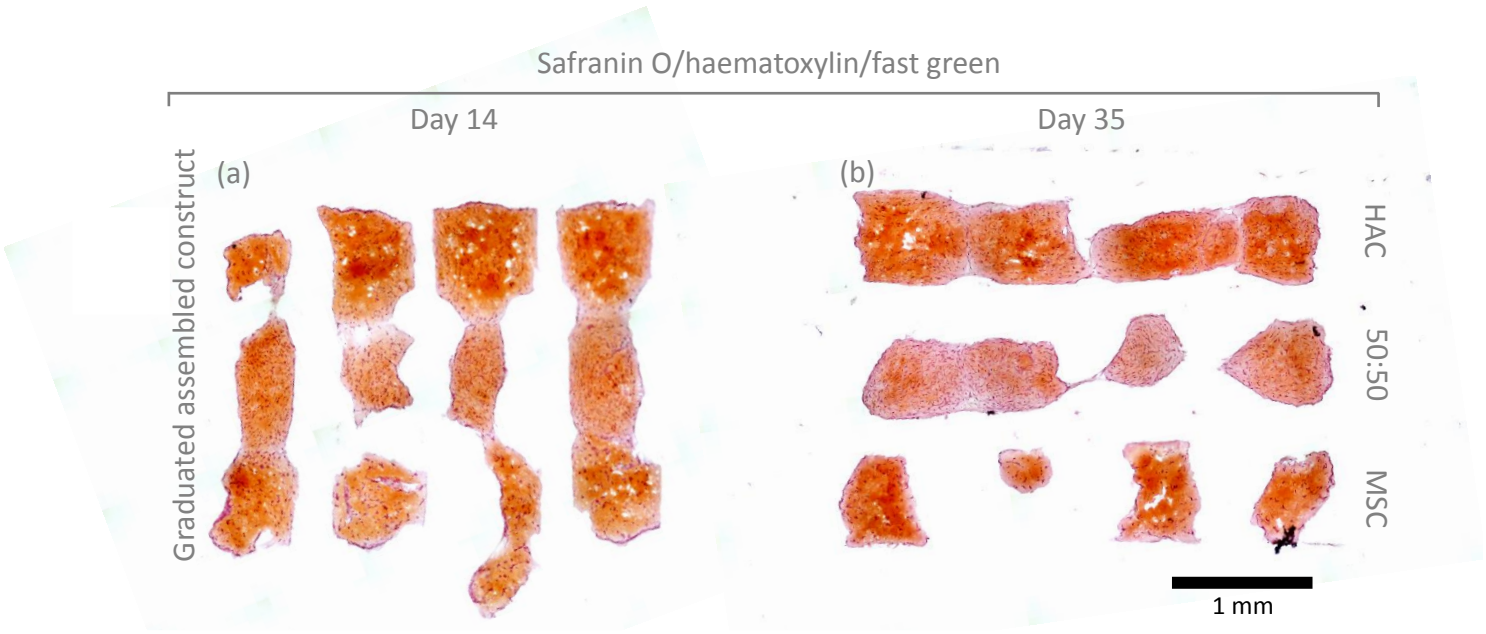

Figure 5.A-x. Histological staining (safranin O/haematoxylin/fast green) for graduated assembled construct (HAC, co-culture (50% HAC and 50% MSC) and MSC laden 9.5% GelMA-0.5% HepMA microspheres) and micro-tissues on (a) day 14 and (b) day 35. *Scale bar = 1 mm for all images.*

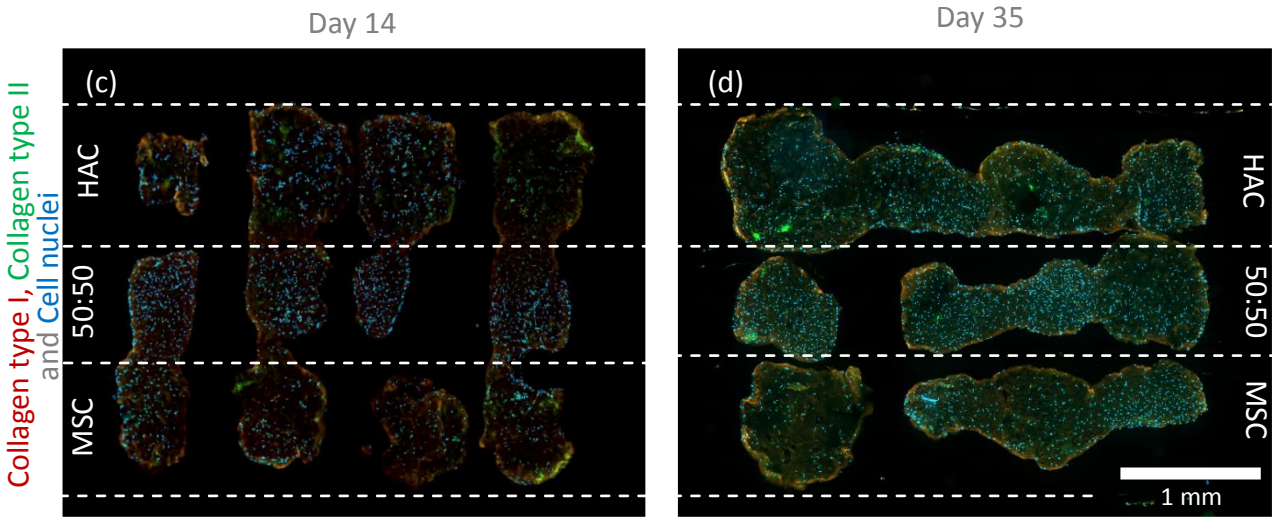

Figure 5.A-xi. Immunofluorescence staining for Collagen type I, Collagen type II and Hoechst 33342 (cell nuclei) imaged using a confocal fluorescence microscopy for a graduated assembled construct (HAC, co-culture (50% HAC and 50% MSC) and MSC-laden 9.5% GelMA-0.5% HepMA microspheres) on day 14 and 35. The dotted lines shows the division in the construct with different cell types. *Scale bar = 1 mm for all images.*

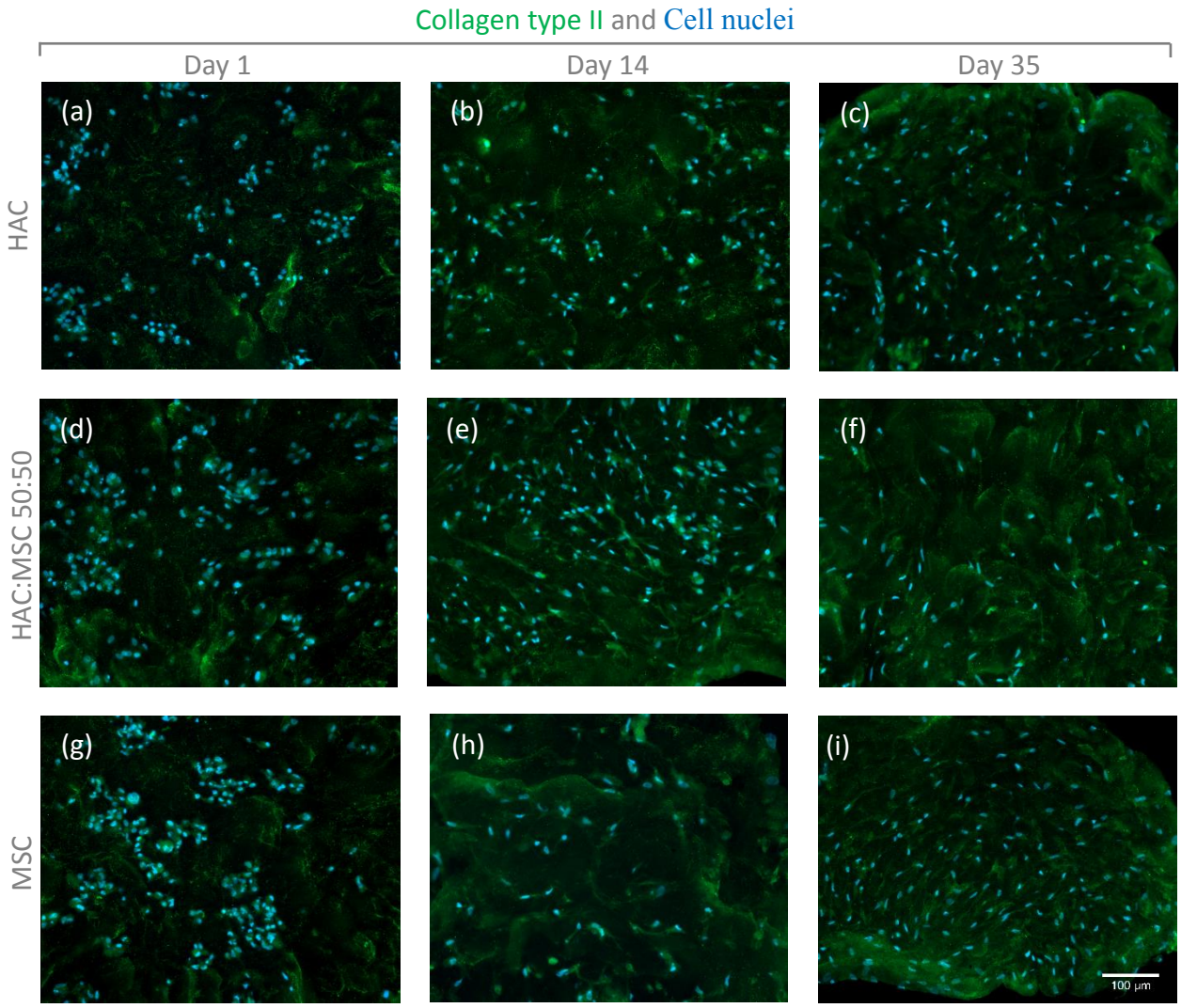

Figure 5.A-xii. Immunofluorescence staining for Collagen type II and Hoechst 33342 (cell nuclei) imaged using a fluorescence microscopy for HAC, co-culture (50% HAC and 50% MSC) and MSC laden 9.5% GelMA-0.5 HepMA microspheres that were assembled as a construct on day 1, 14 and 35. *Scale bar = 100 µm for all images.*

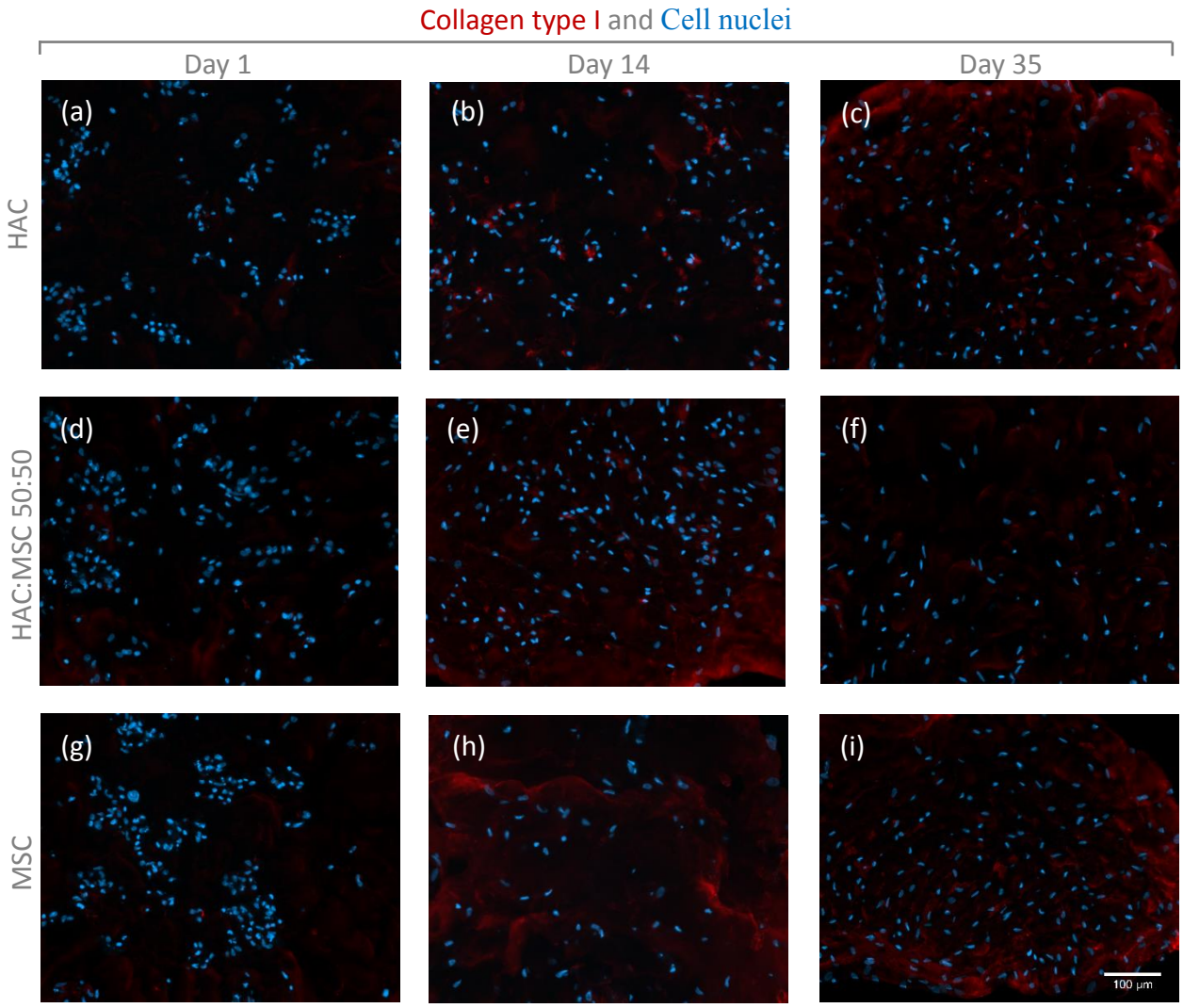

Figure 5.A-xiii. Immunofluorescence staining for Collagen type I and Hoechst 33342 (cell nuclei) imaged using a fluorescence microscopy for HAC, co-culture (50% HAC and 50% MSC) and MSC laden 9.5% GelMA-0.5 HepMA microspheres that were assembled as a construct on day 1, 14 and 35. *Scale bar = 100 µm for all images.*

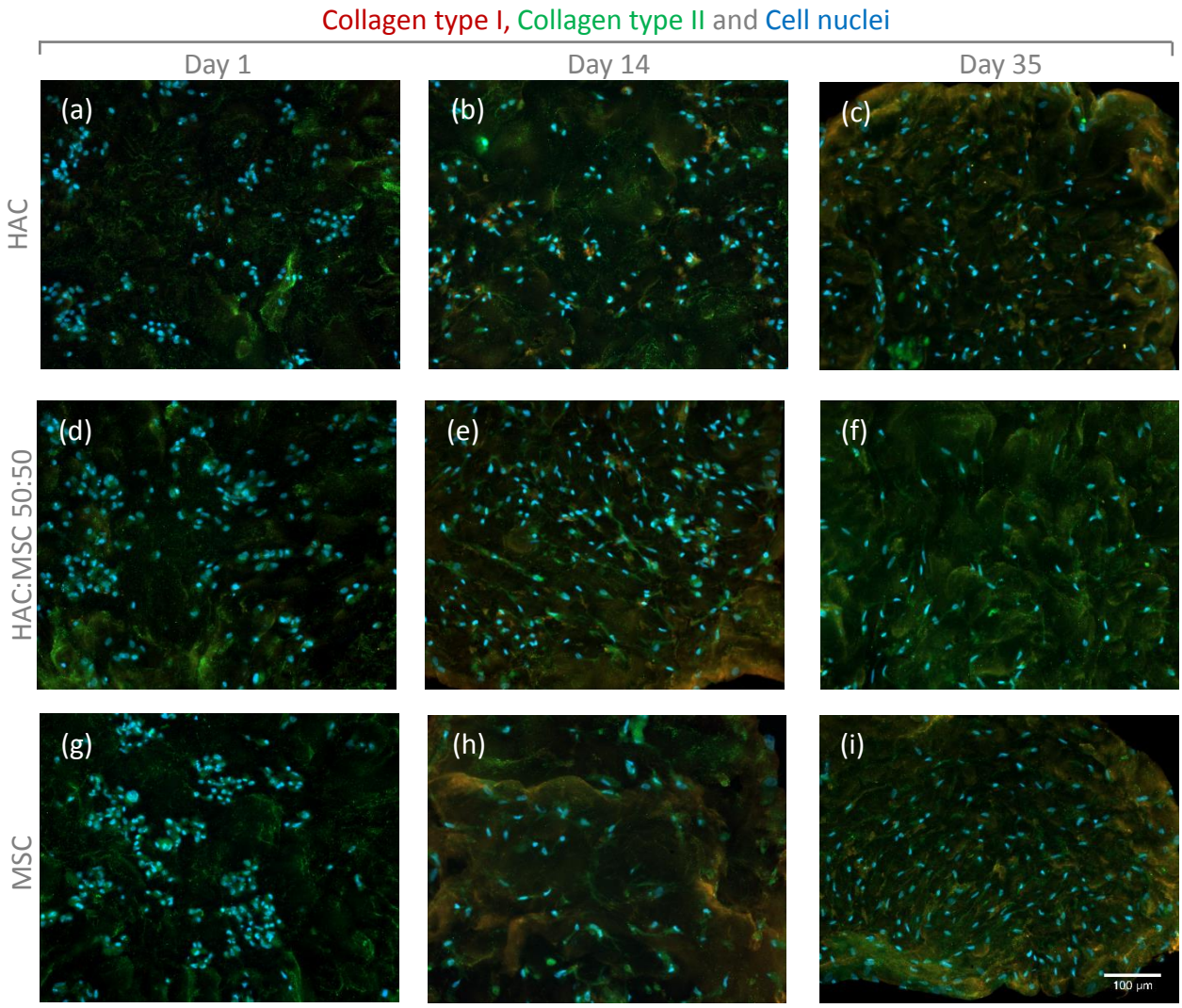

Figure 5.A-xiv. Immunofluorescence staining for Collagen type I, Collagen type II and Hoechst 33342 (cell nuclei) imaged using a fluorescence microscopy for HAC, co-culture (50% HAC and 50% MSC) and MSC laden 9.5% GelMA-0.5 HepMA microspheres that were assembled as a construct on day 1, 14 and 35. *Scale bar = 100 µm for all images.*

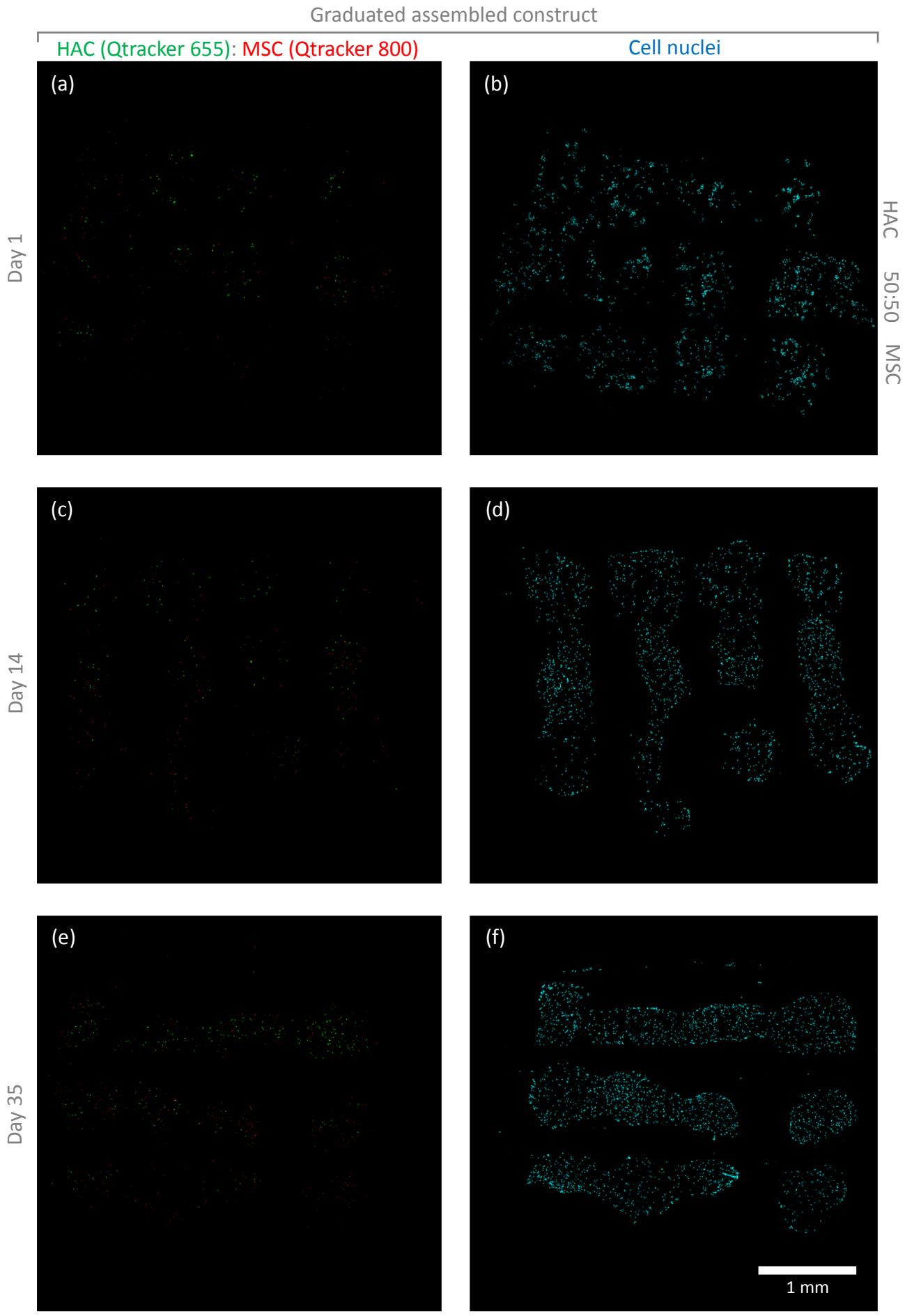

Figure 5.A-xv. Confocal microscope images of the sectioned graduated assembled construct (HAC, co-culture (50% HAC and 50% MSC) and MSC laden 9.5% GelMA-0.5 HepMA microspheres) on day 1, 14 and 35. HAC (Qtracker 655), MSC (Qtracker 800) and Hoechst 33342. *Scale bar = 1 mm for all images.*

Appendix 6.A

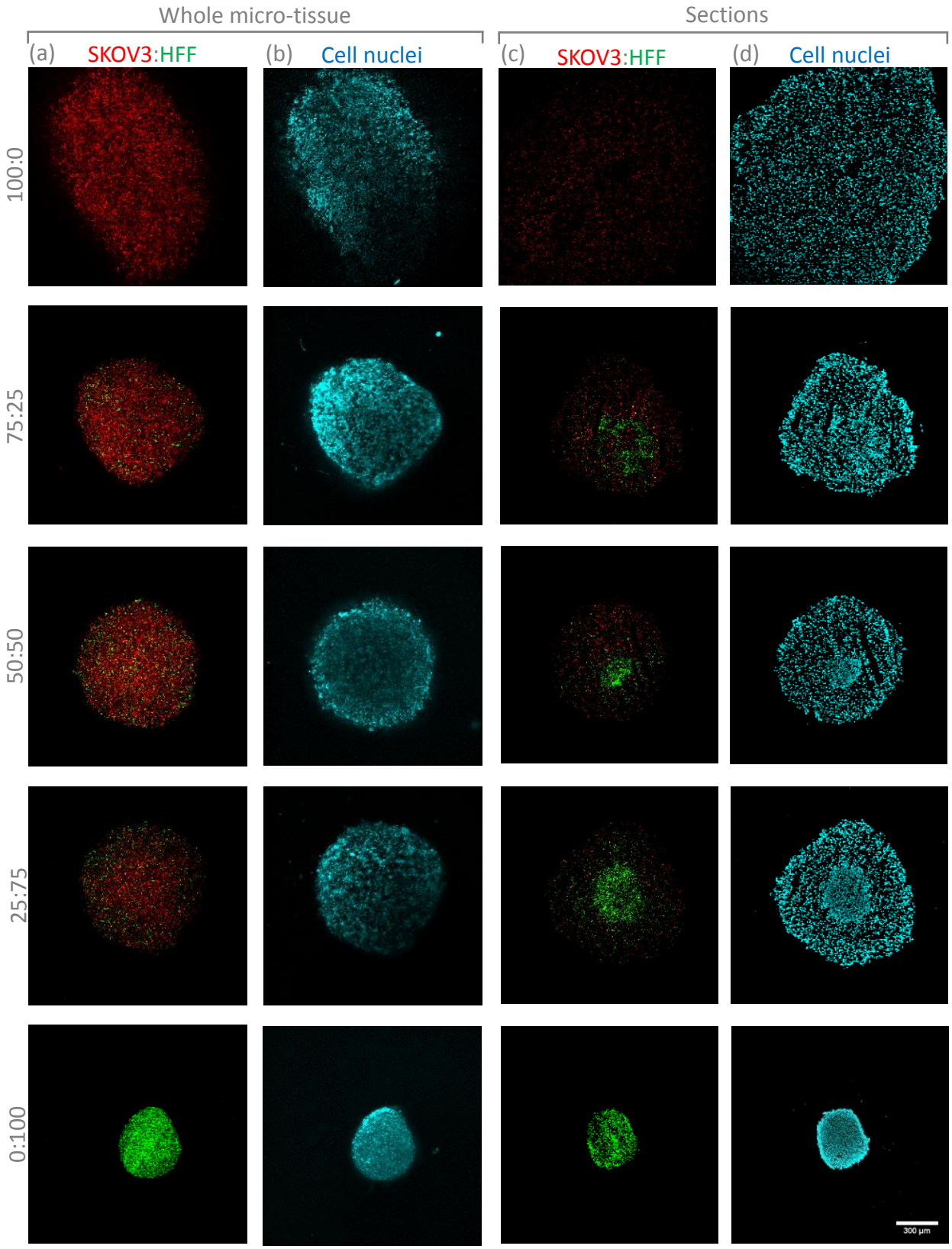

Figure 6.A-i. Fluorescence microscope images of whole micro-tissues (a and b) and micro-tissues sections (c and d) with SKOV3 (Qtracker 800; red) and HFF (Qtracker 655; green) (a and c), and Hoechst 33342 (cell nuclei, blue; b and d). The ratio of SKOV3 to HFF are in rows. *Scale bar = 300 µm for all images.*

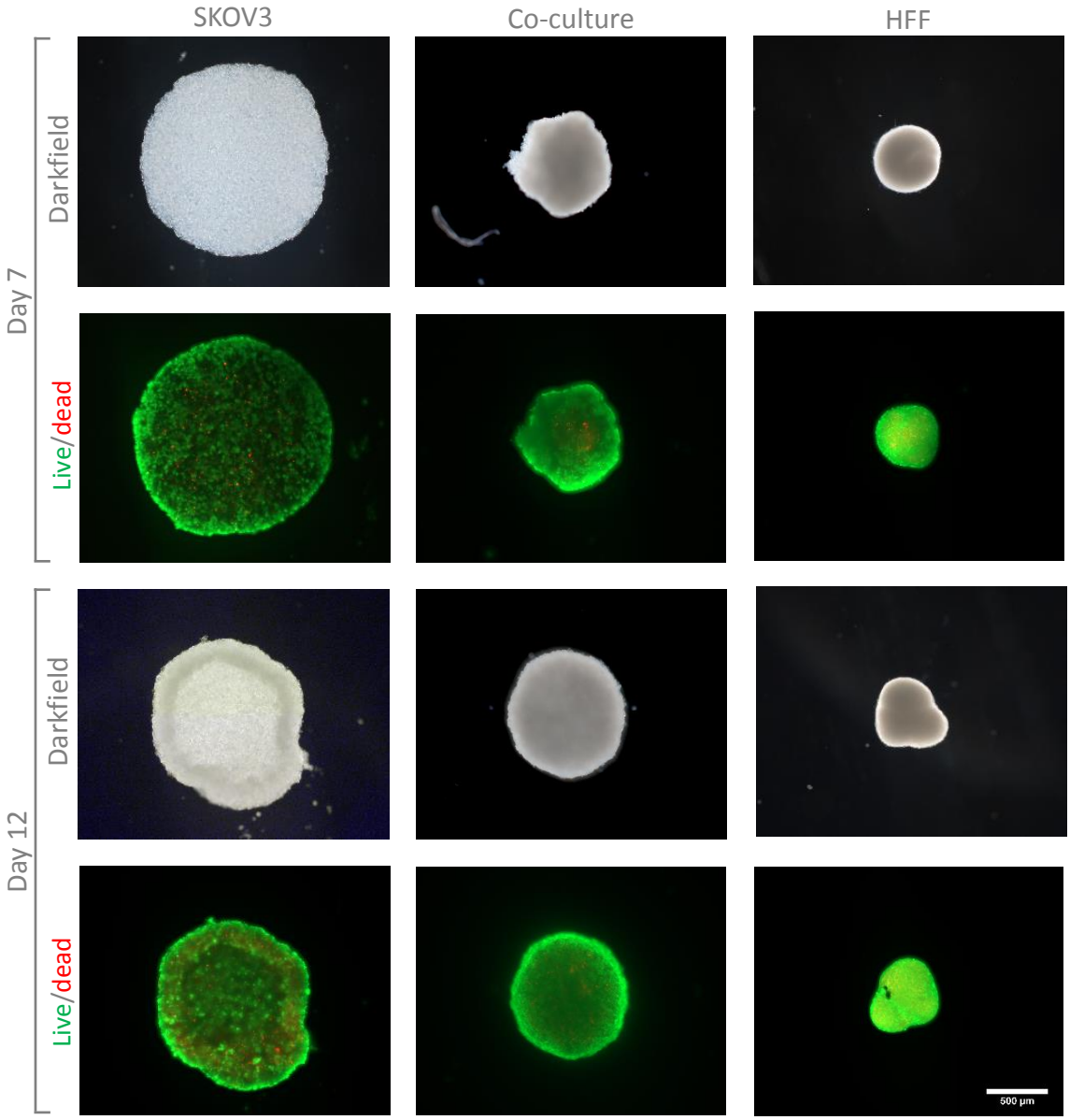

Figure 6.A-ii. Fluorescence microscopy and darkfield images of SKOV3, co-culture and HFF micro-tissues on day 7 and day 12. The samples were stained with Calcein AM (live cells, green) and Propidium Iodide (dead cells, red). *Scale bar = 500 µm for all images.*

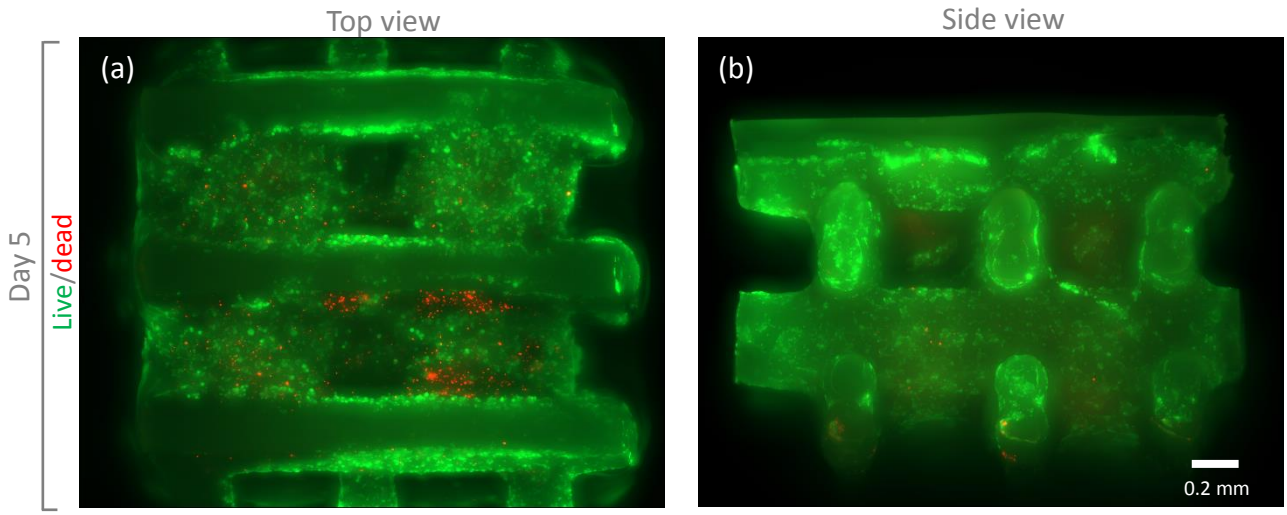

Figure 6.A-iii. Fluorescence microscopy of assembled cancer construct after 5 days of assembly (a) top view and (b) side view. The samples were stained with Calcein AM (live cells, green) and Propidium Iodide (dead cells, red). *Scale bar = 0.2 mm for all images.*

The visual inspection of the live/dead fluorescence microscopy images of micro-tissues (Figure 6.A-ii) on day 7 and 12 showed mostly viable cells which was also true of the assembled scaffold (Figure 6.A-iii) after 5 days in culture.

Appendix 7.A

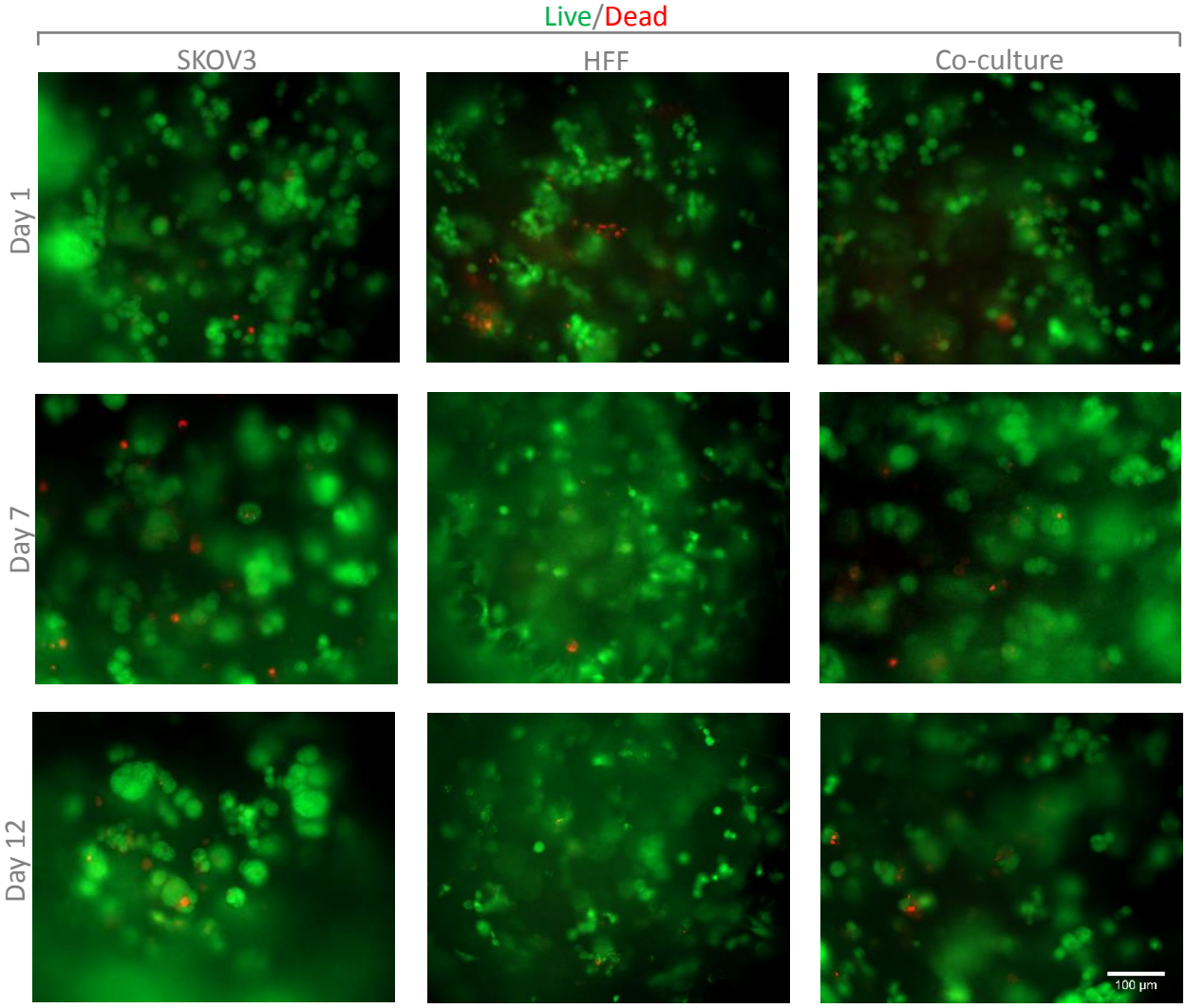

Figure 7.A-i. Fluorescence microscopy images of SKOV3, HFF, and co-culture encapsulated microspheres on day 1, 7 and 12 stained with Calcein AM (live cells, green) and Propidium Iodide (dead cells, red). *Scale bar = 100 µm for all images.*

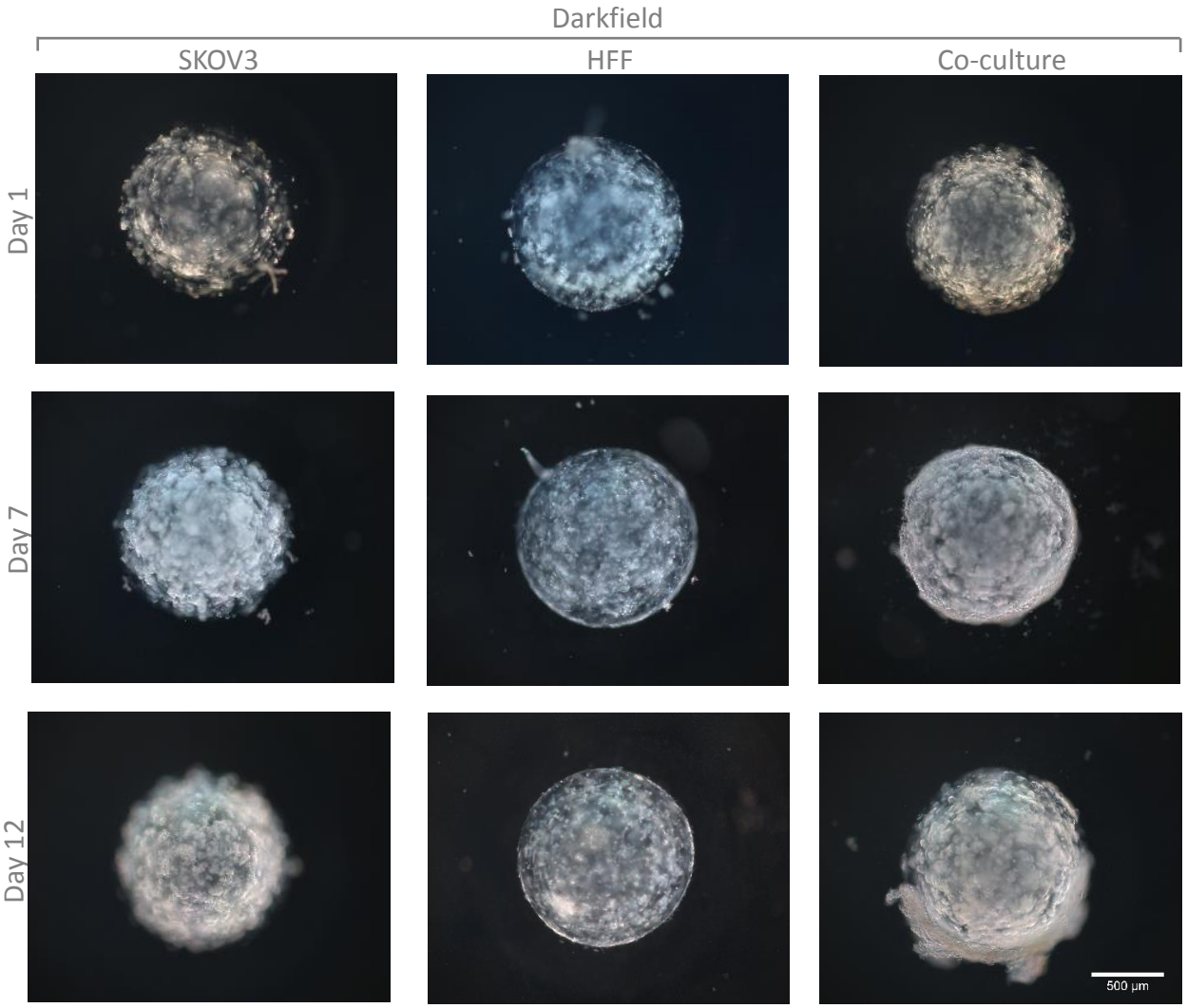

Figure 7.A-ii. Darkfield microscopy images of SKOV3, HFF, and encapsulated microspheres on day 0, 7 and 12. *Scale bar = 500 µm for all images.* For higher magnification images Figure 7.A-iii.

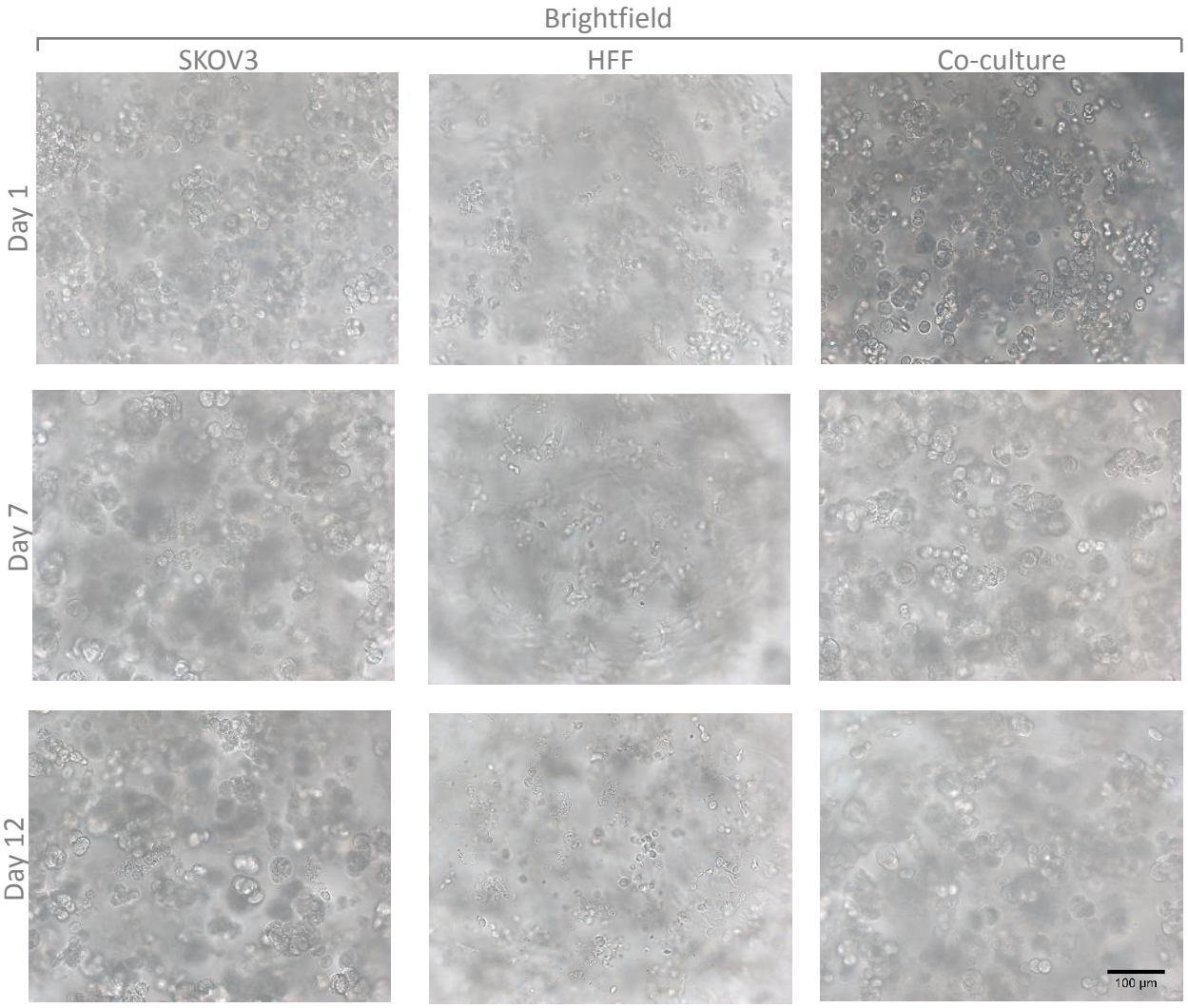

Figure 7.A-iii. Brightfield microscopy images of SKOV3, HFF and co-culture encapsulated microspheres on day 0, 7 and 12. *Scale bar = 100 µm for all images.* For lower magnification image see Figure 7.A-ii.

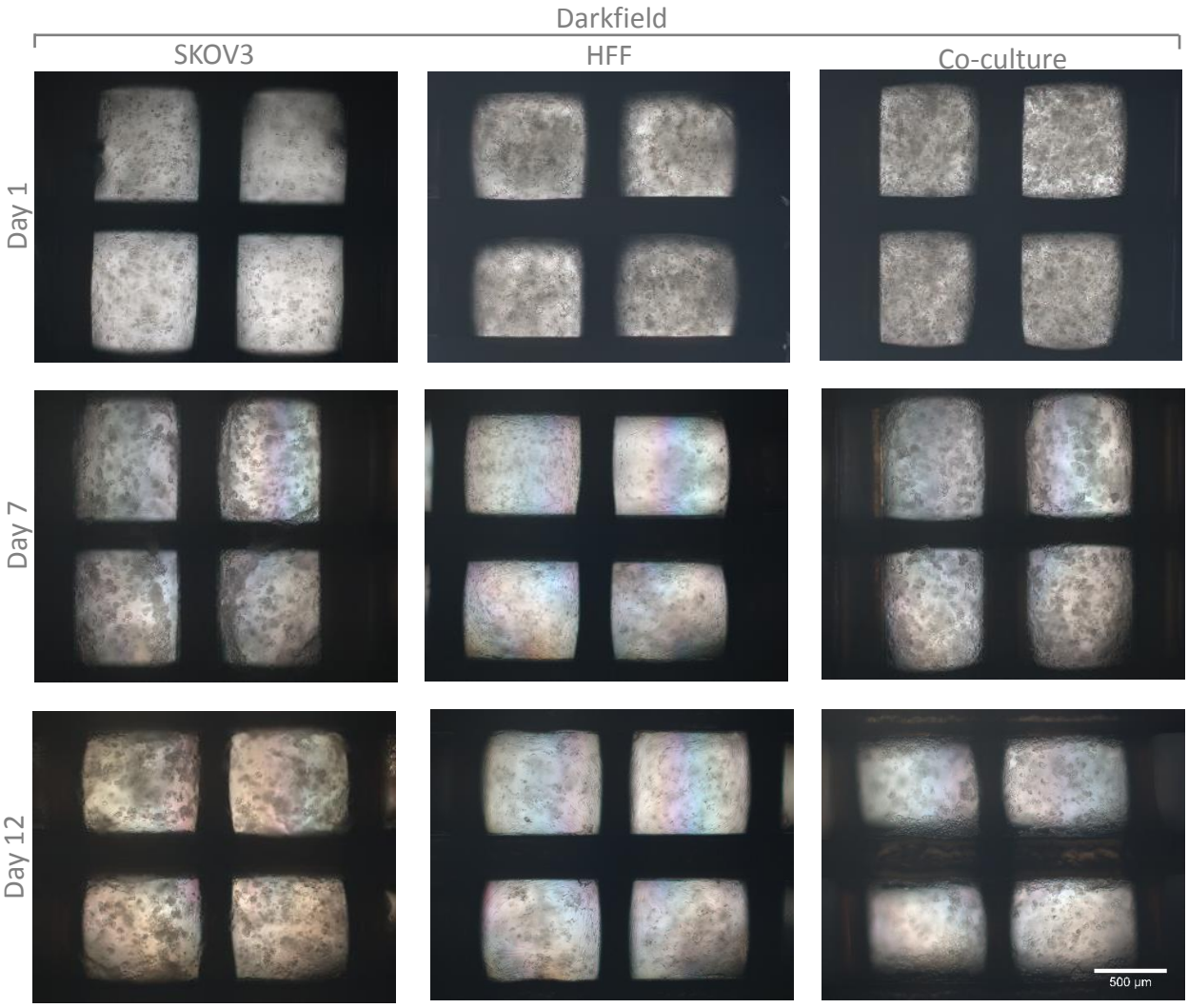

Figure 7.A-iv. Darkfield microscopy images of SKOV3, HFF, and co-culture encapsulated microspheres on day 0, 7 and 12 stained. *Scale bar = 500 µm for all images.*

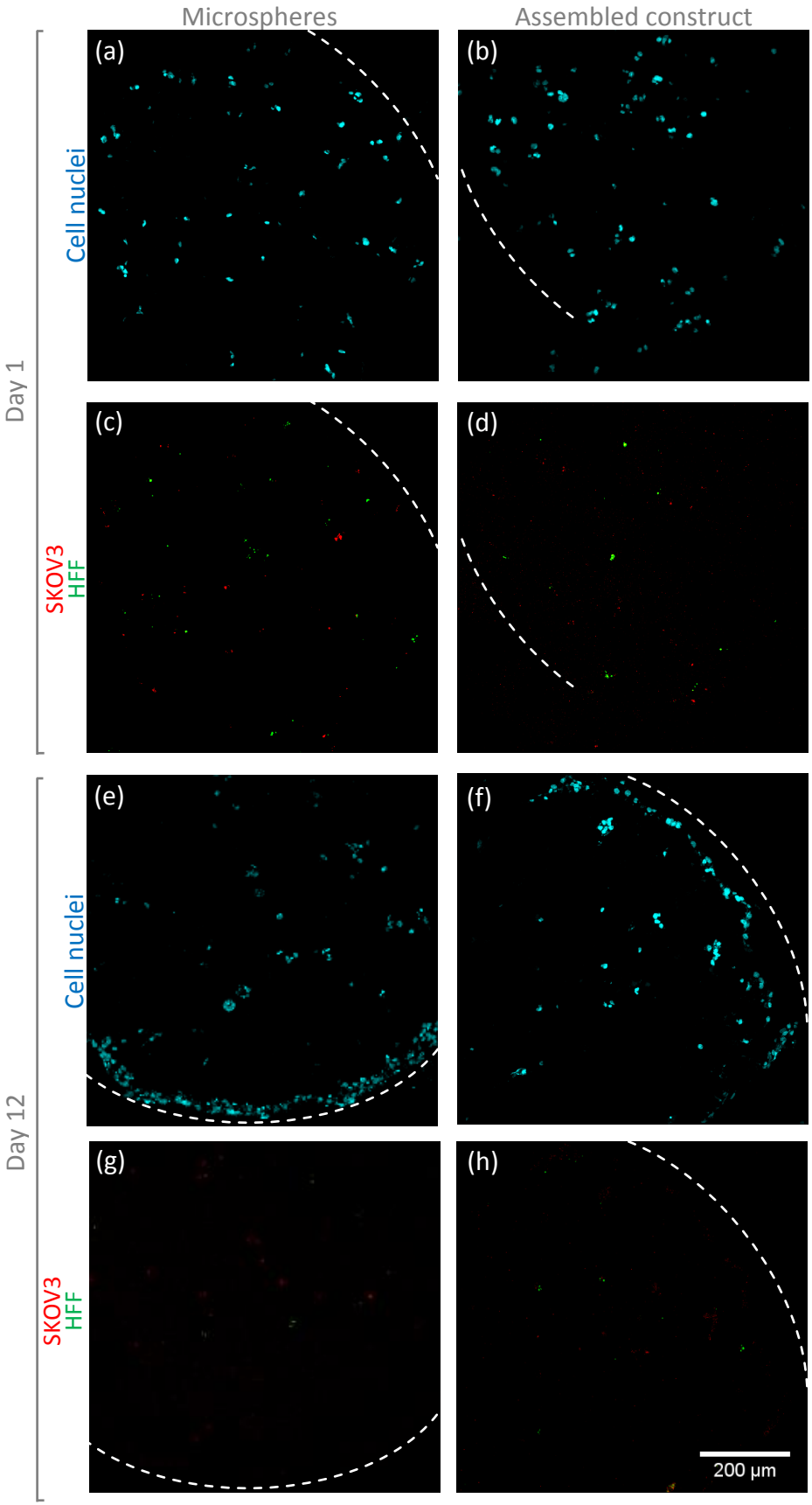

Figure 7.A-v. Fluorescence microscope images of the co-culture (SKOV3:HFF 75:25) microspheres and assembled construct sections on Day 1 and 12. SKOV3 (Qtracker 800, red), HFF (Qtracker 655, green) and Hoechst 33342 (cell nuclei, blue). The dotted line represent the outer edge of the sample. *Scale bar = 200 µm for all images.*

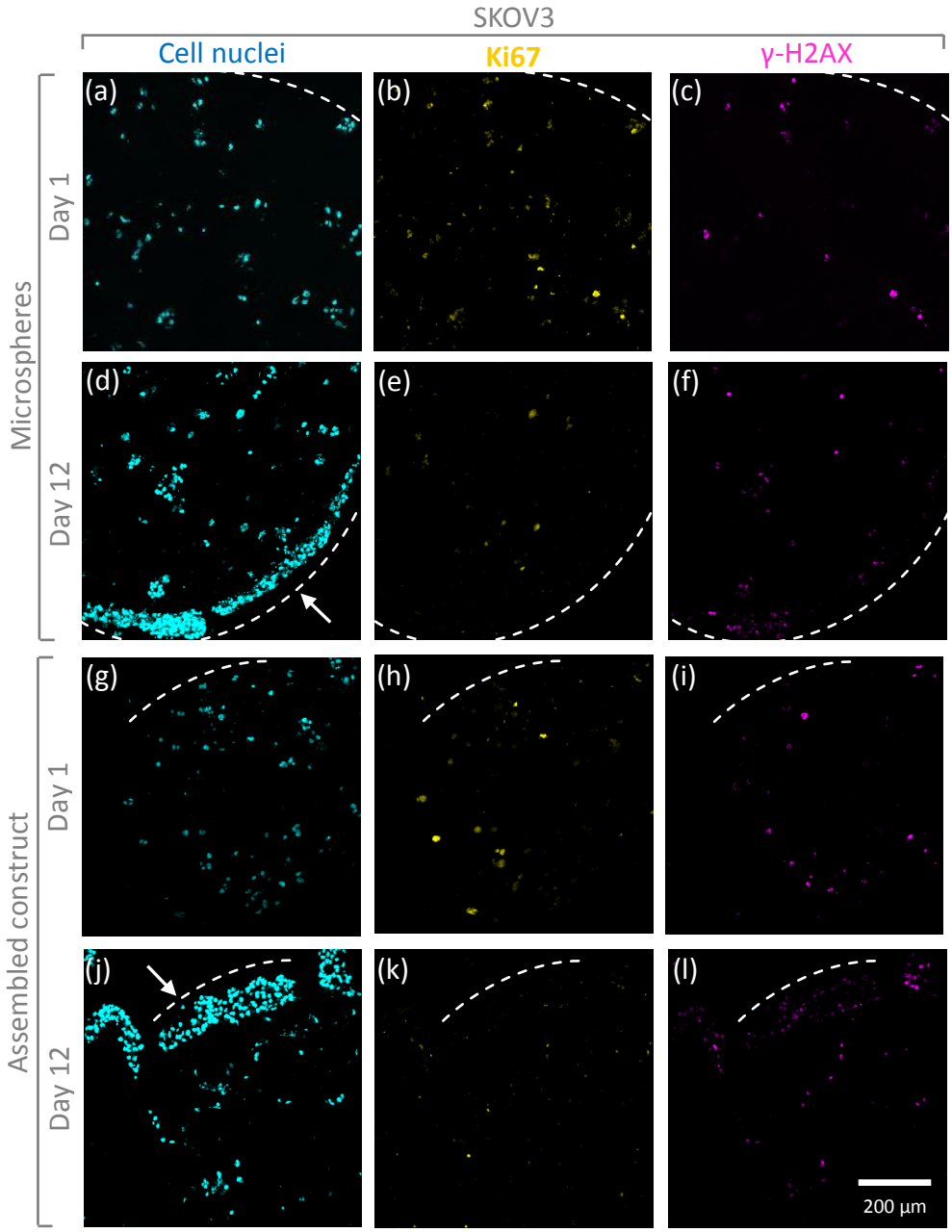

Figure 7.A-vi. Immunofluorescence staining for Ki67 (yellow), γ-H2AX (magenta), and Hoechst 33342 (cell nuclei, blue) imaged using a confocal microscope for SKOV3 microspheres and assembled construct on day 1 and day 12 (no drug control). Arrows point to the monolayer and the dotted line represent the outer edge of the sample. *Scale bar = 200 µm for all images.*

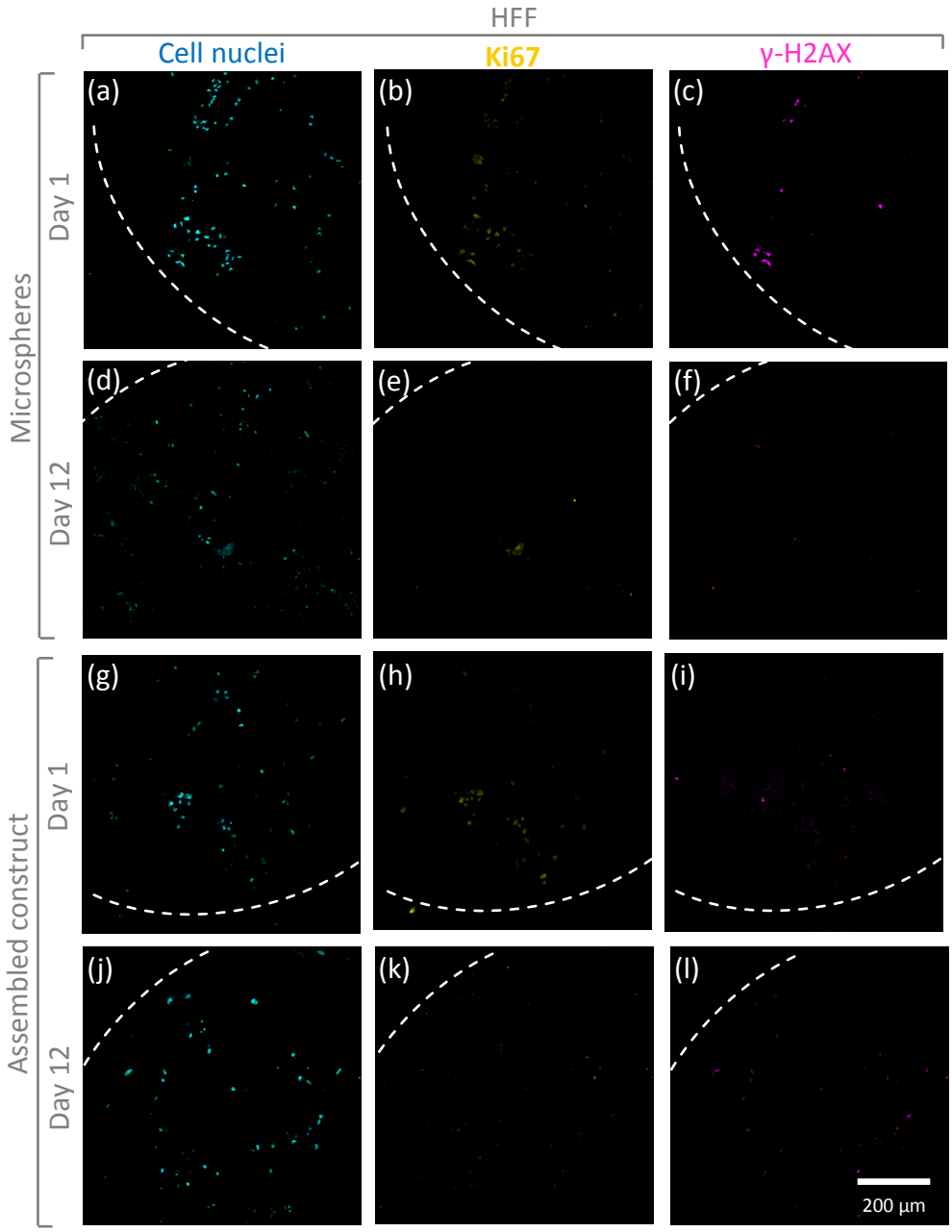

Figure 7.A-vii. Immunofluorescence staining for Ki67 (yellow), γ-H2AX (magenta), and Hoechst 33342 (cell nuclei, blue) imaged using a confocal microscope for HFF microspheres and assembled construct on day 1 and day 12 (no drug control). Arrows point to the monolayer and the dotted line represent the outer edge of the sample. *Scale bar = 200 µm for all images.*

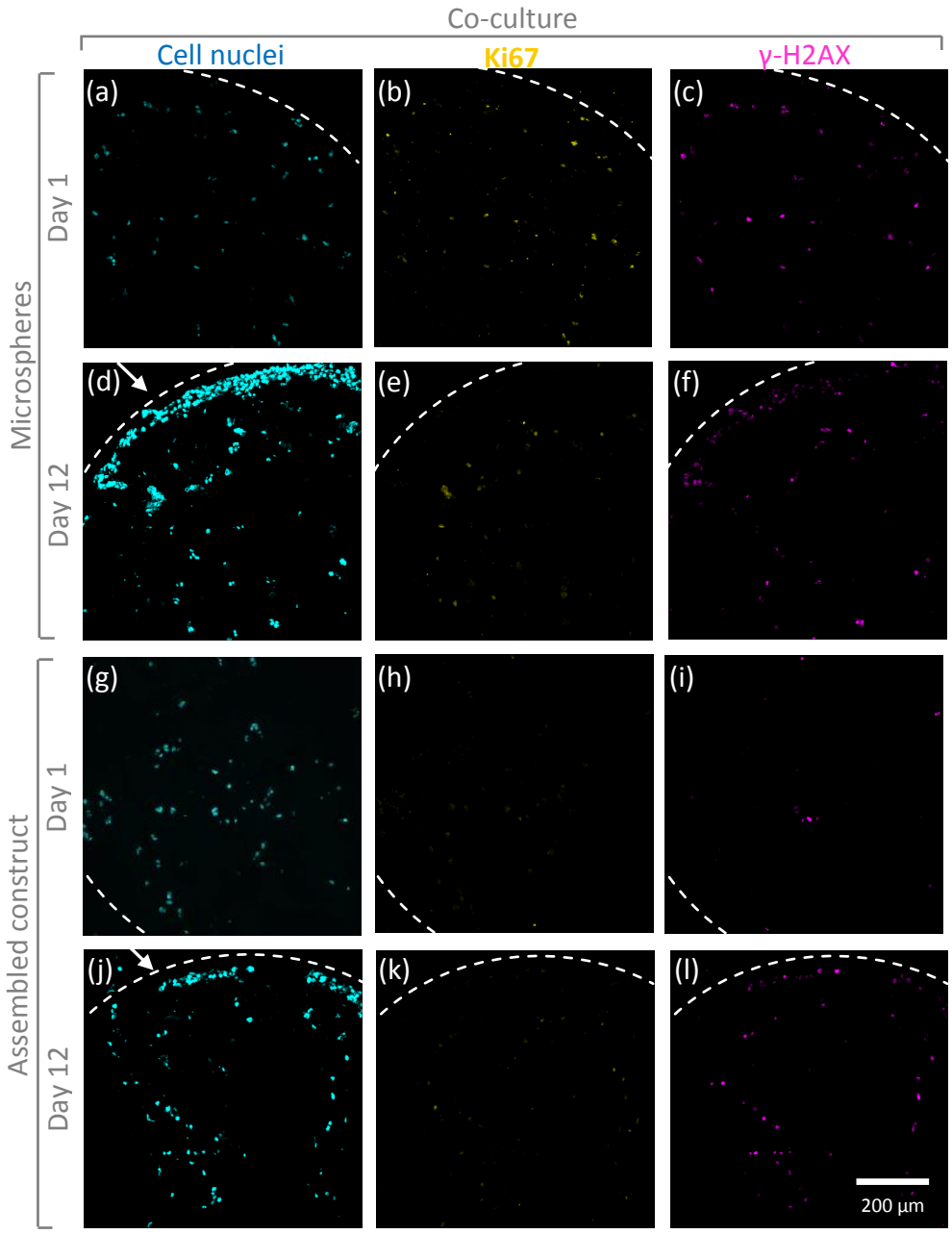

Figure 7.A-viii. Immunofluorescence staining for Ki67 (yellow), γ-H2AX (magenta), and Hoechst 33342 (cell nuclei, blue) imaged using a confocal microscope for co-culture (SKOV3:HFF 75:25) microspheres and assembled construct on day 1 and day 12 (no drug control). Arrows point to the monolayer and the dotted line represent the outer edge of the sample. *Scale bar = 200 µm for all images.*

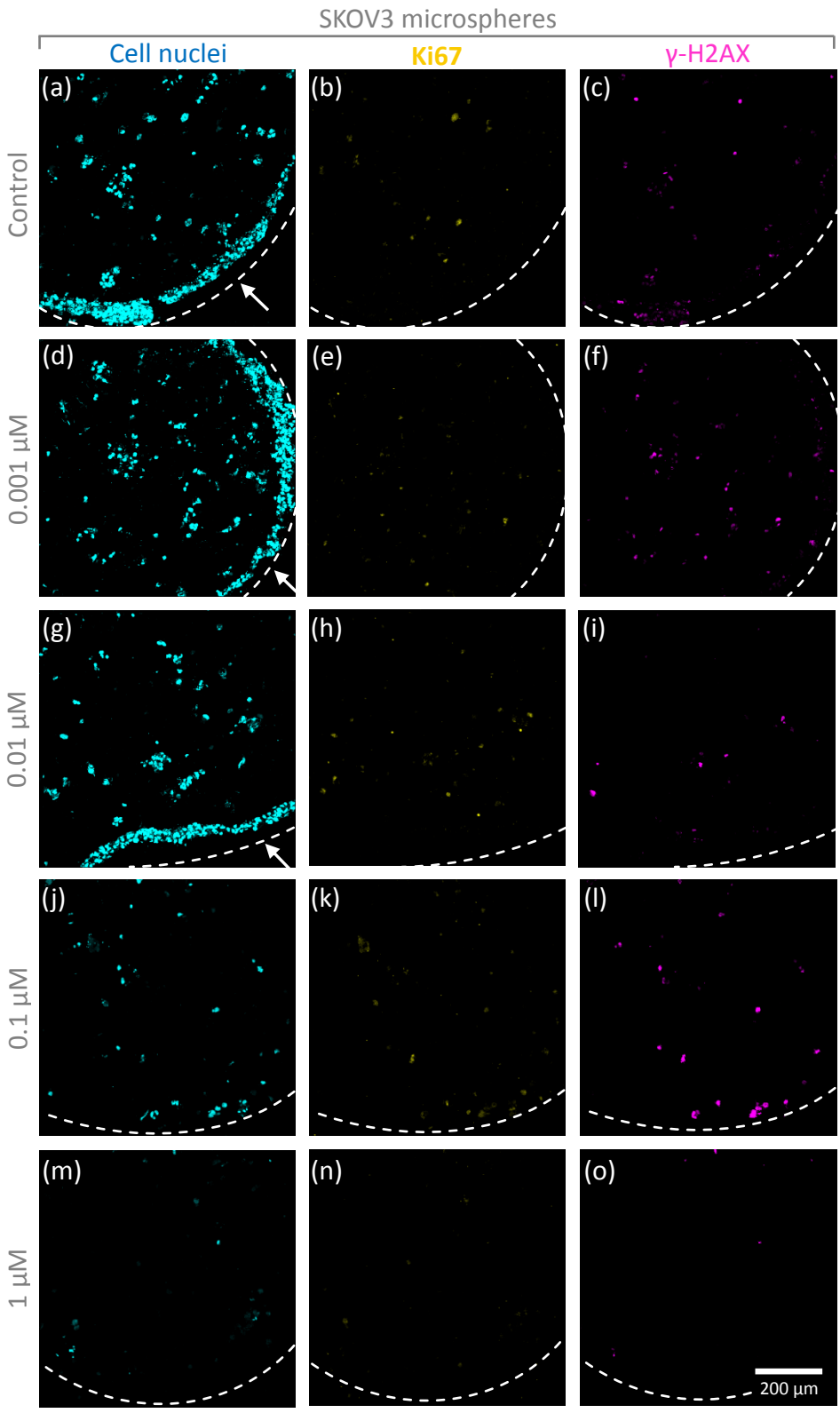

Figure 7.A-ix. Immunofluorescence staining for Ki67 (yellow), γ-H2AX (magenta), and Hoechst 33342 (cell nuclei, blue) imaged using a confocal microscope for SKOV3 microspheres for no drug control, 0.001 µM, 0.01 µM, 0.1 µM and 1 µM concentration of doxorubicin. Arrows point to the monolayer and the dotted line represent the outer edge of the sample. *Scale bar = 200 µm for all images.* See Figure 7.A-xv for higher magnification images.

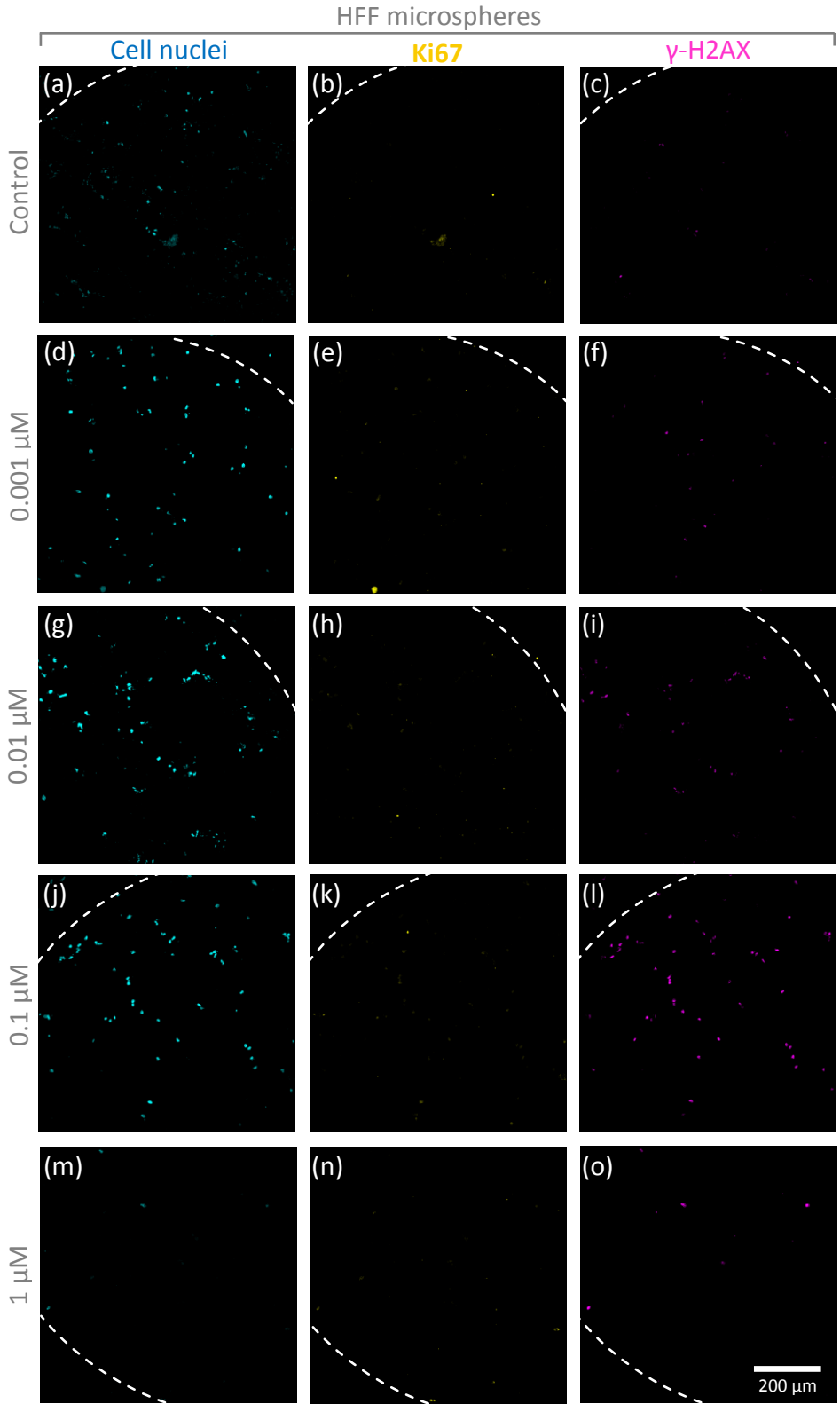

Figure 7.A-x. Immunofluorescence staining for Ki67 (yellow), γ-H2AX (magenta), and Hoechst 33342 (cell nuclei, blue) imaged using a confocal microscope for HFF microspheres for no drug control, 0.001 µM, 0.01 µM, 0.1 µM and 1 µM concentration of doxorubicin. The dotted line represent the outer edge of the sample. *Scale bar = 200 µm for all images.* See for Figure 7.A-xv higher magnification images.

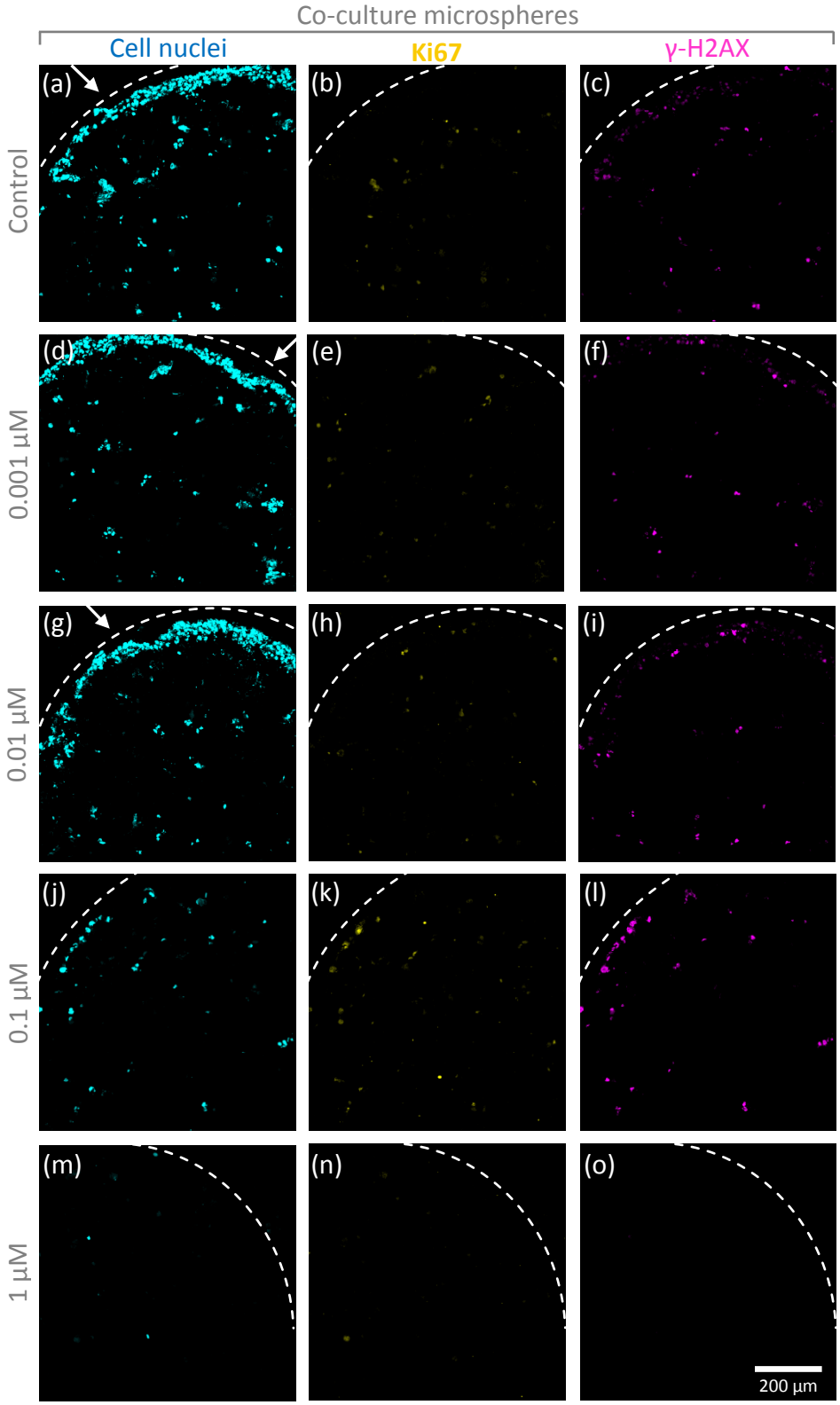

Figure 7.A- xi. Immunofluorescence staining for Ki67 (yellow), γ-H2AX (magenta), and Hoechst 33342 (cell nuclei, blue) imaged using a confocal microscope for co-culture (SKOV3:HFF 75:25) microspheres for no drug control, 0.001 µM, 0.01 µM, 0.1 µM and 1 µM concentration of doxorubicin. Arrows point to the monolayer and the dotted line represent the outer edge of the sample. *Scale bar = 200 µm for all images.* See for Figure 7.A-xv higher magnification images.

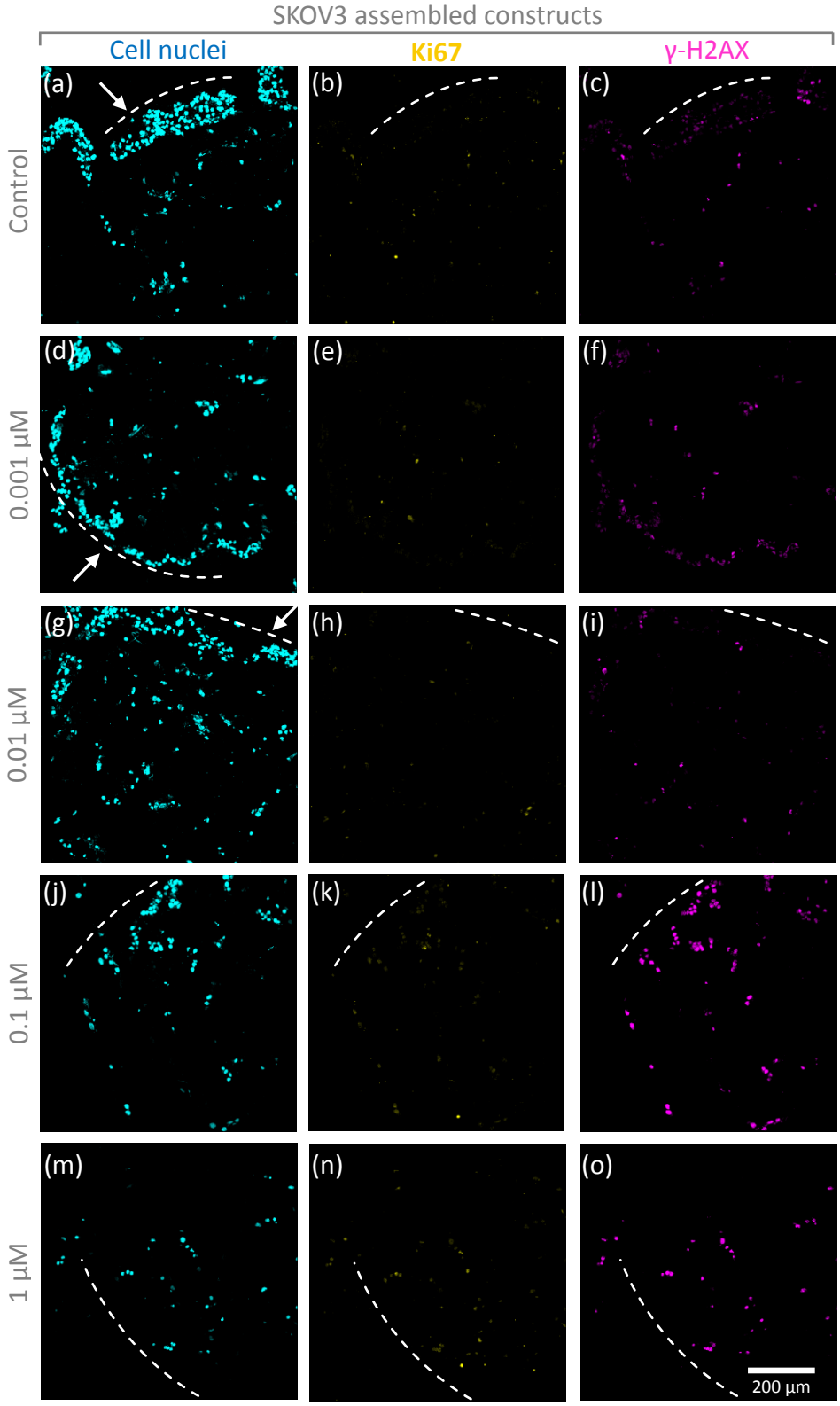

Figure 7.A-xii. Immunofluorescence staining for Ki67 (yellow), γ-H2AX (magenta), and Hoechst 33342 (cell nuclei, blue) imaged using a confocal microscope for SKOV3 assembled construct for no drug control, 0.001 µM, 0.01 µM, 0.1 µM and 1 µM concentration of doxorubicin. Arrows point to the monolayer and the dotted line represent the edge of the sample. *Scale bar = 200 µm for all images.* See for Figure 7.A-xvi higher magnification images.

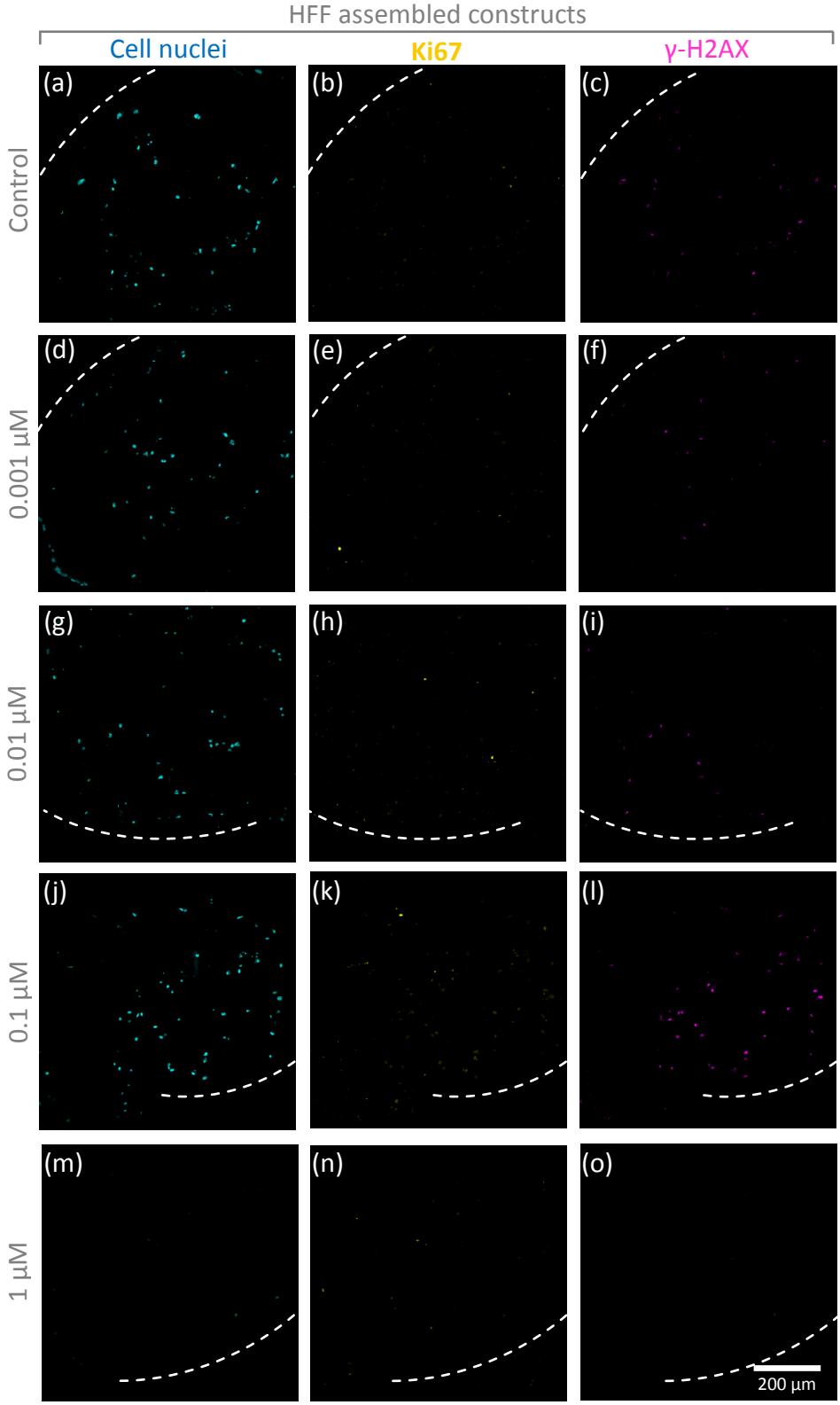

Figure 7.A-xiii. Immunofluorescence staining for Ki67 (yellow), γ-H2AX (magenta), and Hoechst 33342 (cell nuclei, blue) imaged using a confocal microscope for HFF assembled construct for no drug control, 0.001 µM, 0.01 µM, 0.1 µM and 1 µM concentration of doxorubicin. The dotted line represent the edge of the sample. *Scale bar = 200 µm for all images.* See Figure 7.A-xvi for higher magnification images.

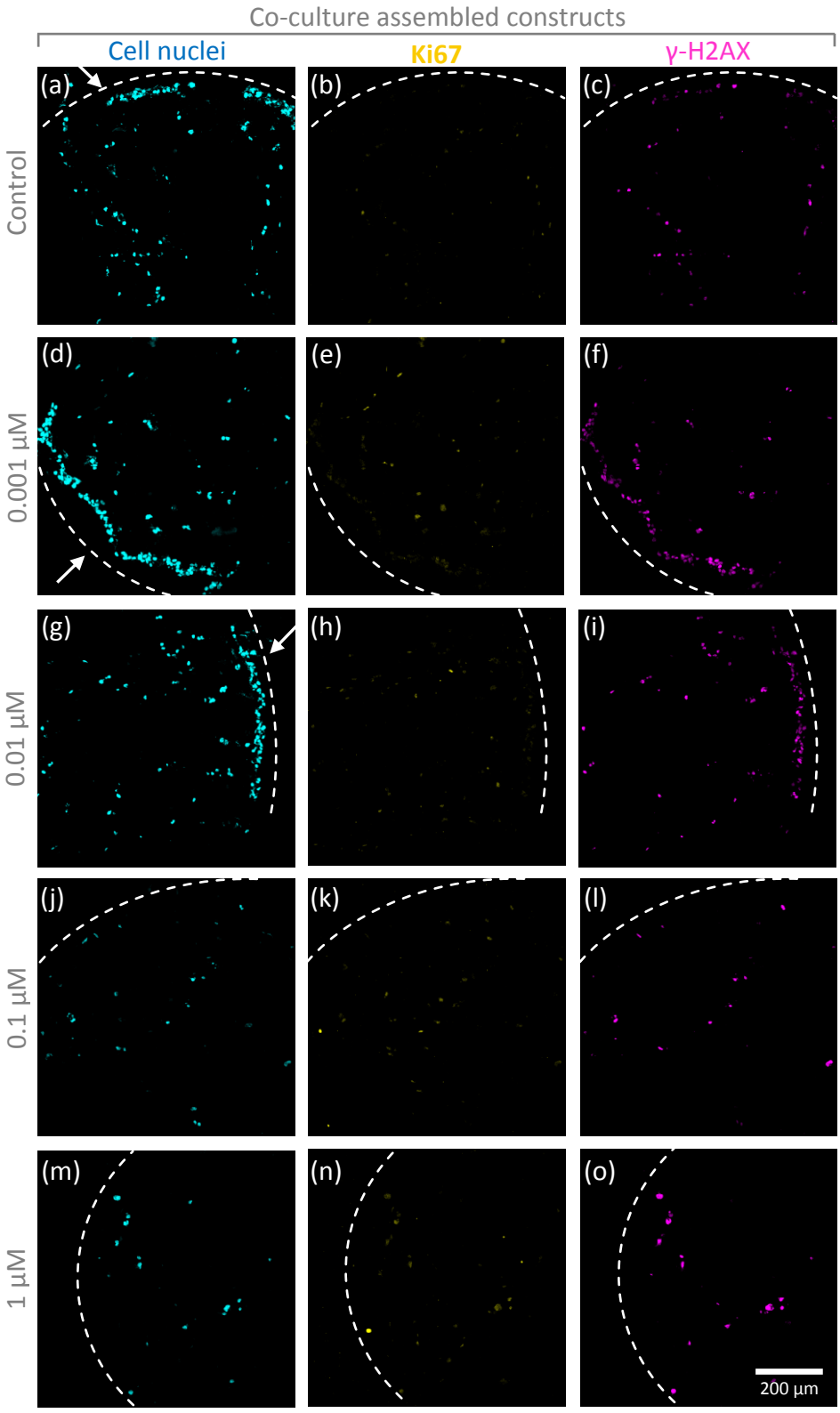

Figure 7.A-xiv. Immunofluorescence staining for Ki67 (yellow), γ-H2AX (magenta), and Hoechst 33342 (cell nuclei, blue) imaged using a confocal microscope for co-culture (SKOV3:HFF 75:25) assembled construct for no drug control, 0.001 µM, 0.01 µM, 0.1 µM and 1 µM concentration of doxorubicin. The dotted line represent the outer edge of the sample. *Scale bar = 200 µm for all images.* See for Figure 7.A-xvi higher magnification images.

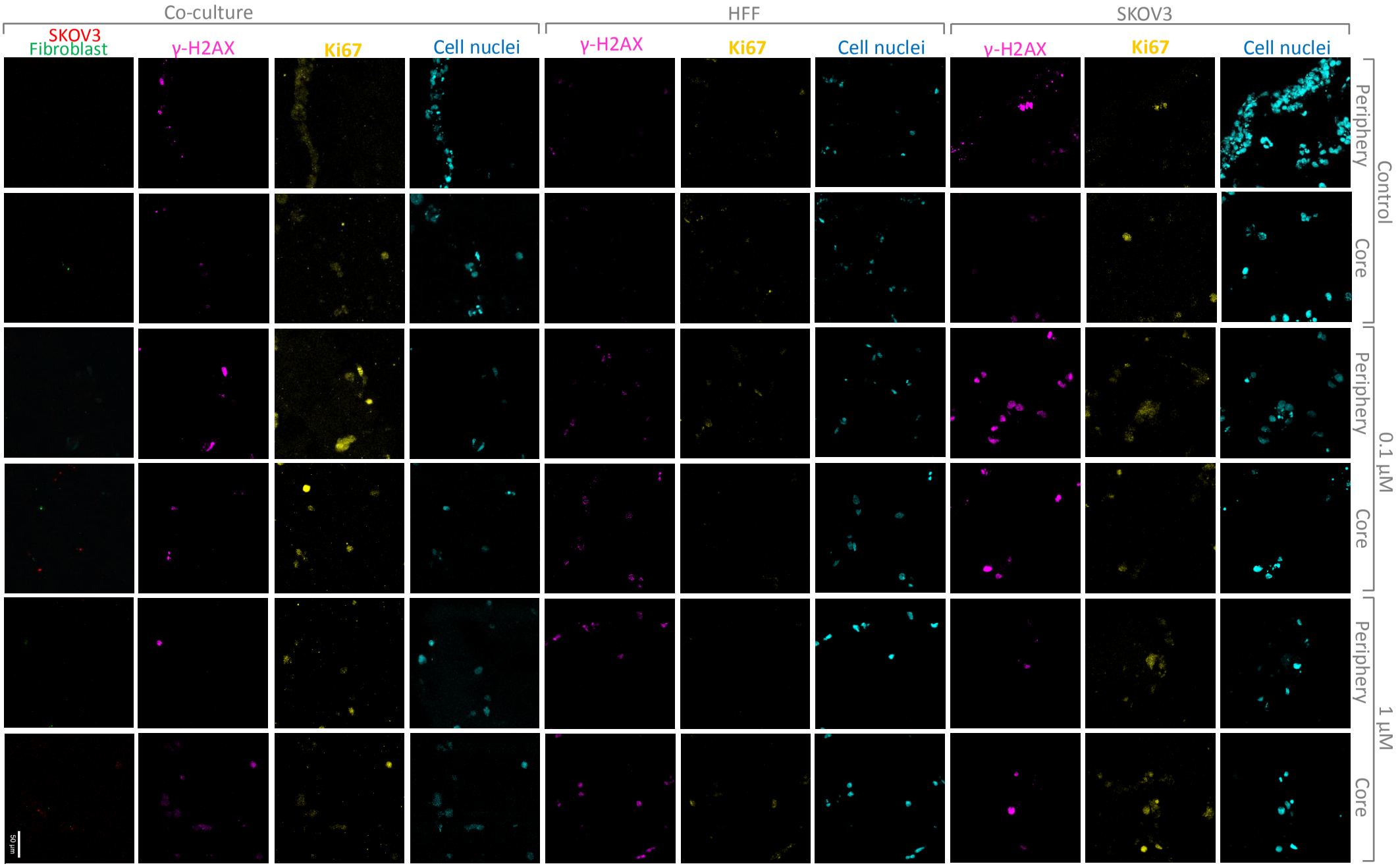

Figure 7.A-xv. Immunofluorescence staining for Ki67 (yellow), γ-H2AX (magenta), Hoechst 33342 (cell nuclei, blue), and SKOV3 (Qtracker 800) and HFF (Qtracker 655) imaged using a confocal microscope for SKOV3, HFF and co-culture (SKOV3:HFF 75:25) microspheres for no drug control, 0.001 µM, 0.01 µM, 0.1 µM and 1 µM concentration of doxorubicin. *Scale bar = 50 µm for all images.*

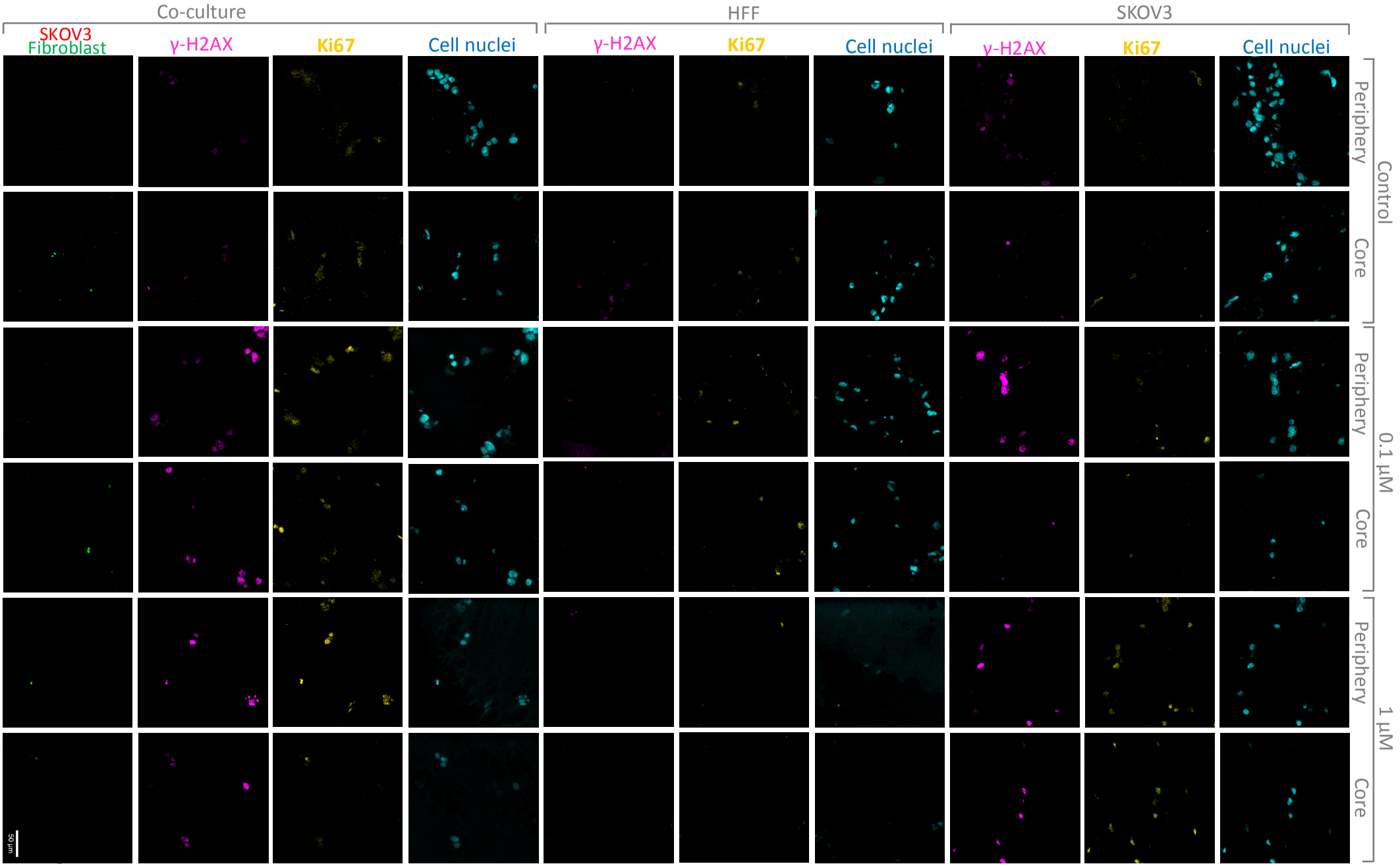

Figure 7.A-xvi. Immunofluorescence staining for Ki67 (yellow), γ-H2AX (magenta), Hoechst 33342 (cell nuclei, blue), and SKOV3 (Qtracker 800) and HFF (Qtracker 655) imaged using a confocal microscope for SKOV3, HFF and co-culture (SKOV3:HFF 75:25) assembled constructs for no drug control, 0.001 µM, 0.01 µM, 0.1 µM and 1 µM concentration of doxorubicin. *Scale bar = 50 µm for all images.*